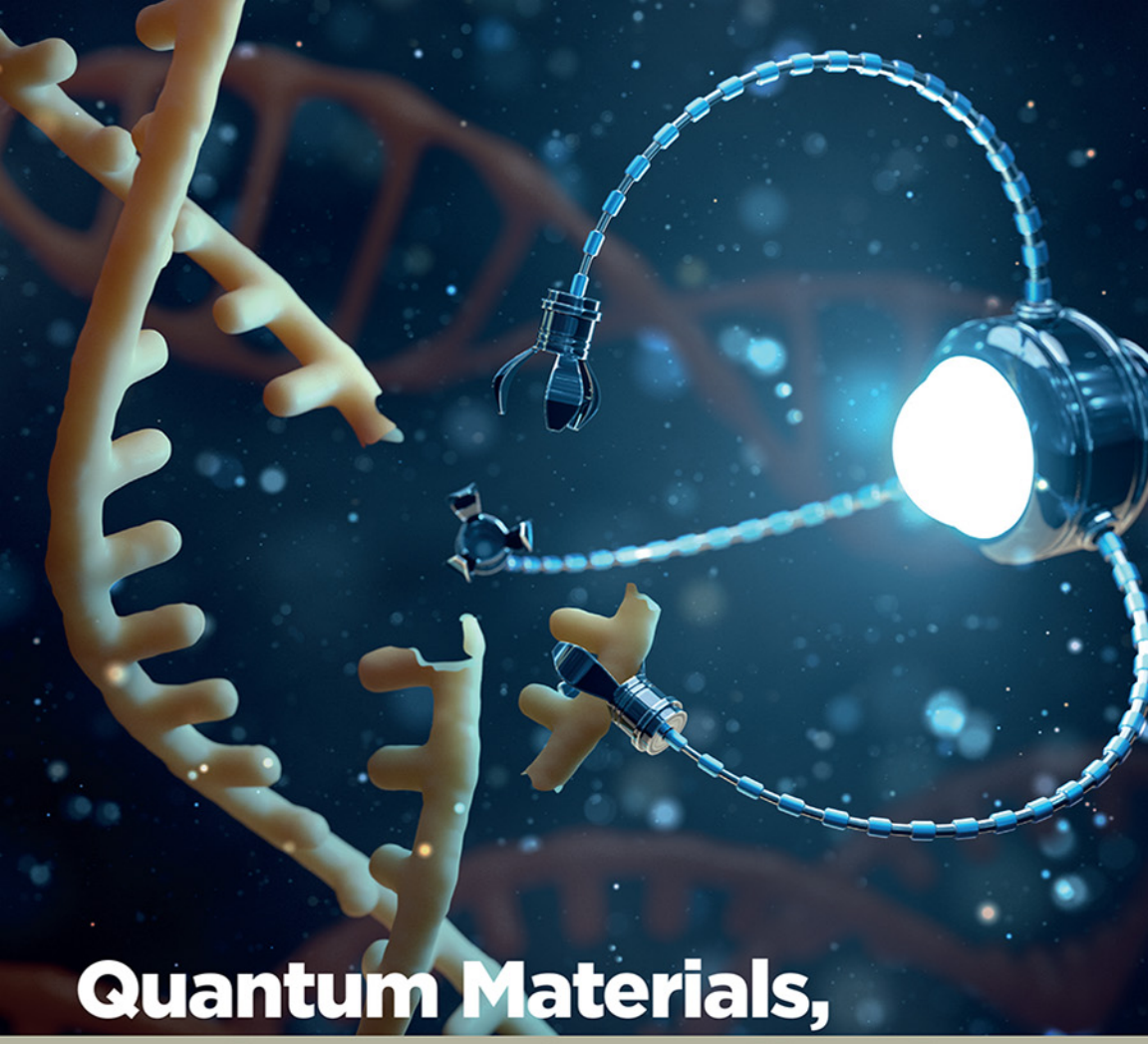

Quantum Materials, Devices, and Applications

Edited by
Mohamed Henini
Marcelo Oliveira Rodrigues

ELSEVIER

Quantum Materials, Devices, and Applications

This page intentionally left blank

Quantum Materials, Devices, and Applications

Edited by

Mohamed Henini

School of Physics and Astronomy, University of Nottingham, Nottingham, Nottinghamshire, United Kingdom

Marcelo Oliveira Rodrigues

Laboratory of Medicinal and Technological Chemistry, University of Brasília, Brasília, DF, Brazil

ELSEVIER

Elsevier
Radarweg 29, PO Box 211, 1000 AE Amsterdam, Netherlands
The Boulevard, Langford Lane, Kidlington, Oxford OX5 1GB, United Kingdom
50 Hampshire Street, 5th Floor, Cambridge, MA 02139, United States

Notices

Knowledge and best practice in this field are constantly changing. As new research and experience broaden our understanding, changes in research methods, professional practices, or medical treatment may become necessary.

Practitioners and researchers must always rely on their own experience and knowledge in evaluating and using any information, methods, compounds, or experiments described herein. In using such information or methods they should be mindful of their own safety and the safety of others, including parties for whom they have a professional responsibility.

To the fullest extent of the law, neither the Publisher nor the authors, contributors, or editors, assume any liability for any injury and/or damage to persons or property as a matter of products liability, negligence or otherwise, or from any use or operation of any methods, products, instructions, or ideas contained in the material herein.

ISBN: 978-0-12-820566-2

Publisher: Matthew Deans
Acquisitions Editor: Kayla Dos Santos
Editorial Project Manager: Tim Eslava
Production Project Manager: Surya Narayanan Jayachandran
Cover Designer: Christian J. Bilbow

Typeset by MPS Limited, Chennai, India

Contents

This page intentionally left blank

List of contributors

Adalberto Benavides-Mendoza Department of Horticulture, Autonomous Agricultural University Antonio Narro, Saltillo, Mexico

Nichollas Serafim Camargo Nanoceuticals Innovation Hub, Aparecida de Goiânia, Goiás, Brazil

Rubén J. Camargo Escuela de Ingeniería Química, Cali, Colombia

Alex Fabiano Cortez Campos Laboratory for Environmental and Applied Nanoscience, University of Brasília, Brasília, DF, Brazil

Camila Magalhães Cardador Department of Genetics and Morphology, Institute of Biological Sciences, University of Brasília, Brasilia, Federal District, Brazil

Marcos Antônio Corrêa Department of Drugs and Medicines, School of Pharmaceutical Sciences, São Paulo State University (UNESP), Araraquara, São Paulo, Brazil

Carime V. da Silva Rodrigues Laboratory of Medicinal and Technological Chemistry, University of Brasília, Chemistry Institute (IQ-UnB), Campus Universitário Darcy Ribeiro, Brasília, Distrito Federal, Brazil

Yajie Dong NanoScience Technology Center, University of Central Florida, Orlando, FL, United States; College of Optics and Photonics, University of Central Florida, Orlando, FL, United States; QLEDCures LLC, Orlando, FL, United States; Department of Materials Science & Engineering, University of Central Florida, Orlando, FL, United States

Sumit Durgapal Department of Pharmaceutical Sciences, Bhimtal Campus, Kumaun University, Nainital, Uttarakhand, India

Alberto Escarpa Department of Analytical Chemistry, Physical Chemistry and Chemical Engineering, University of Alcala, Alcalá de Henares, Madrid, Spain; Chemical Research Institute "Andrés M. del Río", University of Alcala, Alcalá de Henares, Madrid, Spain

Guilherme Alves Ferreira Nanoceuticals Innovation Hub, Aparecida de Goiânia, Goiás, Brazil

Maria Gazouli Laboratory of Biology, School of Medicine, National and Kapodistrian University of Athens, Athens, Greece

José Antonio González-Fuentes Department of Horticulture, Autonomous Agricultural University Antonio Narro, Saltillo, Mexico

Carmine Granata National Research Council, Institute of Applied Science and Intelligent Systems, Pozzuoli (Napoli), Italy; Department of Mathematics and Physics, University of Campania "L. Vanvitelli", Caserta, Italy

Mohamed Henini School of Physics and Astronomy, University of Nottingham, Nottingham, Nottinghamshire, United Kingdom

Antonio Juárez-Maldonado Department of Botany, Autonomous Agricultural University Antonio Narro, Saltillo, Mexico

Beatriz Jurado-Sánchez Department of Analytical Chemistry, Physical Chemistry and Chemical Engineering, University of Alcala, Alcalá de Henares, Madrid, Spain; Chemical Research Institute "Andrés M. del Río", University of Alcala, Alcalá de Henares, Madrid, Spain

Raymond J. Lanzafame QLEDCures LLC, Orlando, FL, United States

Alka Lohani School of Pharmaceutical Sciences, IFTM University, Moradabad, Uttar Pradesh, India

João Paulo Figueiró Longo Department of Genetics and Morphology, Institute of Biological Sciences, University of Brasília, Brasilia, Federal District, Brazil

Gisele A. Medeiros Laboratory of Medicinal and Technological Chemistry, University of Brasília, Chemistry Institute (IQ-UnB), Campus Universitário Darcy Ribeiro, Brasília, Distrito Federal, Brazil

Marek T. Michalewicz Sano Centre for Computational Personalised Medicine, International Research Foundation, Kraków, Poland

Pierfrancesco Morganti Academy of History of Healthcare Art, Rome, Lazio, Italy

Brenno A.D. Neto Laboratory of Medicinal and Technological Chemistry, University of Brasília, Chemistry Institute (IQ-UnB), Campus Universitário Darcy Ribeiro, Brasília, Distrito Federal, Brazil

Marcelo Oliveira Rodrigues Laboratory of Medicinal and Technological Chemistry, University of Brasília, Brasília, DF, Brazil

Eliane Vieira Rosa Federal Institute of Education, Science and Technology Goiano, Campus Ceres, Ceres, GO, Brazil; Green Nanotechnology Group, University of Brasília, Brasília, DF, Brazil

Anthony Sasse RMIT University, Melbourne, VIC, Australia

Paolo Silvestrini Department of Mathematics and Physics, University of Campania "L. Vanvitelli", Caserta, Italy

Marcelo Henrique Sousa Green Nanotechnology Group, University of Brasília, Brasília, DF, Brazil

John Spencer Department of Chemistry, University of Sussex, Brighton, United Kingdom

Gonzalo Rodrigo Tortella-Fuentes Chemical Engineering Department, Universidad de La Frontera, Temuco, Chile

Manuel A. Triana NanoScience Technology Center, University of Central Florida, Orlando, FL, United States; College of Optics and Photonics, University of Central Florida, Orlando, FL, United States

Christos Veros Laboratory of Biology, School of Medicine, National and Kapodistrian University of Athens, Athens, Greece

Antonio Vettoliere National Research Council, Institute of Applied Science and Intelligent Systems, Pozzuoli (Napoli), Italy

Shin-Tson Wu College of Optics and Photonics, University of Central Florida, Orlando, FL, United States

This page intentionally left blank

Quantum dots and bioimaging

1

Christos Veros and Maria Gazouli
Laboratory of Biology, School of Medicine, National and Kapodistrian University of Athens, Athens, Greece

1.1 Introduction

Nanotechnology is an ever-growing subfield of materials science, with a lot of great applications already. It is about the manipulation of matter on the nanometer scale (nanomaterials). Within this rather newly emerged technology, semiconductor nanocrystals with significant potential in biomedicine, known as quantum dots (QDs), have been created. QDs consist of groups II−VI and III−V elements and exhibit unique optical, physicochemical, and electronic properties due to their size and tightly packed structure. In specific, QDs can be fluorescent under light sources of specific wavelengths and, together with their advantages compared to organic dyes, offer a great new technique for bioimaging [1].

The word "quantum" stands for the minimum and discrete unit of a physical property. This means that QDs are tiny particles, sized from 1 to 10 nm, and each one has unique characteristics according to their compound. They all have a "core−shell" conformation that offers them better optical features and less toxicity. Both core and shell of a QD consist of compounds with semiconductor characteristics, with core being more reactive and shell providing the QD structure with stability and other features that make it useful for applications. QDs that belong to the III−V groups show less cytotoxicity and greater stability, because of their covalent bonds compared to the ionic bonds of II−VI elements. As is described later, QDs have some incomparable advantages, such as bright and clear luminescence with high extinction coefficient (absorption of light) and narrow emission spectrum, together with the possibility to image and target different types of cells at the same time. It is noteworthy that the energy of light absorption is directly associated with the configuration of electrons of the material; thus how is photoluminescence achieved in QDs [1−3]?

Electrons are considered to move at specific radii and energy levels around the nucleus. Energy is transmitted to semiconductor electrons in the form of photons and forces them to reach temporarily a higher energy state (excitation) when transmitted energy exceeds the energy difference between excited and initial (ground) states. The created energy difference is called bandgap. Subsequently, excited electrons move back to the initial radius to secure higher stability. The relaxation of energy can emit radiation (photons). The energy of the photons determines the color

Quantum Materials, Devices, and Applications. DOI: https://doi.org/10.1016/B978-0-12-820566-2.00007-7

of light that is emitted and depends on the bandgap. The larger the bandgap is, the more energy is demanded for electron excitation and the more the photon energy is. As energy increases, the color of the light differentiates from red to violet [1–3].

Interestingly, the size and the shape of semiconductor crystals can be altered to achieve different conductive properties. In specific, a smaller size of a QD is equivalent to a larger bandgap. As a result, more energy is released after light exposure when crystal returns to ground state. This is called quantum confinement: manipulating the size of QDs changes the color of the light they emit after excitation. By decreasing the size of QDs the emitted light color shifts from red to violet. Within these realms, QDs have narrow emission peaks, depending on the given energy and the size and composition of the core. Emission spectra do not rely on the excitation energy, as long as it surpasses the bandgap energy. The importance of quantum confinement lies in the fact that by using QDs of various shapes and sizes, we get a distinct light emission from each QD under the same light exposure. This offers the opportunity to image multiple targets simultaneously, making QDs highly advantageous for bioimaging [1,4,5].

It becomes evident that core characteristics are critical for the properties observed in QDs. However, shells are necessary in QD configuration, especially for biological applications. The reason is that the core shows high reactivity—and toxicity—and its crystalline form results in blinking (intermittent luminescence despite continuous light exposure). QDs are created by a method of epitaxy in organic or, preferably, aqueous colloidal solutions. The most commonly used QDs contain cadmium in their core (CdSe, CdTe), while shell often consists of CdS or ZnS, which are characterized by high quantum yield (QY). Hence, their surface is usually covered with hydrophobic ligands, which makes them insoluble in water. Various strategies are used to overcome this and increase their functionality in aqueous media, such as replacing initial ligands with hydrophilic ones, capping with silica shells, or combining the initial hydrophobic cap with amphiphilic ligands [3,6,7].

QDs find applications in a broad spectrum of technological fields, from nonbiological (quantum transistors, detectors, data analysis techniques, and QD LEDs) to biological, such as bioimaging, biolabeling, drug delivery, biosensing, and theranostics (which stands for simultaneous therapy and diagnostics in cancer). Their significant technological use in biomedicine is based on their ability to be easily conjugated with small molecules or substances—for example, peptides, oligonucleotides, or antibodies—that attach to targets (cells or tissues) and detect them easily and efficiently. QDs offer a large outer surface to which biomolecules can be attached and shape their functionalization, depending on the target tissue or cell. Numerous research articles have proposed a wide variety of QD conjugates that can be used with high specificity, such as antibodies for antigens of cancer cells or ligands to receptors [1,3,6].

Even though QDs have already been used in optics and electronics, their use in biomedicine is still limited in animal research. Despite their evident benefits in bioimaging and other biological applications, most QDs have been associated with high degree of cytotoxicity, given that most QD cores include cadmium. Cadmium is widely accused of the cytotoxic effects that are met in the use of QDs in cells.

Their pharmacological and toxic features depend on the environmental conditions together with the core and shell composition and their physicochemical properties. Recent studies have explored and proposed new materials that show lower degree or no signs of toxicity; in fact, such QDs that are made of silicon or carbon/graphene or those that do not contain cadmium (Cd-free) look very promising in biomedical technology. Research regarding the toxicity of QDs is ever-increasing to circumvent their drawbacks and take advantage of their unique properties and great translational potentials in the future [1,6,8−11].

1.2 Applications of quantum dots in bioimaging

QDs exhibit beneficial physicochemical properties compared to conventional organic dyes that have been widely used until today (Table 1.1). First, QDs show greater resistance to degradation, allowing them to be detected for longer time periods. Second, their inorganic nature and light intensity provide them with better photostability. Third, QDs have broad excitation and narrow emission spectra, contrary to the narrow excitation and broad emission spectra of organic agents. In addition, QDs have a greater difference between the absorption and the emission peak (Stokes shift). Their fluorescent capacity lasts longer, has a higher signal-to-noise ratio, and gives 10−20 brighter results than organic fluorophores. QDs are also tunable in size and can be easily attached to biomaterials. Last, organic dyes are more susceptible to environmental conditions [1].

In addition, QDs have unique optical, electronic, and luminescence features, owing to their efficiency as FRET (fluorescence resonance energy transfer) donors. This means that QDs show wide light absorption spectra, narrow light emission spectra, lower photobleaching, and high QY—which stands for the frequency of the occurrence of an event per photon absorbed by the medium. Together with quantum confinement, these features allow a tracking of multiple targets at the same time [1,2,6].

Table 1.1 Quantum dot properties, compared to organic dyes.

Properties of quantum dots
Resistance to degradation
Better photostability
Broad excitation spectrum and narrow emission spectrum
Larger Stokes shift
Higher S/N
Higher brightness
Size-tunable (quantum confinement)
High QY

QY, Quantum yield.

In light of these, QDs have great potentials in bioimaging. Literature regarding their use for in vitro and in vivo bioimaging has expanded over the past two decades. In vitro techniques in research are crucial, because the behavior of molecules or substances can be tested under secure and highly controlled conditions. Thus they act as a stepping-stone before a new technology can be safely applied to living organisms.

In vitro studies have used QDs for biomolecular tracking, cellular imaging, drug delivery, and gene technology. They have offered a great deal of useful information about QDs regarding their functionality, credibility, but also their cytotoxicity. In addition, QDs have already managed to illuminate cellular pathways and give hope for potential use in cancer imaging and treatment [6,8].

In regard to in vivo research, QDs have been applied to living organisms, especially rodents. Newer modifications on structure and conjugation of QDs with other molecules have made their use feasible with lower cytotoxicity and high specificity. Examples in literature include the use of QDs for tracking their biodistribution, labeling cells, lymph node/vasculature/tumor imaging, even for whole-body imaging. An emergence of new QD-complexes enlarges their utility in various fields. Nevertheless, their application in human medicine and imaging is not feasible yet; toxicity issues have to diminish to a greater extent before QDs could be used in humans without concerns [6,8].

QDs can be an important tool in multimodal imaging as well. Multimodal imaging refers to the simultaneous use of different imaging modalities, to make a good use of their advantages while at the same time overcome their disadvantages. Both in vitro and in vivo experiments show good prospects after combining QD with magnetic resonance imaging (MRI), positron−emission tomography (PET), and computed tomography (CT). Resulting images are of better temporal and/or spatial resolution and accuracy [8].

1.3 Quantum dots and in vitro bioimaging

As mentioned in the previous section, QDs have been widely used in vitro bioimaging to enhance cellular imaging, delivery of drugs, and gene technology among others (Fig. 1.1). More specifically, examples include the illustration of cells moving to other body regions to create metastases or the revelation of the fate of a stem cell after its differentiation. QDs can also provide important information about the endocytosis mechanism and their distribution in their targets intracellularly. Furthermore, QDs offer the possibility of multiple targeting, an extremely useful feature in bioimaging [8].

1.3.1 Cell imaging

To detect biomolecules inside the cell, QD complex needs to enter the cell. The most common way is through the process of endocytosis. Endocytosis involves

Figure 1.1 In vitro applications of quantum dots.

intracellular access of a substance, while the latter is surrounded by a part of cell membrane.

QDs can penetrate the cell via passive or active transportation. Passive transportation of QDs inside the cell occurs via electrostatic reaction with the cell membrane. When QDs are not conjugated with biomolecules and do not have a specific target, their absorption from the cell and their intracellular aggregation is defined by their physical properties and capping of their shell, together with environmental conditions—such as temperature and type of the cell and the medium of incubation. For these reasons, positively charged QDs, often capped with carboxylic groups, of a small size at 37°C favor the endocytic pathway. In fact, positive charge in appropriately capped and small-sized QDs can promote a penetration of the nucleus. Yet, cell penetration is not secured under these circumstances, and QDs may need to be encapsulated with carbohydrates, vesicles, or nanogels. On the contrary, the active internalization of QDs requires interactions between ligands and cell membrane receptors. Transferrin and antibodies have been used as ligands in the past; however, cell-penetrating peptides have appeared to be more useful for triggering their uptake from the cell. These peptides are used to contain the HIV translational activator Tat protein, which has been replaced by newer peptides that are characterized by strong positive charge in their N-terminal and, consequently, enhance endocytosis [8].

Major issue in the process of endocytosis is that QD-complexes may stay encapsulated in lysosomes or endosomes and cannot be released in the cytoplasm to reach their targets. To deal with this possible scenario, various methods have been proposed, including applying osmotic pressure, using biodegradable polymeric nanospheres (which are pH-dependent and can be particularly useful in solid tumors that are characterized by acidic microenvironment), and photoinduced rupture of endosomal membrane. In addition, QDs can be conjugated with peptides that are rich in histidine or arginine or with cholera toxin B, which offer a direct internalization of the complex into the cell.

Apart from active and passive internalization of QDs, direct administration into the cell (via electroporation and microinjection) has been proposed too. These

methods risk to induce cell death or nonspecific accumulation of QDs in the intracellular fluid. Nanoneedles and newer technologies have been explored to overcome these issues with more viable results. Last, biomolecular tracking does not always involve a penetration of QDs into the cell, for example, when the research aims to detect receptors on the surface of plasma membrane [8].

When QDs are released in the cytoplasm, they can easily detect and track their target. Depending on their conjugates, QD-complexes have been used as sensors of specific molecules or ions (oxygen, calcium, and chloride), temperature, or pH conditions. They have also been reported to track cell differentiation and metabolic pathways, and, importantly, to detect cancer cells. Studies that used QDs in early-stage undifferentiated cells (stem cells) did not badly impact viability, proliferation, or fate of these cells. It is noteworthy that in all experiments, QDs showed high specificity in marking their targets. Time of retention inside the cell should be taken into account though, when QDs remain intracellularly, are beneficial for imaging reasons but can raise toxicity issues [9].

1.3.2 Molecular targeting

Nanoparticles such as QDs have been used to detect and track specific molecules. This is feasible due to the conjugation of QDs with antibodies and other ligands of high specificity for desired targets. Experiments on living cells attempt to trace molecular motility, and accumulation inside the cell or on the surface of cell membrane. Furthermore, other studies focused on perinuclear and intranuclear accumulation of QDs, which was realized through electroporation. QDs can optimize fluorescent in situ hybridization (FISH) techniques and reveal possible alterations in human chromosomes, provided they can access the interion of the cell through receptors on the cell membrane. Discovery of more techniques to ameliorate transportation and halftime of QDs decrease cytotoxicity and contribute to the emergence of new functionalities is necessary, so that they reveal physiological and pathophysiological pathways in the cells. For example, the use of multiple QDs emitted luminescence for enough time to track the movement of kinesins in live cells [1,6,8].

1.3.3 Drug delivery

Structural features of QDs make them advantageous in the regulation of drug delivery to specific cell or tissue targets. QDs, especially when capped with polyethylene glycol (PEG), are characterized by long retention in blood circulation, while their large surface offers space for binding both with drugs and ligands for detecting the desired cell or substance. At the same time, according to their capping and functionalization, QDs may indicate high EPR (enhanced permeability and retention) effect that allows them to detect and remain longer bound to their target. High specificity of target detection has increased QD use in drug transportation. Normal drug delivery often leads its temporally and spatially uncontrolled distribution. Most of the side effects observed after drug administration can be attributed to the uptake of

the substance by cells other than the targeted ones. Hence, QDs may be able to decrease side effects of drugs and, respectively, increase their efficacy [8].

Drug delivery with QDs has been reported in inflammation, pulmonary diseases, and, most importantly, in cancer research. Anticancer medication has been accused for the development of usual and hazardous side effects, mostly due to triggering cell apoptotic mechanisms. QDs are often conjugated with PEG (to increase circulation time) and are encapsulated in liposomes or micelles. Thanks to other functionalities, they are able to detect proteins that are expressed in tumor cells or antigens on their surface. However, their release from these liposomes to cytoplasm may be limited; consequently, biodegradable micelles have been introduced. Furthermore, QDs inside HPC-PAA (hydroxypropylcellulose-polyacrylic acid) nanogels, which are sensitive to temperature and pH changes, offer simultaneous tumor cell imaging (because of their acidic microenvironment) and regulated drug delivery [8].

It has been common in drug development to face various levels of efficiency of the same substance in different people with the same disease. This variance has been mainly attributed to polymorphisms in their genetic code, known as single-nucleotide polymorphisms (SNPs). SNPs may affect the expression of proteins that are crucial for susceptibility in a specific drug, including those that participate in the metabolism or transportation of the drug. In light of these, QDs conjugated with oligonucleotides can detect such polymorphisms, contribute in assessing drug efficiency and linking specific SNPs to phenotypes of the disease [6].

It is evident that controlled drug delivery with the use of QDs is crucial not only for imaging, but also for therapy of tumors. This has led to the emergence of a new field, known as theranostics. Theranostics are described further in Section 1.5. Apart from theranostics, QDs can be used for structural and pharmacological analysis and screening of drugs. QDs can be attached to drugs, of which the content and pharmacological characteristics (biodistribution, metabolism, and excretion) are not known and reveal useful information about them [6].

1.3.4 Gene technology

Gene technology refers to delivery of oligonucleotides of DNA or RNA up to whole genes into cells to regulate gene expression. Viral vectors and liposomes have been used for gene delivery until today. Nevertheless, these carriers exhibited limited efficiency together with a high risk of oncogenesis. To this end, QDs conjugated with DNA or RNA sequences have been proposed as an alternative in the field [8].

Gene silencing, by the process of RNAi (RNA interference), has been applied widely in research. In this technique, small-interfering RNA (si-RNA) is delivered to the cell to knock down a particular protein. si-RNA transduction to the nucleus is not feasible because of the negative charge of both si-RNA and nucleic DNA. To overcome this, viral and nonviral transporters have been in use. However, the first ones increased the possibility of inducing inflammation, while the latter (such as liposomes) were characterized by low efficiency. As a result, complexes of polymer-capped QDs are used more and more nowadays. In addition, since successful knockdown may last long, QDs may be more useful compared to organic dyes

and fluorescent proteins, as they luminesce for longer periods of time. RNAi combined with QDs could be a part of cancer treatment, as it can inhibit the expression of oncogenes.

Suicide gene therapy is another field of gene technology where QDs could be helpful. This procedure requires the transfection of cancer cells with a gene that can activate the expression of an enzyme. The role of the enzyme often involves the activation of a particular drug. In other words, drug could be active only in target cells and induce their apoptosis/necrosis. QDs can deliver the gene selectively to tumor cells by identifying their antigens or other molecules and microenvironmental conditions. After their administration, QDs were easy to track and ensure the time that they transfected the cell, so that the drug could be given [8].

1.3.5 Multimodal imaging

Multimodal imaging refers to the combination of different imaging techniques at the same time and conditions. To achieve that, a single QD with various simultaneous functional roles should be created.

Simultaneous MRI and fluorescent imaging has been attempted and would be highly beneficial in bioimaging. A combination of these techniques could circumvent the low temporal resolution of MRI and ameliorate its spatial resolution. To this end, QDs conjugated with gadolinium (Gd)-complexes have been produced. Gd has been used as a contrast agent in MRI both in research and clinical practices. In addition, magnetic and paramagnetic materials can be used as coating to QDs to make their handling easy through magnetic fields. Since these materials can impact the photophysical features of QDs, new nanoparticles need to be generated. Consequently, silicon coating of such nanomaterials has been useful due to the observation that these new QD-complexes maintained the original characteristics of all compounds and offered sufficient biocompatibility and potentials for further functionalization. Such silicon-capped QDs were used in imaging of apoptotic cells after myocardial infarction [8].

1.4 Quantum dots and in vivo bioimaging

Recently, QDs have intruded in in vivo bioimaging (Fig. 1.2). Because of their aforementioned physicochemical properties, their use has expanded over the years. Nevertheless, it is still limited to animal research because of the low level of light depth and the consequent inability to image deep tissues, as well as their potential cytotoxicity and unspecified compatibility for living organisms. This is not the case for QDs only; the same limitations stand for organic dyes too. As a result, QDs have been used for labeling cells, imaging of the whole body, the vascular system or tumor tissues, theranostics, and multimodal imaging, among others [8].

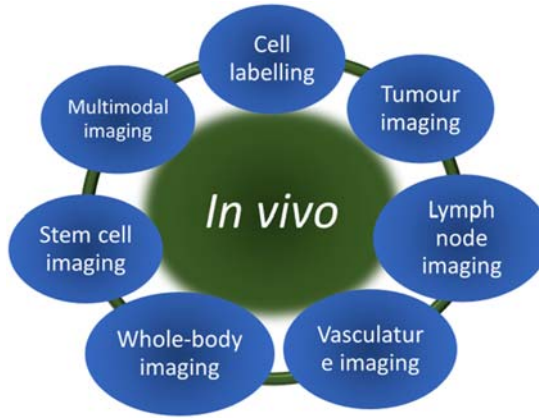

Figure 1.2 In vivo applications of quantum dots.

Techniques that have been in use for human bioimaging are characterized by specific properties:

1. spatial and temporal resolution,
2. ionizing or nonionizing excitation energy,
3. ability of deep-tissue imaging,
4. biocompatibility,
5. defined detection threshold.

We have already discussed about the advantageous features of QDs, together with the possibility to define them with various functionalities and detect multiple targets with one-light source. Fluorescent imaging with the use of QDs offers high temporal and, in particular, spatial resolution. Its excitation energy is nonradiative and less harmful than ionizing technologies, such as CT. Deep-tissue penetration can be achieved by creating QDs of which the structure allows emission at near-infrared (NIR) wavelengths, from 650 to 900 nm. Two-photon imaging is mainly used in imaging in vivo as it enables excitation at these wavelengths. An NIR window is preferred because the extinction coefficients of water and hemoglobin are rather low as well as are autofluorescence of the tissue. Last, fluorescent imaging is noninvasive and safe for skin exposure [8].

One method to enable the excitation of QD electrons in deeper tissues is bioluminescence resonance energy transfer (BRET) that is an alternative method to FRET. Excitation at visible light range can be problematic due to scattering and high absorption from the skin and other tissues. In BRET, energy is transferred from self-exciting proteins to adjacent similar proteins. Protein luciferase (luc) has been used as a BRET donor when conjugated with QDs. When oxidized, it releases nonionizing energy to QDs. In particular, it was found that when QDs emit light in the NIR window, scattering is decreased and allows multiple-target imaging. Interestingly, QD-luc complex can be excited directly via FRET as well, although, in this case, the complex showed a level of instability. BRET imaging can be useful in whole-body imaging as well, although it has limitations. QD BRET-based probes have been used in the detection of DNA and illumination of interactions between cellular proteins [5,8].

Synthesis of QDs plays a crucial role in their activity and utility. To be able to detect their targets efficiently, QDs need to be properly capped with specific functionalities, including binding to ligands, enabling electrostatic interactions, or being encapsulated in liposomes or micelles. This coating might be necessary because conditions of the microenvironment (pH, oxidation) may disturb specific binding to targets. It is already mentioned that PEGylated QDs appear to have longer half-life and, resultingly, blood circulation and more efficient aggregation in target tissue. Recent findings indicate the importance of PEG coating, due to the fact that QDs encapsulated in PEG-micelles achieved fast accumulation and required only half of the usual concentration. Another example of the significance of QD composition is the use of CdTeSe-CdS core−shell configuration, which facilitates NIR imaging and, resultingly, deeper tissue penetration. This configuration showed a low level of toxicity in rodents, and its nonspecific accumulation in reticuloendothelial system (RES) decreased relatively soon [7,8].

Biocompatibility needs to be optimized in order for QDs to be used in human bioimaging and medicine. To this end, biodistribution, cytotoxicity, half-life time, and the specificity of target detection are the factor that should be improved.

1.4.1 Cell labeling

As was reported in the previous paragraphs, QDs have been used in vitro for marking cells with specific components. Recent studies have used QD-complexes in vivo to tag the cellulose in plant cells, ganglion cells in birds, even *Escherichia coli* bacteria. to label whole cells, multifunctional QDs that can attach to specific biomolecules intra- or extracellularly are necessary. Such biomolecules can be proteins, oligonucleotides, and ions inside the cells, or receptors located on plasma membrane. In this way, we can identify the type of a group of cells and distinguish normal from cancer cells. More specific applications of cell tagging are described next [1].

1.4.2 Tumor imaging

One of the main aims of cell labeling is to enable cancer cells tagging, for imaging, and therapeutic reasons. QDs, functionalized with fluorophores and ligands that are specific to the target, have been a research topic in tumor imaging. This can provide information about antigens of cancer cells, their motility, and generation of metastases. QDs can be administered subcutaneously and be attached to antibodies that are specific to tumor cells. This specific labeling can facilitate a surgical removal of the tumor or delivery of anticancer drugs [6,8].

QDs that are PEG-capped and conjugated with peptides or antibodies can circumvent and reduce their nonspecific uptake from RES and specifically detect their target. Indeed, antibodies against alpha-fetoprotein have been used for hepatocellular carcinoma or, against prostate-specific membrane antigen for prostate cancer, have been described. In some cases, QDs were also conjugated to anticancer medication molecules, including doxorubicin, paclitaxel, or pseudopolyrotaxanes. In this

way, specific drug delivery is possible and side effects are reduced. For instance, QDs conjugated with bevacizumab selectively attached to vascular endothelial growth factor expressing cancer cells and delivered the drug efficiently both in vivo and in vitro. These experiments that involved drug delivery were crucial compared to corresponding experiments in vitro, since they allow researchers to examine their effect in living organisms [8,12].

Imaging of cancer cell motility in blood circulation and lymph flow are better described in the following paragraphs. Drug delivery and other techniques, where QDs act as theranostic agents, are discussed Section 1.5.

1.4.3 Lymph node imaging

One of the main criteria for a tumor to be malignant is the movement of undifferentiated cells to other body regions. The first stop in this movement is lymphatic system. Lymph is the liquid that clears tissues and organs by removing useless products and toxins. Cancer cells enter lymphatic system and migrate to lymph nodes, a phenomenon that is called lymph node metastasis. Studies proposed that NIR QDs, which can produce images of deeper tissues, would be a good alternative in imaging lymph nodes for potential metastases (lymph node mapping—LNM), having said that little is known about their toxicity. Within these realms, more researchers tested novel types of QDs that did not contain cadmium. These types exhibited low toxicity and good compatibility with blood. NIR-QD complexes were also used for tracking discreet lymphatic flows in vivo and their flux to separate nodes. Overall, QDs, in particular, more recent types that were heavy metal-free and circumvented signs of toxicity offered an efficient solution in imaging of LNM [6,8].

1.4.4 Vasculature imaging

Imaging of blood vessels and circulation is another biomedical field where QDs could be applicable. For vasculature imaging, two-photon excitation and emission in NIR window are required. CdSe-ZnS QDs were used in hundreds of micrometers and did not indicate any signs of intermittency in luminescence (blinking), while CdMnTe-Hg QDs managed to image efficiently tissues as deep as $1.5-2$ mm. CdTe-CdSe QDs have been proposed to be practical in coronary vasculature in rodents. Furthermore, PEGylated coating was described as a method to increase spatial resolution in depicting generation of new tiny blood vessels in tumor. In fact, PEGylated QDs kept on emitting light of high brightness for a long period of time (>9 h), making surgical operations feasible. Regarding vasculature imaging in tumors, another study traced integrins and VCAM-1. These became visible due to changes in intensity and colors of fluorescent QDs. Even more promising results were acquired by recent findings, which indicated that QDs could remain in blood circulation for days, with no signs of toxicity or autofluorescence. These suggested that QDs can be biocompatible and useful in deep-tissue imaging [6,8].

1.4.5 Whole-body imaging

Whole-body imaging with fluorescence is still in an early stage. Results obtained till now come from superficial tissues, because of several difficulties that lead to low penetration in deep tissues, such as scattering. Modeling studies have proposed two emission windows. Their wavelengths are around 700−900 nm for the NIR-I window and 1200−1600 nm for the NIR-II window. Another issue to be resolved is the nonspecific liver, spleen, and lung uptake. QDs should be characterized by long half-life time and circulation in blood, to increase their penetration in desired tissues. QDs can be functionalized with a fluorescent molecule and a targeting moiety (e.g., antibody) [6].

QD paradigms of whole-body imaging include tagging endothelial cells in rodents, which signal angiogenesis that occurs in tumors, as well as tracking cell motility in blood or lymph vessels. Recent studies have generated nanoparticles embedded with metals, such as silver, copper, and iron. Their findings showed that silver has more pronounced fluorescence ability and could be more promising in biological research [6].

1.4.6 Stem cell imaging

Stem cells are undifferentiated cells that play a major role in regenerative medicines. Their imaging can provide useful information about their function, differentiation, as well as efficiency and safety when they are transplanted in vivo, providing a useful tool to assess their significance in stem cell therapy. QDs have many advantages due to low scattering, absorption, and autofluorescence, which are typically observed in classic fluorescent agents. QDs used in stem cell imaging are mostly conjugated with octa-arginine (R8), because it is not toxic, has easy synthesis, and displays short transduction time. Recent in vivo studies of QDs emitting at the NIR-I window observed the motility of transplanted human mesenchymal stem cells in the area of a wound, with some of them showing aggregation in lungs, while studies of NIR-II QDs showed better imaging of deeper tissues than with NIR-I-emitting QDs. In any case, more appropriate QDs need to be created to optimize the imaging of transplanted stem cells [9].

1.4.7 Multimodal imaging

Attempts to achieve multimodal imaging in vivo have been described as well. Apart from combining the advantages and accuracy of each technique, it is practically significant in living organisms to avoid multiple administrations. In multifunctional imaging the overall spatial and temporal resolution, sensitivity, and specificity are better than that of each separate technique. Resultingly, it can provide information about cellular and subcellular interactions and biodistribution. For instance, PET combined with NIR-QD complexes have been used in tumor imaging with good results. To achieve simultaneous MR and QD fluorescent imaging, various methods have been reported. First, manganese was conjugated to QDs to

provide them with paramagnetic properties. Second, Gd was bound to QD complexes to add contrast in MRI and the results were checked with two-photon imaging. Last, QDs encapsulated in liposomes together with CT contrast agents made a combination of CT and fluorescent imaging possible in animal paradigms [6].

1.5 Quantum dots and theranostics

Theranostics is a combination term of the words therapy and diagnostics and refers to the simultaneous therapy and diagnosis that can be achieved with the use of QDs. As was mentioned already, one form of theranostics can be accomplished through the specific drug delivery that can be realized in vivo with QDs. Long circulation time and the possibility for various functionalities are required to conduct targeted drug delivery. It has already been used in cancer and other diseases research as a method for therapy. In addition to this, other established techniques have attempted to combine the benefits of QDs [6].

Photodynamic therapy (PDT): PDT is a method for cancer therapy. It is based on the light-induced damage of cancer cells. In specific a substance that acts as a light sensor (photosensitizer) is delivered to the target group of cells. A photosensitizer often is a porphyrin-type pigment and is able to absorb the light of particular wavelength and energy. Next, the photosensitizer makes a use of absorbed energy to trigger oxygen activation and conversion into reactive oxygen species (ROS) and, in particular, singlet oxygen (O^{-}). Singlet oxygen stimulates apoptotic or necrotic pathways in the target cells, leading to cell death. It can also affect DNA and proteins, induce peroxidation of lipids, and cause damage to the tumor microenvironment. Although this technique induces damage to restricted groups of cells (cells that contain the photosensitizer and a few of their neighbor cells only), some degree of retention of singlet oxygen molecules exists for days after PDT. These molecules aggregate in skin and eyes, resulting in increased sensitivity to daylight [6].

To avoid these effects the photosensitizer was encapsulated in porous nanoparticles. In this way the ability to induce oxygen reactions remained intact, while the 1-nm size of holes prevented the outflow of reactive oxygen. Furthermore, it was found that QDs could also play the role of the photosensitizer. It has already been discussed that QDs get activated by the light absorption of specific wavelengths. After exposure to ultraviolet light, QDs absorb energy that is high enough to stimulate nearby oxygen molecules and convert them to ROS. Again, QDs show a great extent of specificity, because they can result in light-induced cytotoxicity that occurs only to cells that are adjacent to them [6].

Photothermal therapy (PTT): The idea behind this technique is very similar to the principles of PDT. In PTT, instead of a photosensitizer, a substance that converts energy acquired from light absorption to heat is used. This material localizes near tumor cells and gets triggered under NIR light. Under these conditions, it destroys cancer cells. It becomes evident that QDs that get stimulated in

wavelengths of NIR light can act as such materials and induce specific cell death of cancer cells [6].

1.6 Other applications of quantum dots

It becomes evident that QDs have a lot to offer in bioimaging. However, due to their great specificity and unique properties, QDs can be used for biosensing; that is to say, qualitative or quantitative identification of biomolecules in a group of cells or a tissue.

Tissue samples can be extracted and be tested for the presence of a disease through biopsy methods. Appropriate reagents are added to the sample so that abnormalities can be identified. QDs can be very practical in diagnosis, mainly thanks to their selective binding to a great variety of biomolecules and the possibility to detect multiple targets within one sample. Studies have tested multiple targeting by using different QDs conjugated with each one of distinct antibodies; these could successfully detect target molecules. Furthermore, when combined with two-photon or electron microscopy, spatial resolution was improved and results could be even visualized in three dimensions. QDs have been applied for biosensing reasons in tumors, microbial infections, and allergies. In the last two cases, QD-antibody complexes exhibited high selectivity and specificity compared to common techniques, such as ELISA, as for the detection of bacterial/viral antigens or allergens [6,8].

Regarding tumor detection, QDs could be useful in decoding the molecular and cellular profile of cancer tissues. This could be proved extremely useful in cancer diagnosis and therapy, since there is a vast heterogeneity in this disease, even among tumors that affect the same organ and complicates their treatment. Identification of each distinct cancer type can contribute to the development of more personalized treatment and improved prognosis of the disease. QDs could also optimize the efficiency of diagnostic assays, such as FISH, in which they can trace mRNA or protein markers with high sensitivity and selectivity. In addition, QDs could be practical in tissue microarrays (TMA), a technique for biomarker screening. Thanks to these nanoparticles, we may be able to build appropriate software that identifies specific tumor types, according to their antigens found on TMA. Nevertheless, this scenario requires an optimized affinity of antibodies for specific antigens, an improved degree of QD penetration in deep tissues, and a standardization of biomarkers for diseases, to be realized [8].

Other examples of biosensing applications include biochips/microarrays and neuroscience. Biochips refer to techniques of quantitative measurements of protein expression or the presence of completely structured, functional proteins, as well as the level of their functionality. Studies reported a concomitant measurement of fluorescence and electrochemical signals, for the presence and functionality of proteins, while others indicated that when used for cancer biomarkers, including CEA and CA125, QD gave more rapid and reliable results than ELISA. As for their use in

neuroscientific field, QDs have depicted synaptic function and interactions between neurons and glial cells (e.g., astrocytes and microglia) successfully [6].

Tissue engineering is another field where QDs can be applied. This field aims to test and develop new connective tissues that can be used eventually as fully functional organs, which can be implanted back to the donor of a transplant. In particular, bones feature nanosized particles on their surface. As a result, the implant can be rejected if its surface is smooth. Since QDs show higher biocompatibility than other nanoparticles, they could be attached to the surface of the bone prosthetic and improve the chance of rejection [1].

Last, QDs have been widely used in nonbiological systems as well. In fact, these applications started before their use in biomedical field, due to the lack of toxicity concerns. QDs already play a significant role in technologies, such as quantum transistors, oscillators, filters, detectors, data analysis techniques, and QD light−emitting devices LEDs, providing each one with great benefits thanks to their unique properties [1].

1.7 Toxicity issues

Before describing the toxicity issues that arise from the usage of QDs, it would be useful to mention their pharmacological properties. These properties that include absorption, distribution, metabolism, and excretion correspond to their physicochemical features as well as to environmental conditions.

QDs are delivered via the parenteral route, although dermal and respiratory administrations have also been reported. There is no sufficient information about the interaction between QDs and blood, even though it is hypothesized that they interact with serum proteins. When delivered to a living organism, QDs tend to accumulate to specific targets, as well as to RES in a nonspecific manner. RES involves the liver, the spleen, and the lymph system. Furthermore, QDs can be also found in the kidney and the lungs. Their uptake from target cells is mainly mediated by the process of endocytosis. Their metabolism depends on their size and composition and may occur hours to weeks after their administration. QD cores are not metabolized, while the rest of the configuration degrades under oxidative conditions. Remaining cadmium originated from the core is toxic for kidneys; having said that, QDs that are smaller than 5 nm can undergo renal filtration and prevent kidney toxicity [1,2,8].

Regarding toxicity, it is found that it depends on the size and charge of QDs, the concentration used in imaging, the biochemical valence of their coating and their consistency against destabilizing conditions of oxidation, photolysis, and mechanical forces. Core composition is crucial for toxicity, due to the existence of cytotoxic Cd^{+}. In fact the vast aggregation of QDs in spleen could be attributed to the protective role of ZnS shell, which prevents the efflux of Cd from the core. Systemic toxic effects of QD use involve edema (ocular, pericardial, and in yolk sac), spinal curvature, and tail malformation [1].

The first step of cytotoxicity mechanism that leads to cell death involves the dissolution of the core−shell configuration. Under oxidative or UV light conditions,

the shell degrades and cadmium cations are released. These cations get reduced (they gain electrons) and activate a cascade of reactions that end up to cell death. In particular, QDs, of which the core consists of CdSe, are assumed to induce apoptosis. Another possible mechanism for cytotoxicity can be attributed to the generation of ROS. These products, including singlet oxygen and free radicals, are formed by energy that is transferred from QDs to adjacent oxygen molecules. Subsequently, ROS can destroy genetic materials. Furthermore, inflammation has been observed in some cases due to the retention of organic molecules after QD metabolism and excretion. In some cases, instability was caused from intracellular pH changes, due to QDs interacting with macromolecules or ions. Last, increased autophagy was reported to occur in cells that interacted with QDs. Even though autophagy leads to cell apoptosis, its role is protective in favor of its neighboring cells. It is noteworthy that organic dyes have similar toxic effects in biological systems, and that is why they are not used in living organisms either [6,8].

These mechanisms were observed in vitro. In vivo ones offer the opportunity to study side effects on the larger scale of whole organisms instead of individual cells. These effects are highly related to distribution and other pharmacological features of QDs. QDs are usually injected into the animal, mainly via IV administration. Thus they enter the bloodstream and most probably interact with serum proteins. In this way, proteins may engulf the whole core−shell configuration of QDs and their coating and result in the reduction of their functionality and disturbed biodistribution. Next, QDs are metabolized and excreted through urine and/or feces. Rapid excretion is crucial to avoid toxic effects that occur due to prolonged retention inside the cells and tissues. In particular, effects on kidney function, on lungs (pulmonary vascular thrombosis), and, interestingly, on CNS (hippocampal impairments of synaptic plasticity with observable impact on spatial memory) have been described in literature [8].

Toxicity issues highlighted the importance of structural stability of QDs (Fig. 1.3). The covalent bond in III−V QDs is preferred to the ionic one in II−VI QDs due to its greater stability. In addition, high dosages of QDs are not recommended; low dosages that have been used in vivo did not cause long-term effects in animals. Research has also turned to the generation of novel materials that can be used safely in QD synthesis, with optimized preparation techniques [1].

1.8 Novel types of quantum dots

1.8.1 Cadmium-free quantum dots

Since cadmium appears to be the prevalent cause of cytotoxicity, there have been significant attempts to generate QDs that do not contain cadmium. Such types of QDs have been manufactured and are extensively offered on the market. Most recent types of Cd-free QDs include I−III−VI QDs, for instance, $AgInS_2$, $CuInS_2$, and $CuInSe_2$, which exhibit similar properties with classic QDs and a very low level of toxicity. They can also emit light at NIR wavelengths, making them advantageous for in vivo

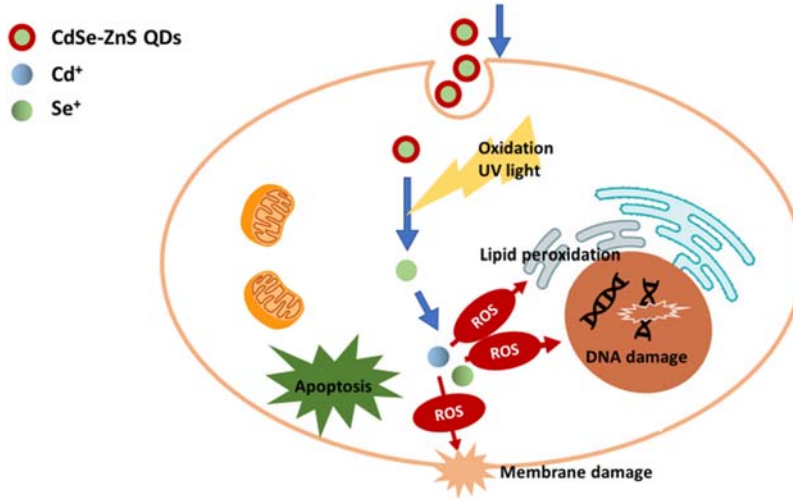

Figure 1.3 Cytotoxic mechanisms proposed for Cd^{+} quantum dots.

applications. Their use has already been reported in stem cells imaging, without affecting their viability and proliferation [6].

1.8.2 Silicon quantum dots

Another novel type of biocompatible QDs is silicon dot. Silicon dots are also characterized by size-dependent physicochemical and optical properties that resemble the ones observed in metal QDs. Their functionality depends on their superficial coating and conjugation with other molecules. Their difference compared to classic QDs lies upon the fact that their degradation produces silicic acid, with no signs of toxicity. Si-QDs are excreted rapidly via urine and they also appear to accumulate in the liver. In vitro applications indicated enhanced uptake by cancer cells and a great imaging potential of cancer cells and of their interior organelles, especially when they were capped with PEG. In vivo studies pointed out their safety even at high dosage, compared to Cd-QDs. They were applied successfully in tumor, vasculature, and lymph node imaging, where they achieved multiple-target detection and NIR emission. Newer types of Si-QDs, which have increased QY, photo- and pH-stability, biocompatibility, are constantly generated and can be suggested for prolonged cellular labeling.

1.8.3 Carbon/graphene quantum dots

Nanotechnological progress has achieved to create carbon-based QDs (CQDs). Because of their organic nature, CQDs (or graphene QDs) are less expensive and nontoxic for cells. They also exhibit similar features to aforementioned QDs, and relevant studies have acclaimed them to be very promising in biomedicine. They are nonspecifically distributed to heart, liver, kidneys, and spleen as well as to their

target tissues. Studies have showed that they are fully excreted after 24 h. Applications of CQDs in vivo have described great benefits in bioimaging, due to their NIR emission. They have been used for molecular detection, cellular labeling (stem cells, cancer cells), drug delivery, and PDT [11].

1.9 Conclusion

It becomes evident that QDs possess unique qualities and advantages over classic fluorescent organic dyes. Literature regarding their applications in biomedicine, particularly in bioimaging, is ever-growing, and the results can be acclaimed as highly promising. Nevertheless, concerns about their toxicity in living organisms still exist, and it is crucial to confirm their safety before we can take the advantage of the significant benefits they could offer.

References

[1] N. Bajwa, N. Mehra, K. Jain, N. Jain, Pharmaceutical and biomedical applications of quantum dots, Artif. Cells Nanomed. Biotechnol. 44 (2016) 758−768.
[2] E. Abbasi, T. Kafshdooz, M. Bakhtiary, N. Nikzamir, N. Nikzamir, M. Nikzamir, et al., Biomedical and biological applications of quantum dots, Artif. Cells Nanomed. Biotechnol. 44 (2016) 885−891.
[3] S. Pleskova, E. Mikheeva, E. Gornostaeva, Using of quantum dots in biology and medicine, Adv. Exp. Med. Biol. 1048 (2018) 323−334.
[4] W. Algar, K. Susumu, J. Delehanty, I. Medintz, Semiconductor quantum dots in bioanalysis: crossing the valley of death, Anal. Chem. 83 (23) (2011) 8826−8837.
[5] T. Pisanic II, Y. Zhang, T. Wang, Quantum dots in diagnostics and detection: principles and paradigms, Analyst 139 (12) (2014) 2968−2981.
[6] J. Yao, P. Li, L. Li, M. Yang, Biochemistry and biomedicine of quantum dots: from biodetection to bioimaging, drug discovery, diagnostics, and therapy, Acta Biomater. 74 (2018) 36−55.
[7] A. Karakoti, R. Shukla, R. Shanker, S. Singh, Surface functionalization of quantum dots for biological applications, Adv. Colloid Interface Sci. 215 (2015) 28−45.
[8] K. Wegner, N. Hildebrandt, Quantum dots: bright and versatile in vitro and in vivo fluorescence imaging biosensors, Chem. Soc. Rev. 44 (14) (2015) 4792−4834.
[9] H. Yukawa, Y. Baba, In vivo fluorescence imaging and the diagnosis of stem cells using quantum dots for regenerative medicine, Anal. Chem. 89 (5) (2017) 2671−2681.
[10] S. Chinnathambi, S. Chen, S. Ganesan, N. Hanagata, Silicon quantum dots for biological applications, Adv. Healthcare Mater. 3 (1) (2013) 10−29.
[11] P. Namdari, B. Negahdari, A. Eatemadi, Synthesis, properties and biomedical applications of carbon-based quantum dots: an updated review, Biomed. Pharmacother. 87 (2017) 209−222.
[12] M. Gazouli, P. Bouziotis, A. Lyberopoulou, J. Ikonomopoulos, A. Papalois, N. Anagnou, et al., Quantum dots-bevacizumab complexes for in vivo imaging of tumors, In Vivo 28 (2014) 1091−1096.

2D quantum materials and sensors devices

2

Beatriz Jurado-Sánchez[1,2] *and Alberto Escarpa*[1,2]
[1]Department of Analytical Chemistry, Physical Chemistry and Chemical Engineering, University of Alcala, Alcalá de Henares, Madrid, Spain, [2]Chemical Research Institute "Andrés M. del Río", University of Alcala, Alcalá de Henares, Madrid, Spain

2.1 Introduction

Quantum materials are newly developed materials that were born to address the growing needs of quantum information. The myriad of quantum materials includes graphene, two-dimensional (2D) nanomaterials, multifunctional oxides, superconductors, and heavy-fermion systems. As a key feature, such materials exhibit quantum mechanical effects at macroscopic length scales, leading novel ordered phases and unique attributes for sensing devices, LED, photodetectors, and sensors [1−3]. The first distinct feature is the quantum confinement effect that occurs when the physical dimension of the particles−materials is similar or even smaller than quantum particles, thus leading to novel properties not found in the bulk materials. One representative example of materials exhibiting quantum confinement effects are quantum dots or exfoliated 2D nanomaterials. The second characteristic, related with the low dimensionality, is the possibility for multiple body interactions such as electron−electron and spin−valley; typical of magnetic materials; and superconductors. The third property is the contribution of its topology and the Berry phase to exotic properties such as the quantum spin Hall effect in insulators. The fourth feature is the utilization of noncharged degrees of freedom of charge carriers (spin, valley, and pseudospin) in low-energy electronics and quantum computations. Quantum materials normally display one or all the previously mentioned features [2,4−6].

In the field of analytical chemistry, quantum materials have been exploited for the preparation of novel sensors for gas detection, optical detection, biosensing, electrochemical detection, and bioimaging [7−9]. Graphene was the first discovered quantum material used for analytical applications with unusual and unpreceded properties arising from the quantum confinement effect of the electrons. Indeed, graphene displays extremely high room-temperature mobility, optical transparency, and excellent electrical conductivities that have been exploited since 2004 in insulators and sensors [10−13]. New 2D nanomaterials beyond graphene have revealed themselves as new rising stars in the field of quantum materials and sensor devices. Fig. 2.1 illustrates an overview of the number of publications, during the last 10 years, on the development of sensing devices based on 2D nanomaterials. As can

Quantum Materials, Devices, and Applications. DOI: https://doi.org/10.1016/B978-0-12-820566-2.00003-X

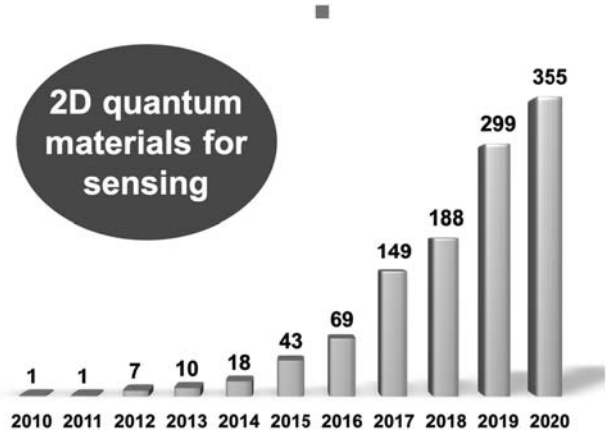

Figure 2.1 Graph bar showing the number of publications (last 10 years) of 2D quantum materials for sensing. *2D*, Two dimensional.
Source: Scopus; keywords: 2D nanomaterials; sensors.

be seen, the trend of publications increases exponentially with a great increase in the last 2 years.

The most widely explored 2D nanomaterials for sensor devices are transition metal dichalcogenides (TMDs) and oxides (TMOs), MXenes, metal-organic frameworks (MOFs) and covalent-organic frameworks (COFs), black phosphorous (BP), boron nitride (h-BN), germanene and its composites with graphene, and other materials. Such materials are similar to graphene in terms of quantum properties but still surpass it in some aspects, including ultralow thickness, strong quantum confinement, and reduced Coulomb screening. These enhanced properties allow for the integration of 2D nanomaterials on biological tissues and skin with minimal mechanical damage, holding considerable promise for wearable sensors and biosensors [9]. The presence of new emerging phases in 2D nanomaterials along with the strong quantum confinement effect results in a high conductivity and remarkable high charge mobility (even superior to graphene) ideal to improve the properties of strain, flexible sensors, and for electrochemical detection [5,14–16].

In this chapter, we will describe cutting-edge advances (last 3 years) of sensor based on quantum materials. The focus will be targeted to new 2D nanomaterials, as graphene itself can be the topic of a complete chapter and even a whole book. On the first section, we will describe the types and properties of 2D quantum materials used in sensing devices. On the second section, we will give a recent overview on the use of such materials for gas sensing, electrochemical (bio)-sensing, optical sensing, and photodetectors. A brief overview and future trends of such rapidly developing field will be given in the conclusion.

2.2 Types of quantum materials for sensing applications

2.2.1 2D nanomaterials

2D materials are an emerging class of sheetlike nanomaterials with a high ratio of lateral size (nanometers to micrometers) to thickness (angstroms to nanometers). The quantum properties of such materials arise from the ultralow thickness after exfoliation, which is lower than 5 nm (equivalent to few atoms). The resulting properties such as ultrahigh room-temperature carrier mobility, tunable bandgaps, and high specific surface area are particularly attractive for sensors development and in applications in semiconductors and biosensors. We will give a brief overview here on the main properties and preparation methods with a special emphasis on the role in the design in quantum materials−based sensors [17,18]. Fig. 2.2 illustrates an overview of the materials and related structures, which will be described here.

The following section is rearranged by mentioning the main characteristics of each 2D nanomaterials from the left to right order established in Fig. 2.2.

2.2.1.1 Transition metal dichalcogenides

TMDs are compounds with the general chemical formula of MX_2, where M is a transition metal (Mo, W, and Nb) and X represents a chalcogen (S, Se, Te, or combinations). TMDs display a layered crystal structure (see Fig. 2.2), with van der Waals forces across the adjacent layers and each individual 2D sheet held together through strong covalent bonds [19]. The different directions of the bonds and/or stacking from the result in different crystal structures include anisotropic 1T′, 1T (trigonal), 2H (hexagonal), or 3R (rhombohedral). For example, the 2H structure has an atomic stacking sequence, whereas a 1H structure indicates a single-layer structure of a 2H phase [20].

Figure 2.2 Summary of quantum nanomaterials used in sensor devices and related structures.

Among the most salient properties of TMDs the quantum confinement in such materials results in an indirect bandgap that shifts from 1 to almost 2 V (in the bulk material in the exfoliated monolayer, respectively), which have been exploited to design different field-effect transistors (FET) for gas and other biomarkers sensing [21,22]. The second feature lies in the different phases, which promotes electron transfer and migration for the preparation of semiconductors and optical sensors [20]. On the third aspect the high surface areas, interfacial contact areas, and the presence of reactive functional groups for further functionalization result in rapid charge transfer to design electrochemical biosensors and enzyme-linked immunoassays [23].

2.2.1.2 Transition metal oxides

Compared with the progress in TMDs, few developments have been achieved so far with 2D TMOs due to the difficulties during its fabrication and exfoliation. The general formula of TMOs is MO_3, where M is a transition metal (Mo, Ta, and V) [24]. A schematic of the typical crystal structure is depicted in Fig. 2.2. As can be seen, the layered structure is composed of individual polyhedrals and octahedrals that share the edges with the surrounding units and create the 2D layers. Different layers can be stacked by van der Waals forces to form the bulk material [25,26].

With regard to the quantum properties the presence of the oxygen ion and the hybridization of the orbitals create a shift in the Fermi levels that allow them to act as semiconductors and active parts in electrochemical (bio)-sensors [27]. In addition, TMOs possess tunable bandgaps and strong d−d transitions for its use in FET and optical sensors based on Forster resonance energy transfer when conjugated with fluorophores and other probes in optical detection schemes [28,29].

2.2.1.3 MXenes

MXenes are compounds synthetized by a direct exfoliation of the corresponding MAX phases with the general formula $M_{n+1}AX_n (n = 1, 2, \text{or } 3)$, where M is a transition metal (Sc, Ti, Zr, V, Cr, Mn, Nb, Hf, Ta, and Mo), A is an element from group 12 to 16 of the periodic table (Cd, Al, Si, P, S, Ga, Ge, As, In, Sn, Tl, and Pb), and X is either carbon or nitrogen. Greater n values indicate more stability on the MXene structure [30−32]. MAX phases have a hexagon-layered structure, in which the M layers are packed together with the X atoms filling the octahedral sites (see Fig. 2.2). The element A is the key for the tailored exfoliation of different MXenes, as is intercalated into the $M_{n+1}X_n$ layers. As such, the A layer can be exfoliated with strong etching solutions hydrogen fluoride (HF) forming MXenes with different structures, including M_2X, M_3X_2, or M_4X_3. More importantly, the exfoliation process imparts the MXene surfaces with multiple functional groups (OH^-, F^-) that improve the electronic conductivity. Such rich chemistry holds considerable promise to develop a myriad of gas sensors, electrochemical sensors, or optical-based sensing strategies. In addition, as will be fully described, the increased surface area of MXenes and the biocompatibility allow for the immobilization of a high loading of (bio)-receptors to improve the overall analytical properties of a myriad of (bio)-sensors [33,34].

2.2.1.4 Metal-organic and covalent-organic frameworks

MOFs are crystalline porous materials in which metal ions (Fe, Co, and Zn) are linked to organic ligands and imidazole rings to form a coordinated layered structure (see Fig. 2.2). Different coordination modes hold considerable promise to tune MOFs structure. In addition, such materials are highly porous with a high surface area. There is no general formula for MOF crystals and such compounds are classified according to their shape/asymmetry (IRMOF-1—IRMOF-16, and isoreticular MOFs), their discovery place (UiO, MIL, and LIC), or the zeolite topology (ZIF, zeolitic imidazolate framework) [35,36]. COFs are similar to MOFs but in this case covalent bonds are responsible for the binding of "light" elements (B, C, and N) to the organic ligands. The resulting crystalline individual layered structures stack together via van der Waals bonds [37]. Due to its tunability, MOFs and COFs are very promising for fabricating fluorescent sensors with built-in fluorescence or combined with other receptors, the high surface area and rich functional groups also facilitate modification for electrochemical biosensors development, and the unpreceded electron mobility and availability of free sites (in other words, the extremely high surface to ratio area) are ideal for gas biosensors development.

2.2.1.5 Black phosphorous and hexagonal boron nitride

BP, also known as phosphorene, displays a single element—layered structure with a basic unit of six phosphorous atoms held together by van der Waals. Each P atom is bonded to three other atoms resulting an orthorhombic-pleated honeycomb structure. The individual layers stack together through van der Waals forces either in a zigzag or armchair conformations (see Fig. 2.2) that result in outstanding anisotropic properties [38]. BP has excellent carrier mobility [1000 $cm^2 (V\ s)^{-1}$] and is very sensitive to electrical perturbation, being thus particularly attractive to detect the sorption and desorption of gases in gas sensors or immunosensors coupled to electric resistance sensors. In addition, BP has a direct bandgap of ~ 2 eV, making it a suitable material for optoelectronics; whereas the relatively high surface area and functional groups allow to develop fluorescence biosensors [39].

h-BN also has a hexagonal structure packed into crystal layers structure similar to that of graphite. The hexagonal structure is composed by boron and nitrogen atoms bonded by covalent bonds and the layers stacked together by van der Waals forces (see Fig. 2.2). This configuration results in a high Young's modulus of 780 GPa with a very high surface area and electronic mobility for the design of biosensors as described for BP [40].

2.2.2 Heterostructures and nanocomposites

In heterostructures and nanocomposites, two dissimilar quantum materials together or mixed with other nanomaterials are combined, resulting in a new material system with novel properties arising at the interface of both materials [1]. Indeed, as will be further described, most sensors based on quantum materials are assembled from

heterostructures and nanocomposites with complementary Fermi velocities, electronic bands, and magnetic ordering to further improve the overall performance. One excellent example is the combination of semiconductors with different bandgaps. This leads to the generation of quantum well or holes at the interface of the semiconductor heterostructures, increasing the conductivity, or imparting new properties for gas sensing [41].

Another important emerging property, when combining quantum materials into heterostructures and nanocomposites, is the proximity effect or the appearance of new properties into a material by the proximity of a second material. For example, a bandgap can be introduced into gapless pristine graphene by combining it with h-BN due to the symmetry of the lattice get inverted [42].

As a third relevant new property, the creation of heterostructures can change the twist angle between two atomic layers to tailor the electronic and other properties. A good example is graphene, which can be combined with TMDs and other materials, resulting in the break of the twisted bilayer and imparting the resulting material with superconductivity for sensors development [43]. As a conclusion, by judicious choice of the material and its combinations is crucial to further explore the potential of quantum materials for sensor devices.

2.2.3 Synthesis of 2D quantum materials for sensing

As the properties of 2D materials are directly influenced by the thickness and surface properties, it is important to choose the best procedure to tailor the material behavior in further quantum-sensing development. Top-down approaches compromise different procedures to break bulk quantum material crystals into individual layers. Bottom-up approach involves the assembly/deposition of precursors into substrates or in solution [44].

Top-down methods include mechanical cleavage, mechanical force−assisted liquid exfoliation, ion intercalation−assisted liquid exfoliation, ion exchange−assisted liquid exfoliation, oxidation-assisted liquid exfoliation, and selective etching−assisted liquid exfoliation. The abovementioned methods are only applicable for layered bulk crystals. Bottom-up approaches include wet-chemical processes, physical or chemical vapor deposition (CVD), and ion intercalation or nanocrystal self-assembly [9,45,46]. Fig. 2.3 illustrates a summary of the most prominent synthetic routes.

Mechanical cleavage is a well-known technique used by Geim and Novoselov for graphene synthesis. The procedure consists of the mechanical removal of layers of bulk crystals by using adhesive tapes. It can be applied to synthetize TMDs, BP, and h-BN. The procedure yet cannot be applied to mass scale production and lacks on precision. Liquid-phase exfoliation is a convenient alternative that consisted of applying ultrasound or mechanical forces to the materials in solution. Surfactants can be added to aid the exfoliation. Ion intercalation−assisted liquid exfoliation relies in the intercalation of cations into the interspacing of layered bulk crystals to form ion-intercalated compounds, which can be next easily exfoliated into single- or few-layer nanosheets under mild sonication treatment in a specific solvent.

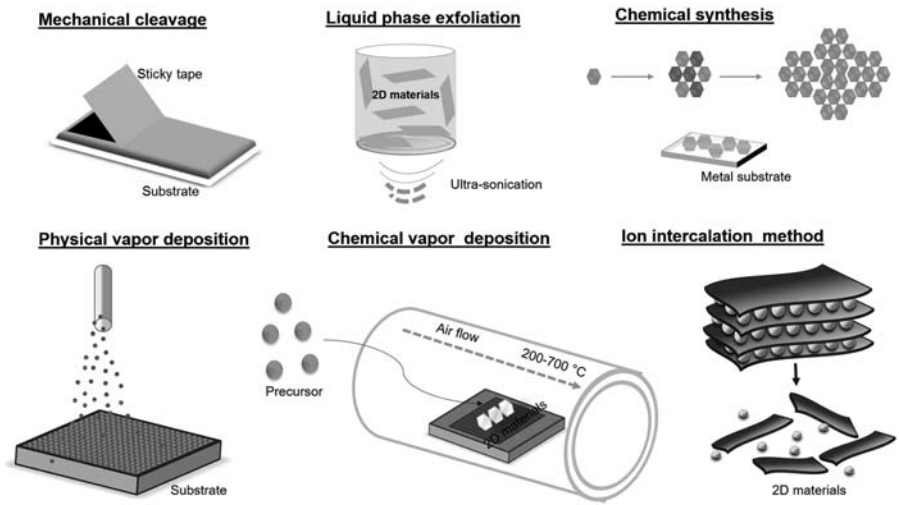

Figure 2.3 Summary of top-down and bottom-up approaches for the synthesis of quantum (2D) nanomaterials for sensing. *2D*, Two dimensional.
Source: Reprinted with permission from C. Murugan, V. Sharma, R.K. Murugan, G. Malaimegu, A. Sundaramurthy, Two-dimensional cancer theranostic nanomaterials: Synthesis, surface functionalization and applications in photothermal therapy, J. Control. Release 299 (2019) 1−20, Copyright 2019, Elsevier.

Chemical syntheses involve chemical reactions between different precursors in solution. The final layered materials are highly soluble in water and other organic solvents. Chemical and physical vapor depositions are the most commonly used bottom-up approaches to obtain quantum materials with high purity and precise control over the number of layers, crystallinity, and thus on the subsequent performance of the material in sensing. Substrates are placed in a pressure chamber and irradiated with vapors of the precursor materials/chemicals, which deposit then onto the substrate.

2.3 Sensors based on quantum materials

Table 2.1 summarizes different sensors based on quantum materials from gas sensors to photodetectors and on-body sensors. More details will be given in the following sections.

2.3.1 Gas sensors

High-performance gas sensors for air and breath monitoring are crucial for detecting hazardous gases to monitor air quality on big cities or for diagnosis monitoring-purposes, which can impact both the environment and public health [33]. The main

Table 2.1 Summary of quantum materials−based sensors.

Materials	Analytes	Type of detection	Analytical characteristics	References
Gas sensing				
MoS_2/Pt	H_2	Electromechanical	Fast speed sensing	[47]
MoS/h-BN	NO_x	FET	LOD: ppt levels	[48]
MoS_2/GO	VOCs NO_2	FET	–	[49]
rGO-SnS_2	NO_2	Electromechanical	LOD: 5 mg L^{-1}	[50]
SnO_2/GO	H_2S	Electromechanical	LR: 10−100 mg L^{-1} LOD: 0.043 mg L^{-1}	[51]
ReS_2	NO_2	Sweep voltammetry (I−V curves)	LOD: 50 μg L^{-1}	[52]
$Ti_3C_2T_x$-F MXene	Ethanol	Electromechanical	LR: 5−120 mg L^{-1}	[53]
$Ti_3C_2T_x$ MXene/CuO nanoparticles	Toluene	Electromechanical	LOD: 0.32 mg L^{-1}	[54]
$Ti_3C_2T_x$ MXene	Acetone Ethanol Methanol NH_4	Electromechanical	LOD: 9.27 mg mL^{-1} (acetone)	[55]
V_2CT_x	H_2 Acetone Methane H_2S	Electromechanical	LOD: 25 mg mL^{-1}	[56]
BP−dyes	NH_3, HCl	UV−Vis	–	[57]
BP−dyes	NO_2	Electromechanical	LOD: 3.3 μg L^{-1}	[58]

Tellurene nanoflakes	NO_2	Electromechanical	LOD: 0.214 μg L^{-1}	[59]
Electrochemical (bio)-sensing				
MoS_2/polyimide composites	Hormones	CV Competitive immunoassay	Flexible sensor	[60]
MoS_2/carbon black composites	Oleuropein Hydroxytyrosol	CV DPV	LR: 0.3−100 μM LOD: 0.1 μM	[61]
MoS_2/carbon black composites	Catechins	CV DPV	LR: 0.12−25 μM LOD: 0.2 μM	[62]
WS_2/carbon black/AuNPs hybrid	Caffeic acid Sinapic acid *p*-Coumaric acid	DPV	LOD: 0.1−0.4 μM	[63]
MX_2	Flavonoids	CV	–	[64]
MoS_2 h-BN	DNA	Nanopore sensors	–	[6]
Nb_2C MXene/ZnS	Dopamine	DPV	LR: 0.09−0.82 μM LOD: 1.39 μM	[65]
Ti_3C_2 MXene/MWCNT	Pharmaceuticals	CV	LR: 0.0011−61 μM LOD: 0.00028 μM	[66]
Ti_3C_2 MXene	Glucose	Chronoamperometry	LR: 50 − 27,750 μM LOD: 23.0 μM	[67]
$Ti_3C_2T_x$ MXene/ink	Human motion	Electromechanical	Flexible sensors Potential for real-time on-skin monitoring	[68]

(*Continued*)

Table 2.1 (Continued)

Materials	Analytes	Type of detection	Analytical characteristics	References
ZIF MOFs-PB	H_2O_2 Glucose	CV Chronoamperometry	LR: 0.2 − 6.0 mM (H_2O_2);1.4 μM−1.5 mM (glucose)	[69]
h-BN	Myoglobin	Electrochemical aptasensing	LR: 0.1−100 mg L^{-1} LOD: 0.035 mg L^{-1}	[70]
Optical sensing				
Ag/$PtSe_2$/WS_2 Au/$PtSe_2$/WS_2	–	SPR	–	[71]
Ti_3C_2 MXene-AuNPs	CEA	SPR	LR: 0.2−2 × 10^7 fM LOD: 0.07 fM	[72]
Ti_3C_2 MXene	HPV	Fluorescence	LOD: 100 pM	[73]
Ti_3C_2 MXene QDs		Fluorescence		[74]
COF	F	Fluorescence	LOD: 5 ppb	[75]
BP−dyes	Crystal violet	SERS	–	[57]
Photodetectors				
ZnO QDs−decorated Zn_2SnO_4 nanowires	–	UV−Vis	–	[76]
$BiVO_4$ photoanode/$Ti_3C_2T_x$ MXene	Hg	Voltammetry (current density)	LR: 1 pM−2 nM LOD: 1 pM	[77]

BP, Black phosphorous; *CEA*, carcinoembryonic antigen; *COF*, covalent organic framework; *CV*, cyclic voltammetry; *DPV,* differential pulse voltammetry; *FET*, field effect transistor; *GO*, graphene oxide; *h-BN*, boron nitride; *HPV*, human papillomavirus; *LOD*, limit of detection; *LR*, linear range; *MOF*, metal organic frameworks; *MWCNT*, multiwalled carbon nanotube; *QD*, quantum dot; *rGO*, reduced graphene oxide; *SERS*, surface enhanced-Raman scattering; *SPR*, surface Plasmon resonance; *VOC*, volatile organic compound; *ZIF,* zeolite imidazolate framework.

focus is directed to the detection at part per millions and even part per billions concentration of highly reactive gases, including NO_2, H_2S, and volatile organic compounds (VOCs). As such, the sensors should have a short response time, high selectivity with a wide linear range (LR), and low detection limits. A convenient solution to achieve such performance is to use materials with high surface area, reactive functional groups or sites for the adsorption of gas molecules, and high electric conductivity to convert the interaction into electrical signal. 2D quantum materials display the abovementioned requirements and as such, TMDs, TMOs, MXenes, BP, h-BN, and nanocomposites have been used for this purpose. Table 2.1 summarizes selected examples of such sensors indicating the type of material used, target gas, and main analytical characteristics and features. Some selected examples on sensor design and specific applications are illustrated in Fig. 2.4.

MoS_2 is the most widely used TMD for gas sensing, and different heterostructure-based sensors have been developed. Kim et al. [47] prepared PtNP-decorated MoS_2 hollow spheres for H_2 sensing by Pickering emulsion. The structures possess a high free volume and surface area in a densely packed structure, which is crucial for the enhanced gas sensing. To design the sensor the material

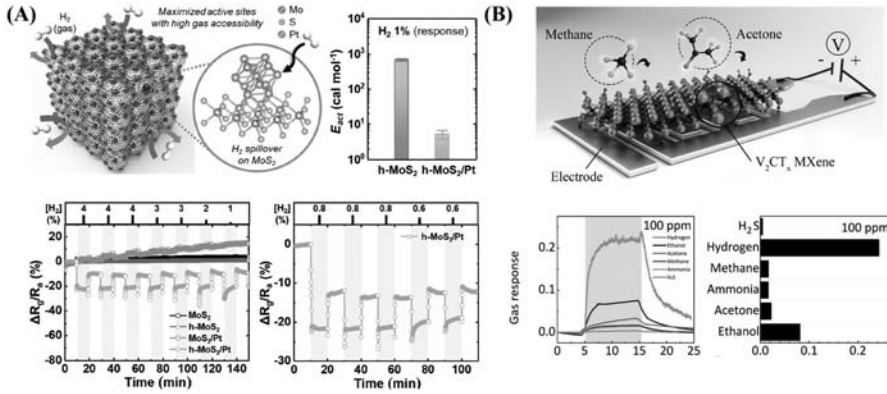

Figure 2.4 Quantum materials−based gas sensors: (A) hollow structure of a Pt-decorated MoS_2 sensor for H_2 sensing. The top part shows the schematic of the sensing mechanism and the calculated activation energies (E_{act}) for H_2 reaction on the sensors. The bottom part shows the resistance changes of MoS_2, h-MoS_2, MoS_2/Pt, and h-MoS_2/Pt in response to 1%−4% and 0.4%−0.8% of H_2. (B) V_2CT_x gas sensor: schematic drawing, resistance variation, and gas response toward 100 ppm of hydrogen, ethanol, acetone, methane, ammonia, and hydrogen sulfide.

Source: Reprinted with permission from (A) C.H. Park, W.T. Koo, Y.J. Lee, Y.H. Kim, J. Lee, J.S. Jang, et al., Hydrogen sensors based on MoS_2 hollow architectures assembled by Pickering emulsion, ACS Nano 14 (2020) 9652−9661, Copyright 2020, American Chemical Society; (B) E. Lee, A. Vahid Mohammadi, Y.S. Yoon, M. Beidaghi, D.J. Kim, Two-dimensional vanadium carbide MXene for gas sensors with ultrahigh sensitivity toward nonpolar gases, ACS Sens. 4 (2019) 1603−1611, Copyright 2012, American Chemical Society.

was dispersed in ethanol (200 μL) and then drop-casted in an Al_2O_3 sensing patterned with two parallel Au electrodes on the front and a Pt microheater on the back. The electrodes were introduced in a sealed chamber and exposed to the H_2. The resistances of the sensor were monitored in real time and used as analytical signal. The sensing mechanism is illustrated in Fig. 2.4A and is based on gas diffusion inside the sensing layers and surface-active sites in MoS_2. Also, the PtNPs dissociate H_2 molecules to promote surface reaction with MoS_2. Such changes are converted into resistivity and monitored. The combination of both materials results in the reduction of the activation energies (E_{act}), which results in shorter sensing times and improved analytical performance (see Fig. 2.4A). The sensing performance was compared with other materials (see Fig. 2.4A, bottom), and the results further illustrated that h-MoS_2/Pt exhibited significant changes in resistance with fast response and recovery speed, as compared with the negligible changes in resistance of the control materials. Detection of H_2 at a low level of 0.05% was achieved with the sensor. MoS_2 has been also combined with graphene into a heterostructure for the development of an FET sensor for VOCs and NO_2 sensing [49]. The MoS_2/graphene heterostructure is synthesized over gold-sensing electrodes by physical stacking of single layers of the TMD over graphene, resulting in an electron transfer to graphene that ultimately changes FET charge neutrality point. MoS_2 has also been combined with h-BN to develop an FET sensor that can detect NO_x down to 6 ppb levels [48]. Novel TMDs such as SnS_2 (combined with graphene) and ReS_2 have been used for NO_2 detection at ppb levels [50,52].

TMOs/graphene nanocomposites are also convenient materials for gas sensing such as H_2S. SnO_2 nanowires have been combined into reduced graphene oxides (rGOs) nanosheets by colloidal approaches and further spin-coated onto ceramic substrates to develop a chemiresistive gas sensor [51]. For the sensor construction the composite materials were assembled into a ceramic substrate that was connected into a commercial sourcemeter system. The sensor response was set as the ratio of the baseline resistance in the presence of clean air and in the presence of the target gas, respectively. The coupling of SnO_2/graphene enhanced the overall electron transfer and reduced the sensing time, improving the overall performance of the sensor. When exposed to H_2S gas, the electron flow across the H_2S/SnO_2 interfaces to the electrodes is enhanced by favorable electron transfer from SnO_2 nanowires to the rGO nanosheets, leading to an excellent performance for the detection of 50 ppm of the gas.

MXenes−based gas sensors offer an excellent sensitivity and a low limit of detections (LODs) as compared with other 2D nanomaterials [55]. Yet, MXenes are prone to oxidative degradation; thus several strategies by surface functionalization or combination with other compounds have been proposed. Stanciu et al. [53] functionalized $Ti_3C_2T_x$ MXene with fluoroalkylsilane, improving the material stability and introducing functional groups for a selective and sensitive detection of VOCs in a gas-based chemosensor. Authors evaluated the sensing behavior to strong-oxidizing (electron-accepting) NO_2 and electron-donating VOCs (acetone and ethanol). The positive variations of resistance were observed regardless the gas type, indicating that the charge carrier is hindered when a gas molecule is absorbed. Yet,

the stronger adsorption energy of ethanol over other gases results in the highest sensor response. In a similar resistive sensor, $CuO/Ti_3C_2T_x$ MXene hybrids prepared by self-assembly were used for toluene sensing with nearly five times higher sensitivity than that of the pristine CuO nanoparticles and the MXene [54]. A novel MXene carbide was also explored for detecting polar and nonpolar chemical species, including hydrogen and methane with a LOD down to 2 ppm. As schematically depicted in Fig. 2.4B, the oxygen terminal groups on the surface of V_2CT_x flakes contribute significantly to interaction with the target gas, leading to changes in the resistance. The typical gas responses were calculated to be 0.08, 0.03, 0.012, 0.012, 0.24, and 0.005 for ethanol, acetone, ammonia, methane, hydrogen, and hydrogen sulfide, respectively, with the highest gas response obtained for hydrogen [56].

BP is another quantum material that offers interesting capabilities for gas sensing. Thus colorimetric (UV−Vis) gas sensing has been achieved using dye−BP composites prepared by Langmuir − Blodgett technology. Tetraphenylporphyrin tetrasulfonic acid hydrate, a dye that display different aggregation modes (and in turn, color changes) under different pHs, was evaluated. After exposure to the film to HCl and NH_3 the gas atmosphere affects the molecular structure of the dyes with changes in corresponding colors that can be used to detect such compounds [57]. Another dye, benzyl viologen, has been combined with BP to design a resistivity gas sensor to detect NO_2 at low levels (50 ppb). The dye effectively passivates BP to prevent high-energy adsorption sites that can prevent the reversibility of the system and, in turn, increase the reproducibility of the system [58]. Tellurene nanoflakes sensors have been used for a highly sensitive detection of NO_2 (0.2 ppb) when used in interdigitated electrodes for resistance measurements. Tellurene structure and quantum properties greatly increase the electrical conductivity for such enhanced performance [59]. Germanene derivatives also offer considerable promise for gas sensing [78].

2.3.2 Electrochemical (bio)-sensors

According to the IUPAC, electrochemical sensors are a category of chemical sensors designed by coupling the receptor part of the device to an electrochemical transducer. As such, they consist in three essential components: (1) a receptor that binds the sample, (2) the sample or analyte, and (3) a transducer to convert the reaction into a measurable electrical signal [79]. Quantum materials can be used for electrode modification to modulate and increase the electron transfer in the electrode or imparting it with additional properties to enhance the overall performance in electrochemical sensors. We will explain a brief selection here. On the first example, MoS_2 was used to fabricate a flexible platform by direct CVD on a polyimide substrate. Such platform was directly used as an electrode that can be used as the working electrode in flexible sensors. The schematic of the fabrication of the sensors and a photograph of the resulting device is depicted in Fig. 2.5A. The quantum properties of MoS_2 impart the sensor with enhanced electrical conductivity for highly sensitive detection of parathyroid hormone (PTH), triiodothyronine (T3), and thyroxine (T4) by cyclic voltammetry. Enzyme-linked

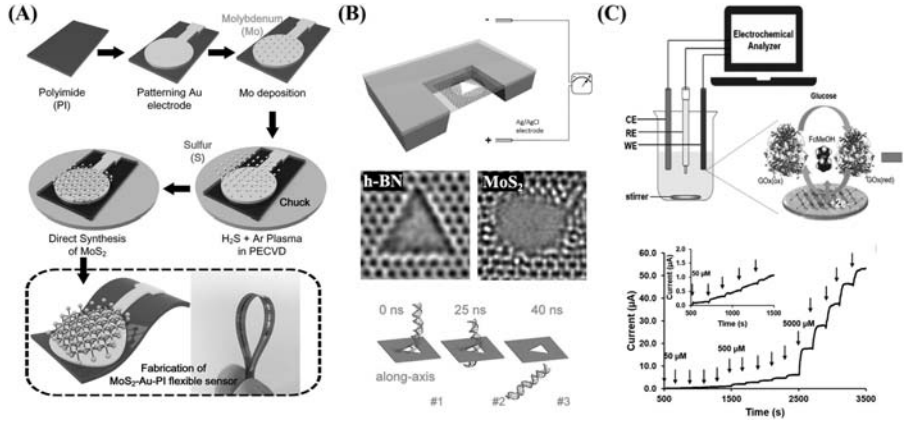

Figure 2.5 Quantum materials−based (bio)-electrochemical sensors. (A) Schematic of the fabrication of MoS_2 flexible electrodes for hormones sensing. (B) Triangular MoS_2 and h-BN nanopore biosensor membranes for DNA translocation sensing: schematic of the device, HRTEM images on the nanopores, and simulation of DNA translocation through the h-BN nanopore. (C) Schematic of a pristine Ti_3C_2 electrochemical biosensor for glucose detection by chronoamperometry. *h-BN*, Boron nitride.
Source: Reprinted with permission from (A) H.U. Kim, H.Y. Kim, H. Seok, V. Kanade, H. Yoo, K.Y. Park, et al., Flexible MoS_2-polyimide electrode for electrochemical biosensors and their applications for the highly sensitive quantification of endocrine hormones: PTH, T3, and T4, Anal. Chem. 92 (2020) 6327−6333, Copyright 2020, American Chemical Society; (B) K. Liu, M. Lihter, A. Sarathy, S. Caneva, H. Qiu, D. Deiana, et al., Geometrical effect in 2D nanopores, Nano Lett. 17 (2017) 4223−4230, Copyright 2017, American Chemical Society; (C) H.L. Chia, C.C. Mayorga-Martinez, N. Antonatos, Z. Sofer, J.J. Gonzalez-Julian, R.D. Webster, et al., MXene titanium carbide-based biosensor: strong dependence of exfoliation method on performance, Anal. Chem. 92 (2020) 2452−2459, Copyright 2020, American Chemical Society.

(T3-BSA, T4-BSA, or PTH) antibodies were used to detect the antigen concentration (T3-BSA, T4-BSA, or PTH) in a competitive enzyme-linked immunoassay. The method was successfully applied for the detection of the hormones at pg L^{-1} levels in serum from real patients [60].

MoS_2 and WS_2 have been combined with carbon black into a hybrid material used for screen-printed electrode modification in the detection of catechins and phenols in complex samples such as olive oil and cocoa. Compared with the use of each nanomaterials alone, the hybrid exhibits improved charge-transfer ability with high electrical conductivity and enhanced electrocatalysis, also preventing electrode fouling [61−63]. A comprehensive study comparing the electrochemical performance of MX_2 nanosheet-based electrodes (where M: Mo or W; X: S or Se) prepared by sonochemical exfoliation revealed that the best results in terms of electrochemical performance were obtained for selenides. In addition, antifouling properties extensive to all MX_2 were demonstrated and the electrochemical mechanism behind was proposed [64].

MoS_2 (and h-BN) also displays nanopores in the structure that can be used to develop single-molecule nanopore−based (bio)-sensors, as illustrated by Radenovic et al. for DNA analysis [6]. For the nanopores preparation, authors deposited MoS_2 and h-BN over a small opening of SiN_x membranes by CVD. This resulted in atomic-scale defects that were exploited for further sensing based on the ionic blockage induced by DNA translocation. The device/membrane was assembled between two reservoirs filled with saline solution connected to a current amplifier to apply bias across the membrane (see Fig. 2.5B). The geometrical effect of the nanopores (circular for MoS_2 and triangular for h-BN) was modeled to study the role in the sensing performance. The simulations and results demonstrate that the devices can be used for DNA sequencing, as DNA translocation exhibits changes in the resistance of the pore (with can be measured) both for MoS_2 and h-BN nanopores [6].

MXenes are also promising materials for electrochemical (bio)-sensor designs, yet the potential has been started to be explored very recently. Nb_2C/ZnS nanocomposites have been used for dopamine sensing by differential pulse voltammetry. The composite was used for the direct modification of a glassy-carbon electrode, achieving enhanced sensitivity and selectivity in the detection of dopamine when compared with bare materials, with a low LOD (1.4 μM) and a wide LR [65]. Multiwalled carbon nanotubes (MWCNTs)/Ti_3C_2 MXene/chitosan nanocomposites have been employed to modified glassy-carbon electrodes for ifosfamide, acetaminophen, domperidone, and sumatriptan detection by cyclic voltammetry and adsorptive stripping differential pulse voltammetry. The composites display enhanced electrocatalytic activities toward the oxidation of target analytes for the detection of the analytes at levels as low as 3×10^{-4} μM, with high selectivity in urine and other complex samples [66]. Pristine Ti_3C_2 has been used as a transducer for electrochemical glucose biosensing by chronoamperometry (see Fig. 2.5C). High sensitivity and selectivity have been achieved, with a LOD of 23.0 μM, lower or comparable to recent glucose biosensors [67]. In a more sophisticated configuration, $Ti_3C_2T_x$ MXene/ink composites have been used to construct strain-wearable sensors, which hold considerable promise to monitor real-time human motion or metabolites such as glucose for future on-body biosensing [68].

2D leaflike ZIFs (Co-ZIF and Fe-ZIF) have been combined with Prussian blue, resulting in a greatly enhanced electron/mass transfer for highly selective and sensitive glucose and H_2O_2 biosensing with a high selectivity and very low LOD of 0.02 μM and 1.08 nM, respectively, in human serum [69]. Gold nanoparticles−decorated h-BN composites, prepared by a hydrothermal method, were used to modify a tin oxide electrode. The electrode was used as a transducer to immobilize a thiol-functionalized DNA aptamer for electrochemical detection of myoglobin. A LOD of 35 ng mL^{-1} was achieved, holding considerable promise for point-of-care diagnosis [70].

2.3.3 Optical sensors

Quantum materials have also been explored in optical sensing. Indeed, the interaction between light and quantum materials can produce changes in the intensity or spectral shift of compounds that can be monitored as analytical signal by different

means. The unique properties of quantum materials can be exploited to develop optical biosensing platforms including fluorescence, photoluminescence, surface plasmon resonance (SPR), or surface-enhanced Raman scattering (SERS). Some details and selected references will be discussed in this section.

The synergy between TMDs and graphene has been explored to enhance the sensitivity of SPR biosensors. Thus $Ag/PtSe_2/WS_2$ and $Au/PtSe_2/WS_2$ structures, respectively, show up to a 1.8 increase in sensitivity when compared with conventional Ag- and Au- based sensors [71]. Ti_3C_2 MXene-MWCNTs-polydopamine-AgNPs nanocomposites have been also used as substrates to enhance SPR biosensing of monoclonal anti-CEA antibody detection. Fig. 2.6 illustrates the preparation of the biosensor. On a first step the MXene is modified with gold nanoparticles followed by the immobilization of staphylococcal protein A (SPA) to orient the immobilization of CEA antibodies (Ab). For sensing, different concentrations of CEA were mixed with MWCNTs-Ag composites modified with Ab_2, followed addition with the MXene-modified composites to generate a sandwich. This result in a signal change, directly related with the concentration of the analyte, which can be used

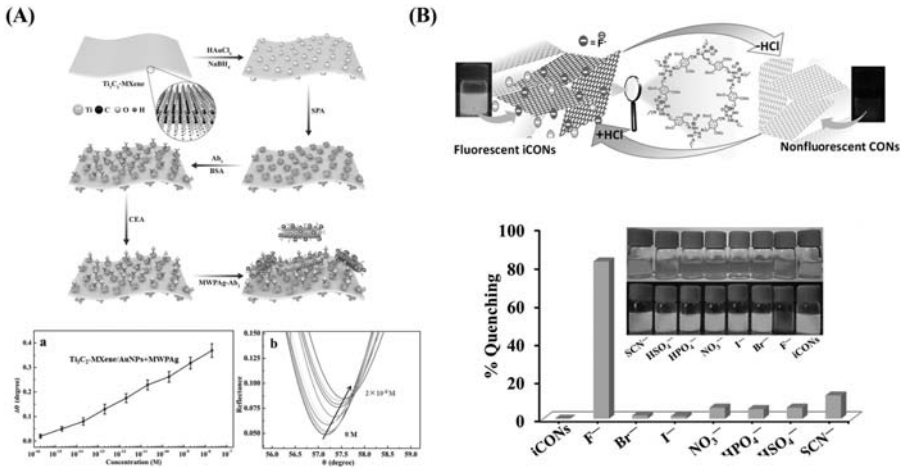

Figure 2.6 (A) Schematic of an MXene-based biosensor for CEA antigen detection and related contact angle measurements and calibration. (B) COFs for fluorine ion sensing: schematic of the sensing mechanism and corresponding quenching plot. *CEA*, Carcinoembryonic antigen; *COF*, covalent organic framework; *SPR*, surface plasmon resonance.

Source: Reprinted with permission from (A) Q. Wu, N. Li, Y. Wang, Y. Liu, Y. Xu, S. Wei, et al., A 2D transition metal carbide MXene-based SPR biosensor for ultrasensitive carcinoembryonic antigen detection, Biosens. Bioelectron. 144 (2019) 111697, Copyright 2019, American Chemical Society; (B) H. Singh, M. Devi, N. Jena, M.M. Iqbal, Y. Nailwal, A. De Sarkar, et al., Proton-triggered fluorescence switching in self-exfoliated ionic covalent organic nanosheets for applications in selective detection of anions, ACS Appl. Mater. Interfaces 12 (2020) 13248−13255, Copyright 2020, American Chemical Society.

for calibration (see Fig. 2.6). A LOD of 0.07 fM was achieved with good method performance in serum samples [72].

Fluorescence approaches also explore the rich surface chemistry of MXenes for ON−OFF bioassays. For example, Ti_3C_2 has been used for the analysis of human papillomavirus (HPV). The MXene can efficiently quench specific dye-labeled single-stranded DNA (ssDNA) along with different affinities for ssDNA and double-stranded DNA. Under the absence of the analyte the fluorescence of the solution is quenched. In the presence of HPV a duplex structure is formed with the complementary target (ssDNA), with a clear enhance in the fluorescence intensity, which can be related with the concentration of the analyte. A LOD of 100 pM was achieved with excellent capabilities for direct detection in cervical scrapes samples [73]. In an attractive approach, chlorine and nitrogen codoped Ti_3C_2 MXene quantum dots with hydroxyl radical scavenging properties hold considerable promise for fluorescence-detection approaches [74].

COFs have been used for fluoride ions sensing. A schematic of the sensing mechanism and corresponding quenching in the presence of several ions and the target analyte is illustrated in Fig. 2.6B. As can be seen, the method displays a high selectivity with a low LOD of 5 ppb [75].

The combination of quantum materials such as BP and ZnO with dyes can result in a great enhancement of the SERS signal for the detection of several analytes. As such, BP has been modified with the dye tetraphenylporphyrin tetrasulfonic acid hydrate and used as SERS substrate for highly enhanced crystal violet detection. The synergetic effect between BP and dye increases electromagnetic and other chemical effects that are mainly responsible for such behavior [57]. Similarly, the functionalization of ZnO with probes was tested with positively charged molecules of crystal violet and negatively charged molecules of methyl orange, and ~700-fold improvement in the SERS response was achieved, holding considerable promise for future live biomolecular detection as illustrated for tryptophan [80].

2.3.4 Photodetectors

Photoelectrochemical sensing is a cutting-edge analytical topic that relies on photoactive materials excited by external light to produce photocurrent readout signal. 2D quantum materials possess unique structures and outstanding photoelectric properties that have been explored to achieve such aim [16,81]. We will give a brief overview of some selected representative examples.

ZnO quantum dots−decorated Zn_2SnO_4 nanowires have been used as ultraviolet photodetectors based on the generation of heterojunctions. The coupling of both materials results in about 10 times higher photocurrent and, in turn, better detection performance. The material was integrated into a 10×10 device array to develop flexible ultraviolet photodetectors for ultraviolet image sensors [76]. A $Ti_3C_2T_x$ MXene/$BiVO_4$ heterojunction electrode was used to develop a highly sensitive photoelectrochemical platform, which was constructed for Hg^{2+} determination with a LOD down to 1 pM. The sensing principle relies on the modification of the film with glutathione. In the presence of Hg^{2+} the photocurrent of the electrode

decreases significantly due to chelation with the glutathione in a concentration-dependent manner [77].

2.4 Conclusions

In this chapter, we have presented a comprehensive overview on the use of the unique properties of quantum materials for the development of a myriad of (bio)-sensor devices in the analytical chemistry field. Among the myriad of quantum materials, 2D nanomaterials are the most commonly employed for such purpose, as revealed by the increasing number of publications and studied in the last 2−3 years. One important application is the development of gas sensors based on quantum materials, with many relevant applications in environmental monitoring and health-care assurance and testing. The most commonly used 2D materials for this purpose were nanocomposites materials exploring the synergetic effect among TMDs, TMOs, MXenes, BP, and h-BN, being the most commonly used detection mode electrochemical resistance. Such sensors hold considerable promise for real-time gas monitoring with many applications and room at the bottom for more applications in the near future. Another important aspect is devoted to the design of electrochemical and optical biosensors, where the high conductivity of quantum materials and increased surface area greatly improve the analytical characteristic and sensing performance. MXenes are the most commonly used quantum materials for such purpose. As previously indicated, the combination of different quantum materials into nanocomposites and heterostructures result in novel phenomena and improved properties that benefit the sensing events. Still, many challenges lie ahead, including scalable and cost-effective synthesis (especially in the case of MXenes), uniformity, or the exploration of toxicology concerns.

Overall, the field of 2D materials is advancing at a rapid pace, with the preliminary and recent studies presented here further supporting the advantages and improved sensing performance of different procedure based on 2D nanomaterials. As such, they hold considerable promise to develop wearable sensors, point-of-care devices, and gas sensors in a myriad of biomedical, analytical, and environmental applications.

Acknowledgments

B. J.-S. acknowledges support from the Ministry of Economy, Industry, and Competitiveness (RYC-2015-17558, cofinanced by EU) from the University of Alcala (CCG19/CC-029) and from the Community of Madrid (CM/JIN/2021-012). A. E. acknowledges financial support from the Ministry of Economy, Industry, and Competitiveness (CTQ2017-86441-C2-1-R) and the TRANSNANOAVANSENS program (S2018/NMT-4349) from the Community of Madrid. B. J.-S and A.E. acknowledge grant PID-2020-118154GB-I00 funded by MCIN/ AEI/ 10.13039/501100011033.

References

[1] C.N. Lau, F. Xia, L. Cao, Emergent quantum materials, MRS Bull. 45 (2020) 340−347.
[2] F. Giustino, M. Bibes, J.H. Lee, F. Trier, R. Valentí, S.M. Winter, et al., The 2020 quantum materials roadmap, J. Phys. Mater. 3 (2020) 042006.
[3] Enter 2D quantum materials, Nat. Mater. 19 (2020) 1255.
[4] D.N. Basov, R.D. Averitt, D. Hsieh, Towards properties on demand in quantum materials, Nat. Mater. 16 (2017) 1077−1088.
[5] Y. Khan, S.M. Obaidulla, M.R. Habib, A. Gayen, T. Liang, X. Wang, et al., Recent breakthroughs in two-dimensional van der Waals magnetic materials and emerging applications, Nano Today 34 (2020) 100902.
[6] K. Liu, M. Lihter, A. Sarathy, S. Caneva, H. Qiu, D. Deiana, et al., Geometrical effect in 2D nanopores, Nano Lett. 17 (2017) 4223−4230.
[7] M. Modayil Korah, T. Nori, S. Tongay, M.D. Green, Harnessing biological applications of quantum materials: opportunities and precautions, J. Mater. Chem. C 8 (2020) 10498−10525.
[8] M. Chen, D. Liu, X. Du, K.H. Lo, S. Wang, B. Zhou, et al., 2D materials: excellent substrates for surface-enhanced Raman scattering (SERS) in chemical sensing and biosensing, Trends Anal. Chem. 130 (2020) 115983.
[9] B. Wang, Y. Sun, H. Ding, X. Zhao, L. Zhang, J. Bai, et al., Bioelectronics-related 2D materials beyond graphene: fundamentals, properties, and applications, Adv. Funct. Mater. 30 (2020) 2003732.
[10] K.S. Novoselov, A.K. Geim, S.V. Morozov, D. Jiang, Y. Zhang, S.V. Dubonos, et al., Electric field effect in atomically thin carbon films, Science 306 (2004) 666−669.
[11] C.I.L. Justino, A.R. Gomes, A.C. Freitas, A.C. Duarte, T.A.P. Rocha-Santos, Graphene based sensors and biosensors, Trends Anal. Chem. 91 (2017) 53−66.
[12] S. Kochmann, T. Hirsch, O.S. Wolfbeis, Graphenes in chemical sensors and biosensors, Trends Anal. Chem. 39 (2012) 87−113.
[13] X.-M. Chen, G.-h Wu, Y.-q Jiang, Y.-r Wang, X. Chen, Graphene and graphene-based nanomaterials: the promising materials for bright future of electroanalytical chemistry, Analyst 136 (2011) 4631−4640.
[14] Y. Chen, X. Gu, Y. Li, X. Du, L. Yang, Y. Chen, Recent advances in topological quantum materials by angle-resolved photoemission spectroscopy, Matter 3 (2020) 1114−1141.
[15] L.M. Schoop, Layer-cake 2D superconductivity, Science 370 (2020) 170.
[16] B. Wang, S. Zhong, P. Xu, H. Zhang, Booming development and present advances of two dimensional MXenes for photodetectors, Chem. Eng. J. 403 (2021) 126336.
[17] C. Tan, X. Cao, X.-J. Wu, Q. He, J. Yang, X. Zhang, et al., Recent advances in ultrathin two-dimensional nanomaterials, Chem. Rev. 117 (2017) 6225−6331.
[18] M. Zhao, Y. Huang, Y. Peng, Z. Huang, Q. Ma, H. Zhang, Two-dimensional metal−organic framework nanosheets: synthesis and applications, Chem. Soc. Rev. 47 (2018) 6267−6295.
[19] M. Chhowalla, H.S. Shin, G. Eda, L.-J. Li, K.P. Loh, H. Zhang, The chemistry of two-dimensional layered transition metal dichalcogenide nanosheets, Nat. Chem. 5 (2013) 263−275.
[20] D. Voiry, A. Mohite, M. Chhowalla, Phase engineering of transition metal dichalcogenides, Chem. Soc. Rev. 44 (2015) 2702−2712.
[21] A. Splendiani, L. Sun, Y. Zhang, T. Li, J. Kim, C.-Y. Chim, et al., Emerging photoluminescence in monolayer MoS_2, Nano Lett. 10 (2010) 1271−1275.

[22] T.A. Su, M. Neupane, M.L. Steigerwald, L. Venkataraman, C. Nuckolls, Chemical principles of single-molecule electronics, Nat. Rev. Mater. 1 (2016) 16002.
[23] B. He, A sandwich-type electrochemical biosensor for alpha-fetoprotein based on Au nanoparticles decorating a hollow molybdenum disulfide microbox coupled with a hybridization chain reaction, New J. Chem. 41 (2017) 11353−11360.
[24] S. Balendhran, S. Walia, H. Nili, J.Z. Ou, S. Zhuiykov, R.B. Kaner, et al., Two-dimensional molybdenum trioxide and dichalcogenides, Adv. Funct. Mater. 23 (2013) 3952−3970.
[25] R. Enjalbert, J. Galy, A refinement of the structure of V_2O_5, Acta Crystallogr. C. 42 (1986) 1467−1469.
[26] K. Kalantar-zadeh, J.Z. Ou, T. Daeneke, A. Mitchell, T. Sasaki, M.S. Fuhrer, Two dimensional and layered transition metal oxides, Appl. Mater. Today 5 (2016) 73−89.
[27] M. Osada, T. Sasaki, Exfoliated oxide nanosheets: new solution to nanoelectronics, J. Mater. Chem. 19 (2009) 2503−2511.
[28] Y. Wang, K. Jiang, J. Zhu, L. Zhang, H. Lin, A FRET-based carbon dot−MnO_2 nanosheet architecture for glutathione sensing in human whole blood samples, Chem. Commun. 51 (2015) 12748−12751.
[29] Z. Zhao, H. Fan, G. Zhou, H. Bai, H. Liang, R. Wang, et al., Activatable fluorescence/MRI bimodal platform for tumor cell imaging via MnO_2 nanosheet−aptamer nanoprobe, J. Am. Chem. Soc. 136 (2014) 11220−11223.
[30] M. Naguib, V.N. Mochalin, M.W. Barsoum, Y. Gogotsi, 25th Anniversary Article: MXenes: a new family of two-dimensional materials, Adv. Mater. 26 (2014) 992−1005.
[31] Z.W. Seh, K.D. Fredrickson, B. Anasori, J. Kibsgaard, A.L. Strickler, M.R. Lukatskaya, et al., Two-dimensional molybdenum carbide (MXene) as an efficient electrocatalyst for hydrogen evolution, ACS Energy Lett. 1 (2016) 589−594.
[32] M. Magnuson, M. Mattesini, Chemical bonding and electronic-structure in MAX phases as viewed by X-ray spectroscopy and density functional theory, Thin Solid Films 621 (2017) 108−130.
[33] K. Deshmukh, T. Kovářík, S.K. Khadheer Pasha, State of the art recent progress in two dimensional MXenes based gas sensors and biosensors: a comprehensive review, Coord. Chem. Rev. 424 (2020) 213514.
[34] X. Zhu, Y. Zhang, M. Liu, Y. Liu, 2D titanium carbide MXenes as emerging optical biosensing platforms, Biosens. Bioelectron. 171 (2021) 112730.
[35] M. Safaei, M.M. Foroughi, N. Ebrahimpoor, S. Jahani, A. Omidi, M. Khatami, A review on metal-organic frameworks: synthesis and applications, Trends Anal. Chem. 118 (2019) 401−425.
[36] H.C. Zhou, J.R. Long, O.M. Yaghi, Introduction to metal−organic frameworks, Chem. Rev. 112 (2012) 673−674.
[37] S.-Y. Ding, W. Wang, Covalent organic frameworks (COFs): from design to applications, Chem. Soc. Rev. 42 (2013) 548−568.
[38] A. Brown, S. Rundqvist, Refinement of the crystal structure of black phosphorus, Acta Crystallogr. 19 (1965) 684−685.
[39] S. Anju, J. Ashtami, P.V. Mohanan, Black phosphorus, a prospective graphene substitute for biomedical applications, Mater. Sci. Eng., C 97 (2019) 978−993.
[40] L. Liu, Y.P. Feng, Z.X. Shen, Structural and electronic properties of h-BN, Phys. Rev. B 68 (2003) 104102.
[41] A. Ohtomo, H.Y. Hwang, A high-mobility electron gas at the $LaAlO_3/SrTiO_3$ heterointerface, Nature 427 (2004) 423−426.

[42] A. Avsar, J.Y. Tan, T. Taychatanapat, J. Balakrishnan, G.K.W. Koon, Y. Yeo, et al., Spin−orbit proximity effect in graphene, Nat. Commun. 5 (2014) 4875.
[43] R. Bistritzer, A.H. MacDonald, Moiré bands in twisted double-layer graphene, Proc. Natl. Acad. Sci. U.S.A. 108 (2011) 12233−12237.
[44] C. Murugan, V. Sharma, R.K. Murugan, G. Malaimegu, A. Sundaramurthy, Two-dimensional cancer theranostic nanomaterials: synthesis, surface functionalization and applications in photothermal therapy, J. Control. Release 299 (2019) 1−20.
[45] X. Cai, Y. Luo, B. Liu, H.-M. Cheng, Preparation of 2D material dispersions and their applications, Chem. Soc. Rev. 47 (2018) 6224−6266.
[46] G. Guan, M.-Y. Han, Functionalized hybridization of 2D nanomaterials, Adv. Sci. 6 (2019) 1901837.
[47] C.H. Park, W.T. Koo, Y.J. Lee, Y.H. Kim, J. Lee, J.S. Jang, et al., Hydrogen sensors based on MoS_2 hollow architectures assembled by Pickering emulsion, ACS Nano 14 (2020) 9652−9661.
[48] A. Ali, O. Koybasi, W. Xing, D.N. Wright, D. Varandani, T. Taniguchi, et al., Single digit parts-per-billion NO_x detection using MoS_2/hBN transistors, Sens. Actuators, A: Phys. 315 (2020) 112247.
[49] T. Pham, P. Ramnani, C.C. Villarreal, J. Lopez, P. Das, I. Lee, et al., MoS_2-graphene heterostructures as efficient organic compounds sensing 2D materials, Carbon 142 (2019) 504−512.
[50] M. Cheng, Z. Wu, G. Liu, L. Zhao, Y. Gao, B. Zhang, et al., Highly sensitive sensors based on quasi-2D rGO/SnS_2 hybrid for rapid detection of NO_2 gas, Sens. Actuators, B: Chem. 291 (2019) 216−225.
[51] Z. Song, Z. Wei, B. Wang, Z. Luo, S. Xu, W. Zhang, et al., Sensitive room-temperature H_2S gas sensors employing SnO_2 quantum wire/reduced graphene oxide nanocomposites, Chem. Mater. 28 (2016) 1205−1212.
[52] J. Zeng, Y. Niu, Y. Gong, Q. Wang, H. Li, A. Umar, et al., All-dry transferred ReS_2 nanosheets for ultrasensitive room-temperature NO_2 sensing under visible light illumination, ACS Sens. 5 (2020) 3172−3181.
[53] W.Y. Chen, S.N. Lai, C.C. Yen, X. Jiang, D. Peroulis, L.A. Stanciu, Surface functionalization of $Ti_3C_2T_x$ MXene with highly reliable superhydrophobic protection for volatile organic compounds sensing, ACS Nano 14 (2020) 11490−11501.
[54] A. Hermawan, B. Zhang, A. Taufik, Y. Asakura, T. Hasegawa, J. Zhu, et al., CuO nanoparticles/$Ti_3C_2T_x$ MXene hybrid nanocomposites for detection of toluene gas, ACS Appl. Nanomater. 3 (2020) 4755−4766.
[55] E. Lee, A. VahidMohammadi, B.C. Prorok, Y.S. Yoon, M. Beidaghi, D.J. Kim, Room temperature gas sensing of two-dimensional titanium carbide (MXene), ACS Appl. Mater. Interfaces 9 (2017) 37184−37190.
[56] E. Lee, A. VahidMohammadi, Y.S. Yoon, M. Beidaghi, D.J. Kim, Two-dimensional vanadium carbide MXene for gas sensors with ultrahigh sensitivity toward nonpolar gases, ACS Sens. 4 (2019) 1603−1611.
[57] R. Wang, X. Yan, B. Ge, J. Zhou, M. Wang, L. Zhang, et al., Facile preparation of self-assembled black phosphorus-dye composite films for chemical gas sensors and surface-enhanced raman scattering performances, ACS Sustain. Chem. Eng. 8 (2020) 4521−4536.
[58] H. Ren, Y. Zhou, Y. Wang, X. Zhu, C. Gao, Y. Guo, Improving room-temperature trace NO_2 sensing of black phosphorus nanosheets by incorporating benzyl viologen, Sens. Actuators, B: Chem. 321 (2020) 128520.

[59] H. Cui, K. Zheng, Z. Xie, J. Yu, X. Zhu, H. Ren, et al., Tellurene nanoflake-based NO_2 sensors with superior sensitivity and a sub-parts-per-billion detection limit, ACS Appl. Mater. Interfaces 12 (2020) 47704−47713.
[60] H.U. Kim, H.Y. Kim, H. Seok, V. Kanade, H. Yoo, K.Y. Park, et al., Flexible MoS_2-polyimide electrode for electrochemical biosensors and their applications for the highly sensitive quantification of endocrine hormones: PTH, T3, and T4, Anal. Chem. 92 (2020) 6327−6333.
[61] D. Rojas, F. Della Pelle, M. Del Carlo, E. Fratini, A. Escarpa, D. Compagnone, Nanohybrid carbon black-molybdenum disulfide transducers for preconcentration-free voltammetric detection of the olive oil o-diphenols hydroxytyrosol and oleuropein, Microchim. Acta 186 (2019) 363.
[62] F. Della Pelle, D. Rojas, A. Scroccarello, M. Del Carlo, G. Ferraro, C. Di Mattia, et al., High-performance carbon black/molybdenum disulfide nanohybrid sensor for cocoa catechins determination using an extraction-free approach, Sens. Actuators, B: Chem. 296 (2019) 12665.
[63] F. Della Pelle, D. Rojas, F. Silveri, G. Ferraro, E. Fratini, A. Scroccarello, et al., Class-selective voltammetric determination of hydroxycinnamic acids structural analogs using a WS_2/catechin-capped AuNPs/carbon black−based nanocomposite sensor, Microchim. Acta 187 (2020) 296.
[64] F. Della Pelle, D. Rojas, F. Silveri, G. Ferraro, E. Fratini, A. Scroccarello, et al., VI transition metal dichalcogenides as antifouling transducers for electrochemical oxidation of catechol-containing structures, Electrochem. Commun. 115 (2020) 106718.
[65] N. Arif, S. Gul, M. Sohail, S. Rizwan, M. Iqbal, Synthesis and characterization of layered Nb_2C MXene/ZnS nanocomposites for highly selective electrochemical sensing of dopamine, Ceram. Int. 47 (2021) 2388−2396.
[66] P.K. Kalambate, Dhanjai, A. Sinha, Y. Li, Y. Shen, Y. Huang, An electrochemical sensor for ifosfamide, acetaminophen, domperidone, and sumatriptan based on self-assembled MXene/MWCNT/chitosan nanocomposite thin film, Microchim. Acta 187 (2020) 402.
[67] H.L. Chia, C.C. Mayorga-Martinez, N. Antonatos, Z. Sofer, J.J. Gonzalez-Julian, R.D. Webster, et al., MXene titanium carbide-based biosensor: strong dependence of exfoliation method on performance, Anal. Chem. 92 (2020) 2452−2459.
[68] Z. Ma, K. Ma, S. Lu, S. Wang, X. Liu, B. Li, et al., Flexible $Ti_3C_2T_x$ MXene/ink human wearable strain sensors with high sensitivity and a wide sensing range, Sens. Actuators, A: Phys. 315 (2020) 112304.
[69] C. Chen, D. Xiong, M. Gu, C. Lu, F.Y. Yi, X. Ma, MOF-derived bimetallic CoFe-PBA composites as highly selective and sensitive electrochemical sensors for hydrogen peroxide and nonenzymatic glucose in human serum, ACS Appl. Mater. Interfaces 12 (2020) 35365−35374.
[70] M. Adeel, M.M. Rahman, J.J. Lee, Label-free aptasensor for the detection of cardiac biomarker myoglobin based on gold nanoparticles decorated boron nitride nanosheets, Biosens. Bioelectron. 126 (2019) 143−150.
[71] M.M. Rahman, M.M. Rana, M.S. Rahman, M.S. Anower, M.A. Mollah, A.K. Paul, Sensitivity enhancement of SPR biosensors employing heterostructure of $PtSe_2$ and 2D materials, Opt. Mater. 107 (2020) 110123.
[72] Q. Wu, N. Li, Y. Wang, Y. Liu, Y. Xu, S. Wei, et al., A 2D transition metal carbide MXene-based SPR biosensor for ultrasensitive carcinoembryonic antigen detection, Biosens. Bioelectron. 144 (2019) 111697.

[73] X. Peng, Y. Zhang, D. Lu, Y. Guo, S. Guo, Ultrathin Ti_3C_2 nanosheets based "OFF-ON" fluorescent nanoprobe for rapid and sensitive detection of HPV infection, Sens. Actuators, B: Chem. 286 (2019) 222−229.
[74] L. Zhao, Z. Wang, Y. Li, S. Wang, L. Wang, Z. Qi, et al., Designed synthesis of chlorine and nitrogen co-doped Ti_3C_2 MXene quantum dots and their outstanding hydroxyl radical scavenging properties, J. Mater. Sci. Technol. 78 (2021) 30−37.
[75] H. Singh, M. Devi, N. Jena, M.M. Iqbal, Y. Nailwal, A. De Sarkar, et al., Proton-triggered fluorescence switching in self-exfoliated ionic covalent organic nanosheets for applications in selective detection of anions, ACS Appl. Mater. Interfaces 12 (2020) 13248−13255.
[76] L. Li, L. Gu, Z. Lou, Z. Fan, G. Shen, ZnO quantum dot decorated Zn_2SnO_4 nanowire heterojunction photodetectors with drastic performance enhancement and flexible ultraviolet image sensors, ACS Nano 11 (2017) 4067−4076.
[77] Q. Jiang, H. Wang, X. Wei, Y. Wu, W. Gu, L. Hu, et al., Efficient $BiVO_4$ photoanode decorated with $Ti_3C_2T_x$ MXene for enhanced photoelectrochemical sensing of Hg(II) ion, Anal. Chim. Acta 1119 (2020) 11−17.
[78] Z. Cui, C. Xiao, Y. Lv, Q. Li, R. Sa, Z. Ma, Adsorption behavior of CO, CO_2, H_2, H_2O, NO, and O_2 on pristine and defective 2D monolayer ferromagnetic Fe_3GeTe_2, Appl. Surf. Sci. 527 (2020) 146894.
[79] A. Hulanicki, S. Glab, F. Ingman, Chemical sensors: definitions and classification, Pure Appl. Chem. 63 (1991) 1247−1250.
[80] R. Haldavnekar, K. Venkatakrishnan, B. Tan, Functionalized, complementary live-charge quantum surface-enhanced raman scattering probes for biomolecular detection, ACS Appl. Nanomater. 3 (2020) 6945−6961.
[81] J. Wang, Z. Liu, Recent advances in two-dimensional layered materials for photoelectrochemical sensing, Trends Anal. Chem. 133 (2020) 116089.

This page intentionally left blank

Superconducting quantum magnetic sensing

3

Antonio Vettoliere[1], *Paolo Silvestrini*[2] *and Carmine Granata*[1,2]
[1]National Research Council, Institute of Applied Science and Intelligent Systems, Pozzuoli (Napoli), Italy, [2]Department of Mathematics and Physics, University of Campania "L. Vanvitelli", Caserta, Italy

3.1 Principles of superconducting quantum magnetic sensing

3.1.1 Introduction

Thanks to their extraordinary properties, superconductors allow for ultrahigh magnetic sensing. In particular, the superconducting quantum interference devices (SQUIDs) are among the most sensitive detectors of magnetic flux and field known, with an equivalent energy sensitivity that approaches the quantum limit (Fig. 3.1). Thanks to their unique properties, SQUID devices are widely used in several applications [1−4] such as biomagnetism, magnetic microscopy, nondestructive evaluation (NDE), geophysics, astrophysics, quantum information, particle physics, and, recently, also in nanoscience.

The purpose of this chapter is to give a brief overview of SQUID devices and their main applications. Before that, we will briefly recall the main characteristics of superconductors. There are materials that, at temperatures close to absolute zero, do not offer any resistance to the passage of current. They are superconducting materials. The temperature at which the transition between normal and superconducting phases occurs is called the critical temperature (T_c) [5−7]. It is important to stress that it is a phase transition and that the resistance after the transition is exactly zero. Superconductivity was discovered in 1911 by physicist Heike Kamerlingh Onnes, while studying a sample of mercury at temperatures close to absolute zero (Onnes is most famous for being able to create liquid helium). At about 4K, the resistivity of mercury to the passage of current suddenly becomes zero: this means that the electrons are able to move in the material without losing energy, in a kind of "perpetual motion" (typically we speak of supercurrent). Another extraordinary effect presented by superconductors is the Meissner−Ochsenfeld effect, discovered in 1933 [5−7]. If you cool a superconductor, in a magnetic field, currents are created on the surface of the superconductor, which induce a magnetic field opposite to that applied. Basically it means that a superconductor behaves like a perfect diamagnet. This effect is what allows to obtain a stable magnetic levitation. On the basis of the value of the T_c, we can divide the superconductors into two categories: low critical temperature

Quantum Materials, Devices, and Applications. DOI: https://doi.org/10.1016/B978-0-12-820566-2.00001-6

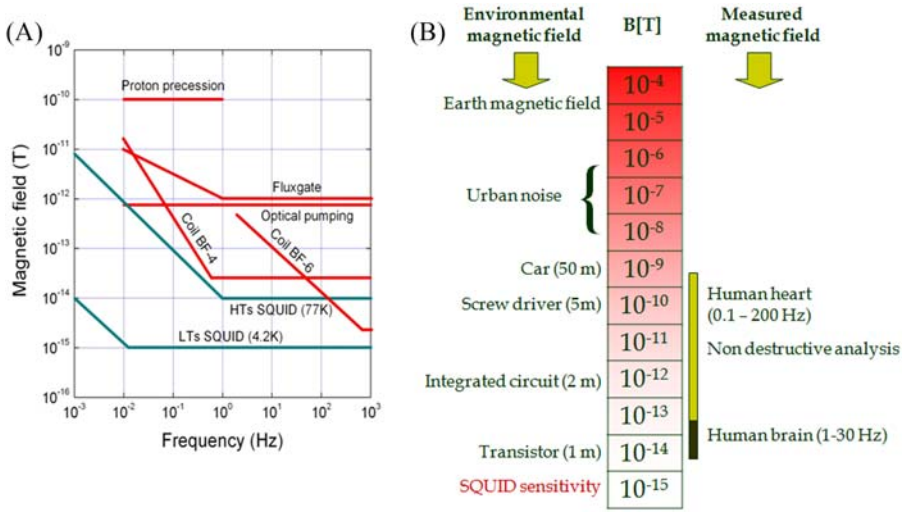

Figure 3.1 (A) Comparison of SQUID magnetic sensitivity with other devices as a function of the frequency. (B) Amplitudes of the environment magnetic signals and the biomagnetic signal. The SQUID sensitivity is the lowest among them. *SQUID*, Superconducting quantum interference device.

superconductors, typically metals, ($T_c < 10$K) and superconductors with high critical temperature superconductors (HTSs), typically ceramic compounds ($T_c < 140$K) [6].

Classical physics is not enough to explain the behavior of superconductors, and it is necessary to use the laws of quantum mechanics. In the 1950s the physicists, Bardeen, Cooper, and Schrieffer (BCS), developed a theory to describe the phenomenon of superconductivity. The BCS theory predicts that in superconductors the electrons unite to form pairs, called Cooper pairs, and that these pairs (supercurrent) carry the electric charge instead of the single electrons. However, these pairs no longer behave as fermions, but as bosons, obeying completely different physical laws and being able to move more freely in the material.

3.1.2 Josephson effect and flux quantization in a superconducting ring

The Josephson effect was predicted in 1962 by Brian Josephson [8,9]. He stated that a supercurrent could tunnel through an insulating barrier separating two superconductors. A Josephson junction is schematically represented by two superconductors separated by a thin insulation barrier (Fig. 3.2). If the junction is biased with a dc current, the voltage across it remains zero up to a current value called Josephson critical current I_0 due to the cooper pair-tunneling through the insulation barrier. This so-called dc Josephson effect occurs due to the overlap of the macroscopic wave functions in the barrier region (Fig. 3.2).

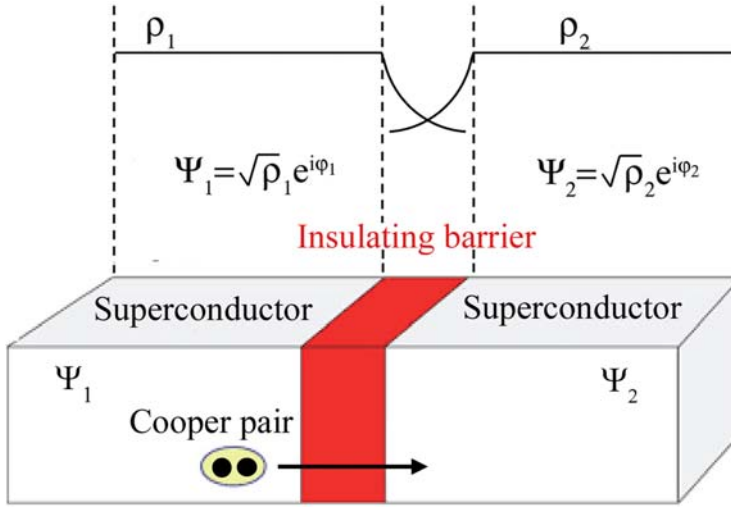

Figure 3.2 Scheme of a Josephson junction. A thin insulator barrier (few nm) separates the two superconductors (tunnel junction). The overlap of the macroscopic wave functions allows the tunneling of the Cooper pair.

When the bias current is greater than I_0, the junction switches in a resistive state where the tunnel is due to the single electrons.

The fundamental equations of the Josephson effect are as follows:

$$I = I_0 \sin \phi \tag{3.1}$$

$$\frac{\partial \phi}{\partial t} = \frac{2e}{\hbar} V \tag{3.2}$$

where I_0 is the critical current and φ is the phase difference between the macroscopic wave functions of the cooper pairs relative to the two superconductors, and V is the voltage across the junction. If the voltage across the junction is constant, the phase difference is a linear function of the time $\varphi = (2e/h)V \cdot t + \varphi_0$, which, substituted in the first Josephson equation, gives an oscillating current at nonzero voltage: $I = I_0 \sin(2\pi ft + \varphi_0)$ where $f = (2e/h)V/2\pi$ (486.6 MHz μV^{-1}). This effect, known as the Josephson ac effect [10], has been successfully employed in metrology and several other applications [2]. An exhaustive review of the Josephson effect can be found in Ref. [9]. An overlap of the macroscopic wave functions of the two superconductors, which implies the Josephson effect, can be also obtained by using different structures such as Dayem bridges (nanoconstrictions of superconductor) or other structures [9].

From the application point of view, the use of Josephson junctions involves various fields, ranging from metrology to radiation detectors and more generally a stimulating new electronics that exploits the characteristics of superconducting devices: high speed, low dissipation, and low dispersion.

The magnetic flux quantization states that the magnetic flux treading a superconducting loop exists only in multiples of the flux quantum ($\Phi = n\Phi_0$, $\Phi_0 = h/(2e)$) = 2.07×10^{-15} T m^2, where h is the Plank constant and e is the electron charge [11]. Physically, it is due to the Meissner effect. In the case of a superconducting ring, the discrete quantities of flux can be trapped into the ring rather than expelled as in a continuous superconductor. This magnetic flux is sustained by a persistent circulating current inside the ring, $J = \Phi/L$, where L is the inductance of the ring and $\Phi = B \cdot S$ is the applied magnetic flux.

3.1.3 Working principle of a SQUID

The operation principle of a SQUID is based on the Josephson effect and the flux quantization in a superconducting ring. Here, we will provide the principle of operation of a SQUID, while an exhaustive analysis can be found in Refs. [1,2]. A dc-SQUID sensor is a converter of magnetic flux into a voltage having an extremely low magnetic flux noise. Basically, it consists of a superconducting ring interrupted by two Josephson junctions. The voltage across the SQUID is a periodic function of the external magnetic flux treading the SQUID ring with a period equal to the flux quantum Φ_0. The typical SQUID configuration is schematically shown in Fig. 3.3. The two Josephson junctions are in a parallel configuration, so the critical current of the SQUID is $I_c = I_1 + I_2$ or $I_c = 2I_0$, if the Josephson junctions are identical. In the presence of an external magnetic field treading the SQUID loop, I_c oscillates with a period of one flux quantum. This is due to the interference of superconducting wave functions in the two arms of the SQUID and analog to the two slit interference in optics. It is the basis of the working principle of a SQUID. If the SQUID is biased with a constant current at a value greater than I_c (Fig. 3.4A), the voltage across it also oscillates (Fig. 3.4B). By measuring the SQUID output voltage, it is possible to obtain the magnetic flux treading the SQUID.

Why is SQUID so sensitive? The superconductivity is one of the most spectacular manifestations of the macroscopic quantum physics. Being a macroscopic object as a superconductor described by a wave function, there are macroscopic physical

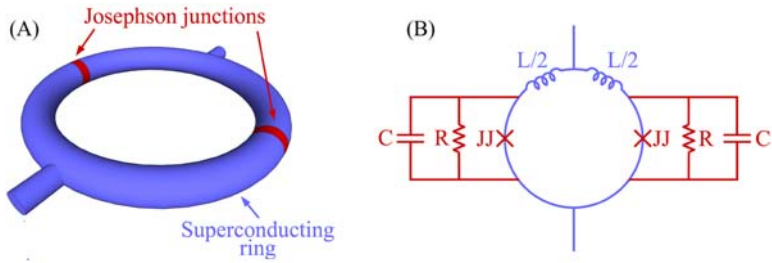

Figure 3.3 (A) Scheme of a SQUID: a superconducting ring interrupted by two Josephson junctions. (B) Equivalent electric circuit of a dc-SQUID in the framework of the resistively and capacitively shunted model of a Josephson junction [12]. *SQUID*, Superconducting quantum interference device.

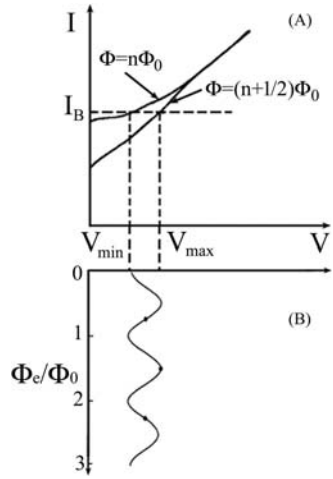

Figure 3.4 (A) Current−voltage characteristics at integer and half-integer values of applied flux. The bias current I_B sets the operation point. (B) SQUID voltage as a function of the external magnetic flux in unit of Φ_0. The SQUID voltage across the SQUID is a periodically function of the external magnetic flux through the superconducting ring with a period equal to the elementary magnetic flux quantum ($\Phi_0 = 2.07 \times 10^{-15}$ Wb). *SQUID*, Superconducting quantum interference device.

quantities related to quantum physical constant. In the case of the SQUID, the voltage across it (few tens of μV) is related to the quantum flux that is a very small quantity from a macroscopic point of view. Moreover, by using suitable readout electronics, the SQUID can measure a magnetic flux less than $10^{-6}\Phi_0$ per bandwidth unit, resulting in an ultralow noise sensor.

3.1.4 Main characteristics and magnetic noise of a SQUID

This section provides a more detailed analysis of the main characteristics and magnetic noise of a SQUID. Fig. 3.3B reports the equivalent electrical circuit of a SQUID obtained in the framework of the resistively shunted junction model [12].

In this model, the Josephson junction has a critical current I_0 and is in parallel with a capacitance C and resistance R having a current noise source associated with it. The R value is related to the hysteresis in the current−voltage ($I-V$) characteristic of a junction or a SQUID. In particular, if the Stewart−McCumber parameter $\beta_c = 2\pi I_c CR^2/\Phi_0 < 1$, there is no hysteresis [13].

It can be shown that the flux quantization in the presence of a superconducting ring, including two Josephson junctions, can be written as [9]

$$\phi_1 - \phi_2 = 2\pi\frac{\Phi}{\Phi_0} = 2\pi\frac{\Phi_e + LJ}{\Phi_0} \tag{3.3}$$

where φ_1 and φ_2 are the phase differences of the superconducting wave functions across the two junctions. $\Phi = \Phi_e + LJ$ is the total flux threading the SQUID loop given by the external flux Φ_e and the self-flux produced by the screening current circulating into the SQUID loop with an inductance L. The circulating current can be expressed as $J = (I_1 - I_2)/2$.

First, we consider the case of zero voltage state. Appling the Kirchhoff laws at the circuit of Fig. 3.3B, combining Eqs. (3.1) and (3.3), and supposing that the junctions are identical:

$$I_c(\Phi) = I_1 + I_2 = I_0(\sin\phi_1 + \sin\phi_2) = 2I_0 \sin\phi \cos\left(\pi\frac{\Phi}{\Phi_0}\right) \tag{3.4}$$

$$\frac{\Phi - \Phi_{ext}}{\Phi_0} = \frac{LJ}{\Phi_0} = \frac{LI_0(\sin\phi_1 - \sin\phi_2)}{\Phi_0} = \beta_L \cos\phi \sin\left(\pi\frac{\Phi}{\Phi_0}\right) \tag{3.5}$$

where $\varphi = (\varphi_1 + \varphi_2)/2$, while $\beta_L = 2LI_0/\Phi_0$ is the inductance parameter. It is one of the most important parameters, since the SQUID characteristic strongly depends on the β_L value.

If the SQUID inductance is very small, $\beta_L \approx 0$, consequently, $\Phi \approx \Phi_e$, the SQUID critical current has a simple cosinusoidal behavior, and the modulation depth, defined as $\Delta I_c = I_c(\Phi_e = 0) - I_c(\Phi_e = \Phi_0/2)$, is equal to $2I_0$, that is, the SQUID critical current modulates to zero.

If β_L is not zero, ΔI_c decreases by increasing the β_L value as shown in Fig. 3.5, where I_c, as a function of the external magnetic flux, is reported for two different β_L values. The curves have been obtained by numerically solving Eqs. (3.4) and (3.5). Note that for $\beta = 0.01$, the modulation depth is about $2I_0$, as expected.

The voltage state involves the presence of an oscillating current, and voltage as predicted by the second Josephson effect Eq. (3.2). In this case, the equations describing the SQUID dynamic are obtained by including the current terms due to the voltage across the resistance (V/R) and the capacitance (CdV/dt) in the Kirchhoff law. Considering Eq. (3.2) and applying the Kirchhoff law to both SQUID arms, we obtain the following two equations:

$$\begin{aligned}
\frac{I_c}{2} + J &= I_0 \sin\phi_1 + \frac{\Phi_0}{2\pi R}\frac{d\phi_1}{dt} + \frac{\Phi_0 C}{2\pi}\frac{d^2\phi_1}{dt^2} + I_{N,1} \\
\frac{I_c}{2} - J &= I_0 \sin\phi_2 + \frac{\Phi_0}{2\pi R}\frac{d\phi_2}{dt} + \frac{\Phi_0 C}{2\pi}\frac{d^2\phi_2}{dt^2} + I_{N,2}
\end{aligned} \tag{3.6}$$

The two equations in Eq. (3.6), together with Eq. (3.5), provide a complete description of the SQUID characteristics. The voltage is given by $V = 1/2[d(\varphi_1(t) + \varphi_2(t))/dt]$. The terms $I_{N,1}$ and $I_{N,2}$ are the Nyquist noise associated with the shunt resistors R. As we said, the voltage across the SQUID is an oscillatory function of time (see Fig. 3.5B), in the case of $I_b/I_0 = 6$, the oscillation period is equal to about half of $\Phi_0/(2\pi I_0 R)$ that considering a typical SQUID parameters

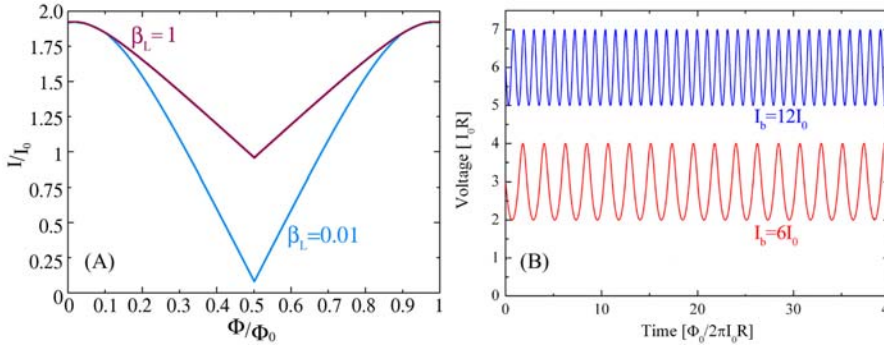

Figure 3.5 (A) Critical current of a SQUID as function of the external magnetic flux threading the loop for two different β_L values. (B) Voltage across a SQUID as a function of the time normalized to $\Phi_0/(2\pi I_0 R)$ for two different current biases. Increasing the bias current, the voltage frequency increases, while the amplitude decreases. *SQUID*, Superconducting quantum interference device.

($I_0 = 10\ \mu A$, $R = 3\ \Omega$) corresponds to a frequency of about 50 GHz. However, during the working operation, a voltage average is typically measured.

The average value of $V(t)$ allows us to calculate the current−voltage characteristic (I−V), the voltage−magnetic flux characteristic (V−Φ), and the voltage responsivity, namely, the slope of the V−Φ curve in the magnetic bias point $V_\Phi = \partial V/\partial \Phi_e$. The power spectral density (PSD) of $V(t)$ gives the PSD of the voltage noise (S_V) and of the magnetic flux noise ($S_\Phi = S_V/V_\Phi{}^2$). In the simplest case, where $I_{N,1} = I_{N,2} = 0$ and β_L, $\beta_C \ll 1$, Eqs. (3.5) and (3.6) can be easily solved, providing the following equation for the SQUID I−V characteristic:

$$V(\Phi_e, I) = \frac{R}{2}\sqrt{I^2 - \left(2I_0 \cos\left(\pi \frac{\Phi_e}{\Phi_0}\right)\right)^2} \tag{3.7}$$

The voltage swing or peak-to-peak modulation defined as $\Delta V_S = V(\Phi_0/2) - V(\Phi_0)$ is given by

$$\Delta V_S(I) = \left[\frac{R\,I}{2} - \frac{R}{2}\sqrt{I^2 - (2I_0)^2}\right] \tag{3.8}$$

The maximum value is obtained for $I = 2I_0$, that is, $\Delta V_S = I_0 R$.

In more general case, Eqs. (3.5) and (3.6) are numerically solved [14,15], providing $\varphi_1(t)$ and $\varphi_2(t)$, which allow one to compute all the SQUID characteristics.

Fig. 3.6 reports the I−V characteristics computed for $\Phi_e = 0$ and $\Phi_e = \Phi_0/2$ and V−Φ characteristics for three different values of I_B/I_0 ratio and $\beta_L = 1$, $\beta_c = 0$ for all curves. As expected, the I−V characteristic does not show hysteresis, while the V−Φ characteristics have a periodic behavior with a period equal to Φ_0. The V−Φ

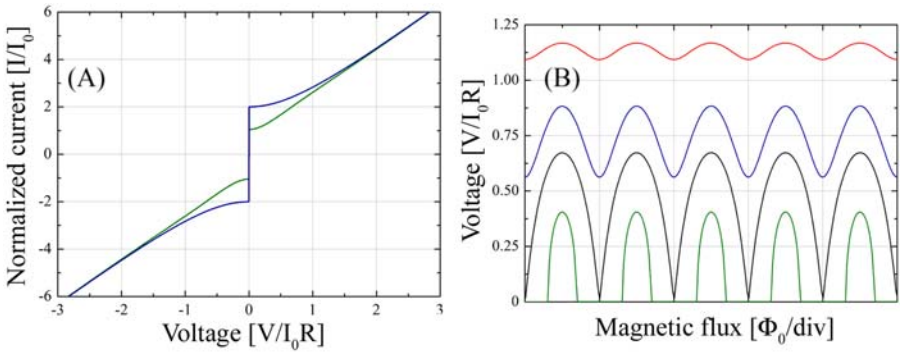

Figure 3.6 (A) Current−voltage characteristics computed for $\Phi_e = 0$ and $\Phi_0/2$. (B) Voltage−magnetic flux characteristics computed for $I_B/I_0 = 1.5$ (*lower curve*), 2.0 (*middle curve*), and 2.5 (*upper curve*). In both figures, $\beta_L = 1$ and $\beta_c = 0$.

amplitude ($V(0) - V(\Phi_0/2)$) depends on the bias current and β_L value and reaches its maximum for $I_B = 2I_0$.

From Fig. 3.6B, it is evident the periodic dependence of the voltage across the SQUID on the external magnetic flux treading the SQUID ring. Hence, a nonhysteretic SQUID can be considered a magnetic flux−voltage transducer and can be employed as a magnetic flux detector. In this case, $\Delta\Phi_e = \Delta V/V_\Phi$. Typically, in this configuration, the SQUID is biased with a constant current close to I_c and an external magnetic flux $\Phi_e = \Phi_0/4$ to maximize the V_Φ.

If the signals to measure are much smaller than the flux quantum, the SQUID can work in small signal mode. In such a configuration, it is flux biased at a voltage−flux characteristic where the responsivity is the maximum. Since every continuous signal in a suitable small range around a point can be approximated to a linear signal, the response of the SQUID is linear with the external magnetic flux. If the signals to detect are greater than the flux quantum, the SQUID response has to be linearized. To do it, a flux-locked-loop (FLL) configuration is used [16].

In such a scheme the output voltage is converted into a current by a resistor and fed back into the SQUID as a flux, via a coil coupled to the sensor, nulling the input magnetic flux (Fig. 3.7). So the SQUID works as a null detector of magnetic flux. The voltage across the feedback resistor is proportional to the magnetic flux input. The FLL linearizes the SQUID output increasing the linear dynamic range. Due to the SQUID's very low output voltage noise, direct voltage readout mode generally leads to a reduction of intrinsic SQUID sensitivity. To solve this problem, complicated schemes such as ac-flux modulation in combination with an impedance matching were often used [17]. In recent years, a second generation of SQUID sensors, with a large flux-to-voltage transfer, has been proposed to allow a direct-coupled readout scheme without flux modulation [1]. In comparison with the standard electronics, the direct-coupled readout schemes are simpler, more compact, and less expensive. In particular, circuits based on additional positive feedback (APF) are very effective [18]. Such a circuit consists of a coil (APF coil) connected to a resistor (APF resistor) put in parallel with the SQUID. The APF circuit

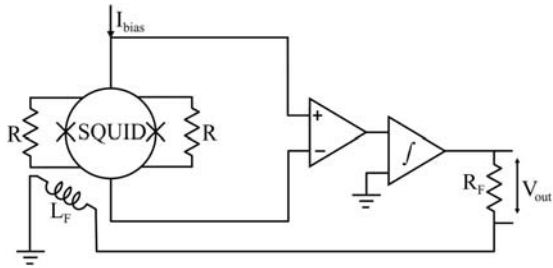

Figure 3.7 Flux-locked-loop configuration used to increase the linear dynamic range of the SQUID sensors. *SQUID*, Superconducting quantum interference device.

renders the magnetic flux−voltage characteristics asymmetric inducing an increase of voltage responsivity on one side of the characteristic. In such a way the contribution to the flux noise due to the readout electronics is reduced.

One of the most important factors of merit of a SQUID device is the magnetic flux noise or more precisely the spectral density of magnetic flux noise. The importance of the noise in Josephson devices has stimulated many theoretical and experimental investigations leading to an exhaustive comprehension of the main mechanisms responsible for the different noise.

In the case of a shunted dc-SQUID, this noise is essential due to the Nyquist noise associated with the shunt resistor R with a current spectral density $S_I = 4k_BT/R$, where k_B is the Boltzmann constant and T the temperature [19].

The SQUID noise is computed by solving numerically Eqs. (3.5) and (3.6), where the $I_{N,1}$ and $I_{N,2}$ are the resistor Nyquist noise. An important parameter is $\Gamma = 2\pi k_BT/(I_0\Phi_0)$ that takes into account the spectral density of the Nyquist current noise relative to the shunt resistors ($S_I = 4\Gamma$). The spectrum of the voltage noise for a bias current $I_B = 2.1I_0$ and two different values of Γ are reported in Fig. 3.8A. The spectra have been computed by averaging 60 spectra of time traces $V(t)$ reported in the inset of Fig. 3.8A and obtained by averaging 40 $V(t)$.

The voltage responsivity V_Φ, the PSD of the voltage S_V, and the spectral density of magnetic flux $S_\Phi{}^{1/2} = S_V{}^{1/2}/V_\Phi$ as a function of the bias current I_B are, respectively, reported in Fig. 3.8B−D for $\beta_L = 1$, $\beta_C = 0$, $\Phi = 0.25$, Φ_0, and $\Gamma = 0.05$. From the figure, we observe that the minimum of $S_\Phi{}^{1/2}$ corresponds to about $1.6I_c$, where the values of S_V and V_Φ are as follows:

$$S_V \cong \frac{0.8I_0\, R\Phi_0}{2\pi} = 16k_B\, TR; \quad V_\Phi \approx \frac{R}{L} \Rightarrow S_\Phi^{1/2} = \frac{S_V{}^{1/2}}{V_\Phi} \cong 4\sqrt{\frac{k_BT}{R}}L \tag{3.9}$$

To compare SQUID with different inductances, SQUID noise is often presented as the noise energy for unit bandwidth:

$$\varepsilon \cong \frac{S_\Phi}{2\,L} \cong \frac{8\,k_B\,T\,L}{R} \tag{3.10}$$

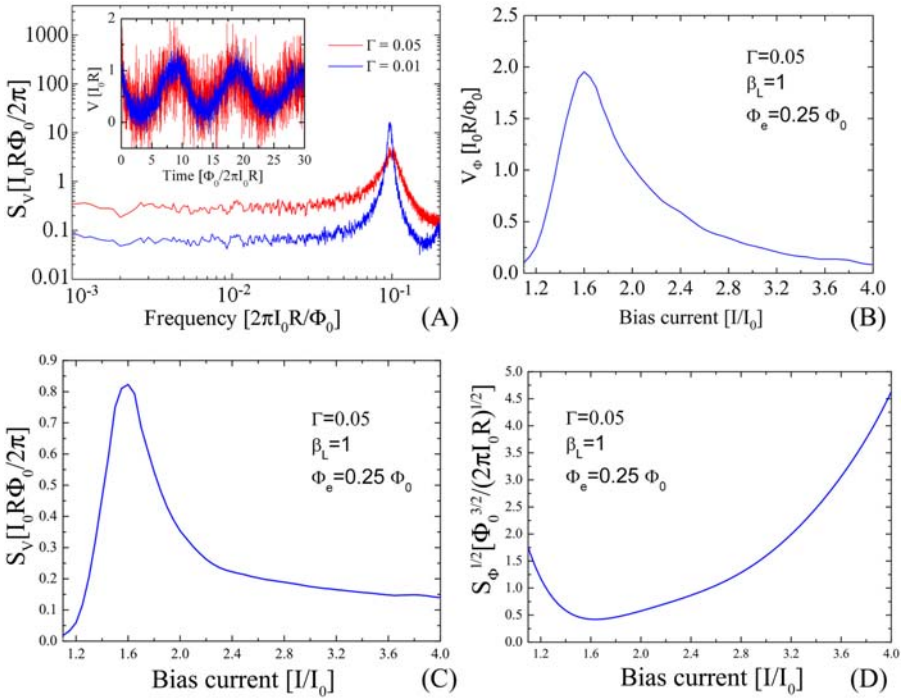

Figure 3.8 (A) Spectrum of the voltage noise for a bias current $I_B = 2.1I_0$ and two different noise parameter values: $\Gamma = 0.01$ and 0.05. The inset shows the time traces $V(t)$, obtained by averaging 40 $V(t)$. (B) Voltage responsivity as a function of the bias current. (C) Power spectral density value in the white region of the voltage noise as a function of the bias current. (D) Spectral density of the magnetic flux noise as a function of the bias current. It has been obtained by taking the ratio $S_V^{1/2}/V_\Phi$.

It is expressed in the unit of $\hbar$. A SQUID can reach an energy resolution as low as few $\hbar$; in other words, it is limited by quantum mechanics uncertainty principle. It has been proved that the conditions $\beta_L = 1$ and $\Phi = 0.25\Phi_0$ optimize the SQUID performances [19]. Hence to reduce the flux noise of a SQUID, we have to reduce the inductance of the loop, increase the shunt resistance value preserving the conditions $\beta_C \ll 1$, $\Gamma \ll 1$, $\beta_L = 1$.

3.2 Main SQUID configurations

A SQUID is essentially a magnetic flux detector. However, it can detect with ultra-high sensitivity of any physical quantities that can be converted in a magnetic flux trading the SQUID loop. Depending on the quantity to measure, it is needed to employ a suitable SQUID sensor design. In this section, we report the basic principle of the main SQUID configurations.

3.2.1 Magnetometer and gradiometer

In the case of a bare SQUID, the rms magnetic field noise $S_B^{1/2}$ is simply given by $S_\Phi^{1/2}/A_\ell$, where A_ℓ is the geometrical area of the superconducting loop. Since the flux noise increases with the ring inductance (Eq. 3.9), it is not possible to increase the magnetic field sensitivity by increasing the geometrical area of the SQUID ring.

Therefore, to increase the magnetic field sensitivity, a superconducting flux transformer is employed. It consists of a superconducting primary coil working as a magnetic flux pick-up (pick-up coil) connected in series with a superconducting secondary coil magnetically coupled to the SQUID (input coil) (Fig. 3.9). When a magnetic flux Φ_p is applied, due to Meissner effect, a screening current flows into pick-up coil to nullify the total magnetic flux. Such screening current flows also in the input coil inducing a magnetic flux Φ_S into the SQUID loop [14]:

$$\Phi_S = \frac{M_i}{L_i + L_P}\Phi_p = \frac{k_i\sqrt{LL_i}}{L_i + L_p}\Phi_p \tag{3.11}$$

where L_i and L_p are the inductances of the input coil and the pick-up coil, respectively, k_i is a coupling factor, and M_i is the mutual inductance between the SQUID loop and input coil.

By inverting Eq. (3.11) and considering that $B_p = \Phi_p/A_p$ (A_p is the pick-up coil area), it is possible to obtain the spectral density of the magnetic field noise $S_B^{1/2}(f)$ of the SQUID magnetometer [14]:

$$S_B^{1/2} = \frac{S_{\Phi,p}^{1/2}}{A_p} = \frac{L_p + L_i}{M_i A_p} S_\Phi^{1/2} = B_\Phi S_\Phi^{1/2}; \quad B_\Phi = \frac{L_p + L_i}{M_i A_p} \tag{3.12}$$

where B_Φ is the magnetic flux to magnetic field conversion efficiency or SQUID magnetometer sensitivity. It is a fundamental parameter for a SQUID magnetometer and assumes the minimum value when $L_p = L_i$. Hence, the magnetometer design can be optimized by minimizing the value of B_Φ in Eq. (3.12). If the flux transformer is

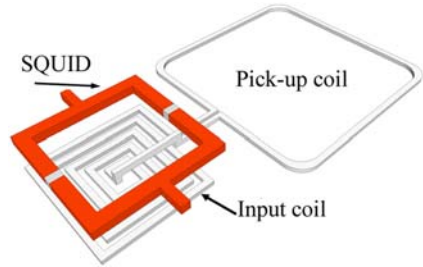

Figure 3.9 Scheme of a SQUID magnetometer. A superconducting flux transformer is inductively coupled to the SQUID loop to increase the effective area of the sensor. *SQUID*, Superconducting quantum interference device.

integrated, an excellent coupling to the SQUID is obtained using a Ketchen-type design [15,20]. The SQUID loop, in a square washer configuration, is coupled to a multiturn thin-film input coil that is connected to a square single turn pick-up loop (Fig. 3.10A). In such a configuration, the SQUID inductance does not depend on the external dimension of the washer but only on the hole dimension. The coupling between the washer and the input coil is very effective, and the input coil inductance is proportional to the turn numbers and the hole inductance. Hence, in this configuration, the input coil inductance can be adjusted to match a suitable load by varying the outer dimension of the washer to accommodate the required number of input coil turns. The Josephson junctions are located on the outer edge of the square loop, away from the higher field region at the center square hole. Therefore a slit through the conductor loop is used, introducing excessive parasitic inductances. Such additional inductance is only partially coupled to the coil turns, reducing the overall coupling efficiency. So, it is preferable to avoid very long slit. Besides, the washer structure does tend to focus flux into the central hole by an amount proportional to the product of outer dimension l and the hole dimension d increasing the flux capture area by a factor $(A_w/A_h)^{1/2}$ (A_w and A_h are the geometrical area of the washer and of the hole, respectively) [21]. The flux-focusing effect is largely employed to fabricate SQUID sensors for several applications.

Typically, a SQUID magnetometer with a square pick-up coil of about 1 cm^2 exhibits a magnetic flux noise as low as 1 fT $Hz^{-1/2}$.

To reduce the equivalent preamplifier flux noise with respect to the SQUID noise in the case of direct-coupling readout scheme, an APF circuit could be integrated on the same chip. It makes the $V-\Phi$ characteristic asymmetric, so, if the SQUID is biased on the steeper side, an effective increase of the SQUID

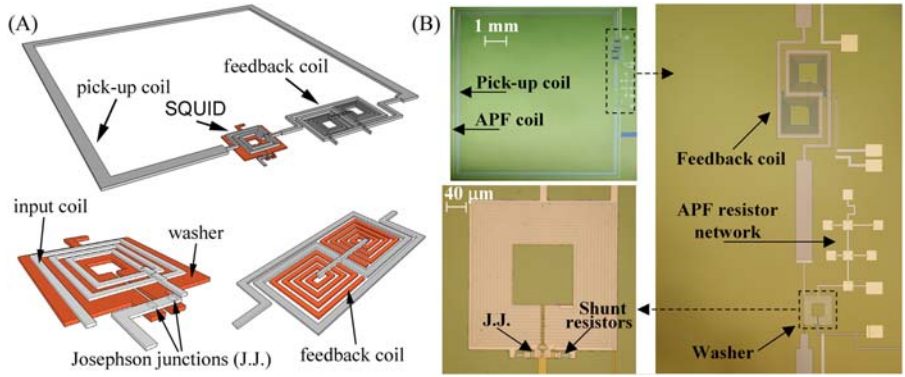

Figure 3.10 (A) Scheme and (B) picture of a fully integrated SQUID magnetometer, including the flux transformer and the feedback coil: a superconducting pick-up loop is inductively coupled to the SQUID by a superconductive multiturn coil located under or over the SQUID washer. An improved feedback coil design allows to reduce cross-talk effect in large multichannel systems. The magnetic field noise of this SQUID magnetometer is 1.5 fT $Hz^{-1/2}$. *SQUID*, Superconducting quantum interference device.

responsivity ($V_\Phi = \partial V/\partial \Phi$) is achieved. The integrated APF circuit includes a resistor network to adjust the APF gain for optimum device operations. The bipolar design of the feedback coil consisting of two multiturn coil allows to reduce crosstalk among neighboring sensors [22].

Another scheme used to increase the effective area of a SQUID is based on multiloop design where n loops are connected in parallel (reminiscent of a wheel with spokes), so that the total SQUID inductance is $L = L_p/n^2 + L_{\text{spoke}}/n$ and the total effective area is given by $A_{\text{eff}} = A_p/n - A_{\text{spoke}}$, where L_p and A_p are the inductance and effective area, respectively, of an equivalent pick-up loop without spokes and L_{spoke} and A_{spoke} are the average parasitic inductance and average parasitic effective area associated with the pair of "spokes" between neighboring loops that form coplanar transmission lines [18,23,24].

The multiloop SQUID magnetometer reported in Fig. 3.11 exhibited a field sensitivity $B_\Phi = 0.46\ \text{nT}/\Phi_0$ and rms magnetic field noise $S_B^{1/2}(f) = 0.9\ \text{fT Hz}^{-1/2}$ [24].

Another multiloop magnetometer realized with low capacitance cross-type Josephson junction exhibited an exceptionally low magnetic field noise, as low as $0.3\ \text{fT Hz}^{-1/2}$ [25].

To detect a magnetic field gradient a pick-up coil consists, usually, of two coils wrapped with the opposite direction. To evaluate the magnetic field gradient along the z direction ($\partial B_z/\partial x$), an axial configuration should be used, while for x- or y-dependent magnetic field gradient ($\partial B_x/\partial y$ or $\partial B_y/\partial x$), a planar configuration has to be employed [1] (Fig. 3.12).

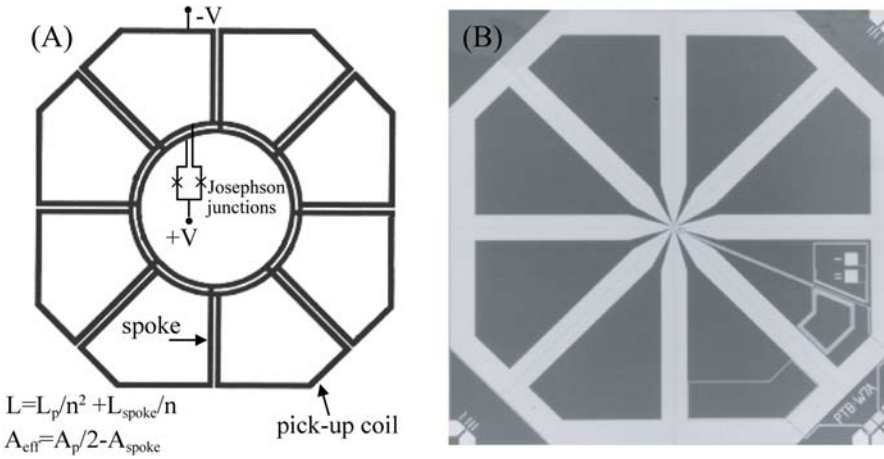

Figure 3.11 (A) Schematic diagram and picture (B) of a multiloop magnetometer. Here eight loops are connected in parallel reducing the SQUID inductance, while the effective loop area is given by the area of the single loop divided by eight minus the area between the "spokes." *SQUID*, Superconducting quantum interference device.
Source: Adapted from D. Drung, S. Knappe, H. Koch, Theory for the multiloop dc superconducting quantum interference device magnetometer and experimental verification, J. Appl. Phys. 77 (1995) 4088–4098.

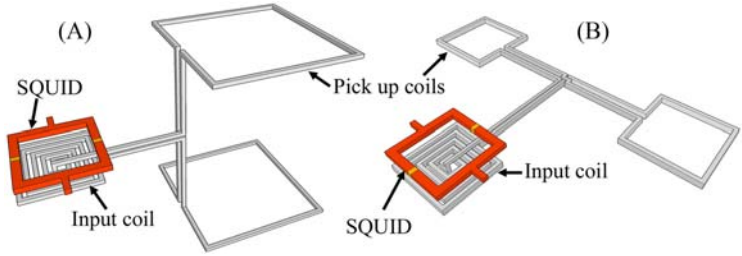

Figure 3.12 Scheme of an axial (A) and a planar gradiometer configuration (B). In the axial case, two coils are wrapped with the opposite direction. In such a way, if a uniform magnetic field is applied, there is no current flowing into the input coil, and subsequently there is no magnetic flux treading the SQUID. *SQUID*, Superconducting quantum interference device.

In both cases, a spatially uniform magnetic field induces in the coils two screening currents having the same amplitude but opposite direction, so that there is no current flowing into the input coil, and subsequently, there is no magnetic flux treading the SQUID. If the magnetic field is nonuniform, the net current circulating into the input coil is nonzero coupling a magnetic flux into the SQUID via mutual inductance M_i; in the planar case [26],

$$\Phi_s = M_i J_s = \frac{2d^3 M_i}{2L_p + L_i}\left(\frac{\partial B_z}{\partial x}\right)$$

where d is the distance between the pick-up coil centers (baseline); thus the noise gradient is expressed by [26]

$$\left.\frac{\partial B_z}{\partial x}\right|_n = \frac{2L_p + L_i}{M_i} = \frac{\Phi_n}{2d^3}$$

where Φ_n is the magnetic flux noise of the SQUID.

In Fig. 3.13, a fully integrated SQUID gradiometer is reported with long baseline planar (50 mm). The pick-up antenna consists of two integrated rectangular coils connected in series and magnetically coupled to a dc-SQUID in a double parallel washer configuration by two series multiturn input coils. Due to their high intrinsic balance and good performances, planar gradiometers may be the elective sensors for biomagnetic application in a soft shielded environment [27].

3.2.2 High-sensitivity current sensor (pico-ammeter)

SQUID sensors are also employed to detect very small changes in various physical quantities such as current or voltage that can be transformed into changes in the magnetic flux treading the SQUID ring. Among them, particular interest is devoted

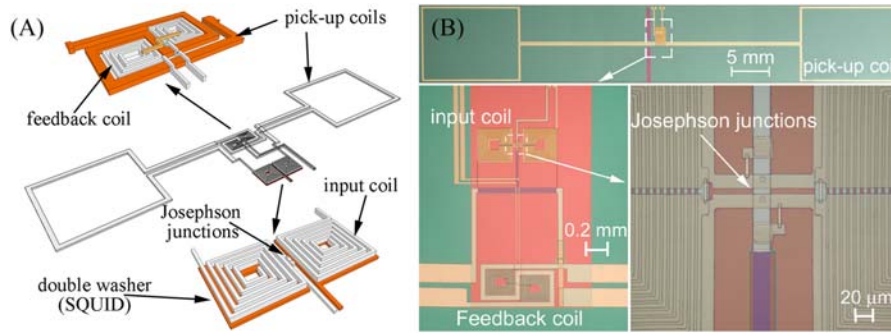

Figure 3.13 (A) Scheme and picture (B) of an integrated planar SQUID gradiometer and its particulars showing the bipolar feedback coil with relative pick-up coil arrangement and the SQUID in a washer shape, including the Josephson junctions, shunt, and damping resistors. The spectral density of the magnetic field noise, referred to one sensing coil, is 3.0 fT $Hz^{-1/2}$ resulting in a gradient spectral noise of 0.6 fT cm^{-1} $Hz^{-1/2}$. *SQUID*, Superconducting quantum interference device.
Source: Adapted from C. Granata, A. Vettoliere, C. Nappi, M. Lisitskiy, M. Russo, Long baseline planar superconducting gradiometer for biomagnetic imaging, Appl. Phys. Lett. 95 (2009) 042502.

to the SQUID-based current sensors because they can be effectively employed as a readout of gravitational wave detectors, transition-edge sensors, and for current-sensing noise thermometry. A suitable way to obtain a practical and reliable SQUID current noise is the design based on the flux transformer that converts easily the electrical current into a magnetic flux treading the SQUID loop and allows to obtain fully integrated sensors (Fig. 3.14). In this case, the magnetic flux coupled to the SQUID loop is $\Phi = M_i$ and the spectral density of the current noise will be [1,17] as follows:

$$S_I^{1/2} = \frac{S_\Phi^{1/2}}{M} = I_\Phi S_\Phi^{1/2}; \quad I_\Phi = \frac{1}{M} \tag{3.13}$$

where M is the mutual inductance between the input coil and the SQUID loop. A suitable way to obtain a practical and reliable SQUID ammeter is to use a flux transformer that converts easily the electrical current into a magnetic flux treading the SQUID loop and allows to obtain fully integrated sensors.

To reject the background magnetic field, which gives an undesirable SQUID signal, it is possible to employ a gradiometric design. In such a configuration (double-washer parallel configuration), two thin-film niobium washers are connected in such a way to form a first-order planar gradiometer with respect to background fields. The external signal is coupled to the SQUID loop by a multiturn input coil via the mutual inductance $M = k(L_i L)^{1/2}$, where L_i is the inductance of the input coil, L is the total SQUID inductance, and k is the coupling constant. Even in this case, excellent coupling to the SQUID is obtained using a Ketchen-type design [15]. Therefore the input coil inductance can be adjusted to

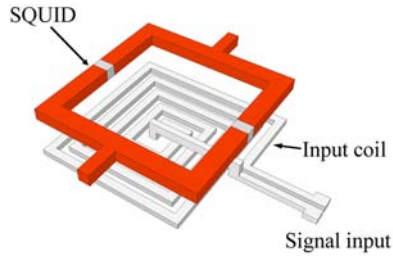

Figure 3.14 Scheme of a SQUID current sensor. The current to detect flows through the input coil that couples a magnetic flux into SQUID loop. By measuring the magnetic flux coupled to the SQUID, it is possible to obtain the current flowing in the input coil. *SQUID*, Superconducting quantum interference device.

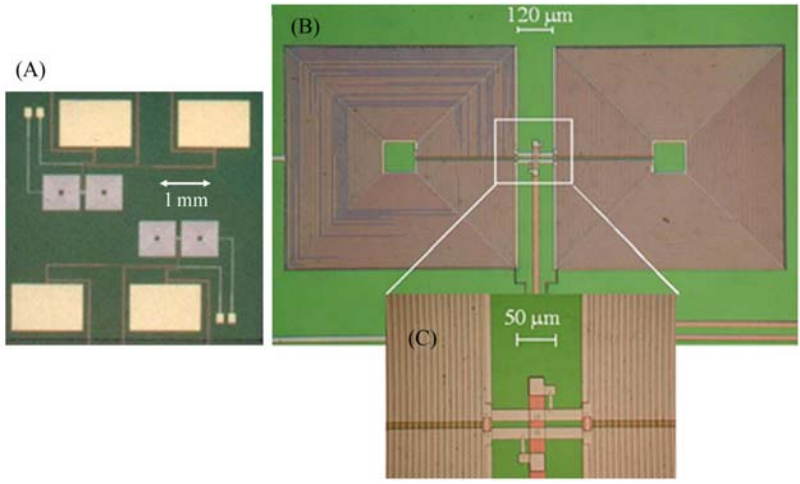

Figure 3.15 (A) Picture of a SQUID current sensor. The big pads are connected to input coil and allow for superconducting soldering if it is coupled to an external superconducting pick-up coil. (B) Parallel double washer in gradiometer configuration that accommodates 40 turns for each washer. (C) Particular of Josephson junctions and shunt resistors, are also visible the turns under the washers. *SQUID*, Superconducting quantum interference device.

match a particular load by varying the outer dimension of the washer to accommodate the required number of input coil turns. In the device reported in Fig. 3.15, the geometry results in a value of SQUID inductance $L = 130$ pH. The outer dimension of the washer (800 μm) accommodates an input coil consisting of 40 turns of a 4-mm wide niobium strip, giving an inductance value of the input coil of about 650 nH. The high input coil inductance allows a good matching with external load inductance. Being the flux noise of the SQUIDs configuration $2\mu\Phi_0\ \mathrm{Hz}^{-1/2}$ measured and an input current sensitivity of 0.2 μA/Φ_0, the resulting spectral density of input current noise is 400 fA $\mathrm{Hz}^{-1/2}$.

An efficient way to couple the signal coil with the SQUID is also obtained by using a double transformer coupling consisting of a matching (intermediary) transformer inserted between the signal coil and the input terminals of the conventional configuration [28–31]. In particular, in Fig. 3.16, an ultrahigh SQUID current sensor is reported [31]. The signal current to magnetic flux transfer factor (current sensitivity) is equal to $62\,\mathrm{nA}/\Phi_0$ measured by using a current-sensing noise thermometer technique. Despite the circuit complexity, the sensor exhibits a smooth and free resonance voltage–flux characteristic ensuring a stable working operation. Considering a SQUID magnetic flux noise $S_\Phi{}^{1/2} = 1.8\mu\Phi_0\,\mathrm{Hz}^{-1/2}$ at $T = 4.2\mathrm{K}$, a current noise as low as $110\,\mathrm{fA\,Hz}^{-1/2}$ is obtained. An even lower current noise ($65\,\mathrm{fA\,Hz}^{-1/2}$) has been obtained by using a SQUID design, based on a cloverleaf structure with four main washers, an input coil inductance of 2860 nH [32].

A SQUID voltmeter can be simply obtained by connecting the signal source in series with the input coil of the SQUID, via a resistance. The noise is essentially limited by the Nyquist noise of the resistance that can vary from 10^{-6} to $100\,\Omega$ giving a spectral density of the voltage noise ranging from 10^{-14} to $10^{-10}\,\mathrm{V\,Hz}^{-1/2}$ [1–4].

3.2.3 High spatial resolution SQUID (microSQUID)

We have seen that, to increase the magnetic field sensitivity, it is needed to increase the detection coil or the SQUID loop dimensions. However, in this way, the spatial

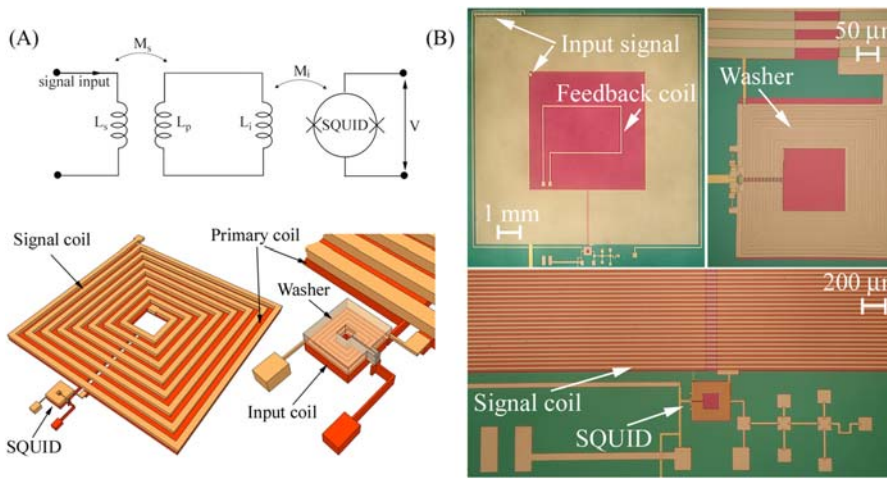

Figure 3.16 (A) Scheme and picture (B) of a high sensitive SQUID current sensor based on double transformer coupling. *SQUID*, Superconducting quantum interference device. *Source*: Adapted from A. Vettoliere, C. Granata, B. Ruggiero, M. Russo, An ultra high sensitive current sensor based on superconducting quantum interference device, in: A. D'amico, C. Di Natale, L. Mosiello, G. Zappa (Eds.), Sensors and Microsystems, Lecture Notes in Electrical Engineering, vol. 109, Springer US, 2012, pp. 175–180 (Copyright Holder: Springer New York) (30° chapter in). https://dx.doi.org/10.1007/978-1-4614-0935-9.

resolution decreases and so, the capability of the SQUID to distinguish two or more magnetic sources close together. A SQUID sensor for magnetic microscopy should have a high spatial resolution, that is, a high capacity to detect magnetic sources as small and close as possible (a few micrometers). It is clear that this objective is achievable if SQUID sensors are made with a very small detection coil, generally with a diameter of the order of 5−10 μm [33,34]. In this case, it is no longer convenient to use a superconducting transformer as in the case of magnetometers or gradiometers. The pick-up coil, usually circular in shape, is connected directly to the superconducting ring via a stripline consisting of two thin superconducting layers separated by an insulating layer (Fig. 3.17A). In this configuration, the pick-up coil is a sort of protuberance of the washer. In other words, the sensitive area of the device is a small part of the washer moved elsewhere to collect the magnetic field or flux in that specific area. The advantage of this configuration lies in the fact that the magnetic flux captured by the pick-up coil is entirely read by the sensor (it is as if the magnetic flux were completely transferred to the SQUID). So in this case, the defined flow gain G_Φ, as the ratio between the flow read by the SQUID (Φ_r) and the flow applied to the pick-up coil (Φ_P), is practically equal to 1 [35].

When analyzing the surface of a sample, the body of the SQUID (washer) should be insensitive to ambient magnetic fields or to those coming from the sample. To this aim a gradiometric configuration of the SQUID could be very useful. In the configuration shown in Fig. 3.17B, the pick-up coil is connected to a SQUID in a gradiometric configuration (double washer in parallel). In this case, the connection

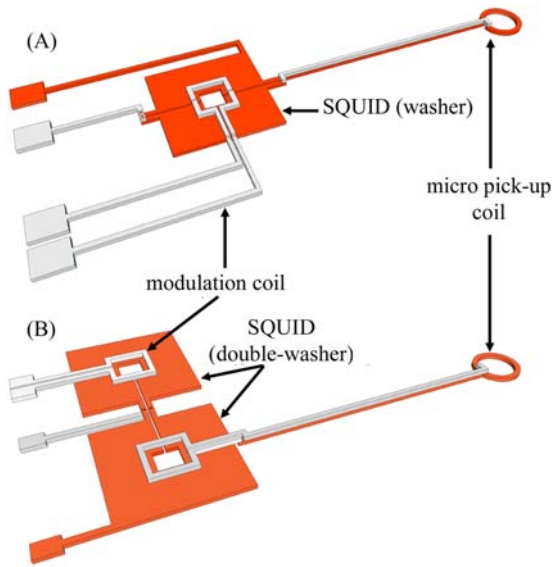

Figure 3.17 (A) Scheme of a microSQUID in direct-coupling magnetometric configuration. (B) Inductive coupling configuration and gradiometric SQUID (parallel double washer). *SQUID*, Superconducting quantum interference device.

is inductive, in other words, the pick-up coil is connected through a stripline to a square-shaped coil with a single turn inductively coupled to a single lobe of the double washer. In this case the flow gain is given by [35]

$$\frac{\Phi_r}{\Phi_p} = \frac{k\sqrt{L_h L_c}}{2(L_h + L_s + L_p)} \approx \frac{kL_h}{2(L_h + L_s + L_p)} \tag{3.14}$$

where L_h is the inductance of the hole of a single washer, L_s is the inductance of the stripline, L_p is the inductance of the pick-up coil, L_c is the inductance of the single coil coupled to the washer, and k is the coupling constant between the single coil and the washer. In this configuration the flux gain value is about half compared to the previous magnetometric configuration.

Note that the stripline structure is insensitive to fields normal to the plane containing the sensor; therefore it does not disturb its response. The distances between the pick-up coils and the washer are of the order of 1−2 mm. This configuration is highly insensitive to environmental magnetic fields and to any homogeneous magnetic fields used to excite the sample to be analyzed.

In Fig. 3.18, pictures of microSQUID based on the two different configurations explained previously are reported. In both cases the devices are equipped with a modulation coil that allows to modulate the SQUID and to tune it at optimal working point if a small signal mode operation is used.

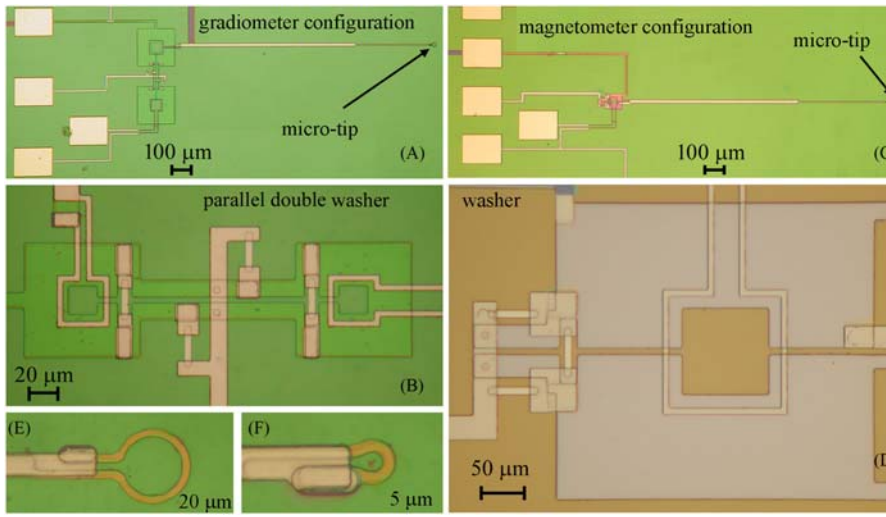

Figure 3.18 (A) Picture of a microSQUID with a micro tip magnetically coupled to a parallel double washer. (B) Particular of parallel double washer were the shunt resistors, the Josephson Junctions, and the modulation coil are visible. (C) Picture of a microSQUID in a pure magnetometer configuration. (D) Particular of the single washer where shunt resistors and Josephson junctions are visible. (E) and (F) Picture of microtips having a diameter of 20 and 5 μm respectively. *SQUID*, Superconducting quantum interference device.

If the measurement involves an applied magnetic field as in the case of micro-susceptometers, the measurement process should cancel the sensor's response to the applied field itself. To aid this cancelation process, microSQUID could be designed with two, nominally identical, counterwound pick-up loops [36]. These loops are separated by about 1 mm on the sensor chip, so that one loop can be located in close proximity to the sample, while the other loop is far from the sample substrate to avoid unwanted coupling. The symmetry of the design leads to both a geometric cancelation of a uniform applied field and a balanced inductance between the two arms of the SQUID, which leads to improved electrical performance (Fig. 3.19).

As expected, microSQUIDs exhibit poor magnetic field sensitivity. In fact for a micro-pick-up coil area ranging from 4 to 25 μm^2, we have $B_\Phi = 1/A_p = 80-500\ \mu T/\Phi_0$ and so a high value of magnetic field noise spectral density $S_B^{1/2}$ $80-500\ pT\ Hz^{-1/2}$ (here a magnetic flux noise of $1\mu\Phi_0\ Hz^{-1/2}$ has been assumed).

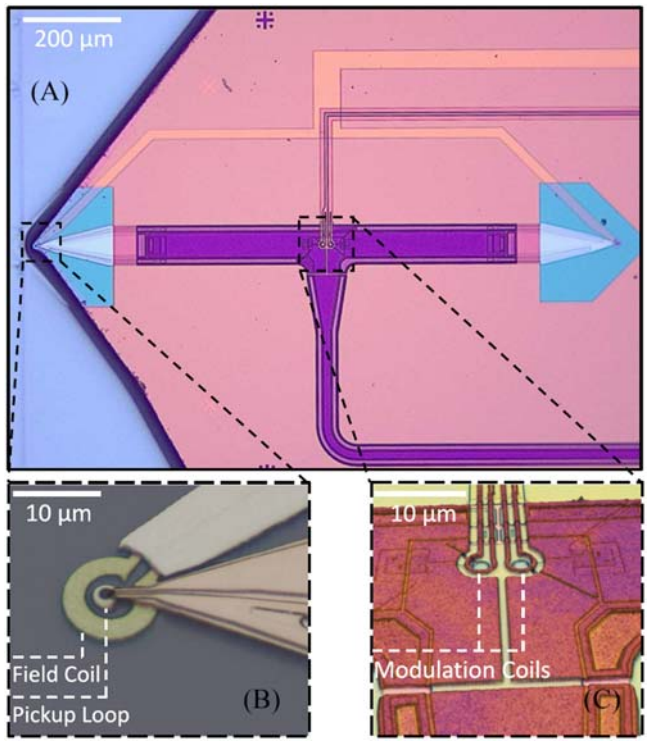

Figure 3.19 (A) Picture of a microSQUID, showing the gradiometric design, with two pick-up loops, modulation coils, and field coils. The chip is polished so that one pick-up loop is near the edge of the chip. (B) A zoom-in on the sensing point, showing the pick-up loop surrounded by the field coil. (C) A zoom-in on the modulation coils. *SQUID*, Superconducting quantum interference device.
Source: Adapted from Y. Shperber, N. Vardi, E. Persky, S. Wissberg, M.E. Huber, B. Kalisky, Scanning SQUID microscopy in a cryogen-free cooler, Rev. Sci. Instrum. 90 (2019) 053702.

3.2.4 Spin sensor (nanoSQUID)

In the last years, one of the most ambitious goals of the high-sensitivity magnetometry is the investigation of the magnetic properties of nanoscale objects such as nanoparticles, magnet molecules, cold atom clouds, nanowire, single electronic spin [37,38]. Nano-sized SQUID or nanoSQUID [39–42] is one of the most promising sensors for nanoscale applications because it exhibits ultrahigh magnetic moment sensitivity reaching few Bohr magnetons (electron magnetic moment) or spins per unit of bandwidth and allows direct magnetization changes detection in small nano-object systems. In the last decade, great efforts have been focused on the development of nanoSQUIDs, making such a nanosensor a powerful tool to study the magnetic properties of the nanoparticles at a microscopic level.

Why a nanoSQUID is able to detect very small magnetic moment? Consider the sketch reported in Fig. 3.20, where a representation of the magnetic flux lines related to a magnetic moment oriented in the z direction and SQUID having three different coil sizes are reported.

In the largest coil case (external coil), we can see that only few field lines contribute to the total flux threading the loop, the others return within the loop and will give no net contribution to the magnetic flux. By decreasing the detection coil size, the number of flux lines that return within the loop decreases and the net magnetic flux increases. In the smallest coil (inner coil), all field lines give a contribution to the magnetic flux. On the other side, if the size of coil tends to infinite, there is no net magnetic flux linkage into the loop because all flux lines return within the loop.

Now we will provide for a more formal demonstration of the previous statement for a simple case and will give the definition of the spin or magnetic moment sensitivity.

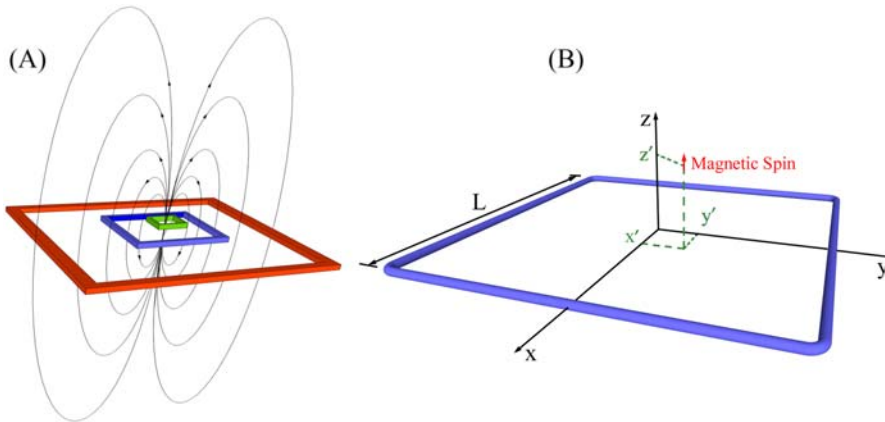

Figure 3.20 (A) Schematic representation of magnetic flux lines of a magnetic moment located in center of a SQUID flux capture area for three different loop sizes. (B) Scheme of a square SQUID detection coil, including an elementary magnetic moment (Bohr magneton or spin) located in a generic position $P = (x', y', z')$. *SQUID*, Superconducting quantum interference device.

Let us consider the elementary magnetic moment (μ_B) or a single spin positioned over a square coil with a side length L and oriented along the z-axis (Fig. 3.20B). We also suppose that the SQUID coil is composed of an idealized filamentary square loop and that the spin lies in the same plane of the SQUID loop and it is located in its center, in other words $x' = y' = z' = 0$. To obtain the magnetic flux through the SQUID loop, we have to calculate the surface integral on the loop area of the magnetic field produced by the magnetic moment μ_B. It is equivalent to calculate the line integral of the vector potential associated to μ_B across the contour ring. Under the aforementioned assumptions, the Cartesian components of the magnetic vector potential $A(\mathbf{r})$ at generic position $r(x,y,z)$, are as follows:

$$A_x = -\frac{\mu_0\,\mu_B}{4\pi}\,\frac{y}{r^3}; \qquad A_y = \frac{\mu_0\,\mu_B}{4\pi}\,\frac{x}{r^3} \tag{3.15}$$

where μ_0 is the magnetic vacuum permeability, and $r = [x^2 + y^2 + z^2]^{1/2}$. The magnetic flux due to the elementary magnetic moment is as follows:

$$\Phi_\mu = \oint \vec{A} \cdot d\vec{s} \tag{3.16}$$

where the integral is considered along the closed line of the SQUID loop. The contribution of the four sides of the square loop can be calculated as [43]

$$\Phi_\mu = \frac{\mu_0\mu_B}{4\pi}\left(2\int_{-L/2}^{L/2} dx \frac{L/2}{\left[(L/2)^2 + x^2\right]^{3/2}} + 2\int_{-L/2}^{L/2} dy \frac{L/2}{\left[(L/2)^2 + y^2\right]^{3/2}}\right) = \frac{2\sqrt{2}\mu_0\mu_B}{\pi L} \tag{3.17}$$

In the case of circular loop, the same calculation leads to the following formula: $\Phi_\mu = \mu_0\,\mu_B/2a$, where a is the coil radius [43].

A relevant figure of merit of a nanoSQUID is the minimum detectable spin number per bandwidth unit or spectral density of the spin noise $S_n^{1/2}$. It can be obtained by taking the ratio of the spectral density of the flux noise $S_\Phi^{1/2}$ and the net magnetic flux due to the single spin (Bohr magneton) [42,43]:

$$S_n^{1/2} = \frac{S_\Phi^{1/2}}{\Phi_\mu} = \frac{S_\Phi^{1/2}\pi L}{2\sqrt{2}\mu_0\mu_B}(\text{square loop}) \tag{3.18}$$

$$S_n^{1/2} = \frac{S_\Phi^{1/2}}{\Phi_\mu} = \frac{S_\Phi^{1/2}2a}{\mu_0\mu_B}(\text{circular coil}) \tag{3.19}$$

As expected, in both cases, the spin sensitivity increases by decreasing the side length L or the diameter $2a$ of the SQUID loop. It is worth stressing that the spin sensitivity strongly depends on the position of the magnetic moment within the

SQUID loop and on the distance from the SQUID plane. In particular, the sensitivity of a nanoSQUID increases (or equivalently $S_n^{1/2}$ decreases) when the magnetic nano-object to investigate is located close to the sides or to the corners of the nanoSQUID loop [43].

The principle of the magnetization measurement with a nanoSQUID can be summarized as follows: a variation of magnetization of a magnetic object produces a magnetic flux change, which is proportional to the magnetization by a coupling factor depending on the geometry of the SQUID pick-up loop and the sample [40,42,44].

We have seen that the capability of a SQUID to measure small magnetic nano-objects depends on the detection coil size. In particular, if we consider a flux noise of $0.1-1.0\mu\Phi_0\,\mathrm{Hz}^{-1/2}$, we can estimate by the formulas (3.18) and (3.19) that a sensitivity of few Bohr magnetons per bandwidth unit requires a loop side length of 100 nm or a radius of 50 nm in the case of circular loop.

To this purpose, nanoSQUIDs are typically fabricated by using electron-beam lithography [45] or the focused ion beam [46] sculpting techniques.

SQUIDs, having an effective area much smaller than 1 μm^2, require deep submicron Josephson junctions to maintain the detection size as designed. However, a typical SQUID employs two Josephson tunnel junctions (JTJ) consisting in a superconductor−insulator−superconductor trilayer that are limited by photolithographic process to about 1 μm.

Good alternatives to tunnel junctions are superconducting nanobridges [47] (or Dayem nanobridges) that consist of nanoconstrictions in a superconducting film with a length and a width less than 1 μm. Nanobridge junctions show a much higher critical current and they can be made by the same superconducting material as the rest of the SQUID in a single-layer superconducting thin film. Thus the fabrication of nanoSQUIDs based on nanobridges is relatively simple being obtained by a single nanopatterning step, avoiding the alignment of several layers on top of each other [48−51].

However, in the last years, the researchers also considered possibility to employ nano-sized JTJ to improve the performance of nanoSQUIDs [52−58] developing nanoSQUID based on sandwich type nanojunctions. Compared to nanoSQUID based on the Dayem nanobridges, the main advantages of those based on JTJ are a better control of the critical current, a high modulation depth (up to 70% of the maximum critical current), and the nonhysteretic behavior at $T = 4.2$K. Due to very low capacitance values, these Josephson nanojunctions are usually nonhysteretic. It is also worth to mention the other nanoSQUIDs types: the carbon nanotube (CNT) and nanoSQUID [59] where the Josephson elements are two CNTs, nanoSQUIDs fabricated on the apex of a sharp quartz tip (SOT—SQUID on a Tip) [60,61] and HTS nanoSQUIDs based on grain boundary nanojunctions [62−64]. In Fig. 3.21, scanning electron micrograph (SEM) images of some nanoSQUIDs are shown.

As regards the spin sensitivity exhibited by nanoSQUIDs, it reaches a value as low as few spin $\mathrm{Hz}^{-1/2}$. However, it is worth noting that it does not mean that actually we are able to detect the single spin because there are other important factors to consider such as the environment noise and the preparation of the experimental state (manipulation of the single spin and the excitation magnetic field).

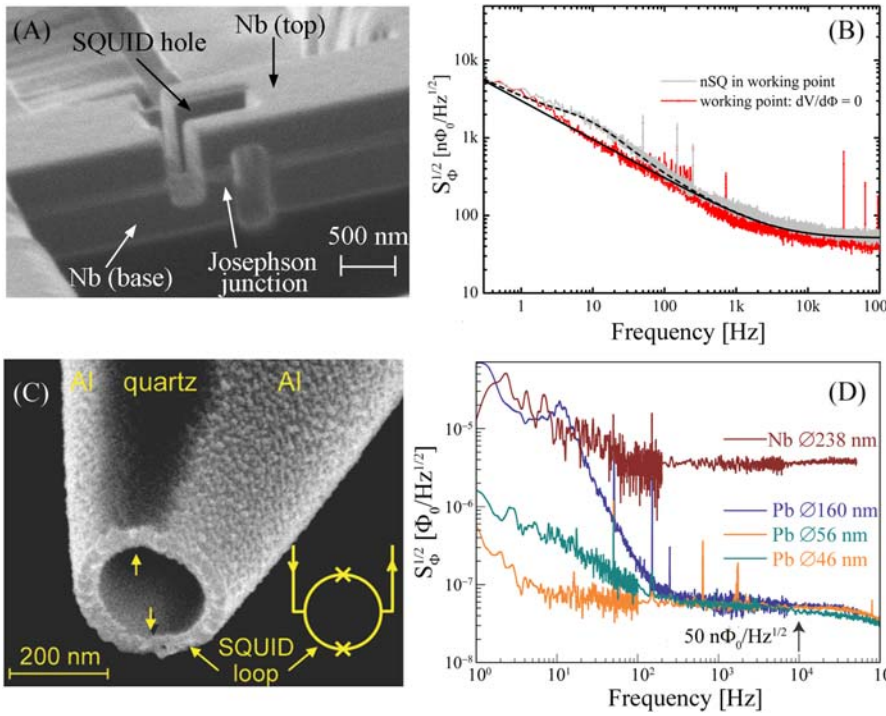

Figure 3.21 (A and C) SEM images of a three-dimensional nanoSQUID based on sandwich nanojunction and of a nanoSQUID on a quartz tip, respectively. (B and D) Spectral density of magnetic flux noise for both nanosensors. In (D), the four spectra refer to different nanoSQUID tip sizes. *SEM*, Scanning electron micrograph; *SQUID*, superconducting quantum interference device. *Source*: Adapted from (A and C) C. Granata, A. Vettoliere, R. Russo, M. Fretto, N. De Leo, V. Lacquaniti, Three-dimensional spin nanosensor based on reliable tunnel Josephson nanojunctions for nanomagnetism investigations, Appl. Phys. Lett. 103 (2013) 102602, 1–4 and A. Finkler, Y. Segev, Y. Myasoedov, M.L. Rappaport, L. Ne'eman, D. Vasyukov, et al., Self-aligned nanoscale SQUID on a tip, Nano Lett. 10 (2010) 1046–1049, respectively; (B and D) M. Schmelz, A. Vettoliere, V. Zakosarenko, N. De Leo, M. Fretto, R. Stolz, et al., 3D nanoSQUID based on tunnel nano-junctions with an energy sensitivity of 1.3 h at 4.2 K, Appl. Phys. Lett. 111 (2017) 032604 and D. Vasyukov, Y. Anahory, L. Embon, D. Halbertal, J. Cuppens, L. Neeman, et al., A scanning superconducting quantum interference device with single electron spin sensitivity, Nat. Nanotechnol. 8 (2013) 639–644, respectively.

3.3 Main SQUID applications

Due to their ultrahigh sensitivity, SQUIDs are widely employed in many applications [2–4]. In Fig. 3.22, the sensitivity required by main SQUID applications, as a function of the frequency, is reported together with the SQUID-magnetometer sensitivity. Here, we will provide a brief overview of the main applications. More details can be found in Refs. [2–4].

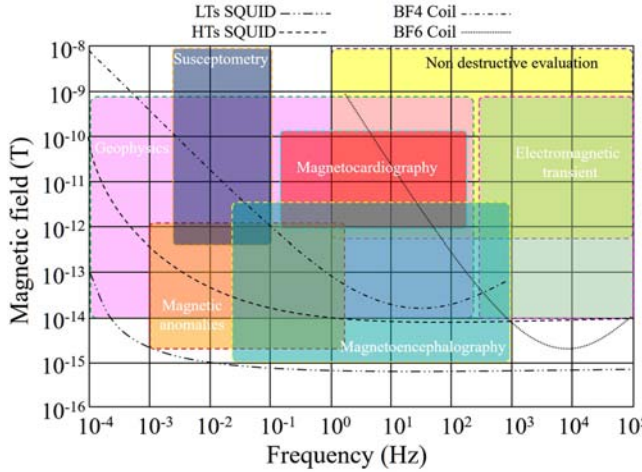

Figure 3.22 Bandwidth of main SQUID applications. We can see that SQUID magnetometer based on LTSs is able to cover all applications. *LTS*, Low critical temperature superconductor; *SQUID*, superconducting quantum interference device.

3.3.1 Biomagnetism

Biomagnetism, namely, the study of magnetic field associated with the electric activity in the human body, is one of the most important applications of SQUIDs [65]. In the following, we will focus on magnetoencephalography (MEG), which is the most relevant topic of biomagnetism [66–68]. MEG is a noninvasive neurophysiologic technique that measures the magnetic fields generated by the neuronal activity using ultrahigh sensitivity magnetic sensors (SQUIDs).

The system (Fig. 3.23A) to perform MEG measurements is typically based on an array of some hundreds of ultrahigh-sensitive SQUID magnetometers arranged in a helmet shape to cover entirely the subject's head [68,69]. This geometry requires a careful wiring and the SQUID sensors have been designed to minimize crosstalk. The sensorial helmets are immerged in helium bath by employing high-performance fiberglass Dewar having a magnetic field noise at most comparable to the SQUID sensors one. The low heat transfer guarantees up to about 7 days of measurement with one refill of helium. Since the magnetic signals generated by the human brain are at least eight orders of magnitude smaller than the magnetic disturbances, the MEG system is housed in a magnetically-shielded room (MSR), which drastically reduces environmental noise. The MSR consists of several layers of high-permeability materials (μ-metal) for magnetic shielding in conjunction with one or more aluminum plates for additional eddy-current shielding (Fig. 3.23B). In the aluminum layers, a time-varying magnetic field induces electrical currents that circulating in the aluminum layer generate a magnetic field that tends to cancel the changes of the applied magnetic field. The shielding efficiency is proportional to the frequency of the external magnetic field and depends on both the layer thickness

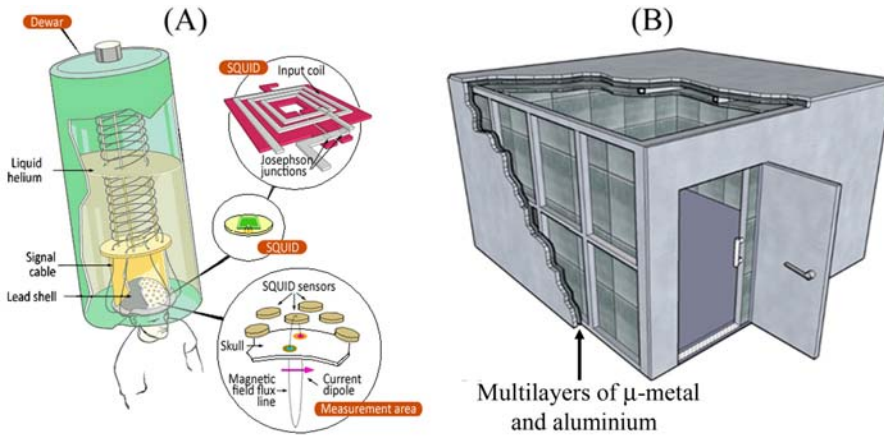

Figure 3.23 (A) Schematic representation of a system for magnetoencephalography. (B) Sketch of a magnetic shielding room based on concentric layers of μ-metal and aluminum.

and the conductivity of the material. At relatively low frequency (below 10 Hz), the eddy-current shielding is no longer effective and shielding is provided by low hysteresis ferromagnetic materials with high magnetic permeability. Usually, an Fe−Ni alloy with small percentages of elements such as Mo, Cu, Cr, or Al is used allowing to obtain a μ_r value as high as 10^4 H m^{-1}. All the electric connections are designed to block any magnetic noise propagating through the connection wires. The shielding factor exhibited by an MRS is typically best of 60 dB at 1 Hz and 100 dB at 50 Hz. The MEG system is also equipped with an integrated nonmagnetic electroencephalography (EEG)-channels cap, with ultrathin wires, which is optimal for usage inside an MEG helmet. This system allows data to be stored digitally and analyzed using both commercial and open-source programs. Scalp EEGs can be inspected visually in real time. It is also possible to record electrooculograms and electrocardiograms (ECGs) using additional electrodes. Moreover, visual and auditory stimuli and seven external triggers can be used.

As example of an MEG system, we report, in Fig. 3.24A and B, a multichannel system, including 163 SQUID magnetometers arranged in a help shape operating in a clinical environment. In Fig. 3.24C and D, the topographic distribution over the head of the power-spectrum in the range of 10−12 Hz, performed with the MEG system, is reported [69]. The measurements were performed on a subject with open eyes (Fig. 3.24C) and with closed eyes. As expected, major activation in the occipital region when the subject was recorded in resting state with closed eyes was observed (alpha rhythm).

MEG is a purely passive method, that is, a completely noninvasive measurement requiring no contrast agent, magnetic field, or x-ray and allows a direct measurement of neural oscillations [67]. The extremely high temporal resolution of MEG allows for an assessment of brain activity on a timescale not accessible to other brain functional imaging methods, that is, single-photon emission computed

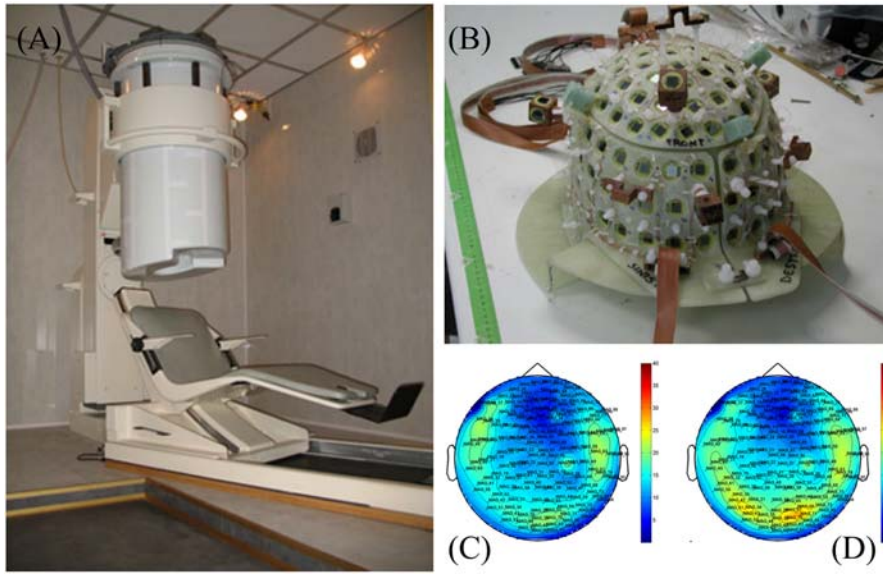

Figure 3.24 (A) MEG system inside the magnetically shielded room operating in a clinic for neurodegenerative diseases. The Dewar is made of fiberglass. (B) Helmet-shaped array consisting of 163 fully integrated SQUID magnetometers. (A and D) Topographic distribution over the head of the power-spectrum in the range of 10−12 Hz after the application of the noise-reduction algorithm for a subject recorded in resting state with open eyes (C) and closed eyes (D) (alpha rhythm). *MEG*, Magnetoencephalography; *SQUID*, superconducting quantum interference device.
Source: Adapted from S. Rombetto, C. Granata, A. Vettoliere, M. Russo, Multichannel system based on a high sensitivity superconductive sensor for magnetoencephalography, Sensors 14 (2014) 12114−12126.

tomography, positron emission tomography, or functional magnetic resonance imaging (fMRI). This is particularly important given the evidence that neural oscillations might represent an intrinsic physiological process by which communication among neurons occurs. Compared to EEG, MEG offers a better source localization, due to the reduced signal distortion. In fact, MEG measurements are not distorted or attenuated by the insulating layers such as the skull, tissues, or anatomical open spaces as in the EEG. The magnetic fields are recorded outside the head and then analyzed to localize the sources of the activity within the brain. This is an ill-posed problem, and there are a number of techniques that differ in various regards (for instance, in the assumptions used to introduce constraints) [67]. The location of the sources can be superimposed on anatomical images, such as MRI (i.e., either the native MRI or a template MRI) to provide information about both structure and function of the brain. MEG possesses both a good spatial and an excellent temporal resolution, thus allowing the investigation of both physiological and pathological processes in neurology. The MEG recording of brain magnetic activity enables

the investigation of neuronal activity such as cognitive processes, language perception, memory encoding and retrieval, and higher level tasks.

MEG is also a useful tool for the identification of early diagnostic biomarker in numerous diseases, as it allows the study of brain functions and facilitates the investigation of both spontaneous and evoked activities. Nowadays, MEG is used in some clinical conditions such as preoperative assessment of brain tumors and intractable epilepsy (presurgical mapping). Furthermore, MEG is useful to investigate neurological conditions such as neurodegenerative diseases, multiple sclerosis, amyotrophic lateral sclerosis (ALS) and migraine, as well as to investigate the autism spectrum disorders (ASDs) and the functional recovery after stroke. In the following, we will provide more detail about the clinical applications of the MEG [66–68].

3.3.1.1 MEG and cognitive disorders

The pathogenesis of neurodegenerative disorders, such as Alzheimer's disease (AD) or frontotemporal degeneration, is still poorly understood and the exact correlation between pathological findings (such as amyloid plaques and neurofibrillary tangles), and the neurodegenerative process is unclear. Moreover, the large heterogeneity of the clinical presentations of these diseases has no unambiguous explanation. In connectomics, AD is described as a "disconnection syndrome," and the evidence of a correspondence between hubs and regions most susceptible to amyloid deposition suggests a greater vulnerability to AD insults by the most active areas, with a higher basal metabolism. The aim of the current work is to exploit these properties to improve early classification of patients.

3.3.1.2 MEG and Parkinson's disease

Parkinson's disease (PD) is the most common basal ganglia disorders. As of today, the etiology of PD is still unknown, and the diagnosis remains a clinical one. With our MEG (based on magnetometers), we aim at the reconstruction of the activity of the basal ganglia. This is especially interesting, since correlations between α-synuclein and altered neuronal activity have been described. In this framework, we explore how different cross-talks among brain areas underlie the symptoms and/or the therapeutic response.

3.3.1.3 MEG and ALS

ALS is one of the most devastating brain disorders. While classically considered to be targeting the motor neurons, recently it has become evident that a much more complex pathophysiological mechanism underlies ALS. Most interestingly, an association between ALS and frontotemporal dementia has been described. We would like to know better how the whole brain evolves as the disease progresses. Hence, we perform network analysis on MEG recording of ALS patients at various stages of the disease.

3.3.1.4 MEG and migraine

Migraine affects roughly 15% of the world population. We aim at understanding how the same stimulus is processed differently in the brain of migraine patients as compared to controls. Indeed, cortical hyperexcitability has been described as one of the hallmarks of migraine. We used a median nerve stimulation paradigm to try to quantify this phenomenon.

3.3.1.5 MEG and depression

According to the World Health Organization, depression affects about 350 million people worldwide. The diagnosis of depression is based on clinical criteria, since we lack a clear definition of the pathophysiological mechanisms leading to this condition. Furthermore, the clinical responsiveness to treatment is assessed empirically. Recently, it has been shown that the activity of the prefrontal cortex is altered in depressive disorders. Furthermore, complexity analysis applied to MEG was shown to identify patients from controls. By recording MEG before and after treatment, we hope to identify connectivity markers of responsiveness to treatment.

3.3.1.6 MEG and ASDs

ASDs are defined by restricted/stereotyped behaviors and social impairments and have a massive impact on both the individuals with ASD and society itself. The biological bases are unknown, and a fully effective treatment has yet to be realized. Given the neurodevelopmental basis of ASD, MEG emerges as an important investigatory tool to explore novel early biomarkers useful not only for diagnostic and prognostic purposes, but also for stratification and response indices for treatment development.

Another interesting issue of biomagnetism is the *magnetocardiography* (MCG) which is a noninvasive electrophysiological mapping technique that provides unprecedented insight into the generation, localization, and dynamic behavior of electric current in the heart [62]. The aim of the MCG measurement is to determine the spatiotemporal magnetic field distribution produced by the cardiac electric activity in a measurement plane just above the thorax. MCG signals, unlike ECG, are not attenuated by surrounding anatomical structures, tissues, and body fluids, thereby providing more accurate information.

3.3.2 Nondestructive evaluation

The nondestructive analysis of materials and composites is becoming increasingly important, and various techniques have been developed to meet the different needs and demands of the production and business world. Among them, SQUID has been shown to have the highest sensitivity to the detection of the weak magnetic anomalies induced by the presence of defects, especially when these are present deep in the material to be analyzed [70,71]. The results were obtained in the vast majority of cases from single-SQUID systems that scanned small areas (of the order of tens of cm in the case of NDEs on “large” areas, and a few mm in the case of SQUID scanning microscopes).

Nondestructive analysis based on SQUIDs is a technique for finding defects in materials by studying the electrical and/or magnetic properties of materials.

In this technique, SQUIDs are used for the detection of very small anomalies in the magnetic field produced by the sample to be characterized. If the analyzed sample has homogeneous properties (absence of defects), the intensity of the magnetic field produced by the sample and detected by the SQUID will also be homogeneous, while the presence of defects will cause nonuniformities as shown in Fig. 3.25.

To detect the nonuniformities in the magnetic field originating from the presence of defects, it is necessary to scan in at least one direction, and generally, it is preferable to mount the material under examination on a plane that can be moved in $X-Y$ by means of computer-controlled motors (Fig. 3.26). The magnetic field detected by the SQUID is most often generated by currents circulating in the material under examination: the presence of defects in the material changes the local conductivity inducing an anomaly in the distribution of the currents and consequently in the

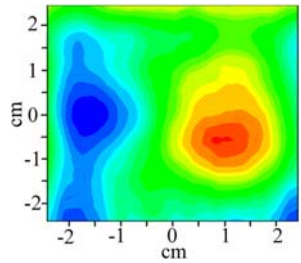

Figure 3.25 Distribution of the magnetic field read by a SQUID in the case of a sample with a defect produced by the impact of a body with an energy of 5 J on a composite material. *SQUID*, Superconducting quantum interference device.

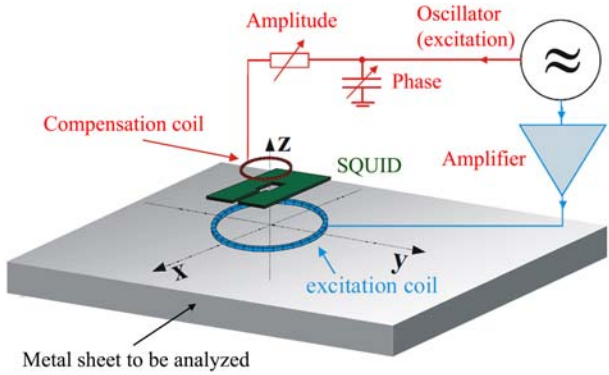

Figure 3.26 Scheme of a nondestructive analysis measurement based on SQUID sensors. The magnetic field produced by eddy currents is measured by a SQUID magnetometer or a gradiometer. *SQUID*, Superconducting quantum interference device.

magnetic field generated by them. Unfortunately, even the presence of different materials inside the piece to be analyzed, such as rivets inside the wings of an airplane, generates nonuniformity of currents and therefore of magnetic field. It is therefore important to use software that, from the measured magnetic field, evaluates the currents that generates it and compares them with the expected currents to establish the presence of damage, its position (superficial or deep), its nature (fracture, delamination, inclusions, and detachment), and its severity. In fact, the NDE should not only provide a qualitative indication of the presence of defects, but also a quantitative one. The thresholds within which the pieces under analysis can be accepted and beyond which they must be discarded, therefore, must be established.

In general, the sources of the magnetic fields produced by the materials under investigation can be intrinsic as in the case of the galvanic currents flowing in a corroded sample or an external source of magnetic field can be used to excite the samples. In the latter case, the external magnetic field can be generated both electrically and magnetically (electric or magnetic excitation). In the case of magnetic excitation, the test sample is placed in a uniform magnetic field and the residual magnetization variation is measured. In the electrical case, ac or dc current is introduced into the sample through the injection current (directly introduced into the sample through a pair of wires connected to a power generator) or through the induction method in which the eddy currents are generated inside the area to be investigated using suitable coils crossed by alternating current (Fig. 3.26). The SQUID is sensitive to weak magnetic fields even in continuous and therefore the need to use an alternating current is substantially due to the need to induce currents in the material to be analyzed. Furthermore, the use of an alternating current makes it possible to use a lock-in as an amplifier that amplifies only the SQUID signal at the frequency equal to the excitation frequency allowing one to exclude (or in any case significantly reduce) from reading those signals at different frequencies. Most of the prototypes of single-channel SQUID systems were based on the eddy-current system. They therefore provide an excitation coil and the detection of the magnetic field generated by the currents induced in the sample. The presence of an external coil for excitation implies that the SQUID must be positioned in an area in which the field generated by the coil is zero in the plane of the SQUID so that the flux of the magnetic field through the ring of the SQUID is zero. The procedure to nulling the signal read by the SQUID in the presence of the excitation coil only is essential for correct system operation, and various solutions can be adopted.

The advantages of the SQUID for NDE include high sensitivity (about $10-100\ \mathrm{fT\ Hz^{-1/2}}$), wide bandwidth (from dc to 10 kHz), and broad dynamic range (>80 dB). Moreover, the ability of SQUIDs to operate down to zero frequency allows them to sense much deeper flaws than traditional techniques, to detect and monitor the flow of steady-state corrosion currents, and to image the static magnetization of paramagnetic materials.

3.3.3 Magnetic microscopy

As mentioned previously, micro-sized SQUIDs have been widely employed for scanning magnetic microscopy, allowing very interesting application in view of

fundamental studies such as imaging of magnetic vortices in superconducting structure, symmetry of the order parameter in the high-T_c superconductor, study of magnetic materials properties, and susceptibility of micrometric material particles [2,72]. In a scanning SQUID microscope (SSM) the sample is scanned by a SQUID, which measures the magnetic field on the sample surface with a high spatial resolution (less than 10 μm). The collected data can be converted into a color image of the magnetic field coming from the sample. Such images can refer to both static fields and alternating fields. Compared to other magnetic imaging techniques, SQUID microscopes are characterized by a wide bandwidth and a high resolution in terms of magnetic flux and magnetic field, but by a moderate spatial resolution.

SSMs have been employed to produce magnetic images from a huge variety of sources, ranging from currents generated by an embryo in a chicken egg, to persistent currents associated with the quantization of magnetic flux in a superconductor. They have also been successfully applied in nondestructive analyses such as the localization of defects in single-microchip and multiple-microchip modules of semiconductor.

SQUID microscopes can be made essentially in four different categories (Fig. 3.27). In the first case (Fig. 3.27A) the sample is at cryogenic temperatures, typically equal to that of the SQUID. In many of these cryogenic microscopes the sample and the SQUID are in vacuum so that only the temperature of the sample can be modified (in particular, increased) thanks to suitable heaters placed in thermal contact with the

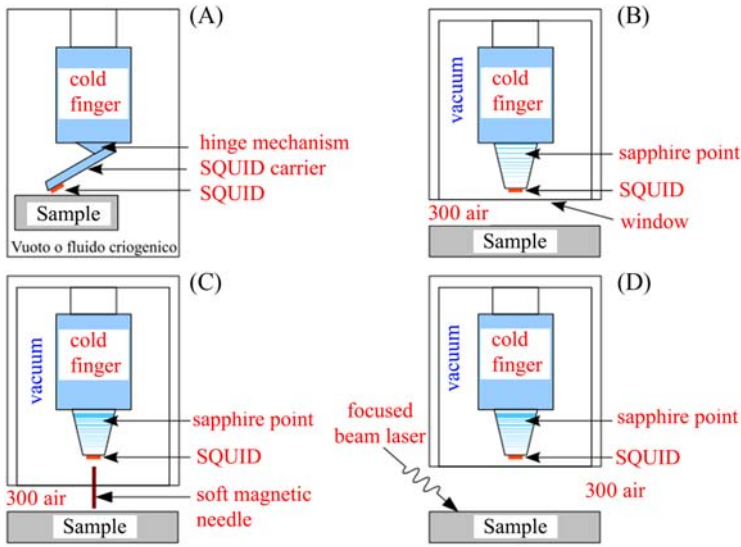

Figure 3.27 Main configurations of a SQUID microscope. In the configuration (A), the sample is at cryogenic temperature, while in the (B) the samples are placed in the air at room temperature. The configuration (C) includes a high magnetic permeability needle tha couples a magnetic flux in the SQUID, the last configuration (D) involves the use of a focused laser beam to generate currents in the sample, in this way the magnetic field generated by currents is coupled in the SQUID. *SQUID*, Superconducting quantum interference device.

sample. These types of microscopes were used essentially for basic physics measurements such as the experimental study of the symmetry of the order parameter in superconductors at high critical temperatures, very useful for understanding the various still unknown mechanisms of superconductivity at high temperatures.

The second type of SQUID microscopes (Fig. 3.27B) is specifically designed to acquire images of samples placed in air at room temperature. Of course, in these types of microscopes at room temperature, the SQUID must still be at cryogenic temperatures; therefore special precautions are necessary in making the instrument. One of the major applications of these types of microscopes is the magnetic imaging of computer microchips aimed at the nondestructive search for defects. Such microscopes had some commercial success as they have been shown to be able to successfully detect fabrication problems such as searching for short circuits in multichip modules. A key factor in the success of these tools has also been the availability of reliable and efficient techniques for converting magnetic signals into images of the source currents that generate the magnetic field.

The third type of SQUID microscope (Fig. 3.27C) provides, for the presence of a needle, with high magnetic permeability coupled inductively to the SQUID pick-up coil. The local magnetic fields generated by the sample polarize the magnetic needle that couples a magnetic flux in the SQUID. The major advantage of this type of approach is obviously the spatial resolution although that is achieved at the cost of worse sensitivity in terms of field resolution and magnetic flux.

The fourth type of SQUID microscopes (Fig. 3.27D) involves the use of a focused laser beam to generate currents in the sample. These laser microscopes were mainly used for the analysis of semiconductor wafers; in this case, the laser light generates a current that varies with the local density of the carriers.

To cool the SQUID sensor to its operating temperature (typically below 9K), it is mounted inside (bottom) of a glass fiber cryostat or Dewar (Fig. 3.27) filled with liquid helium ($T = 4.2$K). To avoid the heating of liquid helium through thermal conduction, the helium container and the SQUID are separated from the outer casing of the Dewar by a cavity where the vacuum is carried out. To reduce radiation losses, the surfaces of the interspace are coated with sheets of highly reflective materials (mylar). The control and readout electronics are located on the upper part of the Dewar at room temperature. Of course, the same fabrication technique is also used to realize Dewar for MEG or NDE systems. To allow the reading of magnetic signals coming from samples at room temperature external to the Dewar, just below the sensor, the external casing of the Dewar has a sapphire window a few tens of microns thick, which allows the sensor to be approached at a very small distance from the sample and at the same time preserves the vacuum. The SQUID is cooled by placing it in contact with a sapphire bar that ensures thermal coupling with liquid helium. The diameter of the sapphire window that separates the SQUID from the sample at room temperature is usually 5−10 mm. In a SQUID scanning microscope the spatial resolution is limited by the size of the micro-pick-up coil and the distance from the sample under investigation, typically, of the order of few μm.

The total noise of a scanning microscope is the result of the magnetic flux noise of the SQUID (typical values are of the order of $1\mu\Phi_0\,\mathrm{Hz}^{-1/2}$), and of the ambient noise.

As we have seen, the magnetic flux noise is proportional to the square root of the superconducting ring area; therefore if the area is decreased to obtain a higher spatial resolution, the SQUID becomes more sensitive to magnetic flux. On the other hand, however, decreasing the area reduces its sensitivity in the magnetic field that is proportional to the area of the SQUID. So if you want to increase the spatial resolution, it is necessary to sacrifice the sensitivity in the magnetic field of the microscope. Typical magnetic field noise values of a SQUID microscope having a spatial resolution of 70 μm are $0.1-1$ pT $Hz^{-1/2}$. Ambient noise can be reduced by placing the instrument in one or more μ-metal shields that are very effective especially for low frequency ambient noise, or by using SQUID gradiometers that are insensitive to background noise.

In the following, we will report some interesting measurement performed with SSM. Further insights into the potential of SQUID microscope can be found in Refs. [2,72].

Frolov et al. [73] used a SQUID microscope based on a microSQUID similar to one reported in Fig. 3.18 to image the spontaneous zero-field currents in superconducting networks of temperature-controlled π-junctions with weakly ferromagnetic barriers (Fig. 3.28). They found an onset of spontaneous supercurrents at the $0-\pi$ transition temperature of the junctions (T about 3K). They image the currents in

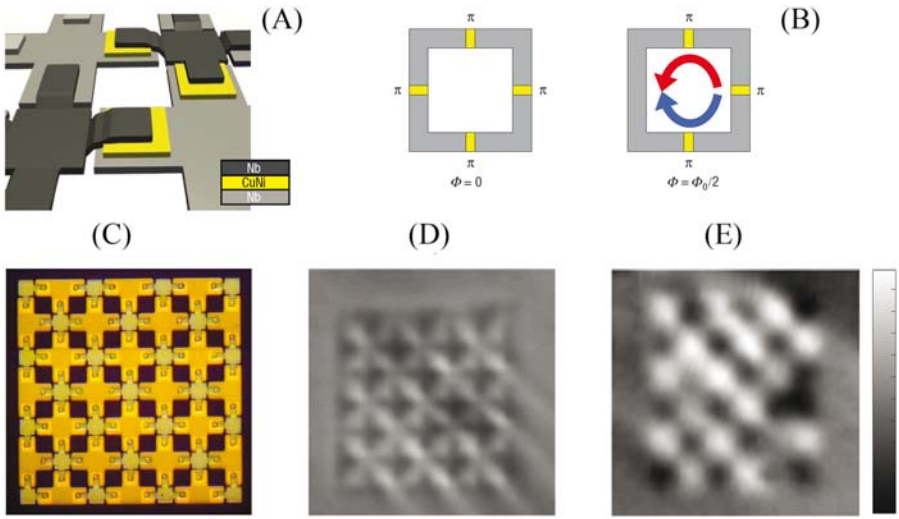

Figure 3.28 (A) Schematic diagram of a single frustrated array cell. (B) Scheme of cells with an even and odd number of π-junctions. (C) Optical image of a 6×6 frustrated SFS array ($Nb-Cu_{47}Ni_{53}-Nb$). (D) and (E) SSM images of the array, including cells with an even number of π-junctions in small applied magnetic flux and an odd number of π-junctions in a zero-applied magnetic field, respectively. *SFS*, Superconductor-Ferromagnet-Superconductor; *SSM*, Scanning SQUID microscope.
Source: Adapted from S.M. Frolov, M.J.A. Stoutimore, T.A. Crane, D.J. Van Harlingen, V. A. Oboznov, V.V. Ryazanov, et al., Imaging spontaneous currents in superconducting arrays of π-junctions, Nat. Phys. 4 (2008) 32.

nonuniformly frustrated arrays consisting of cells with even and odd numbers of π-junctions. In a cell with an even number of π-junctions, the spontaneous flux is zero. In a cell with an odd number of π-junctions, spontaneous currents generate a magnetic flux of order $\pm \Phi_0/2$.

By using a scanning SQUID microscopy equipped with a microSQUID having a 3 μm × 5 μm pick-up loop, Wells et al. [74] measured for the first time a large-scale vortex distribution in a 200-nm tick YBCO film grown by pulsed laser deposition. Due to a strong pinning dominated by out of plane dislocations, the YBCO films enable a vortex glass state, which differs strongly from the vortex lattice. The measurements were performed at $T = 4.2$K in the field cooled state. They applied a magnetic field ($0.1\ \mu T < B_{ext} < 5.5\ \mu T$) perpendicular to the surface of the film. The distance between the YBCO sample and the microSQUID was about 5 μm, and the angle was of 30 degrees. In Fig. 3.29A, the magnetic map of an YBCO film are reported. The brightness of each point shows magnetic field strength, while the round dark spot represents the vortices.

Since, in a scanning SQUID magnetic microscope, the spatial resolution depends by the size of the micro-pick-up coil, the development of nanoSQUIDs fabricated on a

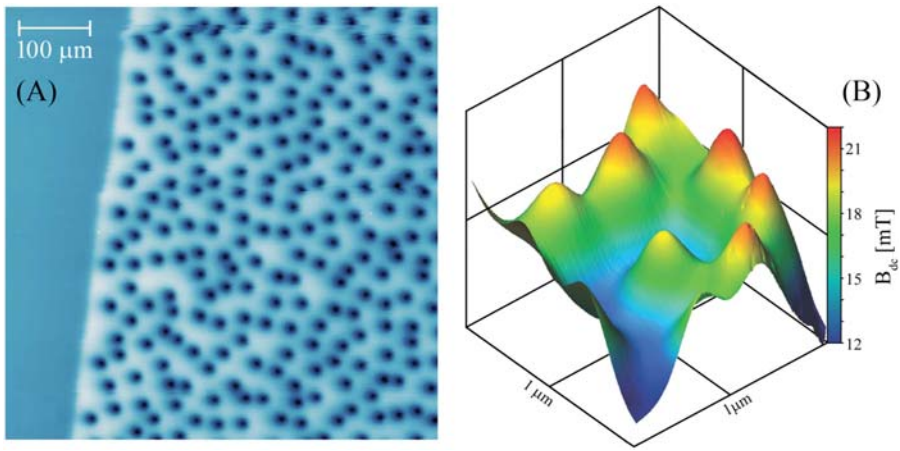

Figure 3.29 (A) Abrikosov vortex image obtained with a scanning SQUID microscope in an YBCO film of 200-nm thickness after field cooling down to 4K at about 7 μT. The average intervortex spacing is 32 μm. (B) Magnetic field distribution generated by ac transport current flowing in a 3-μm-wide Nb strip measured by Pb-based nanoSQUIDs fabricated on a quartz tip having a diameter of 117 nm. *SQUID*, Superconducting quantum interference device.

Source: Adapted from (A) F.S. Wells, A.V. Pan, X.R. Wang, S.A. Fedoseev, H. Hilgenkamp, Analysis of low-field isotropic vortex glass containing vortex groups in YBa2Cu3O7 − x thin films visualized by scanning SQUID microscopy, Sci. Rep. 5 (2015) 8677 and (B) D. Vasyukov, Y. Anahory, L. Embon, D. Halbertal, J. Cuppens, L. Neeman, et al., A scanning superconducting quantum interference device with single electron spin sensitivity, Nat. Nanotechnol. 8 (2013) 639−644.

quartz tip [60,61] appreciably increases the spatial resolution of SSMs. Vasyukov et al. [61] employed the Pb-based nanoSQUID (similar to the one shown in Fig. 3.21C) to image vortices in an Nb thin film (Fig. 3.29B) achieving a very high spatial resolution. During the measurement, the nanoSQUID was placed at a constant height of 50 nm above the sample, and the scanning was performed by an attocube-integrated scanner. The scan areas were $(1 \times 1)\ \mu m^2$ (Fig. 3.28B); the applied fields were $B = 28$ mT. The pronounced peaks displayed in the figure correspond to the vortex centers. The minimum distance between the vortices was 330 nm.

3.3.4 Nanomagnetism

The main application of nanoSQUID is in nanomagnetism, which is the study of small magnetic systems, including magnetic nanoparticles, nanobeads, nanotube, and nanocluster. Recently, there is a growing interest for magnetic nanoparticle applications in biology and nanomedicine, as well as for the study of underlying physics. In particular, the measurements of magnetic relaxation process are very useful for both basic physics investigations like the experimental study of the quantum tunneling of magnetization [75] and applications such as drug delivery or immunoassay techniques [76]. Among the several technique tools employed to investigate the magnetic nanoobjects, those based on nanoSQUIDs allow the most detailed and precise study of magnetic objects at nanometric scale. In the following, we report some examples of nanomagnetism measurements performed with nanoSQUIDs.

The magnetic properties of iron oxide nanoparticle having a diameter ranging from 4 to 8 nm were investigated by Russo et al. [77] and Granata et al. [78] by using the nanoSQUIDs based on both nanobridges and nano-tunnel Josephson junctions. A solenoid surrounding the chip supplied the excitation field coplanar to the SQUID. They measured the field dependence of magnetization at $T = 4.2$K (Fig. 3.30A) for two different sizes of nanoparticles [78]. The hysteretic loops show a coercive field $H_c \cong 290$ G for 8-nm nanoparticles diameter and an $H_c \cong 100$ G for 4-nm nanoparticles diameter indicating an increase of anisotropy as the particle size increases.

Relaxation measurements at $T = 4.2$K for nanoparticles having diameters of 8 and 6 nm were also measured (Fig. 3.30B) [77]. The nanoparticles were cooled in a magnetic field of 10 mT from 300K to 4.2K, then the magnetic field was switched off and the remnant magnetic moment was measured for approximately 1000 s. The data were compared with those obtained by using a commercial system Quantum Design SQUID Magnetometer (Fig. 3.30B, blue/gray squares), confirming the effectiveness of the nanoSQUID measurements. In addition, the nanoSQUID was capable of analyzing the magnetic relaxation behavior in a short-time regime. This feature, unlike the commercial setup, allows to point out the slower magnetic relaxation for short times with respect to that for longer times.

Wernsdorfer et al. [79] studied ferromagnetic nanowires by using microSQUID based on Josepshon nanobridges. In Fig. 3.31A, an SEM image of a microSQUID with a single Ni nanowire is shown. The hysteresis loops, measured by a microSQUID for different angles (θ) between the magnetic field and the wire axis,

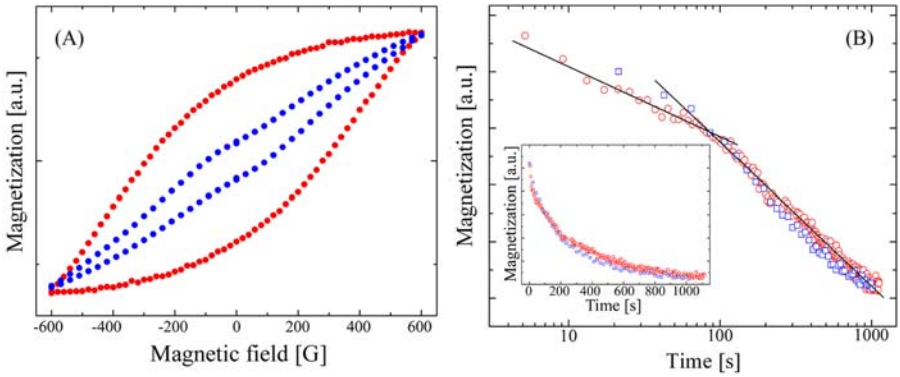

Figure 3.30 (A) Magnetic field dependence of magnetization for iron oxide nanoparticles having a diameter of 4 nm (*blue dots*) and 8 nm (*red dots*) measured at $T = 4.2$K by using a niobium nanoSQUID based on nanobridges. (B) Magnetic relaxation measurement at $T = 4.2$K for 8-nm iron oxide nanoparticles diameter (red circle) compared with a measurement performed by a commercial SQUID instrumentation (*blue squares*). The inset shows the same measurements in a linear scale. *SQUID*, Superconducting quantum interference device.
Source: Adapted from (A) C. Granata, R. Russo, E. Esposito, A. Vettoliere, M. Russo, A. Musinu, et al., Magnetic properties of iron oxide nanoparticles investigated by nanoSQUIDs, Eur. Phys. J. B. 86 (2013) 272 and (B) R. Russo, C. Granata, E. Esposito, D. Peddis, C. Cannas, A. Vettoliere, Nanoparticle magnetization measurements by a high sensitive nano-superconducting quantum interference device, Appl. Phys. Lett. 101 (2012) 122601.

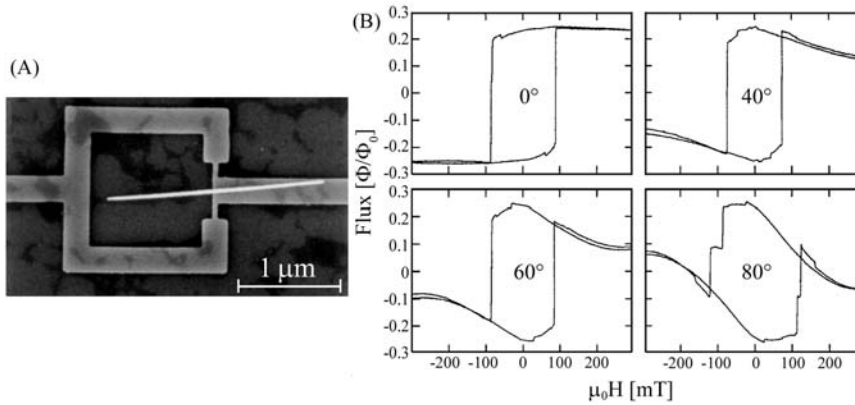

Figure 3.31 (A) SEM images of microSQUID with an Ni nanowire having a diameter of 65 nm. (B) Hysteresis loops of the Ni wire at several values of the angle between the applied field and the wire axis. *SEM*, Scanning electron micrograph; *SQUID*, superconducting quantum interference device.
Source: Adapted from (A) N.L. Adolphi, et al., Characterization of single-core magnetite nanoparticles for magnetic imaging by SQUID relaxometry, Phys. Med. Biol. 55 (2010) 5985–6003 and (B) W. Wernsdorfer, B. Doudin, D. Mailly, K. Hasselbach, A. Benoit, J. Meier, et al., Nucleation of magnetization reversal in individual nanosized nickel wires, Phys. Rev. Lett. 77 (1996) 1873.

are reported in Fig. 3.31B. These measurements provided very useful information about the process of magnetization reversal in nanowire. In particular, the measurements revealed a thermal activated switching following the Arrhenius law according with the Neel−Brown model [80].

Other applications of nanoSQUID are very interesting but there are not yet enough experimental results supporting them but only feasible studies. Among them, it is worth to mention the nanoSQUID readout of an nanoelectromechanical systems resonator [81], the single photon or macromolecule detector [81] and readout for quantum computing [82].

3.3.5 Mentions of other SQUID applications

SQUID systems are also employed in determining the magnetic properties of the earth [2−4]. This concerns both the characterization of specific earth samples (rock magnetometry) and the mapping of the earth magnetic field and its electromagnetic impedance. An important application of SQUID is in *magnetotellurics*, involving the simultaneously measurements of the fluctuating horizontal components of the electric and magnetic fields at the earth's surface originated in the magnetosphere and ionosphere. From these frequency-dependent fields the impedance tensor of the ground can be calculated estimating the spatial variation of the resistivity of the ground. The interesting frequency range is about 10^{-3} to 10^{2} Hz corresponding to a skin depth between about 50 km and 150 m (assuming a resistivity of 10 Ω m). The sensitivity required for magnetotellurics is about 20−30 fT $Hz^{-1/2}$ in the white noise regime and a 1/*f* knee of 1 Hz.

SQUIDs also play a key role in *Metrology* and, in particular, in the development of quantum electrical standards [3,4]. Moreover, SQUID devices have been successfully employed in several experiments of *basic Physic*, including cosmology, astrophysics, general relativity, particle physics, quantum optic, and quantum computing [40].

3.4 Conclusions and perspectives

In this chapter, we have presented a compendium on superconducting quantum sensing and, in particular, of SQUIDs, including the fundamental, the different sensor configurations, and the main applications.

Since their realization (the mid-1960s), the SQUIDs have shown great application potential, in fact, after a few years they were used to carry out the first MEG measurement. During the 1980s and 1990s the development of new manufacturing technologies and, in particular, of niobium technology allowed us to obtain more performing and reliable devices. This has allowed a wide use of SQUID devices and sensors in many fields, including biomedicine, NDE, study of magnetic properties of materials, geophysics, quantum computing, nanomagnetism, and basic physic experiments. Thanks to their peculiarities and extraordinary sensitivity, they have allowed applications and experiments that cannot be carried out in another way.

In conclusion, we would like to stress that these quantum sensors have proven their effectiveness in many applications, and there are still extraordinary potentials to be explored.

References

[1] J. Clarke, A.I. Braginski (Eds.), The SQUID Handbook Vol. I: Fundamentals and Technology of SQUIDs and SQUID Systems, Wiley-VCH Verlag GmbH & Co. KgaA, Weinheim, 2004.

[2] P. Seidel (Ed.), Applied Superconductivity: Handbook on Devices and Applications, Wiley, Weinheim, 2015.

[3] J. Clarke, A.I. Braginski (Eds.), The SQUID Handbook Vol. II: Fundamentals and Technology of SQUIDs and SQUID Systems, Wiley-VCH Verlag GmbH & Co. KgaA, Weinheim, 2006.

[4] R.K. Fagaly, Superconducting quantum interference device instruments and applications, Rev. Sci. Instrum. 77 (2006) 101101.

[5] M. Tinkham, Introduction to the Superconductivity, second ed., Dover Publication INC, 2004.

[6] M. Cyrot, D. Pavuna, Introduction to Superconductivity and High-T_c Materials, World Scientific Press, 1992.

[7] C. Poole, H. Farach, R. Creswick, R. Prozorov, Superconductivity, Elsevier, 2014.

[8] B.D. Josephson, Possible new effects in superconductive tunneling, Phys. Lett. 1 (1962) 251−253.

[9] A. Barone, G. Paterno, Physics and Applications of the Josephson Effect, John Wiley & Sons, New York, 1982.

[10] D.D. Coon, M.D. Fiske, Josephson ac and step structure in the supercurrent tunneling characteristics, Phys. Rev. 138 (1965) A744−A746.

[11] R. Doll, M. Nabauer, Experimental proof of magnetic flux quantization in a superconducting ring, Phys. Rev. Lett. 7 (1961) 51−52.

[12] W.C. Stewart, Current-voltage characteristics of Josephson junctions, Appl. Phys. Lett. 12 (1968) 277−280.

[13] D.E. McCumber, Effect of ac impedance on dc voltage-current characteristics of Josephson junctions, J. Appl. Phys. 39 (1968) 3113−3118.

[14] R. Cantor, DC SQUIDs: design, optimization and practical applications, in: H. Weinstock (Ed.), SQUID Sensors: Fundamentals, Fabrication and Applications, Series E: Applied Sciences, vol. 329, Kluwer Academic Publisher, Dordrecht, 1996, p. 179.

[15] M.B. Ketchen, J.M. Jaycox, Ultra-low-noise tunnel junction dc SQUID with a tightly coupled planar input coil, Appl. Phys. Lett. 40 (1982) 736−738.

[16] D. Drung, Advanced SQUID read-out electronics, in: H. Weinstock (Ed.), SQUID Sensors: Fundamentals, Fabrication and Application, Series E: Applied Sciences, vol. 329, Kluwer Academic Publisher, Dordrecht, 1996, pp. 63−116.

[17] J. Clarke, SQUID fundamentals, in: H. Weinstock (Ed.), SQUID Sensors: Fundamentals, Fabrication and Application, Series E: Applied Sciences, vol. 329, Kluwer Academic Publisher, Dordrecht, 1996, pp. 1−62.

[18] D. Drung, R. Cantor, M. Peters, A.J. Scheer, H. Koch, Low-noise high-speed dc superconducting quantum interference device magnetometer with simplified feedback electronics, Appl. Phys. Lett. 57 (1990) 406−408.

[19] C. Tesche, J. Clarke, DC SQUID: noise and optimization, J. Low Temp. Phys. 29 (1977) 301−331.
[20] M.B. Ketchen, Integrated thin-film dc SQUID sensors, IEEE Trans. Magn. 23 (1987) 1650−1657.
[21] M.B. Ketchen, W.J. Gallagher, A.W. Kleinsasser, S. Murphy, J.R. Clem, dc SQUID flux focuser, in: H.D. Hadlbohm, H. Lubbig (Eds.), SQUID'85: Superconducting Quantum Interference Devices and their Applications, Walter de Gruyter, Berlin, New York, 1985, pp. 865−871.
[22] C. Granata, A. Vettoliere, M. Russo, Improved superconducting quantum interference device magnetometer for low cross talk operation, Appl. Phys. Lett. 88 (2006) 212506.
[23] D. Drung, S. Knappe, H. Koch, Theory for the multiloop dc superconducting quantum interference device magnetometer and experimental verification, J. Appl. Phys. 77 (1995) 4088−4098.
[24] D. Drung, H. Koch, An integrated dc SQUID magnetometer with variable additional positive feedback, Supercond. Sci. Technol. 7 (1994) 242−245.
[25] M. Schmelz, R. Stolz, V. Zakosarenko, T. Schonau, S. Anders, L. Fritzsch, et al., Field-stable SQUID magnetometer with sub-fT $Hz^{-1/2}$ resolution based on sub-micrometer cross-type Josephson tunnel junctions, Supercond. Sci. Technol. 24 (2011) 065009.
[26] M.B. Ketcken, Design of improved integrated thin-film planar dc SQUID gradiometers, J. Appl. Phys. 58 (1985) 4323.
[27] C. Granata, A. Vettoliere, C. Nappi, M. Lisitskiy, M. Russo, Long baseline planar superconducting gradiometer for biomagnetic imaging, Appl. Phys. Lett. 95 (2009) 042502.
[28] B. Muhlfelder, W. Johnson, M.W. Cromar, Double transformer coupling to a very low noise SQUID, IEEE Trans. Magn. 19 (1983) 303−307.
[29] V. Polushkin, E. Gu, D. Glowacka, D. Goldie, J. Lumley, A tightly coupled dc SQUID with an intermediary transformer, Phys. C. 367 (2002) 280−284.
[30] C. Granata, A. Vettoliere, M. Russo, An ultralow noise current amplifier based on superconducting quantum interference device for high sensitivity applications, Rev. Sci. Instrum. 82 (2011) 013901.
[31] A. Vettoliere, C. Granata, B. Ruggiero, M. Russo, An ultra high sensitive current sensor based on superconducting quantum interference device, in: A. D'amico, C. Di Natale, L. Mosiello, G. Zappa (Eds.), Sensors and Microsystems, Lecture Notes in Electrical Engineering, vol. 109, Springer US, 2012 (Copyright Holder: Springer New York). Available from: https://dx.doi.org/10.1007/978-1-4614-0935-9.
[32] V. Zakosarenko, M. Schmelz, R. Stolz, T. Schonau, L. Fritzsch, S. Anders, et al., Femtoammeter on the base of SQUID with thin-film flux transformer, Supercond. Sci. Technol. 25 (2012) 095014.
[33] J.R. Kirtley, J.P. Wikswo, Scanning SQUID microscopy, Annu. Rev. Mater. Sci. 29 (1999) 117−148.
[34] L.N. Vu, M.S. Wistrom, D.J.Van Harlingen, Imaging of magnetic vortices in superconducting networks and clusters by scanning SQUID microscopy, Appl. Phys. Lett. 63 (1993) 1693−1695.
[35] C. Granata, A. Vettoliere, R. Vaccarone, M. Russo, Low critical temperature dc-SQUIDs for high spatial resolution applications, IEEE Trans. on, Appl. Supercond. 17 (2007) 796−799.
[36] Y. Shperber, N. Vardi, E. Persky, S. Wissberg, M.E. Huber, B. Kalisky, Scanning SQUID microscopy in a cryogen-free cooler, Rev. Sci. Instrum. 90 (2019) 053702.

[37] D. Gatteschi, R. Sessoli, Quantum tunneling of magnetization and related phenomena in molecular materials, Angew. Chem. Int. Ed. 42 (2003) 268−287.
[38] S.D. Bader, Colloquium: opportunities in nanomagnetism, Rev. Mod. Phys. 78 (2006) 1−15.
[39] C.P. Foley, H. Hilgenkamp, Why nanoSQUIDs are important: an introduction to the focus issue, Supercond. Sci. Technol. 22 (2009) 064001.
[40] W. Wernsdorfer, From micro to nano-SQUIDs: Applications to nanomagnetism, Supercond. Sci. Technol. 22 (2009) 064013.
[41] L. Hao, C. Granata, Recent trends and perspectives of nanoSQUIDs: introduction to the focus on nanoSQUID and their applications, Supercond. Sci. Technol. 30 (2017) 0050301.
[42] C. Granata, A. Vettoliere, Nano superconducting quantum interference device: a powerful tool for nanoscale investigations, Phys. Rep. 614 (2016) 1−69.
[43] C. Granata, A. Vettoliere, P. Walke, C. Nappi, M. Russo, Performance of nano superconducting quantum interference devices for small spin cluster detection, J. Appl. Phys. 106 (2009) 023925.
[44] M.B. Ketchen, D.D. Awschalom, W.J. Gallagher, A.W. Kleinsasser, R.L. Sandstrom, J. R. Bozen, B. Bumble, Design, fabrication and performance of integrated miniature SQUID susceptometer, IEEE Trans. Magn. 25 (1989) 1212.
[45] M.A. McCord, M.J. Rooks, Chapter 2: Electron beam lithography, in: P. Rai-Choudhury (Ed.), SPIE Handbook of Microlithography, Micromachining and Microfabrication, vol. 1, 2000, pp. 139−250. ISBN: 0-8194-2378-5.
[46] H.D. Wanzenboeck, S. Waid, Chapter 2: Focused ion beam lithography, in: B. Cui (Ed.), Recent Advances in Nanofabrication Techniques and Applications, InTech, 2011, pp. 27−50. ISBN: 978-953-307-602-7.
[47] P.E. Lindelof, Superconducting microbridges exhibiting Josephson properties, Rep. Prog. Phys. 44 (1981) 60.
[48] S.K.H. Lam, D.L. Tilbrook, Development of a niobium nanosuperconducting quantum interference device for the detection of small spin populations, Appl. Phys. Lett. 82 (2003) 1078−1080.
[49] A.G.P. Troeman, H. Derking, B. Boerger, J. Pleikies, D. Veldhuis, H. Hilgenkamp, NanoSQUIDs based on niobium constrictions, Nano Lett. 7 (2007) 2152−2156.
[50] L. Hao, J.C. Macfarlane, J.C. Gallop, D. Cox, J. Beyer, D. Drung, et al., Measurement and noise performance of nano-superconducting-quantum interference devices fabricated by focused ion beam, Appl. Phys. Lett. 92 (2008) 192507. 1−3.
[51] C. Granata, E. Esposito, A. Vettoliere, L. Petti, M. Russo, An integrated superconductive magnetic nanosensor for high-sensitivity nanoscale applications, Nanotechnology 19 (2008) 275501−275506.
[52] J. Nagel, O.F. Kieler, T. Weimann, R. Wolbing, J. Kohlmann, A.B. Zorin, et al., Superconducting quantum interference devices with submicron Nb/HfTi/Nb junctions for investigation of small magnetic particles, Appl. Phys. Lett. 99 (2011) 032506. 1−3.
[53] R. Wölbing, J. Nagel, T. Schwarz, O. Kieler, T.J. Weimann, J. Kohlmann, et al., Nb nano superconducting quantum interference devices with high spin sensitivity for operation in magnetic fields up to 0.5 T, Appl. Phys. Lett. 102 (2013) 192601. 1−4.
[54] C. Granata, A. Vettoliere, R. Russo, M. Fretto, N. De Leo, V. Lacquaniti, Three-dimensional spin nanosensor based on reliable tunnel Josephson nano-junctions for nanomagnetism investigations, Appl. Phys. Lett. 103 (2013) 102602. 1−4.
[55] A. Ronzani, M. Baillergeau, C. Altimiras, F. Giazotto, Micro-superconducting quantum interference devices based on V/Cu/V Josephson nanojunctions, Appl. Phys. Lett. 103 (2013) 052603.

[56] M. Schmelz, Y. Matsui, R. Stolz, V. Zakosarenko, T. Schönau, S. Anders, et al., Investigation of all niobium nano-SQUIDs based on sub-micrometer cross-type Josephson junctions, Supercond. Sci. Technol. 28 (2015) 015004.
[57] M.J. Martínez-Pérez, D. Gella, B. Müller, V. Morosh, R. Wölbing, J. Sesé, et al., Three-axis vector nano superconducting quantum interference device, ACS Nano 10 (2016) 8308.
[58] M. Schmelz, A. Vettoliere, V. Zakosarenko, N. De Leo, M. Fretto, R. Stolz, et al., 3D nanoSQUID based on tunnel nano-junctions with an energy sensitivity of 1.3 h at 4.2K, Appl. Phys. Lett. 111 (2017) 032604.
[59] J.-P. Cleuziou, W. Wernsdorfer, V. Bouchiat, T. Ondarcuhu, M. Monthioux, Carbon nanotube superconducting quantum interference device, Nat. Nanotechnol 1 (2006) 53–59.
[60] A. Finkler, Y. Segev, Y. Myasoedov, M.L. Rappaport, L. Ne'eman, D. Vasyukov, et al., Self-aligned nanoscale SQUID on a tip, Nano Lett. 10 (2010) 1046–1049.
[61] D. Vasyukov, Y. Anahory, L. Embon, D. Halbertal, J. Cuppens, L. Neeman, et al., A scanning superconducting quantum interference device with single electron spin sensitivity, Nat. Nanotechnol 8 (2013) 639–644.
[62] C.H. Wu, Y.T. Chou, W.C. Kuo, J.H. Chen, L.M. Wang, J.C. Chen, et al., Fabrication and characterization of high-Tc $YBa_2Cu_3O_{7-x}$ nanoSQUIDs made by focused ion beam milling, Nanotechnology 19 (2008) 315304.
[63] T. Schwarz, J. Nagel, R. Wolbing, M. Kemmler, R. Kleiner, D. Koelle, Low-noise nano superconducting quantum interference device operating in Tesla magnetic fields, ACS Nano 7 (2013) 844–850.
[64] R. Arpaia, M. Arzeo, S. Nawaz, S. Charpentier, F. Lombardi, T. Bauch, Ultra low noise $YBa_2Cu_3O_7$ nano superconducting quantum interference devices implementing nanowires, Appl. Phys. Lett. 104 (2014) 072603. 1–4.
[65] K. Sternickel, A.I. Braginski, Biomagnetism using SQUIDs: status and perspectives, Supercond. Sci. Technol. 19 (2006) 160–171.
[66] D. Cohen, E. Halgren, Magnetoencephalography, Encycl. Neurosci. 5 (2009) 615–622.
[67] M. Hämäläinen, R. Hari, R. Ilmoniemi, J. Knuutila, O. Lounasmaa, Magnetoencephalography—theory, instrumentation, and applications to noninvasive studies of the working human brain, Rev. Mod. Phys. 65 (1993) 413–497.
[68] C. Del Gratta, V. Pizzella, F. Tecchio, G.L. Romani, Magnetoencephalography—a noninvasive brain imaging method with 1 ms time resolution, Rep. Prog. Phys. 64 (2001) 1759–1814.
[69] S. Rombetto, C. Granata, A. Vettoliere, M. Russo, Multichannel system based on a high sensitivity superconductive sensor for magnetoencephalography, Sensors 14 (2014) 12114–12126.
[70] W.G. Jenks, S.S.H. Sadeghi, J.P. Wikswo, SQUIDs for NDE, J. Phys. D 30 (1997) 293–323.
[71] G.B. Donaldson, The use of SQUIDs for NDE, in: H. Weinstock (Ed.), SQUID Sensors: Fundamentals, Fabrication and Application, Series E: Applied Sciences, vol. 329, Kluwer Academic Publisher, Dordrecht, 1996, pp. 599–628.
[72] J.R. Kirtley, Fundamental studies of superconductors using scanning magnetic imaging, Rep. Prog. Phys. 73 (2010) 126501.
[73] S.M. Frolov, M.J.A. Stoutimore, T.A. Crane, D.J. Van Harlingen, V.A. Oboznov, V.V. Ryazanov, et al., Imaging spontaneous currents in superconducting arrays of π-junctions, Nat. Phys. 4 (2008) 32.
[74] F.S. Wells, A.V. Pan, X.R. Wang, S.A. Fedoseev, H. Hilgenkamp, Analysis of low-field isotropic vortex glass containing vortex groups in $YBa_2Cu_3O_{7-x}$ thin films visualized by scanning SQUID microscopy, Sci. Rep. 5 (2015) 8677.

[75] W. Wernsdorfer, Classical and quantum magnetization reversal studied in nanometer sized particles and clusters, Adv. Chem. Phys. 118 (2001) 99.
[76] N.L. Adolphi, et al., Characterization of single-core magnetite nanoparticles for magnetic imaging by SQUID relaxometry, Phys. Med. Biol. 55 (2010) 5985–6003.
[77] R. Russo, C. Granata, E. Esposito, D. Peddis, C. Cannas, A. Vettoliere, Nanoparticle magnetization measurements by a high sensitive nano-superconducting quantum interference device, Appl. Phys. Lett. 101 (2012) 122601.
[78] C. Granata, R. Russo, E. Esposito, A. Vettoliere, M. Russo, A. Musinu, et al., Magnetic properties of iron oxide nanoparticles investigated by nanoSQUIDs, Eur. Phys. J. B. 86 (2013) 272.
[79] W. Wernsdorfer, B. Doudin, D. Mailly, K. Hasselbach, A. Benoit, J. Meier, et al., Nucleation of magnetization reversal in individual nanosized nickel wires, Phys. Rev. Lett. 77 (1996) 1873.
[80] W.F. Brown, Thermal fluctuations of a single-domain particle, Phys. Rev. 130 (1963) 1677.
[81] L. Hao, D.C. Cox, J.C. Gallop, E.J. Romans, J.C. Macfarlane, J. Chen, Focused ion beam nanoSQUIDs as novel NEMS resonator readouts, IEEE Trans. Appl. Supercond. 19 (2009) 693–696.
[82] J. Tejada, E.M. Chudnovsky, E. del Barco, J.M. Hernandez, T.P. Spiller, Magnetic qubits as hardware for quantum computers, Nanotechnology 12 (2001) 181–186.

This page intentionally left blank

Nano-engineered composites based on carbon nitride as potential agents for the remediation of water with micropollutants

4

Eliane Vieira Rosa[1,2], *Alex Fabiano Cortez Campos*[3], *Marcelo Oliveira Rodrigues*[4], *Mohamed Henini*[5] and *Marcelo Henrique Sousa*[2]

[1]Federal Institute of Education, Science and Technology Goiano, Campus Ceres, Ceres, GO, Brazil, [2]Green Nanotechnology Group, University of Brasília, Brasília, DF, Brazil, [3]Laboratory for Environmental and Applied Nanoscience, University of Brasília, Brasília, DF, Brazil, [4]Laboratory of Medicinal and Technological Chemistry, University of Brasília, Brasília, DF, Brazil, [5]School of Physics and Astronomy, University of Nottingham, Nottingham, Nottinghamshire, United Kingdom

4.1 Introduction

One of the main problems of the growing rate of industrialization is the inappropriate emission of organic and inorganic pollutants into soil and water [1]. A broad range of contaminants from effluents of various sources may accumulate in water or soil and persist in the ecosystems due to their lack of metabolism and biodegradation, which poses serious threats to the environment and human health [2–5]. In general, conventional treatment methods do not effectively remove these contaminants [6–11], therefore the treated effluents often do not meet water quality standards [6,12–16]. It is particularly important in the case of small factories and industries, where the application of traditional remediation techniques is normally expensive and/or unfeasible [9,17].

In this context, remediation methods based on nano-engineered materials have gained increasing attention from the scientific community as an alternative to the traditional decontamination techniques for water and soil pollution remediation [4,18–24]. These materials are manufactured in the size range from 1 to 100 nm, which provides them with a highly reactive and large surface area. As a result, they can be used to remove traces of pollutants and can also be modulated to present not only high selectivity to a target contaminant but also low toxicity [5,7] (Fig. 4.1).

Several materials have been used in research on new nanocomposites for environmental remediation purposes [8,11,25]. Nano-structured carbon nitride (CN) has

Quantum Materials, Devices, and Applications. DOI: https://doi.org/10.1016/B978-0-12-820566-2.00006-5

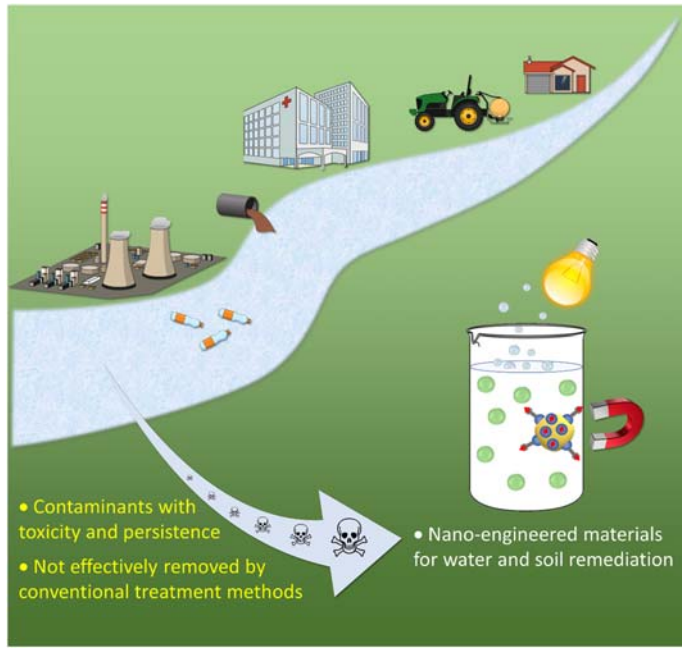

Figure 4.1 Nano-engineered nanocomposites have been emerging as one of alternatives for water and soil remediation. These innovative materials offer potential advantages compared to conventional treatments due to their multifunctional and enhanced properties.

been considered a promising material in this regard due to its ease of synthesis, low cost, high structural, and chemical stability, presence of nontoxic elements (carbon, hydrogen, oxygen, and nitrogen) [10], and photocatalytic (PC) activity [7,26–28]. In its pure form, CN merges high adsorption capacity and remarkable PC activity in a single material, making it effective in the remediation of different pollutants [26–29]. The possibility of modifying CN incorporating different nanocompounds can aggregate new physical and physical–chemical characteristics to the formed nanocomposite where the properties of CN and nanoguest phase are synergically combined. This endows the nanocomposites with higher PC activity and more active and diversified surface sites, which improve their adsorption efficiency and selectivity for a wide number of compounds, extending the capacity to remediate a larger range of pollutants [26,30,31].

Despite the adsorption capacity the presence of a host phase on CN can also improve the remediation performance of the formed nanocomposites in terms of chemical separation. For example, the decoration of CN with magnetic materials allows a fast and easy separation of the nanocomposite loaded with the contaminant by application of an external magnetic field [32]. The magnetically assisted chemical separation is frequently more efficient and cost-effective compared to traditional forms of separation such as centrifugation, filtration, and flotation [5,33]. Also, it minimizes the presence of residual adsorbent in the medium [5,34].

This chapter focuses on the synthesis and application of nano-engineered CN-based composites with different materials as a potential tool for water remediation. Special attention is addressed to the removal of dyes and phenol-based compounds present in industrial rejects, and residual antibiotics in wastewater using adsorption and photodegradation.

4.2 Industrial-origin contaminants and antibiotics: dangerous micropollutants to the environment and health

The global concern about environmental damage is evident as well as with the metabolic diseases and alterations that arise from contact with some contaminants present in the aquatic ambient environment. Particularly, the micropollutants, whose concentrations remaining at trace levels, are bioactive, persistent, and very toxic even at very low concentrations (i.e., up to the microgram per liter range). Also, they are not completely biodegradable and cannot be fully eliminated by traditional wastewater treatment methods. These pollutants are originated from anthropogenic activities and can be found in healthcare products, industrial wastes, agricultural pesticides, and medicines [35].

Concerning the micropollutants from the industrial origin, dyes have been considered major water contaminants [36]. Currently, these materials have been playing a critical role in textile, cosmetic, paper, leather, rubber, and printing industries, which implies a high demand for production [37,38]. Moreover, it is estimated that 10%−15% of the volume of dye production is discarded as wastewater [39]. Besides their persistence in the environment, most of the dyes are carcinogenic and can cause skin and eye irritation and promote biological alterations [38]. For example, rose bengal, which was considered a vital dye, may cause significant ocular irritation after topical ocular instillation [7,40]. Malachite green, a dye highly used in industry, disinfectant materials, and in aquaculture, presents a negative potential action in cell metabolism, interfering in mitochondrial activity [41,42]. Aniline, an ionizable organic compound, is considered toxic and mutagenic and is mainly released in the effluent of pharmaceutical and petrochemical industries [43,44].

Another class of contaminants also focused in this chapter are the endocrine disruptors based on phenols and aromatic compounds [9,45]. Present in industrial waste, their use also ranges from the industrial sector to agricultural and domestic products used in everyday life, including plastics, packings, and some antiseptic sprays and lotions [46,47]. These compounds present harmful effects for human health, acting on the epithelial cells of the skin, eyes, and mucosa [48,49]. Depending on the level of exposure to these compounds, concentrations of phenols can be detected in urine as well as in other biological fluids [47,50,51]. Tang et al., in their research with pregnant women, evaluated different groups of phenols and found an association between the duration of the gestation with the exposure to biphenyl A and benzophenone-3 through the analysis of phenols in the urine.

These authors emphasized that many groups of phenols can cross the placental barrier, thus being able to interfere adversely in fetal growth [47]. Analyzing the presence of different groups of phenols in the urine of infertile men, in comparison with the urine of fertile men, Chen et al. found an association between male infertility and exposure to the following phenols: 4-*tert*-octylphenol, 4-*n*-octylphenol, and 4-*n*-nonylphenol [52]. At the cell level, McCall et al. verified that phenols affect the barrier of human epithelial cells cultivated in vitro using disturbing domains in the plasmatic membrane [46]. Biphenyl polychloride and polybromobiphenyl are phenols that have presented potential as endocrine disruptors, acting as agonists or antagonists of sexual and thyroid hormones [53]. Special attention is given to bisphenol A (BPA), a phenol used in different materials in daily life, including packaging, dental and healthcare products, and toys. The hazard of this compound is enhanced since it can be released in the environment and dissolved in water [54–56]. Recent studies have revealed that BPA has estrogenic activity [54], fertility-disrupting potential [57], and may contribute to obesity and cancer development [55]. Moreover, prenatal exposure to BPA has been considered as an environmental risk factor for the development of autism spectrum disorder [45].

The phthalate esters, widely used in industry to improve flexibility and resistance of plastics [58], are also important contaminants in the group of aromatic compounds. A study carried out by Li et al. evaluated the combined effect of 4-nonylphenol and di-*n*-butyl phthalate in cells of the testicle, related to the support, nutrition and regulation of the germinative cells in the process of spermatozoid production (Sertoli cells). In this research the authors found that exposure to these two compounds can induce the destruction of cell membrane integrity, increasing permeability to these chemical compounds [59].

Antibiotics are also found in the environment, mainly in water, due to their wide use in human and veterinary medicine [25,60]. The presence of antibiotics in water and wastewater can lead to the selection of resistant bacteria and promote potential toxicity for aquatic animals [61]. Some antibiotics, such as sulfamethoxazole (SMX), can persist in the environment due to their low degradability, thus leading to toxicity for the environment and humans [62]. A recent study analyzed the possible effects of toxicity and biological alterations in Nile tilapia fish after exposure to SMX and oxytetracycline [63]. The tests showed that even at low doses or legal doses used in aquaculture, SMX delays performance in growth and feeding efficiencies of the fish. Moreover, low doses of the two antibiotics and legal doses used in agriculture promoted atrophy of the liver and histopathological alterations in the intestinal villi. They also reduced the activity of proteases and lipases in the animals that were exposed. The researchers emphasized that human beings could suffer from consequences caused by the ingestion of fish exposed to these antibiotics.

The possibility of contact with these and other pollutants raises the chance of damage to the health and the environment. The capacity of these compounds to persist, even after conventional treatment, demonstrates the need to develop techniques and materials with effective action against these pollutants, guaranteeing safety in the treatment of water and wastewater. In this context, new materials and nanomaterials offer an opportunity to develop a new generation of

environmental remediation tools with high efficiency and capacity [9,21]. In this regard, nanocomposites based on CN modified with different nanomaterials have been used as promising materials.

4.3 Carbon nitride

CN is a metal-free organic polymer that has a low production cost through facile synthesis routes. Besides, it presents high thermal and chemical stability, low toxicity, and high solubility in water [64–70]. The main features of CN in the environmental field, namely, potential capacity to adsorb different pollutants [34,71–74] and PC activity to degrade them [75–77], are mainly derived from its structure. Among the several allotropes, the graphitic CN (g-CN) has similar carbon network and sp^2 conjugated π structures as a graphene [78] formed by triazine or tri-*s*-triazine units cross-linked by trigonal nitrogen atoms to form extended networks that build stacked layers, as shown in Fig. 4.2. The proportion of triazine or tri-*s*-triazine units depends on the raw materials used and on the condensation process during the synthesis. Besides, g-CN can present residual hydrogen in defects and different surface terminations such as Brønsted and Lewis basic sites, which confers different chemical properties to the material [79–82].

The strong covalent bonds between carbon and nitrogen atoms provide high chemical and thermal stability of g-CN, preventing its photocorrosion under visible light and improving its catalytic activity [71,83,84]. Moreover, the porous body and large surface constituted by sp^2 π-conjugative moieties and primary/secondary/tertiary amines improve the adsorbent–adsorbate affinity through π–π electron coupling, covalent, electrostatic, and hydrogen bonds adsorbate/adsorbent interactions, increasing the g-CN pollutant removal performance (Fig. 4.2). The π-conjugated structure is also responsible for the optical properties of CN, which is considered a semiconductor with a bandgap between 1.5 and 2.70 eV, a very desirable characteristic for applications in photocatalysis processes [80,85–87]. Actually, this property favors the collection of low-energy visible photons (460–827 nm) [85,88] allowing the execution of PC procedures in a configuration similar to the natural environment [89,90].

The photocatalysis using CN catalysts is an important technique that can be applied in different processes of pollutants degradation [91] through the irradiation with different types of light: solar [87,92], visible [86,93], or ultraviolet (UV) [91]. In these processes, radiation activates the CN catalyst at the atomic level, promoting the migration of electrons from the valence band (VB) to the conduction band (CB), with the formation of electronic vacancies holes (h^+) [94]. As schematized in Fig. 4.3, when in aqueous solution, the activation of CN by light can promote the oxidation of superficial hydroxide ions (OH^-) or O_2, producing reactive oxygen species. The main species include hydroxyl radical (•OH), generated by the holes in the VB, and superoxide radical ($\bullet O_2^-$), generated by the accumulated rich electrons in the CB [95]. Typically, degradation of organic pollutants can occur through these

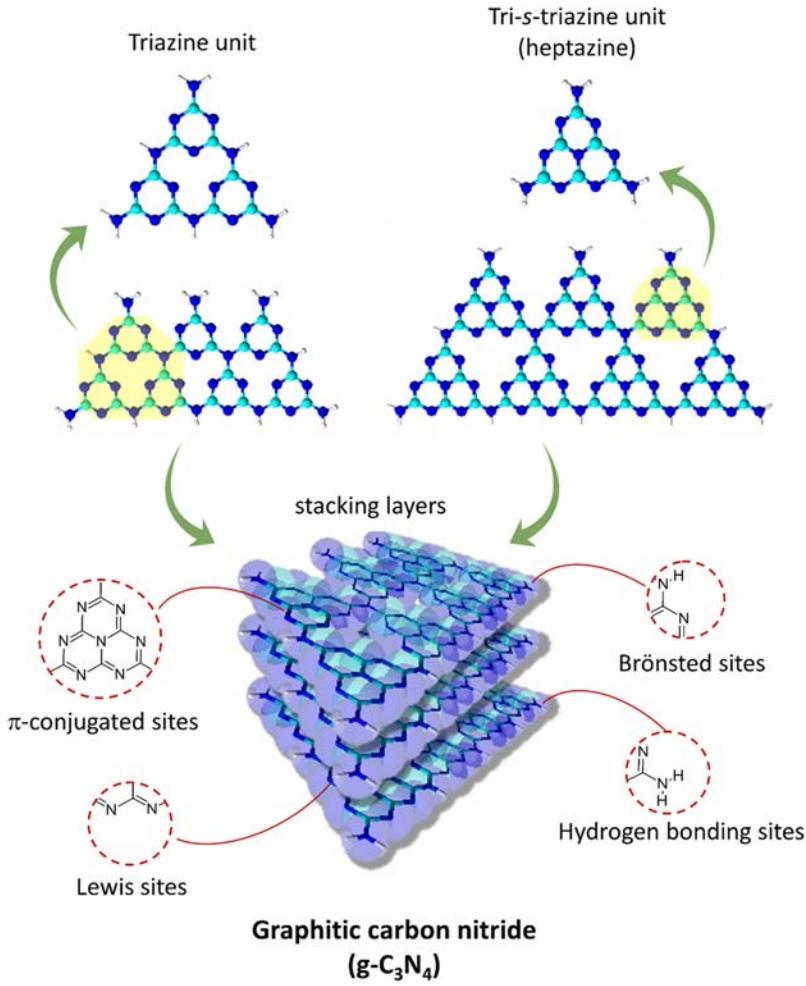

Figure 4.2 g-CN and its unique graphitic π-conjugated stacking 2D structures and terminal groups. *g-CN*, graphitic carbon nitride.

radicals, culminating with an initial decomposition into smaller fragments, followed by the formation of smaller molecules leading to mineralization in nonnoxious forms [94,96].

The synthesis of CN is normally achieved by thermal condensation of carbon/nitrogen-rich raw compounds at temperatures higher than 500°C [97,98]. However, some other less common methods are also employed, such as hydrothermal polyol-mediated [99], microwave-assisted [99,100], and chemical vapor deposition [101]. In this chapter the synthesis using thermal condensations is focused. Particularly, CN has structural properties that can be molded according to the synthesis route [75]. Thus through different protocols, various carbon/nitrogen-rich raw materials

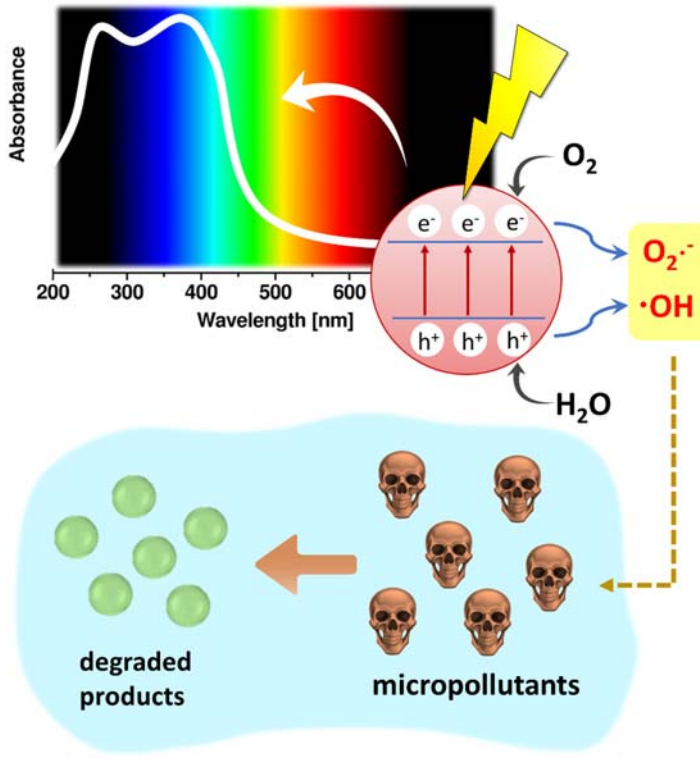

Figure 4.3 Scheme of g-CN activation by solar, visible, or ultraviolet radiation. The main reactive oxygen species generated in the photocatalytic process (•OH and $•O_2^-$) are responsible for pollutant degradation. *g-CN*, graphitic carbon nitride.

have been extensively used, among them melamine, guanidine, cyanamide, dicyandiamide, urea, and thiourea are mostly employed [73,86,87,90,102] (Fig. 4.4). Indeed, there is a correlation between the type of precursor chosen for the synthesis and the final polymeric structure to favor the PC action of CN [28,68,79]. Lan et al. synthesized g-CN using urea, cyanamide, or melamine, employing thermal treatment at 550°C for 4 h, and found that urea promoted a high level of polymerization with a lower number of hydrogen terminations and few structural defects in the product [28]. Otherwise, cyanamide and melamine promoted the formation of similar structures, with a large number of infrastructural spaces, inducing the formation of nitrogen vacancies, which can narrow the band-gap value toward the region of visible light. Research carried out by Zhao et al. demonstrated that under different temperatures at controlled times, the use of melamine, guanidine carbonate, and dicyandiamide promoted the formation of g-CN with different PC activities [80]. The authors found that CN produced by the calcination of melamine at 600°C showed the greatest PC capacity to degrade methyl orange (MO) under irradiation with visible light when compared to g-CN produced by guanidine carbonate and

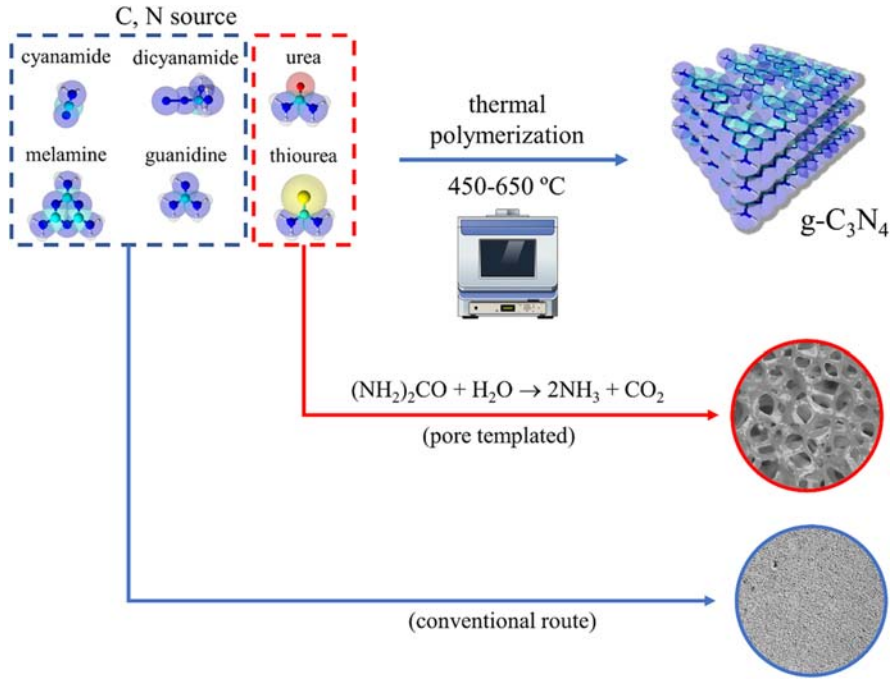

Figure 4.4 Scheme of carbon nitride synthesis through thermal condensation. The final polymeric structure of the material can be tuned according to the precursors used in the synthesis. The use of urea and thiourea as precursors leads to porous structures, which often improve the adsorption capacity and photocatalytic activity of the nanocomposite.

dicyandiamide at different temperatures of synthesis. According to Zhu et al., cyanamide in the presence of NaOH can be converted into g-CN at lower temperatures ($\sim$500°C) and with a greater surface area [68].

It is worth to mention that some "structural defects," which occur during the formation of g-CN due to incomplete condensation of its synthesis precursors, are considered advantageous as they can promote a greater number of superficial bonding sites or facilitate their modification for the optimization of pollutant adsorption [28,71]. Vacancy defects, normally related to nitrogen or carbon gaps or minor defects of nitrogen sp^2 [28], can also regulate and control the band structure improving the PC performance [103].

The presence of pores is also an important factor that can improve the CN adsorptive/catalytic properties. One of the strategies to increase the number of pores in the final structure of CN, which provides a larger number of reactive sites, is the use of templates that can be eliminated at the end of synthesis, not causing interference in the final structure of CN [68,104]. For instance, Wang et al. studied the PC performance of g-CN synthesized from the thermal condensation of melamine and using the pluronic surfactant F68 as the template [7]. They found that the material synthesized through this route presents type IV N_2 adsorption and desorption

isotherms, typical of mesoporous materials. The high efficiency (~90%) in the degradation of rose bengal under irradiation of UV light at 300 W for 6 h was correlated to the presence of larger pores in comparison to CN synthesized without the use of templates.

The use of raw compounds that produce a large volume of gases during the thermal decomposition is also a tool to obtain high porous structures of CN. For example, in the thermal decomposition of urea, the released ammonia (NH_3) can be reused in the process of pyrolysis acting as a supplier of nitrogen for the g-CN while the released carbon dioxide (CO_2) forms bubbles and works as a template, increasing the number and size of pores (Fig. 4.4). Oh et al. synthesized g-CN samples by thermal decomposition using dicyandiamide, melamine, or urea to compare their PC efficiency [75]. The authors found that urea promoted the formation of g-CN with a higher number of pores and best catalytic activity toward the pollutant rhodamine B (RhB) than the product obtained with melamine or dicyanamide. Wang et al. synthesized g-CN adsorbents by heating different combinations of cyanamide and urea in an oil bath at 60°C followed by calcination at 550°C for 2 h [86]. The g-CN obtained from mixtures containing the 1:3 mass ratio (cyanamide:urea) demonstrated PC potential for triethanolamine degradation, which was 10 times greater than the performance of g-CN produced by pure cyanamide. According to the authors, urea-based sample presented a surface five times greater than those produced using cyanamide, indicating that the carbon dioxide formed in the urea pyrolysis process acted as a template.

Xu et al. developed a methodology for the synthesis of nanoporous graphite-like CN through calcination in a furnace using different proportions of dicyandiamide and thiourea. The as-prepared nanomaterials present large surface area and high pollutant adsorption and photodegradation [87]. They found that the higher the proportion thiourea/dicyandiamide, the greater the porosity of the final structure. The results of the PC performance demonstrated that the composition containing a proportion of 80 wt.% of thiourea presented the greatest potential for photodegradation, under simulated solar light irradiation, toward methylene blue (MB) and phenol, during times of 4 and 8 h, respectively. Song et al. evaluated the PC potential of g-CN samples, synthesized from urea by thermal treatment under N_2 flow at 550°C for 4 h and partial N_2 flow at 300°C [29]. The efficiency of catalysts was evaluated to the pollutant rhodamine, and it was confirmed that g-CN produced by the process with interruption of N_2 at 300°C presented a greater surface area, morphology rich in pores, and degradation of 90% of the pollutant (32% more than the other sample) under UV−visible light irradiation.

4.4 Improving the efficiency in environmental remediation applications: the CN nanocomposites

In most decontamination procedures using CN as a photocatalyst, four main steps take place as shown in Fig. 4.5. First, the pollutant must be quantitatively adsorbed

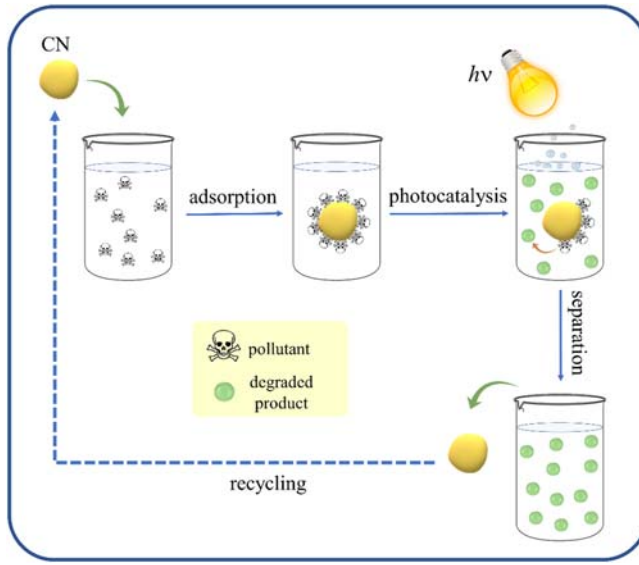

Figure 4.5 Main steps of the water decontamination using nano-engineered materials based on carbon nitride.

onto CN surface. This can be optimized by changing parameters such as pH, ionic strength, and temperature [17,74]. Afterward, photodegradation of the adsorbed contaminant is expected by irradiation of light. The time of irradiation and different light sources are normally controlled in this step to increase the removal efficiency [7,105]. After separating and washing the catalyst to remove the residual contaminant, the CN can be reutilized in several cycles of remediation [106,107].

Although pure CN has been used as a catalyst in pollutant degradation, its band-gap limitations and electron mobility can be overcome by the incorporation of nanocompounds into its structure to improve its removal efficiency and optimize its PC performance in environmental applications [66,68,90,93,108]. Besides the synergistic combination of CN with some nanocompounds (nanoguests) gives origin to new functionalities to the formed nanocomposite, including optical and magnetic stimuli-responsive features [109–111] (Fig. 4.6). Particularly, if the band-gap energy becomes narrower and the photogenerated e^- and h^+ are effectively separated, a possibly induced charge-transfer transition between nanocompounds and g-CN, CB, or VB will result in high performance of the nanocomposite photocatalyst [112,113].

This chapter emphasizes the application of nanocomposites produced by the combination of iron, zinc, and titanium compounds (mainly oxides) with CN as novel and promising materials to remediate water contaminated with two classes of emerging pollutants: dyes and pharmaceutical waste.

Table 4.1 lists a series of CN-based nanocomposites formed by the incorporation of different compounds. Details as the form of the graphitic phase, the composition

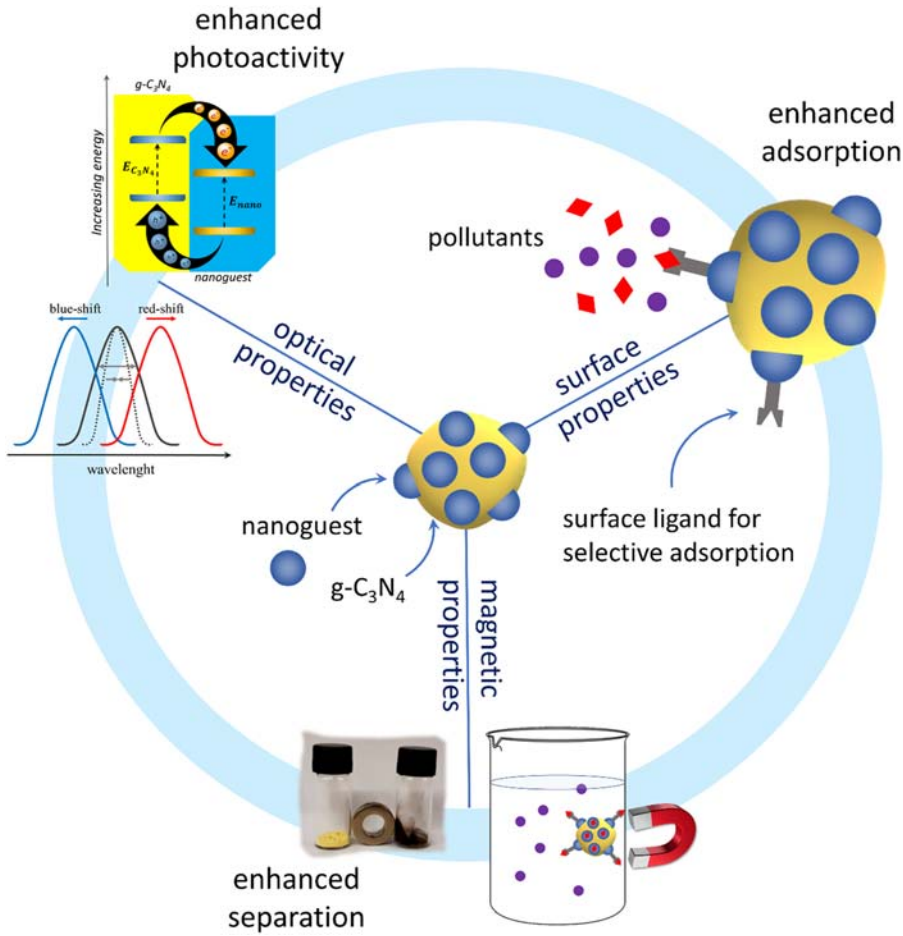

Figure 4.6 The decoration of the g-CN with a nanoguest leads to nanocomposites with multiple functionalities and enhanced properties. It can improve not only the adsorption capacity and the photocatalytic activity of the nanocomposite but also the efficiency of its separation from the medium. *g-CN*, graphitic carbon nitride.

of the material utilized to modify the CN, the removal efficiency, the pollutant studied, and the light utilized for its photodegradation are provided.

The incorporation of CN with iron oxides offers advantageous properties such as increased chemical stability [114], surface area [34], and water solubility [91]. Moreover, these materials can be produced through easy synthesis routes using low-cost and easily acquired raw materials [34,58,91]. Particularly, the incorporation of magnetic iron-based nanoparticles also confers the possibility of magnetic manipulation, improving the separation and reuse of the adsorbents with minimal or no generation of residues [111,115,126,127]. Due to these properties, these nanocomposites

Table 4.1 Carbon nitride (CN)-based nanocomposites incorporated with different compounds and their performance in pollutant remediation.

	CN form	Modifying agents	Pollutants remedied	Percentage of degradation (%)	Radiation used in photocatalytic reaction	References
1	g-CN	α-Fe_2O_3	Rhodamine B	~90	Visible light	[71]
2	g-CN	β-Fe_2O_3	Methyl orange	~90	Visible light and solar light	[92]
3	g-CN	α-Fe_2O_3	4-Nitrophenol	90	Visible light	[114]
4	Nanorod-type of g-CN	γ-Fe_2O_3	Rhodamine B	80	Visible light	[115]
5	Nanospheres of g-CN	Fe_3O_4	Methyl orange	~100	Visible light	[116]
6	g-CN	Fe_2O_3 BiOI	Rhodamine B	≈100	Visible light	[117]
7	mpg-CN	$CoFe_2O_4$	Malachite green Methylene blue Acid orange 7 Rhodamine B	93.4 71.64 57.98 33.22	UV light	[118]
8	mpg-CN	ZnO	Methyl orange	90.8	Visible light	[89]
9	Few-layer nanosheets of g-CN	ZnO	Methylene blue Parachlorophenol	~80	Visible light UV light	[119]
10	g-CN	ZnO	Rhodamine B Phenol	100	UV light and Simulated solar light irradiation	[120]
11	g-CN	ZnO	Phenol	99.5	Simulated solar light irradiation	[48]
12	g-CN	Ag-ZnO	Tetracycline	80.0	Simulated solar light irradiation	[121]
13	g-CN	ZnI_2S_4	Tetracycline	99.0	Visible light	[60]
14	g-CN	$ZnWO_4$	Phenol	30.4	UV light	[122]
15	Membrane with mpg-CN	TiO_2	Sulfamethoxazole	69.0	Simulated solar light irradiation	[123]
16	g-CN	TiO_2	Phenol	98.4	Simulated solar light irradiation and UV light	[124]
17	g-CN	TiO_2	Acid orange	82.0	Simulated solar light irradiation	[125]

g-CN, graphitic carbon nitride; *mpg-CN*, mesoporous graphitic carbon nitride; *UV*, ultraviolet.

have been extensively applied in environmental remediation for the effective removal of toxic metals and organic compounds [5,128,129].

Hu et al. evaluated the nanocomposites of g-CN containing α-Fe_2O_3, at different proportions (up to 0.5% of α-Fe_2O_3), to degrade RhB using visible light [71]. The authors showed that the PC performance of iron oxide-loaded composite was up to 1.3 times higher than that of pure g-CN. This increased PC performance was ascribed to the synergistic effect of decreased band-gap energy and reduced recombination rate of photogenerated electrons−holes pairs caused by α-Fe_2O_3 doping.

The PC activity of g-CN, pure and loaded with β-Fe_2O_3, a metastable phase during the formation of α-Fe_2O_3, was evaluated under both simulated solar light and pure visible light irradiation toward the photodegradation of MO, RhB, and phenol [92]. The authors observed an increase of the surface area upon introducing β-Fe_2O_3 in the g-CN, and an improvement of the photoactivity of β-Fe_2O_3-loaded hybrid, being the best performance with 3.5 wt.% of β-Fe_2O_3. The enhanced light absorption in the visible region was attributed to the presence of β-Fe_2O_3, which promotes charge transfer and separation due to the difference in the CB and VB energies. It leads to a higher PC activity compared to the pure g-CN, coupled with remarkable stability under working conditions. The authors proposed that photogenerated h^+ are the active species responsible for the contaminant degradation in the iron oxide-loaded nanocomposite, while in the pure g-CN the photoactivity was driven by both h^+ and $\bullet O_2^-$. The recyclability of doped nanocomposites was evaluated, and the tests resulted in potentiality and stability being maintained for three consecutive cycles.

Two-dimensional nanosheet structures of g-CN with highly dispersed α-Fe_2O_3 nanoparticles (from 0.1 to 0.8 wt.%) were tested as photocatalysts for 4-nitrophenol (4-NP) degradation by Lin et al. [114] (Fig. 4.7A and B). The authors showed that the absorption edges of α-Fe_2O_3-loaded samples expanded remarkably with a rise in iron oxide loading and that the visible-light responding ability was improved by coupling g-CN with α-Fe_2O_3 (Fig. 4.7C and D). The 4-NP degradation increased significantly with visible-light illumination time and iron oxide content. The best performance was achieved for 0.5 wt.% of α-Fe_2O_3, in the presence of H_2O_2, at pH = 3.5, degrading 90% of the pollutant for 40 min of light exposition, which corresponds to up to six times higher compared to the pure g-CN. As shown by authors, the pH of the reaction medium plays an important role in the degradation of organic pollutants since it influences the generation of hydroxyl radicals, the dissociation of the reactant(s) in solution, and the surface charge of the photocatalyst. The authors also found that there were no significant losses in PC activity after three recycling uses of the nanocomposite.

Wang et al. synthesized a nanorod-type g-CN/Fe_2O_3 composite and compared its efficiency in RhB degradation under irradiation of visible light to that of pure γ-Fe_2O_3 and g-CN [115]. After exposing the pollutant to the nanocomposites in aqueous solution containing hydrogen peroxide at 30%, it was observed that Fe_2O_3/g-CN degraded approximately 80% of the RhB in 5 min and almost 100% in 15 min. According to the authors, the nanorod composite presented better PC activity when compared to pure g-CN as a result of the strong absorption in the visible region and the larger surface area.

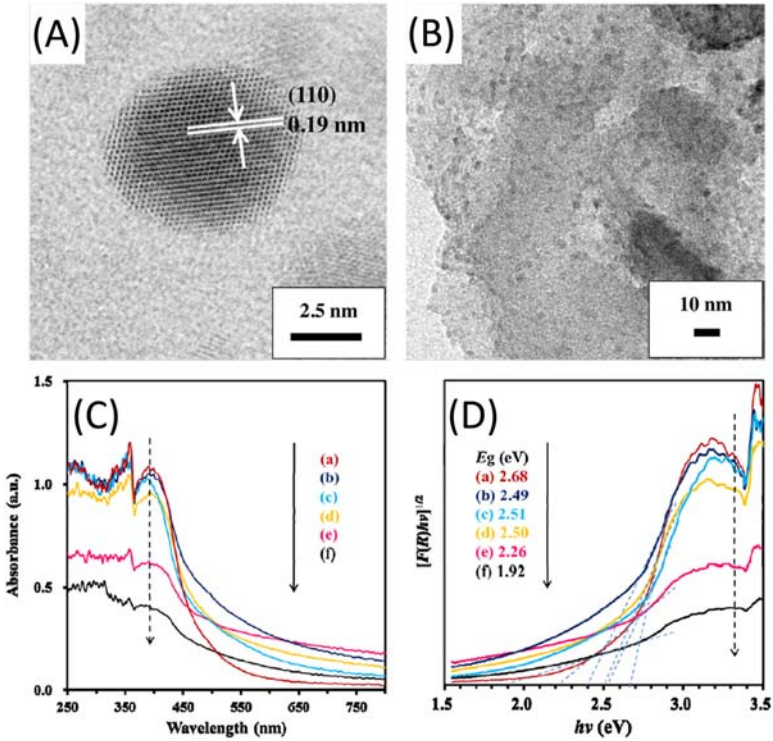

Figure 4.7 TEM images of (A) a single iron oxide nanoparticle incrusted in g-C_3N_4 and (B) the graphitic carbon nitride-supported iron oxide (Fe_2O_3/g-C_3N_4) containing 0.8 wt.% of a-Fe_2O_3. UV−vis diffuse reflectance spectra (C) and $[F(R)hv]^{1/2}$ versus hv plots (D) of g-C_3N_4 with increasing amounts of a-Fe_2O_3: (a) 0.0 wt.%, (b) 0.1 wt.%, (c) 0.3 wt.%, (d) 0.5 wt.%, (e) 0.7 wt.%, and (f) 0.8 wt.% [114]. *TEM*, transmission electron microscopy; *UV*, ultraviolet.

The nanospheres of Fe_3O_4/g-CN with porous structure were produced by a hydrothermal method, with varying proportions of Fe_3O_4 and g-CN, to evaluate their efficiency in MO photodegradation [116]. The experiments demonstrated better PC performance to nanocomposites Fe_3O_4/g-CN against the tested dye, compared to pure g-CN and pure Fe_3O_4, under 150 min after visible light irradiation with total pollutant degradation. The PC activity of the porous Fe_3O_4/g-CN nanospheres reached their maximum for a loading of 2% of Fe_3O_4. The nanocomposites exhibited excellent reusability in five cycles at a ratio of 98%.

Mousavi et al. synthesized magnetic ternary g-CN/Fe_3O_4/BiOI nanocomposites and evaluated their remedial power regarding RhB [117]. Under visible light irradiation the nanocomposite g-CN/Fe_3O_4 (50%)/BiOI (20%) degraded almost 100% of RhB after 180 min of irradiation, while pure g-CN and g-CN/Fe_2O_3 degraded only 32% and 40% of the pollutant, respectively. The authors reported that the nanocomposite properties and their PC potential are associated with synthesis conditions and

that the absorption in the visible light region increased with increasing weight percentage of BiOI, resulting in adequate band-gap values for photocatalysis.

Hassani et al. evaluated the effectiveness of a nanocomposite of monodisperse cobalt ferrite nanoparticles assembled on mesoporous g-CN ($CoFe_2O_4$/mpg-CN) in comparison with pure mpg-CN in the photodegradation of the malachite green, MB, acid orange 7 (AO7), and RhB [118]. The results demonstrated that both are effective for the adsorption of the tested pollutants. The pure mpg-CN presented a PC degradation of 76.38% for MG compared to 93.41% of $CoFe_2O_4$/mpg-CN, both in an environment activated by UV light. In the case of other dyes the PC degradation of the nanocomposite was 71.64% MB, 57.98% AO7, and 33.22% RhB. According to the authors, the heterojunctions among semiconductor materials could provide a great potential driving force to improve the separation between the electron−hole pair to promote a bandgap with a greater range of absorption. This feature, associated with the porous structure of mpg-CN, contributed to the improvement of the PC performance of the composite.

Zinc oxide (ZnO) has featured in many studies because of its nontoxic property, low cost, stability, high catalytic activity [48,130], high electric conductivity, and large suitable bandgap [130]. This compound is considered promising in the area of photocatalysis because of its potential for degrading organic and inorganic pollutants [21,48]. However, isolated ZnO does not absorb visible light, but the incorporation of a nonmetallic component, such as CN, may reduce the bandgap for metallic oxides and extend absorption in the visible region [131,132] and improve its PC efficiency [10].

Le et al. evaluated different composite samples of ZnO particles supported in mpg-CN (mpg-CN/ZnO) in the PC degradation of MO under visible light irradiation [89]. The results showed that the most effective concentration was mpg-CN/ZnO-50 (50% of each component), which presented a photodegradation efficiency of 90.8% for 120 min. According to the authors, in the most efficient nanocomposite (mpg-C_3N_4/ZnO-50), the photogenerated electron−hole pairs were efficiently transferred at the heterostructure interface, leading to greater PC activity under visible light irradiation.

Liu et al. synthesized composites based on ZnO nanoflowers decocted with few-layer g-CN nanosheets (flg-CN/ZnO) as novel photocatalysts to enhance pollutants removal from water [119]. They reported that the elaborated heterostructures are favorable to degrade MB under irradiation with visible light, and parachlorophenol (4-hydroxychlorobenzene) under irradiation with UV light, with a photodegradation efficiency of almost 80%. All nanocomposites produced showed higher PC activity than pure ZnO nanoparticles and the optimal decorating amount of the flg-CN was 30 wt.%. According to the authors, the enhancement of PC property is related to the effective separation and transfer of photogenerated charges stemming from the well-matched band structure between ZnO and flg-CN.

In a research conducted by Wu et al. [120], microspheres produced by the heterojunction of ZnO and g-CN, using solvothermal method and zinc acetate as precursor, were evaluated as photocatalysts for degradation of the pollutants RhB and phenol (Fig. 4.8). Comparing the efficiency and the stability of different

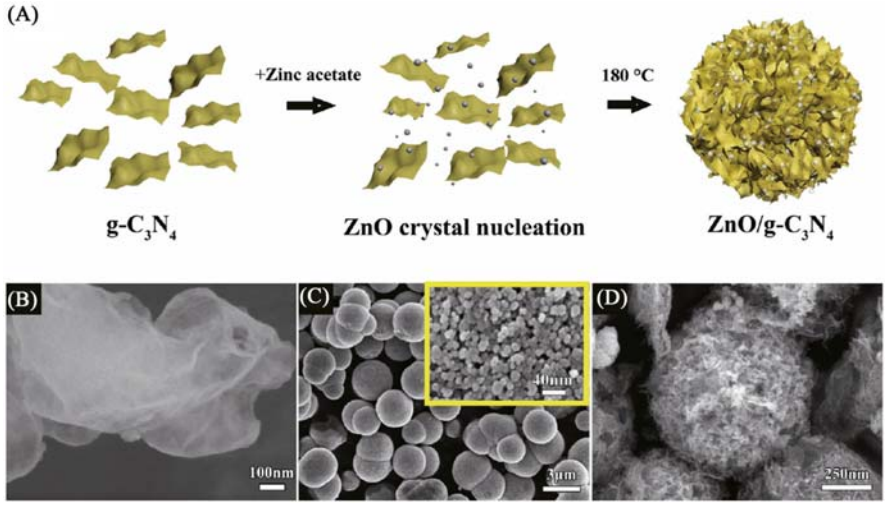

Figure 4.8 (A) Schematic illustration of the synthetic process of hierarchical porous ZnO/g-CN microspherical heterostructure (the gray spheres are ZnO and the dark yellow sheets are g-CN). SEM images of (B) pure g-CN prepared by sintering, (C) pure ZnO and (D) ZnO/g-CN [120]. *g-CN*, graphitic carbon nitride; *SEM*, scanning electron microscopy.

heterostructure combinations concerning pure ZnO and g-CN, the best PC degradation rate occurred with the nanocomposite elaborated using a mass ratio of zinc acetate dihydrate to g-C_3N_4 equals to 1.5 (1.5-ZnO/g-CN). This combination promoted 100% RhB degradation in 30 min under visible UV light irradiation and visible light. The authors investigated the PC stability of 1.5-ZnO/g-CN under simulated solar light and the results show that after five cycles, the degradation rate of RhB is still as high as 95.2%, suggesting a good stability under simulated solar light irradiation. The nanocomposite also presented a high activity of phenol degradation (almost 100%) in 50 min under visible UV light irradiation. The authors pointed out that the combination of these electronic heterostructures with spatial hierarchical structure was an efficient strategy that provided the best performance in the photodegradation of organic pollutants.

A study to evaluate the degradation of phenols using ZnO/g-CN under simulated sunlight irradiation was also carried out by Rosli et al. [48]. The authors found that the optimum amount of g-CN in the composite corresponds to 5 wt.%, which leads to a PC degradation efficiency of 99.5%, with the possibility of reuse for four times. The authors proposed the phenol degradation pathway by the ZnO/g-CN composites, based on the identification of the degradation intermediates. The final products obtained (CO_2 and H_2O) are nontoxic to health or environment.

The combination of g-CN and ZnO was also tested by Panneri et al. adding silver (Ag) as a third component (g-CN-Ag/ZnO) [121]. In the study, different compositions were tested to evaluate their PC degradation and adsorption potentialities for the removal of the antibiotic tetracycline. The g-CN-Ag/ZnO composite exhibited a

high adsorption capacity of tetracycline (47% in the dark and PC degradation of 80% under irradiation with solar light for 60 min) when compared to other combinations of g-C_3N_4−Ag, g-C_3N_4−ZnO, ZnO−Ag, and g-C_3N_4. According to the authors, during sunlight irradiation, nanocomposite excitation creates pairs of electron/holes that can transiently occupy the empty states of the CB in Ag. Concerning g-CN and ZnO, sunlight irradiation excites the electrons in CBs with the simultaneous generation of holes in the VBs. These electrons in the g-CN CB migrate to the ZnO CB. ZnO electrons are transferred to Ag and the reaction with the oxygen from the system takes place, producing the reactive forms of oxygen (e.g., superoxide), which act on the contaminants.

Nanocomposites elaborated through the association of $ZnIn_2S_4$ microflowers, with lamellar g-CN (CN/$Znln_2S_4$) with different mass ratios, were investigated as photocatalysts for tetracycline degradation [60]. The authors found that the composite with loading 50 wt.% g-CN degraded almost 100% of tetracycline in an aqueous solution under visible light irradiation after 120 min of contact. According to the authors, the 50 wt.% proportion of g-CN efficiently promotes the separation of photogenerated electron pairs, leading to better PC performance, while the excess g-CN (above 50 wt.%) leads to an agglomerating state on the $Znln_2S_4$ surface. As a result, the lower contact area of heterojunction decreases the PC activities [133].

In a research done by Zhan et al., films containing the heterojunction of g-CN/$ZnWO_4$ were produced to evaluate their PC activity toward phenol degradation under UV light irradiation [122]. The authors found that all the concentrations of the proposed heterojunction (from 1% to 7% of g-CN) presented greater catalytic activity than the pure forms of $ZnWO_4$ and g-CN. The best concentration was found to be 5% of g-CN, leading to 30.4% of phenol degradation. The authors stated that the photogenerated electrons in the lowest unoccupied molecular orbital of g-CN were directly transferred to the $ZnWO_4$ CB while the photogenerated holes in $ZnWO_4$ were directly transferred to g-CN and the electrons on the $ZnWO_4$ surface could be retained by molecular oxygen to form $\bullet O_2^-$ species, contributing to the efficiency in the PC degradation process.

In its pure form, TiO_2 presents degradation activity for different organic pollutants whose efficiency can be highly improved when this compound is associated with g-CN [128,134]. Yu et al. fabricated a PC membrane for ultrafiltration with a matrix formed by polysulfone incorporated with mpg-CN/TiO_2 composites to evaluate its potential in the photodegradation toward the antibiotic SMX [123]. Different concentrations of g-CN/TiO_2 were tested in association with the matrix, being 1 wt.% of composite loading the most efficient for SMX degradation (69% in 30 h of solar light irradiation). The results are promising to the application in large scale setups concerning pharmaceuticals degradation in water. Moreover, the proposed membrane revealed to be a very efficient host material for photocatalysts immobilization.

Nanotubes of TiO_2 wrapped with g-CN nanoparticles were synthesized by Wang et al. to evaluate photoelectrocatalytic activity in phenol degradation under stimulated solar light [124]. The photoelectrodes elaborated with 10 wt.% of g-CN completely degraded the phenol in 150 min, while the pure TiO_2 degraded only 50% of the pollutant in the same time interval. According to the authors, the outstanding

photoelectric properties and excellent photoelectrocatalytic performance of the proposed nanocomposites are related to the enhanced light-absorption property and improved charge-separation efficiency. The incorporation of g-CN NPs strongly decreases the charge transfer resistance and boosts the charge-separation efficiency of TiO_2. Moreover, the authors pointed out that the photoelectrocatalytic process involved in the phenol degradation over the prepared nanocomposite was much higher than the sum of PC and electrocatalytic processes.

The potential of porous g-CN/TiO_2 nanocomposites with hierarchical heterostructure was tested in the photocatalysis improvement toward acid orange degradation under simulated solar irradiation and at room temperature in comparison to pure g-CN and TiO_2 nanoparticles [125] (Fig. 4.9). The results demonstrated that the nanocomposite g-CN/TiO_2 degraded approximately 82% of acid orange in 10 min, while the pure TiO_2 and g-CN did not present a significant efficiency in degrading this compound. The researchers also confirmed that this heterojunction exhibited a good separation efficiency of electrons and holes, wide light-absorption range, and rapid mass transfer, which make the composite a promising material for PC degradation of pollutants.

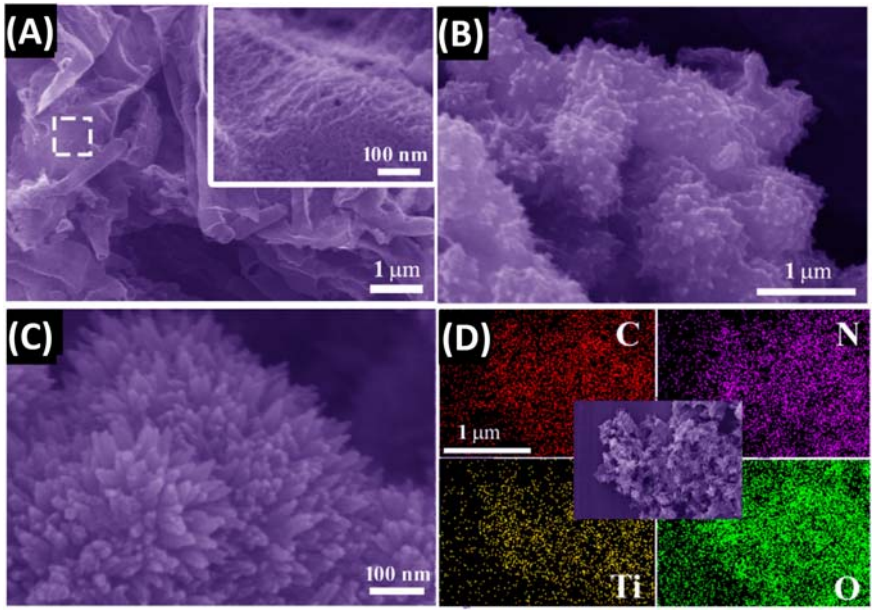

Figure 4.9 FE-SEM image of (A) g-CN nanosheets with rich carbon vacancies. A highly corrugated surface with abundant in-plane holes can be observed. (B) FE-SEM images of the g-CN/TiO_2 nanocomposite with hierarchical heterojunction, showing small needle-like TiO_2 petals. (C) High magnification FE-SEM images of g-CN/TiO_2 nanocomposite. (D) Energy-dispersive X-ray spectroscopy mapping analysis of the g-CN/TiO_2 nanocomposite confirming that TiO_2 is uniformly assembled on the g-CN surface [125]. *FE-SEM*, field emission scanning electron microscopy; *g-CN*, graphitic carbon nitride.

4.5 Final considerations

The presence of micropollutants in water represents a serious threat to human health and the environment. The main traditional water and wastewater treatment technologies do not effectively remove these contaminants, as they remain at trace levels, which make it difficult to meet water quality standards. In this context the development and application of nanotechnology-based methods is a promising alternative, especially using nano-engineered materials based on CN composites, as demonstrated by several laboratory-scale studies. These materials can be designed with multiple functionalities and enhanced properties, which endow them with high efficiency to remediate water with micropollutants and low levels of other contaminants. Moreover, the application of nano-engineered materials in on-site treatment facilities may offer potential advantages in terms of efficiency, environmental friendship, and cost compared to conventional treatments.

In the case of the pilot and full-scale applications, there are still some limitations that must be overcome when using nanotechnology-based methods. Problems such as agglomeration phenomena, leaching, ecotoxicity, regeneration, and reusability require appropriate approaches for ensuring the sustainability and safety of these novel technologies for water treatment. However, these potential drawbacks should not be seen as a technological barrier for real-life applications but as a challenge to be faced. Thus nanotechnology-based methods for environmental remediation and water treatment should be treated as efficient and innovative alternatives with a high potential for effective benefits rather than as risky technologies.

Acknowledgments

The authors gratefully acknowledge the financial support from Conselho Nacional de Desenvolvimento Científico e Tecnológico (CNPq), Coordenação de Aperfeiçoamento de Pessoal de Nível Superior (CAPES), Fundação de Apoio à Pesquisa do Distrito Federal (FAP-DF), Decanato de Pesquisa e Inovação (DPI-UnB), Fundação de Empreendimentos Científicos e Tecnológicos (FINATEC), and Federal Institute of Education, Science, and Technology Goiano—Campus Ceres.

References

[1] J. Trujillo-Reyes, J.R. Peralta-Videa, J.L. Gardea-Torresdey, Supported and unsupported nanomaterials for water and soil remediation: are they a useful solution for worldwide pollution? J. Hazard. Mater. 280 (2014) 487–503. Available from: https://doi.org/10.1016/j.jhazmat.2014.08.029.

[2] K.A. Andrianov, L.M. Volkova, Reactions of (chloromethyl) ethoxysilanes with amines, Bull. Acad. Sci. USSR Div. Chem. Sci. 8 (1959) 255–259. Available from: https://doi.org/10.1007/BF00917371.

[3] S. Sifakis, V.P. Androutsopoulos, A.M. Tsatsakis, D.A. Spandidos, Human exposure to endocrine disrupting chemicals: effects on the male and female reproductive system, Environ. Toxicol. Pharmacol. 51 (2017) 56–70. Available from: https://doi.org/10.1016/j.etap.2017.02.024.

[4] F.L. Rodovalho, G. Capistrano, J.A. Gomes, F.F. Sodré, J.A. Chaker, A.F.C. Campos, et al., Elaboration of magneto-thermally recyclable nanosorbents for remote removal of toluene in contaminated water using magnetic hyperthermia, Chem. Eng. J. 302 (2016) 725–732. Available from: https://doi.org/10.1016/j.cej.2016.05.110.

[5] P.N. Dave, L.V. Chopda, Application of iron oxide nanomaterials for the removal of heavy metals, J. Nanotechnol. 2014 (2014). Available from: https://doi.org/10.1155/2014/398569.

[6] A.S. Adeleye, J.R. Conway, K. Garner, Y. Huang, Y. Su, A.A. Keller, Engineered nanomaterials for water treatment and remediation: costs, benefits, and applicability, Chem. Eng. J. 286 (2016) 640–662. Available from: https://doi.org/10.1016/j.cej.2015.10.105.

[7] Y. Wang, M.F. Ibad, H. Kosslick, J. Harloff, T. Beweries, J. Radnik, et al., Synthesis and comparative study of the photocatalytic performance of hierarchically porous polymeric carbon nitrides, Microporous Mesoporous Mater. 211 (2015) 182–191. Available from: https://doi.org/10.1016/j.micromeso.2015.02.050.

[8] Z. Cai, A.D. Dwivedi, W.-N. Lee, X. Zhao, W. Liu, M. Sillanpää, et al., Application of nanotechnologies for removing pharmaceutically active compounds from water: development and future trends, Environ. Sci. Nano 5 (2018) 27–47. Available from: https://doi.org/10.1039/C7EN00644F.

[9] M.T. Amin, A.A. Alazba, U. Manzoor, A review on removal of pollutants from water/wastewater using different types of nanomaterials, Adv. Mater. Sci. Eng. 2014 (2014). Available from: https://doi.org/10.1155/2014/825910. ID 825910.

[10] S. Kumar, A. Kumar, A. Kumar, R. Balaji, V. Krishnan, Highly efficient visible light active 2D-2D nanocomposites of N-ZnO-g-C_3N_4 for photocatalytic degradation of diverse industrial pollutants, ChemistrySelect 3 (2018) 1919–1932. Available from: https://doi.org/10.1002/slct.201703156.

[11] O.K. Bishoge, L. Zhang, S.L. Suntu, H. Jin, A.A. Zewde, Z. Qi, Remediation of water and wastewater by using engineered nanomaterials: a review, J. Environ. Sci. Heal., A 4529 (2018) 1–18. Available from: https://doi.org/10.1080/10934529.2018.1424991.

[12] E.P. Vejerano, G. Rao, L. Khachatryan, S.A. Cormier, S. Lomnicki, Environmentally persistent free radicals: insights on a new class of pollutants, Environ. Sci. Technol. 52 (2018) 2468–2481. Available from: https://doi.org/10.1021/acs.est.7b04439.

[13] X. Fu-Liu, S.E. Jorgensen, Y. Shimizu, E. Silow, Persistent organic pollutants in fresh water ecosystems, Sci. World J. 2013 (2013) 2–4. Available from: https://doi.org/10.1155/2013/303815.

[14] M. Porta, J. Pumarega, M. Gasull, T. Lopez, Contamination From Endocrine Disrupters of the General Population at Low and High Concentrations, first ed., Elsevier Inc, 2014. Available from: https://doi.org/10.1016/B978-0-12-800095-3.00006-7.

[15] G. Lofrano, G. Libralato, J. Brown, Nanotechnologies for Environmental Remediation: Applications and Implications, Springer Nature, 2017, pp. 1–325. https://doi.org/10.1007/978-3-319-53162-5.

[16] T.T.T. Dang, S.T.T. Le, D. Channei, W. Khanitchaidecha, A. Nakaruk, Photodegradation mechanisms of phenol in the photocatalytic process, Res. Chem. Intermed. 42 (2016) 5961–5974. Available from: https://doi.org/10.1007/s11164-015-2417-3.

[17] M. Anbia, M. Haqshenas, Adsorption studies of Pb(II) and Cu(II) ions on mesoporous carbon nitride functionalized with melamine-based dendrimer amine, Int. J. Environ.

Sci. Technol. 12 (2015) 2649–2664. Available from: https://doi.org/10.1007/s13762-015-0776-3.

[18] A.A. Werkneh, E.R. Rene, Applications of nanotechnology and biotechnology for sustainable water and wastewater treatment, in: X.T. Bui, C. Chiemchaisri, T. Fujioka, S. Varjani (Eds.), Water and Wastewater Treatment Technologies. Energy, Environment, and Sustainability, Springer, Singapore, 2019, pp. 405–430. Available from: https://doi.org/10.1007/978-981-13-3259-3_19.

[19] X. Qu, P.J.J. Alvarez, Q. Li, Applications of nanotechnology in water and wastewater treatment, Water Res. 47 (2013) 3931–3946. Available from: https://doi.org/10.1016/j.watres.2012.09.058.

[20] N.C. Feitoza, T.D. Gonçalves, J.J. Mesquita, J.S. Menegucci, M.K.M.S. Santos, J.A. Chaker, et al., Fabrication of glycine-functionalized maghemite nanoparticles for magnetic removal of copper from wastewater, J. Hazard. Mater. 264 (2014) 153–160. Available from: https://doi.org/10.1016/j.jhazmat.2013.11.022.

[21] Z. Cai, Y. Sun, W. Liu, F. Pan, P. Sun, J. Fu, An overview of nanomaterials applied for removing dyes from wastewater, Environ. Sci. Pollut. Res. 24 (2017) 15882–15904. Available from: https://doi.org/10.1007/s11356-017-9003-8.

[22] F. Brandl, N. Bertrand, E.M. Lima, R. Langer, Nanoparticles with photoinduced precipitation for the extraction of pollutants from water and soil, Nat. Commun. 6 (2015) 1–10. Available from: https://doi.org/10.1038/ncomms8765.

[23] R. Hjorth, C. Coutris, N.H.A. Nguyen, A. Sevcu, J.A. Gallego-Urrea, A. Baun, et al., Ecotoxicity testing and environmental risk assessment of iron nanomaterials for sub-surface remediation – recommendations from the FP7 project NanoRem, Chemosphere 182 (2017) 525–531. Available from: https://doi.org/10.1016/j.chemosphere.2017.05.060.

[24] B. Mu, J. Tang, L. Zhang, A. Wang, Facile fabrication of superparamagnetic graphene/polyaniline/Fe_3O_4 nanocomposites for fast magnetic separation and efficient removal of dye, Sci. Rep. 7 (2017) 5347. Available from: https://doi.org/10.1038/s41598-017-05755-6.

[25] L. Ji, W. Chen, L. Duan, D. Zhu, Mechanisms for strong adsorption of tetracycline to carbon nanotubes: a comparative study using activated carbon and graphite as adsorbents, Environ. Sci. Technol. 43 (2009) 2322–2327. Available from: https://doi.org/10.1021/es803268b.

[26] P. Qiu, C. Xu, H. Chen, F. Jiang, X. Wang, R. Lu, et al., One step synthesis of oxygen doped porous graphitic carbon nitride with remarkable improvement of photo-oxidation activity: role of oxygen on visible light photocatalytic activity, Appl. Catal., B: Environ. 206 (2017) 319–327. Available from: https://doi.org/10.1016/j.apcatb.2017.01.058.

[27] X. Liu, C. Li, Y. Zhang, J. Yu, M. Yuan, Y. Ma, Simultaneous photodegradation of multi-herbicides by oxidized carbon nitride: performance and practical application, Appl. Catal., B: Environ. 219 (2017) 194–199. Available from: https://doi.org/10.1016/j.apcatb.2017.07.007.

[28] H. Lan, L. Li, X. An, F. Liu, C. Chen, H. Liu, et al., Microstructure of carbon nitride affecting synergetic photocatalytic activity: hydrogen bonds vs. structural defects, Appl. Catal., B: Environ. 204 (2017) 49–57. Available from: https://doi.org/10.1016/j.apcatb.2016.11.022.

[29] X. Song, Q. Yang, M. Yin, D. Tang, L. Zhou, Highly efficient pollutant removal of graphitic carbon nitride by the synergistic effect of adsorption and photocatalytic degradation, RSC Adv. 8 (2018) 7260–7268. Available from: https://doi.org/10.1039/c7ra11467b.

[30] B.I. Kharisov, H.V. Rasika Dias, O.V. Kharissova, V. Manuel Jiménez-Pérez, B. Olvera Pérez, B. Muñoz Flores, Iron-containing nanomaterials: synthesis, properties,

and environmental applications, RSC Adv. 2 (2012) 9325−9358. Available from: https://doi.org/10.1039/c2ra20812a.

[31] H. Shi, L. Tan, Q. Du, X. Chen, L. Li, T. Liu, et al., Green synthesis of Fe_3O_4 nanoparticles with controlled morphologies using urease and their application in dye adsorption, Dalton Trans. 43 (2014) 12474−12479. Available from: https://doi.org/10.1039/c4dt01161a.

[32] S. Ye, L.G. Qiu, Y.P. Yuan, Y.J. Zhu, J. Xia, J.F. Zhu, Facile fabrication of magnetically separable graphitic carbon nitride photocatalysts with enhanced photocatalytic activity under visible light, J. Mater. Chem., A. 1 (2013) 3008−3015. Available from: https://doi.org/10.1039/c2ta01069k.

[33] P. Xu, G.M. Zeng, D.L. Huang, C.L. Feng, S. Hu, M.H. Zhao, et al., Use of iron oxide nanomaterials in wastewater treatment: a review, Sci. Total Environ. 424 (2012) 1−10. Available from: https://doi.org/10.1016/j.scitotenv.2012.02.023.

[34] J. Li, J. Fang, P. Ye, D. Wu, M. Wang, X. Li, et al., Peroxymonosulfate activation by iron oxide modified g-C_3N_4 under visible light for pollutants degradation, J. Photochem. Photobiol., A: Chem. 342 (2017) 85−93. Available from: https://doi.org/10.1016/j.jphotochem.2017.04.004.

[35] Y. Gruchlik, K. Linge, C. Joll, Removal of organic micropollutants in waste stabilisation ponds: a review, J. Environ. Manage. 206 (2018) 202−214. Available from: https://doi.org/10.1016/j.jenvman.2017.10.020.

[36] H.S. Rai, M.S. Bhattacharyya, J. Singh, T.K. Bansal, P. Vats, U.C. Banerjee, Removal of dyes from the effluent of textile and dyestuff manufacturing industry: a review of emerging techniques with reference to biological treatment, Crit. Rev. Environ. Sci. Technol. 35 (2005) 219−238. Available from: https://doi.org/10.1080/10643380590917932.

[37] V.K. Gupta, Suhas, Application of low-cost adsorbents for dye removal − a review, J. Environ. Manage. 90 (2009) 2313−2342. Available from: https://doi.org/10.1016/j.jenvman.2008.11.017.

[38] S. Dawood, T.K. Sen, Review on dye removal from its aqueous solution into alternative cost effective and non-conventional adsorbents, J. Chem. Proc. Eng. 1 (2014) 1−11.

[39] K. Hunger (Ed.), Industrial Dyes: Chemistry, Properties, Applications, John Wiley & Sons, Weinheim, 2003. Available from: https://doi.org/10.1002/3527602011.

[40] F.T. Fraunfelder, F.W. Fraunfelder, W.A. Chambers (Eds.), Clinical Ocular Toxicology Drugs, Chemicals and Herbs, Saunders Elsevier, Philadelphia, PA, 2008. Available from: https://doi.org/10.1016/B978-1-4160-4673-8.X0015-0.

[41] A. Stammati, C. Nebbia, I. De Angelis, A.G. Albo, M. Carletti, C. Rebecchi, et al., Effects of malachite green (MG) and its major metabolite, leucomalachite green (LMG), in two human cell lines, Toxicol. In Vitro 19 (2005) 853−858. Available from: https://doi.org/10.1016/j.tiv.2005.06.021.

[42] S. Srivastava, R. Sinha, D. Roy, Toxicological effects of malachite green, Aquat. Toxicol. 66 (2004) 319−329. Available from: https://doi.org/10.1016/j.aquatox.2003.09.008.

[43] K. Yang, W. Wu, Q. Jing, L. Zhu, Aqueous adsorption of aniline, phenol, and their substitutes by multi-walled carbon nanotubes, Environ. Sci. Technol. 42 (2008) 7931−7936. Available from: https://doi.org/10.1021/es801463v.

[44] X.L. Zhang, Z.X. Zhou, X.L. Fan, H.D. Li, QSTR studies on the mutagenicity of anilines, Adv. Mater. Res. 816−817 (2013) 1282−1286. Available from: https://doi.org/10.4028/http://www.scientific.net/AMR.816-817.1282.

[45] S. Thongkorn, S. Kanlayaprasit, D. Jindatip, T. Tencomnao, V.W. Hu, T. Sarachana, Sex differences in the effects of prenatal bisphenol A exposure on genes associated

with autism spectrum disorder in the hippocampus, Sci. Rep. 9 (2019) 1–14. Available from: https://doi.org/10.1038/s41598-019-39386-w.

[46] I.C. McCall, A. Betanzos, D.A. Weber, P. Nava, G.W. Miller, C.A. Parkos, Effects of phenol on barrier function of a human intestinal epithelial cell line correlate with altered tight junction protein localization, Toxicol. Appl. Pharmacol. 241 (2009) 61–70. Available from: https://doi.org/10.1016/j.taap.2009.08.002.

[47] R. Tang, M.J. Chen, G.D. Ding, X.J. Chen, X.M. Han, K. Zhou, et al., Associations of prenatal exposure to phenols with birth outcomes, Environ. Pollut. 178 (2013) 115–120. Available from: https://doi.org/10.1016/j.envpol.2013.03.023.

[48] N.I. Rosli, S. Lam, J. Sin, R.M. Abdul, Photocatalytic performance of ZnO/g-C_3N_4 for removal of phenol under simulated sunlight irradiation, J. Environ. Eng. 144 (2018) 1–12. Available from: https://doi.org/10.1061/(ASCE)EE.1943-7870.0001300.

[49] M. Mousavi, A. Habibi-Yangjeh, Magnetically recoverable highly efficient visible-light-active g-C_3N_4/Fe_3O_4/Ag_2WO_4/AgBr nanocomposites for photocatalytic degradations of environmental pollutants, Adv. Powder Technol. 29 (2018) 94–105. Available from: https://doi.org/10.1016/j.apt.2017.10.016.

[50] K. Hoffman, S.C. Hammel, A.L. Phillips, A.M. Lorenzo, A. Chen, A.M. Calafat, et al., Biomarkers of exposure to SVOCs in children and their demographic associations: the TESIE Study, Environ. Int. 119 (2018) 26–36. Available from: https://doi.org/10.1016/j.envint.2018.06.007.

[51] A. Azzouz, A.J. Rascón, E. Ballesteros, Simultaneous determination of parabens, alkylphenols, phenylphenols, bisphenol A and triclosan in human urine, blood and breast milk by continuous solid-phase extraction and gas chromatography-mass spectrometry, J. Pharm. Biomed. Anal. 119 (2016) 16–26. Available from: https://doi.org/10.1016/j.jpba.2015.11.024.

[52] M. Chen, R. Tang, G. Fu, B. Xu, P. Zhu, S. Qiao, et al., Association of exposure to phenols and idiopathic male infertility, J. Hazard. Mater. 250–251 (2013) 115–121. Available from: https://doi.org/10.1016/j.jhazmat.2013.01.061.

[53] E. Diamanti-Kandarakis, J.P. Bourguignon, L.C. Giudice, R. Hauser, G.S. Prins, A. M. Soto, et al., Endocrine-disrupting chemicals: an Endocrine Society scientific statement, Endocr. Rev. 30 (2009) 293–342. Available from: https://doi.org/10.1210/er.2009-0002.

[54] J. Richard, A. Boergers, C. vom Eyser, K. Bester, J. Tuerk, Toxicity of the micropollutants bisphenol A, ciprofloxacin, metoprolol and sulfamethoxazole in water samples before and after the oxidative treatment, Int. J. Hyg. Environ. Health 217 (2014) 506–514. Available from: https://doi.org/10.1016/j.ijheh.2013.09.007.

[55] A. Shafei, M.M. Ramzy, A.I. Hegazy, A.K. Husseny, U.G. EL-hadary, M.M. Taha, et al., The molecular mechanisms of action of the endocrine disrupting chemical bisphenol A in the development of cancer, Gene 647 (2018) 235–243. Available from: https://doi.org/10.1016/j.gene.2018.01.016.

[56] E. Chen Zee, P. Cornet, G. Lazimi, C. Rondet, M. Lochard, A.M. Magnier, et al., Effets des perturbateurs endocriniens sur les marqueurs de la périnatalité, Gynecol. Obstet. Fertil. 41 (2013) 601–610. Available from: https://doi.org/10.1016/j.gyobfe.2013.08.012.

[57] W.-H. Song, E.A. Mohamed, W.-K. Pang, K.-H. Kang, D.-Y. Ryu, M.S. Rahman, et al., Effect of endocrine disruptors on the ratio of X and Y chromosome-bearing live spermatozoa, Reprod. Toxicol. 82 (2018) 10–17. Available from: https://doi.org/10.1016/j.reprotox.2018.09.002.

[58] M. Wang, X. Yang, W. Bi, Application of magnetic graphitic carbon nitride nanocomposites for the solid-phase extraction of phthalate esters in water samples, J. Sep. Sci. 38 (2015) 445−452. Available from: https://doi.org/10.1002/jssc.201400991.

[59] D. Li, Y. Hu, X. Shen, X. Dai, X. Han, Combined effects of two environmental endocrine disruptors nonyl phenol and di-*n*-butyl phthalate on rat Sertoli cells in vitro, Reprod. Toxicol. 30 (2010) 438−445. Available from: https://doi.org/10.1016/j.reprotox.2010.06.003.

[60] F. Guo, Y. Cai, W. Guan, H. Huang, Y. Liu, Graphite carbon nitride/$ZnIn_2S_4$ heterojunction photocatalyst with enhanced photocatalytic performance for degradation of tetracycline under visible light irradiation, J. Phys. Chem. Solids 110 (2017) 370−378. Available from: https://doi.org/10.1016/j.jpcs.2017.07.001.

[61] H. Bürgmann, D. Frigon, W.H. Gaze, C.M. Manaia, A. Pruden, A.C. Singer, et al., Water and sanitation: an essential battlefront in the war on antimicrobial resistance, FEMS Microbiol. Ecol. 94 (2018). Available from: https://doi.org/10.1093/femsec/fiy101.

[62] A. Dirany, S. Efremova Aaron, N. Oturan, I. Sirés, M.A. Oturan, J.J. Aaron, Study of the toxicity of sulfamethoxazole and its degradation products in water by a bioluminescence method during application of the electro-Fenton treatment, Anal. Bioanal. Chem. 400 (2011) 353−360. Available from: https://doi.org/10.1007/s00216-010-4441-x.

[63] S.M. Limbu, L. Zhou, S.X. Sun, M.L. Zhang, Z.Y. Du, Chronic exposure to low environmental concentrations and legal aquaculture doses of antibiotics cause systemic adverse effects in Nile tilapia and provoke differential human health risk, Environ. Int. 115 (2018) 205−219. Available from: https://doi.org/10.1016/j.envint.2018.03.034.

[64] T. Fiuza, G. Gomide, A.F.C. Campos, F. Messina, J. Depeyrot, On the colloidal stability of nitrogen-rich carbon nanodots aqueous dispersions, C—J. Carbon Res. 5 (2019) 74. Available from: https://doi.org/10.3390/c5040074.

[65] H. Li, Z. Kang, Y. Liu, S.T. Lee, Carbon nanodots: synthesis, properties and applications, J. Mater. Chem. 22 (2012) 24230−24253. Available from: https://doi.org/10.1039/c2jm34690g.

[66] M. Mubeen, K. Deshmukh, D.R. Peshwe, S.J. Dhoble, A.D. Deshmukh, Alteration of the electronic structure and the optical properties of graphitic carbon nitride by metal ion doping, Spectrochim. Acta, A: Mol. Biomol. Spectrosc. 207 (2019) 301−306. Available from: https://doi.org/10.1016/j.saa.2018.09.039.

[67] W.J. Ong, L.L. Tan, Y.H. Ng, S.T. Yong, S.P. Chai, Graphitic carbon nitride (g-C_3N_4)-based photocatalysts for artificial photosynthesis and environmental remediation: are we a step closer to achieving sustainability? Chem. Rev. 116 (2016) 7159−7329. Available from: https://doi.org/10.1021/acs.chemrev.6b00075.

[68] J. Zhu, P. Xiao, H. Li, A.C. Carabineiro, Graphitic carbon nitride: synthesis, properties, and applications in catalysis, ACS Appl. Mater. Interfaces 6 (2014) 16449−16465. Available from: https://doi.org/10.1021/am502925j.

[69] S. Wan, M. Ou, Y. Xiong, Q. Zhong, S. Zhang, Facile preparation of porous carbon nitride for visible light photocatalytic reduction and oxidation applications, J. Mater. Sci. 53 (2018) 11315−11328. Available from: https://doi.org/10.1007/s10853-018-2441-y.

[70] J. Liu, H. Wang, M. Antonietti, Graphitic carbon nitride "reloaded": emerging applications beyond (photo)catalysis, Chem. Soc. Rev. 45 (2016) 2308−2326. Available from: https://doi.org/10.1039/c5cs00767d.

[71] S. Hu, R. Jin, G. Lu, D. Liu, J. Gui, The properties and photocatalytic performance comparison of Fe^{3+}-doped g-C_3N_4 and Fe_2O_3/g-C_3N_4 composite catalysts, RSC Adv. 4 (2014) 24863. Available from: https://doi.org/10.1039/c4ra03290j.

[72] C. Zhou, C. Lai, D. Huang, G. Zeng, C. Zhang, M. Cheng, et al., Highly porous carbon nitride by supramolecular preassembly of monomers for photocatalytic removal of sulfamethazine under visible light driven, Appl. Catal., B: Environ. 220 (2018) 202−210. Available from: https://doi.org/10.1016/j.apcatb.2017.08.055.

[73] Y. Hu, M. Zhang, Z. Xiao, T. Jiang, B. Yan, J. Li, Photodegradation of methyl red under visible light by mesoporous carbon nitride, IOP Conf. Ser. Earth Environ. Sci. 121 (2018) 022030.

[74] R. Hu, X. Wang, S. Dai, D. Shao, T. Hayat, A. Alsaedi, Application of graphitic carbon nitride for the removal of Pb(II) and aniline from aqueous solutions, Chem. Eng. J. 260 (2015) 469−477. Available from: https://doi.org/10.1016/j.cej.2014.09.013.

[75] J. Oh, Y. Shim, S. Lee, S. Park, D. Jang, Y. Shin, et al., Structural insights into photocatalytic performance of carbon nitrides for degradation of organic pollutants, J. Solid State Chem. 258 (2018) 559−565. Available from: https://doi.org/10.1016/j.jssc.2017.11.026.

[76] J. Mei, D. Zhang, N. Li, M. Zhang, X. Gu, S. Miao, et al., The synthesis of Ag_3PO_4/g-C_3N_4 nanocomposites and the application in the photocatalytic degradation of bisphenol A under visible light irradiation, J. Alloys Compd. 749 (2018) 715−723. Available from: https://doi.org/10.1016/j.jallcom.2018.03.251.

[77] B. Fei, Y. Tang, X. Wang, X. Dong, J. Liang, X. Fei, et al., One-pot synthesis of porous g-C_3N_4 nanomaterials with different morphologies and their superior photocatalytic performance, Mater. Res. Bull. 102 (2018) 209−217. Available from: https://doi.org/10.1016/j.materresbull.2018.02.041.

[78] Y. Wei, Y. Zhu, Y. Jiang, Photocatalytic self-cleaning carbon nitride nanotube intercalated reduced graphene oxide membranes for enhanced water purification, Chem. Eng. J. 356 (2018) 915−925. Available from: https://doi.org/10.1016/j.cej.2018.09.108.

[79] V. Devthade, D. Kulhari, S.S. Umare, Role of precursors on photocatalytic behavior of graphitic carbon nitride, Mater. Today Proc. 5 (2018) 9203−9210. Available from: https://doi.org/10.1016/j.matpr.2017.10.045.

[80] Z. Zhao, Y. Ma, J. Fan, Y. Xue, H. Chang, Y. Masubuchi, et al., Synthesis of graphitic carbon nitride from different precursors by fractional thermal polymerization method and their visible light induced photocatalytic activities, J. Alloys Compd. 735 (2018) 1297−1305. Available from: https://doi.org/10.1016/j.jallcom.2017.11.033.

[81] S. Liu, J. Ke, H. Sun, J. Liu, M.O. Tade, S. Wang, Size dependence of uniformed carbon spheres in promoting graphitic carbon nitride toward enhanced photocatalysis, Appl. Catal., B: Environ. 204 (2017) 358−364. Available from: https://doi.org/10.1016/j.apcatb.2016.11.048.

[82] Y. Zheng, Z. Zhang, C. Li, S. Proulx, Surface hydroxylation of graphitic carbon nitride: enhanced visible light photocatalytic activity, Mater. Res. Bull. 84 (2016) 46−56. Available from: https://doi.org/10.1016/j.materresbull.2016.07.003.

[83] F. Hussin, H.O. Lintang, L. Yuliati, Enhanced activity of C_3N_4 with addition of ZnO for photocatalytic removal of phenol under visible light, Malays. J. Anal. Sci. 20 (2016) 102−110. Available from: https://doi.org/10.17576/mjas-2016-2001-11.

[84] H. Yan, Y. Chen, S. Xu, Synthesis of graphitic carbon nitride by directly heating sulfuric acid treated melamine for enhanced photocatalytic H_2 production from water under visible light, Int. J. Hydrogen Energy 37 (2012) 125−133. Available from: https://doi.org/10.1016/j.ijhydene.2011.09.072.

[85] A. Akhundi, A. Habibi-Yangjeh, Novel magnetically separable g-C_3N_4/AgBr/Fe_3O_4 nanocomposites as visible-light-driven photocatalysts with highly enhanced activities, Ceram. Int. 41 (2015) 5634−5643. Available from: https://doi.org/10.1016/j.ceramint.2014.12.145.

[86] X.L. Wang, H.G. Yang, Facile fabrication of high-yield graphitic carbon nitride with a large surface area using bifunctional urea for enhanced photocatalytic performance, Appl. Catal., B: Environ. 205 (2017) 624−630. Available from: https://doi.org/10.1016/j.apcatb.2017.01.013.

[87] J. Xu, Y. Wang, Y. Zhu, Nanoporous graphitic carbon nitride with enhanced photocatalytic performance, Langmuir 29 (2013) 10566−10572. Available from: https://doi.org/10.1021/la402268u.

[88] Q. Zheng, E. Xu, E. Park, H. Chen, D. Shuai, Looking at the overlooked hole oxidation: photocatalytic transformation of organic contaminants on graphitic carbon nitride under visible light irradiation, Appl. Catal., B: Environ. 240 (2019) 262−269. Available from: https://doi.org/10.1016/j.apcatb.2018.09.012.

[89] S. Le, T. Jiang, Y. Li, Q. Zhao, Y. Li, W. Fang, et al., Highly efficient visible-light-driven mesoporous graphitic carbon nitride/ZnO nanocomposite photocatalysts, Appl. Catal., B: Environ. 200 (2017) 601−610. Available from: https://doi.org/10.1016/j.apcatb.2016.07.027.

[90] B. Xu, M.B. Ahmed, J.L. Zhou, A. Altaee, G. Xu, M. Wu, Graphitic carbon nitride based nanocomposites for the photocatalysis of organic contaminants under visible irradiation: progress, limitations and future directions, Sci. Total Environ. 633 (2018) 546−559. Available from: https://doi.org/10.1016/j.scitotenv.2018.03.206.

[91] M. Wang, S. Cui, X. Yang, W. Bi, Synthesis of g-C_3N_4/Fe_3O_4 nanocomposites and application as a new sorbent for solid phase extraction of polycyclic aromatic hydrocarbons in water samples, Talanta 132 (2015) 922−928. Available from: https://doi.org/10.1016/j.talanta.2014.08.071.

[92] K.C. Christoforidis, T. Montini, E. Bontempi, S. Zafeiratos, J.J.D. Jaén, P. Fornasiero, Synthesis and photocatalytic application of visible-light active β-Fe_2O_3/g-C_3N_4 hybrid nanocomposites, Appl. Catal., B: Environ. 187 (2016) 171−180. Available from: https://doi.org/10.1016/j.apcatb.2016.01.013.

[93] G. Mamba, A.K. Mishra, Graphitic carbon nitride (g-C_3N_4) nanocomposites: a new and exciting generation of visible light driven photocatalysts for environmental pollution remediation, Appl. Catal., B: Environ. 198 (2016) 347−377. Available from: https://doi.org/10.1016/j.apcatb.2016.05.052.

[94] M.M. Desipio, R. Thorpe, D. Saha, Photocatalytic decomposition of paraquat under visible light by carbon nitride and hydrogen peroxide, Optik (Stuttg) 172 (2018) 1047−1056. Available from: https://doi.org/10.1016/j.ijleo.2018.07.124.

[95] J. Xiao, Q. Han, Y. Xie, J. Yang, Q. Su, Y. Chen, et al., Is C_3N_4 chemically stable toward reactive oxygen species in sunlight-driven water treatment? Environ. Sci. Technol. (2017). Available from: https://doi.org/10.1021/acs.est.7b04215. acs.est.7b04215.

[96] B. Chai, T. Peng, J. Mao, K. Li, L. Zan, Graphitic carbon nitride (g-C_3N_4)-Pt-TiO 2 nanocomposite as an efficient photocatalyst for hydrogen production under visible light irradiation, Phys. Chem. Chem. Phys. 14 (2012) 16745−16752. Available from: https://doi.org/10.1039/c2cp42484c.

[97] X. Liang, G. Wang, X. Dong, G. Wang, H. Ma, X. Zhang, Graphitic carbon nitride with carbon vacancies for photocatalytic degradation of bisphenol A, ACS Appl. Nano Mater 2 (2019) 517−524. Available from: https://doi.org/10.1021/acsanm.8b02089.

[98] B. Zhu, P. Xia, W. Ho, J. Yu, Isoelectric point and adsorption activity of porous g-C_3N_4, Appl. Surf. Sci. 344 (2015) 188−195. Available from: https://doi.org/10.1016/j.apsusc.2015.03.086.

[99] W. Guan, W. Gu, L. Ye, C. Guo, S. Su, P. Xu, et al., Microwave-assisted polyol synthesis of carbon nitride dots from folic acid for cell imaging, Int. J. Nanomed. 9 (2014) 5071−5078. Available from: https://doi.org/10.2147/IJN.S68575.

[100] Y. Liu, N. Xiao, N. Gong, H. Wang, X. Shi, W. Gu, et al., One-step microwave-assisted polyol synthesis of green luminescent carbon dots as optical nanoprobes, Carbon N. Y. 68 (2014) 258−264. Available from: https://doi.org/10.1016/j.carbon.2013.10.086.

[101] Z.H. Zhang, H.X. Guo, F.W. Yu, Q.H. Xiong, M.S. Ye, X.J. Fan, Preparation of cubic C_3N_4 thin films by low-pressure plasma enhanced chemical vapor deposition, Wuli Xuebao/Acta Phys. Sin. 47 (1998) 1051. Available from: https://doi.org/10.7498/aps.47.1047.

[102] J. Fu, J. Yu, C. Jiang, B. Cheng, g-C_3N_4-based heterostructured photocatalysts, Adv. Energy Mater. 8 (2018) 1−31. Available from: https://doi.org/10.1002/aenm.201701503.

[103] H. Che, L. Liu, G. Che, H. Dong, C. Liu, C. Li, Control of energy band, layer structure and vacancy defect of graphitic carbon nitride by intercalated hydrogen bond effect of NO_3^- toward improving photocatalytic performance, Chem. Eng. J. 357 (2019) 209−219. Available from: https://doi.org/10.1016/j.cej.2018.09.112.

[104] Y. Wang, X. Wang, M. Antonietti, Y. Zhang, Facile one-pot synthesis of nanoporous carbon nitride solids by using soft templates, ChemSusChem 3 (2010) 435−439. Available from: https://doi.org/10.1002/cssc.200900284.

[105] J. Yang, H. Chen, J. Gao, T. Yan, F. Zhou, S. Cui, et al., Synthesis of Fe_3O_4/g-C_3N_4 nanocomposites and their application in the photodegradation of 2,4,6-trichlorophenol under visible light, Mater. Lett. 164 (2016) 183−189. Available from: https://doi.org/10.1016/j.matlet.2015.10.130.

[106] M. Chu, K. Hu, J. Wang, Y. Liu, S. Ali, C. Qin, et al., Synthesis of g-C_3N_4-based photocatalysts with recyclable feature for efficient 2,4-dichlorophenol degradation and mechanisms, Appl. Catal., B: Environ. 243 (2019) 57−65. Available from: https://doi.org/10.1016/j.apcatb.2018.10.008.

[107] S. Panneri, P. Ganguly, B.N. Nair, A.A.P. Mohamed, K.G.K. Warrier, U.N.S. Hareesh, Role of precursors on the photophysical properties of carbon nitride and its application for antibiotic degradation, Environ. Sci. Pollut. Res. 24 (2017) 8609−8618. Available from: https://doi.org/10.1007/s11356-017-8538-z.

[108] M. Sturini, A. Speltini, F. Maraschi, G. Vinci, A. Profumo, L. Pretali, et al., g-C_3N_4-promoted degradation of ofloxacin antibiotic in natural waters under simulated sunlight, Environ. Sci. Pollut. Res. 24 (2017) 4153−4161. Available from: https://doi.org/10.1007/s11356-016-8156-1.

[109] X. Wang, X. Chen, A. Thomas, X. Fu, M. Antonietti, Metal-containing carbon nitride compounds: a new functional organic-metal hybrid material, Adv. Mater. 21 (2009) 1609−1612. Available from: https://doi.org/10.1002/adma.200802627.

[110] A. Akhundi, A. Habibi-Yangjeh, Ternary g-C_3N_4/ZnO/AgCl nanocomposites: synergistic collaboration on visible-light-driven activity in photodegradation of an organic pollutant, Appl. Surf. Sci. 358 (2015) 261−269. Available from: https://doi.org/10.1016/j.apsusc.2015.08.149.

[111] L. Zhu, L. You, Y. Wang, Z. Shi, The application of graphitic carbon nitride for the adsorption of Pb^{2+} ion from aqueous solution, Mater. Res. Express 4 (2017) 075606. Available from: https://doi.org/10.1088/2053-1591/aa7903.

[112] S. Chu, Y. Wang, Y. Guo, J. Feng, C. Wang, W. Luo, et al., Band structure engineering of carbon nitride: in search of a polymer photocatalyst with high photooxidation

property, ACS Catal. 3 (2013) 912−919. Available from: https://doi.org/10.1021/cs4000624.

[113] Q. Zheng, D.P. Durkin, J.E. Elenewski, Y. Sun, N.A. Banek, L. Hua, et al., Visible-light-responsive graphitic carbon nitride: rational design and photocatalytic applications for water treatment, Environ. Sci. Technol. 50 (2016) 12938−12948. Available from: https://doi.org/10.1021/acs.est.6b02579.

[114] H. Lin, Y. Liu, J. Deng, S. Xie, X. Zhao, J. Yang, et al., Graphitic carbon nitride-supported iron oxides: high-performance photocatalysts for the visible-light-driven degradation of 4-nitrophenol, J. Photochem. Photobiol. A: Chem. 336 (2017) 105−114. Available from: https://doi.org/10.1016/j.jphotochem.2016.12.026.

[115] J. Wang, C. Li, J. Cong, Z. Liu, H. Zhang, M. Liang, et al., Facile synthesis of nanorod-type graphitic carbon nitride/Fe_2O_3 composite with enhanced photocatalytic performance, J. Solid State Chem 238 (2016) 246−251. Available from: https://doi.org/10.1016/j.jssc.2016.03.042.

[116] X. Zhou, B. Jin, R. Chen, F. Peng, Y. Fang, Synthesis of porous Fe_3O_4/g-C_3N_4 nanospheres as highly efficient and recyclable photocatalysts, Mater. Res. Bull. 48 (2013) 1447−1452. Available from: https://doi.org/10.1016/j.materresbull.2012.12.038.

[117] M. Mousavi, A. Habibi-Yangjeh, Magnetically separable ternary g-C_3N_4/Fe_3O_4/BiOI nanocomposites: novel visible-light-driven photocatalysts based on graphitic carbon nitride, J. Colloid Interface Sci. 465 (2016) 83−92. Available from: https://doi.org/10.1016/j.jcis.2015.11.057.

[118] A. Hassani, P. Eghbali, A. Ekicibil, Ö. Metin, Monodisperse cobalt ferrite nanoparticles assembled on mesoporous graphitic carbon nitride ($CoFe_2O_4$/mpg-C_3N_4): a magnetically recoverable nanocomposite for the photocatalytic degradation of organic dyes, J. Magn. Magn. Mater. 456 (2018) 400−412. Available from: https://doi.org/10.1016/j.jmmm.2018.02.067.

[119] L. Liu, X. Luo, Y. Li, F. Xu, Z. Gao, X. Zhang, et al., Facile synthesis of few-layer g-C_3N_4/ZnO composite photocatalyst for enhancing visible light photocatalytic performance of pollutants removal, Colloids Surf., A: Physicochem. Eng. Aspects 537 (2018) 516−523. Available from: https://doi.org/10.1016/j.colsurfa.2017.09.051.

[120] S. Wu, H.J. Zhao, C.F. Li, J. Liu, W. Dong, H. Zhao, et al., Type II heterojunction in hierarchically porous zinc oxide/graphitic carbon nitride microspheres promoting photocatalytic activity, J. Colloid Interface Sci. 538 (2019) 99−107. Available from: https://doi.org/10.1016/j.jcis.2018.11.076.

[121] S. Panneri, P. Ganguly, B.N. Nair, A.A.P. Mohamed, K.G. Warrier, U.N.S. Hareesh, Copyrolysed C_3N_4-Ag/ZnO ternary heterostructure systems for enhanced adsorption and photocatalytic degradation of tetracycline, Eur. J. Inorg. Chem. 2016 (2016) 5068−5076. Available from: https://doi.org/10.1002/ejic.201600646.

[122] S. Zhan, F. Zhou, N. Huang, Y. Yang, Y. Liu, Y. Yin, et al., G-C_3N_4/$ZnWO_4$ films: preparation and its enhanced photocatalytic decomposition of phenol in UV, Appl. Surf. Sci. 358 (2015) 328−335. Available from: https://doi.org/10.1016/j.apsusc.2015.07.180.

[123] S. Yu, Y. Wang, F. Sun, R. Wang, Y. Zhou, Novel mpg-C_3N_4/TiO_2 nanocomposite photocatalytic membrane reactor for sulfamethoxazole photodegradation, Chem. Eng. J. 337 (2018) 183−192. Available from: https://doi.org/10.1016/j.cej.2017.12.093.

[124] H. Wang, Y. Liang, L. Liu, J. Hu, W. Cui, Highly ordered TiO_2 nanotube arrays wrapped with g-C_3N_4 nanoparticles for efficient charge separation and increased photoelectrocatalytic degradation of phenol, J. Hazard. Mater. 344 (2018) 369−380. Available from: https://doi.org/10.1016/j.jhazmat.2017.10.044.

[125] Y.N. Li, Z.Y. Chen, M.Q. Wang, L.Z. Zhang, S.J. Bao, Interface engineered construction of porous g-C_3N_4/TiO_2 heterostructure for enhanced photocatalysis of organic pollutants, Appl. Surf. Sci. 440 (2018) 229–236. Available from: https://doi.org/10.1016/j.apsusc.2018.01.106.

[126] A. Habibi-Yangjeh, A. Akhundi, Novel ternary g-C_3N_4/Fe_3O_4/Ag_2CrO_4 nanocomposites: magnetically separable and visible-light-driven photocatalysts for degradation of water pollutants, J. Mol. Catal., A: Chem. 415 (2016) 122–130. Available from: https://doi.org/10.1016/j.molcata.2016.01.032.

[127] A. Akhundi, A. Habibi-Yangjeh, Novel magnetic g-C_3N_4/Fe_3O_4/AgCl nanocomposites: facile and large-scale preparation and highly efficient photocatalytic activities under visible-light irradiation, Mater. Sci. Semicond. Process. 39 (2015) 162–171. Available from: https://doi.org/10.1016/j.mssp.2015.04.052.

[128] N.C. Mueller, B. Nowack, Nanoparticles for remediation: solving big problems with little particles, Elements 6 (2010) 395–400. Available from: https://doi.org/10.2113/gselements.6.6.395.

[129] I. Khan, A. Khalil, F. Khanday, A.M. Shemsi, A. Qurashi, K.S. Siddiqui, Synthesis, characterization and applications of magnetic iron oxide nanostructures, Arabian J. Sci. Eng. 43 (2018) 43–61. Available from: https://doi.org/10.1007/s13369-017-2835-1.

[130] R.C. Pawar, C.S. Lee, Single-step sensitization of reduced graphene oxide sheets and CdS nanoparticles on ZnO nanorods as visible-light photocatalysts, Appl. Catal., B: Environ. 144 (2014) 57–65. Available from: https://doi.org/10.1016/j.apcatb.2013.06.022.

[131] X. Wang, K. Maeda, X. Chen, K. Takanabe, K. Domen, Y. Hou, et al., Polymer semiconductors for artificial photosynthesis: hydrogen evolution by mesoporous graphitic carbon nitride with visible light, J. Am. Chem. Soc. 131 (2009) 1680–1681. Available from: https://doi.org/10.1021/ja809307s.

[132] X. Yang, A. Wolcott, G. Wang, A. Sobo, R.C. Fitzmorris, F. Qian, et al., Nitrogen-doped ZnO nanowire arrays for photoelectrochemical water splitting, Nano Lett 9 (2009) 2331–2336. Available from: https://doi.org/10.1021/nl900772q.

[133] Y. He, Y. Wang, L. Zhang, B. Teng, M. Fan, High-efficiency conversion of CO_2 to fuel over ZnO/g-C_3N_4 photocatalyst, Appl. Catal., B: Environ. 168–169 (2015) 1–8. Available from: https://doi.org/10.1016/j.apcatb.2014.12.017.

[134] R.M. Mohamed, A.A. Ismail, M.W. Kadi, D.W. Bahnemann, A comparative study on mesoporous and commercial TiO_2 photocatalysts for photodegradation of organic pollutants, J. Photochem. Photobiol., A: Chem. 367 (2018) 66–73. Available from: https://doi.org/10.1016/j.jphotochem.2018.08.019.

This page intentionally left blank

Quantum materials for emerging agrochemicals

5

Adalberto Benavides-Mendoza[1], *Antonio Juárez-Maldonado*[2], *Gonzalo Rodrigo Tortella-Fuentes*[3] *and José Antonio González-Fuentes*[1]
[1]Department of Horticulture, Autonomous Agricultural University Antonio Narro, Saltillo, Mexico, [2]Department of Botany, Autonomous Agricultural University Antonio Narro, Saltillo, Mexico, [3]Chemical Engineering Department, Universidad de La Frontera, Temuco, Chile

5.1 Introduction

Different scopes or scales of organization or description are used to study the world. It is customary to schematize this description of the systems in the form of a sequence that indicates the scale of magnitude of the phenomena under study or description, as an example atom on the 10^{-10}-m scale, living organisms on the scale from 10^{-6} to 10^{1} m, and ecosystems on the 10^{3}-m scale. The properties of each scope, going from the smallest to the largest, are partially explained by the features of the previous organization scale that supports it, plus a new set of properties called emergent properties. These new properties are the result of the interactions of the components of the system. In the previous example, living organisms and ecosystems depend on atoms for their existence. Still, they have new and specific properties such as the organization of flows of energy, matter and information, and the evolution across time that are not predictable from the properties of atoms.

The quantum domain considers the behavior and properties of matter, energy, and information on the scale of phenomena where the interactions of particles and their collective excitations intervene. These interactions are manifested in the form of phenomena such as electromagnetic radiation, magnetism, electricity, sound, and conduction. Therefore directly, or indirectly, the quantum domain permeates in all subsequent areas of description: the molecular and supramolecular and the succeeding ones that give rise to phenomena on scales higher than micrometers.

The production of food, energy, and manufactures for a growing human population depends on the manipulation of different properties of matter and on various natural processes that involve transfers of energy and information. Physics and chemistry are responsible for those, as well as disciplines such as medicine, agronomy, ecology, and economics. During the 20th century, a discipline called nanotechnology emerged, which is related to the phenomena and properties found in materials, called nanomaterials (NMs), whose structures are displayed on scales of 10^{-9} m and whose properties are directly dependent on quantum phenomena.

Quantum Materials, Devices, and Applications. DOI: https://doi.org/10.1016/B978-0-12-820566-2.00002-8

Nanotechnological developments are multiple, with applications in practically all areas of knowledge, including biology and medicine. In agriculture, nanotechnology applications have substantially increased in recent years. The uses of nanofertilizers, nanometric soil amendments, nanopesticides, and nanosensors are already present at the commercial level [1]; other applications, such as the use of NMs for genetic transformation with DNA and RNA [2,3], improvement of metabolic activity and photosynthesis [4,5], as well as the use of NMs for biostimulation, and the increase in stress tolerance in cultivated plants [6], are under intense study.

NMs are considered to be structures or aggregates or agglomerates that present at least one external dimension (d) $0.4 < d < 100$ nm [7] or with a volume-specific surface area $>60\ m^2\ cm^{-3}$ [8]. Some authors point out that structures with at least one dimension (1D) <1000 nm can be considered NMs [9,10]. The reality is that at this time, the definitions are somewhat arbitrary, so far without having a functional definition of what constitutes an NM, as well as the threshold of dimensional magnitude for the properties that distinguish an NM from a bulk or micrometric materials [7].

When the size of the structures decreases to the nanometric scale, NMs are obtained that manifest physical, chemical, and optical properties not found in the bulk material. These new properties are what allow highly specialized modern applications of materials whose industrial and craft use dates back to antiquity, such as copper, iron, gold, silver, and silicon. The utilizations of the NMs are multiple and refer to practically all industrial and environmental management areas, communications, energy production, medicine, food, and agricultural and forestry production [11].

NMs are classified according to the number of dimensions outside the nanoscale range. There are all-dimensional or 0D NMs [nanoparticles (NPs); all dimensions ≤ 100 nm], 1D NMs (nanotubes, nanowires, nanofibers, and nanorods; 1D >100 nm), two-dimensional NMs (graphene, nanofilms, nanolayers, and nanocoatings; 2D >100 nm), and three-dimensional NMs (porous materials, zeolites, dispersions, and powders; 3D >100 nm) [12].

A particular class of materials, collectively named quantum materials (QMs), have at least 1D less than the Bohr radius [13], typically from 0.4 to 15 nm, although depending on the material can be up to $d \leq 47$ nm [14]. The small size of the nanostructures of QMs leads to the characteristic of quantum confinement, which occurs when the dimension of the structure is close to the free path length of the electrons. Consequently, delocalized or continuous electronic movement is restricted in one or more dimensions and is confined to certain discrete energy states. This confinement of the electrons produces emergent properties that result from the correlated collective behavior of the electrons, such as superparamagnetism, electrical conduction, optical phenomena derived from the absorption and emission of light, as well as the ability to transform light very efficiently into electricity or heat [15].

The confinement is observed in the different NMs as follows: in 0D NMs called quantum dots, it occurs in 3D; that is, there are 0 free dimensions; in 1D NMs, confinement occurs in 2D; in 2D NMs only 1D shows electron confinement. In 3D porous materials, such as zeolites and nanozeolites, the internal diameters of the

pores can be ≤ 5 nm, with subsequent 1D confinement of electrons [15,16]. The confinement of the electrons results from a geometric restriction or one or more dimensions, that is, it is an effect mainly related to the size or shape of the NM, and it depends to a much lesser extent on the composition. What is primarily variable with the composition of quantum NMs (QNMs) are the specific emergent properties resulting from particle confinement.

A definition of QM is, "solids with exotic physical properties, arising from the quantum mechanical properties of their constituent electrons" [17]. QMs are diverse: superconductors, graphene, topological insulators, Weyl semimetals, quantum spin liquids, spin glasses, and spin ices [15]. However, the attention in this manuscript will focus on those QMs in the NM category in which the authors visualize applications as agrochemicals, including use as fertilizer, soil improver, pesticide, or biostimulant, that is, 0D materials with $d \leq 15$ nm as quantum dots or metallic or semimetallic NPs, of metal and organic oxides, 1D and 2D materials of carbon or silicon, and zeolites and nanozeolites 3D.

Considering the earlier text, the objective of this chapter is to describe the agricultural applications of the class of NMs called QMs or QNMs.

5.2 Nanomaterials and quantum nanomaterials: the applicable properties for agriculture

The responses of organisms against NMs depend fundamentally on the concentration and bioavailability of NMs in the growth medium. The phenomenon of hormesis describes the positive reaction of an organism against a physical, chemical, or biological agent, called an inductor, when this inductor is at low concentration. By increasing the amount, intensity, or concentration of the inducer, the body's response becomes negative. These types of reactions, when plotted, form a figure called an "inverted U." For NMs, this type of hormetic responses has been described [18]; for this reason, the concentration of the NM and the characteristics of the medium that can increase or decrease the bioavailability (such as pH, ionic strength, presence of dissolved organic matter, or inorganic colloids) determine in a substantial way the impact of the NMs on organisms and ecosystems [9]. Many studies have been devoted to verifying the effect of concentration and bioavailability of NMs on living organisms, and plants have been the subject of much attention in this regard.

But beyond the responses to concentration in the medium and bioavailability, which fall into the domain of environmental chemistry and ecosystems, there is another class of properties of the NMs that refer to a physicochemical field of the materials. These physicochemical properties have been less studied. These properties are manifested as intrinsic characters, regardless of the concentration or characteristics of the medium in which the NMs are found.

Two types of basic physicochemical properties have been described that modify the response of organisms in contact with an NM. The first property is the high surface: volume ratio, which manifests itself as sizeable free surface energy that allows the

formation of a corona upon contact with biological and natural fluids. The corona is the interface of the NM with the cells of the organisms. The second property is the chemical composition of NM, which allows the release of specific ions or monomers with effects that can range from biostimulation to toxicity on organisms.

We will mention a third and a fourth property of the NMs that have been studied extensively from the biomedical and industrial point of view but much less addressed in terms of examining the effects on plants. The third property is the earlier mentioned quantum confinement, resulting from the topological restriction on the mobility of electrons, which, among other things, causes surface plasmons and photon emission or photoluminescence. Photon emission is the result of recombination of electrons and holes, and the subsequent photon emission with the energy proportional to the band-gap energy. It is not known to what extent quantum confinement can affect or act synergistically, with the surface-to-volume ratio and with the chemical composition to determine cellular responses. The same seems to be true of the fourth property, superparamagnetism, which is the single-domain magnetism shown by NPs <20 nm composed of ferromagnetic or ferrimagnetic materials. It is not possible to exclude, at this time, that the potential responses of organisms to quantum confinement and superparamagnetism are added to those observed concerning the surface-to-volume ratio and the chemical composition.

The dimensions of the NMs are determinants of the first, third, and fourth properties: the surface-to-volume ratio, quantum confinement, and superparamagnetism. The surface-to-volume ratio increases as the size of the NMs decreases; quantum confinement and superparamagnetism occur from a critical reduction in the dimensional size of the NM, that is, it happens once a threshold showing variations in each material is reached.

The second property, the elemental composition of the NM core, is independent of the magnitude of the dimensions. The different elemental composition of the NM's core causes different reactions with the biomolecules present in an organic fluid or natural environment, producing the release in the ionic or monomeric form of the core components.

All NMs interact with organisms through their high surface free energy, and the biological response to this energy depends fundamentally on the size of the NMs, but also on other characteristics that change the active area of the NMs with respect to its volume, such as the shape, roughness, aspect ratio, and organic corona composition. The first interactions are dependent on surface free energy, and the functional groups of the corona are those that trigger the first cellular responses: changes in the membrane potential, modifications in the activity of integral proteins such as channels, signal transducers, and proteins for the transport of electrons.

The initial changes lead to adjustments in the physiological activity, in the metabolome of the cells, as well as in the gene expression and the subsequent change in the proteome. Under certain conditions of concentration, size, and shape of the NMs, these initial modifications can turn into cellular responses similar to those of defense against stress. Therefore the NMs under the appropriate schemes of agricultural application, that is, avoiding the contamination of soils and water and ensuring safety for consumers, can be used in agricultural practice as biostimulants [6].

The second sequence of cellular responses occurs after interactions between the NM corona-plant cell interfaces. This second chain of reactions depends on the

cellular internalization of the NMs and the interaction of the corona and the core with the proteins and metabolites present in the cytoplasm, in the organelles, and the internal systems of membranes and cytoskeleton. In addition to interactions with inner cell surfaces, NMs may react with different cell metabolites and begin to release core components in ionic or monomeric form. The release of the ions or monomers causes the second chain of signals and cellular adjustments that once again modify physiological activity and gene expression [6].

This biphasic response to free energy and the composition of the NMs makes the prediction of the reactions of biological organisms difficult. In addition, although the responses can be described in a general scope for all organisms, they are highly dependent on the specific organism-environment context. Therefore they present small or full variants depending on the plant species and the growth environment and its characteristics [19]. Electron confinement and superparamagnetism are additional little-explored domains in the response of plant organisms to NMs. It is highly likely that they will add to or interact with cellular reactions to surface energy and the composition of NMs.

Agricultural experimentation directed toward understanding the impact of QNMs on plants is not abundant. Instead, what is available is a certain amount of information on the agricultural use of various NMs with at least 1D ≤ 15 nm (which may place them in the category of QNMs). These NMs with at least one $d \leq 15$ nm have been used as agrochemicals in the areas of fertilizers, pesticides, or biostimulants [20]. In many cases, the use of these materials was thought to take into account the reactivity and the composition—the first and second properties described earlier—but without taking into account the ability to impact plant cells thanks to their quantum or magnetic properties, the third and fourth properties described earlier.

In QNMs, the confinement of the electrons causes them to be present at specific energy levels, which, in interaction with biomolecules (which are also known to carry out quantum processes), could alter the responses of organisms to light, magnetism, and other environmental factors. It is even possible to consider the modification of the functionality and efficiency of the biological nanostructures carrying out an essential segment of the activity of organisms, that is, membranes, proteins, DNAs, and RNAs [21].

In some biological processes such as photosynthesis, they occur unexpectedly long-time quantum coherences in energy transport in the photosynthetic complexes. The energy transduction of photons into energy stored in biomolecule's bonds occurs through the generation of excitons in photosynthetic antennas [22]. NMs have been shown to increase the efficiency of light-harvesting by capturing or reflecting higher amounts of photosynthetic active radiation (PAR) within chloroplasts or by converting by fluorescence the shortwave (UV, violet, and blue) radiation into longwave (red), decreasing heat generation, fluorescence, and the production of reactive oxygen species (ROS) in chloroplast photosystems [10,23].

It is not known if QNMs can modify quantum processes of photosynthesis, such as quantum coherence and electron entanglement, but it is a relevant possibility for the design of QNMs aimed at increasing the efficiency in the use of PAR in photosynthesis. This efficiency, apparently due to fundamental design issues, reaches values between 2% and 6% [24].

Quantum tunneling of electrons and protons/hydride/hydrogen under physiological conditions has been observed in enzymatic catalysis developed by specific proteins of microorganisms, plants, and animals [25]. In principle, it is likely that in the processes where the transports of electrons and protons are involved, that is, in those processes of energy transduction in membranes, chloroplasts and mitochondria, the quantum tunneling is relevant [26,27]. However, the extent of the importance of the phenomenon on the biological scale is still unexplored and subject to controversy [28]. It remains to be answered equally if the QNMs somehow modify the tunneling process that has been described in the proteins.

Likewise, quantum entanglement processes have been described that naturally increase the efficiency of energy transduction, decreasing losses due to heat and fluorescence [29]. Some NMs are known to increase the efficiency of photosynthesis [23]. Still, as far as we know, it has not been systematically described whether QNMs have the general ability to modify biological energy transduction, both in the photosynthesis as in mitochondrial respiration and in other enzymatic processes dependent on the transfer of electrons and protons. It is possible that this last capacity, if it occurs in all QNMs, would be a very relevant property for the design and obtaining of new biostimulants to increase agricultural productivity.

Regarding magnetism, the impact of this phenomenon on biological organisms is well known [30,31], including plants [32]. Proteins from plants and other organisms contain transition metal cofactors, which can be magnetic per se [33] or accumulate in cells as magnetic minerals [34]. Taking into account the earlier text, techniques called magnetopriming have been proposed that are based on the use of magnetic fields to induce particular modulation and stress tolerance responses in crops [35,36]. However, the mechanism of action of magnetism on cells or their components is, in many cases, poorly understood [37].

Nanomagnetism occurs in 0D, 2D, and 3D NMs. In the case of NMs, single-domain superparamagnetism is expected at NPs ≤ 15 nm and has been observed, for example, in the ferritin protein whose function is iron storage [38]. The NM's superparamagnetism allows obtaining materials with characteristics such as hyperthermia, magnetic resonance, magnetic inhomogeneities for tissue contrast, which made them profoundly studied agents in biomedicine, both for the controlled release of bioactive compounds and for hyperthermic treatment during cancer therapy [39−42]. These same characteristics make superparamagnetic NPs candidate materials for use in crops or specific processes in the food industry or environmental engineering [43,44].

Regarding the availability of NMs of different chemical elements with the characteristic of 1D ≤ 15 nm, which could be verified for their potential application as agrochemicals, Table 5.1 presents a list of them. The examples do not necessarily indicate that the material is a QNM. Still, in those cases where the character of QM was not mentioned, the examples were included considering the dimensional criterion $d \leq 15$ nm.

The examples in Table 5.1 do not include chemical elements that are routinely used in agriculture, such as in fertilizers, biostimulants, and pesticides; rather, the selected examples refer to materials whose agricultural use (such as pesticide or

Table 5.1 Examples of chemical elements or materials for which nanomaterials (NMs) are reported with at least one dimension less than 15 nm and therefore can be categorized as quantum NMs.

Elements or materials	NM class	Reported use	References
Bi	Bismuth sulfide nanorods with retractable zinc protoporphyrin molecules	Cancer therapy	[45]
C	Carbon quantum dots	Detection of food contaminants	[46]
C	Carbon quantum dots	Visible light−activated bactericide capacity	[47]
C	Carbon nanotubes	Plant biostimulant	[48]
C	Multiwalled carbon nanotubes	Plant biostimulant	[49]
C	Multiwalled carbon nanotubes	Plant biostimulant	[50]
C	Multiwalled carbon nanotubes functionalized with carboxylic acid	Plant biostimulant	[51]
C-Br	Halogenated carbon nanodots	Biological imaging	[52]
CdSe/ZnS	CdSe/ZnS quantum dot-encapsulated in chitosan nanospheres	Biological imaging	[53]
Cellulose	Cellulose nanofiber and sodium alginate	Delivery of biomolecules	[54]
Chitosan	Chitosan quantum dots	Biomedical applications	[55]
Chitosan	Chitosan−graphene nanocomposites	Carrier of plant nutrients	[56]
Co	Co sulfide NMs	Magnetism, energy	[57]
Ga	Ga_2O_3 nanorods	Photoelectrochemical water splitting	[58]
Hydroxyapatite nanorods	Hydroxyapatite nanorods loaded with parathyroid hormone	Biomedical applications	[59]
I	Iodinated graphene nanoplatelets	Contrast agent for imaging	[60]
I	Iodine oxide NPs	Natural origin	[61]
Graphene	Graphene nanosheets	Plant biostimulant	[62]
Graphene	Graphene oxide sheets	Carrier of plant micronutrients	[63]
Graphene	Graphene oxide sheets	Plant biostimulant	[64]

(*Continued*)

Table 5.1 (Continued)

Elements or materials	NM class	Reported use	References
Graphene	Graphene oxide−Fe(III) composite with phosphate	Carrier of plant nutrients	[65]
Graphene	Graphene quantum dots	Electrochemistry, biological sensing	[66]
Graphene	Graphene quantum dots	Plant biostimulant	[67]
Mo	Molybdenum disulfide quantum dots	Cell imaging, photoluminescence	[68]
Mo	Molybdenum disulfide nanosheets	Photocatalysis and antimicrobial use, wound healing	[69]
Mo	Molybdenum disulfide quantum dots	Neurological theranostics	[70]
Nanofibers	Electrospun nanofibers	Delivery of biomolecules	[71]
Ni	Spin glass nickel oxide NPs	Antimicrobial use. Nontoxicity to human cells	[72]
Ni	Ni sulfide NMs	Magnetic, energy production	[57]
Ni	Bimetallic Ni−Fe NPs	Dehalogenation of TCE	[73]
Polymer dots	Semiconducting polymer nanoparticles	Cellular labeling, imaging, biosensing	[74]
Polymer dots	Semiconducting polymer nanoparticles and a immunostimulant conjugated	Cancer therapy	[75]
Se	Nanocrystals and nanorods	Biomedical applications	[76]
Si	Silicon nanowires	Optical modulation of cellular responses	[77]
Si	Silicon nanowires	Biomedical applications	[78]
Si	Silicon quantum dots	Biological imaging, nanosensors	[79]
Si	Silicon quantum dots with fluorescein isothiocyanate	Imaging and pH sensing	[80]
Zr	Ultrathin ZrS_2 nanodisks	Anodic materials for Li^+ intercalation	[81]

These NMs are not routinely used in agriculture. In almost all cases, tests have not been performed with plants, but they have the potential to be used as agrochemicals or biostimulants. *TCE*, Trichloroethylene.

biostimulant) could become applicable or refers to some cases such as Ni and Mo, which, although they are considered essential elements for plants, are not used ordinarily. The NMs for Ag, Au, Ce, and Ti that have been relatively well studied regarding their effect on plants are not included in Table 5.1. The potential use of the materials listed later presupposes the careful study of their impact on food safety and soil and water contamination.

5.3 Agrochemicals and the niches for quantum materials

In addition to the four properties relevant for agrochemicals and biostimulants mentioned in the previous section (high surface ratio: volume, chemical composition, quantum confinement, and superparamagnetism) for NMs and QNMs, there are other series of properties that they allow characterizing the materials used as agrochemicals, either in bulk or in nano form. Table 5.2 shows some of the characteristics used to describe the different materials. Some features are used both in bulk materials, as in NM or QNM, but others are unique for each scope of the description.

Tables 5.2 and 5.3 allow visualizing various scenarios regarding the use of QNMs as agrochemicals. The scenarios indicate the niches where the QNMs can initially be located, considering the different agrochemical class. If it is assumed that the NMs will behave like QNMs when reaching the threshold $d \leq 15$ nm, then the proposed alternatives for use are as follows:

1. Uses that depend on the composition, for example, a fertilizer with zinc or another essential or beneficial element. In this case, the use of Zn QNM significantly increases the efficiency of the material by making it more bioavailable and more stable against environmental inactivation (e.g., by sunlight or by the fixation on the colloids of the soil). The result is that the nanofertilizers can be applied in less quantity than it should be if it were a bulk material [11,122]. NMs consisting of the 14 essential elements that are applied as fertilizers in crops are included in this composition-dependent use category (N, P, K, Ca, Mg, S, Fe, Zn, Mn, B, Cl, Cu, Mo, and Ni), plus five elements considered beneficial Si, Na, I, Se, and Co.
2. Applications that depend on reactivity, that is, physiological, biochemical responses, or changes in the gene expression and proteomes of plants or their symbiotic organisms in response to the surface free energy of a QNM, that is, that depends on size, surface-to-volume ratio, shape, and aspect ratio of the nanostructure. An example of this alternative is the use of carbon or silicon 3D, 2D, 1D, and 0D QNMs, or quantum dots of the 19 elements remarked earlier and adding the elements Au, Ag, Ti, and Ce additionally. The reactivity of the QNMs in all organisms is higher when $d \leq 15$ nm compared to that observed in larger nanostructures [6,10].
3. Uses related to the ability of QNMs to carry or transport high molecular weight biomolecules, polymers, carbohydrates, and other metabolites and mineral elements to the plant body. In this case, it takes advantage of the large active surface of the 3D, 2D, 1D, and 0D QNMs, resulting from porosity, roughness, and high surface-to-volume ratio [10,123]. Examples of this alternative are the transport to the apoplast of plants or the interior of cells or their organelles of molecules such as DNA or RNA [3], antioxidants [10], pesticides [124,125], biostimulants [126], and fertilizer elements [127]. This type of application resulting from carrying capacity is always associated with the previous group of usages dependent on reactivity. In the biological field, the two effects can be combined or interact synergistically.

Table 5.2 Characteristics used to describe the materials in the macro and micro (bulk material) and nano [nanomaterials (NM) and quantum NM (QNM)] domains of description.

Physical or chemical properties	Bulk materials	NMs	QNMs
Density			
Hardness			
Melting point			
Solubility			
Vapor pressure			
Boiling point			
Composition			
Bandgap[a]			
Magnetism[a]			
Superconductivity[a]			
Plant toxicity[b]			
Insecticide, fungicide, or bactericide action[b]			
Impacts on plant microbiome[b]			
Plant biostimulation[b]			
Plant biofortification[b]			
Pore size			
Hydrofobicity			
Roughness			
Size of the structure			
Shape of the structure			
Aspect ratio			
Z potential			
Surface area:volume			
Surface free energy			
Superparamagnetism			
Electron confinement			
Highly efficient conversion of light to electricity[c]			
Highly efficient conversion of light to heat[c]			

Some of the reported biological impacts on plants are included as functional characteristics.
[a]It is evident in all three areas, but it depends on quantum phenomena.
[b]The toxicity, biostimulation, and the ability to provide essential or beneficial elements for biofortification rely primarily on the composition, and therefore the materials in their bulk and nano forms are capable of inducing them; however, the efficiency with which the three processes are achieved increases substantially when using NMs and QNMs. For these latter cases, the explanation has been found in the increase in reactivity and higher free surface energy, which increases with decreasing the dimensions of the nanostructures and with changing their shape and aspect ratio.
[c]These characteristics seem to explain, in part, the higher photosynthetic and metabolic efficiency of the plants where the QNMs are applied.

4. Applications that depend on the properties derived from the ability of light-harvesting, electron/proton transfer or transport, fluorescence, and quantum confinement [10]. The use of NMs as sensors has been studied to some extent due to their characteristics of fluorescence [128], to magnetism [129], for the capture of ROS [130] or improvement of light-harvesting and electron transport in photosynthetic membranes [23,131]. In other biological processes where magnetism intervenes or in processes that manifest a quantum character (especially tunneling, quantum superposition, and entanglement), the application of QNMs has been less studied.

Table 5.3 Different classes of agrochemicals and the different nanomaterials (NMs) or quantum NMs potentially located or actually located in each category.

Agrochemical class	Example	References
Fertilizers 3D and 0D	N, P, K, Ca, Mg, S, Fe, Zn, Mn, B, Cl, Cu, Mo, Ni nanometric forms	[82]
3D, 2D, 1D, and 0D NMs for shelf-life extension	ZnO NPs, Ag NPs, nano-$CaCo_3$, nanochitosan, nanosilica	[83,84]
2D and 1D organic soil amendments	Carbon NMs	[85−88]
3D and 0D inorganic soil amendments	Nanozeolites	[89]
Biostimulant metabolites (such as antioxidants, vitamins, peptides, and noncoding RNA)	Nanoencapsulated metabolites	[90,91]
Biostimulant beneficial elements	Nanometric forms of Si, Na, I, Se, and Co	[92]
Biostimulant biopolymers	Nanochitosan	[93]
Biopolymers carrying agrochemicals	Nanochitosan-fertilizers or nanochitosan-pesticides	[94,95]
Agrochemical carrier materials	Quantum hybrid NMs	[96,97]
2D, 1D, and 0D materials with biostimulant potential	Carbon NMs	[98,99]
2D, 1D, and 0D materials with biostimulant potential	Hybrid carbon NMs	[100,101]
Biotic elicitors	Pathogenic proteins or toxins, fragments of cell walls, oligosaccharides, small RNA or peptides nanoencapsulated or adsorbed on zeolite, nanozeolite or carbon or silicon materials 2D, 1D, or 0D	[102−104]
NMs that function as growth regulators and biostimulants	Carbon and silicon NMs 2D, 1D, or 0D	[105]
Growth regulator metabolites	Growth regulator biomolecules (e.g., salicylates) nanoencapsulated or adsorbed on zeolite, nanozeolite or 2D, 1D, or 0D materials	[106−108]
Nanoinsecticides	Nanozeolites and zeolites	[109,110]
Insecticides or acaricides	Nanoencapsulated or adsorbed insecticides on zeolite, nanozeolite or 2D, 1D, or 0D materials	[111,112]
Nanofungicides	Ag, Cu, Zn, Se, C quantum dots	[101,113]
Fungicides	Nanoencapsulated or adsorbed fungicides on zeolite, nanozeolite or 2D, 1D, or 0D materials	[114,115]

(*Continued*)

Table 5.3 (Continued)

Agrochemical class	Example	References
Nanobactericides	Ag, Cu, Zn, Se, C quantum dots	[47,116,117]
Bactericides	Bactericides nanoencapsulated or adsorbed on zeolite, nanozeolite or 2D, 1D, or 0D materials	[118,119]
Viral elicitors	Capsid proteins or inactivated virions nanoencapsulated or adsorbed on a matrix of zeolite, nanozeolite or 2D, 1D, or 0D materials	[120,121]

In addition to the applications that the authors of this manuscript have not visualized, new applications will likely emerge shortly since the area of research on QNMs is very dynamic [132] especially in topics potentially related with agriculture such as quantum hybrid materials [133−135], nanobionics [136,137], and synthetic biology [138−140]. The following section presents examples of applications of different QNMs as agrochemicals in crop species.

5.4 Use of quantum materials as agrochemicals

Agrochemicals are solid, liquid, or gaseous materials, either of natural or synthetic origin that are applied exogenously in crop plants, in irrigation water, in the soil or substrate, or in the volume of atmosphere that surrounds the canopy of the plants.

Agrochemicals are classified in different categories according to their use. Table 5.3 shows the types of agrochemicals commonly used and examples of the different nanometric materials located in each group.

In the following sections, some examples of the use of QNMs as agrochemicals will be presented. In a part of the examples a comparison of the efficiency of the material in its bulk form and in its nano form is available.

5.4.1 All-dimensional materials as fertilizers, biostimulants, growth regulators, and pesticides

Some NMs reported in the literature that fall within the category of 0D materials are shown in Table 5.4. Among the various applications presented in these NMs, the use as a biostimulant in plants stands out, with 86% of the references included. However, it is also observed that the use of 0D materials such as fertilizers [141], growth regulators [143], possible soil improvers [144], as well as antimicrobials. In the latter case, the evaluation of iron oxide NPs against phytopathogenic fungi was performed in vitro, presenting excellent results since the growth of the pathogens was inhibited [152]. This class of materials could be used as potential fungicides for direct application to plants.

Table 5.4 Examples of zero-dimensional quantum nanomaterials used as agrochemicals.

Materials	*d* (nm)	Application route/plant species	Observed impact or function	Results	References
Nano-N Nano-P Nano-K	5.78−9.33 4.98−7.66 5.6−9.45	Soil and leaf application/ *Solanum tuberosum*	Fertilizer	Improved tuber and starch yield, NPK nutrient use efficiency, higher harvest index, and lower nitrate content	[141]
SiO_2	5−15	Foliar/*Saccharum officinarum*	Biostimulant	Reduced the adverse effects of chilling by maintaining the maximum photochemical efficiency of PSII, maximum photo-oxidizable PSI (Pm), and photosynthetic gas exchange. Also increased the content of light-harvesting pigments	[142]
ZnS	13.3	Seed priming/*Vigna radiate*	Biostimulant	Increased seed germination, root−shoot length, pigment content, and decreased lipid peroxidation. Increased antioxidant activity	[143]
SiO_2	5−15	Nutritive solution/*Zea mays*	Biostimulant	Ameliorated Al toxicity at growth, physiological, and oxidative damage levels. Stimulated the antioxidant defense systems, increased organic acids accumulation, and metal detoxification	[144]

(*Continued*)

Table 5.4 (Continued)

Materials	*d* (nm)	Application route/plant species	Observed impact or function	Results	References
$Ag@CoFe_2O_4$	10	Seed priming/*Triticum aestivum*	Estimulante	Seed germination was not affected. Root and shoot lengths of seedlings diminished. Increased photosynthetic pigments and the antioxidant enzymes	[145]
Fe-amino acid nano complexes	5−20	Foliar/*Ocimum basilicum*	Estimulante	Increased essential oil yield and antioxidant activity	[146]
Fe_3O_4	10	Irrigation/*Phaseolus vulgaris*	Estimulante and soil amendment	Increase in the contents of total P, extractable P, total K, extractable K, Ca, total Mn, total Fe, and cation exchange capacity and of a decrease in Cl content in soil. Beneficial effect for plant development and health	[147]
CeO_2	6.9	Foliar/*P. vulgaris*	Biostimulant	Increased dry weight and MDA	[148]
CuO	14.3	Nutritive solution/*Oryza sativa*	Biostimulant	Reduced the accumulation of total As	[149]
SiO_2	10−20	Nutritive solution/ *Fragaria* × *ananassa*	Biostimulant	Maintain epicuticular wax structure, chlorophyll content, and carotenoid content and accumulated less proline relative to plants treated only with salt	[150]

SiO_2	7−14	Soil application/*Hordeum vulgare*	Biostimulant	SiO_2 NPs have a protective role in barley plants under nano-NiO stress, and protection against oxidative stress	[151]
Fe_2O_3 and Fe_3O_4	10−30	In vitro/*Trichothecium roseum*, *Cladosporium herbarum*, *Penicillium chrysogenum*, *Alternaria alternata*, *Aspergillus niger*	Antimicrobial agent	Show inhibitory effect on the growth of fungal pathogens	[152]
Ag	8	Root culture/*Brassica rapa*	Biostimulant	Increased glucosinolates and total phenolic and flavonoid concentrations and their transcripts. Promotion of bioactive compounds	[153]
Fe_3O_4	6.7	Seed priming and nutritive solution/*Cucumis sativus*	Fertilizer	Significant increase in biomass, antioxidant enzymes SOD, and POD	[154]
Ag	9.4	Nutritive solution/*Dianthus caryophyllus*	Biostimulant	Enhanced the ornamental quality and extending the vase life of cut "Master" carnation flowers	[155]
Nanoceria	4.6	Foliar/*Arabidopsis thaliana*	Biostimulant	Reduce leaf ROS levels by 52%, including hydrogen peroxide, superoxide anion, and hydroxyl radicals	[130]
Fe_2O_3	<10	Seed priming and nutritive solution/*Solanum lycopersicum*	Biostimulant	Enhanced seed germination, the root, and shoot lengths. Enhanced growth parameters	[156]
Ag	2	Seed priming/*Raphanus sativus*	Biostimulant	Affect the growth, nutrient content, and macromolecule conformation	[157]
TiO_2	12−15	Foliar/*V. radiata*	Biostimulant	Improvement in shoot length, root length, root area, root nodule, chlorophyll content, and total soluble leaf protein	[158]

(*Continued*)

Table 5.4 (Continued)

Materials	*d* (nm)	Application route/plant species	Observed impact or function	Results	References
SiO_2	12	Seed priming/*Lycopersicum esculentum*	Biostimulant	Improved percent seed germination, mean germination time, seed germination index, seed vigor index, seedling fresh weight, and dry weight	[159]
ZnO	10	Soil addition/*Pisum sativum*	Biostimulant	Increased root Elongation. CAT was significantly reduced in leaves, while APOX was reduced in both roots and leaves	[160]
ZnO	3.8	Foliar/*Cyamopsis tetragonoloba*	Biostimulant	Improvement in plant biomass shoot and root length, root area, chlorophyll content, total soluble leaf protein, rhizospheric microbial population, acid phosphatase, alkaline phosphatase, and phytase activity in the rhizosphere. Gum content in clusterbean seeds was improved	[161]

APOX, Ascorbate Peroxidase; *CAT*, Catalase; *MDA*, Malondialdehyde; *NP*, Nanoparticle; *NPK*, Nitrogen, Phosphorus, ans Potassium; *POD*, peroxidase; *ROS*, reactive oxygen species; *SOD*, superoxide dismutase.

Among the 0D NMs classifiable as QNMs, the most used ones are mainly those of Fe, Si, Zn, Ag, and Ce, in addition to others that are used to a lesser extent such as N, P, K, S, and Ti (Table 5.4). Although it is known that NMs based on many chemical elements exist and that they have been studied in crops and with different uses, most do not present the criterion of QM used in this manuscript, that is, a smaller diameter at 15 nm.

5.4.2 One-dimensional materials such as fertilizers, biostimulants, growth regulators, and pesticides

Among the QNMs classified as 1D materials, carbon nanotubes, whether single or multiple walls, are remarkable (Table 5.5). Among the applications that have been studied, its use as a biostimulant stands out, although its usefulness as a carrier of nutrients such as Zn has also been reported [162]. Among the types of nanotubes used, most are multiple-walled (96% of those reported in Table 5.5), although reports with single-walled nanotubes are also found. The use of nanotubes functionalized with COOH has also been reported [171,172], or with NH_2 [178].

As a result of the high surface-to-volume ratio and the high reactivity on cells, carbon nanotubes can be used directly as biostimulants or as ion carriers of fertilizer elements or biomolecules, whether these are pesticides or growth regulators or stress tolerance inducers. In all cases, the objective would be to improve the efficiency in the use of the inputs that are combined with the NMs: nutrients, pesticides, or biostimulants. Its use as a biostimulant is the most studied, reporting a variety of positive effects on plants such as increased yield or biomass production, antioxidant production, tolerance to various types of stress, and enhanced germination. Adverse effects associated with its use have also been reported, generally linked to the synthesis of ROS and oxidative stress, or in some cases, due to the modification of the balance of nutrients in the plant (Table 5.5).

5.4.3 Two-dimensional materials as fertilizers, biostimulants, growth regulators, and pesticides

Among the QNMs classified as 2D materials, graphene stands out. Graphene is a carbon-based material in the form of simple atomic monolayer or multilayer structures. The structure of graphene has a large surface to volume, so the active area of the material is extensive. Furthermore, the presence of delocalized electrons makes graphene capable of conducting electric charge or functioning as a semiconductor. The confinement of electrons in graphene enables photoluminescence and induction of nanomagnetism. These last properties are dependent on the functionalization or doping of graphene [184].

Among the reported applications of graphene in agriculture, it is used as a biostimulant of plants; standing 96% of the references in Table 5.6. Although its use as an antimicrobial has also been reported [192,201], it can be used as a carrier for ions of fertilizers, metabolites, and high molecular weight biomolecules, which could be applied as fertilizers, pesticides, or regulators of growth and stress

Table 5.5 Examples of one-dimensional quantum nanomaterials used as agrochemicals.

Materials	*d* (nm)	Application route/plant species	Observed impact or function	Results	References
MWCNTs–Zn composite	8.54	Seed priming/onion	Carrier of Zn	Increased germination and cell division rate	[162]
MWCNTs	5–15	Seed priming/*Dodonaea viscosa* L.	Biostimulant	Increased germination and biomass	[163]
MWCNTs	6–9	Nutritive solution/*Brassica oleracea* L. var. *italica*	Biostimulant	Growth increase in NaCl stress condition	[164]
MWCNTs	20–70 External 5–10 Internal	Seed priming/*Glycine max*, *Phaseolus vulgaris*, and *Zea mays*	Biostimulant/toxic agent	Increased germination, inhibition of root growth	[165]
MWCNTs	10–20	Seed priming/*Triticum aestivum*, *Z. mays*, *Arachis hypogaea*, and *Allium sativum*	Biostimulant	Increased growth and biomass	[166]
MWCNTs	12.8 External 5.5 Internal	Seeds and seedlings/*Medicago sativa* and *T. aestivum*	Biostimulant/toxic agent	Increased root growth	[167]
MWCNTs	14–30	Seed priming/*Oryza sativa*	Biostimulant	Better yield and productivity of rice	[168]
MWCNTs	5–15 External 3–5 Internal	Seed priming in vitro/*Thymus daenensis*	Biostimulant	Increase in biomass and biosynthesis of antioxidants	[169]
MWCNTs	20–30 External 5–10 Internal	Foliar/*Salvia verticillata*	Biostimulant/toxic agent	Decreases photosynthetic pigments, increases antioxidants	[170]
MWCNTs-COOH	8–15 External 3–5 Internal	Nutritive solution/*Vicia faba*	Toxic agent	Nutrient imbalance, oxidative stress, and increased antioxidant enzyme activity occurred	[171]
MWCNTs-COOH	8–15 External 3–5 Internal	Nutritive solution/*V. faba*	Toxic agent	Produces nutrient imbalance, oxidative stress, and leaf damage	[172]
MWCNTs	13–14	Seed priming/*T. aestivum*	Biostimulant	Growth and yield induction	[48]
MWCNTs	5–15 External 3–5 Internal	Seed priming/*Cucurbita pepo*	Biostimulant/toxic agent	Reduction in germination percentage, root and shoot length, accumulation, and vigor index ia dose-dependent manner. Increase oxidative stress	[173]
MWCNTs	–	Nutritive solution/*Solanum lycopersicum*	Biostimulant	Modification in the metabolome of the fruit	[174]
SWCNTs	1–3 External 0.9–2 Internal	Seed priming/*Hyoscyamus niger*	Biostimulant	Induction of tolerance to moderate drought stress. Reduction of oxidative stress and increase of metabolites	[175]
MWCNTs	6–9	Nutritive solution/*B. oleracea*	Biostimulant	Increase in growth, absorption of water, and net assimilation of CO_2 under salinity	[164]

MWCNTs	–	Seed priming/*S. lycopersicum*	Biostimulant	The germination percentage, and seedling length and weight were enhanced	[176]
MWCNTs	5–15	In vitro/leaf segments of *Satureja khuzestanica*	Biostimulant	Calli growth improved. Induction of antioxidant activity	[177]
MWCNTs MWCNT-NH_2s MWCNT-COOHs	20–30	*Z. mays* and *G. max*	Biostimulant/toxic agent	Stimulated the growth of maize and inhibited the growth of soybean. Increase dry biomass of maize	[178]
MWCNTs	11	Nutritive solution/*Amaranthus tricolor*	Toxic agent	Growth inhibition and cell death. Adverse effects on root and leaf morphology. ROS increased	[179]
MWCNTs	13	Nutritive solution/*Lactuca sativa*, *O. sativa*, *Cucumis sativus*, *A. tricolor*, *Abelmoschus esculentus*, *Capsicum annuum*, *G. max*	Toxic agent	Root and shoot lengths of red spinach, lettuce, and cucumber were significantly reduced. Similar toxic effects occurred regarding cell death and electrolyte leakage	[180]
MWCNTs	13–18	Soil/*Gossypium hirsutum*, *Catharanthus roseus*	Biostimulant	Increased growth, increased fiber biomass, and increased number of flowers and leaves	[181]
Long MWCNTs Short MWCNTs	13–18 <7	Seed priming/*S. lycopersicum*	Biostimulant	Increased germination and growth	[182]
MWCNTs	13–18	In vitro/*Sorghum bicolor* and *Panicum virgatum*	Biostimulant	Increased germination and biomass. Reduction of salinity stress symptoms	[183]

MWCNTs, Multiwalled carbon nanotubes; *ROS*, reactive oxygen species; *SWCNT*, single-walled carbon nanotubes.

Table 5.6 Examples of two-dimensional quantum nanomaterials used as agrochemicals.

Materials	*d* (nm)	Application route/plant species	Observed impact or function	Results	References
Graphene	–	Soil/*Gossypium hirsutum*, *Catharanthus roseus*	Biostimulant	Increased growth, enhanced fiber biomass, improved number of flowers and leaves	[181]
Graphene	–	Seed priming/*Solanum lycopersicum*	Biostimulant	Increased germination and growth	[182]
Graphene	–	In vitro/*Sorghum bicolor* and *Panicum virgatum*	Biostimulant	Increase of germination and biomass. Reduction of salinity damage	[183]
Graphene oxide	0.8−1	Seed priming/*Oryza sativa*	Biostimulant	Increased germination and root growth	[185]
Graphene oxide	0.44−0.78	Nutritive solution/*O. sativa*	Toxic agent	Reduction of biomass and growth, increase of antioxidant enzymes	[186]
Graphene oxide	0.55−1.1	Nutritive solution/*Triticum aestivum*	Toxic agent	Decreased root growth, NO_3 absorption, and NRTs gene expression	[187]
Ag-graphene oxide	57.5	Seed priming/*Medicago sativa*, *Raphanus sativus*, and *Cucumis sativus*	Biostimulant	Increase shoot growth in radish but decrease it in the cucumber. It increases root growth in radish but decreases it in the alfalfa. Induces H_2O_2 production	[188]
Graphene oxide	<1	Soil/*Larix olgensis*	Biostimulant	Biomass increase, induces oxidative stress	[189]
Graphene quantum dots	1.8−3.6	Seed priming and nutritive solution/*Vigna radiata*, *S. lycopersicum*	Biostimulant	Chlorophyll, H_2O_2, MDA, glutathione, proline, and antioxidant enzymes (CAT and GR) increase. Graphene in high concentrations decreases growth	[190]
Graphene oxide	3−6	Seed priming/*T. aestivum*	Biostimulant	Germination and root growth decrease depending on the concentration. Oxidative stress occurs	[191]
Graphene oxide	–	Foliar/*Daucus carota*	Biostimulant and antimicrobial agent	Increased growth, photosynthetic pigments, and proline. A decrease in the incidence of diseases was observed	[192]
Graphene oxide	–	Nutritive solution/*Pisum sativum*	Toxic agent	Photosystem II inhibition. Increased oxidative stress	[193]

Graphene oxide	3.4−7	In vitro/*Plantago major*	Biostimulant	Increased growth of calli cells. However, high concentrations induce oxidative stress	[194]
Graphene	0.5−3	Nutritive solution/*T. aestivum*	Biostimulant	Improves root elongation but induces oxidative stress. Decreases growth, photosynthesis and causes nutrient imbalance	[195]
Sulfonated graphene	–	Nutritive solution/*Zea mays*	Biostimulant	Hormetic effect on plant height and ROS levels	[196]
Graphene oxide	–	Nutritive solution/*Brassica napus*	Biostimulant	Fresh root weight decreased. Higher ABA content, but a lower IAA content	[197]
Graphene oxide	1	In vitro/*Arabidopsis thaliana*	Biostimulant	No effect on growth. Increase in MDA, formation of oxidative stress, and altered activities of antioxidant enzymes	[198]
Graphene quantum dots	5	Seed priming/*Coriandrum sativum* and *Allium sativum*	Biostimulant	Enhance the growth rate	[67]
Graphene	0.5−0.9	Seed priming/*S. lycopersicum*	Biostimulant	Lower biomass accumulation, but exhibited longer stems and roots	[199]
Graphene oxide	–	Seed priming/*Vicia faba*	Biostimulant	Decreases growth parameters and activity of antioxidant enzymes, increase oxidative stress	[200]
Graphene oxide	0.794	In vitro/*Pseudomonas syringae*, *Xanthomonas campestris* pv. *undulosa*, *Fusarium graminearum*, and *Fusarium oxysporum*	Antimicrobial agent	Graphene oxide interacts with the pathogens by mechanically wrapping and locally damaging the cell membrane and finally causing cell lysis	[201]
Graphene oxide	–	Seed priming/*V. faba*	Biostimulant	Significant improvements in *V. faba* health status	[202]
Graphene oxide	1	Seed priming/*Brassica oleracea* var. *capitata*, *S. lycopersicum*, *Lactuca sativa*, *Amaranthus tricolor*, and *Amaranthus lividus*	Toxic agent	Significantly inhibited plant growth and biomass. Increase in ROS and cell death as well as visible symptoms of necrotic lesions	[203]

ABA, Abscisic acid; *CAT*, Catalase; *GR*, Glutathione reductase; *IAA*, Indole-3-acetic acid; *MDA*, Malondialdehyde; *NRTs*, Nitrate transporter genes; *ROS*, reactive oxygen species.

tolerance. As a biostimulant, used in the correct form and concentration, multiple benefits have been reported, such as increased yield or biomass, increased germination, or antioxidant production. On the contrary, adverse effects such as the induction of oxidative stress and damage to photosystems have also been reported, which has an impact on biomass production, growth decrease, among others (Table 5.6).

5.5 Conclusions

The physicochemical properties of NMs are critical determinants in the response of organisms to the exposure of these substances. Two of these properties: a high surface-to-volume ratio and chemical composition are shared by all NMs regardless of their dimensions. The third and fourth properties, quantum confinement and superparamagnetism, only manifest in QNMs. The current development of agrochemical applications of NMs and QNMs is highly oriented toward the use of the first two properties. Both quantum confinement and superparamagnetism, about which little is known about the impact on plant cells, are, however, a potential source of new possibilities for basic and applied research, and for the development of new agrochemicals, whose purpose would be to increase the efficiency of the metabolic processes of crops and their resilience in the face of climate change.

References

[1] X. He, H. Deng, H. Hwang, The current application of nanotechnology in food and agriculture, J. Food Drug. Anal. 27 (2019) 1−21. Available from: https://doi.org/10.1016/j.jfda.2018.12.002.

[2] P. Wang, F.-J. Zhao, P.M. Kopittke, Engineering crops without genome integration using nanotechnology, Trends Plant Sci. 24 (2019) 574−577. Available from: https://doi.org/10.1016/j.tplants.2019.05.004.

[3] R. Chandrasekaran, P. Rajiv, K.A. Abd-Elsalam, Carbon nanotubes: plant gene delivery and genome editing, in: K.A. Abd-Elsalam (Ed.), Carbon Nanomaterials for Agri-Food and Environmental Applications, Micro and Nano Technologies, Elsevier, 2020, pp. 279−296. Available from: https://doi.org/10.1016/B978-0-12-819786-8.00014-1.

[4] Y. Li, W. Li, H. Zhang, Y. Liu, L. Ma, B. Lei, Amplified light harvesting for enhancing Italian lettuce photosynthesis using water soluble silicon quantum dots as artificial antennas, Nanoscale 12 (2020) 155−166. Available from: https://doi.org/10.1039/C9NR08187A.

[5] R. Dong, Y. Li, W. Li, H. Zhang, Y. Liu, L. Ma, et al., Recent developments in luminescent nanoparticles for plant imaging and photosynthesis, J. Rare Earths 37 (2019) 903−915. Available from: https://doi.org/10.1016/j.jre.2019.04.001.

[6] A. Juárez-Maldonado, H. Ortega-Ortíz, A.B. Morales-Díaz, S. González-Morales, Á. Morelos-Moreno, M. Cabrera-De la Fuente, et al., Nanoparticles and nanomaterials as plant biostimulants, Int. J. Mol. Sci. 20 (2019) 162. Available from: https://doi.org/10.3390/ijms20010162.

[7] M. Miernicki, T. Hofmann, I. Eisenberger, F. von der Kammer, A. Praetorius, Legal and practical challenges in classifying nanomaterials according to regulatory definitions, Nat. Nanotechnol. 14 (2019) 208−216. Available from: https://doi.org/10.1038/s41565-019-0396-z.

[8] W. Wohlleben, J. Mielke, A. Bianchin, A. Ghanem, H. Freiberger, H. Rauscher, et al., Reliable nanomaterial classification of powders using the volume-specific surface area method, J. Nanopart. Res. 19 (2017). Available from: https://doi.org/10.1007/s11051-017-3741-x.

[9] A.B. Morales-Díaz, H. Ortega-Ortíz, A. Juárez-Maldonado, G. Cadenas-Pliego, S. González-Morales, A. Benavides-Mendoza, Application of nanoelements in plant nutrition and its impact in ecosystems, Adv. Nat. Sci.: Nanosci. Nanotechnol. 8 (2017) 013001. Available from: https://doi.org/10.1088/2043-6254/8/1/013001.

[10] T.A. Swift, T.A.A. Oliver, M.C. Galan, H.M. Whitney, Functional nanomaterials to augment photosynthesis: evidence and considerations for their responsible use in agricultural applications, Interface Focus. 9 (2019) 20180048. Available from: https://doi.org/10.1098/rsfs.2018.0048.

[11] A. Juárez-Maldonado, S. González-Morales, M. Cabrera-De la Fuente, J. Medrano-Macías, A. Benavides-Mendoza, Nanometals as promoters of nutraceutical quality in crop plants, in: A.M. Grumezescu, A.M. Holban (Eds.), Impact of Nanoscience in the Food Industry, Handbook of Food Bioengineering, Academic Press, 2018, pp. 277−310. Available from: https://doi.org/10.1016/B978-0-12-811441-4.00010-8.

[12] V.V. Pokropivny, V.V. Skorokhod, Classification of nanostructures by dimensionality and concept of surface forms engineering in nanomaterial science, Mater. Sci. Eng., C 27 (2007) 990−993EMRS 2006 Symposium A: Current Trends in Nanoscience − from Materials to Applications. Available from: https://doi.org/10.1016/j.msec.2006.09.023.

[13] IUPAC, IUPAC − Bohr radius (B00693) [WWW document]. <https://doi.org/10.1351/goldbook.B00693>, 2020.

[14] B. Guzelturk, P.L.H. Martinez, Q. Zhang, Q. Xiong, H. Sun, X.W. Sun, et al., Excitonics of semiconductor quantum dots and wires for lighting and displays, Laser Photonics Rev. 8 (2014) 73−93. Available from: https://doi.org/10.1002/lpor.201300024.

[15] P. Ball, Quantum materials: where many paths meet, MRS Bull. 42 (2017) 698−705. Available from: https://doi.org/10.1557/mrs.2017.220.

[16] E. Koohsaryan, M. Anbia, Nanosized and hierarchical zeolites: a short review, Chin. J. Catal. 37 (2016) 447−467. Available from: https://doi.org/10.1016/S1872-2067(15)61038-5.

[17] U.S. DOE, Basic Research Needs Workshop on Quantum materials for Energy Relevant Technology, U.S. Department of Energy, Washington, DC, 2016.

[18] E. Agathokleous, Z. Feng, I. Iavicoli, E.J. Calabrese, The two faces of nanomaterials: a quantification of hormesis in algae and plants, Environ. Int. 131 (2019) 105044. Available from: https://doi.org/10.1016/j.envint.2019.105044.

[19] N. Mitter, K. Hussey, Moving policy and regulation forward for nanotechnology applications in agriculture, Nat. Nanotechnol. 14 (2019) 508−510. Available from: https://doi.org/10.1038/s41565-019-0464-4.

[20] I.O. Adisa, V.L.R. Pullagurala, J.R. Peralta-Videa, C.O. Dimkpa, W.H. Elmer, J.L. Gardea-Torresdey, et al., Recent advances in nano-enabled fertilizers and pesticides: a critical review of mechanisms of action, Environ. Sci.: Nano 6 (2019) 2002−2030. Available from: https://doi.org/10.1039/C9EN00265K.

[21] M. Bizzarri, N. Monti, M. Minini, A. Pensotti, Field-dependent effects in biological systems, Organisms. J. Biol. Sci. 3 (2019) 35−42. Available from: https://doi.org/10.13133/10.13133/2532-5876_5.8.

[22] I.G. Karafyllidis, Quantum transport in the FMO photosynthetic light-harvesting complex, J. Biol. Phys. 43 (2017) 239–245. Available from: https://doi.org/10.1007/s10867-017-9449-4.
[23] J.P. Giraldo, M.P. Landry, S.M. Faltermeier, T.P. McNicholas, N.M. Iverson, A.A. Boghossian, et al., Plant nanobionics approach to augment photosynthesis and biochemical sensing, Nat. Mater. 13 (2014) 400–408. Available from: https://doi.org/10.1038/nmat3890.
[24] W. Junge, Oxygenic photosynthesis: history, status and perspective, Q. Rev. Biophys. 52 (2019). Available from: https://doi.org/10.1017/S0033583518000112.
[25] Z.-X. Liang, J.P. Klinman, Structural bases of hydrogen tunneling in enzymes: progress and puzzles, Curr. Opin. Struct. Biol. 14 (2004) 648–655. Available from: https://doi.org/10.1016/j.sbi.2004.10.008.
[26] V. Stojković, A. Kohen, Enzymatic H transfers: quantum tunneling and coupled motion from kinetic isotope effect studies, Isr. J. Chem. 49 (2009) 163–173. Available from: https://doi.org/10.1560/IJC.49.2.163.
[27] A. de la Lande, N.S. Babcock, J. Řezáč, B. Lévy, B.C. Sanders, D.R. Salahub, Quantum effects in biological electron transfer, Phys. Chem. Chem. Phys. 14 (2012) 5902–5918. Available from: https://doi.org/10.1039/C2CP21823B.
[28] J.P. Bothma, J.B. Gilmore, R.H. McKenzie, The role of quantum effects in proton transfer reactions in enzymes: quantum tunneling in a noisy environment? New J. Phys. 12 (2010) 055002. Available from: https://doi.org/10.1088/1367-2630/12/5/055002.
[29] M. Sarovar, A. Ishizaki, G.R. Fleming, K.B. Whaley, Quantum entanglement in photosynthetic light-harvesting complexes, Nat. Phys. 6 (2010) 462–467. Available from: https://doi.org/10.1038/nphys1652.
[30] M.M. Scanlan, N.F. Putman, A.M. Pollock, D.L.G. Noakes, Magnetic map in nonanadromous Atlantic salmon, PNAS 115 (2018) 10995–10999. Available from: https://doi.org/10.1073/pnas.1807705115.
[31] X. Zhang, K. Yarema, A. Xu, Molecular mechanisms for electromagnetic field biosensing, in: X. Zhang, K. Yarema, A. Xu (Eds.), Biological Effects of Static Magnetic Fields, Springer, Singapore, 2017, pp. 51–79. Available from: https://doi.org/10.1007/978-981-10-3579-1_3.
[32] J.A. Teixeira da Silva, J. Dobránszki, Magnetic fields: how is plant growth and development impacted? Protoplasma 253 (2016) 231–248. Available from: https://doi.org/10.1007/s00709-015-0820-7.
[33] D. Bahadur, J. Giri, Biomaterials and magnetism, Sadhana 28 (2003) 639–656. Available from: https://doi.org/10.1007/BF02706451.
[34] A.M. Hamdan, S. Bijaksana, A. Tjoa, D. Dahrin, K.H. Kirana, Magnetic characterizations of nickel hyperaccumulating plants (*Planchonella oxyhedra* and *Rinorea bengalensis*) from Halmahera, Indonesia, Int. J. Phytorem. 21 (2019) 364–371. Available from: https://doi.org/10.1080/15226514.2018.1524839.
[35] A. Anand, A. Kumari, M. Thakur, A. Koul, Hydrogen peroxide signaling integrates with phytohormones during the germination of magnetoprimed tomato seeds, Sci. Rep. 9 (2019) 1–11. Available from: https://doi.org/10.1038/s41598-019-45102-5.
[36] S. Kataria, L. Baghel, M. Jain, K.N. Guruprasad, Magnetopriming regulates antioxidant defense system in soybean against salt stress, Biocatal. Agric. Biotechnol. 18 (2019) 101090. Available from: https://doi.org/10.1016/j.bcab.2019.101090.
[37] J. Juutilainen, M. Herrala, J. Luukkonen, J. Naarala, P.J. Hore, Magnetocarcinogenesis: is there a mechanism for carcinogenic effects of weak magnetic fields? Proc. R. Soc. B: Biol. Sci. 285 (2018) 20180590. Available from: https://doi.org/10.1098/rspb.2018.0590.

[38] L. Gutiérrez, M. Vujić Spasić, M.U. Muckenthaler, F.J. Lázaro, Quantitative magnetic analysis reveals ferritin-like iron as the most predominant iron-containing species in the murine Hfe-haemochromatosis, Biochim. Biophys. Acta 1822 (2012) 1147−1153. Available from: https://doi.org/10.1016/j.bbadis.2012.03.008.

[39] V.E. Orel, M. Tselepi, T. Mitrelias, A. Rykhalskyi, A. Romanov, V.B. Orel, et al., Nanomagnetic modulation of tumor redox state, Nanomed. Nanotechnol. Biol. Med. 14 (2018) 1249−1256. Available from: https://doi.org/10.1016/j.nano.2018.03.002.

[40] P. Tartaj, M.P. Morales, T. Gonzalez-Carreño, S. Veintemillas-Verdaguer, O. Bomati-Miguel, A.G. Roca, et al., Biomedical applications of magnetic nanoparticles, Reference Module in Materials Science and Materials Engineering, Elsevier, 2016. Available from: https://doi.org/10.1016/B978-0-12-803581-8.02251-7.

[41] A. Fernández-Pacheco, R. Streubel, O. Fruchart, R. Hertel, P. Fischer, R.P. Cowburn, Three-dimensional nanomagnetism, Nat. Commun. 8 (2017) 1−14. Available from: https://doi.org/10.1038/ncomms15756.

[42] M. Levy, C. Wilhelm, N. Luciani, V. Deveaux, F. Gendron, A. Luciani, et al., Nanomagnetism reveals the intracellular clustering of iron oxide nanoparticles in the organism, Nanoscale 3 (2011) 4402−4410. Available from: https://doi.org/10.1039/C1NR10778J.

[43] Y. Jiang, J. Du, H. Tang, X. Zhang, W. Li, L. Wang, et al., Synthesis and application of nanomagnetic immobilized phospholipase C [WWW document]J. Chem. 2019 (2019). Available from: https://doi.org/10.1155/2019/5951793.

[44] K.J. Khorshidi, H. Lenjannezhadian, M. Jamalan, M. Zeinali, Preparation and characterization of nanomagnetic cross-linked cellulase aggregates for cellulose bioconversion, J. Chem. Technol. Biotechnol. 91 (2016) 539−546. Available from: https://doi.org/10.1002/jctb.4615.

[45] Y. Cheng, Y. Chang, Y. Feng, H. Jian, X. Wu, R. Zheng, et al., Bismuth sulfide nanorods with retractable zinc protoporphyrin molecules for suppressing innate antioxidant defense system and strengthening phototherapeutic effects, Adv. Mater. 31 (2019) 1806808. Available from: https://doi.org/10.1002/adma.201806808.

[46] X. Shi, W. Wei, Z. Fu, W. Gao, C. Zhang, Q. Zhao, et al., Review on carbon dots in food safety applications, Talanta 194 (2019) 809−821. Available from: https://doi.org/10.1016/j.talanta.2018.11.005.

[47] M.J. Meziani, X. Dong, L. Zhu, L.P. Jones, G.E. LeCroy, F. Yang, et al., Visible-Light-activated bactericidal functions of carbon "quantum" dots, ACS Appl. Mater. Interfaces 8 (2016) 10761−10766. Available from: https://doi.org/10.1021/acsami.6b01765.

[48] A. Joshi, S. Kaur, K. Dharamvir, H. Nayyar, G. Verma, Multi-walled carbon nanotubes applied through seed-priming influence early germination, root hair, growth and yield of bread wheat (*Triticum aestivum* L.), J. Sci. Food Agric. 98 (2018) 3148−3160. Available from: https://doi.org/10.1002/jsfa.8818.

[49] D.K. Tiwari, N. Dasgupta-Schubert, L.M. Villaseñor Cendejas, J. Villegas, L. Carreto Montoya, S.E. Borjas García, Interfacing carbon nanotubes (CNT) with plants: enhancement of growth, water and ionic nutrient uptake in maize (*Zea mays*) and implications for nanoagriculture, Appl. Nanosci. 4 (2014) 577−591. Available from: https://doi.org/10.1007/s13204-013-0236-7.

[50] M.H. Lahiani, Z.A. Nima, H. Villagarcia, A.S. Biris, M.V. Khodakovskaya, Assessment of effects of the long-term exposure of agricultural crops to carbon nanotubes, J. Agric. Food Chem. 66 (2018) 6654−6662. Available from: https://doi.org/10.1021/acs.jafc.7b01863.

[51] S. Tripathi, S.K. Sonkar, S. Sarkar, Growth stimulation of gram (*Cicer arietinum*) plant by water soluble carbon nanotubes, Nanoscale 3 (2011) 1176−1181. Available from: https://doi.org/10.1039/C0NR00722F.

[52] R. Knoblauch, B. Bui, A. Raza, C.D. Geddes, Heavy carbon nanodots: a new phosphorescent carbon nanostructure, Phys. Chem. Chem. Phys. 20 (2018) 15518−15527. Available from: https://doi.org/10.1039/C8CP02675K.

[53] Y. Lin, L. Zhang, W. Yao, H. Qian, D. Ding, W. Wu, et al., Water-soluble chitosan-quantum dot hybrid nanospheres toward bioimaging and biolabeling, ACS Appl. Mater. Interfaces 3 (2011) 995−1002. Available from: https://doi.org/10.1021/am100982p.

[54] H. Zhang, C. Yang, W. Zhou, Q. Luan, W. Li, Q. Deng, et al., A pH-responsive gel macrosphere based on sodium alginate and cellulose nanofiber for potential intestinal delivery of probiotics, ACS Sustain. Chem. Eng. 6 (2018) 13924−13931. Available from: https://doi.org/10.1021/acssuschemeng.8b02237.

[55] Ł. Janus, M. Piątkowski, J. Radwan-Pragłowska, D. Bogdał, D. Matysek, Chitosan-based carbon quantum dots for biomedical applications: synthesis and characterization, Nanomaterials 9 (2019) 274. Available from: https://doi.org/10.3390/nano9020274.

[56] T. Li, B. Gao, Z. Tong, Y. Yang, Y. Li, Chitosan and graphene oxide nanocomposites as coatings for controlled-release fertilizer, Water Air Soil Pollut. 230 (2019) 146. Available from: https://doi.org/10.1007/s11270-019-4173-2.

[57] C. Gervas, Nickel and Cobalt Sulfide Nanomaterials for Magnetic and Energy Applications (Thesis), University of Zululand, 2018.

[58] W. He, W. Wu, Q. Li, K. Chen, X. Lu, Facile fabrication of Ga_2O_3 nanorods for photoelectrochemical water splitting, ChemNanoMat 6 (2020) 208−211. Available from: https://doi.org/10.1002/cnma.201900583.

[59] J.R. Dave, A.M. Dewle, S.T. Mhaske, P.T. Phulpagar, V.L. Mathe, S.E. More, et al., Hydroxyapatite nanorods loaded with parathyroid hormone (PTH) synergistically enhance the net formative effect of PTH anabolic therapy, Nanomed. Nanotechnol. Biol. Med. 15 (2019) 218−230. Available from: https://doi.org/10.1016/j.nano.2018.10.003.

[60] J.L. Sundararaj, Synthesis and Characterization of Iodine Laden Graphene Nano Platelets via Reduction of Graphene Oxide Using Hydrogen Iodide (Thesis), The Graduate School, Stony Brook University: Stony Brook, NY, 2012.

[61] R.W. Saunders, J.M.C. Plane, Formation pathways and composition of iodine oxide ultra-fine particles, Environ. Chem. 2 (2006) 299−303. Available from: https://doi.org/10.1071/EN05079.

[62] N.A. Younes, M.F.A. Dawood, A.A. Wardany, Biosafety assessment of graphene nanosheets on leaf ultrastructure, physiological and yield traits of *Capsicum annuum* L. and *Solanum melongena* L, Chemosphere 228 (2019) 318−327. Available from: https://doi.org/10.1016/j.chemosphere.2019.04.097.

[63] S. Kabiri, F. Degryse, D.N.H. Tran, R.C. da Silva, M.J. McLaughlin, D. Losic, Graphene oxide: a new carrier for slow release of plant micronutrients, ACS Appl. Mater. Interfaces 9 (2017) 43325−43335. Available from: https://doi.org/10.1021/acsami.7b07890.

[64] S. Shen, Y. Liu, F. Wang, G. Yao, L. Xie, B. Xu, Graphene oxide regulates root development and influences IAA concentration in rice, J. Plant Growth Regul. 38 (2019) 241−248. Available from: https://doi.org/10.1007/s00344-018-9836-5.

[65] I.B. Andelkovic, S. Kabiri, E. Tavakkoli, J.K. Kirby, M.J. McLaughlin, D. Losic, Graphene oxide-Fe(III) composite containing phosphate − a novel slow release fertilizer for improved agriculture management, J. Cleaner Prod. 185 (2018) 97−104. Available from: https://doi.org/10.1016/j.jclepro.2018.03.050.

[66] S. Gupta, T. Smith, A. Banaszak, J. Boeckl, Graphene quantum dots electrochemistry and sensitive electrocatalytic glucose sensor development, Nanomaterials 7 (2017) 301. Available from: https://doi.org/10.3390/nano7100301.

[67] D. Chakravarty, M.B. Erande, D.J. Late, Graphene quantum dots as enhanced plant growth regulators: effects on coriander and garlic plants, J. Sci. Food Agric. 95 (2015) 2772–2778. Available from: https://doi.org/10.1002/jsfa.7106.

[68] Y. Li, X. Wang, M. Liu, H. Luo, L. Deng, L. Huang, et al., Molybdenum disulfide quantum dots prepared by bipolar-electrode electrochemical scissoring, Nanomaterials 9 (2019) 906. Available from: https://doi.org/10.3390/nano9060906.

[69] X. Tian, Y. Sun, S. Fan, M.D. Boudreau, C. Chen, C. Ge, et al., Photogenerated charge carriers in molybdenum disulfide quantum dots with enhanced antibacterial activity, ACS Appl. Mater. Interfaces 11 (2019) 4858–4866. Available from: https://doi.org/10.1021/acsami.8b19958.

[70] P. Yang, S. Ke, L. Tu, Y. Wang, S. Ye, S. Kou, et al., Regulation of autophagy orchestrates pyroptotic cell death in molybdenum disulfide quantum dot-induced microglial toxicity, ACS Biomater. Sci. Eng. 6 (2020) 1764–1775. Available from: https://doi.org/10.1021/acsbiomaterials.9b01932.

[71] R. Sridhar, R. Lakshminarayanan, K. Madhaiyan, V.A. Barathi, K.H.C. Lim, S. Ramakrishna, Electrosprayed nanoparticles and electrospun nanofibers based on natural materials: applications in tissue regeneration, drug delivery and pharmaceuticals, Chem. Soc. Rev. 44 (2015) 790–814. Available from: https://doi.org/10.1039/C4CS00226A.

[72] S. Rakshit, S. Ghosh, S. Chall, S.S. Mati, S.P. Moulik, S.C. Bhattacharya, Controlled synthesis of spin glass nickel oxide nanoparticles and evaluation of their potential antimicrobial activity: a cost effective and eco-friendly approach, RSC Adv. 3 (2013) 19348–19356. Available from: https://doi.org/10.1039/C3RA42628A.

[73] B. Schrick, J.L. Blough, A.D. Jones, T.E. Mallouk, Hydrodechlorination of trichloroethylene to hydrocarbons using bimetallic nickel – iron nanoparticles, Chem. Mater. 14 (2002) 5140–5147. Available from: https://doi.org/10.1021/cm020737i.

[74] C. Wu, D.T. Chiu, Highly fluorescent semiconducting polymer dots for biology and medicine, Angew. Chem. Int. Ed. 52 (2013) 3086–3109. Available from: https://doi.org/10.1002/anie.201205133.

[75] J. Li, D. Cui, J. Huang, S. He, Z. Yang, Y. Zhang, et al., Organic semiconducting pronanostimulants for near-infrared photoactivatable cancer immunotherapy, Angew. Chem. Int. Ed. 58 (2019) 12680–12687. Available from: https://doi.org/10.1002/anie.201906288.

[76] F. Jiang, W. Cai, G. Tan, Facile synthesis and optical properties of small selenium nanocrystals and nanorods, Nanoscale Res. Lett. 12 (2017). Available from: https://doi.org/10.1186/s11671-017-2165-y.

[77] Y. Fang, Y. Jiang, H. Acaron Ledesma, J. Yi, X. Gao, D.E. Weiss, et al., Texturing silicon nanowires for highly localized optical modulation of cellular dynamics, Nano Lett. 18 (2018) 4487–4492. Available from: https://doi.org/10.1021/acs.nanolett.8b01626.

[78] Q. Shen, H. Yang, C. Peng, H. Zhu, J. Mei, S. Huang, et al., Capture and biological release of circulating tumor cells in pancreatic cancer based on peptide-functionalized silicon nanowire substrate, Int. J. Nanomed. 14 (2018) 205–214. Available from: https://doi.org/10.2147/IJN.S187892.

[79] A. Guleria, S. Neogy, D.K. Maurya, S. Adhikari, Blue light-emitting Si quantum dots with mesoporous and amorphous features: origin of photoluminescence and potential applications, J. Phys. Chem. C 121 (2017) 24302–24316. Available from: https://doi.org/10.1021/acs.jpcc.7b07283.

[80] Y. Zhang, D. Hou, X. Yu, Facile preparation of FITC-modified silicon nanodots for ratiometric pH sensing and imaging, Spectrochim. Acta, A: Mol. Biomol. Spectrosc. 234 (2020) 118276. Available from: https://doi.org/10.1016/j.saa.2020.118276.

[81] J. Jang, S. Jeong, J. Seo, M.-C. Kim, E. Sim, Y. Oh, et al., Ultrathin zirconium disulfide nanodiscs, J. Am. Chem. Soc. 133 (2011) 7636−7639. Available from: https://doi.org/10.1021/ja200400n.

[82] J. Estrada-Urbina, A. Cruz-Alonso, M. Santander-González, A. Méndez-Albores, A. Vázquez-Durán, Nanoscale zinc oxide particles for improving the physiological and sanitary quality of a Mexican landrace of red maize, Nanomaterials 8 (2018) 247. Available from: https://doi.org/10.3390/nano8040247.

[83] W. Liu, M. Zhang, B. Bhandari, Nanotechnology − a shelf life extension strategy for fruits and vegetables, Crit. Rev. Food Sci. Nutr. 0 (2019) 1−16. Available from: https://doi.org/10.1080/10408398.2019.1589415.

[84] I. Kim, K. Viswanathan, G. Kasi, S. Thanakkasaranee, K. Sadeghi, J. Seo, ZnO nanostructures in active antibacterial food packaging: preparation methods, antimicrobial mechanisms, safety issues, future prospects, and challenges, Food Rev. Int. 0 (2020) 1−29. Available from: https://doi.org/10.1080/87559129.2020.1737709.

[85] L. Zhao, X. Guan, B. Yu, N. Ding, X. Liu, Q. Ma, et al., Carboxylated graphene oxide-chitosan spheres immobilize Cu^{2+} in soil and reduce its bioaccumulation in wheat plants, Environ. Int. 133 (2019) 105208. Available from: https://doi.org/10.1016/j.envint.2019.105208.

[86] C. Camedda, R.D. Hoelzle, A. Carucci, S. Milia, B. Virdis, A facile method to enhance the performance of soil bioelectrochemical systems using in situ reduced graphene oxide, Electrochim. Acta 324 (2019) 134881. Available from: https://doi.org/10.1016/j.electacta.2019.134881.

[87] Y. Ge, J.H. Priester, M. Mortimer, C.H. Chang, Z. Ji, J.P. Schimel, et al., Long-term effects of multiwalled carbon nanotubes and graphene on microbial communities in dry soil, Environ. Sci. Technol. 50 (2016) 3965−3974. Available from: https://doi.org/10.1021/acs.est.5b05620.

[88] J. Li, L. Xiao, Y. Cheng, Y. Cheng, Y. Wang, X. Wang, et al., Applications of carbon quantum dots to alleviate Cd^{2+} phytotoxicity in *Citrus maxima* seedlings, Chemosphere 236 (2019) 124385. Available from: https://doi.org/10.1016/j.chemosphere.2019.124385.

[89] A. Rastogi, D.K. Tripathi, S. Yadav, D.K. Chauhan, M. Živčák, M. Ghorbanpour, et al., Application of silicon nanoparticles in agriculture, 3 Biotech 9 (2019) 90. Available from: https://doi.org/10.1007/s13205-019-1626-7.

[90] M. Maria Leena, L. Mahalakshmi, J.A. Moses, C. Anandharamakrishnan, Nanoencapsulation of nutraceutical ingredients, in: K. Pal, I. Banerjee, P. Sarkar, D. Kim, W.-P. Deng, N.K. Dubey, K. Majumder (Eds.), Biopolymer-Based Formulations, Elsevier, 2020, pp. 311−352. Available from: https://doi.org/10.1016/B978-0-12-816897-4.00014-X.

[91] S. Ghodke, B. Bhanvase, S. Sonawane, S. Mishra, K. Joshi, Nanoencapsulation and nanocontainer based delivery systems for drugs, flavors, and aromas, in: A.M. Grumezescu (Ed.), Encapsulations, Nanotechnology in the Agri-Food Industry, Academic Press, 2016, pp. 673−715. Available from: https://doi.org/10.1016/B978-0-12-804307-3.00016-8.

[92] H. El-Ramady, T. Alshaal, N. Elhawat, E. El-Nahrawy, A.E.-D. Omara, S. El-Nahrawy, et al., Biological aspects of selenium and silicon nanoparticles in the terrestrial environments, in: A.A. Ansari, S.S. Gill, R. Gill, G. Lanza, L. Newman (Eds.),

Phytoremediation: Management of Environmental Contaminants, vol. 6, Springer International Publishing, Cham, 2018, pp. 235–264. Available from: https://doi.org/10.1007/978-3-319-99651-6_11.

[93] P. Khati, P. Chaudhary, S. Gangola, P. Bhatt, A. Sharma, Nanochitosan supports growth of *Zea mays* and also maintains soil health following growth, 3 Biotech 7 (2017) 81. Available from: https://doi.org/10.1007/s13205-017-0668-y.

[94] G. Asgari-Targhi, A. Iranbakhsh, Z.O. Ardebili, Potential benefits and phytotoxicity of bulk and nano-chitosan on the growth, morphogenesis, physiology, and micropropagation of *Capsicum annuum*, Plant. Physiol. Biochem. 127 (2018) 393–402. Available from: https://doi.org/10.1016/j.plaphy.2018.04.013.

[95] H.M.M. Abdel-Aziz, M.N.A. Hasaneen, A.M. Omer, Nano chitosan-NPK fertilizer enhances the growth and productivity of wheat plants grown in sandy soil, Span. J. Agric. Res. 14 (2016) 0902. Available from: https://doi.org/10.5424/sjar/2016141-8205.

[96] S.Z.N. Ahmad, W.N.W. Salleh, A.F. Ismail, N. Yusof, M.Z.M. Yusop, et al., Adsorptive removal of heavy metal ions using graphene-based nanomaterials: toxicity, roles of functional groups and mechanisms, Chemosphere 248 (2020) 126008. Available from: https://doi.org/10.1016/j.chemosphere.2020.126008.

[97] M. Iqbal, S. Umar, Mahmooduzzafar, Nano-fertilization to enhance nutrient use efficiency and productivity of crop plants, in: A. Husen, M. Iqbal (Eds.), Nanomaterials and Plant Potential, Springer International Publishing, Cham, 2019, pp. 473–505. Available from: https://doi.org/10.1007/978-3-030-05569-1_19.

[98] P. Paramanantham, V.T. Anju, M. Dyavaiah, B. Siddhardha, Applications of carbon-based nanomaterials for antimicrobial photodynamic therapy, in: R. Prasad (Ed.), Microbial Nanobionics: Volume 2, Basic Research and Applications, Nanotechnology in the Life Sciences, Springer International Publishing, Cham, 2019, pp. 237–259. Available from: https://doi.org/10.1007/978-3-030-16534-5_12.

[99] S. Yang, L. Li, Z. Pei, C. Li, X. Shan, B. Wen, et al., Effects of humic acid on copper adsorption onto few-layer reduced graphene oxide and few-layer graphene oxide, Carbon 75 (2014) 227–235. Available from: https://doi.org/10.1016/j.carbon.2014.03.057.

[100] Z. Wang, Y. Gao, S. Wang, H. Fang, D. Xu, F. Zhang, Impacts of low-molecular-weight organic acids on aquatic behavior of graphene nanoplatelets and their induced algal toxicity and antioxidant capacity, Environ. Sci. Pollut. Res. 23 (2016) 10938–10945. Available from: https://doi.org/10.1007/s11356-016-6290-4.

[101] J. Chen, L. Sun, Y. Cheng, Z. Lu, K. Shao, T. Li, et al., Graphene oxide-silver nanocomposite: novel agricultural antifungal agent against *Fusarium graminearum* for crop disease prevention, ACS Appl. Mater. Interfaces 8 (2016) 24057–24070. Available from: https://doi.org/10.1021/acsami.6b05730.

[102] J. Luo, J. Lai, N. Zhang, Y. Liu, R. Liu, X. Liu, Tannic acid induced self-assembly of three-dimensional graphene with good adsorption and antibacterial properties, ACS Sustain. Chem. Eng. 4 (2016) 1404–1413. Available from: https://doi.org/10.1021/acssuschemeng.5b01407.

[103] M.M. Pour, R. Saberi-Riseh, R. Mohammadinejad, A. Hosseini, Nano-encapsulation of plant growth-promoting rhizobacteria and their metabolites using alginate-silica nanoparticles and carbon nanotube improves UCB1 pistachio micropropagation, J. Microbiol. Biotechnol. 29 (2019) 1096–1103. Available from: https://doi.org/10.4014/jmb.1903.03022.

[104] J. Tanum, J. Heo, J. Hong, Spontaneous biomacromolecule absorption and long-term release by graphene oxide, ACS Omega 3 (2018) 5903–5909. Available from: https://doi.org/10.1021/acsomega.8b00537.

[105] Y. González-García, E.R. López-Vargas, G. Cadenas-Pliego, A. Benavides-Mendoza, S. González-Morales, A. Robledo-Olivo, et al., Impact of carbon nanomaterials on the antioxidant system of tomato seedlings, Int. J. Mol. Sci. 20 (2019) 5858. Available from: https://doi.org/10.3390/ijms20235858.

[106] F. Seidi, R. Jenjob, T. Phakkeeree, D. Crespy, Saccharides, oligosaccharides, and polysaccharides nanoparticles for biomedical applications, J. Control. Release 284 (2018) 188–212. Available from: https://doi.org/10.1016/j.jconrel.2018.06.026.

[107] J. Tanum, H. Jeong, J. Heo, M. Choi, K. Park, J. Hong, Assembly of graphene oxide multilayer film for stable and sustained release of nitric oxide gas, Appl. Surf. Sci. 486 (2019) 452–459. Available from: https://doi.org/10.1016/j.apsusc.2019.04.260.

[108] M. Dowaidar, H.N. Abdelhamid, M. Hällbrink, X. Zou, Ü. Langel, Graphene oxide nanosheets in complex with cell penetrating peptides for oligonucleotides delivery, Biochim. Biophys. Acta 1861 (2017) 2334–2341. Available from: https://doi.org/10.1016/j.bbagen.2017.07.002.

[109] N. Eroglu, M. Emekci, C.G. Athanassiou, Applications of natural zeolites on agriculture and food production, J. Sci. Food Agric. 97 (2017) 3487–3499. Available from: https://doi.org/10.1002/jsfa.8312.

[110] S.S. Ibrahim, N.Y. Salem, Insecticidal efficacy of nano zeolite against *Tribolium confusum* (Col., Tenebrionidae) and *Callosobruchus maculatus* (Col., Bruchidae), Bull. Natl Res. Cent. 43 (2019) 92. Available from: https://doi.org/10.1186/s42269-019-0128-4.

[111] S. Song, Y. Wang, J. Xie, B. Sun, N. Zhou, H. Shen, et al., Carboxymethyl chitosan modified carbon nanoparticle for controlled emamectin benzoate delivery: improved solubility, pH-responsive release, and sustainable pest control, ACS Appl. Mater. Interfaces 11 (2019) 34258–34267. Available from: https://doi.org/10.1021/acsami.9b12564.

[112] X. Wang, H. Xie, Z. Wang, K. He, Graphene oxide as a pesticide delivery vector for enhancing acaricidal activity against spider mites, Colloids Surf., B: Biointerfaces 173 (2019) 632–638. Available from: https://doi.org/10.1016/j.colsurfb.2018.10.010.

[113] Q. Sun, J. Li, T. Le, Zinc oxide nanoparticle as a novel class of antifungal agents: current advances and future perspectives, J. Agric. Food Chem. 66 (2018) 11209–11220. Available from: https://doi.org/10.1021/acs.jafc.8b03210.

[114] X. Wang, A. Cai, X. Wen, D. Jing, H. Qi, H. Yuan, Graphene oxide-Fe_3O_4 nanocomposites as high-performance antifungal agents against *Plasmopara viticola*, Sci. China Mater. 60 (2017) 258–268. Available from: https://doi.org/10.1007/s40843-016-9005-9.

[115] C. Li, X. Wang, F. Chen, C. Zhang, X. Zhi, K. Wang, et al., The antifungal activity of graphene oxide–silver nanocomposites, Biomaterials 34 (2013) 3882–3890. Available from: https://doi.org/10.1016/j.biomaterials.2013.02.001.

[116] P.K. Stoimenov, R.L. Klinger, G.L. Marchin, K.J. Klabunde, Metal oxide nanoparticles as bactericidal agents, Langmuir 18 (2002) 6679–6686. Available from: https://doi.org/10.1021/la0202374.

[117] N.A. Travlou, D.A. Giannakoudakis, M. Algarra, A.M. Labella, E. Rodríguez-Castellón, T.J. Bandosz, S- and N-doped carbon quantum dots: surface chemistry dependent antibacterial activity, Carbon 135 (2018) 104–111. Available from: https://doi.org/10.1016/j.carbon.2018.04.018.

[118] A. Guo, Y. Sun, X. Xu, X. Yu, X. Wu, A. Cai, et al., Facile synthesis of polydopamine/reduced graphene oxide nanosheets with incorporated copper ions for high antibacterial performance, Micro Nano Lett. 15 (2020) 114–118. Available from: https://doi.org/10.1049/mnl.2019.0524.

[119] F. Kiani, N.A. Astani, R. Rahighi, A. Tayyebi, M. Tayebi, J. Khezri, et al., Effect of graphene oxide nanosheets on visible light-assisted antibacterial activity of vertically-aligned copper oxide nanowire arrays, J. Colloid Interface Sci. 521 (2018) 119−131. Available from: https://doi.org/10.1016/j.jcis.2018.03.013.

[120] H.-W. Chen, C.-Y. Huang, S.-Y. Lin, Z.-S. Fang, C.-H. Hsu, J.-C. Lin, et al., Synthetic virus-like particles prepared via protein corona formation enable effective vaccination in an avian model of coronavirus infection, Biomaterials 106 (2016) 111−118. Available from: https://doi.org/10.1016/j.biomaterials.2016.08.018.

[121] H. Li, K. Fierens, Z. Zhang, N. Vanparijs, M.J. Schuijs, K. Van Steendam, et al., Spontaneous protein adsorption on graphene oxide nanosheets allowing efficient intracellular vaccine protein delivery, ACS Appl. Mater. Interfaces 8 (2016) 1147−1155. Available from: https://doi.org/10.1021/acsami.5b08963.

[122] R.C. Choudhary, R.V. Kumaraswamy, S. Kumari, S.S. Sharma, A. Pal, R. Raliya, et al., Zinc encapsulated chitosan nanoparticle to promote maize crop yield, Int. J. Biol. Macromol. 127 (2019) 126−135. Available from: https://doi.org/10.1016/j.ijbiomac.2018.12.274.

[123] H.I. Hussain, Z. Yi, J.E. Rookes, L.X. Kong, D.M. Cahill, Mesoporous silica nanoparticles as a biomolecule delivery vehicle in plants, J. Nanopart. Res. 15 (2013) 1676. Available from: https://doi.org/10.1007/s11051-013-1676-4.

[124] M.-R. Song, S.-M. Cui, F. Gao, Y.-R. Liu, C.-L. Fan, T.-Q. Lei, et al., Dispersible silica nanoparticles as carrier for enhanced bioactivity of chlorfenapyr, J. Pestic. Sci. 37 (2012) 258−260. Available from: https://doi.org/10.1584/jpestics.D12-027.

[125] D. Wibowo, C.-X. Zhao, B.C. Peters, A.P.J. Middelberg, Sustained release of fipronil insecticide in vitro and in vivo from biocompatible silica nanocapsules, J. Agric. Food Chem. 62 (2014) 12504−12511. Available from: https://doi.org/10.1021/jf504455x.

[126] Z. Yi, H.I. Hussain, C. Feng, D. Sun, F. She, J.E. Rookes, et al., Functionalized mesoporous silica nanoparticles with redox-responsive short-chain gatekeepers for agrochemical delivery, ACS Appl. Mater. Interfaces 7 (2015) 9937−9946. Available from: https://doi.org/10.1021/acsami.5b02131.

[127] D.L. Ojeda-Barrios, I. Morales, A. Juárez-Maldonado, A. Sandoval-Rangel, L.O. Fuentes-Lara, A. Benavides-Mendoza, Importance of nanofertilizers in fruit nutrition, in: A.K. Srivastava, C. Hu (Eds.), Fruit Crops, Elsevier, 2020, pp. 497−508. Available from: https://doi.org/10.1016/B978-0-12-818732-6.00035-6.

[128] A.K. Srivastava, A. Dev, S. Karmakar, Nanosensors and nanobiosensors in food and agriculture, Environ. Chem. Lett. 16 (2018) 161−182. Available from: https://doi.org/10.1007/s10311-017-0674-7.

[129] E. Govea-Alcaide, S.H. Masunaga, A. De Souza, L. Fajardo-Rosabal, F.B. Effenberger, L.M. Rossi, et al., Tracking iron oxide nanoparticles in plant organs using magnetic measurements, J. Nanopart. Res. 18 (2016) 305. Available from: https://doi.org/10.1007/s11051-016-3610-z.

[130] H. Wu, N. Tito, J.P. Giraldo, Anionic cerium oxide nanoparticles protect plant photosynthesis from abiotic stress by scavenging reactive oxygen species, ACS Nano 11 (2017) 11283−11297. Available from: https://doi.org/10.1021/acsnano.7b05723.

[131] D. Sun, H.I. Hussain, Z. Yi, J.E. Rookes, L. Kong, D.M. Cahill, Mesoporous silica nanoparticles enhance seedling growth and photosynthesis in wheat and lupin, Chemosphere 152 (2016) 81−91. Available from: https://doi.org/10.1016/j.chemosphere.2016.02.096.

[132] D.N. Basov, R.D. Averitt, D. Hsieh, Towards properties on demand in quantum materials, Nat. Mater. 16 (2017) 1077−1088. Available from: https://doi.org/10.1038/nmat5017.

[133] A. Antonacci, V. Scognamiglio, Photosynthesis-based hybrid nanostructures: electrochemical sensors and photovoltaic cells as case studies, TrAC Trends Anal. Chem. 115 (2019) 100–109. Available from: https://doi.org/10.1016/j.trac.2019.04.001.

[134] Y. Li, K. Yang, High-throughput computational design of organic–inorganic hybrid halide semiconductors beyond perovskites for optoelectronics, Energy Environ. Sci. 12 (2019) 2233–2243. Available from: https://doi.org/10.1039/C9EE01371G.

[135] X. Zhang, C. Gong, O.U. Akakuru, Z. Su, A. Wu, G. Wei, The design and biomedical applications of self-assembled two-dimensional organic biomaterials, Chem. Soc. Rev. 48 (2019) 5564–5595. Available from: https://doi.org/10.1039/c8cs01003j.

[136] A.K. Vala, B.P. Dave, Microbial photosynthetic reaction centers and functional nanohybrids, in: R. Prasad (Ed.), Microbial Nanobionics: Volume 1, State-of-the-Art, Nanotechnology in the Life Sciences, Springer International Publishing, Cham, 2019, pp. 269–277. Available from: https://doi.org/10.1007/978-3-030-16383-9_12.

[137] J. Jampílek, K. Kráľová, Impact of nanoparticles on photosynthesizing organisms and their use in hybrid structures with some components of photosynthetic apparatus, in: R. Prasad (Ed.), Plant Nanobionics: Volume 1, Advances in the Understanding of Nanomaterials Research and Applications, Nanotechnology in the Life Sciences, Springer International Publishing, Cham, 2019, pp. 255–332. Available from: https://doi.org/10.1007/978-3-030-12496-0_11.

[138] A. Lishchuk, C. Vasilev, M.P. Johnson, C.N. Hunter, P. Törmä, G.J. Leggett, Turning the challenge of quantum biology on its head: biological control of quantum optical systems, Faraday Discuss. 216 (2019) 57–71. Available from: https://doi.org/10.1039/C8FD00241J.

[139] M. El Karoui, M. Hoyos-Flight, L. Fletcher, Future trends in synthetic biology—a report, Front. Bioeng. Biotechnol. 7 (2019). Available from: https://doi.org/10.3389/fbioe.2019.00175.

[140] D. Leister, Genetic engineering, synthetic biology and the light reactions of photosynthesis, Plant. Physiol. 179 (2019) 778–793. Available from: https://doi.org/10.1104/pp.18.00360.

[141] M.M. Abd El-Azeim, M.A. Sherif, M.S. Hussien, I.A.A. Tantawy, S.O. Bashandy, Impacts of nano- and non-nanofertilizers on potato quality and productivity, Acta Ecol. Sin. 40 (2020) 388–397. Available from: https://doi.org/10.1016/j.chnaes.2019.12.007.

[142] N. Elsheery, V.S.J. Sunoj, Y. Wen, J.J. Zhu, G. Muralidharan, K.F. Cao, Foliar application of nanoparticles mitigates the chilling effect on photosynthesis and photoprotection in sugarcane, Plant Physiol. Biochem., 149, 2020, pp. 50–60. Available from: https://doi.org/10.1016/j.plaphy.2020.01.035.

[143] M. Thapa, M. Singh, C.K. Ghosh, P.K. Biswas, A. Mukherjee, Zinc sulphide nanoparticle (nZnS): a novel nano-modulator for plant growth, Plant. Physiol. Biochem. 142 (2019) 73–83. Available from: https://doi.org/10.1016/j.plaphy.2019.06.031.

[144] A. de Sousa, A.M. Saleh, T.H. Habeeb, Y.M. Hassan, R. Zrieq, M.A.M. Wadaan, et al., Silicon dioxide nanoparticles ameliorate the phytotoxic hazards of aluminum in maize grown on acidic soil, Sci. Total Environ. 693 (2019) 133636. Available from: https://doi.org/10.1016/j.scitotenv.2019.133636.

[145] J. López-Luna, S. Cruz-Fernández, D.S. Mills, A.I. Martínez-Enríquez, F.A. Solís-Domínguez, M. Del Carmen Ángeles González-Chávez, et al., Phytotoxicity and upper localization of $Ag@CoFe_2O_4$ nanoparticles in wheat plants, Environ. Sci. Pollut. Res. Int. 27 (2020) 1923–1940. Available from: https://doi.org/10.1007/s11356-019-06668-9.

[146] V. Tavallali, M. Kiani, S. Hojati, Iron nano-complexes and iron chelate improve biological activities of sweet basil (*Ocimum basilicum* L.), Plant Physiol. Biochem. 144 (2019) 445−454. Available from: https://doi.org/10.1016/j.plaphy.2019.10.021.

[147] A. De Souza, E. Govea-Alcaide, S.H. Masunaga, L. Fajardo-Rosabal, F. Effenberger, L.M. Rossi, et al., Impact of Fe_3O_4 nanoparticle on nutrient accumulation in common bean plants grown in soil, SN Appl. Sci. 1 (2019) 308. Available from: https://doi.org/10.1007/s42452-019-0321-y.

[148] C. Xie, Y. Ma, J. Yang, B. Zhang, W. Luo, S. Feng, et al., Effects of foliar applications of ceria nanoparticles and $CeCl_3$ on common bean (*Phaseolus vulgaris*), Environ. Pollut. 250 (2019) 530−536. Available from: https://doi.org/10.1016/j.envpol.2019.04.042.

[149] X. Wang, W. Sun, X. Ma, Differential impacts of copper oxide nanoparticles and Copper(II) ions on the uptake and accumulation of arsenic in rice (*Oryza sativa*), Environ. Pollut. 252 (2019) 967−973. Available from: https://doi.org/10.1016/j.envpol.2019.06.052.

[150] S. Avestan, M. Ghasemnezhad, M. Esfahani, C.S. Byrt, Application of nano-silicon dioxide improves salt stress tolerance in strawberry plants, Agronomy 9 (2019) 246. Available from: https://doi.org/10.3390/agronomy9050246.

[151] C. Soares, S. Branco-Neves, A. de Sousa, M. Azenha, A. Cunha, R. Pereira, et al., SiO_2 nanomaterial as a tool to improve *Hordeum vulgare* L. tolerance to nano-NiO stress, Sci. Total Environ. 622−623 (2018) 517−525. Available from: https://doi.org/10.1016/j.scitotenv.2017.12.002.

[152] S. Parveen, A.H. Wani, M.A. Shah, H.S. Devi, M.Y. Bhat, J.A. Koka, Preparation, characterization and antifungal activity of iron oxide nanoparticles, Microb. Pathog. 115 (2018) 287−292. Available from: https://doi.org/10.1016/j.micpath.2017.12.068.

[153] I.-M. Chung, K. Rekha, G. Rajakumar, M. Thiruvengadam, Influence of silver nanoparticles on the enhancement and transcriptional changes of glucosinolates and phenolic compounds in genetically transformed root cultures of *Brassica rapa* ssp. *rapa*, Bioprocess. Biosyst. Eng. 41 (2018) 1665−1677. Available from: https://doi.org/10.1007/s00449-018-1991-3.

[154] A. Konate, Y. Wang, X. He, M. Adeel, P. Zhang, Y. Ma, et al., Comparative effects of nano and bulk-Fe_3O_4 on the growth of cucumber (*Cucumis sativus*), Ecotoxicol. Environ. Saf. 165 (2018) 547−554. Available from: https://doi.org/10.1016/j.ecoenv.2018.09.053.

[155] J. Liu, Z. Zhang, H. Li, X. Lin, S. Lin, D.C. Joyce, et al., Alleviation of effects of exogenous ethylene on cut 'Master' carnation flowers with nano-silver and silver thiosulfate, Postharvest Biol. Technol. 143 (2018) 86−91. Available from: https://doi.org/10.1016/j.postharvbio.2018.04.017.

[156] K. Shankramma, S. Yallappa, M.B. Shivanna, J. Manjanna, Fe_2O_3 magnetic nanoparticles to enhance *S. lycopersicum* (tomato) plant growth and their biomineralization, Appl. Nanosci. 6 (2016) 983−990. Available from: https://doi.org/10.1007/s13204-015-0510-y.

[157] N. Zuverza-Mena, R. Armendariz, J.R. Peralta-Videa, J.L. Gardea-Torresdey, Effects of silver nanoparticles on radish sprouts: root growth reduction and modifications in the nutritional value, Front. Plant Sci. 7 (2016). Available from: https://doi.org/10.3389/fpls.2016.00090.

[158] R. Raliya, P. Biswas, J.C. Tarafdar, TiO_2 nanoparticle biosynthesis and its physiological effect on mung bean (*Vigna radiata* L.), Biotechnol. Rep. 5 (2015) 22−26. Available from: https://doi.org/10.1016/j.btre.2014.10.009.

[159] M.H. Siddiqui, M.H. Al-Whaibi, Role of nano-SiO_2 in germination of tomato (*Lycopersicum esculentum* seeds Mill), Saudi J. Biol. Sci. 21 (2014) 13−17. Available from: https://doi.org/10.1016/j.sjbs.2013.04.005.

[160] A. Mukherjee, J.R. Peralta-Videa, S. Bandyopadhyay, C.M. Rico, L. Zhao, J.L. Gardea-Torresdey, Physiological effects of nanoparticulate ZnO in green peas (*Pisum sativum* L.) cultivated in soil, Metallomics 6 (2014) 132−138. Available from: https://doi.org/10.1039/C3MT00064H.

[161] R. Raliya, J.C. Tarafdar, ZnO nanoparticle biosynthesis and its effect on phosphorous-mobilizing enzyme secretion and gum contents in clusterbean (*Cyamopsis tetragonoloba* L.), Agric. Res. 2 (2013) 48−57. Available from: https://doi.org/10.1007/s40003-012-0049-z.

[162] V. Kumar, D. Sachdev, R. Pasricha, P.H. Maheshwari, N.K. Taneja, Zinc-supported multiwalled carbon nanotube nanocomposite: a synergism to micronutrient release and a smart distributor to promote the growth of onion seeds in arid conditions, ACS Appl. Mater. Interfaces 10 (2018) 36733−36745. Available from: https://doi.org/10.1021/acsami.8b13464.

[163] S. Yousefi, D. Kartoolinejad, R. Naghdi, Effects of priming with multi-walled carbon nanotubes on seed physiological characteristics of Hopbush (*Dodonaea viscosa* L.) under drought stress, Int. J. Environ. Stud. 74 (2017) 528−539. Available from: https://doi.org/10.1080/00207233.2017.1325627.

[164] M.C. Martínez-Ballesta, L. Zapata, N. Chalbi, M. Carvajal, Multiwalled carbon nanotubes enter broccoli cells enhancing growth and water uptake of plants exposed to salinity, J. Nanobiotechnol. 14 (2016) 42. Available from: https://doi.org/10.1186/s12951-016-0199-4.

[165] O. Zaytseva, G. Neumann, Differential impact of multi-walled carbon nanotubes on germination and seedling development of *Glycine max*, *Phaseolus vulgaris* and *Zea mays*, Eur. Chem. Bull. 5 (2016) 202−210. Available from: https://doi.org/10.17628/ecb.2016.5.202-210.

[166] D.P. Rao, A. Srivastava, Enhancement of seed germination and plant growth of wheat, maize, peanut and garlic using multiwalled carbon nanotubes, Eur. Chem. Bull. 3 (2014) 502−504. Available from: https://doi.org/10.17628/ecb.2014.3.502-504.

[167] P. Miralles, E. Johnson, T.L. Church, A.T. Harris, Multiwalled carbon nanotubes in alfalfa and wheat: toxicology and uptake, J. R. Soc. Interface 9 (2012) 3514−3527. Available from: https://doi.org/10.1098/rsif.2012.0535.

[168] A. Joshi, L. Sharma, S. Kaur, K. Dharamvir, H. Nayyar, G. Verma, Plant nanobionic effect of multi-walled carbon nanotubes on growth, anatomy, yield and grain composition of rice, BioNanoSci 10 (2020) 430−445. Available from: https://doi.org/10.1007/s12668-020-00725-1.

[169] S. Samadi, M.J. Saharkhiz, M. Azizi, L. Samiei, M. Ghorbanpour, Multi-walled carbon nanotubes stimulate growth, redox reactions and biosynthesis of antioxidant metabolites in *Thymus daenensis* celak. in vitro, Chemosphere 249 (2020) 126069. Available from: https://doi.org/10.1016/j.chemosphere.2020.126069.

[170] N. Rahmani, T. Radjabian, B.M. Soltani, Impacts of foliar exposure to multi-walled carbon nanotubes on physiological and molecular traits of *Salvia verticillata* L., as a medicinal plant, Plant Physiol. Biochem. 150 (2020) 27−38. Available from: https://doi.org/10.1016/j.plaphy.2020.02.022.

[171] H. Rong, C. Wang, X. Yu, J. Fan, P. Jiang, Y. Wang, et al., Carboxylated multi-walled carbon nanotubes exacerbated oxidative damage in roots of *Vicia faba* L. seedlings under combined stress of lead and cadmium, Ecotoxicol. Environ. Saf. 161 (2018) 616−623. Available from: https://doi.org/10.1016/j.ecoenv.2018.06.034.

[172] C. Wang, H. Liu, J. Chen, Y. Tian, J. Shi, D. Li, et al., Carboxylated multi-walled carbon nanotubes aggravated biochemical and subcellular damages in leaves of broad bean (*Vicia faba* L.) seedlings under combined stress of lead and cadmium, J. Hazard. Mater. 274 (2014) 404−412. Available from: https://doi.org/10.1016/j.jhazmat.2014.04.036.

[173] M. Hatami, Toxicity assessment of multi-walled carbon nanotubes on *Cucurbita pepo* L. under well-watered and water-stressed conditions, Ecotoxicol. Environ. Saf. 142 (2017) 274−283. Available from: https://doi.org/10.1016/j.ecoenv.2017.04.018.

[174] D.L. McGehee, M.H. Lahiani, F. Irin, M.J. Green, M.V. Khodakovskaya, Multiwalled carbon nanotubes dramatically affect the fruit metabolome of exposed tomato plants, ACS Appl. Mater. Interfaces 9 (2017) 32430−32435. Available from: https://doi.org/10.1021/acsami.7b10511.

[175] M. Hatami, J. Hadian, M. Ghorbanpour, Mechanisms underlying toxicity and stimulatory role of single-walled carbon nanotubes in *Hyoscyamus niger* during drought stress simulated by polyethylene glycol, J. Hazard. Mater. 324 (2017) 306−320. Available from: https://doi.org/10.1016/j.jhazmat.2016.10.064.

[176] T.A. Ratnikova, R. Podila, A.M. Rao, A.G. Taylor, Tomato seed coat permeability to selected carbon nanomaterials and enhancement of germination and seedling growth [WWW Document]Sci. World J. (2015). Available from: https://doi.org/10.1155/2015/419215.

[177] M. Ghorbanpour, J. Hadian, Multi-walled carbon nanotubes stimulate callus induction, secondary metabolites biosynthesis and antioxidant capacity in medicinal plant *Satureja khuzestanica* grown in vitro, Carbon 94 (2015) 749−759. Available from: https://doi.org/10.1016/j.carbon.2015.07.056.

[178] G. Zhai, S.M. Gutowski, K.S. Walters, B. Yan, J.L. Schnoor, Charge, size, and cellular selectivity for multiwall carbon nanotubes by maize and soybean, Environ. Sci. Technol. 49 (2015) 7380−7390. Available from: https://doi.org/10.1021/acs.est.5b01145.

[179] P. Begum, B. Fugetsu, Phytotoxicity of multi-walled carbon nanotubes on red spinach (*Amaranthus tricolor* L) and the role of ascorbic acid as an antioxidant, J. Hazard. Mater. 243 (2012) 212−222. Available from: https://doi.org/10.1016/j.jhazmat.2012.10.025.

[180] P. Begum, R. Ikhtiari, B. Fugetsu, M. Matsuoka, T. Akasaka, F. Watari, Phytotoxicity of multi-walled carbon nanotubes assessed by selected plant species in the seedling stage, Appl. Surf. Sci. 262 (2012) 120−124. Available from: https://doi.org/10.1016/j.apsusc.2012.03.028.

[181] K. Pandey, M. Anas, V.K. Hicks, M.J. Green, M.V. Khodakovskaya, Improvement of commercially valuable traits of industrial crops by application of carbon-based nanomaterials, Sci. Rep. 9 (2019) 1−14. Available from: https://doi.org/10.1038/s41598-019-55903-3.

[182] M.H. Lahiani, E. Dervishi, I. Ivanov, J. Chen, M. Khodakovskaya, Comparative study of plant responses to carbon-based nanomaterials with different morphologies, Nanotechnology 27 (2016) 265102. Available from: https://doi.org/10.1088/0957-4484/27/26/265102.

[183] K. Pandey, M.H. Lahiani, V.K. Hicks, M.K. Hudson, M.J. Green, M. Khodakovskaya, Effects of carbon-based nanomaterials on seed germination, biomass accumulation and salt stress response of bioenergy crops, PLoS One 13 (2018). Available from: https://doi.org/10.1371/journal.pone.0202274.

[184] A. Margineanu, Biological applications of nanoparticles in optical microscopy, in: C. Vasile (Ed.), Polymeric Nanomaterials in Nanotherapeutics, Micro and Nano Technologies, Elsevier, 2019, pp. 469−495. Available from: https://doi.org/10.1016/B978-0-12-813932-5.00014-5.

[185] J. Li, F. Wu, Q. Fang, Z. Wu, Q. Duan, X. Li, et al., The mutual effects of graphene oxide nanosheets and cadmium on the growth, cadmium uptake and accumulation in rice, Plant. Physiol. Biochem. 147 (2020) 289−294. Available from: https://doi.org/10.1016/j.plaphy.2019.12.034.

[186] P. Zhang, Z. Guo, W. Luo, F.A. Monikh, C. Xie, E. Valsami-Jones, et al., Graphene oxide-induced pH alteration, iron overload, and subsequent oxidative damage in rice (*Oryza sativa* L.): a new mechanism of nanomaterial phytotoxicity, Environ. Sci. Technol. 54 (2020) 3181−3190. Available from: https://doi.org/10.1021/acs.est.9b05794.

[187] Y. Weng, Y. You, Q. Lu, A. Zhong, S. Liu, H. Liu, et al., Graphene oxide exposure suppresses nitrate uptake by roots of wheat seedlings, Environ. Pollut. 262 (2020) 114224. Available from: https://doi.org/10.1016/j.envpol.2020.114224.

[188] M.-J. Kim, W. Kim, H. Chung, Effects of silver-graphene oxide on seed germination and early growth of crop species, PeerJ 8 (2020) e8387. Available from: https://doi.org/10.7717/peerj.8387.

[189] J. Song, K. Cao, C. Duan, N. Luo, X. Cui, Effects of graphene on *Larix olgensis* seedlings and soil properties of Haplic Cambisols in Northeast China, Forests 11 (2020) 258. Available from: https://doi.org/10.3390/f11030258.

[190] P. Feng, B. Geng, Z. Cheng, X. Liao, D. Pan, J. Huang, Graphene quantum dots-induced physiological and biochemical responses in mung bean and tomato seedlings, Braz. J. Bot. 42 (2019) 29−41. Available from: https://doi.org/10.1007/s40415-019-00519-0.

[191] G. Vochita, L. Oprica, D. Gherghel, C.-T. Mihai, R. Boukherroub, A. Lobiuc, Graphene oxide effects in early ontogenetic stages of *Triticum aestivum* L. seedlings, Ecotoxicol. Environ. Saf. 181 (2019) 345−352. Available from: https://doi.org/10.1016/j.ecoenv.2019.06.026.

[192] Z.A. Siddiqui, A. Parveen, L. Ahmad, A. Hashem, Effects of graphene oxide and zinc oxide nanoparticles on growth, chlorophyll, carotenoids, proline contents and diseases of carrot, Sci. Hortic. 249 (2019) 374−382. Available from: https://doi.org/10.1016/j.scienta.2019.01.054.

[193] L. Chen, C. Wang, S. Yang, X. Guan, Q. Zhang, M. Shi, et al., Chemical reduction of graphene enhances in vivo translocation and photosynthetic inhibition in pea plants, Environ. Sci.: Nano 6 (2019) 1077−1088. Available from: https://doi.org/10.1039/C8EN01426D.

[194] M. Ghorbanpour, A.H. Khaltabadi Farahani, J. Hadian, Potential toxicity of nano-graphene oxide on callus cell of *Plantago major* L. under polyethylene glycol-induced dehydration, Ecotoxicol. Environ. Saf. 148 (2018) 910−922. Available from: https://doi.org/10.1016/j.ecoenv.2017.11.061.

[195] P. Zhang, R. Zhang, X. Fang, T. Song, X. Cai, H. Liu, et al., Toxic effects of graphene on the growth and nutritional levels of wheat (*Triticum aestivum* L.): short- and long-term exposure studies, J. Hazard. Mater. 317 (2016) 543−551. Available from: https://doi.org/10.1016/j.jhazmat.2016.06.019.

[196] W. Ren, H. Chang, Y. Teng, Sulfonated graphene-induced hormesis is mediated through oxidative stress in the roots of maize seedlings, Sci. Total Environ. 572 (2016) 926−934. Available from: https://doi.org/10.1016/j.scitotenv.2016.07.214.

[197] F. Cheng, Y.-F. Liu, G.-Y. Lu, X.-K. Zhang, L.-L. Xie, C.-F. Yuan, et al., Graphene oxide modulates root growth of *Brassica napus* L. and regulates ABA and IAA concentration, J. Plant. Physiol. 193 (2016) 57−63. Available from: https://doi.org/10.1016/j.jplph.2016.02.011.

[198] S. Zhao, Q. Wang, Y. Zhao, Q. Rui, D. Wang, Toxicity and translocation of graphene oxide in *Arabidopsis thaliana*, Environ. Toxicol. Pharmacol. 39 (2015) 145−156. Available from: https://doi.org/10.1016/j.etap.2014.11.014.

[199] M. Zhang, B. Gao, J. Chen, Y. Li, Effects of graphene on seed germination and seedling growth, J. Nanopart. Res. 17 (2015) 78. Available from: https://doi.org/10.1007/s11051-015-2885-9.

[200] N.A. Anjum, N. Singh, M.K. Singh, I. Sayeed, A.C. Duarte, E. Pereira, et al., Single-bilayer graphene oxide sheet impacts and underlying potential mechanism assessment in germinating faba bean (*Vicia faba* L.), Sci. Total Environ. 472 (2014) 834−841. Available from: https://doi.org/10.1016/j.scitotenv.2013.11.018.

[201] J. Chen, H. Peng, X. Wang, F. Shao, Z. Yuan, H. Han, Graphene oxide exhibits broad-spectrum antimicrobial activity against bacterial phytopathogens and fungal conidia by intertwining and membrane perturbation, Nanoscale 6 (2014) 1879−1889. Available from: https://doi.org/10.1039/C3NR04941H.

[202] N.A. Anjum, N. Singh, M.K. Singh, Z.A. Shah, A.C. Duarte, E. Pereira, et al., Single-bilayer graphene oxide sheet tolerance and glutathione redox system significance assessment in faba bean (*Vicia faba* L.), J. Nanopart. Res. 15 (2013) 1770. Available from: https://doi.org/10.1007/s11051-013-1770-7.

[203] P. Begum, R. Ikhtiari, B. Fugetsu, Graphene phytotoxicity in the seedling stage of cabbage, tomato, red spinach, and lettuce, Carbon 49 (2011) 3907−3919. Available from: https://doi.org/10.1016/j.carbon.2011.05.029.

This page intentionally left blank

Quantum dot materials, devices, and their applications in photomedicine

6

Manuel A. Triana[1,2], Rubén J. Camargo[3], Shin-Tson Wu[2], Raymond J. Lanzafame[4] and Yajie Dong[1,2,4,5]

[1]NanoScience Technology Center, University of Central Florida, Orlando, FL, United States, [2]College of Optics and Photonics, University of Central Florida, Orlando, FL, United States, [3]Escuela de Ingeniería Química, Cali, Colombia, [4]QLEDCures LLC, Orlando, FL, United States, [5]Department of Materials Science & Engineering, University of Central Florida, Orlando, FL, United States

6.1 Introduction

The optical phenomena and physicochemical processes triggered by the light−matter interaction enable multiple applications of semiconductor nanomaterials and optoelectronic devices in the photomedicine field. Remarkably, quantum dot (QD) materials are considered highly attractive as individual platforms for multimodal applications, and for the development of wearable optoelectronic devices with medical applications. QDs are semiconductor nanocrystals with a radius below the corresponding Bohr radius, exhibiting electronic transitions that resemble an atom's behavior. The most remarkable properties of QDs are their size-tunable emission wavelength, high photoluminescence quantum yield (PL-QY), wide absorption bandwidth, narrow emission bandwidth linked to narrow particle size distribution, and photostability. These unique optical properties along with the mature QD-based technologies have encouraged new applications. Among the most attractive applications of individual QD platforms is their use as fluorescent probes and efficient energy donors in photodynamic therapy (PDT). On the other hand, QD light-emitting diodes (QLEDs) are the QD-based devices attracting most of the attention for multiple applications in the health-care and photomedicine fields. The recent results of QLED-based in vitro studies in PDT and photobiomodulation (PBM) demonstrated the high potential of QLEDs as alternative and cost-effective photomedical light sources. Moreover, the QLEDs' capability for flexible form factors, with simultaneous high power density (PD) and narrow emission bandwidth at clinically relevant red wavelengths, makes them strong candidates for use as light sources that would facilitate wider clinical adoption of PDT and PBM treatments. The photomedical markets include but are not limited to the management of cancer treatment, periodontal disease, dermatology, and chronic wound and ulcer care.

Quantum Materials, Devices, and Applications. DOI: https://doi.org/10.1016/B978-0-12-820566-2.00005-3

The fundamentals of QD materials, QD devices, and phototherapies of high relevance are explained in the first section. This section includes the properties and synthesis of QDs, the evolution and operating principle of QLEDs, and the basics and benefits of PDT and PBM treatments. Subsequently, different types of QDs proposed for light-based theranostic applications are summarized. The next section is dedicated to the development and photomedical application of QD devices, especially QLEDs. This starts with the recent advances in red-emitting QLEDs, followed by the explanation of the most relevant radiometric parameters for phototherapy administration and for the evaluation of the QLEDs as efficient photomedical light sources. Later, the unique features and advantages of flexible QLEDs as alternative photomedical light sources and the results of QLED-based in vitro studies in PDT and PBM are presented. These studies are presented in parallel with the recent photomedical studies using organic light-emitting diodes (OLEDs) as light sources. A perspective about the future of QLEDs in and beyond the current photomedical research areas, along with conceptual designs of QLED-based medical devices, is also discussed. Ultimately, some examples of QD-based devices proposed for health monitoring and diagnostics are given. The latter applications could be included in the other branch of photomedicine that uses light for health monitoring and detecting disease.

6.2 Fundamentals

6.2.1 QD materials: properties and synthesis

In semiconductors, the Bohr radius (R_B) is the characteristic size of a photogenerated exciton (electron−hole pair). QD materials are semiconductor nanocrystals whose size is $<2R_B$, which leads to three-dimensional (3D) confinement of electrons and holes, and to the discretization of the energy levels in the electronic bands. Notably, the electronic and optical properties vary as functions of the degree of confinement, that is, they vary depending on the nanocrystal size. Specifically, the energy difference between the valence and conduction band edges, that is, the band-gap energy (E_g), increases as the degree of confinement increases. The Brus model (1984) [1] derived from the *effective masses approach* is an equation for the predictive calculation of the band-gap energy increment (ΔE_g) as a function of the QD average radius (R):

$$\Delta E_g = E_{g(\mathrm{QD})} - E_{g(\mathrm{bulk})} = \frac{\bar{h}^2\pi^2}{2R^2}\left(\frac{1}{m_e^*} + \frac{1}{m_h^*}\right) - \frac{1.8q^2}{\varepsilon_r R} \tag{6.1}$$

where the effective masses in the first-term count for the internal force effects, which affect the acceleration of electrons within the nanocrystalline solid relative to the electrons in the vacuum. $\hbar = 1.0546 \times 10^{-34}$ J s ($h/2\pi$) (reduced Planck constant), m_e^* is the effective mass of electrons in the conduction band, m_h^* is the

effective mass of holes in the valence band, and ε_r is the dielectric constant. A significant dependence between the effective masses and the nanocrystal size under quantum confinement has also been found. The second term corresponds to the Columbic attraction of the electron−hole pair or exciton, and 1.8 is a dimensionless constant obtained by the numerical solution of the Columbic interaction between neighboring atoms, ignoring the atoms in the distance. It is worth noting that the nature of a ligand bound to the nanocrystal surface can also affect the band-gap energy of colloidal QDs [2]. The size-tunable band-gap energy of QDs implies that the emission wavelength can be tuned by controlling the QD size. Therefore, a desired emission wavelength ranging from ultraviolet (UV) to the near-infrared (NIR) can be obtained by controlling either the nanocrystal size or the chemical composition of the QDs. Fig. 6.1 shows the emission wavelength range of typical QDs with different compositions [3].

QDs can be grown by molecular beam epitaxy on crystalline substrates or can be synthesized as colloids in solutions containing complexes of the constituent atoms. The QDs discussed here are colloidal QDs obtained through the wet route, which are compatible with simple and low-cost solution processing. The simplest colloidal QD structure consists of a nanocrystalline semiconductor core and an organic capping ligand. Such ligand controls the growth during synthesis and stabilizes the QDs in certain solvents. In addition, core−shell and core−shell−shell structures can also be formed by coating the core with other inorganic semiconducting materials. A typical core−shell structure for biological and optoelectronic applications is a type I structure, where the bandgap of the core is smaller than that of the shell material, and both the conduction and valence band edges of the core lie within the

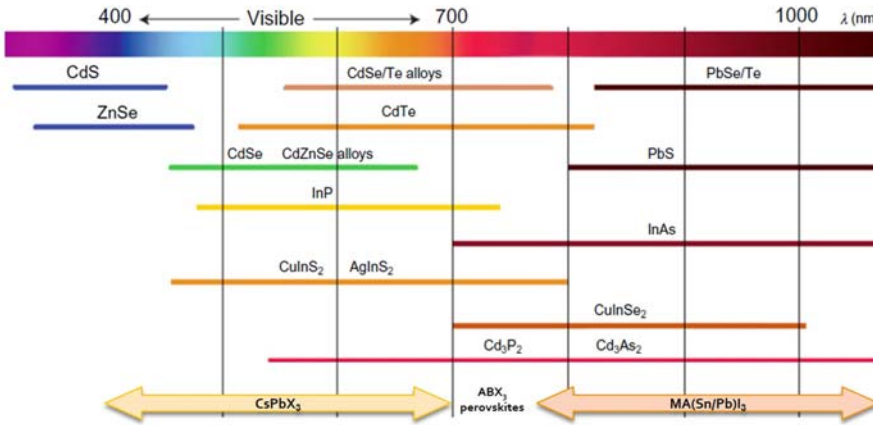

Figure 6.1 Reported spectral ranges of emission for different semiconductor QDs. *QD*, quantum dot.
Source: Adapted from C. Philippot, P. Reiss, Chapter 3 − Synthesis of inorganic nanocrystals for biological fluorescence imaging, in: J.M. de la Fuente, V. Grazu (Eds.), Frontiers of Nanoscience, vol. 4, Elsevier, 2012, pp. 81−114, Copyright (2012), with permission from Elsevier.

bandgap of the shell. Proper coating with a material matching the crystal core lattice can improve the confinement of excitons in the core and passivate the core surface defects, which simultaneously increases the PL-QY of QDs. Moreover, the use of a coating shell can reduce the toxicity and improve the stability of QDs in aqueous solution or biological environments. The most common QD cores comprise elements from groups 12 and 16 (e.g., CdSe, CdTe, CdS, and ZnO); other QD cores recently attracting more attention are formed by elements from groups 13 and 15 (e.g., InAs, InP, InSb, and GaAs). Typical examples of core−shell and core−shell−shell QDs are CdSe/CdS and CdSe/ZnS/CdZnS, respectively.

The two main routes for the synthesis of colloidal QDs are the organometallic synthesis based on thermolysis of the precursors, and the classic aqueous synthesis that uses polyphosphates or thiols as stabilizing agents. For the organometallic route, the formation of colloidal QDs can be divided into three main stages: nucleation, growth, and ripening. During nucleation, the concentration of liquid monomers is partially depleted by the formation of nuclei with approximately the same size. The particles then grow by monomer consumption. Subsequently, as the monomer depletes, the average size increases by competitive growth or Ostwald ripening. During this stage, the bigger particles grow, while the smaller particles shrink and disappear, resulting in the reduction of the net surface energy of the system [4]. The Ostwald ripening is characterized by a slow growth rate, scarcity of the precursor reagents, and, consequently, a broadening of the size distribution. Importantly, the maximum PL-QY and minimum full width at half maximum (FWHM) of the emission spectrum are simultaneously reached at the transition point between the growth and ripening stages. This so-called bright point [5] corresponds to the period when the nanocrystals are practically in equilibrium with the monomer concentration of the solution [6]. However, this point can be moved forward in time by continuous feeding of the precursors to the reaction volume. Small aliquots are normally extracted with a syringe at different reaction times, in order to monitor the QDs growth by measuring the absorption and emission spectra. In the case of the classic aqueous route, the formation process of QDs is similar except for the initial stage, since the nucleation occurs at room or low temperature, creating small nuclei with a broad size distribution and a high density of crystalline structure defects. Therefore, in the conventional aqueous synthesis, this step is followed by heating of the raw solution inside a reflux system to promote the growth of nanocrystals. As expected, the maximum growth temperature in the reflux system is imposed by the boiling temperature of water at atmospheric pressure. Alternatively, the hydrothermal growth of QDs can be carried out by heating the raw solution inside a sealed autoclave, in order to increase the temperature of the aqueous solution above 100°C (under $P > P_{atm}$). Each wet-chemical route has advantages, depending on the synthesis conditions, the resulting properties, and final application of the QDs. QDs obtained by aqueous route and therefore stabilized in water are ideal for direct application in biological systems. The main advantages of the aqueous route are reproducibility, easy scalability, and lower cost and time consumption. QDs grown through the hydrothermal route can achieve relatively narrow FWHM (down to 27 nm) [7] and high PL-QY (up to 84%) [8] using

thiols as stabilizing agents, such as mercaptosuccinic acid [7–9] and mercaptopropionic acid [10]. In addition, QDs emitting in the UV [11], visible [7–10], and NIR [12] ranges can be synthesized by aqueous synthesis.

On the other hand, the advantages of the organometallic route are the production of QDs with narrower FWHM (as low as 22 nm), higher PL-QY (~100%), and high monodispersity, with emission wavelengths also covering the UV [13], visible [14,15], and NIR [16,17] ranges. The high crystallinity of these QDs results from the high temperatures during synthesis and calcination (200°C–360°C), which eliminates surface traps responsible for nonradiative exciton recombination. Accordingly, higher thermal energy promotes a better organization of each atom under the aggregation state into the crystalline network. Meanwhile, one drawback for the biological application of QDs obtained in nonpolar organic solvents is the required postsynthetic surface treatments, in order to replace the native ligand with a hydrophilic ligand and make the QDs dispersible in water. For instance, ligand exchange normally results in simultaneous reduction of the PL-QY. Alternatively, pristine QDs (with native ligands) can be encapsulated with amphiphilic molecules (e.g., phospholipid micelles), thus preserving the original PL-QY but at the expense of an increase in the QD hydrodynamic diameter. One concern related to the final size is that a QD system comparable in size to a large protein could be retained or lasts for longer time within the body after performing its task. The size of the crystalline structure of QDs is usually measured by transmission electron microscopy (TEM), while the hydrodynamic diameter of the QDs in solution can be measured by dynamic light scattering. Finally, different nanostructures under quantum confinement can be obtained depending on shape, such as spherical, cubic, rod-like, and tetrapod-like. Herein, we make special emphasis on spherical QDs since they are the most widely studied and used ones at the present time.

6.2.2 QD devices

QDs are no longer commercially new nanomaterials since pioneering companies started their commercialization in 2001. Subsequently, QDs were first applied in display as remote phosphors through the color enhancement film technology, which has been widely used in wide color gamut liquid crystal displays. Currently, the use of QDs as self-emissive materials in QLEDs is considered their ultimate application in the display and lighting markets due to the QLED capability for 100% Rec. 2020 color gamut, high efficiency, and low cost of manufacturing [18]. The Rec. 2020 is one of the three main color gamut standards, covering the largest area of the visible color space. It is worth noting that the research for display application has been the main actor pushing forward the development of QLEDs for more than 20 years. Nevertheless, there are remaining challenges impeding the full entry of QLEDs into the display and lighting industries. For instance, tailoring of the QD core–shell structure and interfacial energy alignment between QDs and neighboring materials are of utmost importance, in order to improve the charge injection balance and avoid accelerated degradation of the QLED under operation at high brightness. The high brightness ($\geq 10^4$ cd m^{-2}) and external quantum efficiency (EQE $\geq$ 20%)

achieved for all red, green, and blue on-glass QLEDs are promising developments for future lighting applications [19,20]. Green and red Cd-based on-glass QLEDs have already overcome the commercialization requirement for low- and high-brightness (outdoors) display [21–23], that is, $\sim 5x10^4$ h for T_{50} @ 100 cd m^{-2} and $\sim 2x10^3$ h for T_{95} @ 1000 cd m^{-2}. However, the T_{50} operation lifetime of blue on-glass QLEDs is still under the corresponding limit ($1x10^4$ h) [22]. T_{50} and T_{95} are the periods of time when the luminance has dropped to 50 and 95% of its initial value, respectively. Although QDs have a high photochemical resistance to decomposition, the multilayer structure of QLEDs also have oxygen–moisture sensitive materials such as organic molecules or polymers. However, considering that the encapsulation of on-glass rigid QLEDs is already a mature technology, the remaining obstacle to increase the lifetime of blue QLEDs is related to the QD interfacial engineering.

On the other hand, the development of portable and ergonomic systems is pushing forward the application limits of optoelectronics. Moreover, research and development of wearable optoelectronics are promoting new paradigms in the way health care and medicine are administered. New pathways stimulated by this development are a translation of health monitoring and ambulatory therapy to "at home" application, an early detection of disease conditions, and a stimulation of more healthy habits in individuals. For instance, flexible QD-based devices such as QLEDs and QD photodetectors (QDPDs) in the visible and NIR ranges can be integrated in wearable medical device systems with the capability for real-time health monitoring, diagnostics, and light-based therapy. These devices based on colloidal QDs have a multilayer structure and can be made by solution-processing at a low cost. While QLEDs convert an electrical current into light using QDs as an emissive layer, QDPDs absorb light and convert it into an electrical current signal using QDs as the absorber layer. Medical device systems can also take the advantage of the capability of these QD devices for lightweight, thinness, and flexible form factors. However, QLEDs are probably the QD-based devices most frequently integrated in wearable medical systems being produced for research applications to date, since QLEDs are used either as light sources with large emitting areas, or for display in an array of small pixels driven by passive or active matrices. Notably, our group [24–26] recently proposed the use of flexible QLEDs as light sources for light-based therapy, taking the advantage of the unique optical properties of QLEDs at clinically relevant light wavelengths. Similarly, flexible QLEDs have been integrated by others [27] for health monitoring of vital signs.

Besides the fundamental function of the medical device systems, there are important additional challenges for the transition to portable and ergonomic devices. Importantly, the body surface where the device is to be located, the degree of exposure to air and water, and whether the device should operate for long or short times determine other required parameters for the device. Such parameters correspond to specific form factors (e.g., bendability or stretchability), stability in ambient conditions, and the minimum operating lifetime of the devices. In general, the more rigorous or restricted these parameters are, the more complex and expensive is the fabrication process of the devices. For instance, when the device is meant

to be wearable for real-time health monitoring during a long period (days to months), the degradation mechanisms of the device under operation need to be mitigated in order to obtain a sufficient operating lifetime. Exposure to different ambient conditions, while the device is permanently attached to the user, requires either an inert material structure or an effective barrier encapsulation of the device against oxygen and water. In a normal routine, permanent wearing will subject the device to a shower environment (max. water $T \approx 43^{\circ}C$), and sometimes to very high relative humidity ($RH > 50\%$), depending on the outdoor environment. In addition, if the device needs to be attached to a joint of the body (e.g., the wrist), stable operation under elongation and compression of the device will be required during joint movement. Therefore, this application will require a waterproof and stretchable device with long operating lifetime. Meanwhile, if the wearable device is intended for light-based therapy over a short period of time (i.e., seconds to few hours), the operating lifetime needed for the device is less stringent. In addition, the operation of the device under a moderate bending radius (e.g., $\geq$ small finger curvature) and inside a controlled environment (i.e., indoors) further favor the performance and stability of the device over the short treatment period. This application could then be satisfied by a disposable and bendable device with a short operating lifetime and moderate stability. Notably, the use of cost-effective disposable devices for ambulatory and "at home" applications also eliminates the concerns rising from inappropriate reuse, such as overtreatment, undertreatment, and cross-contamination.

6.2.3 Evolution and operating principle of QLEDs

QDs play the role of emissive materials in a QD light-emitting device. The display industry has introduced two types of QD light-emitting devices according to their excitation mechanism. In the first type, the emission results from the QDs photoexcitation, and in the second one, the emission originates from the electroexcitation of QDs by the application of an external electrical field. The photoluminescent devices are normally used as color-converters or down-converters in the display industry. Meanwhile, the self-emissive or electroluminescent devices still need further optimization before they can be commercialized for display and lighting applications. The electroluminescent devices are the key subject of this chapter and correspond to the QLEDs. Four structure types of the QLEDs are also highlighted in the literature according to the evolution of the device structure throughout a period of almost three decades [28]. This QLED's structure evolution is represented in Fig. 6.2. The type I structure was based either on a QD-polymer bilayer [29] or a QD-polymer blend [30] sandwiched between two electrodes, as illustrated in Fig. 6.2A. The performance of these first devices was accordingly low, for instance, the EQE of a device using CdSe core-only QDs (PL-QY $\sim$ 10% in solution) was less than 0.01% (at 100 cd m^{-2}) [30]. Subsequently, the use of QDs with a CdS shell increased the EQE up to 0.22% (at 600 cd m^{-2}) [31]. One of the main issues with these first QLEDs was the poor separation between the charge transport layers (CTLs) and the electroluminescent QD region. A type II structure was introduced in 2002 [32],

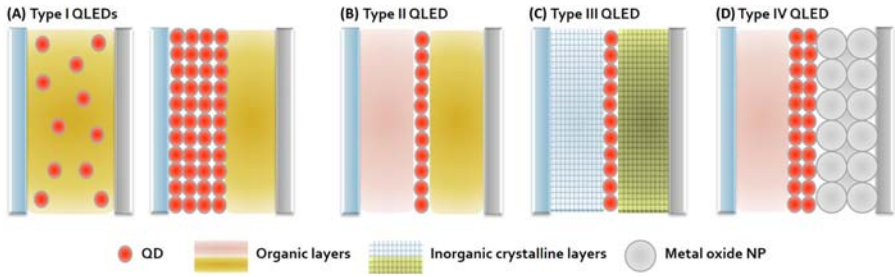

Figure 6.2 Schematic illustration of the QLED's structure evolution from (A) type I, passing through type II (B) and III (C), to type IV (D) QLEDs. *QLED*, quantum dot light-emitting diodes.

which used a QD monolayer between two organic transport materials (see Fig. 6.2B) and demonstrated a higher EQE of 0.5%. The CdSe-ZnS core−shell QDs' monolayer was self-assembled by spin-casting of a blend solution containing the QDs and the hole transport material. Later, Anikeeva et al. [33] demonstrated different color QLEDs by microcontact printing of close-packed QD monolayers, and a maximum EQE of 2.7% for orange-emitting QLEDs. This printing technique enabled better interfacial contact between the hole transport layer (HTL) and the QD monolayer and avoided the exposure of the underlying HTL to solvents, as these preliminary QLEDs had a forward structure. Overall, the efficiency improvement in type II QLEDs was possible since the QD monolayer sandwiched between the two organic thin films decoupled the electroluminescence (EL) process from the charge transport, occurring through the organic layers. In order to address the instability in air at high current densities which is mainly attributed to the organic transport layers, all-inorganic QLEDs corresponding to type III structure were also proposed (see Fig. 6.2C). Mueller et al. [34] sandwiched a QD monolayer between epitaxially grown n- and p-type gallium nitride (GaN), which resulted in EQE $\leq$ 0.01%. Subsequently, Caruge et al. [35] reported red-emitting QLEDs using NiO and ZnO:SnO_2 as p-type and n-type materials, resulting in EQE of nearly 0.1%. Regardless of the improved shelf life (up to 4 A cm^{-2}) of these devices, their low performance could be attributed to damage of the QDs layer caused by deposition of the overlying metal oxide by sputtering. Finally, the type IV structure was a hybrid architecture combining both inorganic and organic CTLs, as illustrated in Fig. 6.2D. Typically, metal oxides and organic molecules or polymers are used to make the electron transport layer (ETL) and HTL of the type IV QLEDs, respectively. QD vision reported a hybrid QLED with a record EQE of 18% in 2013 [36]. Type IV devices can also be all-solution processed by using colloidal metal oxide nanoparticles (NPs) and polymers as the respective transport layers. Qian et al. [37] reported all-solution processed (excluding the electrodes) QLEDs emitting at different colors for the first time. These devices incorporated ZnO NPs as ETL and poly (4-butylphenyl-diphenyl-amine) (poly-TPD) as the HTL and exhibited a maximum brightness of 3.1×10^4 cd m^{-2} for red−orange-emitting devices (600 nm).

Regarding the operating principle, Förster resonance energy transfer (FRET) was suggested as the dominant QD excitation mechanism in type II QLEDs [28]. According to this mechanism, one-type carriers migrate through the QD monolayer, followed by the formation of excitons in an adjacent donor material (luminescent species), and the nonradiative transfer of the excitons' energy to the QDs by the dipole−dipole coupling. For both types III and IV QLEDs the accepted dominant mechanism is direct charge injection, due to the QD film being thicker than one monolayer. In this case, electrons and holes are injected from the respective CTLs into the QDs, forming excitons that subsequently recombine to emit photons. Besides the four structure types mentioned, QLEDs can also be classified according to the transparency of the electrodes, that is, top- or bottom-emitting devices, and according to the injection scheme, that is, forward (regular) or inverted structure. Accordingly, an inverted structure enables a reverse injection scheme in which holes and electrons are injected from the top anode and bottom cathode, respectively. The introduction of the inverted architecture allowed the deposition of a wider variety of organic HTL materials by either thermal evaporation or solution-process techniques on top of the QD layer.

6.2.4 PDT and PBM

PBM, previously known as low-level light therapy, and PDT belong to the branch of photomedicine that uses the application of light at various wavelengths and treatment parameters to manage or cure diseases or conditions [38]. Both PDT and PBM have been already proven as effective noninvasive or minimally invasive phototherapies and their fields of application are of high relevance and growing.

Specifically, PDT has been adopted for the treatment of cancer and other diseases characterized by the presence of unwanted tissues and cells. In addition, antimicrobial PDT (aPDT) has been proposed as an alternative approach to prevent the growth of disease-causing microorganisms. In general, the mechanism of action for PDT requires the combined effect of light, most frequently at a therapeutic window between 600 and 700 nm, an exogenous chromophore or photosensitizer (PS) (i.e., a drug), and molecular oxygen to produce reactive oxygen species (ROS) as a result of light exposure. Consequently, the ROS kill and destroy the unwanted cells and tissues being targeted. In the case of molecular PSs, singlet oxygen ($^1O_2$) is mainly generated through the type II pathway after excitation of the PS. This pathway involves direct energy transfer. A fluence rate between 10 and 200 mW cm^{-2} has been typically used for PDT clinical regimes. Nevertheless, selective tumor cell killing through apoptosis has been demonstrated by application of metronomic PDT (mPDT). mPDT involves long treatment times at low fluence rates (i.e., 0.1−6 mW cm^{-2}) along with continuous and slow administration of the PS.

Meanwhile, PBM treatment is known for induction of beneficial clinical effects such as reduction of pain, inflammation, and edema [39−41]; promotion of wound healing and nerve regeneration [42−47]; prevention of tissue damage [45,47]; hair regrowth [48−50]; and influencing the host response to different disease conditions, including infection and sepsis [51−53]. The basic mechanism of PBM consists of

exposure to deep red or NIR light, at specific irradiances and low doses, and consequent absorption by endogenous cytochrome *c* oxidase, with absorption range of photomedical relevance at 620−900 nm. This light absorption leads to a cascade of effects: increased ATP production, modulation of ROS, and induction of transcription factors [54]. Photostimulatory effects are generally observed at a fluence range of $1-10\ \mathrm{J\ cm^{-2}}$, while photoinhibitory effects are typically observed at a fluence $\geq 20\ \mathrm{J\ cm^{-2}}$ [40,41,46,47,55,56]. Despite the fact that $10\ \mathrm{mW\ cm^{-2}}$ is an irradiance floor value commonly mentioned in the PBM literature, in vitro and in vivo studies using lower irradiances (e.g., $5-8\ \mathrm{mW\ cm^{-2}}$) [40,44,46,47,56−58] have produced positive results. Detailed mechanisms of actions for PDT and PBM, and extended discussion on both phototherapies, can be found elsewhere [26,59]. In section 6.4 the discussion focuses on the application progress of QLEDs as alternative and effective light sources for both PDT and PBM.

6.3 QD materials' development and applications

QDs have found a special niche in medicine, either as individual multifunctional platforms or as components playing a relevant role in medical devices. The versatility and specificity of individual QDs have clearly demonstrated their potential in multimodal applications, including but not limited to drug delivery, bioimaging, phototherapy (mainly PDT and photothermal therapy), and other theranostic applications for both therapy and diagnostics [60−64]. QDs forming part of multifunctional systems can, for instance, simultaneously play the role of an enhanced imaging agent, PS nanocarrier, and efficient energy donor for PDT. Herein, we make special emphasis in the applications of QDs related to photomedicine. Importantly, QDs can perform as PSs due to their semiconductor nature, which enable the catalytic generation of ROS under irradiation at certain light wavelength. Therefore, QDs have been solely used as PSs or as photoactive delivery agents, that is, for delivery of small PS molecules attached to their surface and simultaneous enhancement of the photosensitizing capacity for PDT in vitro and in vivo studies. Generation of either excitons ($E_g^{\mathrm{op}} \leq h\nu < E_g$) or free-charge carriers ($h\nu > E_g$) takes place upon irradiation and light absorption of the QDs, depending on the band-gap energy of the QDs and the wavelength of the incident light. This is followed by diffusion of the excitons or the free charge carriers to the interfacial surface area of the QDs, with electrons and holes moving through the conduction and valence bands, respectively. Subsequently, reduction and oxidation reactions take place at the interphase by electron transfer to or from chemical species of the surrounding environment. Given the relatively large spatial separation between free charge carriers at the QD's surface, type I reactions (involving electron transfer) are more likely to occur than in molecular PSs, leading to generation of different ROS. Thus holes produce highly reactive hydroxyl radicals (•OH) through oxidation of molecular water, and electrons produce superoxide anions $\left(\bullet O_2^-\right)$ through reduction of molecular oxygen; the superoxide anion can also undergo dismutation into

hydrogen peroxide (H_2O_2). In addition, QDs with core made of direct band-gap semiconductors can efficiently emit photons after recombination of electron−hole pairs, resulting in fluorescence of visible or NIR light. This property has been exploited for application of QDs as fluorescence probes for bioimaging, bioanalysis and diagnostics, and as the emissive material in QLEDs. Commonly known semiconductors with direct bandgap are CdS, CdSe, CdTe, InP, InAs, and PbSe. In comparison with organic fluorophores (small dye molecules), QDs offer remarkable advantages such as larger extinction coefficients or absorption, broader absorption bands, higher PL-QY, much longer fluorescence lifetimes, higher photostability, and higher resistance to photochemical decomposition. On the other hand, a very high PL-QY is translated into minimal intersystem crossing to triplet state, that is, minimal generation of singlet oxygen through the type II mechanism. Therefore, given their strong fluorescence and wider excitation range, QDs are preferred as fluorescent probes for bioimaging and efficient energy donors for PDT. In systems using PS molecules attached on the QD's surface, QDs can transfer energy by FRET. In this FRET process the photoexcited QDs transfer energy through nonradiative dipole−dipole coupling to the PS, which subsequently generates singlet oxygen. QDs can be efficient FRET donors by assuring sufficient spectral overlap of the QDs PL emission and the excitation spectrum of the PS. This energy transfer, and therefore the singlet oxygen generation rate, has been found to be highly sensitive to the distance between the QD (donor) and the PS (acceptor). Accordingly, the QD-based FRET degree can be tailored for simultaneous imaging and PDT, allowing it to monitor intracellular uptake, biodistribution, and clearance by detection of the QD fluorescence. The biodistribution refers to the accumulation profile in organs, skin, and muscles. Considering all the mentioned properties, QDs can potentiate and improve the detection, diagnostics, and therapeutics of cancer compared to other systems. In particular, application of QDs in detection allows for single-molecule detection and dynamic tracking in live cell imaging (i.e., dynamic cell imaging), simpler multicolor target detection or multiplexing capability using one single excitation wavelength, and tumor imaging at NIR and IR regions. Fig. 6.3 illustrates potential applications of individual QDs as multimodal platforms in the photomedicine field.

The research and development of these applications to date have revealed several critical factors to determine the functionality of QDs in different QD-based systems. The most important factors normally mentioned are biocompatibility, dark toxicity, phototoxicity, in vitro and in vivo colloidal stability, size control, and surface functionalization capability. The latter determines the selectivity, bio-adhesion, and cellular uptake of the QDs. Importantly, the final application will determine the molecule type for surface functionalization of the QD. Nucleic acids, proteins, peptides, aptamers, and antibodies are some of the molecules commonly bioconjugated to the QD surface via covalent bonding or electrostatic interaction for targeted delivery. For instance, antibody-conjugated QDs can be used to label cancer cells which overexpress the corresponding antigen receptors. Similarly, folic acid (FA)-conjugated QDs are widely used to target many types of human cancer cells which overexpress folate receptors (FRs). Minimum expression of FRs in

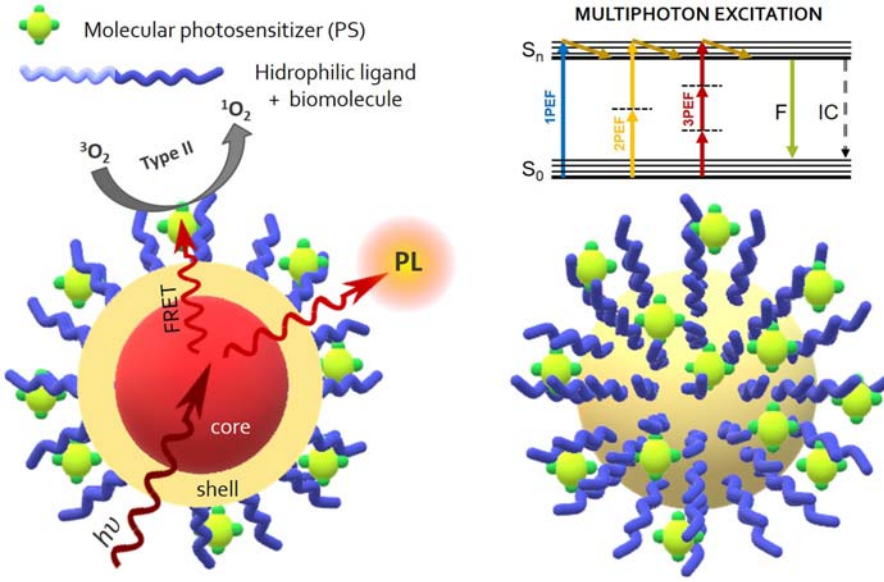

Figure 6.3 Illustration of a QD-PS system with PS anchored to a hydrophilic ligand/biomolecule conjugate. The scheme in the left corresponds to a cross-sectional view of the QD-PS, describing two important processes: QD's fluorescence and FRET energy transfer from the QD to the PS leading to generation of singlet oxygen ($^1O_2$) by the type II pathway. In the right, a 3D scheme of the whole QD-PS system is shown. In addition, the Jablonski diagram represents the multiphoton excitation process in certain QDs leading to single, two, and three photon-excited fluorescence: 1PEF, 2PEF, and 3PEF, respectively. *3D*, three-dimensional; *F*, fluorescence emission; *FRET*, Förster resonance energy transfer; *IC*, internal conversion (heat generation); *PS*, photosensitizer; *QD*, quantum dot.

normal tissues allows for selective cellular uptake of FA-conjugated QDs into cancer cells. For in vivo treatment, these bio-conjugated QDs are expected to accumulate inside tumors via the enhanced permeation and retention (EPR) effect, caused by poor quality vasculature of the solid tumor. Accumulation of the QDs in the tumor site can be tracked over time after a systemic circulation period and through gradual building up of the fluorescence intensity.

Other semiconductor NPs being used in PDT studies, either as PSs or photosensitizing agents, are metal oxides such as titanium oxide (TiO_2) nanocrystals, in which clear observation of the quantum confinement effect requires a subnanometer range [65]. Metal oxide NPs have been proposed in PDT since they offer a proper size (0.1−100 nm) for transport in tumor tissues and through endothelial, vascular, and tumor cell membranes, in addition to favoring the EPR effect. Particularly, TiO_2 is an abundant and nontoxic semiconductor material of great interest. TiO_2 NPs are normally synthesized by the sol−gel method or the Pechini method [66], and subsequently subjected to surface modification before being tested in PDT treatment of cancer cells. Coating of the TiO_2 NPs' surface with metals has

demonstrated highly improved phototoxicity compared to nondoped TiO_2 NPs. For instance, TiO_2 NPs with superficial gold (TiO_2−Au NPs) were successfully tested as PSs under UV irradiation for PDT treatment of cervical cancer cells (HeLa), producing 43.2% cell death [67]. Subsequently in 2016 TiO_2 NPs modified with both gold and FA increased the cytotoxicity of HeLa cells to 78% and simultaneously resulted in null cytotoxicity in Chinese hamster ovary cells. This result evidenced the selectivity of modified TiO_2 NPs during PDT treatment of HeLa cancer cells [68]. Camargo and coworkers also patented TiO_2-based nanocomposites which are highly cytotoxic in PDT treatment of cancer cells under UV photoirradiation. These nanocomposites were comprised of TiO_2 NPs in anatase phase, with either multiwalled carbon nanotubes or FA attached to the NPs' surface. The invention included a method for the synthesis of the nanocomposites, as well as a method for the treatment of cancer [69]. Such modified TiO_2 NPs exhibited high PDT efficacy and selectivity; specifically, cytotoxicity between 80% and 98% was achieved for cervical cancer, leukemia, and breast cancer cells under UV irradiation for less than 40 min. It is worth noting that the TiO_2 NPs in anatase phase have a wide energy bandgap of $\sim$3.2 eV, therefore their use as PSs for PDT treatment of deeply situated tumors would require the use of optical fibers due to the short tissue penetration of UVA-light necessary for excitation. Nevertheless, TiO_2 NPs hold great promise for PDT treatment among metal oxides due to their exceptional photocatalytic efficiency.

Ultimately, the potential toxicity of Cd- and Pb-based QDs is a remaining challenge impeding the full adoption of these QDs for invasive treatment in clinical trials. Even though the core oxidation (producing CdO, PbO) and leakage of free metallic Cd^{2+} and Pb^{2+} ions can be mitigated by core−shelling, the instability of protective layers and ligands, surface cationic charge, and hydrophobicity of functionalized QDs remain important concerns. Alternatively, research in heavy metal-free QDs is ongoing, and gradual but important progress has been made using the background and knowledge gained with Cd-based QDs. The main compositions of these alternative QDs are indium phosphide (InP), carbon (C), silver sulfide (Ag_2S), doped zinc chalcogenides (ZnS or ZnSe), silicon (Si), and ternary QDs such as silver indium sulfide ($AgInS_2$) and copper indium sulfide ($CuInS_2$). Overall, these QDs have shown lower toxicity with in vitro [70−73] and in vivo [73−76] studies when compared to Cd-based QDs composed of either CdSe or CdTe, enabling higher dosage concentration for multiple applications. A key finding of the in vivo studies has been that the accumulation and excretion rate are closely related to the surface nature and the hydrodynamic diameter of the QDs. In addition to low toxicity, these alternative QDs offer other features probing their specificity and multimodal capabilities. For instance, the enhanced Stokes shift from doped zinc chalcogenide QDs suggests the elimination of self-quenching caused by Förster energy transfer or reabsorption [77], which is potentially advantageous for biomedical imaging applications. Mn-doped core−shell $CuInS_2$−ZnS QDs have the potential to work as multimodal contrast agents, simultaneously using the QD emission and the paramagnetic nature of Mn for fluorescence and magnetic resonance imaging [72], respectively. Remarkably, negligible background signals and deeper tissue penetration of light in the NIR-II window

(1000−1700 nm) emitted by Ag_2S QDs, make them superior as contrast agents for in vivo imaging compared to QDs emitting in the NIR-I range (700−950 nm) [17,61,74]. A sharp contrast between the QD emission and tissue autofluorescence and/or scattering should allow high tumor-to-background contrast. Moreover, in vivo imaging by the multiphoton excitation technique is possible using carbon, Si, and doped zinc chalcogenide QDs, due to their characteristic large multiphoton cross sections. This results in two-photon-excited fluorescence from carbon QDs [73] and three-photon-excited fluorescence in the case of Si [76] and doped QDs [78], as illustrated in the Jablonski diagram from Fig. 6.3.

Recently, the characteristics of InP-based QDs have been significantly improved. Samsung Electronics demonstrated core−shell−shell InP/ZnSe/ZnS QDs with PL-QY ~ 100%, and FWHM of 35 nm at emission wavelength of 630 nm [15], achieving almost comparable properties to those of Cd-based QDs. However, the use of precursor tris(trimethylsilyl)phosphine (TMS3P) still poses hazard and instability issues during the synthesis of InP QDs. A relevant advantage of Cd-based QDs for high sensitivity multiplex imaging is their much wider emission range (coverage) compared to that of InP QDs. Overall, there are also important challenges for the heavy metal-free QDs which need to be overcome before they can fully replace Cd-based QDs. Other challenges include poor reproducibility, complex synthesis with no standard procedures, and the need for postsynthetic size refinement to obtain a narrow particle size distribution (small FWHM). Importantly, the use of the size-selective precipitation technique to narrow the FWHM discards a certain portion of the QDs in the raw solution, leading to low production yield of the QD synthesis.

6.4 Development and application of QD devices in photomedicine

6.4.1 QLEDs for photomedical application

6.4.1.1 Recent advances and records in red-emitting QLEDs

After the breakthrough in EQE was reported for type IV QLEDs in 2013 [36], many efforts were dedicated to find the possible causes of efficiency decay at high current densities, also known as “efficiency roll-off.” To date, the main mechanisms proposed for this roll-off behavior at high current density are: the quantum confined Stark effect (QCSE), the Auger recombination (AR), and the Joule-heat generation (J-HG). A study conducted by Shirasaki et al. [79] suggested that an electric-field-induced decrease in QD luminescence efficiency was responsible for the roll-off behavior, and the QCSE was used to predict the EQE roll-off of QLEDs. According to the QCSE, the internal charge accumulation and charge-up at the interfaces form an electric field that induces exciton dissociation. On the other hand, in the AR process the excess energy emitted by an electron−hole recombination is absorbed by a second electron that loses its additional energy in a series of collisions with the lattice and returns to the edge of the band. Both the QCSE and AR are related to

unbalanced charge injection and subsequent accumulation of charge carriers. Therefore, different strategies have been applied to improve the charge injection balance in QLEDs. In this regard, Bae et al. [80] fabricated QLEDs using CdSe−CdS−ZnCdS core−shell−shell QDs in order to partially inhibit the electron injection into the QDs. This strategy led to significant suppression of the roll-off behavior and simultaneous improvement of the EQE, eightfold the EQE of the core−shell QD-based LEDs. In order to improve the injection or avoid the excess of one type of charge carrier, other strategy being used is the addition of injection or blocking layers, respectively. For instance, Mashford et al. [36] implemented a thin layer of HAT-CN as a hole injection layer (HIL) to promote better charge injection balance into the QDs. Dai et al. [81] reported a red forward QLED with a thin PMMA layer inserted between the QD layer and the ZnO NPs ETL, which worked as an electron blocking layer. This thin dielectric layer weakened the electron transfer and improved the charge injection balance in the device, yielding an EQE of up to 20%. Subsequently, our group (2015) [14] reported a low roll-off inverted QLED that used a Cs_2CO_3 hole blocking layer between the ZnO NPs ETL and the QD layer. This red-emitting QLED demonstrated a high brightness of 1.65×10^5 cd m^{-2} at 1 A cm^{-2} and 5.8 V and EQE above 20% without light outcoupling. Ultimately, the excess J-HG at high current densities resulting from the nonradiative recombination current and leakage current, leads to the increase of the device temperature. Sun et al. [82] implemented two strategies to suppress thethermal-induced emission quenching. First, thermal stability of the QDs was improved by replacing conventional oleic acid ligands with 1-dodecanethiol. Then, the Joule heat generated at high current density ($\geq$2 A cm^{-2}) was effectively dissipated by using a sapphire-based substrate, which has a much higher thermal conductivity (42-fold) compared with glass. This research resulted in a green forward QLED with ultrahigh brightness of 1.6×10^6 cd m^{-2} at high current density ($\sim$3.9 A cm^{-2}) and EQE of 10%. With this last approach, it can be concluded that the technical causes of the *efficiency roll-off* behavior can be diverse based on the constituent materials, device architecture, and ultimately, the operating range.

In addition to the efforts for further improvement of the efficiency and operating lifetime, current developments are focused on the design of flexible QLEDs with multiple form factors, the substitution of Cd-based QDs in the devices, and the reduction of fabrication costs for commercialization. Recent and important advances have been achieved in each of these areas, and the recent progress in QLEDs with clinically relevant red emission wavelengths is summarized here. Remarkably, Ding et al. [83] reported a red inverted flexible QLED with EQE of 24.1%, which is the current record efficiency among all QLED devices. This bottom-emitting device used solution-processed silver nanowires (Ag NWs) embedded in a polyimide film as the flexible substrate, which simultaneously worked as transparent conductive electrode and light extraction medium. Thus, the improvement of the light outcoupling efficiency with respect to indium tin oxide (ITO) on-glass substrates enabled a record EQE above the intrinsic limit. Most recently, Samsung Electronics (2019) [15] reported a red forward QLED using InP/ZnSe/ZnS core/shell/shell QDs, which exhibited a maximum EQE of 21.4%, peak brightness of 1×10^5 cd m^{-2}, and T_{50} of 1×10^6 h at an initial

luminance of 100 cd m^{-2}. Therefore this device represents a record in performance for heavy metal-free QLEDs reported to date. Given the importance of cost-effective high-volume manufacturing, solution-processed QLEDs are also of great interest. In this regard, our group reported a QLED with record brightness of 1.46×10^5 cd m^{-2} [84] among the red solution-processed QLEDs with inverted structure. Other electroluminescent devices using emerging perovskites as emissive materials have also been reported. However, the current record for red perovskite QLEDs (EQE up to 21.3%) still have very low brightness ($\sim 10^2$ cd m^{-2}) and extremely short lifetime [85,86]. Table 6.1 summarizes the performance and fabrication techniques of current record QLEDs emitting at red wavelengths relevant for application in photomedicine. The presented QLEDs hold the record in either luminance, EQE, or operating lifetime depending on structure and fabrication techniques.

In the following, we discuss the advances achieved by our group in the development of red-emitting QLEDs with potential application in the photomedicine field. To date, all our QLED based in vitro studies in PDT and PBM have been conducted

Table 6.1 Red-emitting quantum dot light-emitting diodes (QLEDs) with record in luminance, efficiency, or lifetime according to structure and fabrication techniques.

QLEDs	V_{on} (V)	λ_{peak}/ FWHM (nm)	L_{max} (cd m^{-2})	EQE_{max} (%)	T_{50} @ 100 cd m^{-2} (h)	Record category
Cao et al. [23]	1.7	631/21	$\sim 3 \times 10^4$	15.1	**2.2×10^6**	All rigid red QLEDs
Ding et al. [83]	1.95	628/ ~37	~5000	**24.1**	–	All flexible red QLEDs
Chiba et al. [85]	2.8	653/33	500	**21.3**	0.083	Perovskite red QLEDs
Won et al. [15]	~1.9	630/35	**1×10^5**	**21.4**	1×10^6	Cd-free red QLEDs
Shen et al. [19]	<2	~602/ 27	**3.56×10^5**	21.6	1.6×10^6	All forward red QLEDs
Chen et al. [84]	2.0	629/25	**1.46×10^5**	~6.0	–	Solution-processed red QLEDs (inverted)
Triana et al. [87]	1.9	627/29	**4.2×10^4**	8.3	–	Flexible red QLEDs with large pixel (8 mm^2)

The record values are in bolt.
EQE, external quantum efficiency; *FWHM*, full width at half maximum.

using rigid devices. In general, the characteristics of the on-glass inverted QLEDs used for the in vitro studies were narrow FWHM (down to ~22 nm), high PD (up to 25 mW cm^{-2}), low turn-on voltage (1.7 V), and homogeneous illumination. The multilayer structure of the QLEDs was as follows: ITO/ZnO NPs:Cs_2CO_3/CdSe−ZnS−CdZnS QDs/Spiro-2NPB/HAT-CN/Al, were the core−shell−shell QDs work as the emissive layer. These devices were fabricated in an inert atmosphere (N_2 filled glove-box), using both spin-coating and thermal evaporation for deposition of the lower and upper layers, respectively. Before exposure to ambient conditions, the devices were encapsulated using a glass cover with UV-curable epoxy and a getter sheet. The fabrication and full characterization of devices with similar structure were first reported in 2015 [14], demonstrating a record brightness of 1.65×10^5 cd m^{-2} at 5.8 V, which corresponded to pixel size of ~1 mm^2.

Subsequently, our group developed other QLED devices in an effort to obtain cost-effective, stable, flexible QLEDs in the medium run. First, all-solution processed QLEDs were made by spin-coating using the structure shown in Fig. 6.4A: ITO/ZnO NPs:Cs_2CO_3/CdSe−ZnS−CdZnS QDs/poly-TPD/PEDOT:PSS/Al. Essentially, the materials of the HTL and the HIL were replaced by solution-processed polymers in these devices, poly-TPD and poly(ethylenedioxythiophene)/ polystyrenesulfonate (PEDOT:PSS), respectively. Enhanced coverage and uniformity of the hydrophilic PEDOT:PSS-based HIL on hydrophobic poly-TPD was enabled by doping PEDOT:PSS with nonionic surfactant Triton X-100, as illustrated in Fig. 6.4B and C. In addition, the mixed ZnO NPs:Cs_2CO_3 layer efficiently improved the electron injection into the QD emissive layer while blocking holes. The first device of this type reported in 2018 [88] had a peak brightness of 7.54×10^4 cd m^{-2} at 7.7 V and peak EQE of 3.1% (0.8 mm^2 pixel). Later, the performance of these all-solution processed QLEDs was improved by imprinting of speckle image holography (SIH) structures on the poly-TPD HTL surface [84]. A scheme of this method and the resulting pattern on the polymer layers are shown in Fig. 6.4D and E, respectively. The devices with imprinted random grating structures reached a luminance of up to 1.46×10^5 cd m^{-2} at 8 V, with peak EQE approximately twice as high as that of previous devices with planar architecture. Remarkably, these devices have the current record brightness for red-emitting solution-processed QLEDs with inverted structure as mentioned before (see Table 6.1); the corresponding EL spectrum and $J-L-V$ curves are shown in Fig. 6.4F and G, respectively. It was found that the imprinting method simultaneously helped extracting the trapped photons via the SIH structure and also improved the device performance through an imprinting-induced film-compression mechanism. Solution-processed materials are compatible to cost-effective high-volume manufacturing via roll-to-roll (R2R) processing, and all-solution processed QLEDs are preferred for a more cost-effective photomedical application.

Recently, our group developed flexible QLEDs [25,87] with same structure as that of the on-glass QLEDs previously used for photomedical testing. In the latest report [87], the performance of the flexible QLEDs was improved following systematic steps. Briefly, we used ITO on polyethylene naphthalate (PEN) substrates with low sheet resistance (6−8 Ω sq^{-1}), optimized conditions for plasma treatment

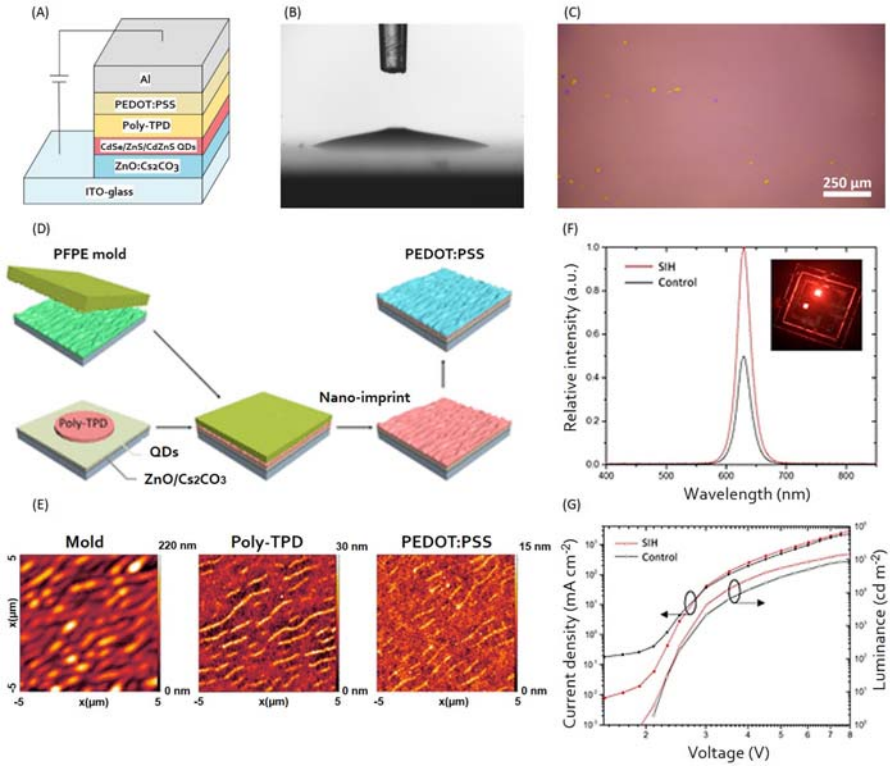

Figure 6.4 (A) Cross-sectional scheme of the inverted red-emitting QLEDs fabricated by all-solution processing. (B) Contact angle image of a PEDOT:PSS: Triton X-100 (500:1) droplet on a poly-TPD surface. (C) Optical microscopy image of spin-coated PEDOT:PSS: Triton X-100 (500:1), demonstrating full coverage of the poly-TPD surface. (D) Schematic illustration of the fabrication process of red-emitting QLEDs with imprinted SIH nanostructures. In the SIH-QLED fabrication, a PFPE stamp was cast from the SIH sample and imprinted onto the poly-TPD layer. (E) AFM images of the PFPE mold, the patterned poly-TPD layer, and the patterned PEDOT:PSS layer on ITO glass substrates. (F) Relative EL spectra at 3 V. (G) *J*−*L*−*V* characteristic curves of the SIH-QLED versus the planar QLED (control). *AFM*, atomic force microscopy; *EL*, electroluminescence; *PEDOT:PSS*, poly(ethylenedioxythiophene)/polystyrenesulfonate; *poly-TPD*, poly(4-butylphenyl-diphenyl-amine); *PFPE*, perfluoropolyether; *QLED*, quantum dot light-emitting diode; *SIH*, speckle image holography.

Source: (A−C) Reproduced by permission from M.A. Triana, H. Chen, D. Zhang, R.J. Camargo, T. Zhai, S. Duhm, et al., Bright inverted quantum-dot light-emitting diodes by all-solution processing, J. Mater. Chem., C 6 (28) (2018) 7487−7492 of The Royal Society of Chemistry. (D−G) Reprinted with permission from H. Chen, Z. He, D. Zhang, C. Zhang, Y. Ding, L. Tetard, et al., Bright quantum dot light-emitting diodes enabled by imprinted speckle image holography nanostructures, J. Phys. Chem. Lett. 10 (9) (2019) 2196−2201. Copyright (2019) American Chemical Society.

and baking of the substrates before processing, and barrier lamination on the top and bottom of the QLEDs for full encapsulation. The barrier film used for encapsulation consisted in an organic coating for planarization stacked between two inorganic layers of amorphous hydrogenated SiN, provided by the Holst Centre [89]. These fabrication conditions enabled flexible QLEDs with high peak luminance of 4.22×10^4 cd m^{-2}, long shelf life, and high peak EQE of 8.3% (included in Table 6.1), demonstrated for pixels of 8 mm^2. Remarkably, the maximum PD of $\sim$71 mW cm^{-2} reached at only 5.8 V largely surpasses the range normally used for low-irradiance PDT and PBM treatments ($\sim$2−10 mW cm^{-2}). In addition, these flexible QLEDs showed low *efficiency roll-off* over the measured range, and the low driving voltage could be supplied from a small battery pack. A lamination sketch, EL spectrum, EQE curve, $J-L-V$ curves, and picture of the flexible QLED are shown in Fig. 6.5A−D, respectively. In addition, the picture from Fig. 6.5E shows a bent flexible QLED with a larger emitting area of 4 cm^2 made with the same process and structure [18,90]. This QLED was lightweight ($\sim$1.4 g) and showed good luminance uniformity over the emitting area (standard deviation

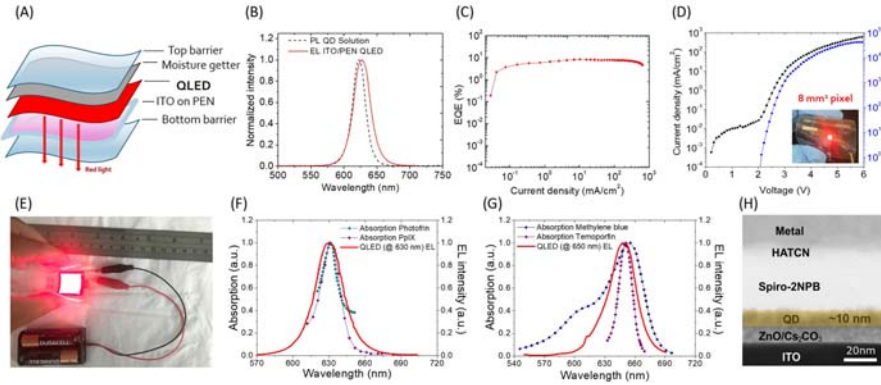

Figure 6.5 (A) Sketch of the flexible QLED sandwiched between two laminated barrier layers and deposited on an ITO-PEN substrate. (B) EL (emission peak at 627 nm) and PL spectra of the flexible QLEDs and QDs, respectively. (C) EQE curve. (D) $J-L-V$ characteristic curves of the flexible QLEDs with record brightness. Inset: the corresponding flexible QLED with 8 mm^2 pixel driven at 3.5 V in air. (E) Picture of flexible QLED with large emitting area (2×2 cm^2) driven at 3 V in air. Overlapping of the (F) absorption spectra of Photofrin and PpIX and the EL spectrum of 630 nm QLED. (G) Absorption spectra of temoporfin and MB and the EL spectrum of 650 nm QLED. (H) Cross-sectional TEM image of a typical QLED showing a QD layer with thickness of approximately 10 nm. *EL*, electroluminescence; *EQE*, external quantum efficiency; *ITO*, indium tin oxide; *MB*, methylene blue; *PEN*, polyethylene naphthalate; *PL*, photoluminescence, *TEM*, transmission electron microscopy; *QD*, quantum dot; *QLED*, quantum dot light-emitting diode.
Source: (A−D) M.A. Triana, S. Wu, Y. Dong, P-105: Bright, large pixel, flexible quantum-dot light-emitting diodes for photomedicine, in: SID Symposium Digest of Technical Papers, vol. 51, 2020, pp. 1748−1751, John Wiley & Sons. Copyright (2020) Wiley-VCH Verlag GmbH & Co. KGaA, Weinheim.

of ~17%). Moreover, the maximum PD for safe operation (2.8 mW cm^{-2} at 4.5 V) was sufficient for low irradiation phototherapy such as mPDT, regardless of the 50x increase in emitting area with respect to 8 mm^2 pixels. Finally, both flexible devices showed a good shelf life after being stored in an inert atmosphere (≥1 month), however, their PD exhibited 20% decay after 1 week in ambient conditions. Therefore, further optimization of the encapsulation is needed before these flexible QLEDs can be used in photomedical testing.

Although the stability and operating lifetime for photomedical applications of flexible QLEDs are reasonably less demanding, the bottom and top lamination strategy cannot guarantee enough stability in ambient air, most likely due to lateral permeation. A highly reliable thin film encapsulation (TFE) typically consists in a hybrid organic−inorganic alternating multilayer barrier, conducted by chemical vapor deposition (CVD) or atomic layer deposition (ALD) of nanoscale inorganic layers alternated with solution deposition of polymer-based layers. When TFE is conducted immediately after the device fabrication the water and oxygen transmission rates can reach very low values. A suitable approach for flexible QLEDs can be the integration of a multilayer barrier between the conductive electrode and the plastic substrate, instead of using bottom lamination which can lead to lateral permeation. For example, multilayer barriers were deposited on plastics by ALD and subsequently used as bottom substrates and top barriers of flexible OLEDs [91]. This resulted in devices with low water transmission rate (WVTR ~10^{-6} g m^{-2} day^{-1}) and long operating lifetime in air and water. Importantly, flexible top barrier lamination is compatible with high-volume manufacturing through R2R processing, and due to the similar nature of OLEDs and QLEDs, this mature encapsulation strategy could be adopted with QLEDs. However, TFE by CVD and ALD still has a low production throughput. The use of solution-processed materials such as reduced graphene oxide for encapsulation [92−94] and hydrophobic polymers for planarization [95,96], could make the encapsulation simpler and more promising for the development of cost-effective flexible QLEDs as disposable light sources in ambulatory PDT and PBM.

In addition to the previous improvements in fabrication cost, performance, and form factor of the QLEDs, our group has demonstrated that controlled spectra overlapping for targeted phototherapy is possible by simply tuning the peak emission wavelength of the QDs. QDs with high PL-QY, narrow emission spectra (FWHM < 30 nm), and different peak emission wavelengths were precisely obtained by tuning the QDs' size during synthesis. Subsequently, QDs with emission peaks at 625 and 646 nm were used to fabricate QLEDs. By considering the ~4−5 nm redshift observed between the EL spectrum of QLEDs and the PL spectrum of the corresponding QDs solution, the QLEDs obtained had emission wavelength around 630 and 650 nm, respectively. This redshift is ascribed to the electric-field-induced Stark effect observed in closely packed QD solid films. QLEDs with EL peaks at ~630 nm match well with porfimer sodium (Photofrin) and protoporphyrin IX (PpIX), while QLEDs with EL peak at ~650 nm can be used for excitation of temoporfin and methylene blue (MB), respectively. Photofrin (abs. peak @ 630 nm) is approved by the Food & Drug Administration (FDA) and used for various PDT treatments of cancer, while PpIX (fourth Q band ~630 nm)

is an endogenous PS that accumulates after administration of aminolevulinic acid (ALA). This PS has been developed for a wide range of applications and it is FDA approved for PDT treatment of actinic keratosis. Temoporfin (652 nm) is a PS used for PDT treatment of squamous cell carcinoma of the head and neck, and MB (max. abs. peak $\sim$655 nm) is a PS used for antibacterial and antiviral PDT. Overlapping of the QLEDs EL spectra and absorption spectra of the PSs is shown in Fig. 6.5F for Photofrin and PpIX, and Fig. 6.5G for temoporfin and MB. Importantly, QLEDs with EL peak centered at $\sim$650 nm can also be used for PBM treatment paradigms to promote wound healing, among other applications. Although the absorption of endogenous cytochrome c oxidase is wide, 650 nm is in the wavelength range that has been demonstrated to be particularly efficacious.

Finally, an important concern under current debate is the potential toxicity of the QDs composition, specifically the toxicity effect of Cd-based QDs. In consequence, the Restriction of Hazardous Substances (RoHS) directive restricted the Cd content of QD conversion materials in display to $<0.2\ \mu g\ mm^{-2}$ of the light emitting area [97]. Although toxicity might be critical when using individual QDs as theranostic agents, the use of Cd-based QLEDs for external applications does not pose a critical risk. Some structural reasons that make Cd absorption or ingestion very unlikely during QLED irradiation of the body's skin or the oral cavity are as follows. The deep position of the QD layer in the QLED stack and the encapsulation can effectively prevent leakage of any toxic Cd^{+2} ions. In addition, noncontact irradiation of soft tissues inside the oral cavity can be performed by supporting the QLED inside a transparent plastic holder. To further support this rationale, we also estimated the Cd content in the emissive area of our QLEDs using transmission electron microscopy (TEM). From the cross-sectional images obtained with TEM (Fig. 6.5H), the thickness of the QD layer in our devices was approximately 10 nm. Assuming that the spherical QDs were 100% solid Cd, we estimated a mass Cd content per emissive area of $0.0453\ \mu g\ mm^{-2}$, which is far below the RoHS restriction. Most importantly, this value was overestimated considering the other elements in the core−shell−shell structure of the QDs (CdSe−ZnS−CdZnS) and the lower density of QD layers compared with bulk crystalline layers. Therefore the estimated value was likely much higher than the actual Cd concentration. On the other hand, assuming the ingestion of the full Cd content in a 25-mm^2 pixel QLED (2.16 μg) during an oral treatment session, the dose corresponding to a 80-kg person [$\sim 0.03\ \mu g\ (kg\ day)^{-1}$] would also be far below the EPA limit [$1\ \mu g\ (kg\ day)^{-1}$] [98], which corresponds to the oral minimal risk level. In the near future, positive data collected after preclinical trials in animals is expected to encourage these claims, although the transition to Cd-free QLEDs is also feasible as the performance of Cd-free QDs becomes satisfactory.

6.4.1.2 *Radiometric parameters for QLED performance and phototherapy administration*

The parameters and efficiencies for evaluation of the QLED performance depend on the specific application field. Therefore, in the case of QLEDs intended for

application in display, widely adopted parameters are brightness or luminance (L) in terms of cd m^{-2}, color purity related to the FWHM of the EL spectrum, and the current efficiency (CE) with units of candela/ampere (cd A^{-1}). Nits are also commonly used units for the brightness of displays, with 1 nit $= 1$ cd m^{-2}. When it comes to lighting applications, the luminous power efficiency (lm W^{-1}) of the QLED is a more suitable efficiency, for which lumen (lm) is the unit of luminous flux and watt (W) is the unit for electric power going through the QLED. The equivalent units for luminance in terms of lumens are lm m^{-2} sr^{-1}, with 1 lm m^{-2} $sr^{-1} = 1$ cd m^{-2}. Most importantly, candelas and lumens are photometric units weighed according to the spectral response of the human eye, with green light at 555 nm having the greatest weight, as it stimulates the eye more than other visible light of equal radiometric power. Accordingly, the CE is only applicable to the visible range of light and can reach high values in optimized green-emitting QLEDs ($\sim$40–80 cd A^{-1}). Therefore this efficiency is particularly relevant for display applications, for which a device output is rated according to the human eye response.

On the other hand, the application of QLEDs as light sources in photomedicine requires the use of different terminology and parameters, in order to evaluate ideal and efficient irradiation of tissues and cells using a wider range of light, including nonvisible light in the NIR range. For example, a narrow emission bandwidth is an important characteristic of the light source for efficient use of photons and is a more suitable expression in photomedicine than color purity. In addition, phototherapy uses radiometric parameters instead of photometric parameters, since light delivery on a specific target is measured in terms of energy and its quality does not depend on the eye responsivity to light. Therefore ideal and efficient irradiation with visible and nonvisible light in phototherapy depends on parameters such as the excitation energy of the PS (J or eV), irradiance or fluence rate (I or ϕ) (W cm^{-2}), fluence (F) (J cm^{-2}), and exposure time (t) (s). The last parameters are correlated as follows:

$$F = I * t \tag{6.2}$$

or

$$F = \phi \times t \tag{6.3}$$

where F corresponds to total fluence or delivered dose, and t is the irradiation time. Two equations for the fluence are distinguished here, since either the irradiance I or the fluence rate ϕ must be used depending on the location of the target. Specifically, the irradiance corresponds to the incident power on an area at a superficial target, such as the skin and the oral mucosa. Meanwhile, the fluence rate considers the optical power being delivered inside a sphere and crossing the surface unit area of the sphere in all directions. Therefore, the fluence rate applies to light sources inside volume targets, such as tumors, where both the absorption and scattering effects are important. A scheme representing light propagation in biological tissue is shown in Fig. 6.6A. Accordingly, the evaluation of the superficial

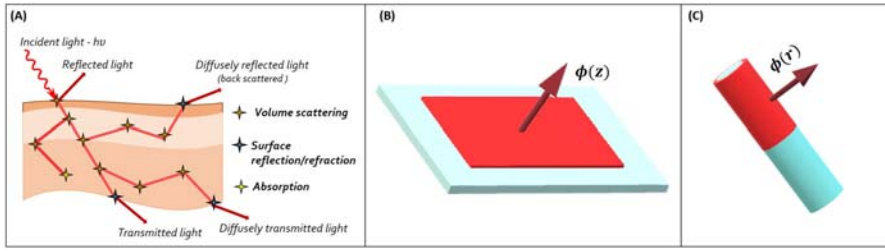

Figure 6.6 (A) Multiple phenomena occurring to photons when they hit biological tissue: direct and diffuse reflection, direct and diffuse transmission, scattering and absorption. Elaborated according to [38]. 3D representations of flexible QLEDs with (B) planar and (C) cylindrical form factor. *3D*, Three-dimensional; *QLEDs*, quantum dot light-emitting diodes.

irradiance and the fluence rate at the target depth are critical to determine the right amount of energy for treatment. In particular, the light propagation inside biological tissue is a critical parameter to predict the right fluence for interstitial and intraoperative PDT treatments. The finite element method (numerical model) and the Monte Carlo method (algorithm model) are often used to compute the light propagation in complex tissues and heterogeneous media, respectively. However, there are analytical expressions that can provide a quick estimation of the fluence rate distribution in a homogeneous medium depending on the geometry of the light source. Here we present equations derived from the Boltzmann transport equation for simple light source geometries, which represent the flexible QLEDs with flat and cylindrical form factor illustrated in Fig. 6.6B and C. The equations describe the steady-state diffusion of light from a planar source and a line source using 1D planar diffusion and 2D cylindrical diffusion, respectively [99].

$$\phi(z) = P_{pl}\frac{e^{-z/\delta}}{2\mu_a\delta} \tag{6.4}$$

$$\phi(r) = P_{cyl}\sqrt{\frac{2\delta}{\pi r}}\frac{e^{-r/\delta}}{2\pi\mu_a\delta^2} \tag{6.5}$$

where z and r correspond to the distance between the source and the position of the point where the fluence rate is estimated. Importantly, the application of these equations from the diffusion theory is appropriate when the distance from the light source is longer than the MFP' (over several mm), and the point is inside the boundaries of the homogeneous medium. P_{pl} is the power for planar geometry (W cm^{-2}); P_{cyl} is the power for cylindrical geometry (W cm^{-1}); δ is the optical penetration depth (cm), $\sqrt{D/\mu_a}$; D is the diffusion coefficient (cm); μ_a is the absorption coefficient (cm^{-1}); MFP′ is the transport mean free path (cm), $1/(\mu_a + \mu_s')$; μ_s' is the reduced scattering coefficient (cm^{-1}), $\mu_s(1-g)$; μ_s is the scattering coefficient (cm^{-1}); g is the anisotropy parameter [ ].

On the other hand, the fluence equation for surface irradiation Eq. (6.2) can be directly applied when the distance between light source and target is fixed, and when the PD output of the light source is stable over the treatment time. If the power of the light source has a gradual or exponential decay over time, the correct total fluence must be integrated from the calibrated curve: I versus t. Here, the PD output is the total optical power delivered per unit area ($\mathrm{W\,cm^{-2}}$) by the light source at certain driving voltage. In the case of collimated lasers, the PD is obtained as the measured power divided by the measured beam area of the laser. In the case of large-area flat QLEDs, the PD can be calculated from the measured radiance R ($\mathrm{W\,cm^{-2}\,sr^{-1}}$) and using the following expression for Lambertian sources with homogeneous light distribution:

$$\mathrm{PD} = \pi \times R \tag{6.6}$$

The measured radiance counts for the radiant intensity emitted from a known unit area of the light source. It is worth noting that the PD thus calculated corresponds to the irradiance "at skin" (max. available) when the light source is in direct contact with the target. This is important as a reference considering the variation of the irradiance with the distance between the target and the light source.

Regarding the efficiency of the QLED device, the EQE is not relative to eye sensitivity and is probably the most general efficiency for use in any field. The EQE counts for the total output of photons across the emission spectrum (visible and nonvisible range) relative to the total amount of electrons injected into the QLED device $\left(N_p/N_e\right)$. A normal experimental setup for the measurement of the EQE requires complex and expensive components such as integrating spheres and monochromators. Nevertheless, the elementary approach is a widely used and cost-effective method for calculation of the EQE (with moderate deviation), which can be applied to LED sources with nearly Lambertian beam distributions. This method only requires the measurement of the EL spectrum and the characteristic curve $R{-}J$ or $L{-}J$ of the QLED device. The calculation of the output optical power of the light source will then depend on the characteristic curve obtained, that is, on whether the radiance or luminance was measured. When the radiance is measured, the total number of photons emitted $\left(N_p\right)$ can be obtained by integration over the emission range as follows:

$$N_p = \int_{w1}^{w2} \frac{\pi R(\lambda)\lambda}{hc} d\lambda \tag{6.7}$$

where $\pi R(\lambda)$ and hc/λ are the PD and the energy of a photon at certain wavelength, respectively. In addition, the total radiance (R_t) can be expressed as

$$R_t = \int_{w1}^{w2} R(\lambda) d\lambda = \kappa \int_{w1}^{w2} I(\lambda) d\lambda \tag{6.8}$$

where $I(\lambda)$ is the relative EL intensity and κ is a constant. Then combining Eqs. (6.7) and (6.8), N_p can be rewritten as

$$N_p = \frac{k\pi}{hc}\int_{w1}^{w2} I(\lambda)\lambda d\lambda \tag{6.9}$$

The constant κ can be directly calculated from Eq. (6.8), after the measurement of R_t at certain current density (J) and the numerical integration of $I(\lambda)$ over the emission range of the EL spectrum. Finally, the expression for the EQE obtained by replacing N_p and the number of injected electrons $N_e = JA/q$ is as follows:

$$\mathrm{EQE} = \frac{k\pi q}{hcJA}\int_{w1}^{w2} I(\lambda)\lambda d\lambda \tag{6.10}$$

where J, A, and q are the current density, the emissive area of the device, and the electron charge, respectively. This equation can also be solved by numerical integration of the product $I(\lambda)\lambda$ using the $I(\lambda)$ values obtained from the EL spectrum.

An equation for monochromatic light sources to convert brightness or luminance to radiance is as follows:

$$R = \frac{L}{K \times V(\lambda)} \tag{6.11}$$

$$V(\lambda) = 1.019e^{-285.4(\lambda-0.559)^2}$$

where the units of R and L are (W m^{-2} sr^{-1}) and (cd m^{-2}), respectively. K is a constant equal to 683 lm W^{-1} and $V(\lambda)$ is the empirical function of the photopic response. $V(\lambda)$ gives the spectral response of the human eye to wavelengths in the visible range. Thus this function reaches its maximum value (equal to 1) at 555 nm, the wavelength at which the human eye is most sensitive to light, as mentioned before.

For nonmonochromatic light sources, conversion from luminance to radiance requires more rigorous calculation using the EL spectrum data. According to Eq. (6.11), integration over the emission wavelength range gives the following expression:

$$R = \frac{1}{683}\int_{w_1}^{w_2} \frac{L(\lambda)}{V(\lambda)} d\lambda \tag{6.12}$$

In addition, the absolute luminance measured can be expressed as

$$L_t = \int_{w_1}^{w_2} L(\lambda)d\lambda = \alpha\int_{w_1}^{w_2} I(\lambda)V(\lambda)d\lambda \tag{6.13}$$

where α is a constant. Then combining Eqs. (6.12) and (6.13), R can be rewritten as

$$R = \frac{\alpha}{683}\int_{w_1}^{w_2} I(\lambda)d\lambda \; = \; \int_{w1}^{w2} R(\lambda)d\lambda \tag{6.14}$$

The value of α is calculated from Eq. (6.13), replacing the absolute luminance (L_t) measured and by numerical integration of the product $I(\lambda)V(\lambda)$. Then the equivalent radiance can be directly computed from Eq. (6.14).

However, simple conversion using Eq. (6.11) is also a good approach for a light source with a narrow emission spectrum and unimodal Gaussian distribution. In this case, $V(\lambda)$ is calculated using the corresponding peak wavelength of the EL spectrum. For instance, a calculation of the radiance using Eq. (6.11) led to a deviation of $\sim$16% with respect to Eq. (6.14) for an EL spectrum with FWHM of 29 nm. When data unavailability and time consumption are limiting factors, a moderate standard deviation is acceptable.

Ultimately, when the QLED emits only in the visible range and its characteristic curve is measured as $L{-}J$ (using a luminance meter), an expression for the N_p and the EQE can be similarly obtained by combination of Eqs. (6.7) and (6.14):

$$N_p = \frac{\alpha\pi}{683hc}\int_{w_1}^{w_2} I(\lambda)\lambda d\lambda \tag{6.15}$$

$$EQE = \frac{\alpha\pi q}{683hcJA}\int_{w_1}^{w_2} I(\lambda)\lambda d\lambda \tag{6.16}$$

6.4.2 QLEDs for PDT and PBM

6.4.2.1 Emergence of QLEDs as alternative photomedical light sources

Regardless of the remaining challenges for commercial application, the QLED is a growing technology, and development on new features of QLEDs such as lightweight, thinness, and flexible form factors have encouraged the application of QLEDs in other fields. Remarkably, QLEDs can fit the light source profile currently required for widespread clinical adoption of PDT and PBM. An ideal light source to enable wider application of phototherapies must have narrow emission spectrum matching the absorption peaks of PSs, relatively high PD, low heat radiation, and flexible form factors with homogeneous emission. Wider application will also require a lower cost per treatment for adoption of PDT and PBM by small clinics and low-resource populations. The rationale of the technical requirements is as follows. By matching the peak emission of the light source with the absorption peak of the PS, the phototherapy can take more advantage of photons and be more

effective for treatment at a specific excitation wavelength. Moreover, a high overlap of the mentioned spectra can reduce heat generation through thermal loss of photons, thus avoiding pain and discomfort to patients. A relatively high PD can guarantee sufficient energy for excitation of the PS. All these positive effects are improved when each condition is combined with a narrow emission bandwidth. The flexibility, lightweight, and thinness are all required features for an ergonomic photomedical light source, which enable practical "at home" and ambulatory treatment of the skin and the oral cavity. Ultimately, a light source with homogeneous large emission area can guarantee a more uniform irradiation at all points of the target, eliminating the need for multiple sweeps over a large target area.

There is an urgent need for suitable light sources in the marketplace that can fulfill the profile for widespread adoption, considering the quality of life improvement of patients and the high benefits of phototherapy. At present, commercially available light sources used for PDT and PBM in clinical settings are lasers and inorganic LEDs. Lasers have been widely used in medicine and offer a broad PD range ($>100\ \text{mW cm}^{-2}$) with very narrow FWHM (<5 nm). However, the main drawbacks for wide adoption of laser-based PDT and PBM are the high cost per treatment (equipment, operation, and trained staff), the need for optical fibers and diffusive optics, the bulkiness of the laser system, and frequent in-office visits. On the other hand, inorganic LEDs have highly stable output power ($10-100\ \text{mW cm}^{-2}$), narrow FWHM (15−20 nm), and much lower cost per treatment compared to lasers. Nevertheless, LED arrays are normally rigid and heavy, and the irradiated area is inhomogeneous due to the point-source nature of LEDs [100]. Consequently, the limitations of these commercial light sources motivated the search for alternative devices, and current research is focused on two relevant candidates: QLEDs and OLEDs.

OLEDs were first proposed as light-emitting bandages for PDT in 2009 by two companies: Polymertronics and Lumicure [101]. The same year, Samuel's group reported an open pilot study of ambulatory PDT using a low-irradiance OLED for treatment of nonmelanoma skin cancer [102]. ALA-assisted PDT resulted in clearance of 7 out of 12 patients. In addition, the comparison to inorganic LED-based PDT ($\sim 80\ \text{mW cm}^{-2}$) demonstrated that the OLED-based PDT ($\sim 5\ \text{mW cm}^{-2}$) was convenient for "at home" treatment and less painful, eliminating the need for analgesia or skin cooling. After a long while (5−6 years), two more OLED-based photomedical studies were reported in 2015. In one work, the Anders group proposed OLED-based PBM for wound healing stimulation for the first time [103]. The authors used in vitro and in vivo models to investigate the effects of OLED radiation on cellular function and cutaneous wound healing, respectively. The effects of these devices on enhancing diabetic wound healing were comparable to those observed with in vivo laser-based experiments ($\text{PD} \leq 10\ \text{mW cm}^{-2}$ and $F \leq 5\ \text{J cm}^{-2}$). In the other work, Guo et al. [104] reported on OLED-based mPDT for glioma mouse models. The authors demonstrated a longer survival time in a mouse model with glioblastoma after a single ALA dose and OLED irradiation at a low fluence rate (PD: $3\ \text{mW cm}^{-2}$ and F: $40\ \text{J cm}^{-2}$) for 3.7 h. Regardless of its promising debut on the field, the OLEDs used for preliminary and subsequent

photomedical studies were still rigid (on-glass) and had broad emission spectra (>30 nm) falling out of the desirable range. Importantly, a broad emission spectrum can have two main negative effects. One is the sum of simultaneous effects masking important individual effects at specific wavelengths. The second negative effect is the resultant lower power delivered at the desired wavelength, leading to reduced energy for excitation of the PS. Accordingly, the interrupted report of OLED-based studies during this first stage could be in consonance with the development rate of the OLED technology.

In 2017 QLEDs were proposed by our group as alternative light sources for PDT and PBM for the first time [24]. These and subsequent QLED-based in vitro studies showed satisfactory results, comparable to those of commercial LED-based experiments. The results included destruction of cancer cells with PDT [18,24,90], cell metabolism increase [24,105] and cell migration promotion for wound healing [106] with PBM, and bacteria killing with aPDT [25]. Consequently, our QLED work stimulated the recent revival of the OLED photomedicine research that demonstrated important technical advances in comparison with the OLED devices used in early photomedical studies. The current leading groups in the OLED-based photomedicine research are the Samuel group and the Choi group, a leading flexible OLED team. For instance, the Choi group developed adhesive transferable OLEDs with ultrathin thickness (10 μm) resulting in multiple form factors, narrower emission bandwidth (down to 34 nm), and emission wavelength tunability [91]. In addition, Samuel's group implemented a p−i−n (p-doped, intrinsic, n-doped) structure to enable enhanced conductivity of the transport layers and subsequent higher PD at low driving voltage. This work resulted in a flexible red OLED with large pixel (4 cm^2) and PD up to 9.85 mW cm^{-2} at 3.82 V [107]. Both research groups implemented the microcavity effect by adjusting the thickness of the HTL to tune the peak emission wavelength of the red flexible OLEDs over a wide range. Regardless of these advances, the PD peak of OLEDs was in general below the maximum of red QLEDs with a similar peak emission wavelength. Conventionally, OLEDs with fluorescent or phosphorescent emitters cannot achieve high PD in the deep red region due to significant *efficiency roll-off* at high current density [108], and the lack of efficient deep red emitters with narrow emission spectra [109].

On the other hand, the intrinsic characteristics of flexible QLEDs promise full realization of the ideal light source profile previously described. The satisfactory results found for QLED-based PDT and PBM studies are also one step toward real application. Technically, flexible QLEDs can comply not only with the form factors offered by the mature flexible OLEDs but also can overcome the PD and broad emission spectrum limitations of OLEDs. It is worth noting that the narrower bandwidth and higher PD at red wavelengths of QLEDs might be even more relevant for actual human trials, in which the light reflectance of the skin, subsurface scattering, and diffuse scattering inside tissue are important. The recent demonstration of flexible QLEDs by our group [26,87], with large pixel (8 mm^2), high-PD ($\sim$71 mW cm^{-2} at 627 nm), narrow FWHM (27 nm), turn-on voltage of 1.9 V, and

EQE up to 8.3%, promise a competitive performance for efficient photomedical application. Importantly, a closed-packed array of these pixels can uniformly irradiate over the target surface, similarly as using a single larger pixel. It is also worth noting to highlight the advantages intrinsic to QDs. These properties are the size-tunable emission wavelength, stability, and easy processability, which result attractive for wide emission wavelength coverage and low-cost fabrication of QLEDs, respectively. The emission wavelength tuning and narrow emission spectrum are possible simply by controlling the conditions of the QDs' synthesis, eliminating the need for additional engineering during the QLED fabrication.

A detailed discussion of the preliminary QLED-based in vitro studies, in parallel with recent OLED-based studies in photomedicine, is given in the next section.

6.4.2.2 QLED-based in vitro studies

The first QLED-based photomedical studies reported in 2017 presented results on PDT and PBM in vitro tests [24,105]. The cross-sectional structure, EL spectrum, and design pattern of the red-emitting QLEDs used for all in vitro testing are shown in Fig. 6.7A–C, respectively. A typical on-glass QLED had 2×2 pixels (16 mm^2 each), as shown in inset of Fig. 6.7B and in Fig. 6.7C. Fig. 6.7D shows a setup of cell cultures for in vitro experiments with bottom QLED illumination.

For the PBM study, three cell lines were cultured: a human epithelial cell line (Hep-2 cells) and two murine fibroblast cell lines (L929 and 3T3). QLED irradiation of the culture wells was performed to deliver 4 J cm^{-2} in 10 min at $\sim$8 mW cm^{-2}. For comparison, a parallel PBM experiment was performed with a commercial inorganic LED (Quantum Devices, Barneveld, WI), and the irradiation conditions were similar (4 J cm^{-2} in 10 min) except for the peak emission wavelength of the LED (670 nm). Cell metabolism was assessed by 3-(4,5-dimethylthiazol-2-yl)-2,5-diphenyltetrazolium bromide (MTT) assay, a common colorimetric assay to evaluate cell metabolic activity at 24 h postirradiation. QLED photoirradiation successfully increased the cell metabolism for the three cell lines HEp-2, L929, and 3T3, by 27.9%, 12.5%, and 26.2%, respectively, as compared to nonphotoirradiated control cultures. The bar chart in Fig. 6.7G summarizes the results of the MTT assay and the cell metabolic enhancement, respectively. Importantly, the results were comparable to those of the parallel LED in vitro experiment despite the fact that the peak wavelength of the QLED and LED devices differed.

The parallel PDT in vitro experiment induced photosensitization of A431 cells in 3D cultures with ALA administration, which led to accumulation of PpIX prior to light activation. A431 cells are a human cell line from an epidermoid carcinoma of the skin. They are also used in studies of the cell cycle and cancer-associated cell signalling pathways since they express abnormally high levels of the epidermal growth factor receptor. Another PDT experiment was performed in parallel using an inorganic LED with a similar spectral emission but with higher irradiance. In order to deliver a total light dose of 30 J cm^{-2} in both experiments, irradiation with the QLED and LED lasted 4.75 h ($\sim$1.8 mW cm^{-2}) and 4 min ($\sim$130 mW cm^{-2}),

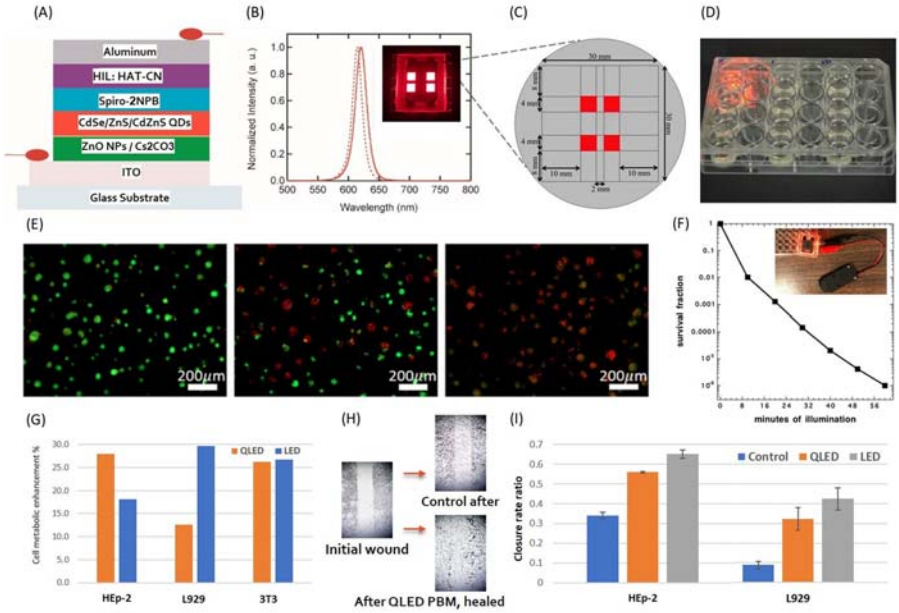

Figure 6.7 (A) Cross-sectional structure of the red-emitting QLEDs used for in vitro testing. (B) Typical EL (*solid line*) and PL spectra (*dashed line*) of QLEDs and corresponding QDs used for in vitro studies, respectively. The inset is a picture of a typical on-glass QLED with all 4 pixels lighting up simultaneously. (C) Pattern of the QLED with 4 pixels (16 mm^2 each) shown in (B). (D) Setup of cell cultures for in vitro PDT and PBM experiments with bottom QLED illumination. (E) Fluorescent vital-dye labeled 3D cultures 24-h post-PDT treatment. Calcein labels live cells green, while ethidium bromide labels dead cells red. Cultures are shown in the following order: control cells without light treatment (left), LED-based PDT (center), and QLED-based PDT (right). (F) Survival fraction evolution of MRSA under QLED-based PDT using photofrin as PS. The inset corresponds to the experimental setup with QLED-pixel powered by a 6-V battery pack. (G) Cell metabolism enhancement of cells lines HEp-2, L929, and 3T3 after irradiation with either QLED or LED, and respect to control cultures. (H) Cell migration observed with PBM in vitro test based on a 2D scratch model. (I) CRR of cell lines HEp-2 and L929, 24 h after irradiation with QLED, LED, and without irradiation (control systems). The irradiation conditions corresponding to these results were: 4 J cm^{-2} in 10 min at $\sim$8 mW cm^{-2}. *3D*, three-dimensional; *CRR*, closure rate ratio; *EL*, electroluminescence; *MRSA*, methicillin-resistant *Staphylococcus aureus*; *PDT*, photodynamic therapy; *PL*, photoluminescence; *PBM*, photobiomodulation; *PS*, photosensitizer; *QD*, quantum dot; *QLED*, Quantum dot light-emitting diode.
Source: (A and B) Y. Dong, J.-M. Caruge, Z. Zhou, C. Hamilton, Z. Popovic, J. Ho, et al., 20.2: Ultra-bright, highly efficient, low roll-off inverted quantum-dot light emitting devices (QLEDs), in: SID Symposium Digest of Technical Papers, vol. 46 (1), 2015, pp. 270−273, John Wiley & Sons. Copyright (2015) Wiley-VCH Verlag GmbH & Co. KGaA, Weinheim. (D and E) H. Chen, J. He, R. Lanzafame, I. Stadler, H.E. Hamidi, H. Liu, et al., Quantum dot light emitting devices for photomedical applications, J. Soc. Inf. Disp. 25 (3) (2017)

(*Continued*)

respectively. The total fluence per session must be similar when comparing treatments with different light sources, so that the results obtained can be compared. At 24 h post-PDT treatment, the 3D cultures were labeled using a fluorescent vital-dye technique. Calcein labeled live cells green while ethidium bromide labeled dead cells red. Fig. 6.7E shows the images for control cells without light treatment, cells with LED-based PDT, and cells with QLED-based PDT, from left to right. Finally, both QLED and LED devices achieved photodestruction of 3D tumor nodules. Most importantly, the quantitative image processing of multiple replicates revealed a slightly higher PDT efficacy for the QLED, based on the residual tumor viabilities: 0.61 ± 0.04 and 0.53 ± 0.08 for LED and QLED, respectively. Recently, we also reported an in vitro PDT test on TR146 cells [18,90], a human squamous cell carcinoma whose primary tumor originated in the buccal mucosa. In this test a light dose of 66 J cm^{-2} was delivered over a period of 150 min using LEDs and QLEDs. According to the residual cell viabilities, 0.65 ± 0.03 and 0.52 ± 0.06 measured for LEDs and QLEDs, respectively, a higher efficacy of the QLED-based in vitro PDT was once again observed over commercial LEDs, attributed to better irradiation uniformity of the QLED-based PDT.

Another in vitro study to evaluate the effect of QLED-based PBM in wound healing was conducted in 2018 using a "2D scratch model" [106]. Cultures of HEp-2 and L929 cells with a confluent monolayer were scored to leave a scratch of $\sim 0.4-0.5$ mm in width. Photoirradiation of the culture wells was performed with a QLED emitting at 626 nm, in order to deliver either 2 J cm^{-2} in 5 min or 4 J cm^{-2} in 10 min at ~ 8 mW cm^{-2}. A parallel experiment was carried out using a commercial NASA LED array with an emission peak at 670 nm and with the same light dosages and culture conditions. The scratch width was monitored over time and the closure rate ratio (CRR) results at 24 h measured the degree of promotion of cell migration as compared to the control cultures, as shown in Fig. 6.7H and I. The best CRRs for both QLED and LED treatments resulted from delivering a fluence of 4 J cm^{-2} in 10 min. In addition, slightly higher CRRs were observed for LEDs. This discrepancy was attributed to the difference in peak wavelength for irradiation, since longer red wavelengths are known to be more effective in promoting wound healing. In conclusion, this study demonstrated for the first time the potential of QLED-based PBM for impaired wound healing treatments and suggested that further optimization of cell migration promotion could be achieved at longer wavelengths.

An in vitro study reported in 2018 further evaluated the QLED efficacy for aPDT [25]. This study revealed that QLED-based aPDT can effectively kill methicillin-resistant *Staphylococcus aureus* (MRSA), an antibiotic-resistant bacterium. MRSA

177–184, John Wiley & Sons. Copyright (2017) Wiley-VCH Verlag GmbH & Co. KGaA, Weinheim. (F) H. Chen, T.-H. Yeh, J. He, C. Zhang, R. Abbel, M.R. Hamblin, et al., Flexible quantum dot light-emitting devices for targeted photomedical applications, J. Soc. Inf. Disp. 26 (5) (2018) 296–303, John Wiley & Sons. Copyright (2018) Wiley-VCH Verlag GmbH & Co. KGaA, Weinheim.

bacterium was treated with 10-μM photofrin and 100-mM potassium iodide, and then irradiated with a QLED powered by a simple 6 V battery pack. Only one 16 mm^2 pixel was turned on as shown in the inset of Fig. 6.7F. Remarkably, the survival fraction of MRSA dropped to less than 10^{-6} after 1 h irradiation, as observed in Fig. 6.7F. Then, this result simultaneously demonstrated the high efficacy and simplicity of QLED-based aPDT for infection treatment, and promises inactivation of pathogens without the risk of inducing resistance.

Subsequently, the introduction of QLEDs in the photomedicine field encouraged recent OLED studies in photomedicine after a long gap, as mentioned in the previous section. The recent photomedical studies from Choi's and Samuel's groups represent the state-of-the-art OLED-based work, dedicated to PBM for wound healing and aPDT for infection treatment, respectively. In 2018, the Choi group of KAIST published the in vitro wound healing effects of PBM using flexible OLEDs for the first time [110]. Notably, irradiation at 5 mW cm^{-2} with a 650 nm patch OLED on cultured normal human fibroblasts effectively stimulated fibroblast proliferation and migration, 58% and 46% over the control, corresponding to 6 J cm^{-2} for 20 min and 3 J cm^{-2} for 10 min, respectively. Later in the same year, the group conducted a cell migration test to investigate the OLED PBM effect on epidermal keratinocyte cells 12 h after irradiation with 3 J cm^{-2} at 5 mW cm^{-2} for 10 min [111]. The study confirmed a better wound-healing promotion at a longer peak emission wavelength of 650 nm by 31.5% over the control group. In 2019 the same group reported transferable and free form OLEDs as wearable and disposable light sources for skin wound photomedicine [91]. Briefly, this study showed a 26% and 32% increase in cell proliferation and migration after irradiation of keratinocytes, respectively; a 39% increase of epidermis thickness for a skin equivalent model; a 14% skin area increase and a 21% re-epithelialization improvement in an organ culture model. The best conditions found in terms of the keratinocyte response (5 mW cm^{-2} at 670 nm for 10 min) were subsequently used for the two model experiments. Fig. 6.8A and B shows the in vitro wound healing effect using keratinocytes and the cell migration test using a scratch-wound healing assay, respectively. The organ culture model consisted in a rat skin cryo-wound model, and corresponding evolution of the reference and irradiated wounds is shown in Fig. 6.8C.

In parallel with these PBM studies, Samuel's group revisited the OLED photomedicine topic after ~10 years and reported top-emitting flexible OLEDs for aPDT [107]. The team performed in vitro PDT for killing *S. aureus* with both on-glass and flexible OLEDs. In both cases, administration of 5 μg mL^{-1} of MB and OLED irradiation for 3 h led to more than 99% killing of bacteria at optical density 0.001 (see bar charts in Fig. 6.8D). In 3 h, the on-glass and flexible OLEDs delivered fluences of 54 and 64.8 J cm^{-2} at 5 and 6 mW cm^{-2}, respectively. Overall, these preliminary results suggested that flexible OLED devices can be as effective as on-glass devices, but with important additional features for ergonomic and practical application. Comparative experiments with the available commercial light sources (lasers or LEDs) will be needed to further validate the benefits and efficacy of flexible OLED-based phototherapy.

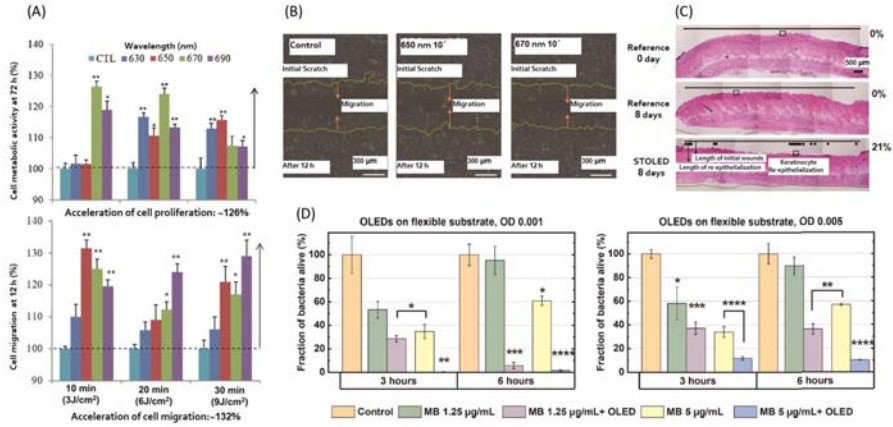

Figure 6.8 (A) Bar charts of keratinocyte cell proliferation test 72 h after light irradiation (upper), and migration test 12 h after light irradiation (lower). Bars correspond to control sample and samples under OLEDs irradiation with peak wavelengths at 630, 650, 670, and 690 nm. (B) Migrated cell images 12 h after light irradiation for control, 650 and 670 nm (10 min irradiation). (C) Effect of irradiating rat skin with a 670 nm OLED on organ culture in the cryo-wound model. Thin lines indicate the length of initial wounds, while thick lines indicate the length of re-epithelialization. (D) Bar charts of OLED-based aPDT for killing *Staphylococcus aureus*, showing the fraction of bacteria alive for a range of illumination conditions and PS (MB) concentrations. Control corresponds to sample with no light and no PS. *aPDT*, antimicrobial photodynamic therapy; *MB*, methylene blue; *PS*, photosensitizer; *OLED*, organic light emitting diode.
Source: (A–C) Adapted from Y. Jeon, H.-R. Choi, J.H. Kwon, S. Choi, K.M. Nam, K.-C. Park, et al., Sandwich-structure transferable free-form OLEDs for wearable and disposable skin wound photomedicine, Light: Sci. Appl. 8 (1) (2019) 114. CC BY 4.0. (D) Reproduced from C. Lian, M. Piksa, K. Yoshida, S. Persheyev, K.J. Pawlik, K. Matczyszyn, et al., Flexible organic light-emitting diodes for antimicrobial photodynamic therapy, NPJ Flexible Electron. 3 (1) (2019) 18. CC BY 4.0.

6.4.2.3 *Perspective of QLEDs in the photomedicine field and device concepts*

The high potential of QLEDs to escalate the adoption of photomedicine promises wide coverage of multiple health-care markets such as cancer treatment, periodontal disease, dermatology (especially cosmetic dermatology), and chronic wound and ulcer care. However, a focused single market targeting the treatments and settings where QLEDs are currently most needed is necessary for a smooth start and as a first target for device development. PDT treatment of oral cancer and PBM treatment for diabetic wound healing were recently proposed [25] as target treatments for initial photomedical applications of flexible QLEDs. These two treatment market segments were considered to be the more promising due to the technical feasibility, high social impacts, and commercialization potential. Accordingly, the high incidence of oral cancer in low-resource populations (e.g., in India), the high cost and negative side

effects of current treatments, and the limitations of mainstream light sources for wide adoption of PDT, are demanding an alternative light source. In addition, the unsatisfactory results of existing multidisciplinary treatments for impaired wound healing also merit the introduction of QLEDs for targeted PBM.

A set of basic technical requirements for near-future introduction of flexible QLEDs in the photomedicine market has been discussed elsewhere [26]. The design of the QLED-based medical device might vary between different photomedical applications, depending on the characteristics of the location to be treated. Therefore, the form factor of the flexible QLED and the QLED holder would need to be modified when the spatial characteristics of the location change. Accordingly, the main usable form factors of flexible QLEDs are summarized as being foldability, stretchability, bendability, and minimum bending radius. On the other hand, the same operating requirements such as minimum operating lifetime, minimum shelf life, and PD range can satisfy and cover a wide range of both PDT and PBM applications. Naturally, treatment of easy-to-access locations are preferred for early application of QLEDs, for example, the locations for the targeted treatments previously mentioned, that is, the oral cavity and the skin. Herein, we present preliminary conceptual designs of QLED devices for ambulatory and "at home" treatment of the skin and oral cavity, which were designed with SolidWorks.

The first design proposed for treatment of the skin corresponds to a bendable bandage-type device with a moderate minimum bending radius ($<$6.5 mm), and for one-time fit on a curved surface [26]. The average radius of the small finger in children between 3 and 10 years of age is 6.5 mm [112]. In Fig. 6.9A and B, we illustrate the application of the bandage-type device on body limbs (finger and arm), which could be used by the patient in the comfort of the home, following the dosage instructions prescribed by the doctor. Such a bandage should be adhesive on the edges and contain both the flexible QLED and the power source (e.g., coin cell batteries). A customized design might also be needed for the bandage, for example, in order to avoid direct contact of the QLED with the skin. While skin cancer, inflammation, tendinopathies, and arthritic conditions might allow contact, other conditions such as diabetic wound healing and treating superficial bacterial infections may require a small space in the bandage to avoid direct contact with the emitting surface of the QLED for a variety of reasons.

The second conceptual design corresponds to a mouthguard-type device for treatment of the oral cavity. This design is also proposed for both ambulatory and "at home" treatment, and should be practical for patient self-application after dosage instructions from the doctor. As illustrated in Fig. 6.9C, the device has a mouthguard-type plastic holder with a handle in the front. The plastic holder fits the lower teeth and has a notch matching the inferior labial frenulum (see Fig. 6.9D). The handle is used to position the device inside the mouth and to contain the coin cell batteries for operation of the QLEDs. Once the device is in place, the plastic holder should be bitten by the patient to keep it in place. Well positioned flexible QLEDs supported in this oral plastic device are expected to irradiate different soft tissues, mainly the tongue, hard and soft palate, and the buccal mucosa.

These early-phase designs have not been tested or proven but are proposed as a basis for the future development of QLED-based medical prototypes.

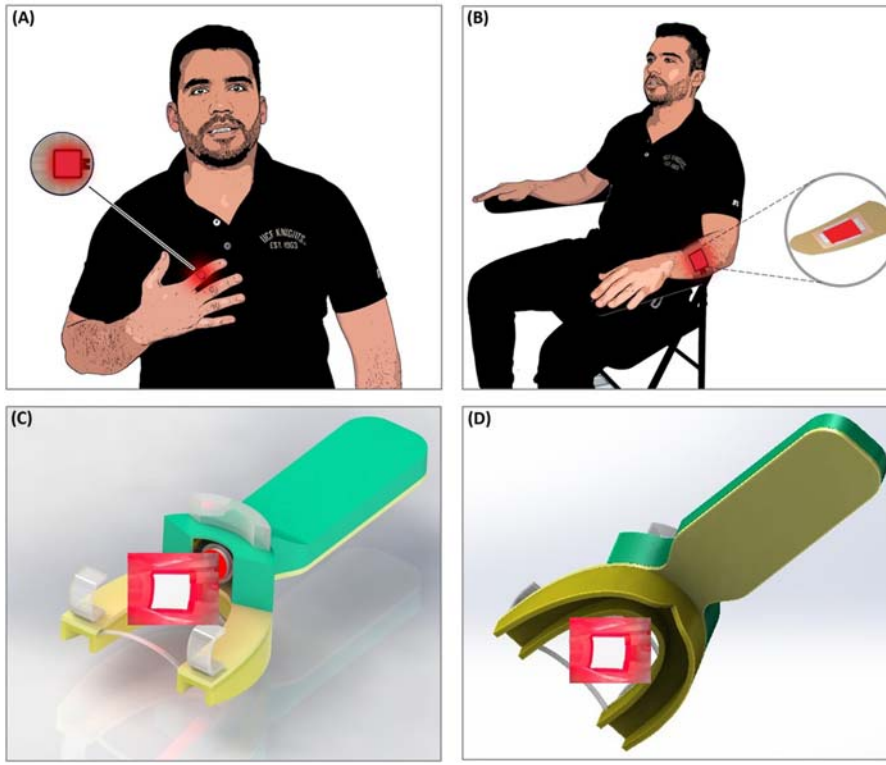

Figure 6.9 Conceptual design of bandage-type QLED device for phototherapy of skin diseases and conditions, applied on the patient's (A) finger and (B) arm, respectively. (C) Conceptual design of mouthguard-type QLED device for phototherapy of the oral cavity. It illustrates an oral plastic device which supports the flexible QLEDs. (D) Lower view of the mouthguard-type QLED device, where the U-shaped case for the lower teeth and the notch for the inferior labial frenulum can be observed. *QLED*, quantum dot light-emitting diode.

The gradual introduction of QLEDs to other applications will require the design and fabrication of new prototypes, according to the specific needs of the treatment scenario. Currently, lasers are normally used for internal treatment of organs and lesions, since coherent light can be easily coupled into flexible optical fibers. Thus light delivery inside the body can be accomplished via endoscopes or transcutaneous insertion of fibers through needles [38]. These laser systems also use different types of diffusers for light delivery (i.e., frontal, cylindrical, and spherical) and are most often used in the PDT field, specifically for interstitial and intraoperative PDT of malignant tumors. For example, when a solid tumor is deep-seated and tumor resection is impractical or impossible, interstitial PDT is a good approach for volume irradiation and destruction of the tumor. When tumor resection is achievable, intraoperative PDT is used as an adjunct to surgery [113], particularly in cases where the resection cavity surface is the target. The application of flexible QLEDs in phototherapy could be extended to internal treatment with the development of

new devices exhibiting multiple form factors, eliminating the need for optical fibers and diffusers. For instance, the development of ultrathin stretchable QLEDs can be easily wrapped around the tip of a probe. Fabrication of the QLED by dip-coating of the functional layers directly onto a cylindrical probe working as electrode is in principle also possible. Moreover, encapsulated flexible QLEDs could also be attached or applied to the tissue target inside the body and wirelessly powered for the application of mPDT. This approach was proposed as an alternative local treatment for tumor in delicate organs [114] and was tested by implantation of a wireless sandwiched LED on the inner surface of the dorsal skin of mice.

6.4.3 QD devices for health monitoring and diagnostics

The great potential of QLEDs promises widespread use and integration of QLED-based displays in all kinds of wearable medical devices, as information input/output ports. Ultrathin QLED displays are also good competitors to inorganic micro-LEDs, polymer LEDs, and OLEDs under current research [115]. Importantly, flexible QLED displays can be integrated with touch interfaces, wearable sensors, memories, micro-controllers, wireless communication units, power sources, [116], etc. All of these components can be mounted in a flexible printed circuit board, in order to show real-time data processed from the wearable sensors. Kim et al. [115] reported a fully integrated QLED display with a touch user interface that directly showed sensor data. This device visualized the real-time ambient temperature and step counts measured by the integrated sensors attached to the wearer's skin, as shown in Fig. 6.10B. In addition, the passively driven ultrathin QLED display had sufficient brightness of $674\,\mathrm{cd\,m^{-2}}$ at $6\,V_{pp}$ (max. brightness of iPhone 7 is $625\,\mathrm{cd\,m^{-2}}$) when all 16×16 pixels were on (see Fig. 6.10A).

A portable device system may also integrate several QD-based devices which interact with each other to monitor/perform diagnostic and therapeutic functions. For instance, QDPDs and QLEDs working either as light sources or displays. Integration of QD-based devices to make disposable medical sensors for pulse oximetry is one potential application being explored. Conventional pulse oximeters can simultaneously measure pulse rate and arterial blood oxygenation, using two inorganic LEDs with different peak emission wavelengths (in the red and NIR) and an inorganic photodetector. Meanwhile, the proposed solution-processed organic optoelectronic sensors are cost-effective but still have some limitations. Lochner et al. [117] reported an all-organic pulse oximeter composed of two OLEDs (emission peaks at 532 and 626 nm) and a flexible organic polymer photodiode, shown in Fig. 6.10D. Besides the heart rate obtained directly from the photoplethysmography (PPG) signals, the arterial oxygen saturation was computed from the ratio of transmitted light at two different wavelengths. The latter takes advantage of the difference in absorptivity between oxygenated hemoglobin and deoxygenated hemoglobin at different light wavelengths. A schematic model of the transmitted light pathway through blood and tissue over several cardiac cycles is shown in Fig. 6.10C. The PPG signals obtained with both OLEDs preserved similar shapes as the signal of other oximeter systems, regardless of the evident reduction in the

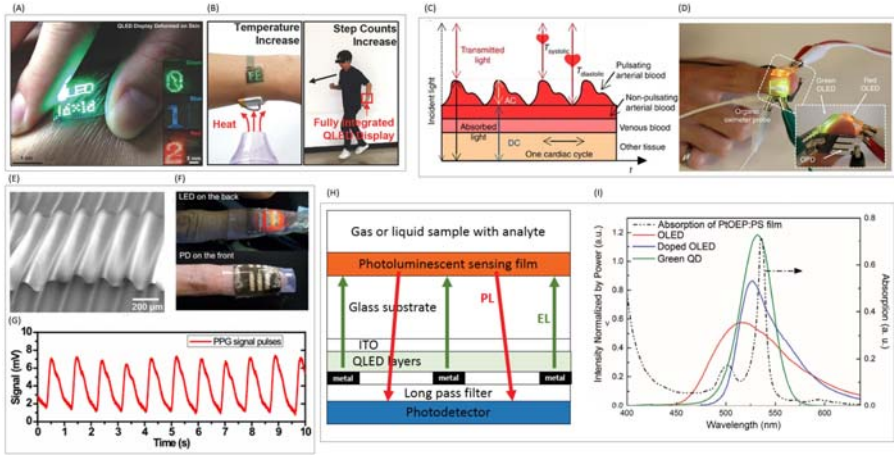

Figure 6.10 (A) Ultrathin QLED display (16 × 16 QLED) on deformed skin. The insets show the RGB QLED displays. (B) Integrated wearable system subjected to external heat (left) and the running wearer (right). The skin-mounted QLED shows the measured information. (C) Model for the pulse oximeter's light transmission path through pulsating arterial blood, nonpulsating arterial blood, venous blood, and other tissues over several cardiac cycles. (D) Organic oximeter with red and green OLEDs in one side and OPD placed on the opposite side of the subject's finger. The light emitted from the OLEDs and transmitted through the finger is collected with the OPD. (E) Perspective scanning electron micrograph of a wavy QLED with a titled angle of 75 degrees formed by a 70% prestrain. (F) QD-based epidermal PPG sensor with wavy QLEDs operating at 8.4 V and QDPD wrapped around the forefinger of a subject. (G) Real-time record of PPG signals over several pulse periods under illumination from the red QLED. (H) Schematic structure of a compact back detection QLED based PL sensor. (I) Emission spectra of OLED, doped OLED, and green QDs (*solid lines*), along with the absorption spectrum of PtOEP:PS sensing film (*dashed line*). *OLED*, organic light-emitting diode; *OPD*, organic polymer photodiode; *PL*, photoluminescence; *PPG*, photoplethysmography; *QD*, quantum dot; *QLED*, quantum dot light-emitting diode.

Source: (A and B) J. Kim, H.J. Shim, J. Yang, M.K. Choi, D.C. Kim, J. Kim, et al., Ultrathin quantum dot display integrated with wearable electronics, Adv. Mater. 29 (38) (2017) 1700217, John Wiley & Sons. Copyright (2018) Wiley-VCH Verlag GmbH & Co. KGaA, Weinheim. (C and D) Reprinted from C.M. Lochner, Y. Khan, A. Pierre, A.C. Arias, All-organic optoelectronic sensor for pulse oximetry, Nat. Commun. 5 (1) (2014) 1−7. Copyright (2014), with permission from Springer Nature. (E−G) Reprinted with permission from T.-H. Kim, C.-S. Lee, S. Kim, J. Hur, S. Lee, K.W. Shin, et al., Fully stretchable optoelectronic sensors based on colloidal quantum dots for sensing photoplethysmographic signals, ACS Nano. 11 (6) (2017) 5992−6003. Copyright (2017) American Chemical Society. (H and I) J. He, H. Chen, S.T. Wu, Y. Dong (Eds.), 27-4: Distinguished student paper: integrated sensing platform based on quantum dot light emitting diodes, in: SID Symposium Digest of Technical Papers, Wiley Online Library, 2016, John Wiley & Sons. Copyright (2016) Wiley-VCH Verlag GmbH & Co. KGaA, Weinheim.

signal magnitude. Overall, the low optical power output of red-emitting OLEDs resulting in low PPG signal intensity, and the lower tissue penetration of green light suggest further development in specific directions. In addition, the motion induced errors and the optical energy losses produced by the reduced contact area between skin and rigid OLEDs need to be addressed. The cost-effective fabrication and flexible form factors, in addition to the characteristic narrower emission bandwidth and higher optical PD of red and NIR QLEDs could enhance the performance of pulse oximeter sensors as compared to OLED-based sensors. Kim et al. [27] reported a fully stretchable QD-based sensor for continuous monitoring of blood waves via PPG signal recording. The epidermal PPG sensor was integrated by a QLED and a QDPD, both stretchable and attached onto a 300-μm thick Ecoflex film. The stretchability and crack-free internal structure of the sensor under elongation was enabled by coupling the ultrathin devices with a prestrained elastomer (see Fig. 6.10E). After lamination of the sensor around the forefinger of a subject (shown in Fig. 6.10F), the PPG signal pulses were measured by QLED illumination (1000 cd m^{-2} at 618 nm) and detection of the light transmitted by the QDPD (see the graphic in Fig. 6.10G). CdSe/CdS/ZnS core−shell−shell QDs and PbS QDs (abs. peak at 1100 nm) were used as emissive and active materials of the red-emitting QLED and QDPD, respectively. Importantly, tight adhesion of the patch-type stretchable devices to the skin and nail avoided light leakage and reduced the parasitic short-circuit current produced by ambient light. Furthermore, this firm adhesion allowed the measurement of accurate signals regardless of the subject's movement or the device's location on the body, for example, joints and distal appendages such as fingers and ears.

Finally, our group also proposed the use of QLEDs as the excitation sources in compact PL-based sensors [118] to overcome OLEDs' limitations of low brightness, broad emission spectra, and long radiative lifetime. A schematic structure of the proposed QLED-based PL sensor with back detection is shown in Fig. 6.10H. The compact sensor consists of a sensing film with PL dependent on the analyte concentration, the QLED as the excitation source, and a photodetector to measure the PL of the sensing film. To estimate the improvement in power utilization of the QLED-based sensor due to narrow and wavelength-fit emission peak, the emission spectra of OLED and doped OLED devices were compared with a green QDs spectrum as illustrated in Fig. 6.10I. As a result, by tuning the EL peak wavelength to better fit the absorption of the sensing film (PtOEP:PS film as example), the energy efficiency can be improved by over 57%, to as much as 63% with a narrower QD emission band. In addition, QLED-based sensing systems can be further simplified by removing unnecessary components. For instance, the band pass filter for excitation light, and therefore the filter patterning, is not necessary. Moreover, in radiative lifetime (τ)-based detection mode the long pass filter is also possibly removable, considering the negligible QLED EL decay time, typically $\sim$15 ns in contrast to at least $\sim$100 ns decay time for OLEDs. It is then envisioned that simple, low-cost, high-efficiency, and signal-noise free QLED-based sensing platforms will also be highly competitive for portable medical sensing applications.

6.5 Conclusion and outlook

The unique optical properties of colloidal QDs, notably their size-tunable emission wavelength, high PL−QY, narrow emission bandwidth, and photostability, make them highly desirable for fluorescence and EL-based applications in the photomedicine field. The capacity of individual QDs to simultaneously perform as a fluorescent probe, PS nanocarrier, and efficient energy donor for PDT, are evidence of the wide multimodal application of QDs. Proper engineering of the core−shelling, encapsulation, and surface functionalization of the QDs will play a decisive role for the effective and safe application of QD-systems as theranostic agents in living systems. In particular, the biodistribution and clearance from living organisms will be key topics of study in order to reduce the toxicity of QDs. The current research is pointing out two main approaches for the reduction of QDs toxicity, one of which is the use of efficient and suitable QDs composed of green or less toxic elements, and the other is enhancing their fast and safe clearance from the body by controlling the size and surface chemistry of the QDs.

Although QLEDs and OLEDs are still early in the path to real photomedical application, the in vitro and in vivo studies in PDT and PBM have demonstrated exciting results comparable to those of commercial LEDs and lasers. In addition, their similarity as conformable surface light sources and the knowledge gained with new photomedical testing and device development, can contribute to the progress of both technologies enabling their final translation to human clinical trials. Importantly, the additional advantages of flexible QLEDs such as high PD and narrow-emission bandwidth at red wavelengths promise a competitive future for QLEDs in the photomedicine and health-care fields. We believe that the mature Cd-based QLEDs with record efficiency and brightness can pave the way for application of emerging Cd-free QLEDs in the photomedical field, as research advances in the development of new QD materials. Finally, among the QD devices, QLEDs are probably the devices most frequently integrated to wearable medical systems currently being developed and being used in research applications. It is clear that the introduction of QLEDs in the photomedicine market can be a challenging pathway due to the multidisciplinary nature of the application. However, a deep understanding and close collaborative progress on the QLED device development, medical treatments, and regulatory approval process, will be key factors for the successful realization of QLED devices and technologies in this growing field of high relevance.

References

[1] L.E. Brus, Electron−electron and electron-hole interactions in small semiconductor crystallites: the size dependence of the lowest excited electronic state, J. Chem. Phys. 80 (9) (1984) 4403−4409.

[2] P.R. Brown, D. Kim, R.R. Lunt, N. Zhao, M.G. Bawendi, J.C. Grossman, et al., Energy level modification in lead sulfide quantum dot thin films through ligand exchange, ACS Nano 8 (6) (2014) 5863−5872.

[3] C. Philippot, P. Reiss, Chapter 3 – Synthesis of inorganic nanocrystals for biological fluorescence imaging, in: J.M. de la Fuente, V. Grazu (Eds.), Frontiers of Nanoscience, vol. 4, Elsevier, 2012, pp. 81–114.
[4] B.D. Dickerson, D.M. Irving, E. Herz, W.B.S. Claus RO Jr., K.E. Meissner, Synthesis kinetics of CdSe quantum dots in trioctylphosphine oxide and in stearic acid, Appl. Phys. Lett. 86 (17) (2005) 171915.
[5] M. Eck, M. Krueger, Correlation between CdSe QD synthesis, post-synthetic treatment, and BHJ hybrid solar cell performance, Nanomaterials 6 (6) (2016) 115.
[6] L. Qu, X. Peng, Control of photoluminescence properties of CdSe nanocrystals in growth, J. Am. Chem. Soc. 124 (9) (2002) 2049–2055.
[7] M.A. Triana, O.A. Jaramillo-Quintero, R.J. Camargo, M.E. Rincón, Direct assembly of thioacid capped quantum dots in solid-state hybrid photovoltaics, effect of QDs size and thermal annealing, RSC Adv. 7 (22) (2017) 13543–13551.
[8] Y. Zhu, Z. Li, M. Chen, H.M. Cooper, G.Q.M. Lu, Z.P. Xu, One-pot preparation of highly fluorescent cadmium telluride/cadmium sulfide quantum dots under neutral-pH condition for biological applications, J. Colloid Interface Sci. 390 (1) (2013) 3–10.
[9] J. Tan, Y. Liang, J. Wang, J. Chen, B. Sun, L. Shao, Facile synthesis of CdTe-based quantum dots promoted by mercaptosuccinic acid and hydrazine, New J. Chem. 39 (6) (2015) 4488–4493.
[10] F. Wei, X. Lu, Y. Wu, Z. Cai, L. Liu, P. Zhou, et al., Synthesis of highly luminescent CdTe/CdS/ZnS quantum dots by a one-pot capping method, Chem. Eng. J. 226 (2013) 416–422.
[11] Z. Fang, Y. Li, H. Zhang, X. Zhong, L. Zhu, Facile synthesis of highly luminescent UV-blue-emitting ZnSe/ZnS core/shell nanocrystals in aqueous media, J. Phys. Chem., C. 113 (32) (2009) 14145–14150.
[12] G.-X. Liang, L.-L. Li, H.-Y. Liu, J.-R. Zhang, C. Burda, J.-J. Zhu, Fabrication of near-infrared-emitting CdSeTe/ZnS core/shell quantum dots and their electrogenerated chemiluminescence, Chem. Commun. 46 (17) (2010) 2974–2976.
[13] J. Kwak, J. Lim, M. Park, S. Lee, K. Char, C. Lee, High-power genuine ultraviolet light-emitting diodes based on colloidal nanocrystal quantum dots, Nano Lett. 15 (6) (2015) 3793–3799.
[14] Y. Dong, J.-M. Caruge, Z. Zhou, C. Hamilton, Z. Popovic, J. Ho, et al., 20.2: Ultra-bright, highly efficient, low roll-off inverted quantum-dot light emitting devices (QLEDs), in: SID Symposium Digest of Technical Papers, vol. 46 (1), 2015, pp. 270–273.
[15] Y.-H. Won, O. Cho, T. Kim, D.-Y. Chung, T. Kim, H. Chung, et al., Highly efficient and stable InP/ZnSe/ZnS quantum dot light-emitting diodes, Nature 575 (7784) (2019) 634–638.
[16] R. Xie, K. Chen, X. Chen, X. Peng, InAs/InP/ZnSe core/shell/shell quantum dots as near-infrared emitters: bright, narrow-band, non-cadmium containing, and biocompatible, Nano Res. 1 (6) (2008) 457–464.
[17] Y. Zhang, G. Hong, Y. Zhang, G. Chen, F. Li, H. Dai, et al., Ag_2S quantum dot: a bright and biocompatible fluorescent nanoprobe in the second near-infrared window, ACS Nano 6 (5) (2012) 3695–3702.
[18] M.A. Triana, E-L. Hsiang, C. Zhang, S.-T. Wu, Y. Dong. Luminescent Nanomaterials for Energy Efficient Display and Healthcare. ACS Energy Letters 7 (3) (2022) 1001–1020.
[19] H. Shen, Q. Gao, Y. Zhang, Y. Lin, Q. Lin, Z. Li, et al., Visible quantum dot light-emitting diodes with simultaneous high brightness and efficiency, Nat. Photonics 13 (3) (2019) 192–197.

[20] Y. Yang, Y. Zheng, W. Cao, A. Titov, J. Hyvonen, J.R. Manders, et al., High-efficiency light-emitting devices based on quantum dots with tailored nanostructures, Nat. Photonics 9 (4) (2015) 259–266.
[21] X. Li, Q. Lin, J. Song, H. Shen, H. Zhang, L.S. Li, X. Li, Z. Du, Quantum-Dot Light-Emitting Diodes for Outdoor Displays with High Stability at High Brightness, Adv. Optical Mater. 8 (2) (2020) 1901145.
[22] C. Pu, X. Dai, Y. Shu, M. Zhu, Y. Deng, Y. Jin, X. Peng, Electrochemically-stable ligands bridge the photoluminescence - electroluminescence gap of quantum dots, Nat. Commun. 11 (1) (2020) 937.
[23] W. Cao, C. Xiang, Y. Yang, Q. Chen, L. Chen, X. Yan, et al., Highly stable QLEDs with improved hole injection via quantum dot structure tailoring, Nat. Commun. 9 (1) (2018) 2608.
[24] H. Chen, J. He, R. Lanzafame, I. Stadler, H.E. Hamidi, H. Liu, et al., Quantum dot light emitting devices for photomedical applications, J. Soc. Inf. Disp. 25 (3) (2017) 177–184.
[25] H. Chen, T.-H. Yeh, J. He, C. Zhang, R. Abbel, M.R. Hamblin, et al., Flexible quantum dot light-emitting devices for targeted photomedical applications, J. Soc. Inf. Disp. 26 (5) (2018) 296–303.
[26] M.A. Triana, A.A. Restrepo, R.J. Lanzafame, P. Palomaki, Y. Dong, Quantum dot light-emitting diodes as light sources in photomedicine: photodynamic therapy and photobiomodulation, J. Phys.: Mater. 3 (3) (2020) 032002.
[27] T.-H. Kim, C.-S. Lee, S. Kim, J. Hur, S. Lee, K.W. Shin, et al., Fully stretchable optoelectronic sensors based on colloidal quantum dots for sensing photoplethysmographic signals, ACS Nano 11 (6) (2017) 5992–6003.
[28] Y. Shirasaki, G.J. Supran, M.G. Bawendi, V. Bulović, Emergence of colloidal quantum-dot light-emitting technologies, Nat. Photonics 7 (1) (2013) 13–23.
[29] V.L. Colvin, M.C. Schlamp, A.P. Alivisatos, Light-emitting diodes made from cadmium selenide nanocrystals and a semiconducting polymer, Nature 370 (6488) (1994) 354–357.
[30] B. Dabbousi, M. Bawendi, O. Onitsuka, M. Rubner, Electroluminescence from CdSe quantum-dot/polymer composites, Appl. Phys. Lett. 66 (11) (1995) 1316–1318.
[31] M. Schlamp, X. Peng, A. Alivisatos, Improved efficiencies in light emitting diodes made with CdSe (CdS) core/shell type nanocrystals and a semiconducting polymer, J. Appl. Phys. 82 (11) (1997) 5837–5842.
[32] S. Coe, W.-K. Woo, M. Bawendi, V. Bulović, Electroluminescence from single monolayers of nanocrystals in molecular organic devices, Nature 420 (6917) (2002) 800–803.
[33] P.O. Anikeeva, J.E. Halpert, M.G. Bawendi, V. Bulovic, Quantum dot light-emitting devices with electroluminescence tunable over the entire visible spectrum, Nano Lett. 9 (7) (2009) 2532–2536.
[34] A.H. Mueller, M.A. Petruska, M. Achermann, D.J. Werder, E.A. Akhadov, D.D. Koleske, et al., Multicolor light-emitting diodes based on semiconductor nanocrystals encapsulated in GaN charge injection layers, Nano Lett. 5 (6) (2005) 1039–1044.
[35] J. Caruge, J.E. Halpert, V. Wood, V. Bulović, M. Bawendi, Colloidal quantum-dot light-emitting diodes with metal-oxide charge transport layers, Nat. Photonics 2 (4) (2008) 247–250.
[36] B.S. Mashford, M. Stevenson, Z. Popovic, C. Hamilton, Z. Zhou, C. Breen, et al., High-efficiency quantum-dot light-emitting devices with enhanced charge injection, Nat. Photonics 7 (5) (2013) 407–412.

[37] L. Qian, Y. Zheng, J. Xue, P.H. Holloway, Stable and efficient quantum-dot light-emitting diodes based on solution-processed multilayer structures, Nat. Photonics 5 (9) (2011) 543−548.
[38] Y.-Y. Huang, P. Mroz, M.R. Hamblin, Basic Photomedicine, Department of Dermatology, Harvard Medical School, 2009, p. 414. Available from: http://photobiology.info/Photomed.html.
[39] R.T. Chow, M.I. Johnson, R.A. Lopes-Martins, J.M. Bjordal, Efficacy of low-level laser therapy in the management of neck pain: a systematic review and meta-analysis of randomised placebo or active-treatment controlled trials, Lancet 374 (9705) (2009) 1897−1908.
[40] J. Tuner, L. Hode, The New Laser Therapy Handbook: A Guide for Research Scientists, Doctors, Dentists, Veterinarians and Other Interested Parties Within the Medical Field, Prima Books AB;, New York, 2010.
[41] R. Chow, P. Armati, E.-L. Laakso, J.M. Bjordal, G.D. Baxter, Inhibitory effects of laser irradiation on peripheral mammalian nerves and relevance to analgesic effects: a systematic review, Photomed. Laser Surg. 29 (6) (2011) 365−381.
[42] W. Yu, J.O. Naim, R.J. Lanzafame, Effects of photostimulation on wound healing in diabetic mice, Lasers Surg. Med. 20 (1) (1997) 56−63.
[43] I. Stadler, R.J. Lanzafame, R. Evans, V. Narayan, B. Dailey, N. Buehner, et al., 830-nm irradiation increases the wound tensile strength in a diabetic murine model, Lasers Surg. Med. 28 (3) (2001) 220−226.
[44] R.J. Lanzafame, Laser and light treatment for wound healing, in: K. Nouri (Ed.), Dermatologic Surgery: Step by Step, John Wiley & Sons Ltd, Hoboken, NJ, 2013, pp. 360−367.
[45] R.J. Lanzafame, I. Stadler, R. Cunningham, A. Muhlbauer, J. Griggs, R. Soltz, et al., Preliminary assessment of photoactivated antimicrobial collagen on bioburden in a murine pressure ulcer model, Photomed. Laser Surg. 31 (11) (2013) 539−546.
[46] R.J.S.I. Lanzafame, The recalcitrant wound: using low-level light therapy to manage non-healing wounds and ulcers, in: M.R. Hamblin, T. Agrawal, M. de Sousa (Eds.), Handbook of Low-Level Laser Therapy, Jenny Stanford Publishing;, New York, 2017, pp. 581−596.
[47] R.J. Lanzafame, S. de la Torre, G.H. Leibaschoff, The rationale for photobiomodulation therapy of vaginal tissue for treatment of genitourinary syndrome of menopause: an analysis of its mechanism of action, and current clinical outcomes, Photobiomodul. Photomed. Laser Surg. 37 (7) (2019) 395−407.
[48] R.J. Lanzafame, R.R. Blanche, A.B. Bodian, R.P. Chiacchierini, A. Fernandez-Obregon, E.R. Kazmirek, The growth of human scalp hair mediated by visible red light laser and LED sources in males, Lasers Surg. Med. 45 (8) (2013) 487−495.
[49] R.J. Lanzafame, R.R. Blanche, R.P. Chiacchierini, E.R. Kazmirek, J.A. Sklar, The growth of human scalp hair in females using visible red light laser and LED sources, Lasers Surg. Med. 46 (8) (2014) 601−607.
[50] M. Myakishev-Rempel, I. Stadler, O. Polesskaya, A.S. Motiwala, F.B. Nardia, B. Mintz, et al., Red light modulates ultraviolet-induced gene expression in the epidermis of hairless mice, Photomed. Laser Surg. 33 (10) (2015) 498−503.
[51] W. Yu, L.H. Chi, J.O. Naim, R.J. Lanzafame, Improvement of host response to sepsis by photobiomodulation, Lasers Surg. Med. 21 (3) (1997) 262−268.
[52] I. Stadler, R. Evans, B. Kolb, J.O. Naim, V. Narayan, N. Buehner, et al., In vitro effects of low-level laser irradiation at 660 nm on peripheral blood lymphocytes, Lasers Surg. Med. 27 (3) (2000) 255−261.

[53] R.J. Lanzafame, One man's light: mechanistic convergence of photobiomodulation and biological effects, Photomed. Laser Surg. 32 (5) (2014) 243–244.
[54] J.F. Turrens, Mitochondrial formation of reactive oxygen species, J. Physiol. 552 (Pt 2) (2003) 335–344.
[55] P. Avci, A. Gupta, M. Sadasivam, D. Vecchio, Z. Pam, N. Pam, et al., Low-level laser (light) therapy (LLLT) in skin: stimulating, healing, restoring, Semin. Cutan. Med. Surg. 32 (1) (2013) 41–52.
[56] R.J. Lanzafame, I. Stadler, A.F. Kurtz, R. Connelly, P. Brondon, D. Olson, Reciprocity of exposure time and irradiance on energy density during photoradiation on wound healing in a murine pressure ulcer model, Lasers Surg. Med. 39 (6) (2007) 534–542.
[57] M. Keijzer, S.L. Jacques, S.A. Prahl, A.J. Welch, Light distributions in artery tissue: Monte Carlo simulations for finite-diameter laser beams, Lasers Surg. Med. 9 (2) (1989) 148–154.
[58] R.J. Lanzafame, Light dosing and tissue penetration – it's complicated, Photobiomodul. Photomed. Laser Surg. 38 (8) (2020) 1–4.
[59] M.R. Hamblin, Y. Huang, Handbook of Photomedicine, CRC Press – Taylor & Francis, Boca Raton, FL, 2013.
[60] Y. Park, S. Jeong, S. Kim, Medically translatable quantum dots for biosensing and imaging, J. Photochem. Photobiol., C: Photochem. Rev. 30 (2017) 51–70.
[61] K.J. McHugh, L. Jing, A.M. Behrens, S. Jayawardena, W. Tang, M. Gao, et al., Biocompatible semiconductor quantum dots as cancer imaging agents, Adv. Mater. 30 (18) (2018) 1706356.
[62] C. Zhu, Z. Chen, S. Gao, B.L. Goh, I.B. Samsudin, K.W. Lwe, et al., Recent advances in non-toxic quantum dots and their biomedical applications, Prog. Nat. Sci.: Mater. Int. 29 (6) (2019) 628–640.
[63] S. Kargozar, S.J. Hoseini, P.B. Milan, S. Hooshmand, H.W. Kim, M. Mozafari, Quantum dots: a review from concept to clinic, Biotechnol. J. (2020) 2000117.
[64] D. Wang, Y. Zhu, X. Wan, X. Zhang, J. Zhang, Colloidal semiconductor nanocrystals for biological photodynamic therapy applications: recent progress and perspectives, Prog. Nat. Sci.: Mater. Int. (2020).
[65] N. Satoh, T. Nakashima, K. Kamikura, K. Yamamoto, Quantum size effect in TiO_2 nanoparticles prepared by finely controlled metal assembly on dendrimer templates, Nat. Nanotechnol. 3 (2) (2008) 106–111.
[66] M.A. Vargas, Y.H. Ochoa, Y. Ortegón, P. Mosquera, J.E. Rodríguez, R.J. Camargo, Nanopartículas de TiO_2, fase anatasa, sintetizadas por métodos químicos, Ing. Desarrollo 29 (2) (2011) 186–201.
[67] R.J. Camargo, Efecto fotocatalítico del TiO_2-Au sobre células de cáncer de cuello uterino, Ing. Compet. 14 (2) (2012) 191–198.
[68] M.J. Basante, O. Gutierrez, R.J. Camargo, Evaluacion de la citotoxicidad inducida por TIO_2 modificado funcionalizado con folato y oro sobre lineas celulares de HeLa y CHO, Inf. Tecnol. 27 (5) (2016) 63–68.
[69] R.J. Camargo, J.O. Gutiérrez, M.J. Basante, W.D. Criollo, Synthesis of Nanocompounds Comprising Anatase-Phase Titanium Oxide and Compositions Containing Same for the Treatment of Cancer. US Patent 10,603,381, 2020.
[70] K.-T. Yong, H. Ding, I. Roy, W.-C. Law, E.J. Bergey, A. Maitra, et al., Imaging pancreatic cancer using bioconjugated InP quantum dots, ACS Nano 3 (3) (2009) 502–510.
[71] L. Liu, R. Hu, I. Roy, G. Lin, L. Ye, J.L. Reynolds, et al., Synthesis of luminescent near-infrared $AgInS_2$ nanocrystals as optical probes for in vivo applications, Theranostics 3 (2) (2013) 109–115.

[72] K. Ding, L. Jing, C. Liu, Y. Hou, M. Gao, Magnetically engineered Cd-free quantum dots as dual-modality probes for fluorescence/magnetic resonance imaging of tumors, Biomaterials 35 (5) (2014) 1608–1617.
[73] S.-T. Yang, X. Wang, H. Wang, F. Lu, P.G. Luo, L. Cao, et al., Carbon dots as non-toxic and high-performance fluorescence imaging agents, J. Phys. Chem., C. 113 (42) (2009) 18110–18114.
[74] Y. Zhang, Y. Zhang, G. Hong, W. He, K. Zhou, K. Yang, et al., Biodistribution, pharmacokinetics and toxicology of Ag_2S near-infrared quantum dots in mice, Biomaterials 34 (14) (2013) 3639–3646.
[75] T. Pons, E. Pic, N. Lequeux, E. Cassette, L. Bezdetnaya, F. Guillemin, et al., Cadmium-free $CuInS_2$/ZnS quantum dots for sentinel lymph node imaging with reduced toxicity, ACS Nano 4 (5) (2010) 2531–2538.
[76] F. Erogbogbo, K.-T. Yong, I. Roy, R. Hu, W.-C. Law, W. Zhao, et al., In vivo targeted cancer imaging, sentinel lymph node mapping and multi-channel imaging with biocompatible silicon nanocrystals, ACS Nano 5 (1) (2011) 413–423.
[77] P. Wu, X.-P. Yan, Doped quantum dots for chemo/biosensing and bioimaging, Chem. Soc. Rev. 42 (12) (2013) 5489–5521.
[78] J.H. Yu, S.-H. Kwon, Z. Petrášek, O.K. Park, S.W. Jun, K. Shin, et al., High-resolution three-photon biomedical imaging using doped ZnS nanocrystals, Nat. Mater. 12 (4) (2013) 359–366.
[79] Y. Shirasaki, G.J. Supran, W.A. Tisdale, V. Bulović, Origin of efficiency roll-off in colloidal quantum-dot light-emitting diodes, Phys. Rev. Lett. 110 (21) (2013) 2174031–2174035.
[80] W.K. Bae, Y.-S. Park, J. Lim, D. Lee, L.A. Padilha, H. McDaniel, et al., Controlling the influence of Auger recombination on the performance of quantum-dot light-emitting diodes, Nat. Commun. 4 (1) (2013) 26611–26618.
[81] X. Dai, Z. Zhang, Y. Jin, Y. Niu, H. Cao, X. Liang, et al., Solution-processed, high-performance light-emitting diodes based on quantum dots, Nature 515 (7525) (2014) 96–99.
[82] Y. Sun, Q. Su, H. Zhang, F. Wang, S. Zhang, S. Chen, Investigation on thermally induced efficiency roll-off: toward efficient and ultrabright quantum-dot light-emitting diodes, ACS Nano 13 (10) (2019) 11433–11442.
[83] K. Ding, Y. Fang, S. Dong, H. Chen, B. Luo, K. Jiang, et al., 24.1% external quantum efficiency of flexible quantum dot light-emitting eiodes by light extraction of silver nanowire transparent electrodes, Adv. Opt. Mater. 6 (19) (2018) 1800347.
[84] H. Chen, Z. He, D. Zhang, C. Zhang, Y. Ding, L. Tetard, et al., Bright quantum dot light-emitting diodes enabled by imprinted speckle image holography nanostructures, J. Phys. Chem. Lett. 10 (9) (2019) 2196–2201.
[85] T. Chiba, Y. Hayashi, H. Ebe, K. Hoshi, J. Sato, S. Sato, et al., Anion-exchange red perovskite quantum dots with ammonium iodine salts for highly efficient light-emitting devices, Nat. Photonics 12 (11) (2018) 681–687.
[86] Z. Wei, J. Xing, The rise of perovskite light-emitting diodes, J. Phys. Chem. Lett. 10 (11) (2019) 3035–3042.
[87] M.A. Triana, S. Wu, Y. Dong, P-105: Bright, large pixel, flexible quantum-dot light-emitting diodes for photomedicine, in: SID Symposium Digest of Technical Papers, vol. 51, 2020, pp. 1748–1751.
[88] M.A. Triana, H. Chen, D. Zhang, R.J. Camargo, T. Zhai, S. Duhm, et al., Bright inverted quantum-dot light-emitting diodes by all-solution processing, J. Mater. Chem., C 6 (28) (2018) 7487–7492.

[89] P. van de Weijer, P.C.P. Bouten, S. Unnikrishnan, H.B. Akkerman, J.J. Michels, T.M. B. van Mol, High-performance thin-film encapsulation for organic light-emitting diodes, Org. Electron. 44 (2017) 94−98.
[90] M.A. Triana, H. El Hamid, J. Celli, R. Lanzafame, S.-T. Wu, Y. Dong, Quantum Dot Light-Emitting Diode Based Photomedicine: In Vitro Results to Date and Tunable Features for Targeted Phototherapy, Proc. 28th Int. Display Workshops 28 (2021) 810−813.
[91] Y. Jeon, H.-R. Choi, J.H. Kwon, S. Choi, K.M. Nam, K.-C. Park, et al., Sandwich-structure transferable free-form OLEDs for wearable and disposable skin wound photomedicine, Light: Sci. Appl. 8 (1) (2019) 114.
[92] H. Yamaguchi, J. Granstrom, W. Nie, H. Sojoudi, T. Fujita, D. Voiry, M. Chen, G. Gupta, A.D. Mohite, S. Graham, M. Chhowalla, Reduced Graphene Oxide Thin Films as Ultrabarriers for Organic Electronics, Adv. Energy Mater. 4 (2014) 1300986.
[93] Y. Su, V. Kravets, S. Wong, et al., Impermeable barrier films and protective coatings based on reduced graphene oxide, Nat Commun 5 (2014) 4843.
[94] H.K. Seo, M.H. Park, Y.H. Kim, S.J. Kwon, S.H. Jeong, T.W. Lee, Laminated graphene films for flexible transparent thin film encapsulation. ACS applied materials & interfaces. 8 (23) (2016) 14725−31.
[95] D.-W. Shin, Y.-H. Suh, S. Lee, B. Hou, S.D. Han, Y. Cho, et al., Waterproof flexible InP@ZnSeS quantum dot light-emitting diode, Adv. Opt. Mater. 8 (6) (2020) 1901362.
[96] L. Wang, C. Ruan, M. Li, J. Zou, H. Tao, J. Peng, et al., Enhanced moisture barrier performance for ALD-encapsulated OLEDs by introducing an organic protective layer, J. Mater. Chem., C 5 (16) (2017) 4017−4024.
[97] C.-O. Gensch, Y. Baron, M. Blepp, Consultant's Report on Cadmium Exemptions for RoHS, 2016, pp. 1−114. Available from: <https://rohs.exemptions.oeko.info/fileadmin/user_upload/reports/20160601_Final_Report_RoHS_Pack_10_Cd_QDs.pdf>.
[98] P.G. Tucker, Cadmium Toxicity What Are the U.S. Standards for Cadmium Exposure?, 2011, pp. 1−63. Available from: <https://www.atsdr.cdc.gov/csem/cadmium/docs/cadmium.pdf>.
[99] S.L. Jacques, B.W. Pogue, Tutorial on diffuse light transport, J. Biomed. Opt. 13 (4) (2008) 041302.
[100] H. Moseley, J. Allen, S. Ibbotson, A. Lesar, A. McNeill, M. Camacho-Lopez, et al., Ambulatory photodynamic therapy: a new concept in delivering photodynamic therapy, Br. J. Dermatol. 154 (4) (2006) 747−750.
[101] J. Evans, High-tech bandages lighten the load of light therapy, Nat. Med. 15 (7) (2009) 713.
[102] S.K. Attili, A. Lesar, A. McNeill, M. Camacho-Lopez, H. Moseley, S. Ibbotson, et al., An open pilot study of ambulatory photodynamic therapy using a wearable low-irradiance organic light-emitting diode light source in the treatment of nonmelanoma skin cancer, Br. J. Dermatol. 161 (1) (2009) 170−173.
[103] X. Wu, S. Alberico, E. Saidu, S. Rahman Khan, S. Zheng, R. Romero, et al., Organic light emitting diode improves diabetic cutaneous wound healing in rats, Wound Repair Regen. 23 (1) (2015) 104−114.
[104] H.-W. Guo, L.-T. Lin, P.-H. Chen, M.-H. Ho, W.-T. Huang, Y.-J. Lee, et al., Low-fluence rate, long duration photodynamic therapy in glioma mouse model using organic light emitting diode (OLED), Photodiagn. Photodyn. Ther. 12 (3) (2015) 504−510.
[105] R.J. Lanzafame, I. Stadler, Y. Dong, H. Chen, S.-T. Wu, J. He, Preliminary studies of a novel red-emitting quantum dot LED source for photobiomodulation applications, Lasers Surg. Med. 49 (2017) 57−58.

[106] R.J. Lanzafame, I. Stadler, Y. Dong, H. Chen, J. He, J. Blackman, et al., Preliminary studies of a novel red-emitting quantum dot LED source for photobiomodulation for In Vitro model of the wound healing, Lasers Surg. Med. 50 (4) (2018) 359−360.
[107] C. Lian, M. Piksa, K. Yoshida, S. Persheyev, K.J. Pawlik, K. Matczyszyn, et al., Flexible organic light-emitting diodes for antimicrobial photodynamic therapy, NPJ Flexible Electron. 3 (1) (2019) 18.
[108] C. Murawski, K. Leo, M.C. Gather, Efficiency roll-off in organic light-emitting diodes, Adv. Mater. 25 (47) (2013) 6801−6827.
[109] C.-H. Chen, L.-C. Hsu, P. Rajamalli, Y.-W. Chang, F.-I. Wu, C.-Y. Liao, et al., Highly efficient orange and deep-red organic light emitting diodes with long operational lifetimes using carbazole−quinoline based bipolar host materials, J. Mater. Chem., C 2 (30) (2014) 6183−6191.
[110] Y. Jeon, H.-R. Choi, M. Lim, S. Choi, H. Kim, J.H. Kwon, et al., A wearable photobiomodulation patch using a flexible red-wavelength OLED and its in vitro differential cell proliferation effects, Adv. Mater. Technol. 3 (5) (2018) 1700391.
[111] Y. Jeon, H.-R. Choi, J.H. Kwon, S. Choi, K.-C. Park, K.C. Choi, 22-4: Wearable photobiomodulation patch using attachable flexible organic light-emitting diodes for human keratinocyte cells, in: SID Symposium Digest of Technical Papers, vol. 49 (1), 2018, pp. 279−282.
[112] B. Hohendorff, C. Weidermann, K.J. Burkhart, P.M. Rommens, K.J. Prommersberger, M.A. Konerding, Lengths, girths, and diameters of children's fingers from 3 to 10 years of age, Ann. Anat. 192 (3) (2010) 156−161.
[113] E. Henderson, B. Lai, L. Lilge, Data acquisition for interstitial photodynamic therapy, in: M. Vadursi (Ed.), Data Acquisition, Intech Open, Rijeka, Croatia, 2010, pp. 265−280.
[114] Y. Lee, D.-H. Kim, Wireless metronomic photodynamic therapy, Nat. Biomed. Eng. 3 (1) (2019) 5−6.
[115] J. Kim, H.J. Shim, J. Yang, M.K. Choi, D.C. Kim, J. Kim, et al., Ultrathin quantum dot display integrated with wearable electronics, Adv. Mater. 29 (38) (2017) 1700217.
[116] M.K. Choi, J. Yang, T. Hyeon, D.-H. Kim, Flexible quantum dot light-emitting diodes for next-generation displays, NPJ Flexible Electron. 2 (1) (2018) 10.
[117] C.M. Lochner, Y. Khan, A. Pierre, A.C. Arias, All-organic optoelectronic sensor for pulse oximetry, Nat. Commun. 5 (1) (2014) 1−7.
[118] J. He, H. Chen, S.T. Wu, Y. Dong (Eds.), 27-4: Distinguished student paper: integrated sensing platform based on quantum dot light emitting diodes, in: SID Symposium Digest of Technical Papers, Wiley Online Library, 2016.

Carbon dots (C-dots): fluorescence processes and bioimaging

7

Gisele A. Medeiros[1], *Carime V. da Silva Rodrigues*[1], *John Spencer*[2] *and Brenno A.D. Neto*[1]

[1]Laboratory of Medicinal and Technological Chemistry, University of Brasília, Chemistry Institute (IQ-UnB), Campus Universitário Darcy Ribeiro, Brasília, Distrito Federal, Brazil, [2]Department of Chemistry, University of Sussex, Brighton, United Kingdom

7.1 Introduction

Carbon-based materials are of paramount importance for a diverse range of technologies used nowadays [1−5]. Among these materials, carbon dots (C-dots), also known as carbon nanodots, occupy a prominent position because of their attractive features, especially as light-emitting materials, as reviewed elsewhere [6−11]. The physicochemical properties of such materials are a consequence of their nanometric small sizes (typically in the range of 1−100 nm), but C-dots have typical sizes down to 10 nm [12]. One major advantage of using C-dots is that these derivatives commonly display very low cytotoxicity, thus rendering them attractive nanomaterials for bioapplication.

Beyond these few characteristics, C-dots exhibit tunable photoluminescence properties and multicolor emissions that are in turn intimately associated with excitation wavelengths. The C-dot cores are formed from stacking multiple graphene fragments (π-conjugated domains at the C-dot core), whereas the surface, characteristically oxidized, may bear functional groups or other organic structures. The possibility of modulating the size, functional groups at the C-dots surface and irradiation wavelengths, may aid in the biological application of these carbon-based nanomaterials. The possibility of functionalizing the C-dots surface may also help in the prediction of specific biological responses. Another important feature related to C-dots is that these nanometric carbonaceous derivatives may be synthesized from several sources and in general they are produced by means of low-cost materials.

When designing C-dots, it is important to bear in mind some attractive characteristics aiming at an efficient bioimaging application of the nanomaterial [13]. Initially, narrow nanoparticle size distribution is a desired feature and the photoluminescent properties are intimately associated with the size distribution. Currently, with several synthetic methods available for the synthesis of C-dots [14], great improvements have been reported, especially using hydrothermal methodologies. Tunable emissions associated with narrow emissions are also important considering the production of well-resolved images [15].

Quantum Materials, Devices, and Applications. DOI: https://doi.org/10.1016/B978-0-12-820566-2.00004-1

A rational use of the surface chemistry aiming at tuning both the physicochemical and the photophysical properties of the material [16,17] is vital to a successful application of the designed C-dot in specific bioimaging [18], or for any other light technology application of the nanomaterial [19]. The science behind the rationale for the surface functionalization (or oxidation) to attach small molecules or to control the organic functional groups noted at the exterior side of the nanoparticles is known as surface engineering. It is important to remember that chemical functional groups have a unique role for the C-dots' interaction with the biological interface, thus rendering the surface engineering a protagonist during the designing process of new functionalized C-dots. Finally, when bioimaging is the main goal, it is important to work with C-dots down to 10 nm [20]. Carbon nanoparticles of small size ($<$10 nm) allow for more precise intracellular targeting and faster internalization.

In this chapter, we will disclose some important contributions to bioimaging application of C-dots and describe their emission mechanisms to associate the emitting colors and cellular responses with the design process and rationale of the carbon nanoparticle derivatives.

7.2 C-dots fluorescent emissive processes

When C-dots are smaller than the exciton Bohr radius, quantum confinement effects become a viable option. To understand this effect, it is interesting to visualize (Fig. 7.1) the electronic movement possibilities similar to those distinguished in the studies of conductor and semiconductor materials. A change in the valence and conduction bands is observed, that is, continuous energy bands, toward discrete energy levels; thus the bandgaps also change upon the decrease of the 3D nanomaterial size. The net result is notorious in the bandgap transitions that are characteristically observed in the ultraviolet to the visible regions accompanied with improvement to fluorescent quantum yields [12]. In other words, the effect is basically related to the electronic movement restriction inside a small size nanometric system independently whether it is a 1D, 2D, or 0D limitation (as seen in Fig. 7.1) [21]. The emission of C-dots may be sometimes observed in the near-infrared region of the electromagnetic spectrum.

When the C-dots have large conjugated π-domains (basically the C-dot core) and minimum functional groups at the surface, the fluorescence is basically a result of the quantum confinement effect. As expected, by adjusting the size of the π-domains, it is possible to tune the C-dot bandgap. The larger the π-domains, the smaller is the bandgap and redshift is observed. This is the reason why as the C-dots size decreases (typically from 8 to 1 nm), a clear energy gap augmentation is noted as a consequence of a lower extent of the sp^2 content and therefore the lower π-conjugation in the C-dot cores. The net result is a blue shifting of the fluorescence emission. Several strategies may be used to control the C-dots size, as reviewed elsewhere [14].

It is important to differentiate two features regarding C-dots structure and emissive processes. First, the core size of the nanomaterial is not straight associated

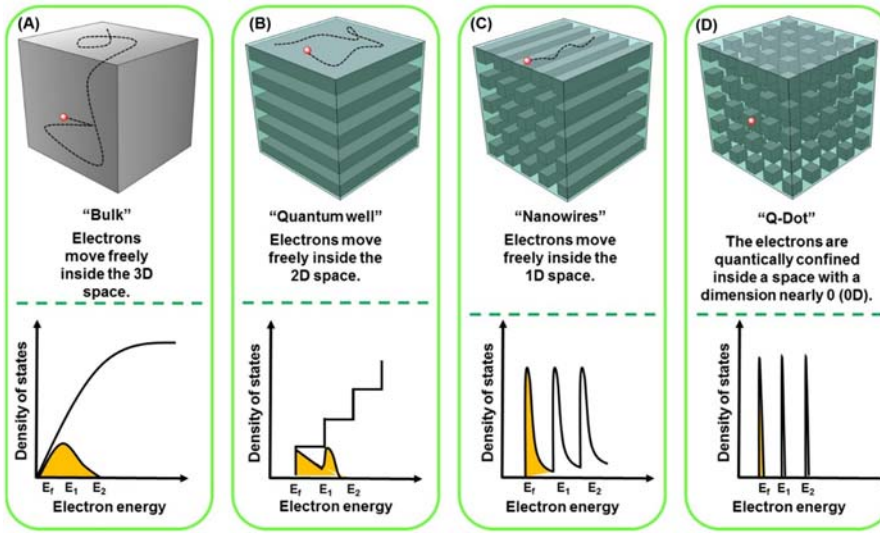

Figure 7.1 Electron movement restriction and quantum confinement effect. (A) No electron movement restriction is imposed and a free movement is allowed in the 3D space. (B) The electron movement is restricted between two layers, thus in a 2D space. (C) The electron movement is restricted in a 1D space due to quantum restrictions (nanowire or nanotube). (D) The electron movement is restricted in all directions (0D space) due to quantum restrictions (i.e., a dot).

with its surface oxidation degree. The surface effect will be analyzed in due course in this chapter. These two distinct parts play important and different roles in the fluorescence emission of the C-dots; thus it is possible to synthesize smaller particles with redshift effect as a consequence of the functional groups (or molecules) attached to the carbonaceous nanomaterial surface.

When C-dots are synthesized, although good size control is possible using optimized/developed conditions, these carbon-based nanodots have a size distribution and, as a consequence, different volumes are noted for the carbonaceous materials. A broadening is therefore observed when emission spectra are acquired and the Gaussian distribution may be observed in both the sizes and in the emissions spectra of the C-dots, as better visualized in Fig. 7.2. In this sense, controlled synthesis affording narrow distributions is most desirable aiming at a better control of the fluorescence emission due to the C-dots.

Surface engineering is another topic of paramount importance when considering the emissive properties of C-dots since surface defect states may also play a role in the C-dots fluorescence emissions. In general, defects are referred to as spherical shells (boundary regions) that are distinct from the carbon cores domains. Defect states are known to be complexes and, in the same particle, different defect states may be noted. As a consequence, excitation-dependent luminescence is a commonly observed phenomenon for C-dots. The defect states are usually generated from

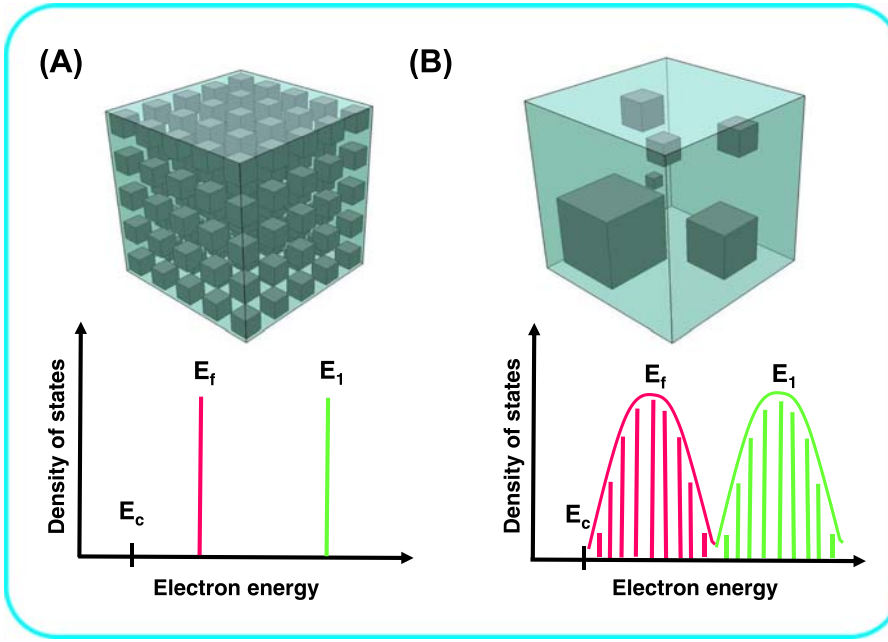

Figure 7.2 Density of states in C-dots. (A) Ideal behavior in which the nanoparticles have the same size/volume (top and left). (B) As a consequence of the Gaussian distribution of the particles sizes (top and right), a corresponding Gaussian distribution is observed in the emission frequencies. E_c = energy in the bottom in the conduction band-like state, E_f = energy in the fundamental level, E_1 = energy in the excited state.

surface oxidation processes, and frequently these defects act as traps for excitons, thus affording a fluorescence emission from defect states. The most commonly noted behavior is that the more oxidized the surface, the more defects are formed; thus redshifts in the emissions are the outcome of the process. When irradiated, photons with the appropriate energy, in relation to the bandgaps, will accumulate in the adjacent defects and then return to the ground states emitting at different wavelengths (usually in the visible to near-infrared regions).

Considering that different functional groups may be found at the C-dot surface, bearing different degrees of defects, and that these functional groups have their own energy levels, thereby producing a series of emission traps, as described elsewhere [22–24]. In this sense, choosing functional groups at the C-dots surface may allow for the color emission adjustment, especially because different functional groups have different abilities to supply electrons [25].

It is important to consider that C-dots may incorporate fluorophores, that is, molecules like fluorescent dyes, at their structures or associated with different metals. The presence of such molecules or metals may result in different effects over the C-dot fluorescent emission. In general, the dyes may help in the light absorption and in electron transfer processes. For some cases, quenching effects

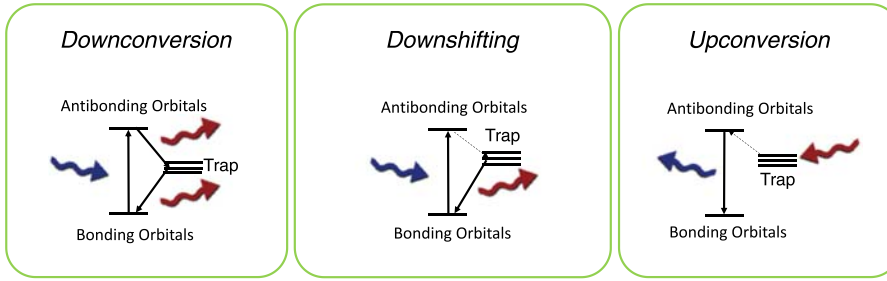

Figure 7.3 C-dots possible emissive processes considering a downshifting and both the possibilities of down- and upconversion.

may also be noted, especially when metals are present in the dyes' structures or coordinate with the C-dot structure [13].

Down- and upconversion processes are equally discussed for C-dots. In a general way, although this topic is largely discussed [26–33], C-dots may undergo downshifting, down- and upconversion processes, as seen in Fig. 7.3. Although it is a controversial issue, upconversion is accepted for C-dots even considering the possibility of multiphoton absorptions processes [34–36].

7.3 C-dots in bioimaging experiments

In this section, we intend to highlight the most recent advances for intracellular bioimaging using C-dots and modified C-dots, which also contributed to the comprehension of the fluorescence emission process associated with the carbonaceous materials. C-dots are attractive materials for imaging live cells also due to their small sizes and fast internalization processes. C-dots, in addition to the advantage of easy surface functionalization, which, where appropriate, allow for the targeting of specific organelles or components inside the cells. Indeed, as already demonstrated, the molecule used to functionalize the C-dots surface (e.g., cysteine) may actually affect the cellular energy metabolism [37].

In a recent work, Liu and coworkers [38] demonstrate the ability of C-dots synthesized from folic acid to target tumor cells. The hydrothermal aqueous synthesis allowed for the obtention of C-dots with fluorescent quantum yields up to 94%, that is, bright carbon nanoparticles. The use of folic acid in the synthesis also afforded C-dots with folate residues in the C-dots surface. Folic acid is known for its targetability to cancer cells characteristic, [39,40] being therefore used to differentiate healthy and tumoral cells.

After the hydrothermal treatment in aqueous media, the folic acid afforded C-dots bearing the residues of the acid in the surface of the nanoparticles. The average size was of 5.4 ± 2.2 nm. One important feature noted in the work [38] was that the C-dots had no fluorescence dependence of the excitation wavelength. This behavior, which is indeed unusual and highly dependent on the surface engineering,

pointed to a few features of the prepared nanoparticles. First, it indicated the single-energy level of the material surface, which was likely very well passivated by the folate residues from the hydrothermal synthesis. As a consequence, traps are not dominating the surface, thus allowing for single-energy level radioactive decays and favoring a high fluorescent quantum yield of the material.

The bioimaging experiments (Fig. 7.4) indicated the fundamental role of folate receptors to the C-dots internalization. Overexpressing folate receptor-Hela cells internalized the fluorescent nanoparticles very fast, whereas those with a regular quantity of these receptors showed almost no fluorescence, thus indicating that folate receptors are the essential factor for both the selective cell targeting and the carbon nanoparticles uptaking. Folate receptor positive SKOV3 cells were also tested and returned similar results, thus indicating this essential role of the folate receptors for the selective targeting and internalization.

Wei and coworkers [41] applied the hydrothermal methodology to obtain fluorescent and small C-dots from rose-heart radish. The nanoparticles had fluorescent quantum yields nearly 14% (aqueous solutions) and could be applied in cellular

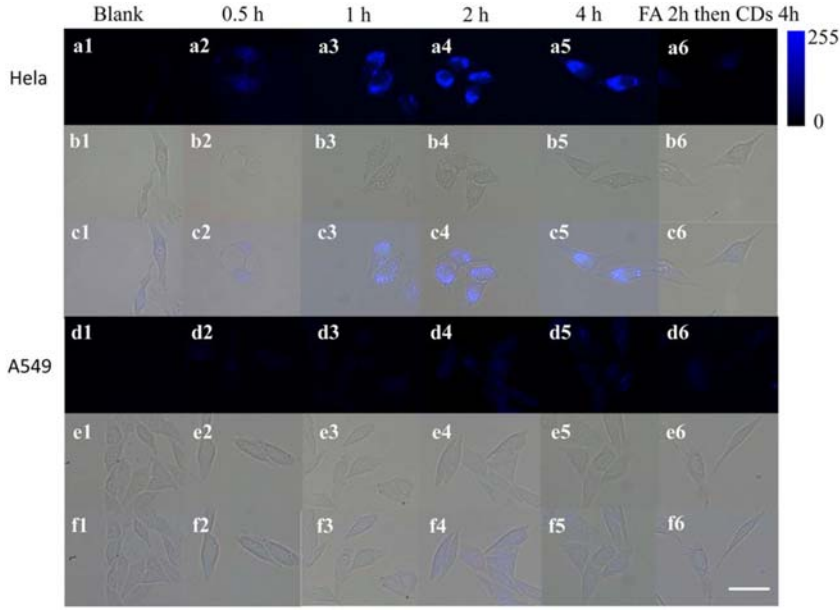

Figure 7.4 Fluorescence images of Hela and A549 incubated with the C-dots synthesized from folic acid (100 μg mL^{-1}) at 37°C for different incubated time, 0 h (a1, d1), 0.5 h (a2, d2), 1 h (a3, d3), 2 h (a4, d4), and 4 h (a5, d5). As another control, Hela and A549 pretreated at 37°C for 2 h with excess folic acid for folate receptor saturation, and then incubated with CDs (100 μg mL^{-1}) at 37°C for 4 h (a6, d6). Bright-field images are shown in (b) and (e). The overlay images are shown in (c) and (f). Scale bar of 10 μm.
Source: Reproduced with permission. Copyright 2018 Springer Nature.

bioimaging experiments as will be discussed herein. On average, 3.6-nm nanoparticles were obtained and, as highlighted, the particles were most observed to be between 1 and 6 nm, that is, down to 10 nm as expected for C-dots. The characterization of the as-prepared carbonaceous nanoparticles indicated the presence of several functional organic groups in the surface such as $-NH_2$, $-OH$, and $-CO_2H$.

The photoproperties of the as-prepared C-dots were also investigated and showed excitation-dependent emissions, as noted for most of the reported C-dots. By increasing the excitation wavelengths, redshifts could be observed for the material. The results pointed that, although there are several functional groups in the material surface, the presence of traps played a role over the photoluminescence of the C-dots. The difference in the size and therefore the different number of functional groups in the surface also contributed to different surface states and, thus, also contributed to the excitation-dependent emission properties of the C-dots. The excitation-dependent emission effect could, in principle, allow for the visualization of the emissive particles in different channels when applied in bioimaging experiments. The quenching effect was also observed in the presence of several metals aiming at sensing a specific metal. Results showed Fe^{3+} had a pronounced quenching effect even in the presence of interference ions, thus pointing to the selectivity of the material to the transition metal ion. It also pointed to the selective detection of the metal in bioimaging experiments.

SiHa cells were initially tested in the bioimaging experiments of the as-prepared C-dots. The excitation-dependent emission feature of the nanoparticles has been used to monitor the C-dots emissions inside the cells after the cellular uptake, that is, in the blue, green, and red channels (Fig. 7.5). This feature proved to be important because it allowed for authors to select in which channel the cellular process would be monitored. This characteristic, depending on the experiment, may be advantageous to follow an intracellular event. The internalization process proved to be fast and the cells could be observed emitting blue, green, and red when, respectively, irradiated at 405, 488, and 543 nm. When incubated with Fe^{3+} ions and followed by dynamic fluorescence imaging a quenching process was monitored. The quenching effect could be dynamically monitored and the fluorescence decreased as a consequence of the metal ions internalization.

The hydrothermal treatment of citric acid and neutral red dye afforded a solid that was characterized as red emitting C-dots [42]. The synthetic procedure was evaluated, and it was shown that the increase in the temperature also resulted in quantum yields increase as well, although some blueshift was also noted. Shorter reaction times also resulted in redshifts. By optimizing the synthetic conditions, C-dots of 3.4 nm (on average) could be obtained and characterized.

The photophysical evaluation of the as-synthesized C-dots indicated the excitation-independent emission property, therefore indicating a nearly uniform surface for the nanoparticles. The designed C-dots proved to be highly stable and the pH effect indicated optimal emissions between 2 and 8. Above and below these values, a decrease in the fluorescence could be observed as the net result of protonation or deprotonation of the surface functional groups such as $-NH_2$, $-OH$, or $-CO_2H$. The quantum yield of the particles was nearly 12%.

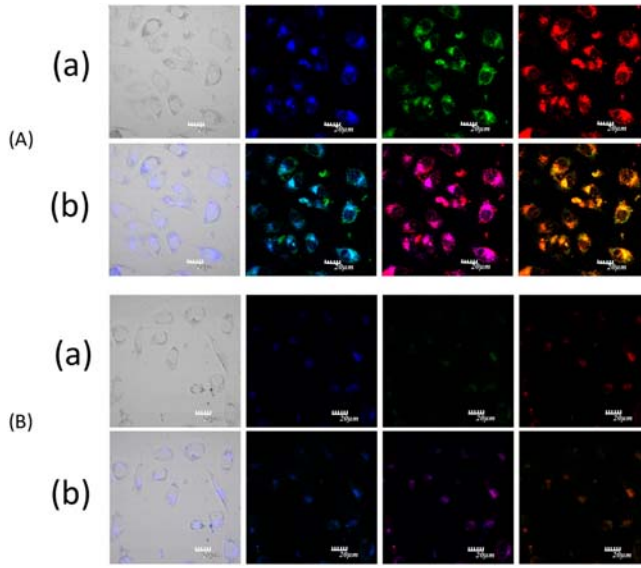

Figure 7.5 Laser scanning confocal microscopy images of SiHa cells incubated with (A) 0.50 mg mL^{-1} of the C-dots, (B) 0.50 mg mL^{-1} of the C-dots and 100-μM Fe^{3+} at 37°C for 3 h. The first left panels of the (a) lines show the bright-field images of SiHa cells. The second, third, and fourth panels of the (a) lines are cell images taken at $\lambda_{ex}/\lambda_{em}$ of 405/450 ± 25, 488/520 ± 25, and 543/650 ± 25 nm, respectively. The first panels of the (b) lines are the merged images of the first and second panels of the (a) lines. The second panels of the (b) lines are the merged images of the second and third panels of the (a) lines. The third panels of the (b) lines are the merged images of the second and fourth panels of the (a) lines. The fourth panels of the (b) lines are the merged images of the third and fourth panels of the (a) lines.
Source: Reproduced with permission. Copyright 2017 Elsevier.

Some metals were tested (by titration experiments), and Pt^{2+}, Au^{3+}, or Pd^{2+} showed more significant effects over the photoluminescence of the material. The presence of these metals afforded a quenching over the fluorescence of the C-dots, and limits of detection of 0.886, 3.03, and 3.29 μM were, respectively, observed. Pt^{2+} proved to undergo a dynamic quenching, whereas strong inner filter effect was taking place for the other two metals.

Bioimaging experiments (Fig. 7.6) were performed since no cytotoxicity could be noted for the C-dots. The application of the as-synthesized C-dots as bioimaging probes afforded red and intensive emissions using PC12 cells and zebrafish as the models. After Pt^{2+} addition, the intense red emission could be quenched in both experiments. Similar results could be obtained by an addition of Au^{3+} or Pd^{2+} indicating that the rationally designed carbon nanoparticles could be used to detect these metals in solution and in biological systems.

We have disclosed [43] the synthesis of small surface−modified C-dots (nearly 4 nm) using cow manure as the carbon source. Reproducible results could be

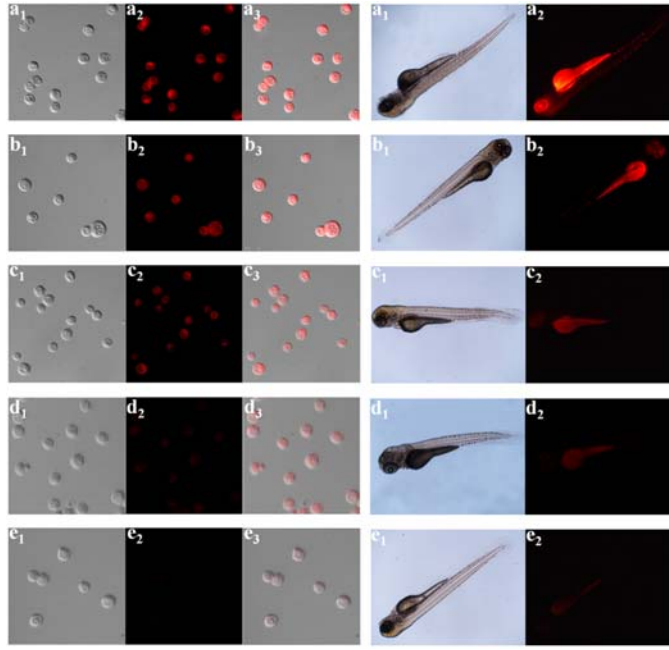

Figure 7.6 (Left) Confocal imaging of Pt^{2+} in PC12 cells. (a1−e1) Bright-field images. (a2−e2) Black field images of the C-dots in PC12 cells with the different concentrations of Pt^{2+} (0, 25, 50, 150, and 300 μM). (a3−e3). Overlay images. (Right) Fluorescence imaging of Pt^{2+} in ZF. (a1−e1) Bright-field images. (a2−e2) Fluorescence images of the CDs in ZF with the various concentrations of Pt^{2+} (0, 30, 60, 100, and 150 μM).
Source: Reproduced with permission. Copyright 2018 American Chemical Society.

obtained independently whether cow manure or glucose was used to the synthesis of the C-dots. Cow manure is a rich source of cellulose, which is a glucose-based polymer. By a simple chemical modification of the as-prepared nanomaterial, that is, the surface passivation with ethylenediamine, bright green C-dots emitters could be obtained. The C-dots exhibited a high quantum yield of fluorescence value (0.65) with an intense fluorescent green emission.

The surface-passivated material proved to be stable after 8 h of constant light irradiation and no notable decrease of the fluorescence emission was observed, indicating, therefore the high stability of the material. Under different pH values (3−9), intense and bright emission was also noted. The nanomaterial was also emissive in temperatures ranging from 5°C to 80°C. The excitation-dependent luminescence of the C-dots allowed the emission to be tuned in three different channels (blue, green, and red), although the green emission was considerably more intense.

The carbonaceous nanomaterial had no cellular cytotoxicity, thus prone to be used in bioimaging experiments. The cellular imaging experiments using MCF-7 cells (Fig. 7.7) showed that the modified C-dots were capable of associating in the cells' nuclei selectively with and intense green emission.

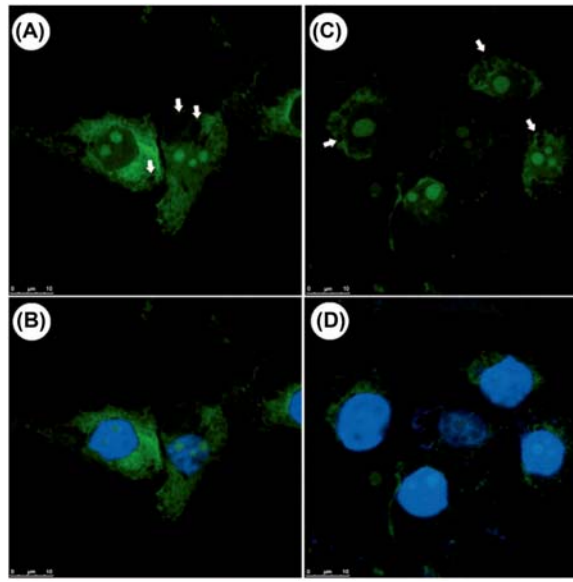

Figure 7.7 Cellular bioimaging experiments for the modified C-dots with the MCF-7 cell line: parts (A) and (B) show the modified C-dots stain pattern (green) for the fixed cells, whereas parts (C) and (D) show the staining for live cells. The fluorescent signals are shown to be mostly associated with the nucleoli of all cells. Parts (B) and (D) also show the nucleus staining with commercially available DAPI (blue). Note the arrows to indicate voids ("holes") in the cytoplasm, thereby showing no association with these organelles. The cytoplasmic associations (pattern and distribution) are with ribosomal components. Reference scale bar 10 mm.
Source: Reproduced with permission. Copyright 2014 Wiley-VCH Verlag GmbH & Co. KGaA, Weinheim.

7.4 Summary and outlook

Although C-dots were discovered more than a decade ago and thousands of findings are already disclosed, we are just scratching the surface of knowledge regarding the synthetic control, tuning the photophysical properties and possible application of these fascinating materials in bioimaging experiments. There is still much room for improvements, creative application of C-dots, and the surface engineering aimed at specific intracellular responses. Several groups are applying C-dots with success and trying to disclose the "secrets" behind the photoluminescence of these nanometric materials.

The possibility of accessing these virtually nontoxic nanomaterials using the most unusual carbon sources is just an additional appeal. Their highly stable emissions and recent progress toward a more controlled synthesis and fluorescence emission properties are fostering new discoveries and pushing the limits of light technology applications. Their advantageous photophysical properties along

with their easy handling and storage are helping in the furthering of the promising technology of C-dots for bioimaging.

In this chapter, we have described some selected examples of relevant works to highlight the recent progress toward the comprehension of the emissive properties of C-dots and their cellular responses in specific imaging experiments. We hope readers will be challenged by this new and exciting area where we are still taking baby steps yet will soon be moving with large steps.

References

[1] A. Verhagen, A. Kelarakis, Carbon dots for forensic applications: a critical review, Nanomaterials 10 (2020) 1535.
[2] Y. Wang, Y. Xia, Optical, electrochemical and catalytic methods for in-vitro diagnosis using carbonaceous nanoparticles: a review, Microchim. Acta 186 (2019) 50.
[3] J.B. Essner, G.A. Baker, The emerging roles of carbon dots in solar photovoltaics: a critical review, Environ. Sci. Nano 4 (2017) 1216−1263.
[4] S. Kumar, G. Saeed, L. Zhu, K.N. Hui, N.H. Kim, J.H. Lee, 0D to 3D carbon-based networks combined with pseudocapacitive electrode material for high energy density supercapacitor: a review, Chem. Eng. J. 403 (2021) 126352.
[5] L. Xie, Z. Jin, Z. Dai, Y. Chang, X. Jiang, H. Wang, Porous carbons synthesized by templating approach from fluid precursors and their applications in environment and energy storage: a review, Carbon 170 (2020) 100−118.
[6] S. Tajik, Z. Dourandish, K. Zhang, H. Beitollahi, Q.V. Le, H.W. Jang, et al., Carbon and graphene quantum dots: a review on syntheses, characterization, biological and sensing applications for neurotransmitter determination, RSC Adv. 10 (2020) 15406−15429.
[7] M.J. Molaei, The optical properties and solar energy conversion applications of carbon quantum dots: a review, Sol. Energy 196 (2020) 549−566.
[8] M.J. Molaei, Principles, mechanisms, and application of carbon quantum dots in sensors: a review, Anal. Methods 12 (2020) 1266−1287.
[9] X. Kou, S. Jiang, S.-J. Park, L.-Y. Meng, A review: recent advances in preparations and applications of heteroatom-doped carbon quantum dots, Dalton Trans. 49 (2020) 6915−6938.
[10] C. Ji, Y. Zhou, R.M. Leblanc, Z. Peng, Recent developments of carbon dots in biosensing: a review, ACS Sens. 5 (2020) 2724−2741.
[11] H. Ehtesabi, Z. Hallaji, S. Najafi Nobar, Z. Bagheri, Carbon dots with pH-responsive fluorescence: a review on synthesis and cell biological applications, Microchim. Acta 187 (2020) 150.
[12] F. Yan, Z. Sun, H. Zhang, X. Sun, Y. Jiang, Z. Bai, The fluorescence mechanism of carbon dots, and methods for tuning their emission color: a review, Microchim. Acta 186 (2019) 583.
[13] H. Ali, S. Ghosh, N.R. Jana, Fluorescent carbon dots as intracellular imaging probes, Wiley Interdiscip. Rev.: Nanomed. Nanobiotechnol. 12 (2020) e1617.
[14] N. Panwar, A.M. Soehartono, K.K. Chan, S. Zeng, G. Xu, J. Qu, et al., Nanocarbons for biology and medicine: sensing, imaging, and drug delivery, Chem. Rev. 119 (2019) 9559−9656.

[15] Y.P. Sun, B. Zhou, Y. Lin, W. Wang, K.A.S. Fernando, P. Pathak, et al., Quantum-sized carbon dots for bright and colorful photoluminescence, J. Am. Chem. Soc. 128 (2006) 7756–7757.
[16] J.-J. Hu, X.-L. Bai, Y.-M. Liu, X. Liao, Functionalized carbon quantum dots with dopamine for tyrosinase activity analysis, Anal. Chim. Acta 995 (2017) 99–105.
[17] L. Chai, J. Zhou, H. Feng, C. Tang, Y. Huang, Z. Qian, Functionalized carbon quantum dots with dopamine for tyrosinase activity monitoring and inhibitor screening: in vitro and intracellular investigation, ACS Appl. Mater. Interfaces 7 (2015) 23564–23574.
[18] S.K. Misra, I. Srivastava, J.S. Khamo, V.V. Krishnamurthy, D. Sar, A.S. Schwartz-Duval, et al., Carbon dots with induced surface oxidation permits imaging at single-particle level for intracellular studies, Nanoscale 10 (2018) 18510–18519.
[19] Z.Y. Li, L. Wang, Y. Li, Y.Y. Feng, W. Feng, Frontiers in carbon dots: design, properties and applications, Mater. Chem. Front. 3 (2019) 2571–2601.
[20] L. Yang, W. Jiang, L. Qiu, X. Jiang, D. Zuo, D. Wang, et al., One pot synthesis of highly luminescent polyethylene glycol anchored carbon dots functionalized with a nuclear localization signal peptide for cell nucleus imaging, Nanoscale 7 (2015) 6104–6113.
[21] J. Mao, Z. Liu, Z. Ren, Size effect in thermoelectric materials, NPJ Quantum Mater. 1 (2016) 16028.
[22] S. Kiran, R.D.K. Misra, Mechanism of intracellular detection of glucose through nonenzymatic and boronic acid functionalized carbon dots, J. Biomed. Mater. Res., A 103 (2015) 2888–2897.
[23] H.C. Yang, F.M. Li, C.Z. Zou, Q.T. Huang, D.J. Chen, Sulfur-doped carbon quantum dots and derived 3D carbon nanoflowers are effective visible to near infrared fluorescent probes for hydrogen peroxide, Microchim. Acta 184 (2017) 2055–2062.
[24] Y. Xu, M. Wu, X.Z. Feng, X.B. Yin, X.W. He, Y.K. Zhang, Reduced carbon dots vs oxidized carbon dots: photo- and electrochemiluminescence investigations for selected applications, Chem. Eur. J. 19 (2013) 6282–6288.
[25] B. Yuan, S. Guan, X. Sun, X. Li, H. Zeng, Z. Xie, et al., Highly efficient carbon dots with reversibly switchable green-red emissions for trichromatic white light-emitting diodes, ACS Appl. Mater. Interfaces 10 (2018) 16005–16014.
[26] Y. Zhang, X. Lan, S.H. Park, L. Wang, D. Liu, J. Shi, Rational design of efficient near-infrared photon conversion channel via dual-upconversion process for superior photocatalysts, Carbon 169 (2020) 111–117.
[27] C. Wang, R. Xue, A. Gulzar, Y. Kuang, H. Shao, S. Gai, et al., Targeted and imaging-guided chemo-photothermal ablation achieved by combining upconversion nanoparticles and protein-capped gold nanodots, Chem. Eng. J. 370 (2019) 1239–1250.
[28] H. Tan, G. Gong, S. Xie, Y. Song, C. Zhang, N. Li, et al., Upconversion nanoparticles@-carbon dots@meso-SiO_2 sandwiched core-shell nanohybrids with tunable dual-mode luminescence for 3D anti-counterfeiting barcodes, Langmuir 35 (2019) 11503–11511.
[29] D. Li, C. Liang, E.V. Ushakova, M. Sun, X. Huang, X. Zhang, et al., Thermally activated upconversion near-infrared photoluminescence from carbon dots synthesized via microwave assisted exfoliation, Small 15 (2019) 1905050.
[30] C. Zheng, L. Huang, Q. Guo, W. Chen, W. Li, H. Wang, Facile one-step fabrication of upconversion fluorescence carbon quantum dots anchored on graphene with enhanced nonlinear optical responses, RSC Adv. 8 (2018) 10267–10276.
[31] S. Gogoi, R. Khan, NIR upconversion characteristics of carbon dots for selective detection of glutathione, New J. Chem. 42 (2018) 6399–6407.

[32] H. Wang, J. Yi, Y. Yu, S. Zhou, NIR upconversion fluorescence glucose sensing and glucose-responsive insulin release of carbon dot-immobilized hybrid microgels at physiological pH, Nanoscale 9 (2017) 509–516.
[33] Q. Ma, J. Wang, Z. Li, D. Wang, X. Hu, Y. Xu, et al., Near-infrared-light-mediated high-throughput information encryption based on the inkjet printing of upconversion nanoparticles, Inorg. Chem. Front. 4 (2017) 1166–1172.
[34] S.Y. Lim, W. Shen, Z. Gao, Carbon quantum dots and their applications, Chem. Soc. Rev. 44 (2015) 362–381.
[35] J. Ke, X. Li, Q. Zhao, B. Liu, S. Liu, S. Wang, Upconversion carbon quantum dots as visible light responsive component for efficient enhancement of photocatalytic performance, J. Colloid Interface Sci. 496 (2017) 425–433.
[36] S. Zhu, J. Zhang, S. Tang, C. Qiao, L. Wang, H. Wang, et al., Surface chemistry routes to modulate the photoluminescence of graphene quantum dots: from fluorescence mechanism to up-conversion bioimaging applications, Adv. Funct. Mater. 22 (2012) 4732–4740.
[37] F. Li, Y.Y. Li, X. Yang, X.X. Han, Y. Jiao, T.T. Wei, et al., Highly fluorescent chiral N-S-doped carbon dots from cysteine: affecting cellular energy metabolism, Angew. Chem. Int. Ed. 57 (2018) 2377–2382.
[38] H.F. Liu, Z.H. Li, Y.Q. Sun, X. Geng, Y.L. Hu, H.M. Meng, et al., Synthesis of luminescent carbon dots with ultrahigh quantum yield and inherent folate receptor-positive cancer cell targetability, Sci. Rep. 8 (2018) 1086.
[39] C. Chen, J. Ke, X.E. Zhou, W. Yi, J.S. Brunzelle, J. Li, et al., Structural basis for molecular recognition of folic acid by folate receptors, Nature 500 (2013) 486–489.
[40] Y. Song, W. Shi, W. Chen, X. Li, H. Ma, Fluorescent carbon nanodots conjugated with folic acid for distinguishing folate-receptor-positive cancer cells from normal cells, J. Mater. Chem. 22 (2012) 12568–12573.
[41] W. Liu, H.P. Diao, H.H. Chang, H.J. Wang, T.T. Li, W.L. Wei, Green synthesis of carbon dots from rose-heart radish and application for Fe^{3+} detection and cell imaging, Sens. Actuators, B: Chem. 241 (2017) 190–198.
[42] W.L. Gao, H.H. Song, X. Wang, X. Liu, X.B. Pang, Y. Zhou, et al., Carbon dots with red emission for sensing of Pt^{2+}, Au^{3+}, and Pd^{2+} and their bioapplications in vitro and in vivo, ACS Appl. Mater. Interfaces 10 (2018) 1147–1154.
[43] C. D'Angelis do E. S. Barbosa, J.R. Corrêa, G.A. Medeiros, G. Barreto, K.G. Magalhães, et al., Carbon dots (C-dots) from cow manure with impressive subcellular selectivity tuned by simple chemical modification, Chem. Eur. J. 21 (2015) 5055–5060.

This page intentionally left blank

Quantum tunneling nanoelectromechanical system devices for biomedical applications

8

Marek T. Michalewicz[1] *and Anthony Sasse*[2]
[1]Sano Centre for Computational Personalised Medicine, International Research Foundation, Kraków, Poland, [2]RMIT University, Melbourne, VIC, Australia

8.1 MEMS and NEMS sensors and sensing in biomedical applications

8.1.1 Existing MEMS devices

Explosive growth in semiconductor fabrication and nanotechnology, its promise of a multitude of new applications and products, as well as the continuing reduction in the scale of microelectronic systems create an opportunity for sensors and diagnostic devices in biomedical applications that operate in an *almost* noninvasive manner and are characterized by ultrasmall dimensions and extreme sensitivity.

Several general reviews describe a variety of sensing technologies and their application areas in biomedicine [1−6]. Specifically, biomedical sensors in micro/nanoelectromechanical systems (MEMS) and (NEMS) are reviewed in Refs. [1,2,6−10]. Specialist conferences devote a large part of their program to nanosystems and sensing in biomedicine [11].

Wearable sensors, typically accelerometers or gyroscopes, are used to observe and analyze exoskeleton system [12], human body joints angles [13], cervical range of motion [14], human motion [15], or Parkinson's disease [10].

Other wearable sensor applications include monitoring of vital signs [16], imbalance disorders [17], wrist pulse signal acquisition [18], measurement of blood flow variation [19], oxygenation [16], or seismocardiography [20,21]. Wearable sensor selection is presented in Ref. [22].

Continual progress in reducing sensors' size, sensitivities, signal transmission, and analysis and new methods to supply or harvest energy enable a nearly noninvasive or minimally invasive application of implantable sensors. Implantable pressure sensors [23] are used for blood pressure monitoring [24] or intracranial pressure measurements [25]. Other examples of implantable devices and sensors [26] include minimally invasive catheters [27], cardiac and bladder catheters [4], MEMS accelerometers to detect heart bypass surgery complications [28], retinal implants [29], electronic contact lenses [30], and sensors for regenerative medicine [31].

Quantum Materials, Devices, and Applications. DOI: https://doi.org/10.1016/B978-0-12-820566-2.00009-0

Another class of biomedical sensors are chemical sensors [32] such as microfluidic pH-sensing MEMS chip [33] or alcohol vapor sensor based on multiwalled carbon nanotube [34] or oral/salivary monitoring MEMS [35]. Some are used in nanomechanical infra-red (IR) spectroscopy [36] or for intradermal glucose monitoring [16,37].

Newly discovered and perfected materials such as liquid crystal polymers [25], microbial nanocellulose [38], hydrogels [39], nanocomposites [40], functionalized nanowires [41], and graphene [42] enable new sensing principles and new sensor designs.

A number of physical phenomena are used in sensing. Some of these include the following:

- *Piezoresistive* devices exploit the relatively strong piezoresistive effect in silicon. Silicon piezoresistors are placed in the supports of a proof mass, acting as strain gauges as the proof mass moves in response to acceleration.
- *Piezoelectric* sensors use a piezoelectric material, such as ZnO, which generates a charge directly from the displacement of the proof mass. Piezoelectric and piezoresistive nanodevices are reviewed in Ref. [43], force sensors in Ref. [44], pressure sensors in Ref. [45], and piezoresistive sensors for bones stress and characterization are described in Refs. [46–48].
- *Capacitive*: MEMS-based capacitive accelerometers operate by sensing the capacitance changes between electrodes fixed to a proof mass and electrodes fixed to the accelerometer package. Acceleration causes displacement of the proof mass, and the change in capacitance can be measured. Capacitive accelerometers are widely deployed in low-cost, large-volume automotive applications, but it is also possible to produce higher precision devices for other more demanding applications, such as inertial navigation or accelerometers for medical diagnosis or therapy use [17]. Capacitive accelerometers can be made using bulk or surface micromachining, and both lateral and vertical structures are possible.
- *Optoelectronic* sensors are reviewed in Ref. [49] and their use in cardiorespiratory vital sign measurements are discussed in Ref. [50].
- *Resonant magnetic field* sensors [7].

8.1.2 Unique advantages of quantum tunneling NEMS devices

Quantum tunneling devices have advantages over devices that utilize the above transduction mechanisms, for example:

- Piezoelectric transducers require high voltages; the extension range depends on the length of the piezoelectric element and the applied voltage. The brittle piezo element is an active part of a sensor and often fails (breaks) in dynamic measurement applications.
- Piezoresistive accelerometers exhibit an uncompensated temperature coefficient of around 0.2°C, which means that temperature compensation is required. This compensation can involve such process steps as laser-trimming, inevitably adding cost. Piezoresistive accelerometers also tend not to be stable over time.
- MEMS-based piezoresistive accelerometers are produced using bulk micromachining, with feature sizes that make integration with microelectronics difficult.
- As discussed above, capacitive accelerometers require the measurement of extremely small changes in capacitance, which limits resolution.

Several capacitance sensing MEMS accelerometer designs have been reported with thermal noise in the order of 1 $\mu g/\sqrt{\text{Hz}}$ in an air environment. An improvement of 100 times is to be expected when operating in a vacuum. These capacitor-based designs have not been driven to vacuum-based techniques because of the difficulties in measuring device output much below these levels. Resolution of movement down to 10 nm has stretched the capabilities of capacitive sensing and the associated amplifier techniques. The quantum tunneling measurements should be capable of providing resolution of movement such that 50 nm represents a full-scale output.

This capability has no parallel in traditional sensor technology and opens up the possibility of an entirely new class of biomedical NEMS devices.

Power systems required for prolonged sensors and devices useful for life operation, especially in case of implantable devices, may be battery-based, thermo-voltaic, photovoltaic, micro fuel cell, electrostatic, capacitive, electromagnetic, piezoelectric, and energy-harvesting systems [16,30,43,51–53].

Wiring for minimally invasive implantable sensors with thousands of channels for in vivo neuronal recording, medical diagnostics, and electrochemical sensing was presented in Ref. [54].

Communication is often realized through wireless means, such as in MEMS microphones [55], MEMS for pressure sensing in the gastrointestinal (GI) tract [56], or MEMS-based accelerometer [57].

Wearable antennas for medical monitoring systems were discussed in Ref. [58].

Data transmission from biomedical sensors [16] and data processing and analysis are also important topics tackled with modern approaches such as convolutional neural networks [21], support vector machine [59], artificial intelligence [60], data fusion for multiple MEMS-based cardiac and respiratory gating [61], and various calibration methods for accelerometers [15].

Mechanical dynamic NEMS sensors are useful in a range of biomedical applications such as:

Measurand	Sensor
Motion (velocity, acceleration)	Accelerometers
Sound	Ultrasensitive microphones
Force (pressure)	Pressure meters [44,62]
Flow	Flow meters [63]

8.1.3 Further prospects for ultrasmall and sensitive medical NEMS sensors in biomedicine

- *Pressure sensors* are used for *nearly noninvasive* medical monitoring for postoperative intracardiac and intracranial monitoring.

Current technology requires placement of infection-prone catheters connecting the target site with external pressure transducers, with an only short term of the order of three to seven measurements possible. Long-term implantable sensors will revolutionize postoperative care and will enable placement at multiple sites, for

example, left atrium, left ventricle, pulmonary artery, superior vena cava, aorta, or radial artery. These pressure sensors will be able to discern basal versus superior cranial pressures. They will enable highly accurate diagnosis and allow optimization of medical care and will help to detect adverse events earlier.

- *Blood pressure monitoring*
  Periarterial NEMS devices will provide constant 24/7, long-term, accurate data measurement allowing optimization of medical therapy, instead of sphygmomanometers that have not changed in over 150 years.
- *Other sites* where pressure sensing using ultraminiaturized pressure sensors would be used are glaucoma = intra-ocular pressure, renal artery stenosis, peripheral vascular disease (carotids, limbs), abdominal aortic aneurysm (where transmural pressure/tension will predict the timing of rupture), vertebral disc pressure, and bladder.
- *Associated flow meters* will allow pressure/flow analysis. Nanotech devices will be easily incorporated into the large variety of stents currently being inserted. Examples of their use include coronary artery, abdominal aorta, peripheral arteries such as carotid and limbs, and stents are being developed for bronchi (airways).
- *Sensors for motion localization*, for example, eyes in sleep, limb in sleep.
- *Flow meters*
  - Vascular flow
    Critical blood flow scenarios: coronary, renal, carotid (pre-, peri-, postoperative). Vascular spasm detection—cerebral: subarachnoid hemorrhages, migraine, neonatal cardiac malformations
  - Flow meters: Airflow used for acute cases, such as asthma or sleep apnea, or for chronic cases such as nasal, chronic obstructive pulmonary disease = COPD or others.

  All these applications could be realized as wearable, patient-based network, either internally placed, or externally worn, or in close proximity such as in mattresses in association with a low-power wireless network such as passive radiofrequency technology, to allow continuous or intermittent computer-based monitoring in a home, step-down facility, or hospital environment.
- *Ultrasensitive microphones*

Ultrasensitive microphones and microphone networks can be used for ultrasound tests, investigation of structure/function of organs, in neonatology where organs can be observed for normal development, organ transplant monitoring, and for loss of function, such as in cardiac transplantation of the progress of the left ventricle and atria. Ordinary organs will be able to be closely observed, such as in cardiac failure, and more precise treatments tailored as a result.

8.2 Quantum tunneling

Tunneling of particles (electrons, protons, alpha particles [64–66]) is an exclusively quantum phenomenon arising out of the particle-wave duality. It can only be explained by the laws of quantum physics. In the quantum realm particles such as an electron, proton, or alpha particle can penetrate energy barriers higher than the energy of that particle, and appear on the "other side" in a "ghostlike" manner. The

history of the earliest studies of tunneling phenomena gives a fascinating insight into the development of modern quantum physics [67,68].

Several Nobel Prizes in Physics were awarded for contributions related to quantum tunneling effect:

- de Broglie, for conceptualizing particle-wave duality [69];
- Bethe, for explanation of energy production in the Sun and stars [70,71];
- Josephson, for theoretical predictions of the properties of a supercurrent through tunnel barrier—Josephson effect [72];
- Esaki and Giaever, for experimental discoveries regarding tunneling phenomena in semiconductors and superconductors, respectively [73,74];
- Binnig and Rohrer, for the design of the scanning tunneling microscope (STM) [75].

Quantum tunneling explains fundamental processes in nature from astrophysics, for example, physics of energy production in stars, to life science, for example, electron transfer in respiratory complexes of mitochondria and enzymes [76–80], but it is also the essence of a number of modern technologies, devices, and measurement techniques.

Magnetoencephalography is an imaging technique used to measure the magnetic fields produced by electrical activity in the brain via extremely sensitive magnetometers, typically superconducting quantum interference devices that are built with superconducting tunneling Josephson junctions.

STM "is widely regarded as the instrument that opened the door to nanotechnology and a wide range of explorations in fields as diverse as electrochemistry, semiconductor science, and molecular biology" [81].

Other useful tunneling devices we should mention are *tunneling diodes* or *quantum computer designs based on Josephson junctions*.

We will not expose here the details of quantum tunneling ideas and formalism but merely direct the reader to textbooks on quantum mechanics, or specialist monographs such as [82,83].

8.3 Design and proof of concept for quantum tunneling NEMS sensors

8.3.1 Different designs of quantum tunneling sensors

The whole class of sensors, such as accelerometers, pedometers, and pressure and flow meters, can be constructed on the basis of motion measurement in time and time derivatives. Here we describe a type of NEMS motion sensors based on quantum tunneling between arrays of nanowires. The ideas described below were developed by one of the authors with coworkers at Quantum Precision Instruments Asia Private Limited (Quantum-π) in Singapore between 2004 and 2008 [84–90].

The proposed devices were branded *dynamic nanoTrek*. Their operation is based on a variable overlap area of the quasi-1D nanowire electrodes placed on two opposing atomically flat surfaces.

The intellectual property rights [86] describe a novel technology for ultrasensitive monolithic quantum tunneling NEMS sensors. Arrays of quasi-1D nanowires are fabricated on two substrates. When a small bias is applied between the two sets of nanowires that are essentially in a parallel configuration, a tunneling current flows between them. The substrates are allowed to slide laterally with respect to each other, with separation between a set of nanowires kept constant. The tunnel current is an extremely sensitive measure of the overlap area of nanowires on both the opposing substrates. These NEMS devices unlike their predecessors [91–96] are not cantilever, beam, or point tip devices.

This new and unique technology has not been implemented yet. Despite the considerable technical challenges, the theoretical and experimental bases of the project are well substantiated. The first working linear encoder of position based on quantum tunneling has been demonstrated. The sensing element consisted of 12,000 nanowires, each 90-nm wide and 5-mm long ($\sim$1:55,000 aspect ratio of width-to-length of nanowires), on a sensing area of 5×4.3 mm [90].

Binnig and Rohrer were awarded the Nobel Prize in Physics for constructing and successful demonstration of the STM [75]. Soon after their feat, several groups attempted to build cantilever or beam geometry sensors based on quantum tunneling through a variable interelectrode gap [91–96]. Despite considerable efforts and some successes, cantilever geometry quantum tunneling dynamic sensors have not achieved broad commercial success. Here, we propose a different principle of operation for quantum tunneling devices. *nanoTrek* devices are not cantilever or beam devices. They are based on a constant interelectrode separation, but variable tunneling area between two sets of nanowire arrays deposited on two separate substrates. These sensors are unlike any previously built or designed MEMS/NEMS devices [97–102].

8.3.2 Quantum tunneling NEMS devices based on overlapping arrays of nanowires

The concept of tunneling between systems of conductors with a variable area has never been exploited before. In the design of a tunneling sensor proposed here, arrays of nanowires (quasi-1D conductors) are deposited on two substrates. Nanowires are made of a suitably chosen metal (TaN, Au/Ti, Ag, selectively doped substrate, or other) and are from few to 250 nm in width and a few μm to several mm in length. The nanowires are separated by several to 250-nm wide insulator strips (e.g., substrate in damascene process). An important parameter of the device is the pitch, defined as a sum of the nanowire width and the adjacent insulator strip width.

The two substrates can be brought into close proximity. Preferred embodiment is for the substrates to be monolithically integrated and held in place by flexible support structures. When a small bias (not more than few volts) is applied between the two sets of nanowires, a tunneling current flows between them. The plates are allowed to slide laterally with respect to each other, but the intersubstrate normal separation remains constant. The current is an extremely sensitive, oscillatory

(not exponential!) measure of the overlap area or shadowing of the nanowires on the opposing substrates.

In the static mode of operation, nanoTrek is a transducer of position or translation. It can operate in coarse grain and large translation resolution when one plate is translated with respect to the other by more than one pitch length. The fine-grain and small translation resolution will be achieved when translation is less than one pitch length. In fine-grain resolution mode, *nanoTrek* will have subnanometer linear sensitivity. This mode of operation can be thought of as a quantum tunneling linear encoder of position. Proof of concept for this type of device has been constructed and demonstrated.

In the dynamic mode of operation, where devices are coupled with integrated inbuilt timers and nano-spring equilibrium position return mechanisms, *nanoTrek* devices will constitute an entire family of new, exceedingly sensitive NEMS sensors. Due to specific geometry and mechanism of operation, a *nanoTrek* sensor will not be prone to problems inherent in earlier cantilever tunneling sensors such as tip-counter electrode crashing and subsequent short-circuiting and tip damage, drift, low current signal, and an exponential characteristic response.

There are several challenging issues in developing this kind of NEMS devices posing substantial technical risk, but also offering a high potential reward, listed here:

- Developing fabrication techniques for 3D monolithic devices with 2D arrays of quasi-1D nanowires on opposing (internal, hidden) surfaces.
- Fabrication of nanowires, few-to-100-nm wide with nearly atomically smooth surfaces.
- Developing packages for stand-alone sensors that can be only 50−100 μm in size.
- Developing robust digital signal processing (DSP) for the low-level electrical nanosystems.
- Optimizing the application-specific vibrational response of the nanosensors.
- Integration of sensing, power, and communication facilities on a single chip in a single package.
- Controlling the dimensions, compositions, and shapes of fabricated nanowires with sufficient precision.
- In alternative embodiments, we propose the use of two separate chips and soft-matter spacer (this is the embodiment used in our linear encoder), which leads to very subtle issues of selection, application, and life-time issues regarding soft-matter spacer.
- Spacer nanotribology, including stiction, adhesion, and frequency response.
- Device encapsulation and containment of the liquid or soft-matter spacer.
- Electrical connectivity, or nano-micro-macro signal transfer and communication from a stand-alone or sensor-in-a-network to the macroscopic world.
- Packaging and modularity.
- Thermal and vibrational response, noise, and robustness of the devices.
- Behavior in hostile environments.
- Micropower and network integration.

Other research groups, using a variety of approaches, have addressed some of the above challenges in a different context—especially in the multitude of ways for fabricating nanowires. A good example of such an early work is the molecular memory research done by Phil Kuekes, James Heath, R. Stanley Williams, and

others at Caltech, and Hewlett-Packard and few early molecular electronics companies [103] that were fabricating arrays of nanowires on two substrates forming a square grid crossbar separated by a layer of multistate memory molecules [104–107]. In contrast to that work, *nanoTrek* will be an electromechanical system with a movable nanowire substrates (Table 8.1).

The greatest remaining technical challenges are as follows:

Monolithic 3D integration

This is the most challenging aspect of proof-of-concept work. We propose at least two different alternative approaches to address this challenge:

- 3D monolithic, seven-mask process that uses the creation of several layers and embedded elements (nanowires, suspension springs, terminal connections, etc.) and elective removal of gap material using isotropic wet etching described in detail below (including process flow chart);
- hybrid process where two complementary parts of the device are fabricated on two wafers and subsequently joined to form a device—the risk and the great unknown here is that in MEMS practice, *void* spaces are of an order of microns and we must reduce it to less than 10 nm.

Fabrication of uniform nanowires with atomically smooth surfaces

2D parallelism and constant separation between plates

Another challenging aspect of this design is the achievement and control of a constant, predetermined and extremely small of less than 10 nm, intersubstrate separation, as well as the 2D intersubstrate parallelism. Note that the plates are to be of the order of 100×100 μm.

Signal transfer and packaging

The entire fabrication process has to be compatible with existing microelectronics fabrication processes. Apart from the core *nanoTrek* sensing element, the sensors will require on-chip-integrated electronics to provide control and signal conditioning, communication, and micropower (if possible). For various sensor applications where the device needs to interact with the outside environment, tailored packaging schemes will need to be designed. A major risk arising from bonding and packaging is the possibility that the mechanical and thermal stress induced during these processes will cause damage or impair performance. The risk is that all existing bonding techniques might affect the device behavior in an unacceptable way, so alternative methods may need to be developed. For devices that would operate in harsh environments, the packaging requirements will be considerably more rigorous than conventional microelectronic components.

Noise relating to low outputs

Noise from the electronics that interfaces the macro world to the sensing elements is the factor that limits the overall resolution for most accelerometer designs [109]. This is because the outputs of the sensing elements in accelerometers are often extremely small in both absolute and relative terms. For capacitive accelerometers the change in capacitance that corresponds to a particular acceleration may be extremely small. It was shown that for an example set of sensing element characteristics, a 1-mg acceleration would cause a change in capacitance of only 10 ppm [110]. We expect similar factors to influence quantum tunneling sensors, especially critical is very small electrodes area and relatively large interelectrode separation ($\sim$10 nm).

Table 8.1 Key technical factors.

Key factors	Technical targets	Commercial requirements	Current practice	Associated technical barriers	Innovative technical approaches
Production of atomically smooth surfaces	<1 nm	No "micro-tips" formation	Achievable, for example, Chemical Mechanical Planarization (CMP) process	Entire wafer area undulation, especially 8″ wafers	Sensor area very small—undulations *not visible* at this scale
Maintenance of proof mass to substrate spacing	<1 nm variation	Related to spring constant of proof mass (very stiff in the direction parallel to normal to two plates)	No known applicable current practice	Very detailed NEMS mechanical modeling, nanometer dimensions tolerances	Use of soft-matter spacer or novel MEMS structure
Low thermal noise structure	10 ng/$\sqrt{Hz}$	500 ng/$\sqrt{Hz}$	90 ng/$\sqrt{Hz}$ [108]	Low damping	Structure with low damping; vacuum packaging
Nanowire width and spacing	10 nm/ 10 nm	90 nm	100 nm (mainstream complementary metal−oxide−semiconductor (CMOS) process), 10 nm (nanoimprint lithography and atomic layer epitaxy (ALE))	Nanowires on internal opposing surfaces of plates	Novel 3D process, eeactive ion etching (RIE), hybrid process, separate plates solution

MEMS, Microelectromechanical system; *NEMS*, nanoelectromechanical system.

Thermal noise

Accelerometer proof masses are affected by mechanical-thermal noise. Thermal noise is usually not a restricting factor in the performance of capacitive accelerometers, due to the higher noise level related to position sensing. All devices are characterized by inherent 1/f noise, characteristic of various types of noise in the electronics that limits the overall performance.

Micropower, networking, integration

Each of the key issues mentioned in this paragraph is a topic of intense current research [111–129]. Individually none would perhaps be considered an extraordinary challenge but combining all into a working, robust quantum tunneling dynamic NEMS sensor of minute dimensions poses substantial technical issues and risks (Table 8.2).

Many methods were successfully developed to fabricate arrays of nanowires [130–163].

The most successful embodiments of proof-of-principle *nanoTrek* devices, so far, have been fabricated at Singapore's A*STAR Institute of Microelectronics (IME) and tested at Institute of Materials Research and Engineering (IMRE). Test results have been published in peer-reviewed conference proceedings [87,89,90]. The publications demonstrate the achievement of large arrays of 12,000 nanowires, each wire of 90-nm width and 5-mm length that displays voltage- and displacement-dependent current characteristics consistent with the quantum tunneling theory. To maintain controlled and uniform separation between the opposing arrays of nanowires, these devices have used soft-matter spacers (PFPE or Zdol, lubricant used in hard disk drives) with good results achieved. The two figures below represent second-generation *nanoTrek* devices fabricated at IME in Singapore (Fig. 8.1).

Table 8.2 Technical success criteria.

Technical criterion	Target	Explanation
Atomically smooth substrates	<1 nm	Required to avoid formation of *micro-tip* tunneling electrodes
Tunneling current signal level	>1 nA	Required for compact digital signal processing (DSP) electronics
Variation in peak quantum tunneling current between devices	10%	Required for uniformity in mass-scale product
Device noise floor	$< 10\ \mathrm{ng}/\sqrt{\mathrm{Hz}}$	Includes thermal noise, quantum tunneling current noise, and readout circuit
Shock resistance	20 g	Required for device robustness
Network of many sensors	>20	Depending on application
Distance between each sensor in distributed wireless network	>5 m	Required for large engineering structures monitoring
Power for each sensor in wireless network sustained for at least	1 year	Required for maintenance-free operation (ideally energy harvesting power sources should be used)

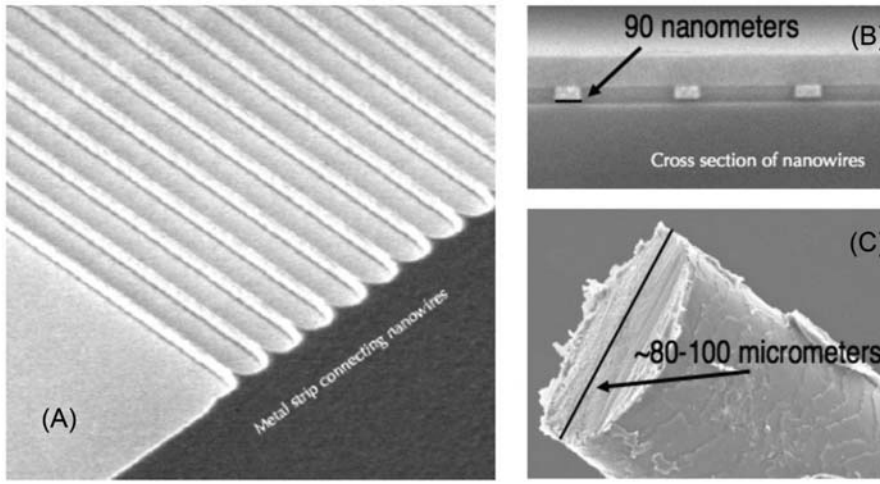

Figure 8.1 (A) Tilted view SEM image of TaN metal line nanowires before planarization. The fabrication of the *nanoTrek* devices was done at the IME using an 8″semiconductor processing line. TaN is the metal of choice for nanowires due to its favorable surface and other properties. The sub-100-nm lines having a 360-nm pitch were patterned using a Nikon KrF lithography scanner with an alternating phase shift mask. Dry etching was used to transfer the resist patterns into the metal layer followed by USG deposition and chemical mechanical polishing (CMP). (B) A cross-sectional scanning electron microscope image of TaN nanowires. The width of the nanowires is nominally 90 nm and their pitch is 360 nm. The specimen was fabricated for Quantum-π at IME, Singapore. (C) STM image of a human hair. *IME*, Institute of Microelectronics.

8.3.3 Proof-of-concept tunneling current measurements, NEMS conceptual designs, and proposed fabrication processes

Quantum-π has tested a quantum tunneling current-based linear position encoder at the IMRE facilities in Singapore. With the relative positions of the top and bottom nanowire arrays held fixed, all tests showed strongly nonohmic current-voltage characteristics in good agreement with quantum tunneling theory. When the arrays were laterally displaced, with constant vertical separation and a fixed applied voltage, oscillatory current versus position curves were obtained. Fig. 8.2 shows a typical result. The high tunneling current values observed, compared to other tunneling devices such as STMs, is due to the very large total area of nanowire electrodes in the present devices (Figs. 8.3–8.5).

8.4 New quantum tunneling metrology for cantilever-based devices

Atomic resolution scanning probe microscopy (SPM) [164] includes the original STM, which was originally developed at the IBM Laboratories in Zurich [165],

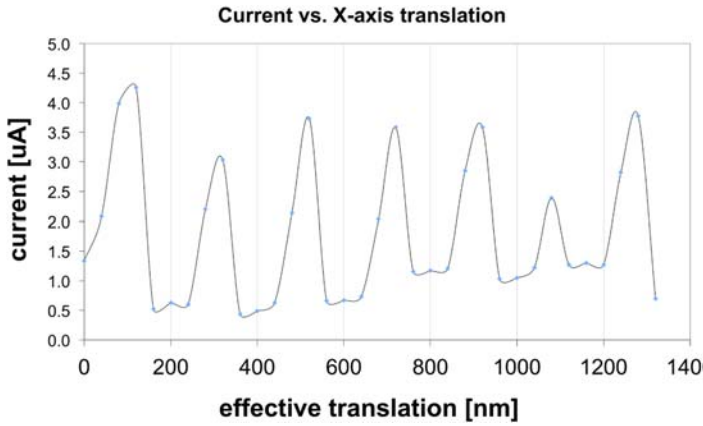

Figure 8.2 The measured quantum tunneling current versus translation in a proof-of-concept quantum tunneling linear position encoder obtained by Quantum-π at IMRE, Singapore [90]. *IMRE*, Institute of Materials Research and Engineering.

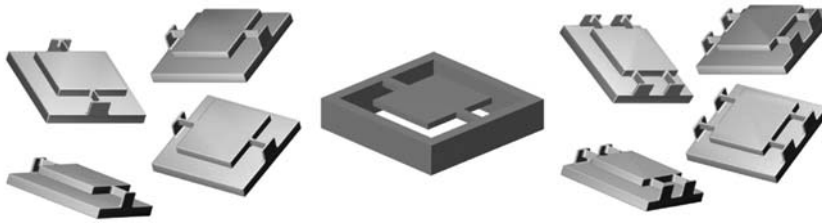

Figure 8.3 It depicts perspective views of 3D *nanoTrek* monolithically integrated devices. The all-important arrays of embedded nanowires on the bottom surface of the top plate and on the top surface of bottom substrate are not depicted here. See the process flow diagram in Fig. 8.5 for the nanowire locations and their proposed method of fabrication.

various kinds of atomic force microscopes (AFMs) [166,167], and many derivative kinds of STM probes. These local atomic resolution probing techniques are considered to be the basic metrology techniques in nanotechnology and in many modern biological, materials, and engineering applications [168–170].

Some 4000 AFM-related papers were published by 2005 alone, with several thousands of them published since the original paper [166]. More than 500 patents related to various forms of SPM have been filed worldwide. AFMs are critically important instruments in biology and life science, physics, chemistry, surface science, semiconductor manufacturing, materials science, and nanotechnology. AFMs have been sent to space with the Rosetta European Space Agency mission and NASA is planning to send AFM in its mission to Mars to analyze particle size distribution in cometary and Martian material.

SPM-like microcantilever devices have wide range of applications as chemical sensors. Several devices were built to serve a function an artificial nose [171–173].

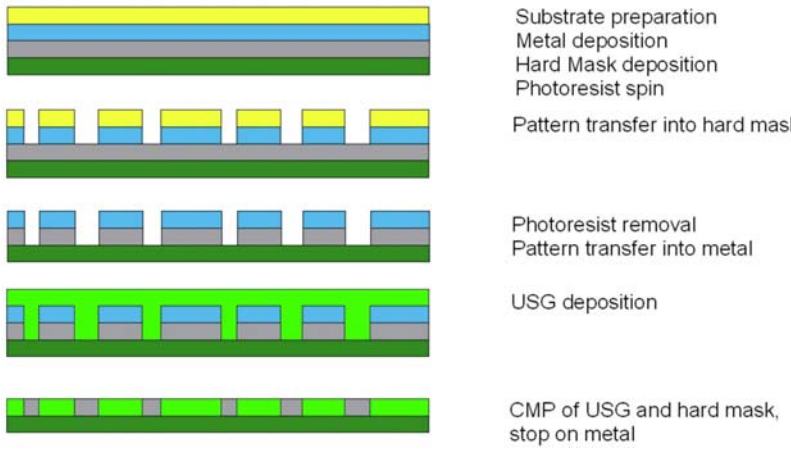

Figure 8.4 Process steps for current nanoTrek fabrication. Please note the process is identical to the first steps 1−4 in a considerably more elaborate process depicted in Fig. 8.5.

Microcantilevers (and microcantilever arrays) were built as prototypes of memory devices [174,175], atomic force-guided scanning Hall probe microscopy [176], or force metrology sensors [177,178].

George et al. [179] built a cantilever-based device to measure kinetics on blood platelet contraction, although in that case, a nickel wire cantilever was in a quite different embodiment than typical STM or AFM arrangement. Katta and Sandanalakshmi [180] present a molecular mass biosensor with four cantilevers with a goal to establish a classification scheme for tropical and subtropical diseases. Piezoresistive microcantilever-based system for biochemical sensing was demonstrated by Nag et al. [181]. Wu et al. have demonstrated that microcantilevers of different geometries were effective to detect two forms of prostate-specific antigen over a wide range of concentrations in a background of human serum albumin and human plasminogen [182].

The dominant tip deflection sensing technique is based on an optical laser beam metrology. However, optical metrology to measure cantilever bending has several limitations making cantilever-based measurements difficult, time-consuming, or even impossible in certain situations. There are several *pain-points* of the optical cantilever metrology that can be solved with proposed below quantum tunneling metrology. The need to phase out optical metrology for AFM cantilevers has been motivating researchers to find alternative metrology solution. Just two notable examples include tunneling point-contact solution from IBM/Stanford University team [183] and MOSFET-embedded cantilevers from Northwestern University team [184]. A new and complimentary cantilever deflection metrology where direct electrical detection of cantilever deflection using quantum tunneling would be desirable is described here.

In 2010 Quantum-Pi proposed to develop new AFM cantilevers metrology based on quantum tunneling. The technology is protected by patents [88].

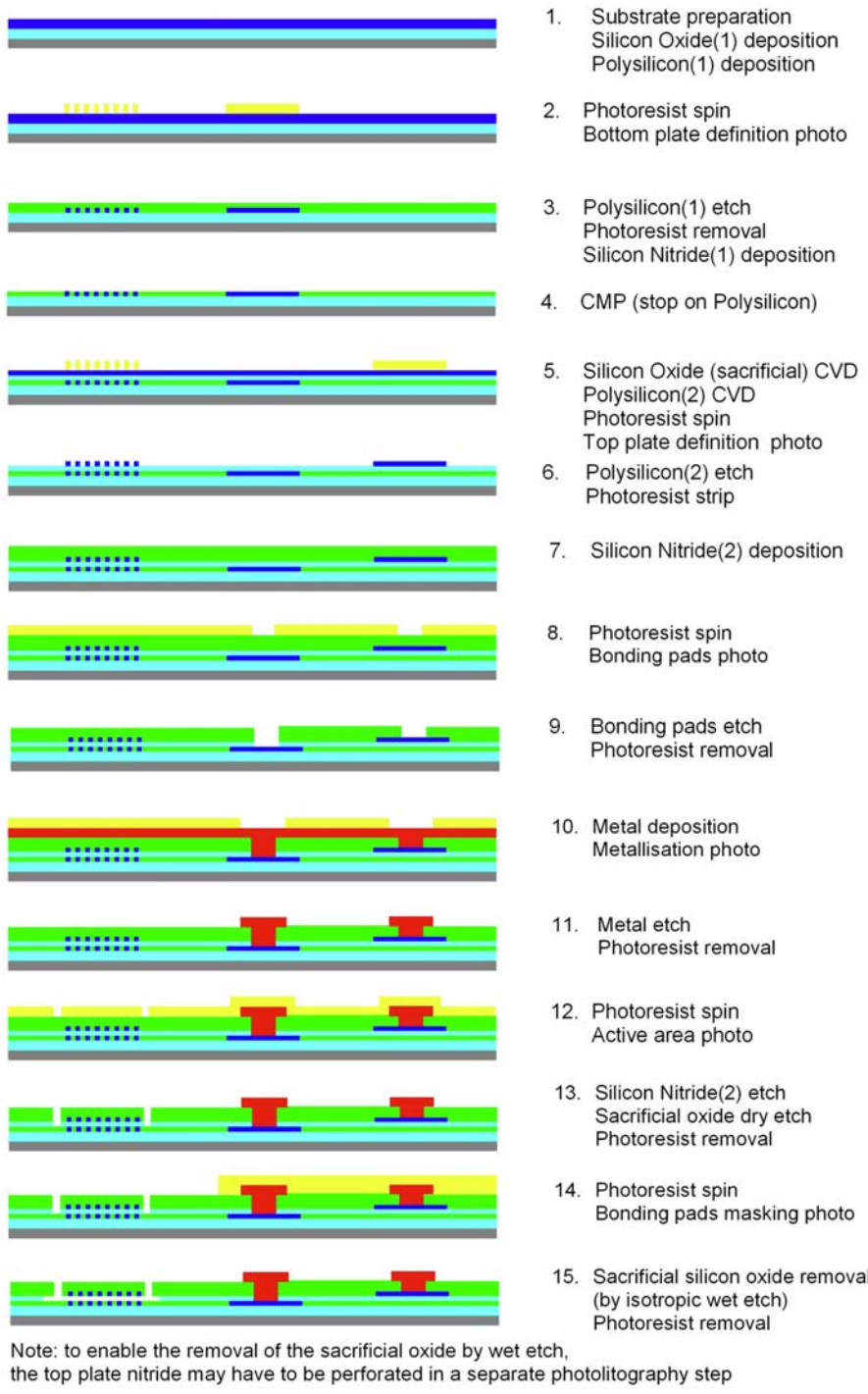

Figure 8.5 Suggested process flow for fabrication of 3D monolithic structures like those in Fig. 8.3, including the nanowire arrays and electrical connections.

8.4.1 Quantum tunneling cantilevers: proof-of-concept description

The quantum tunneling cantilever device concept is illustrated in Fig. 8.6A. It consists of kind of superlattice consisting of alternating layers of few to less than hundred nanometers thick conducting material, separated by insulating layers. The tunneling current flows from the cantilever across the narrow gap of at most few tens of nanometers to opposing layers that are part of the substrate structure (frame). The entire structure can be monolithically integrated (as shown in Figs. 8.6B and 8.7).

The most innovative step in the proposed proof of concept is to fabricate a monolithically integrated quantum tunneling effect cantilever device. This includes the development of a suitable material system comprising a number of alternating conductive and insulating layers, each of the order of a few to less than hundred

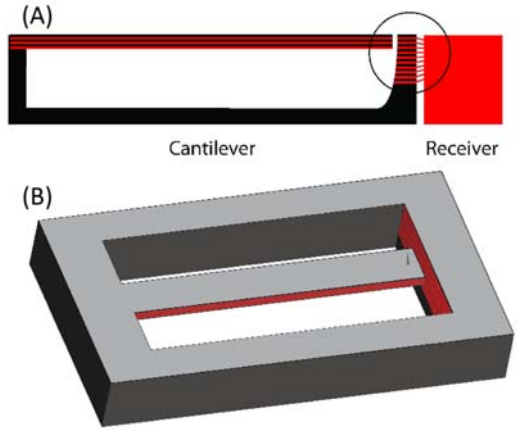

Figure 8.6 The quantum tunneling cantilever in cross section (A) and perspective (B). Idea diagram, the dimensions are not in proportional scale. The circled portion is shown in more detail in Fig. 8.7. This is a schematic diagram and the dimensions are not to scale.

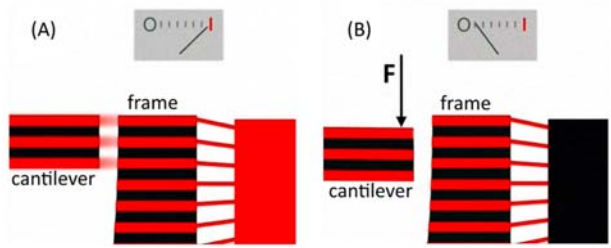

Figure 8.7 Detail of the circled region in the previous figure. Panel (A) illustrates the cantilever position when conducting nanolayers are aligned with surrounding frame conducting layers—quantum tunneling current is strong. Panel (B) shows the cantilever deflection, misalignment of opposing conducting layers leading to minimum of tunneling current.

nanometers thick with a separate electrical contact to each layer forming a *superlattice* vertical structure. However, the most challenging fabrication step will be the creation of a high aspect ratio *tunneling gap* of maximum few tens of nanometers wide, 2−4 μm deep, and 20−100 μm long, as illustrated in Fig. 8.6 (not to scale).

Another innovative aspect of the device fabrication is the double-sided processing of the wafer. The cantilever devices could be fabricated on an 8-in silicon on insulator (SOI) substrate. To produce the required structures, it will be necessary to carry out *double-sided* wafer processing, meaning that process steps are to be carried out on both the front and back sides of the wafer. On the wafer front side the cantilever structure will be defined through the deposition and etching of several metals and dielectric layers. The wafer backside will be etched selectively to achieve a very thin silicon membrane (2−4 μm thick) that constitutes the main mechanical structure of the cantilever. In the last step, one end of the cantilever will be separated from surrounding area by focused ion beam or other processes to form the tunneling gap of at most few tens of nanometers.

The technological challenges include achieving the required precision alignment of the structures created on the front and the back of the substrate and the stopping of the back side etch on the buried oxide layer to form a cantilever of precisely the required thickness. The key and novel technological benefit of such a device is that quantum tunneling current is very sensitive to cantilever deflection, varying by as much as 100% for small deflections of the order of a few nanometers. In comparison the fractional current change in a comparable piezoresistive device is five orders of magnitude smaller on the order of 10^{-3}% per nanometer. Although optical metrology employed widely in almost all SPMs provides sufficient resolution in many applications, it also requires dedicated pieces of optics (laser, detectors) and very elaborate calibration and environmental control (temperature, humidity, vibrations) not suitable for many in situ sensors required in biomedical applications.

The quantum tunneling effect cantilever conceptual design presented here provides all electronic means of deflection measurement that is integrated within the cantilever with the following advantages:

- superior feature resolution and speed performance compared to all other SPM cantilever technologies;
- simplicity and reduced cost of SPM systems;
- compact and robust design for applications where access is limited;
- compatibility with a broad range of submerged, chemical, and ultrahigh vacuum environments;
- extremely small size and possibility of using it in situ in biomedical applications.

Cantilevers are replaced almost daily by users of SPMs as the tips get blunted or crashed and only new replacement cantilevers can ensure accuracy. The quantum tunneling cantilever sensors are expected to be compatible with existing commercial SPMs while providing superior performance to the existing technologies in terms of sensitivity, simplicity of use, and cost. The cost of optical metrology components in SPMs, including cantilever preparation (i.e., gold layer deposition), will be shifted into consumables (cantilevers) in a fashion similar to printing cartridges

in modern printers. Other important advantages of quantum tunneling cantilevers include smaller footprint (through elimination of optical metrology elements), a very important feature, especially in ultrahigh vacuum instruments where space is at premium. In biological AFMs operating in liquid, quantum tunneling cantilevers solve the currently difficult problem of optical metrology calibration in the presence of liquids of often unknown refractive index.

8.5 Final word: future prospects for NEMS in biomedical applications

The wide adoption of quantum tunneling NEMS in biomedical research, diagnostics, patient observation, and treatment is still at a concept stage. Over the last 20 years, there were notable and successful examples of producing proof-of-concept quantum tunneling sensors and NEMS, but we are still rather far away from mass production and adoption of such devices in medical field. However, with incredible advances in semiconductor and material processing at nanoscale driven by microelectronics, computer industry, and MEMS/NEMS, we may expect that quantum tunneling sensors built following designs outlined above or others will become available sometime. The idea of *smart dust* [185] dates back to concepts proposed by Kris Pister at University of California, Berkeley back in the 1990s. Smart dust is still a subject of research and development and projects are being funded by various agencies. Quantum tunneling transduction, as outlined in this chapter, is very well suited to provide sensing mechanism in smart dust sensors. A proof-of-concept design of nanorobots for exposing cancer cells was presented by Dolev et al. [186]. The authors hope that this contribution provided outline of quantum tunneling transduction mechanism and its application in biomedical NEMS sensors and will lead to further fruitful explorations, research and technical discussions, and creation of new quantum tunneling NEMS biomedical sensors.

Acknowledgments

We wish to thank Jan Miśkiewicz for his help in collecting up-to-date literature on medical sensors, Jakub Kopeć for his help in organizing the references, and Dr. Andrzej Radliński for proofreading the manuscript.

References

[1] P. Rolfe, Impact of micro and nano sensors in biomedical measurement, Key Eng. Mater. 437 (2010) 299–303.
[2] P. Rolfe, Micro- and nanosensors for medical and biological measurement, Sens. Mater. 24 (6) (2012) 275–302.

[3] S. Bhattacharya, A.K. Agarwal, N. Chanda, A. Pandey, A.K. Sen, S. Kumar, et al., Introduction to Environmental, Chemical, and Medical Sensors, Energy, Environment, and Sustainability, 2018.
[4] P. French, In-vivo microsystems: a review, Sensors 20 (17) (2020) 1–22.
[5] V.S. Naresh, S.S. Pericherla, P.S.R. Murty, S. Reddi, Internet of Things in healthcare: architecture, applications, challenges, and solutions, Comput. Syst. Sci. Eng. 35 (6) (2020) 411–421.
[6] D.-J. Li, H.-Y. Chen, C.-R. Liu, K. Fan, G.-F. Wang, A review on MEMS/NEMS-based biosensor, Tien Tzu Hsueh Pao/Acta Electronica Sinica 49 (6) (2021) 1228–1236.
[7] A.L. Herrera-May, L.A. Aguilera-Cortes, P.J. Garcia-Ramiŋrez, E. Manjarrez, Resonant magnetic field sensors based on MEMS technology, Sensors 9 (10) (2009) 7785–7813.
[8] V.M. Aponte, D.S. Finch, D.M. Klaus, Considerations for non-invasive in-flight monitoring of astronaut immune status with potential use of MEMS and NEMS devices, Life Sci. 79 (14) (2006) 1317–1333.
[9] G. Ciuti, L. Ricotti, A. Menciassi, P. Dario, MEMS sensor technologies for human centred applications in healthcare, physical activities, safety and environmental sensing: a review on research activities in Italy, Sensors 15 (3) (2015) 6441–6468.
[10] G.R.K. Prasad, S. Shameem, N. Srinivasulu, C. Renukavalli, B. Manasa, P.S.S. Babu, Design and analysis of proof mass based micro sensor for early detection of Parkinson's disease, Int. J. Eng. Technol. (UAE) 7 (1.5) (2018) 146–151.
[11] Jeffrey Da-Jeng YAO, Conference General Chair, The 14th IEEE International Conference on Nano/Molecular Medicine and Engineering, Nanomed, in: IEEE International Conference on Nano/Molecular Medicine and Engineering, NANOMED, 2020, IEEE, December, 2020.
[12] S.A. Mineev, V.A. Novikov, I.V. Kuzmina, R.A. Shatalin, I.V. Grin, Goniometric sensor interface for exoskeleton system control device, Biomed. Eng. 49 (6) (2016) 357–361.
[13] A.D. Caballero, J.J.C. Lopez, An accelerometer-based embedded system-on-chip for measuring human-body joint angles, in: Pan American Health Care Exchanges, PAHCE, 2013.
[14] R. Raya, R. Garcia-Carmona, C. Sanchez, E. Urendes, O. Ramirez, A. Martin, et al., An inexpensive and easy to use cervical range of motion measurement solution using inertial sensors, Sensors 18 (8) (2018).
[15] A. Nez, L. Fradet, P. Laguillaumie, T. Monnet, P. Lacouture, Simple and efficient thermal calibration for MEMS gyroscopes, Med. Eng. Phys. 55 (2018) 60–67.
[16] Y. Khan, A.E. Ostfeld, C.M. Lochner, A. Pierre, A.C. Arias, Monitoring of vital signs with flexible and wearable medical devices, Adv. Mater. 28 (22) (2016) 4373–4395.
[17] M. Szermer, P. Zając, P. Amrozik, C. Maj, M. Jankowski, G. Jabłoński, et al., A capacitive 3-axis MEMS accelerometer for Medipost: a portable system dedicated to monitoring imbalance disorders, Sensors 21 (10) (2021).
[18] C. Chen, Z. Li, Y. Zhang, S. Zhang, J. Hou, H. Zhang, A 3D wrist pulse signal acquisition system for width information of pulse wave, Sensors 20 (1) (2019).
[19] W. Iwasaki, H. Nogami, S. Takeuchi, M. Furue, E. Higurashi, R. Sawada, Detection of site-specific blood flow variation in humans during running by a wearable laser Doppler flowmeter, Sensors 15 (10) (2015) 25507–25519.
[20] P. Castiglioni, A. Faini, G. Parati, M. Di Rienzo, Wearable seismocardiography, in: Annu Int Conf IEEE Eng Med Biol Soc., 2007, pp. 3954–3957.
[21] H. Lee, M. Whang, Heart rate estimated from body movements at six degrees of freedom by convolutional neural networks, Sensors 18 (5) (2018).

[22] J.B. Wendt, M. Potkonjak, Medical diagnostic-based sensor selection, in: Proceedings of IEEE Sensors, 2011, pp. 1507−1510.
[23] I. Clausen, T. Glott, Development of clinically relevant implantable pressure sensors: perspectives and challenges, Sensors 14 (9) (2014) 17686−17702.
[24] P. Cong, D.J. Young, B. Hoit, W.H. Ko, Novel long-term implantable blood pressure monitoring system with reduced baseline drift, in: Annual International Conference of the IEEE Engineering in Medicine and Biology—Proceedings, 2006, pp. 1854−1857.
[25] P. Sattayasoonthorn, J. Suthakorn, S. Chamnanvej, J. Miao, A.G.P. Kottapalli, LCP MEMS implantable pressure sensor for intracranial pressure measurement, in: IEEE International Conference on Nano/Molecular Medicine and Engineering, NANOMED, 2013, pp. 63−67.
[26] J. Lu, L. Zhang, D. Zhang, S. Matsumoto, H. Hiroshima, R. Maeda, et al., Development of implantable wireless sensor nodes for animal husbandry and MedTech innovation, Sensors 18 (4) (2018).
[27] J.F.L. Goosen, Silicon sensors for catheters and guide wires, in: Proceedings of SPIE—The International Society for Optical Engineering, vol. 4590, 2001, pp. 75−85.
[28] C. Lowrie, M.P.Y. Desmulliez, L. Hoff, O.J. Elle, E. Fosse, Fabrication of a MEMS accelerometer to detect heart bypass surgery complications, Sens. Rev. 29 (4) (2009) 319−325.
[29] D.D. Zhou, R.J. Greenberg, Microsensors and microbiosensors for retinal implants, Front. Biosci. 10 (1) (2005) 166−179.
[30] M. Frei, J. Martin, S. Kindler, G. Cristiano, R. Zengerle, S. Kerzenmacher, Power supply for electronic contact lenses: abiotic glucose fuel cells vs. mg/air batteries, J. Power Sources 401 (2018) 403−414.
[31] B.S. Klosterhoff, M. Tsang, D. She, K.G. Ong, M.G. Allen, N.J. Willett, et al., Implantable sensors for regenerative medicine, J. Biomech. Eng. 139 (2) (2017).
[32] H.H. Weetall, Chemical sensors and biosensors, update, what, where, when and how, Biosens. Bioelectron. 14 (2) (1999) 237−242.
[33] C.-F. Lin, G.-B. Lee, C.-H. Wang, H.-H. Lee, W.-Y. Liao, T.-C. Chou, Microfluidic pH-sensing chips integrated with pneumatic fluid-control devices, Biosens. Bioelectron. 21 (8) (2006) 1468−1475.
[34] M.L.Y. Sin, G.C.T. Chow, C.K.M. Fung, W.J. Li, P. Leong, K.W. Wong, et al., Ultra-low-power alcohol vapor sensors based on multi-walled carbon nanotube, in: Proceedings of 1st IEEE International Conference on Nano Micro Engineered and Molecular Systems, 1st IEEE-NEMS, 2006, pp. 1198−1202.
[35] Y. Li, P. Denny, C.M. Ho, C. Montemagno, W. Shi, F. Qi, et al., The oral fluid MEMS/NEMS chip (OFMNC): diagnostic and translational applications, Adv. Dent. Res. 18 (1) (2005) 3−5.
[36] A.J. Andersen, E.K.P. Kumar, T.L. Andresen, S. Yamada, A. Boisen, S. Schmid, Nanomechanical IR spectroscopy for the fast analysis of picogram samples of engineered nanomaterials, in: 18th International Conference on Miniaturized Systems for Chemistry and Life Sciences, MicroTAS 2014, 2014, pp. 2552−2553.
[37] F. Ribet, G. Stemme, N. Roxhed, Ultra-miniaturization of a planar amperometric sensor targeting continuous intradermal glucose monitoring, Biosens. Bioelectron. 90 (2017) 577−583.
[38] J.D. Yuen, L.C. Shriver-Lake, S.A. Walper, D. Zabetakis, J.C. Breger, D.A. Stenger, Microbial nanocellulose printed circuit boards for medical sensing, Sensors 20 (7) (2020).
[39] M. Caldorera-Moore, N.A. Peppas, Micro- and nanotechnologies for intelligent and responsive biomaterial-based medical systems, Adv. Drug. Deliv. Rev. 61 (15) (2009) 1391−1401.

[40] C.S. Boland, Stumbling through the research wilderness, standard methods to shine light on electrically conductive nanocomposites for future healthcare monitoring, ACS Nano 13 (12) (2019) 13627−13636.
[41] A. Kumar, S. Aravamudhan, M. Gordic, S. Bhansali, S.S. Mohapatra, Ultrasensitive detection of cortisol with enzyme fragment complementation technology using functionalized nanowire, Biosens. Bioelectron. 22 (9−10) (2007) 2138−2144.
[42] D. Liepmann, K. Aran, P.M. Ajayan, S. Viswanathan, P. Li, V. Renugopalakrishnan, Graphene protein field effect biomedical sensor for glucose measurements, in: Materials Research Society Symposium Proceedings, vol. 1725, 2015, pp. 50−54.
[43] M. Salim, D. Salim, D. Chandran, H.S. Aljibori, A.S. Kherbeet, Review of nano piezoelectric devices in biomedicine applications, J. Intell. Mater. Syst. Struct. 29 (10) (2018) 2105−2121.
[44] J. Lee, W. Choi, Y.K. Yoo, K.S. Hwang, S. Lee, S. Kang, et al., A micro-fabricated force sensor using an all thin film piezoelectric active sensor, Sensors 14 (12) (2014) 22199−22207.
[45] P. Song, C. Si, M. Zhang, Y. Zhao, Y. He, W. Liu, et al., A novel piezoresistive MEMS pressure sensors based on temporary bonding technology, Sensors 20 (2) (2020).
[46] J. Fernando Alfaro, L.E. Weiss, P.G. Campbell, M.C. Miller, C. Heyward, J.S. Doctor, et al., Bioimplantable bone stress sensor, in: Annual International Conference of the IEEE Engineering in Medicine and Biology—Proceedings, vol. 7, 2005, pp. 518−521.
[47] S. Bhalla, R. Suresh, Condition monitoring of bones using piezo-transducers, Meccanica 48 (9) (2013) 2233−2244.
[48] S. Bhalla, Bone characterization using piezo-transducers as bio-medical sensors, smart materials in structural health monitoring, control and biomechanics, Advanced Topics in Science and Technology in China, Springer, 2012.
[49] Z. Bielecki, T. Stacewicz, J. Wojtas, J. Mikołajczyk, D. Szabra, A. Prokopiuk, Selected optoelectronic sensors in medical applications, Opto-Electron. Rev. 26 (2) (2018) 122−133.
[50] V. Blazek, B. Venema, S. Leonhardt, P. Blazek, Customized optoelectronic in-ear sensor approaches for unobtrusive continuous monitoring of cardiorespiratory vital signs, Int. J. Ind. Eng. Manage. 9 (4) (2018) 197−203.
[51] J. Lueke, W.A. Moussa, MEMS-based power generation techniques for implantable biosensing applications, Sensors 11 (2) (2011) 1433−1460.
[52] M.M.N. Aldeer, R.P. Martin, R.E. Howard, Tackling the fidelity-energy trade-off in wireless body sensor networks, in: Proceedings—2017 IEEE 2nd International Conference on Connected Health: Applications, Systems and Engineering Technologies, CHASE 2017, 2017, pp. 7−12.
[53] S. Mohsen, A. Zekry, K. Youssef, M. Abouelatta, A self-powered wearable wireless sensor system powered by a hybrid energy harvester for healthcare applications, Wireless Personal Commun. 116 (4) (2021) 3143−3164.
[54] A.S. Sadek, R.B. Karabalin, J. Du, M.L. Roukes, C. Koch, S.C. Masmanidis, Wiring nanoscale biosensors with piezoelectric nanomechanical resonators, Nano Lett. 10 (5) (2010) 1769−1773.
[55] A.S. Sezen, S. Sivaramakrishnan, S. Hur, R. Rajamani, W. Robbins, B.J. Nelson, Passive wireless MEMS microphones for biomedical applications, J. Biomech. Eng. 127 (6) (2005) 1030−1034.
[56] A. Arshak, K. Arshak, D. Waldron, D. Morris, O. Korostynska, E. Jafer, et al., Review of the potential of a wireless MEMS and TFT microsystems for the measurement of pressure in the GI tract, Med. Eng. Phys. 27 (5) (2005) 347−356.

[57] A. Sabato, M.Q. Feng, Feasibility of frequency-modulated wireless transmission for a multi-purpose MEMS-based accelerometer, Sensors 14 (9) (2014) 16563–16585.
[58] G.A. Conway, W.G. Scanlon, Wearable antennas for medical monitoring systems, in: 2015 International Workshop on Antenna Technology, iWAT 2015, 2015, pp. 19–21.
[59] S. Schellenberger, K. Shi, T. Steigleder, F. Michler, F. Lurz, R. Weigel, et al., Support vector machine-based instantaneous presence detection for continuous wave radar systems, in: Asia-Pacific Microwave Conference Proceedings, APMC, vol. 2018, November 2019, pp. 1465–1467.
[60] H. Haick, N. Tang, Artificial intelligence in medical sensors for clinical decisions, ACS Nano 15 (3) (2021) 3557–3567.
[61] M.J. Tadi, E. Lehtonen, J. Teuho, J. Koskinen, J. Schultz, R. Siekkinen, A computational framework for data fusion in MEMS-based cardiac and respiratory gating, Sensors 19 (19) (2019).
[62] Y. Wei, Q. Xu, An overview of micro-force sensing techniques, Sens. Actuator A Phys. 234 (2015) 359–374.
[63] H. Herzog, A. Klein, H. Bleckmann, P. Holik, S. Schmitz, G. Siebke, et al., μ-Biomimetic flow-sensors—introducing light-guiding PDMS structures into MEMS, Bioinspiration Biomim 10 (3) (2015).
[64] R. Gurney, E.U. Condon, Wave mechanics and radioactive disintegration, Nature 122 (1928) 439. Available from: https://www.nature.com/articles/122439a0.pdf.
[65] R. Gurney, E.U. Condon, Quantum mechanics and radioactive disintegration, Phys. Rev. 33 (1929) 127.
[66] G. Gamov, Zur quantentheorie des atomkernes, Z. Phys. 51 (1928) 204–212. https://doi.org/10.1007.
[67] E.U. Condon, Tunneling—how it all started, Am. J. Phys. 46 (13) (1978) 319–323. Available from: https://doi.org/10.1119/1.11306.
[68] E. Merzbacher, The early history of quantum tunneling, Phys. Today 55 (8) (2002) 44. Available from: https://doi.org/10.1063/1.1510281.
[69] L. de Broglie, Nobel lecture: the wave nature of the electron. <https://www.nobelprize.org/uploads/2016/04/broglie-lecture.pdf>, 1929.
[70] H. Bethe, Nobel lecture: energy production in stars. <https://www.nobelprize.org/uploads/2016/04/broglie-lecture.pdf>, 1967.
[71] O. Klein, The Nobel Prize in physics 1967: presentation speech. <https://www.nobelprize.org/prizes/physics/1967/ceremony-speech/>, 1967.
[72] B. Josephson, Nobel lecture: the discovery of tunnelling superconductors. <https://www.nobelprize.org/uploads/2018/06/josephson-lecture_new.pdf>, 1973.
[73] L. Esaki, Nobel lecture: long journey into tunneling. <https://www.nobelprize.org/uploads/2018/06/esaki-lecture.pdf>, 1973.
[74] I. Giaever, Nobel lecture: electron tunneling and superconductivity. <https://www.nobelprize.org/uploads/2018/06/giaever-lecture.pdf>, 1973.
[75] G. Binnig, H. Rohrer, Scanning tunneling microscopy—from birth to adolescence, Rev. Mod. Phys. 59 (13) (1987) 615–626. Available from: https://www.nobelprize.org/uploads/2018/06/rohrer-lecture.pdf.
[76] C.C. Moser, T. Farid, S.E. Chobot, P.L. Dutton, Electron tunneling chains of mitochondria, Biochim. Biophys. Acta 1757 (2006) 1096–1109.
[77] C.C. Moser, J.L. Anderson, P.L. Dutton, Guidelines for tunneling in enzymes, Biochim. Biophys. Acta. 1797 (9) (2010) 1573–1586. Available from: https://doi.org/10.1016/j.bbabio.2010.04.441.

[78] T. Hayashi, A.A. Stuchebrukhov, Electron tunneling in respiratory complex I, Proc. Natl. Acad. Sci. U.S.A. 107 (45) (2010) 19157–19162.
[79] T. Hayashi, A.A. Stuchebrukhov, Quantum electron tunneling in respiratory complex I, J. Phys. Chem. B 115 (18) (2011) 5354–5364. Available from: https://doi.org/10.1021/jp109410j.
[80] E. Gnandt, K. Dörner, M. Strampraad, S. de Vries, T. Friedrich, The multitude of iron-sulfur clusters in respiratory complex I, Biochim. Biophys. Acta 1857 (18) (2016) 1068–1072.
[81] <https://www.ibm.com/ibm/history/ibm100/us/en/icons/microscope/>.
[82] M. Razavy (Ed.), Quantum Theory of Tunneling, World Scientific, 2003.
[83] H. Mizuta, T. Tanouhe (Eds.), The Physics and Applications of Resonant Tunnelling Diodes, Cambridge, 1995.
[84] M. Michalewicz, Tunnelling current between two quasi-1-dimensional conductors, in: Eighth Foresight Conference on Molecular Nanotechnology, 2000.
[85] M. Michalewicz. Measurements Using Tunnelling Current Between Elongate Conductors, (2004) US Patent 6,707,308.
[86] M. Michalewicz, Z. Rymuza, Quantum Tunneling Transducer Device, (2004) PCT/AU2004/000523.
[87] M. Michalewicz, P. Glowacki, Z. Rymuza, N. Lumpkin, S. Bremner, E. Radlinska, 3D monolithic devices utilizing quantum tunneling between 2D arrays of quasi-1D nanowires, in: Nanoelectronic Devices for Defense & Security Conference, Crystal City, VA, 2007.
[88] M. Michalewicz, P. Slodowy, Sensor Device and Method, Patent (2007) PCT/SG2007/000278.
[89] M. Michalewicz, P. Glowacki, N. Singh, B. Subrmanian, N. Gosvami, Quantum tunneling between large arrays of nanowires—new sensing principle, applications in defense and security and demonstration of nanoTrek functionality, in: Nanoelectronic Devices for Defense & Security Conference, Crystal City, VA, 2007.
[90] M. Michalewicz, P. Glowacki, N. Singh, B. Subrmanian, N. Gosvami, nanoTrek—quantum tunneling linear encoder for sub-nanometer positional metrology with centimeters range, in: NSTI Nanotech Conference, Santa Clara, CA, 2007.
[91] T. Kenny, W. Kaiser, H. Rockstad, J. Reynolds, J. Podosek, E. Vote, Wide-bandwidth electromechanical actuators for tunneling displacement transducers, J. Microelectromech. Syst. 3 (3) (1994) 97–104.
[92] J. Kaiser, Tunnel-Effect Displacement Sensor, Tech. Rep., NTIS Tech Notes, April 1990, p. 346.
[93] R. Kubena, G. Atkinson, Method of Manufacturing Single-Wafer Tunneling Sensor, United States Patent 5,665,253, September 1997.
[94] W. Kaiser, S. Waltman, T. Kenny, Tunnel Effect Measuring Systems and Particle Detectors, United States Patent 5,265,470, November 1993.
[95] W. Kaiser, S. Waltman, T. Kenny, Tunnel Effect Measuring Systems and Particle Detectors, United States Patent 5,293,781, March 1994.
[96] P. Hartwell, M. Bertsch, S. Miller, K. Foster, N. MacDonald, Single mask lateral tunneling accelerometer, in: Proceedings of the IEEE International Conference on Micro Electro Mechanical Systems (MEMS), 1998.
[97] S.M. Sze (Ed.), Semiconductor Sensors, John Wiley & Sons, Inc., New York, 1994.
[98] S. Lyshevski, MEMS and NEMS: Systems, Devices, and Structures, CRC Press, Boca Raton, FL, 2002.

[99] I. Busch-Vishniac, Electromechanical Sensors and Actuators, Springer, New York, 1999.
[100] L. Ristic, Sensor Technology and Devices, Artech House, Boston, MA, 1994.
[101] T.-R. Hsu, MEMS and Microsystems: Design and Manufacture, McGraw-Hill, Boston, MA, 2002.
[102] J. Pelesko, Modeling MEMS and NEMS, Chapman & Hall/CRC, Boca Raton, FL, 2003.
[103] Zettacore, Corp. Rolltronics, Molecular Electronics Corp. (MEC) (2001).
[104] P. Kuekes, S. Williams, J. Heath, Molecular Wire Crossbar Memory, (2000) United States Patent 6,128,214.
[105] J. Heath, D. Leif, G. Markovich, Single-Electron Solid State Electronic Device, (2000) United States Patent 6,159,620.
[106] P. Kuekes, S. Williams, J. Heath, Molecular-Wire Crossbar Interconnect (MWCI) for Signal Routing and Communications, (2001) United States Patent 6,314,019.
[107] J. Heath, S. Williams, P. Kuekes, Chemically Synthesized and Assembled Electronics Devices, (2002) United States Patent 6,459,095.
[108] E.B. Cooper, E.R. Post, S. Griffith, J. Levitan, S.R. Manalis, M.A. Schmidt, et al., High-resolution micromachined interferometric accelerometer, Appl. Phys. Lett. 76 (22) (2000) 3316−3318.
[109] B. Boser, Electronics for micromachined inertial sensors, in: International Conference on Solid-State Sensors and Actuators, Proceedings 2, vol. 2, 1997, pp. 1169−1172.
[110] B. Boser, R. Howe, Surface micromachined accelerometers, IEEE J. Solid-State Circuits 31 (3) (1996) 366−375.
[111] S. Linder, Power Semiconductors, EPFL Press, Lausanne, 2006.
[112] R. Natarajan, Power System Capacitors (Power Engineering), CRC Press, Boca Raton, FL, 2005.
[113] E.J. Brandon (Ed.), Micropower and Microdevices: Proceedings of the International Symposium, Electrochemical Society, Pennington, NJ, 2002.
[114] S. Bailey, R. Raffaelle, Handbook of Photovoltaic Science and Engineering, John Wiley & Sons, Inc., 2002. Ch. Photovoltaics for space.
[115] S. Bailey, R. Raffaelle, Practical Handbook of Photovoltaics: Fundamentals and Applications, Elsevier Advanced Technology, 2003. Ch. Operation of solar cells in a space environment.
[116] K. Worden, W. Bullough, J. Haywood, Smart Technologies, World Scientific Pub. Co., 2003.
[117] E. Callaway, Wireless Sensor Networks: Architectures and Protocols, Auerbach Publications, Boca Raton, FL, 2004.
[118] M. Ilyas, I. Mahgoub, Handbook of Sensor Networks: Compact Wireless and Wired Sensing Systems, CRC Press, 2005.
[119] R.R. Brooks, S. Iyengar, Distributed Sensor Networks, Chapman & Hall/CRC, Boca Raton, FL, 2005.
[120] M. Ilyas, M. Imad, Smart Dust: Sensor Network Applications, Architecture and Design, CRC Press, 2006.
[121] S.-L. Wu, Y.-C. Tseng, Wireless Ad Hoc Networking: Personal-Area, Local-Area, and the Sensory-Area Networks, Auerbach, 2007.
[122] M. Ilyas, M. Imad, Sensor Network Protocols, CRC Press, 2006.
[123] Y. Xiao, Security in Sensor Networks, Auerbach, 2006.
[124] S. Bandyopadhyay, S. Roy, T. Ueda, Enhancing the Performance of Ad Hoc Wireless Networks With Smart Antennas, Auerbach Publications, Boca Raton, FL, 2006.

[125] W. Jie, Handbook on Theoretical and Algorithmic Aspect of Sensor, Ad Hoc Wireless, and Peer-to-Peer Networks, Auerbach, Boca Raton, FL, 2006.
[126] H. Eren, Wireless Sensors and Instruments: Networks, Design, and Applications, CRC Press, Boca Raton, FL, 2005.
[127] N. Bulusu, S. Jha, Wireless Sensor Networks, Artech House, Boston, MA, 2005.
[128] D. Hall, S.A. McMullen, Mathematical Techniques in Multisensor Data Fusion, Artech House, Boston, MA, 2004.
[129] A. Vasilakos, W. Pedrycz, Ambient Intelligence, Wireless Networking, and Ubiquitous Computing, Artech House, Boston, MA, 2006.
[130] Le Roy H. Hackett Jr., Process and Mask for Ion Beam Etching of Fine Patterns, (1981) United States Patent 4,275,286.
[131] S. Berger, J. Gibson, R. Camarda, R. Farrow, H. Huggins, J. Kraus, et al., Fabrication of nanostructure arrays using projection electron-beam lithography, in: W.P. Kirk, M.A. Reed (Eds.), Nanostructures and Mesoscopic Systems, Academic Press, 1992, pp. 95–104. Available from: https://www.sciencedirect.com/science/article/pii/B9780124096608500158.
[132] J. McClelland, Handbook of Nanostructured Materials and Nanotechnology, vol. 1, Academic Press, San Diego, CA, 2000. no. 141, Ch. Nanofabrication via atom optics.
[133] R.J. Celotta, R. Gupta, R.E. Scholten, J.J. McClelland, Nanostructure fabrication via laser-focused atomic deposition (invited), J. Appl. Phys. 79 (8 Part 2B) (1996) 6079–6083.
[134] J.J. McClelland, W.R. Anderson, C.C. Bradley, M. Walkiewicz, R.J. Celotta, E. Jurdik, et al., Accuracy of nanoscale pitch standards fabricated by laser-focused atomic deposition, J. Res. Natl. Inst. Stand. Technol. 108 (2) (2003) 99–113.
[135] M. Bartek, P.T.J. Gennissen, P.J. French, P.M. Sarro, R.F. Wolffenbuttel, Study of selective and non-selective deposition of single- and polycrystalline silicon layers in an epitaxial reactor, in: International Conference on Solid-State Sensors and Actuators, Proceedings, vol. 2, 1997, pp. 1403–1406.
[136] D. Routkevitch, A.A. Tager, J. Haruyama, D. Almawlawi, M. Moskovits, J.M. Xu, Nonlithographic nano-wire arrays: fabrication, physics, and device applications, IEEE Trans. Electron. Devices 43 (10) (1996) 1646–1658.
[137] D. Routkevitch, T. Bigioni, M. Moskovits, J.M. Xu, Electrochemical fabrication of CDS nanowire arrays in porous anodic aluminum oxide templates, J. Phys. Chem. 100 (33) (1996) 14037–14047.
[138] B.W. Gregory, J.L. Stickney, Electrochemical atomic layer epitaxy (ECALE), J. Electroanal. Chem. 300 (1–2) (1991) 543–561.
[139] R. Schuster, V. Kirchner, P. Allongue, G. Ertl, Electrochemical micromachining, Science 289 (5476) (2000) 98–101.
[140] A. Blondel, J.P. Meier, B. Doudin, J. Ansermet, Giant magnetoresistance of nanowires of multilayers, Appl. Phys. Lett. 65 (23) (1994) 3019–3021.
[141] W. Li, J.A. Virtanen, R.M. Penner, Nanometer-scale electrochemical deposition of silver on graphite using a scanning tunneling microscope, Appl. Phys. Lett. 60 (10) (1992) 1181–1183.
[142] H. Stormer, L. Pfeiffer, K. West, K. Baldwin, Cleaved edge overgrowth: a route to atomically precise lower dimensional structures, in: W.P. Kirk, M.A. Reed (Eds.), Nanostructures and Mesoscopic Systems, Academic Press, 1992, pp. 51–62. Available from: https://www.sciencedirect.com/science/article/pii/B9780124096608500110.
[143] R. De Picciotto, H.L. Stormer, L.N. Pfeiffer, K.W. Baldwin, K.W. West, Four-terminal resistance of a ballistic quantum wire, Nature 411 (6833) (2001) 51–54.

[144] G. Timp, M. Prentiss, R. Behringer, N. Bigelow, J. Cunningham, Can a device be made with atomic precision? in: W.P. Kirk, M.A. Reed (Eds.), Nanostructures and Mesoscopic Systems, Academic Press, 1992, pp. 75–84. Available from: https://www.sciencedirect.com/science/article/pii/B9780124096608500134.
[145] W. Smith, E. Ehrichs, A. de Lozanne, Direct writing of nickel wires using a scanning tunneling microscope/scanning electron microscope system, in: W.P. Kirk, M.A. Reed (Eds.), Nanostructures and Mesoscopic Systems, Academic Press, 1992, pp. 85–94. Available from: https://www.sciencedirect.com/science/article/pii/B9780124096608500146.
[146] A.M. Morales, C.M. Lieber, A laser ablation method for the synthesis of crystalline semi-conductor nanowires, Science 279 (5348) (1998) 208–211.
[147] Y.F. Zhang, Y.H. Tang, N. Wang, D.P. Yu, C.S. Lee, I. Bello, et al., Silicon nanowires prepared by laser ablation at high temperature, Appl. Phys. Lett. 72 (15) (1998) 1835–1837.
[148] N. Wang, Y.H. Tang, Y.F. Zhang, D.P. Yu, C.S. Lee, I. Bello, et al., Transmission electron microscopy evidence of the defect structure in Si nanowires synthesized by laser ablation, Chem. Phys. Lett. 283 (5–6) (1998) 368–372.
[149] C.K. Ober, Self-assembly: persistence pays off, Science 296 (5569) (2002) 859–861.
[150] S.-W. Lee, C. Mao, C.E. Flynn, A.M. Belcher, Ordering of quantum dots, using genetically engineered viruses, Science 296 (5569) (2002) 892–895.
[151] J.R. Heath, F.K. LeGoues, A liquid solution synthesis of single crystal germanium quantum wires, Chem. Phys. Lett. 208 (3–4) (1993) 263–268.
[152] A. Baski, D. Kendall, Strongly Textured Atomic Ridge and Dot Fabrication, (2002) United States Patent 6,413,880.
[153] M. Moskovits, J. Xu, Nanoelectric Devices, (1996) United States Patent 5,581,091.
[154] S.-T. Lee, N. Wang, C.-S. Lee, I. Bello, Growth Method for Silicon Nanowires and Nanoparticle Chains From Silicon Monoxide, (2001) United States Patent 6,313,015.
[155] T. Kamins, Y.-L. Chang, Method of Aligning Nanowires, (2001) United States Patent 6,248,674.
[156] J. Ying, Z. Zhang, L. Zhang, M. Dresselhaus, Process for Fabricating an Array of Nanowires, (2001) United States Patent 6,231,744.
[157] J. Ying, Z. Zhang, L. Zhang, M. Dresselhaus, Nanowire Arrays, (2002) United States Patent 6,359,288.
[158] V. Fleury, D. Barkey, Runaway growth in two-dimensional electrodeposition, Europhys. Lett. 36 (4) (1996) 253–258.
[159] C.A. Huber, T.E. Huber, M. Sadoqi, J.A. Lubin, S. Manalis, C.B. Prater, Nanowire array composites, Science 263 (5148) (1994) 800–802.
[160] K. Shimoyama, S. Nagao, Y. Inoue, K. Kiyomi, N. Hosoi, K. Fujii, et al., Fabrication of quantum wire structures by in-situ gas etching and selective-area metalorganic vapor phase epitaxy regrowth, J. Cryst. Growth 145 (1–4) (1994) 734–739.
[161] M. Ogura, X.-L. Wang, H. Matsuhata, T. Tada, A. Hamoudi, S. Ikawa, et al., Fabrication of quantum wire and minute buried heterostructure by in situ etching and selective MOCVD growth, Jpn. J. Appl. Phys. 35 (2 Suppl. B) (1996) 1353–1357.
[162] T. Kyotani, L.-F. Tsai, A. Tomita, Preparation of ultrafine carbon tubes in nanochannels of an anodic aluminum oxide film, Chem. Mater. 8 (8) (1996) 2109–2113.
[163] N. Wang, Y.H. Tang, Y.F. Zhang, C.S. Lee, I. Bello, S.T. Lee, Si nanowires grown from silicon oxide, Chem. Phys. Lett. 299 (2) (1999) 237–242.
[164] G. Friedbacher, H. Fuchs, Classification of scanning probe microscopies, Pure Appl. Chem. 71 (1999) 1337–1357.

[165] F.J. Giessibl, C.F. Quate, Exploring the nanoworld with atomic force microscopy, Phys. Today 59 (12) (2006) 44–50.
[166] G. Binnig, C. Quate, C. Gerber, Atomic force microscope, Phys. Rev. Lett. 56 (1986) 930–933.
[167] C. Gerber, H. Lang, How the doors to the nanoworld were opened, Nat. Nanotechnol. 1 (2006) 3–5.
[168] U. Grunewald, S. Müller-Pfeiffer, Market overview: sensors for scanning force microscopy, Sens. Update 3 (1) (1998) 327–351.
[169] M.J. Brukman, D.A. Bonnell, Probing physical properties at the nanoscale, Phys. Today 61 (6) (2008) 36–42.
[170] M.T. Postek, R.J. Hocken, Instrumentation and metrology for nanotechnology, in: Report of the National Nanotechnology Initiative Workshop January 27–29, National Nanotechnology Coordination Office, Gaithersburg, MD, 2004. <https://www.nano.gov/Instrumentation-and-Metrology>.
[171] H. Lang, M. Baller, R. Berger, C. Gerber, J. Gimzewski, F. Battiston, et al., An artificial nose based on a micromechanical cantilever array, Analytica Chim. Acta 393 (1) (1999) 59–65.
[172] H.P. Lang, M. Hegner, C. Gerber, Cantilever array sensors, Mater. Today 8 (4) (2005) 30–36. Available from: https://www.sciencedirect.com/science/article/pii/S1369702105007923.
[173] H. Lang, et al., An artificial nose based on microcantilever array sensors, J. Phys. Conf. Ser. 61 (2007) 663.
[174] P. Vettiger, et al., The millipede: more than one thousand tips for future AFM data storage, IBM J. Res. Dev. 44 (2000) 323–340.
[175] P. Vettiger, et al., The millipede-nanotechnology entering data storage, IEEE Trans. Nanotechnol. 1 (2002) 39–55.
[176] A. Brook, S. Bending, J. Pinto, A. Oral, D. Ritchie, H. Beere, et al., Integrated piezoresistive sensors for atomic force-guided scanning hall probe microscopy, Appl. Phys. Lett. 82 (2003) 3538–3540.
[177] E. Peiner, L. Doering, M. Balke, A. Christ, Silicon cantilever sensor for micro-/nanoscale dimension and force metrology, Microsyst. Technol. 14 (2008) 441–451.
[178] Scanning Probe Microscopy (SPM), Atomic Force Microscopy and SPM Lithography - Methods of Operation, https://www.azonano.com/article.aspx?ArticleID=1209 (last accessed 2022.05.13); A Guide to Scanning Probe Microscopy and its Applications, https://www.azonano.com/article.aspx?ArticleID=5175 (last accessed 2022.05.13)
[179] M.J. George, K.R. Aroom, M.A. Skibber, T. Sharma, C.E. Wade, C.S. Cox, et al., A useful device to measure kinetics of platelet contraction, ASAIO J. 64 (4) (2018) 529–535.
[180] M. Katta, R. Sandanalakshmi, Simultaneous tropical disease identification with PZT-5H piezoelectric material including molecular mass biosensor microcantilever collection, Sens. Bio-Sens. Res. 32 (2021) 100413.
[181] S. Nag, N.S. Kale, V.R. Rao, D.K. Sharma, An ultra-sensitive δ r/r measurement system for biochemical sensors using piezoresistive micro-cantilevers, in: Proceedings of the 31st Annual International Conference of the IEEE Engineering in Medicine and Biology Society: Engineering the Future of Biomedicine, EMBC 2009, 2009, pp. 3794–3797.
[182] G. Wu, R. Datar, K. Hansen, T. Thundat, R. Cote, A. Majumdar, Bioassay of prostate specific antigen (PSA) using microcantilever, Nat. Biotechnol. 19 (2001) 856–860.

[183] M. Poggio, M. Jura, C. Degen, M. Topinka, H. Mamin, D. Goldhaber-Gordon, et al., An off-board quantum point contact as a sensitive detector of cantilever motion, Nat. Phys. 4 (2008) 635−638.
[184] G. Shekhawat, S.-H. Tark, V.P. Dravid, Mosfet-embedded microcantilevers for measuring deflection in biomolecular sensors, Science 311 (5767) (2006) 1592−1595.
[185] <https://www.nanowerk.com/smartdust.php>.
[186] S. Dolev, R.P. Narayanan, M. Rosenblit, Design of nanorobots for exposing cancer cells, Nanotechnology 30 (31) (2019).

This page intentionally left blank

Quantum dots: an emerging implication of nanotechnology in cancer diagnosis and therapy

9

Alka Lohani[1], *Sumit Durgapal*[2] *and Pierfrancesco Morganti*[3]
[1]School of Pharmaceutical Sciences, IFTM University, Moradabad, Uttar Pradesh, India, [2]Department of Pharmaceutical Sciences, Bhimtal Campus, Kumaun University, Nainital, Uttarakhand, India, [3]Academy of History of Healthcare Art, Rome, Lazio, Italy

9.1 Introduction

Cancer is the second leading cause of death in the world behind cardiovascular disease. It is considered to be the cause of one out of every six deaths worldwide [1]. While the overall number of cancer fatalities is rising, this is most likely due to aging and growing populations. Breast cancer (11.6%), lung cancer (11.4%), colorectal cancer (10%), prostate cancer (7.3%), and stomach cancer (5.6%) are the most common cancers [2]. Cancer is defined by the American Cancer Society as "A category of diseases characterized by unregulated development and spread of abnormal cells, which can result in mortality if the spread is not controlled" [3]. In cancer, some of the body's cells grow uncontrollably and spread to other parts of the body. If cancer is diagnosed and treated early, fatality rates can be lowered. Modern imaging tools and morphological inspection of tissues (histopathology) or cells (cytology), which aid in the early detection of malignant growth, have made it easier to detect and cure cancer.

The potential for cancer diagnosis and treatment using nanotechnology is enormous. Nanotechnology is a fantastic science that can not only improve cancer diagnostics but also provide detection strategies with greater reliability, susceptibility, and specificity. It has resulted in the development of nanomaterials with novel surface architecture and characteristics, thereby opening up new possibilities for molecular manipulation. The fabrication of biocompatible quantum dot (QD) nanomaterials for the diagnosis and treatment of cancer is an area of enormous interest. This chapter highlights the QDs as an emerging application of nanotechnology, specifically for the diagnosis and therapy of cancer.

9.2 Pathophysiology of cancer

Cancer is defined as the abnormal development of a group of cells that defies the normal cell division rule. These cells are referred to as cancer cells. Cancer is a

Quantum Materials, Devices, and Applications. DOI: https://doi.org/10.1016/B978-0-12-820566-2.00008-9

disease in which a normal cell is transformed into a cancer cell through a process known as carcinogenesis. The transformation of a normal cell into a cancer cell is induced by a number of causes. Carcinogens are the factors or agents that cause cancer. Researchers classify cancer causes into two categories: (1) cancer caused by environmental factors that include lifestyle factors (e.g., tobacco use, nutrition, and physical activity), Natural occurring exposure to ultraviolet light, infectious agents and radon gas, and medical treatments (e.g., radiation and medicine); (2) cancer caused by genetic factors [4]. The damage to the genetic structure of normal cells is widely acknowledged as the pathogenesis of cancer (e.g., gene expression disturbances, mutation, and activation of genes that promote tumor and inactivation of tumor suppressor genes).

Normal human cells usually grow and divide to produce newer cells; therefore the older cells are constantly shed and replaced with new cells. This process is hampered, in case of the deadly condition grows inside the body. As a result, the cells become entirely unusual, as damaged cells coexist with new cells in the body, even when they are not required. These unwanted cells continue to divide indefinitely, causing the tumor to spread (Fig. 9.1). The tumor could be benign or cancerous. Benign tumors are not considered destructive since they grow slowly and do not damage other body tissues or spread to the other parts of the body. Malignant tumors, on the other hand, spread uncontrollably, resulting in rapid tumor growth. These tumors then target other organs of the body via numerous pathways such as the lymphatic system and blood, eventually forming new cancers.

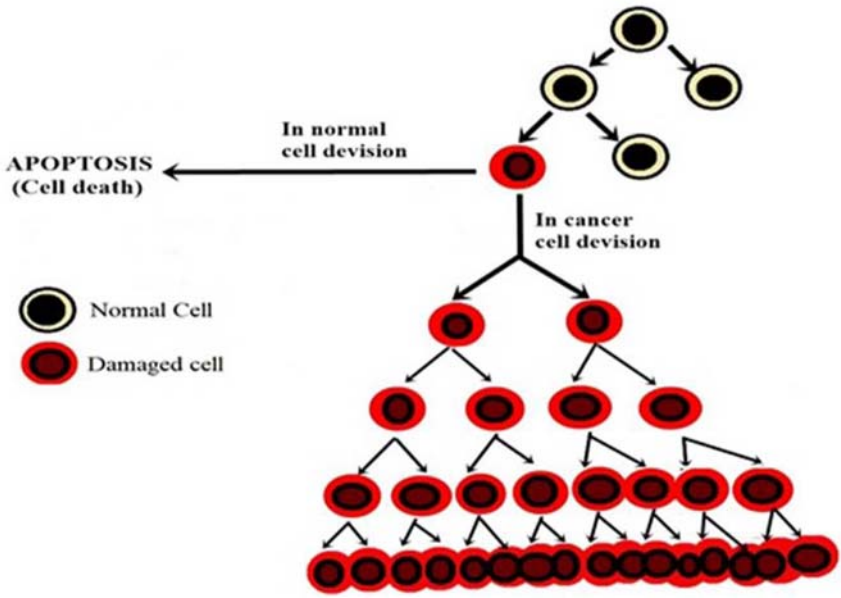

Figure 9.1 Cell division in normal and cancer cell.

9.3 Present diagnostic methods

Early detection is critical to the effective treatment of the disease in cancer control. As a result, mortality associated with the disease is greatly reduced. In recent years, modern imaging tools and morphological inspection of cells (cytology) or tissues (histopathology) aid in early detection of malignant growth and have made it easier to detect and cure cancer. Imaging techniques such as magnetic resonance imaging (MRI), X-rays, ultrasound, and endoscopy can potentially distinguish the malignant tumor when there is a notable change in the tissue [5]. These methods do not differentiate between benign and malignant tumors. There is a risk of damage to normal tissues or incomplete cancer eradication with all these methods. There are few screening tests available for various types of cancers and many of them are not very reliable. In addition, noninvasive screening methods are not accessible for different types of cancer and only a small percentage of patients follow screening criteria. Overdiagnosis and overtreatment are risks with individuals being detected and treated for cancers that are not life-threatening or causing symptoms. In overdiagnosis, patients are exposed to unnecessary physical harm due to invasive diagnostic tests and treatment as well as the psychological stresses associated with the cancer diagnosis. In combating cancer, half the battle is won if the cancer is detected in an early stage. Thus the development of advanced technologies for the identification of malignant tumor in the initial stages is a challenging task.

9.4 Nanotechnology in cancer

Nanotechnology has achieved major heights in the recent decade. It has revolutionized the way cancer is detected and treated [6]. Nanotechnology has the ability to target cancer biomarkers and cancer cells selectively, diagnose a single small cancer cell with high sensitivity, deliver the drug to the cancer cell with high specificity and monitoring the progress of cancer therapy progress, and annihilation of only cancer cells [7]. A number of nanomaterials are used today in molecular imaging to diagnose cancer and monitor its progression. Certain advanced nanomaterials used to detect cancer include supermagnetic nanoparticles, nanoshell, QDs, nanosponge, dendrimers, nanodiamonds, and nanowires. The design and development of QDs has advanced considerably in recent due to the increased interest in inorganic particles and versatile and unique characteristics of QDs.

9.5 Quantum dots

Since the past 20 years, low-dimensional nanosized systems have established a new field of research in condensed-matter physics [8]. Using modern semiconductor processing techniques, it is possible to artificially create quantum confinement of only a few electrons. These artificial structures, designed and fabricated in the laboratory,

have much in common with atoms. Usually they are called "QDs". The term QDs was coined by an American physicist Mark Arthur Reed [9]. With the discovery of quantum-size effects in the optical spectra of semiconductor nanocrystals, by Alexei Ekimov in a glass matrix [10] and Louis E. Brus in colloidal solution [11], sparked the interest in QDs. QDs are nanosized (typically ranged between 2 and 10 nm), highly crystalline, semiconductor crystals that demonstrate quantum mechanical behavior. QDs are usually composed of heavy metals such as indium, cadmium, copper, zinc, selenium, tellurium or their combinations, and oxides. Earlier QDs were composed of zinc oxides, zinc sulfides, cadmium sulfides, copper selenide, and cadmium selenide. In today's scenario the new classes of QDs from carbon origin such as grapheme dots and carbon dots are also found to be a potential candidate for various biomedical applications [12]. QDs are zero-dimensional nanomaterials and have a higher density of states in comparison to higher dimensional nano-structures, which result in the unique optical and transport properties of QDs [13]. The dimensional similarities between the biological macromolecules and QDs can allow nanotechnology to be integrated with biology, resulting in a variety of benefits in medical science, molecular biology, and cell biology. When semiconductor crystals are produced small enough, quantum effects start to exist, limiting the energies at which electrons and holes (the absence of an electron) can exist in the nanocrystal [14]. Since energy is proportional to wavelength the particle's optical properties can be optimized depending on its size. By regulating the size of crystal, they can be made to emit or absorb particular wavelengths/color of light. QDs have a semiconductor core that is over-coated with a shell (e.g., ZnS) to enhance optical properties as well as a cap that allows for increased solubility in aqueous buffers [15].

9.6 Properties of quantum dots

9.6.1 Optical properties

Because of their small size, QDs have unique optical properties [16]. Special optical properties of QDs include bandgap, Stokes shift, fluorescence, brightness, and photostability.

9.6.1.1 Band-gap energy

Electrons (in atoms/molecules) typically occupy distinct energy levels. However, in solids, these energy levels combine to form bands. Those electrons that are used to bind the atoms are present in the valence energy band, whereas the leftover electrons are able to move freely around. For many materials, there is an energy gap between the two bands. The distance between the valence band and the conduction band of electrons is known as a bandgap [17]. Essentially, the bandgap represents the minimum energy required to excite an electron up to a conduction band state leaving behind a hole [18] (Fig. 9.2).

An exciton is formed when an electron and a hole join together. A photon with longer wavelength will be emitted when this exciton recombines (i.e., the excited

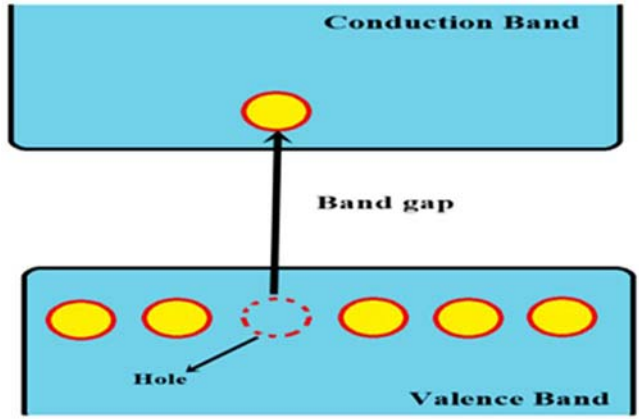

Figure 9.2 Representation of band-gap energy.

electron returns to its ground state). This phenomenon is known as fluorescence [19]. Quantum confinement generally results in a widening of the bandgap with a decrease in the size of the QDs (Fig. 9.3). QDs exhibit size-dependent discrete levels of energy. As the energy gap increases, the size of QDs decreases, resulting in a size-dependent rainbow of colors. Small QDs emit light with higher energy that is bluish in color and larger QDs emit lower energy light that is red in color. As the emission wavelength depends on the QDs size, their fluorescence can be readily controlled by changing their size during the QDs synthesis process [20].

9.6.1.2 Stokes shift

Stokes shift is one of most common features of QDs. The photoluminescence red-shift, relative to absorption (also known as the Stokes shift), is commonly observed in semiconductor QDs and is one of the important features that determines the optical properties of QDs. Stokes shift refers to the difference between the wavelength at which a molecule emits light and the wavelength at which it was excited [21].

The whole emission spectra of QDs can be detected if the excitation and emission spectra of QDs are separated by a higher distance (Fig. 9.4). This improves the detection sensitivity of QDs. QDs can be utilized for multicolor detection with a single wavelength−excitation source because of their extraordinarily large Stokes shifts (up to 400 nm). Because the excitation and emission spectra of QDs are separated by such a great distance, the detection sensitivity of QDs is improved because the full emission spectrum may be monitored.

9.6.1.3 Fluorescence

The emission of light by a substance that has absorbed light or other electromagnetic radiation is known as fluorescence. An external light source of a specific

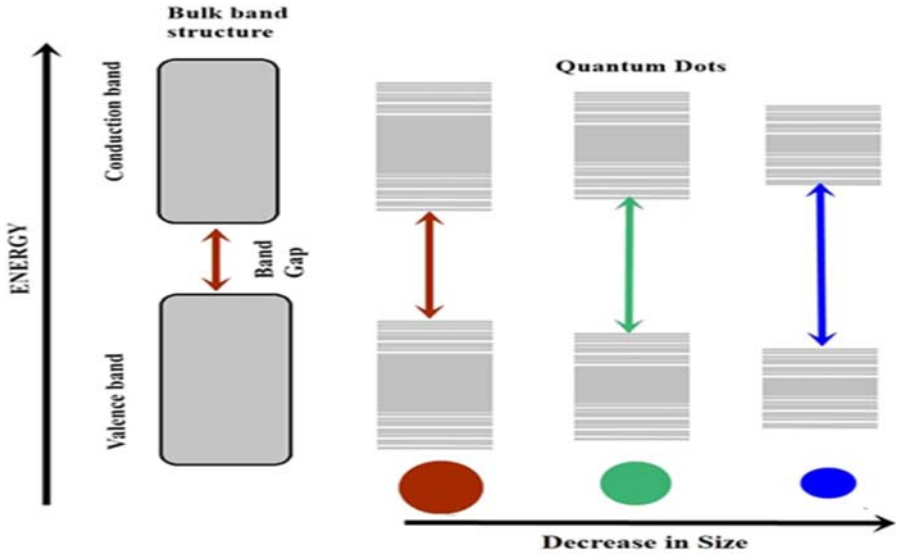

Figure 9.3 Splitting of energy levels in QDs due to the quantum confinement effect and the influence of bandgap on the size of QDs. *QD*, Quantum dot.

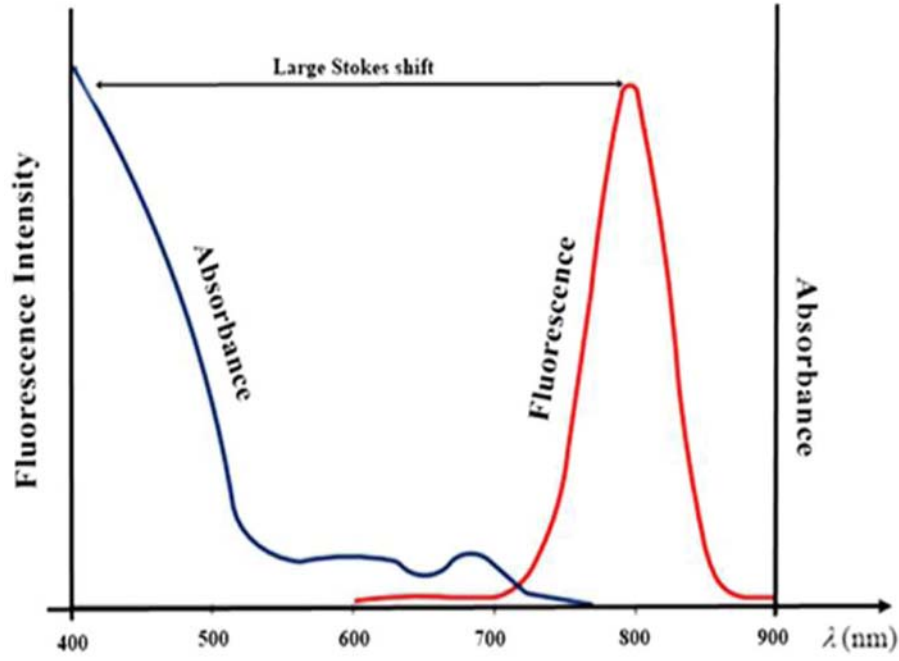

Figure 9.4 Representation of Stokes shift.

wavelength excites fluorescent molecules. The molecule absorbs a photon of this wavelength, causing an electrical transition from a ground to an excited state. The excited molecule returns to the ground state in a radiative transition after transitory vibration relaxation to the lowest excited electronic state, generating longer wavelength photons, which is fluorescence [22]. Fluorescence is widely used in microscopy and an important tool for imaging and detection purpose. The fluorescence phenomenon happens in three steps: (1) excitation of fluorophore by the absorption of light energy; (2) vibrational relaxation of excited state electrons to the lowest energy level; and (3) fluorophore returns to its ground state accompanied by the emission of light [23]. Cell metabolism can be determined from the spontaneous fluorescence produced in cells and tissues.

The average residence period of fluorescent molecules in the excited state before they return to the ground state is referred to as fluorescence lifetime (Fig. 9.5). Fluorescence lifetime imaging microscopy exhibits great performance with high sensitivity and specificity, allowing for the precise location of the cancer tissue, and has a strong potential for application in cancer research and clinical diagnosis [22]. QDs have the ability to emit fluorescence with wavelengths that vary depending on their size.

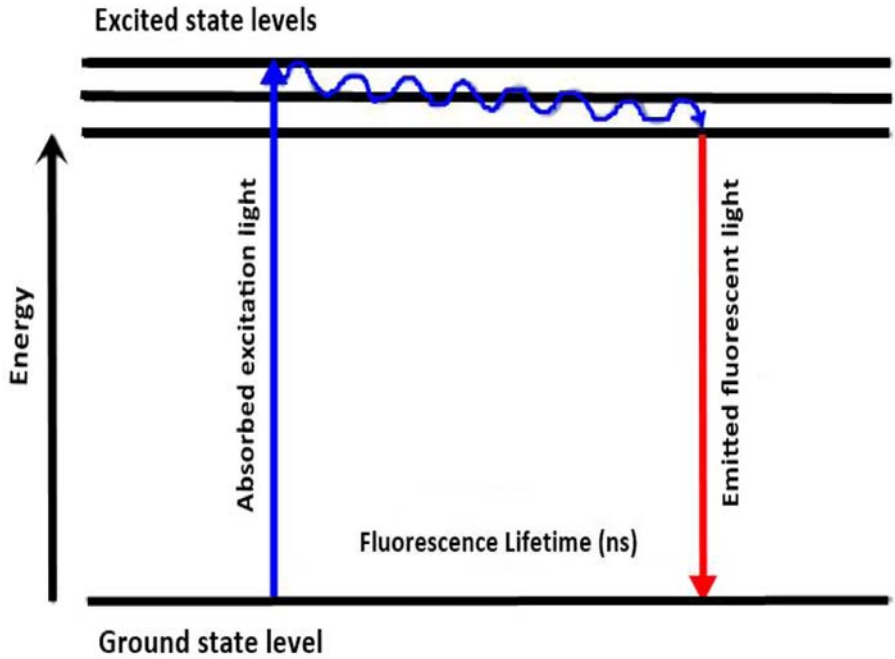

Figure 9.5 QDs have the ability to absorb light at a specific wavelength and then emit light of a longer wavelength after a short period of time called fluorescence lifetime. *QD*, Quantum dot.

9.6.1.4 Brightness and photostability

The fluorescence intensity of a fluorescent molecule is referred to as its brightness. A higher brightness improves the detected signal; hence it is a crucial property of a fluorophore. To show a signal against the typically autofluorescent background prevalent in biological systems, sufficient fluorescence brightness is required. Photobleaching causes conventional organic fluorophores to lose their ability to fluoresce after repeated exposure to excitation light. Here QDs have emerged as bright and photostable nanomaterials. Because of their tremendous brightness and extended photostability, QDs are particularly said to be an excellent probe for multicolor fluorescence imaging in biological applications [24]. Overlap between total excitation and emission bands can be minimized by preventing reabsorption of emitted light into neighboring QDs that improves the brightness and clarity of fluorescing QDs.

9.7 Quantum dots in cancer diagnosis and therapy

Recent advances in QDs technology have already had a significant impact on cancer therapy. Following are the applications of QDs in cancer diagnosis and therapy.

9.7.1 Identification of the molecular targets

In the detection and diagnosis of cancer at an early stage, molecular biomarkers are very crucial. These are the substances/processes in the body that indicate the presence of cancer. Molecular biomarkers include proteins, gene rearrangements, gene mutations, proteins, carbohydrates, RNA, and lipids. If a set of biomarkers are capable to quantify and statistically identify between cancer cells and normal cells, then the assay of biomarkers becomes very beneficial for the screening and diagnosis of cancer, risk assessment, monitoring of disease prognosis, and the prediction of cancer treatment [25,26]. As a result, cancer biomarkers must go through rigorous analytical and clinical validation. But these markers are present at very low concentrations. So, highly sensitive methods having low detection limits are required. A novel approach for detecting biomarkers is through the application of nanotechnology where QDs can be coupled with biomolecules (specific for the target) to increase the specificity and sensitivity [27]. High molar extinction coefficients of QDs ($0.5-5 \times 10^6\ M^{-1}\ cm^{-1}$) make them extremely sensitive probe for identifying low-abundance targets [28,29].

Recently, Zhang et al. explored the significance of graphene QD (GQD)-based nanocomposites to diagnose cancer biomarker "APE1 (apurinic/apyrimidinic endonuclease-1)" in living cells [30]. APE1 is an essential DNA repair enzyme that is overexpressed in most cancers and is identified as a crucial biomarker for effective diagnosis and therapy of cancer. They designed biocompatible nanocomposites by combining meticulously designed unimolecular DNA and fine-sized GQDs; when these nanocomposites were used as diagnostic probes, researchers observed that a

modest amount of cellular APE1 was able to trigger a massive accumulation of fluorescence signals in living cells. They claimed that these GQD-based nanocomposites can detect the APE1 in identical cells under diverse cell conditions and may be used to detect numerous cancer cells with highly sensitivity and specificity. Freitas et al. reported first electrochemical immunosensing strategy based on QDs as electrochemical label for in situ detection of HER2-ECD (Human Epidermal Growth Factor Receptor-2, a breast cancer biomarker) [31].

Au et al. developed a sensitive and specific molecular probe to assess breast cancer margins by using aqueous QDs (AQDs) conjugated with antibodies specific to breast cancer markers such as Tn-antigen. The AQD-Tn mAb probe was found to be sensitive and specific in identifying cancer area quantitatively while remaining unaffected by tissue heterogeneity. The AQD therapy had no effect on the surgical specimen's integrity. Furthermore, the AQD-Tn mAb approach was able to determine margin status within 30 min following tumor removal, showing that it has the potential to be a reliable intraoperative margin assessment method [32] (Fig. 9.6).

9.7.2 Mapping of a sentinel lymph node

Lymph node metastasis is one of the most important prognostic signs of cancer. A sentinel lymph node (SLN) is the first lymph node to which cancer cells are most likely to spread from a primary tumor. Sometimes, there can be more than one SLN. SLN mapping is done to identify the lymph nodes that are at higher risk of malignancy to limit complete lymphadenectomy methods and the morbidities that come with them [33]. SLN mapping is used to detect cancer in various organs (such as breast, thyroid, colon, skin, head, and neck). A surgical approach, named SLN biopsy, is used to identify/remove the SLN to determine if the cancer has spread, and if so, how far. SLN mapping requires higher detection sensitivity and low false negative rate [34]. Various methods are available for SLN mapping that include peritumoral injection of radioisotopes (e.g., Technetium Tc99m Albumin Aggregated), use of isosulfan blue (blue dye), or combination of both [35]. Unfortunately, high background signal and radiation exposure, drainage patterns unpredictability, skip metastasis, and inability to scan lymphatic tracers limit these techniques [36]. Because of these limitations, better and more reliable imaging methods have been developed. Fluorescent semiconductor nanocrystals (QDs) of an appropriate size and emission wavelength allow SLN biopsy to be done more rapidly and effectively with high sensitivity. QDs can be applied to map SLN in breast [37,38], gastrointestinal tract [36], skin [39], esophageal SLN [40], and ovary [41].

Kim et al. worked on near-infrared (NIR) fluorescent type II QDs for SLN mapping and suggested under situations of high fluence rate and prolonged exposure to biological fluids at core body temperature, type II NIR QDs may perform well in the mapping of SLN for cancer. They reported that when QDs were injected intradermally into a mouse's paw, NIR QDs entered the lymphatic system and moved to an axillary area within minutes, which could be seen in imaging. The analysis of resected tissue revealed that NIR QDs were entirely trapped in the SLN and limited to the outermost rim of the SLN. Authors reported that because of their unique

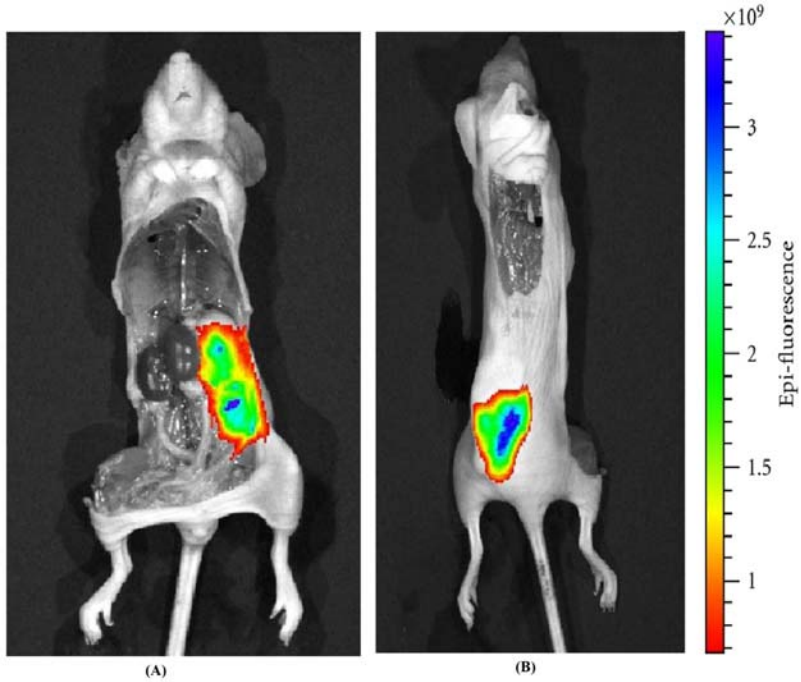

Figure 9.6 Whole mouse tumor imaging: (A) ventral site where the tumor was exposed; (B) Dorsal site, tumor was underneath the skin. Other organs had negative signal, indicating AQTD-Tn mAb prove was specific and sensitive to the tumor [32]. *AQTD*, Aqueous quantum dot.

optical characteristics and high sensitivity, type II NIR QDs give direct visual guidance to the surgeon throughout the SLN mapping technique, reducing incision and dissection errors and allowing real-time confirmation of complete resection [42].

9.7.3 Cancer imaging

Computed tomography scanning, MRI, positron emission tomography, single-photon emission−computed tomography, ultrasound, and X-ray imaging are some of the most common imaging techniques utilized for the cancer diagnosis. Signals that can transmit through dense tissue are used in these approaches and image contrast is generated by changes in signal attenuation through different tissue types. Because there is a difference between structure and anatomy of normal and cancer tissue, various tumors can be identified using image contrast produced with or without exogenous contrast agents. Despite significant technological advancements in diagnostic radiology, conventional cancer imaging techniques do not offer sensitivity, specificity, and high resolution. Organic fluorophores have several limitations that include instability on exposure to photoirradiation that results in degradation

and photobleaching. This means that it does not fluoresce constantly over an extended period of time [43]. Narrow excitation range of conventional organic fluorophores makes simultaneous excitation of different fluorophores very difficult, leading to incompatibility for multicolor imaging.

Since their discovery, QDs have emerged as a strong molecular imaging tool. The excellent properties of QDs such as high brightness, long-term photostability, narrow and size tunable light emission, and broad excitation for multiplex imaging make them better candidates in place of dye or other conventional diagnostic methods. QDs are 20−50 times brighter than the organic dyes. They are less hazardous than typical organic dyes due to their inorganic characteristics [44]. Higher Stokes shifts and an NIR (650−900 nm) emission spectrum of QDs allow better separation and prevent any interference of QTD fluorescence from the background autofluorescence emitted by hemoglobin, cells, or by water [45]. For cancer imaging purpose, this becomes very beneficial as higher background autofluorescence are commonly seen in paraffin-embedded and formalin-fixed tissue specimens. Furthermore, different colors of QDs can be stimulated simultaneously by a single-light source with low spectrum overlap and can emit light of different wavelengths. This results in considerable benefits for multiplexed detection of target molecules. Multicolor QD probes can be used to view and analyze several molecular targets at the same time. This causes reduction in the amount of tissue specimen required for biomarker analysis. Broad excitation range and narrow emission peak of QDs allow multiplex bioimaging with a single source [46].

Liang et al. used CdSe/ZnS QDs, with a maximum emission wavelength of 590 nm (QD590) linked to alpha-fetoprotein (AFP) monoclonal antibody (Ab), to detect AFP in cytoplasm of HCCLM6 (human hepatocellular carcinoma cell line). QD−AFP−Ab probes for targeted imaging of human hepatocellular carcinoma xenograft developing in nude mice by injecting them into the tail vein of the lung metastasis model. The whole-body imaging showed that the majority of probes were found in the lung metastases of the model in comparison to control (Fig. 9.7A and B). The lung imaging revealed that the lung metastases had high fluorescence (Fig. 9.7C and D). The specific binding of QD−AFP−Ab probes to metastases was also confirmed by HE staining (Fig. 9.7E) and CLSFM (Fig. 9.7F) using sections of lung tissues. The results revealed that QD-based probes have good specificity, stability, and biocompatibility for selective cancer targeting in the liver cancer model system [47].

9.7.4 Drug delivery

The process of drug delivery involves administration of drug, release, and transfer of drug across the biological membranes to the desired site. Many anticancer drugs in clinical trials may have drawbacks such as toxicity, nonselectivity, and poor site targeting [48]. The use of QDs is a promising approach that has generated a lot of interest in cancer drug delivery due to their unique properties such as small size, water solubility, cell membrane permeability, easy synthesis, high drug-loading capacity, low toxicity, potential functionalization, fluorescence emission, photochemical, catalytic, electronic, and

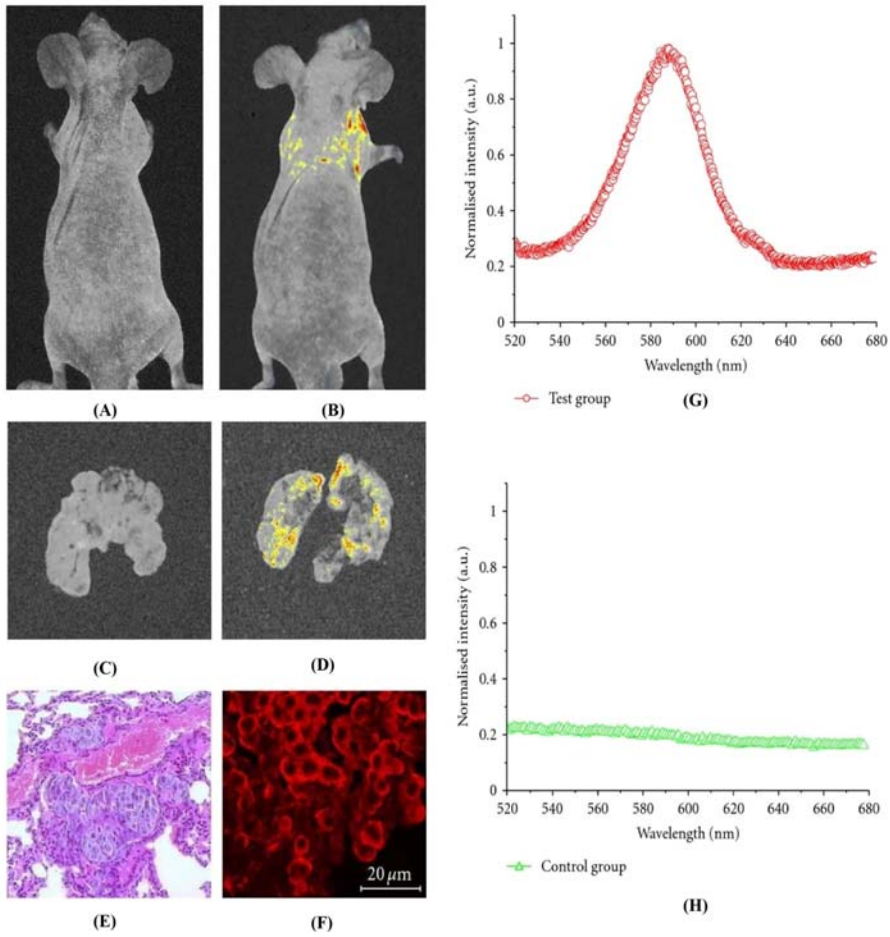

Figure 9.7 In vivo targeting and imaging of lung metastasis model with QD−AFP−Ab probes. (A and B) As compared with the control group (A), the whole-body imaging showed that the QD fluorescence was localized in the lung metastases of the model (B). (C and D) As compared with the control group (C), the lung imaging also showed that there was bright fluorescence in the lung metastases (D). (E) Microphotography of tumor metastasis to lungs, replacing the normal lung tissue with massive tumor cells obviously (HE stain, 200 ×). (F) The confocal microscopic imaging of tumor metastasis to lungs, which showed the specific binding of QD−AFP−Ab probes to tumor cells. Scale bar: 20 mm. (G and H) The spectra analysis of the test group (G) and the control group (H) showed that the fluorescence spectra of metastases in the test group were the same with those of QD−AFP−Ab probes, but there was no characteristic 590 nm peak of the QD at those in the control group [47]. *Ab*, Antibody; *AFP*, alpha-fetoprotein; *QD*, quantum dot.

optical properties [49]. As an anticancer drug delivery carrier, QDs should have the following properties [50]: (1) compatibility with the anticancer drug; (2) high drug encapsulation efficiency; (3) easy preparation and purification; (4) good strength and stability; (5)

low toxicity; and (6) prolonged in vivo residence time. One of the main advantages of the QDs is its ability to deliver drugs directly to cancer cells. Tumor cells possess unique proteins on their membrane that can be recognized by a specific Ab, ligand, or peptide binding. The functional QDs have been efficiently used to target tissues that require addition of molecules (such as antibodies, peptides, or other ligands) to the QDs surface. Surface modification and conjugation properties of QDs possess certain important characteristics for efficient drug delivery such as high affinity, receptor binding specificity, improved drugs absorption, distribution, and elimination. The conjugation ability of QDs along with small size range promotes QDs as an outstanding candidate with the potential to cross the physiological membrane as well as ability to reach varied tissues (such as lymphatic vessel or liver or blood) facilitating intracellular internalization and cellular uptake [51]. Thus QDs enhance maximum uptake by allowing the drug to be targeted to the desired site. Ruzycka-Ayoush et al. [52] reported that QD−11-mercaptoundecanoic acid (MUA)−FA−DOX nanoconjugates can be considered as an efficient drug delivery system for treating cancer in human alveolar basal−epithelial cells. For this purpose the QDs were modified with MUA, L-cysteine, and lipoic acid decorated with folic acid and used to target doxorubicin (DOX) to folate receptors on adenocarcinomic human alveolar basal-epithelial cells (A549). Results confirmed the cytotoxicity of QD conjugates against A549 cells. Recently, Qi et al. [53] reported that GQDs suppress the growth of tumor by selectively damaging cancer cell DNA. Results showed that the functionalized GQDs adsorb on DNA via the $\pi-\pi$ and electrostatic interactions, which causes the DNA damage, upregulation proteins related to cell apoptosis, and ultimately the suppression of cancer cell growth. Vahedi et al. [54] used GQDs as drug carriers and also as an imaging agent for cancer cells. To optimize drug dose, to reduce side effects in healthy cells, and to target cancer cells, hyaluronic acid was decorated on the surface of GQDs. Drug-loading capacity of GQDs were found to be 98.02%. Authors reported that the prepared QDs were biocompatible and reduced HeLa cell viability.

Table 9.1 presents some research reports on QDs in cancer.

9.8 Toxicity of quantum dots

QDs used for clinical applications must have a low level of toxicity [63]. Discussions of QDs toxicity can be somewhat perplexing because of a variety of QDs has been synthesized by the researchers. However, there is still a lack of research on QD toxicity in the literature. QDs used for imaging and therapeutic applications have been shown to have effects on biological systems at the cellular, subcellular, and on protein levels [64]. Each type of QD has its own set of physical and chemical properties, which determine its toxicity potential (or lack thereof) such as size of QD, charge, surface functionality, concentration, and outer coating. Zinc oxide (ZnO) is generally regarded as a safe substance by the FDA, but ZnO-based QDs can be toxic because of their size. The surface area is indirectly proportional to the size of QDs; as the size decreases, larger surface area will be available and QD will be more reactive. As a result, QDs with small size can be more toxic

Table 9.1 Recent state-of-the-art: reported research on quantum dots (QDs) in cancer.

Test material	Findings	References
GQDs	GQD, the new generation members of graphene-family, have shown promising applications in anticancer therapy. The results of biological tests underlined the low cytotoxicity of the GQD sample and the cytotoxic activity of the drug delivery system against the investigated cancer cell lines with a higher or similar potency to that exerted by the benzofuran structure alone, thus opening new possibilities for the use of this drug or other anticancer agents endowed of cytotoxicity and serious side effects	[55]
InP/ZnS QDs	InP/ZnS QDs were synthesized and functionalized with folate (QD-FA), D-glucosamine (QD-GA), or both (QD-FA-GA). The bifunctionalized QDs were further conjugated with doxorubicin (QD-FA-GA-DOX). The FA-functionalized QDs showed significantly higher uptake in the FR-positive OVCAR-3 cells, nonetheless the GA-functionalized QDs resulted in an indiscriminate uptake in both cell lines. In conclusion, our findings indicated that DOX-conjugated FA-armed QDs can be used as theranostics for simultaneous imaging and therapy of cancer	[56]
GQDs	GQDs were found to exhibit a strong blue photoluminescence with a significantly high quantum yield. Results showed that the robust functionality, luminescence stability, nanosecond lifetime, biocompatibility, and low toxicity of GQDs could be a promising probe for cancer therapeutic applications	[57]
Titanium nitride MXene QDs	In vitro and in vivo assessments of Ti_2N QDs demonstrate that they possess excellent biocompatibility, photoacoustic effect, and photothermal therapy efficiency. Ti_2N QDs showed obvious aggregation in tumors after 4 h postinjection. Ti_2N QDs with appropriate degradation property also show an applicable excretion rate from the body in vivo, which ensures sufficient stability in circulation to accomplish therapeutics roles and then can be smoothly discharged from the body after that. These results indicate the high potential of biodegradable Ti_2N QDs in cancer treatment	[58]

(*Continued*)

Table 9.1 (Continued)

Test material	Findings	References
Polydopamine-functionalized black phosphorus QDs	Polydopamine-functionalized black phosphorus QDs were found to have excellent biodegradability and good biocompatibility and hold great potential for cancer theranostics	[59]
Carboxylated GQDs	A drug delivery system was synthesized through a crosslink reaction of carboxylated GQDs, NH2-PEG-NH2, and folic acid. Cell image results indicated that the QDs system entered into human cervical cancer cells mainly through macropinocytosis-dependent pathway. In vivo experiments showed the outstanding antitumor ability and low systemic toxicity of this nanodrug delivery system	[60]
ZnO QDs	pH responsive delivery system based on ZnO QDs for controlled release of drugs were prepared. ZnO@P(CBMA-*co*-DMAEMA) loaded with Doxorubicin can achieve lysosomal acid degradation and the release of DOX after endocytosis by tumor cells, resulting in synergistic treatment of cancer, which is attributed to a combination of the anticancer effect of Zn^{2+} and doxorubicin	[61]
PEGylated MoS_2 QDs	A drug delivery system based on MoS_2 QDs was successfully developed by covalently grafting MoS_2 QDs with diamine-terminated oligomeric PEG and then loading with a fluorescent antineoplastic anthracycline drug, DOX. The MoS_2-PEG-DOX nanoassembly can be effectively taken up by U251 cells, and an accelerated DOX release is then triggered by intracellular acid condition, which in turn diminishing unwanted side effects derived by the incorporation of DOX into healthy cells. These findings demonstrated that MoS_2-PEG-DOX could be promising for high treatment efficacy with minimal side effects in future therapy	[62]

DOX, Doxorubicin; *GQD*, graphene quantum dots; *PEG*, polyethylene glycol.

than large ones. Furthermore, the shape and charge of QDs are two important factors affecting their toxicity. The process of membrane warping during endocytosis/phagocytosis can be influenced by the shape of the QD [64]. Endocytosis of spherical QDs is easy and quick than that of rod-shaped QDs. As far as the charge of QD is concerned, cationic surface is considered to be more toxic than anionic surface [65]. QDs toxicity also depends on environmental conditions such as oxidation, photolysis, and mechanical stability as after oxidative or photolytic degradation of the core coating, QDs have been discovered to be cytotoxic [66]. Concerns about the toxicity of QDs are also related to the chemical composition of QDs, particularly in the case of QDs that contain heavy metal ions such as cadmium (Cd), mercury (Hg), selenium (Se), and tellurium (Te).

With the changes in physicochemical, environmental, and composition of QDs, the toxicity can be reduced. Surface modification of QDs can influence the in vivo distribution and clearance and can reduce the decomposition in biological environment may lead to reduction in toxicity. The cytotoxicity of QDs can also be reduced by using inorganic coating materials.

9.9 Conclusion and future prospects

With early detection and improved diagnostic cancer imaging the future may hold hope for the prevention and cure of cancer. In the nanotechnology area, QDs are considered unique nanoparticles for their versatility and unique properties that include good resistance to photobleaching, narrow and symmetric emission peak, and higher excitation coefficient broader absorption range. High brightness and photostability of QDs provides a realistic means of monitoring the early stages of cancer. Drug delivery system based on QDs offers greater possibilities for designing and developing multifunctional therapeutic and diagnostic systems. In spite of their extraordinary features for effective cancer diagnosis and treatment, there is still a lot of research to be done ahead of a clinically effective drug delivery system. Current challenges include synthesizing monodisperse, stable nanoparticles with no long-term cytotoxic and genotoxic effects. Although QDs are already used as diagnostic cancer imaging probes, several challenges are still need to be overcome before this can be realized. It is possible to further improve QD-based technology for tissue biomarker analysis beyond its current state. The spectral imaging detection is currently limited to 10 colors. But faster computers and improved software could analyze hundreds of cancer biomarkers simultaneously in a single-tissue sample. To leverage the potential of QDs for identifying cancer in its early stages, delivery of cancer drugs to target site and monitoring treatment results, persistent and coordinated exploration efforts should be pursued.

References

[1] F. Bray, J. Ferlay, I. Soerjomataram, R.L. Siegel, L.A. Torre, A. Jemal, Global cancer statistics 2018: GLOBOCAN estimates of incidence and mortality worldwide for 36 cancers in 185 countries, CA: Cancer J. Clin. 68 (6) (2018) 394−424.

[2] H. Sung, J. Ferlay, R.L. Siegel, M. Laversanne, I. Soerjomataram, A. Jemal, et al., Global cancer statistics 2020: GLOBOCAN estimates of incidence and mortality worldwide for 36 cancers in 185 countries, CA: Cancer J. Clin. 71 (3) (2021) 209−249.
[3] SEER Training Modules 2000, Introduction to collaborative stage, ICD-O-3, and summary stage 2000. U. S. National Institutes of Health, National Cancer Institute. (Accessed on 01.08.2021). <https://training.seer.cancer.gov/>.
[4] A.M. Kabel, M.A. Abd Elmaaboud, Cancer: role of nutrition, pathogenesis, diagnosis and management, World J. Nutr. Health 2 (4) (2014) 48−51.
[5] T. Hussain, Q.T. Nguyen, Molecular imaging for cancer diagnosis and surgery, Adv. Drug Delivery Rev. 66 (2014) 90−100.
[6] V. Jaishree, P.D. Gupta, Nanotechnology: a revolution in cancer diagnosis, Indian J. Clin. Biochem. 27 (3) (2012) 214−220.
[7] F. Alexis, J.W. Rhee, J.P. Richie, A.F. Radovic-Moreno, R. Langer, O.C. Farokhzad, New frontiers in nanotechnology for cancer treatment, Urol. Oncol. 26 (1) (2008) 74−85.
[8] S.M. Reimann, M. Manninen, Electronic structure of quantum dots, Rev. Mod. Phys. 74 (2002) 1283−1286.
[9] B. Hou, Colloidal quantum dots: the artificial building blocks for new-generation photo-electronics and photochemistry, Isr. J. Chem. 59 (8) (2019) 637−638.
[10] A.I. Ekimov, A.L. Efros, A.A. Onushchenko, Quantum size effect in semiconductor microcrystals, Solid State Commun. 56 (1985) 921−924.
[11] R. Rossetti, S. Nakahara, L.E. Brus, Quantum size effects in the redox potentials, resonance Raman spectra, and electronic spectra of CdS crystallites in aqueous solution, J. Chem. Phys. 79 (1983) 1086−1088.
[12] A.M. Smith, H. Duan, A.M. Mohs, S. Nie, Bioconjugated quantum dots for in vivo molecular and cellular imaging, Adv. Drug Delivery Rev. 60 (2008) 1226−1240.
[13] A.P. Alivisatos, Semiconductor clusters, nanocrystals, and quantum dots, Science 271 (1996) 933−937.
[14] K. Sanderson, Quantum dots go large, Nature 459 (2009) 760−761.
[15] A. Valizadeh, H. Mikaeili, M. Samiei, S.M. Farkhani, N. Zarghami, A. Akbarzadeh, et al., Quantum dots: synthesis, bioapplications, and toxicity, Nanoscale Res. Lett. 7 (1) (2012) 480.
[16] P. Hawrylak, Optical properties of quantum dots. NATO Science Series (Series 3: High Technology) in: M.L. Sadowski, M. Potemski, M. Grynberg (Eds.), Optical Properties of Semiconductor Nanostructures, Springer, Dordrecht, 2000, pp. 319−336.
[17] F. Capasso, Band-gap engineering: from physics and materials to new semiconductor devices, Science 235 (4785) (1987) 172−176.
[18] E.O. Chukwuocha, M.C. Onyeaju, T.S. Harry, Theoretical studies on the effect of confinement on quantum dots using the Brus equation, World J. Condens. Matter Phys. 2 (2012) 96−100.
[19] E. Petryayeva, W.R. Algar, I.L. Medintz, Quantum dots in bioanalysis: a review of applications across various platforms for fluorescence spectroscopy and imaging, Appl. Spectrosc. 67 (3) (2013) 215−252.
[20] H.S. Mansur, Quantum dots and nanocomposites, Wiley Interdiscip. Rev. Nanomed. Nanobiotechnol. 2 (2) (2010) 113−129.
[21] G.G. Stokes, On the change in refrangibility of light, Philos. Trans. R. Soc. Lond. 142 (2013) 463−562.
[22] Z. Wang, Y. Zheng, D. Zhao, Z. Zhao, L. Lixin, P. Artem, et al., Applications of fluorescence lifetime imaging in clinical medicine, J. Innovative Opt. Health Sci. 11 (1) (2018).

[23] A.J. Welch, C. Gardner, R. Richards-Kortum, E. Chan, G. Criswell, J. Pfefer, et al., Propagation of fluorescent light, Lasers Surg. Med. 21 (2) (1997) 166–178.
[24] E.C. Arnspang, P. Kulatunga, B.C. Lagerholm, A single molecule investigation of the photostability of quantum dots, PLoS One 7 (8) (2012) e44355.
[25] M.K. Wagner, F. Li, J. Li, X.F. Li, X.C. Li, Use of quantum dots in the development of assays for cancer biomarkers, Anal. Bioanal. Chem. 397 (2010) 3213–3224.
[26] N.L. Henry, D.F. Hayes, Cancer biomarkers, Mol. Oncol. 6 (2) (2012) 140–146.
[27] T.A. Zhukov, M. Dybiec, J.Z. Zhang, P.B. Zhukov, S. Ostapenko, T.A. Sellers, Quantum dots for cancer biomarker panels, Cancer Res. 65 (9) (2005) 184.
[28] C.A. Leatherdale, W.K. Woo, F.V. Mikulec, M.G. Bawendi, On the absorption cross section of CdSe nanocrystal quantum dots, J. Phys. Chem. B 106 (31) (2002) 7619–7622.
[29] L.D. True, X. Gao, Quantum dots for molecular pathology: their time has arrived, J. Mol. Diagn. 9 (1) (2007) 7–11.
[30] H. Zhang, S. Ba, Z. Yang, T. Wang, J.Y. Lee, T. Li, et al., Graphene quantum dot-based nanocomposites for diagnosing cancer biomarker APE1 in living cells, ACS Appl. Mater. Interfaces 12 (12) (2020) 13634–13643.
[31] M. Freitas, M.M. Neves, H.P. Nouws, C. Delerue-Matos, Quantum dots as nanolabels for breast cancer biomarker HER2-ECD analysis in human serum, Talanta 208 (2020) 120430.
[32] G.H.T. Au, W.Y. Shih, W.-H. Shih, L. Mejias, V.K. Swami, et al., Assessing breast cancer margins ex vivo using aqueous quantum-dot-molecular probes, Int. J. Surg. Oncol. 2012 (2012).
[33] R.W. Holloway, N.R. Abu-Rustum, F.J. Backes, J.F. Boggess, W.H. Gotlieb, W.J. Lowery, et al., Sentinel lymph node mapping and staging in endometrial cancer: a Society of Gynecologic Oncology literature review with consensus recommendations, Gynecol. Oncol. 146 (2) (2017) 405–415.
[34] J.N. Barlin, F. Khoury-Collado, C.H. Kim, M.M. Leitao Jr, D.S. Chi, Y. Sonoda, et al., The importance of applying a sentinel lymph node mapping algorithm in endometrial cancer staging: beyond removal of blue nodes, Gynecol. Oncol. 125 (3) (2012) 531–535.
[35] G. Peley, I. Sinkovics, G. Liszkay, J. Toth, I. Peter, E. Farkas, et al., The role of intraoperative gamma-probe-guided sentinel lymph node biopsy in the treatment of malignant melanoma and breast cancer, Orv. Hetil. 140 (42) (1999) 2331–2338.
[36] E.G. Soltesz, S. Kim, S.W. Kim, R.G. Laurence, M. Alec, C.P. Parungo, et al., Sentinel lymph node mapping of the gastrointestinal tract by using invisible light, Ann. Surg. Oncol. 13 (3) (2006) 386–396.
[37] M. Helle, E. Cassette, L. Bezdetnaya, T. Pons, A. Leroux, F. Plénat, et al., Visualisation of sentinel lymph node with indium-based near infrared emitting quantum dots in a murine metastatic breast cancer model, PLoS One 7 (8) (2012) e44433.
[38] A. Robe, E. Pic, H.P. Lassalle, L. Bezdetnaya, F. Guillemin, F. Marchal, Quantum dots in axillary lymph node mapping: biodistribution study in healthy mice, BMC Cancer 8 (1) (2008) 1–9.
[39] C.P. Parungo, S. Ohnishi, S.W. Kim, S. Kim, R.G. Laurence, E.G. Soltesz, et al., Intraoperative identification of esophageal sentinel lymph nodes with near-infrared fluorescence imaging, J. Thorac. Cardiovasc. Surg. 129 (4) (2005) 844–850.
[40] M. Kleppe, T. Van Gorp, B.F. Slangen, A.J. Kruse, B. Brans, I.N. Pooters, et al., Sentinel node in ovarian cancer: study protocol for a phase 1 study, Trials 14 (1) (2013) 1–6.

[41] M.H. Ko, S. Kim, W.J. Kang, J.H. Lee, H. Kang, S.H. Moon, et al., In vitro derby imaging of cancer biomarkers using quantum dots, Small 5 (10) (2009) 1207−1212.
[42] S. Kim, Y.T. Lim, E.G. Soltesz, A.M. De Grand, J. Lee, A. Nakayama, et al., Near-infrared fluorescent type II quantum dots for sentinel lymph node mapping, Nat. Biotechnol. 22 (1) (2004) 93−97.
[43] X.T. Zheng, A. Ananthanarayanan, K.Q. Luo, P. Chen, Glowing graphene quantum dots and carbon dots: properties, syntheses, and biological applications, Small 11 (14) (2015) 1620−1636.
[44] P.K. Tiwari, S. Mugdha, G. Kumar, A. Mohsen, Pivotal role of quantum dots in the advancement of healthcare research, Comput. Intell. Neurosci. 9 (2021) 1−9.
[45] S. Muralidhara, K. Malu, P. Gaines, B.M. Budhlall, Quantum dot encapsulated nanocolloidal bioconjugates function as bioprobes for in vitro intracellular imaging, Colloids Surf., B: Biointerfaces 182 (2019) 110348.
[46] U. Badılı, F. Mollarasouli, N.K. Bakirhan, Y. Ozkan, S.A. Ozkan, Role of quantum dots in pharmaceutical and biomedical analysis, and its application in drug delivery, Trends Anal. Chem. 131 (2020) 116013.
[47] D.C. Liang, J. Liu, X.F. Yu, M. He, X.F. Pei, Z.Y. Tang, et al., The biocompatibility of quantum dot probes used for the targeted imaging of hepatocellular carcinoma metastasis, Biomaterials 29 (31) (2008) 4170−4176.
[48] Z. Liu, et al., Targeted drug delivery: carbon-quantum-dots-loaded mesoporous silica nanocarriers with pH-switchable zwitterionic surface and enzyme-responsive pore-cap for targeted imaging and drug delivery to tumor, Adv. Healthcare Mater. 5 (12) (2016) 1380.
[49] B. Loretz, R. Jain, P. Dandekar, C. Thiele, H. Yamada, B. Mostaghaci, et al., Chances of nanomaterials for pharmaceutical applications, in: W. Luther, A. Zweck (Eds.), Safety Aspects of Engineered Nanomaterials, Pan Stanford Publishing, Singapore, 2013, pp. 279−317.
[50] M.X. Zhao, B.J. Zhu, The research and applications of quantum dots as nano-carriers for targeted drug delivery and cancer therapy, Nanoscale Res. Lett. 11 (207) (2016) 1−9.
[51] S. Parveen, R. Misra, S.K. Sahoo, Nanoparticles: a boon to drug delivery, therapeutics, diagnostics and imaging, Nanomedicine 8 (2) (2012) 147−166.
[52] M. Ruzycka-Ayoush, P. Kowalik, A. Kowalczyk, P. Bujak, A.M. Nowicka, M. Wojewodzka, et al., Quantum dots as targeted doxorubicin drug delivery nanosystems in human lung cancer cells cancer, Nanotechnology 12 (1) (2021) 1−27.
[53] L. Qi, T. Pan, L. Ou, Z. Ye, C. Yu, B. Bao, et al., Biocompatible nucleus-targeted graphene quantum dots for selective killing of cancer cells via DNA damage, Commun. Biol. 4 (1) (2021) 1−2.
[54] N. Vahedi, F. Tabandeh, M. Mahmoudifard, Hyaluronic acid−graphene quantum dot nanocomposite: potential target drug delivery and cancer cell imaging, Biotechnol. Appl. Biochem. (2021) 1−12.
[55] D. Iannazzo, A. Pistone, C. Celesti, C. Triolo, S. Patane, S.V. Giofré, et al., A smart nanovector for cancer targeted drug delivery based on graphene quantum dots, Nanomaterials 9 (2) (2019) 282−290.
[56] R. Navazi, M. Eskandani, M. Johari, A. Nemati, H. Akbari, S. Davaran, et al., Doxorubicin-conjugated D-glucosamine-and folate-bi-functionalised InP/ZnS quantum dots for cancer cells imaging and therapy, J. Drug Target 26 (3) (2018) 267−277.
[57] S. Ghorai, I. Roy, S. De, P.S. Dash, A. Basu, D. Chattopadhyay, Exploration of the potential efficacy of natural resource-derived blue-emitting graphene quantum dots in cancer therapeutic applications, New J. Chem. 44 (2020) 5366−5376.

[58] J. Shao, J. Zhang, C. Jiang, J. Lin, P. Huang, Biodegradable titanium nitride MXene quantum dots for cancer phototheranostics in NIR-I/II biowindows, Chem. Eng. J. 400 (2020) 126009.
[59] Z. Li, H. Xu, J. Shao, C. Jiang, E. Zhang, J. Lin, et al., Polydopamine-functionalized black phosphorus quantum dots for cancer theranostics, Appl. Mater. Today 15 (2019) 297−304.
[60] Z. Li, J. Fan, C. Tong, H. Zhou, W. Wang, B. Li, et al., A smart drug-delivery nanosystem based on carboxylated graphene quantum dots for tumor-targeted chemotherapy, Nanomedicine 14 (15) (2019) 2011−2025.
[61] Y. Wang, L. He, B. Yu, Y. Chen, Y. Shen, H. Cong, ZnO quantum dots modified by pH-activated charge-reversal polymer for tumor targeted drug delivery, Polymers 10 (2018) 1272−1286.
[62] L. Liu, J. Hongli, J. Dong, W. Zhang, G. Dang, M. Yang, et al., PEGylated MoS_2 quantum dots for traceable and pH-responsive chemotherapeutic drug delivery, Colloids Surf., B: Biointerfaces 185 (2020) 110590.
[63] Y. Park, S. Jeong, S. Kim, Medically translatable quantum dots for biosensing and imaging, J. Photochem. Photobiol., C: Photochem. Rev. 30 (2017) 51−70.
[64] H. Sun, F. Zhang, H. Wei, B. Yang, The effects of composition and surface chemistry on the toxicity of quantum dots, J. Mater. Chem. B 1 (47) (2013) 6485−6494.
[65] C. Wu, L. Shi, Q. Li, H. Jiang, M. Selke, L. Ba, et al., Probing the dynamic effect of cys-CdTe quantum dots toward cancer cells in vitro, Chem. Res. Toxicol. 23 (1) (2010) 82−88.
[66] R. Hardman, A toxicologic review of quantum dots: toxicity depends on physicochemical and environmental factors, Environ. Health Perspect. 114 (2) (2006) 165−172.

Nanotechnology for cosmetics applications—a journey in innovation

10

João Paulo Figueiró Longo[1], *Nichollas Serafim Camargo*[2], *Guilherme Alves Ferreira*[2], *Camila Magalhães Cardador*[1] *and Marcos Antônio Corrêa*[3]

[1]Department of Genetics and Morphology, Institute of Biological Sciences, University of Brasília, Brasilia, Federal District, Brazil, [2]Nanoceuticals Innovation Hub, Aparecida de Goiânia, Goiás, Brazil, [3]Department of Drugs and Medicines, School of Pharmaceutical Sciences, São Paulo State University (UNESP), Araraquara, São Paulo, Brazil

10.1 Introduction

Nanotechnology, as a field, is a technology with applications in several areas of human knowledge. The field was formally defined as a technological area in the 1980s [1,2] and has advanced significantly since then. The improvements were observed not only in academia, but also across the most different industrial sectors [3]. The number of research groups worldwide, in addition to the number of scientific publications, is important indicators in this direction. Moreover, several industrial fields have seen the incorporation of nanotechnology in their supply chain [4].

For the cosmetic sector, this process was no different, and the field was probably the first one that used nanotechnology in huge markets. As an early adopter, the cosmetic sector released the first nano-products in the 1980s when Dior and L'Oréal incorporated liposomes in their products [5]. Nowadays, the cosmetic sector is currently a global leader in the use of nanoparticles, and thousands of companies use different types of nanosystems in their products. The nature of these nanoparticles is different and includes organic and inorganic particles that have been used to improve some desirable innovative characteristics for cosmetic products [6].

The maturity and complexity of the field is reflected by the suppliers of nanoparticles that illustrate how the supply chain has become specialized recently. Some companies specialize only in inorganic and metallic nanoparticles, and others are dedicated only to organic lipid and polymeric nanosystems. Moreover, some less mainstream companies specialize in nanoparticle characterization, or are dedicated to preclinical and clinical evaluations, and these have generated a complex ecosystem in this field. This is important evidence of the field's maturity, showing how a division of labor has come to offer innovative materials and solutions for the cosmetic sector.

Quantum Materials, Devices, and Applications. DOI: https://doi.org/10.1016/B978-0-12-820566-2.00010-7

Due to this organization, we can observe nanotechnology being applied at different stages in the cosmetic innovation process. The general idea of using nanotechnology is to improve effectiveness, reduce potential toxicity, and eventually create new and desirable properties [6]. In this way, cosmetic ingredients can benefit from nanotechnology at different points along the cosmetic product journey (Fig. 10.1). In other words, nowadays, nanotechnologies are used to improve industrial production, by reducing the time of active ingredient dispersion; as an active carrier that works to keep the ingredients stable over time; or in creating long-lasting effects, sustained release over time, or improving the contact between the active ingredient and the target skin/hair surface [7].

Depending upon the objective, nanotechnology can be included at different stages in cosmetic product development, which means that it can be used as a wide tool to produce different types of innovations. The main idea of this chapter is to present and discuss how these innovations can affect the quality and performance of the cosmetic sector. Furthermore, we will introduce potential benefits that can be incorporated into the field in the next few years.

10.2 Nanocosmetic definitions

Discussions regarding the definition of nanotechnology are not only exclusive to cosmetic applications but are also present in the general nanoscience literature. Historically, the definition most used in the scientific literature was provided by the American National Nanotechnology Initiative, which defines nanoscience as "science, engineering, and technology conducted at the nanoscale (1−100 nm), where unique phenomena enable novel applications in a wide range of fields, from chemistry, physics, and biology, to medicine, engineering, and electronics" [1].

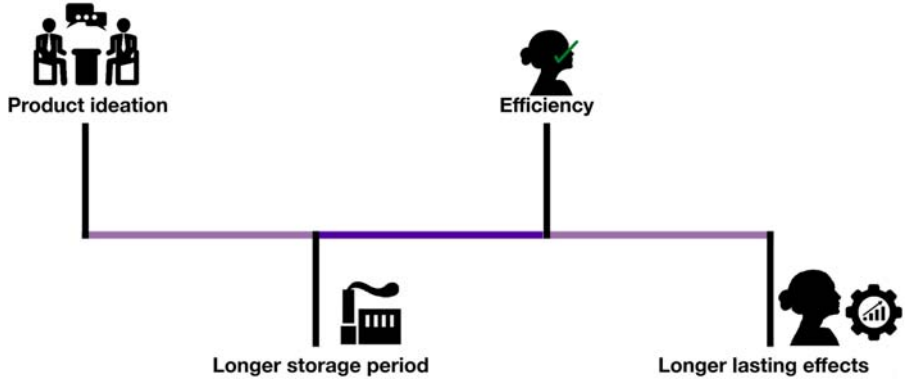

Figure 10.1 Cosmetic ingredients can benefit from nanotechnology at different points along the cosmetic product journey.

This definition has two main aspects: the first is the nanoscale, which needs to be in the range of 1−100 nm, and the second is related to the special properties that are observed in this nanoscale. Historically, as most of the nanotech groups were created in the university's physics and chemistry departments, it is probable that the special properties were observed in inorganic nanoparticles, especially metallic ones in this 1- to 100-nm nanoscale range. However, when the research efforts moved to the biological applications, the researchers also observed that interesting properties could be observed in organic nanomaterials with larger, submicrometric, sizes. In other words, for the biomedical field that includes cosmetics applications, the range of 1−999 nm can also be considered a nanoscale range. Of course, the second aspect, regarding the special properties, needs to be present to fulfill the nanotechnology definition.

In addition to this general discussion, the cosmetics sector also presents some particularities about the definition of nanotechnology. For the European Commission Regulation (1223/2009), nanoparticles are defined as materials intentionally produced in the nanoscale (1−100 nm), which are insoluble or bio-persistent. Thus the definition includes metallic particles, especially the ultraviolet (UV) filters and pigment particles largely used in cosmetics applications. Moreover, organic biodegradable particles, such as liposomes, nanoemulsions (NEs), solid lipid nanoparticles (SLNs), and polymeric systems, are not included in this regulatory definition. Despite this regulatory definition presented by the European Commission, the scientific literature still considers lipid and polymeric nanostructures as nanoparticles used for biomedical purposes, such as dermatological and cosmetic products.

These definitions tend to follow the low toxicological risk of this type of organic system. This approach is also interesting in terms of international regulation, since these organic biodegradable nanosystems could be easily incorporated into cosmetic products. Furthermore, clearer definitions and legislation are fundamental for regulatory predictability that, in turn, facilitates and optimizes the mutation of the entire innovation ecosystem in nanotechnology and cosmetics [7].

10.3 Inorganic nanoparticles used in cosmetics

With these regulatory definitions in mind, we will consider here that the general scientific literature includes both organic and inorganic nanostructures as nanoparticles used in cosmetics products. In terms of volume of sales, inorganic particles are the most common ingredients. These numbers are supported by the use of zinc and titanium oxides as UV blockers, which are extensively used worldwide, and by silver nanoparticles used as antibacterial particles, mainly used in cosmetics as deodorant products. Moreover, gold nanoparticles and silver nanoparticles are present as pigment ingredients in cosmetic products [8,9].

Inorganic nanoparticles used as UV filters, such as zinc and titanium oxides, were also developed in the 1980s and 1990s and nowadays are widely used worldwide. Some evidence shows that more than 40% of American sunscreens use these

types of nanoparticles [8]. This percentage increases significantly (17%−41%) if we compare data from 2007 to 2018 [8]. We do not have data from other markets, but observing the products available nowadays, it seems that this tendency may also be true for other markets all over the world.

Some reasonable points can explain this movement. The first is related to the physical appearance of the product, which is more transparent and can easily be applied over the skin. Due to the granularity of the products containing these nanoparticles, they are applied smoothly, conferring better sensorial feelings for the end users. The second point that supports the increasing number of products that use inorganic nanoparticles is the potential to replace traditional organic UV filters [9].

The use of traditional organic UV filters, mainly represented by oxybenzone and octinoxate, has become controversial in recent decades. There is some evidence that correlates these organic compounds with both health and environmental impacts. Some reports have found that these ingredients can damage coral reefs, which induced the creation of specific legislation to avoid the use of these kinds of sunscreens. Furthermore, some studies have shown that these chemical compounds can promote hormonal dysregulation in animal models, a fact that could also impact human health. Thus this regulatory condition, in addition to the alert about potential toxic health effects, triggered the development of innovative materials, such as nanoparticle UV filters, which could be used to replace conventional organic filters [8].

Regarding the technical benefits of nanotech sunscreens, we can cite the sensorial and the physical aspects of the products. This is a clear example where the nanotech definition fits very well. The production of metal oxides (zinc or titanium) in the nanoscale modifies the macroscopic aspect of the product. This happens because the oxide suspensions will interact differently with the visible light [10]. In terms of physical behavior, small nanoparticles will interact less with longer wavelengths and eventually will interact mostly with the shorter UV wavelengths that have higher energy. With this profile, smaller particles will have a more translucid macroscopic appearance under visible light.

As an example, we explain how the UV filter nanoparticles will interact with the different wavelengths. Due to the size of the nanoparticles, they will interact mostly with the shorter and more dangerous UV wavelengths, and less with the visible wavelengths. This effect is very important, because the objective of sun blockers is exactly to block the high-energy UV wavelengths, which can be absorbed, reflected, or even scattered, thus protecting the biological skin structures [10].

Furthermore, this pattern also explains how the macroscopic aspect of these nanoparticles will be more translucid, or even having a slightly blue aspect. This model is represented in Fig. 10.2, where the more clear appearance of the NE is explained by the fact that almost all light wavelengths can cross the nanodroplets suspensions, while in the microemulsion, the microdroplets block almost all light wavelengths, creating a more opaque appearance. We also present some possible physical interactions, such as absorption, reflection, and diffraction of the UV wavelengths when getting in contact with the UV filter nanoparticles. This behavior of nanoparticle suspensions can also be observed in organic nanoparticles, such as liposomes or lipid nanoparticles, and is exploited by the cosmetic industry as a differential aspect in nano-based cosmetic products.

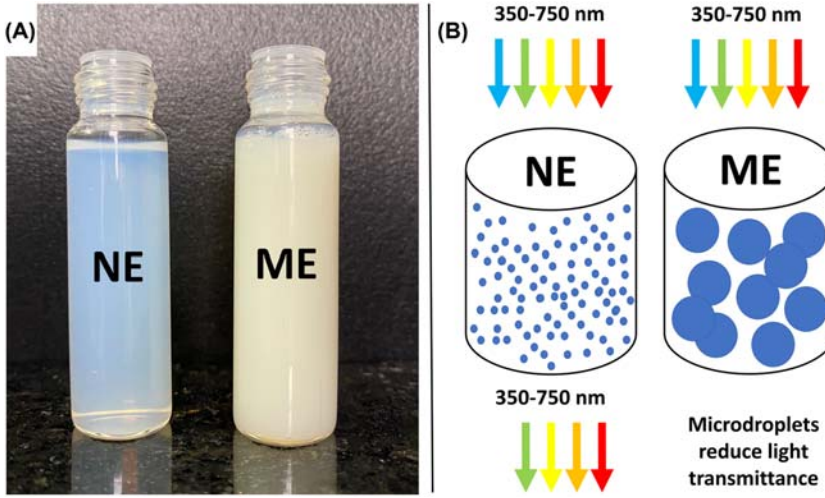

Figure 10.2 (A) The macroscopic aspect of an NE and convention emulsion with microdroplets (ME). (B) The NE and ME interaction with light in different wavelengths. *ME*, microemulsion; *NE*, nanoemulsion.

10.4 Organic nanoparticles used in cosmetics

As commented previously, the first nanoparticle used in the cosmetic industry was the liposome, included in cosmetic products in the 1980s [5]. For these organic structures (Fig. 10.3), there are a high number of nanostructured particles that have been used in cosmetics. The most common, as will be discussed here, are the lipid and polymeric nanoparticles. Each of these nanosystems is used because they solve a specific problem or chemical challenge. In other words, they are applied at different stages of the cosmetic product journey (Fig. 10.1). Briefly, we will introduce the different organic nanoparticles, and then we will discuss the most important problems that these nanotechnologies solve for the cosmetic sector.

10.4.1 Lipid nanoparticles

Lipid nanoparticles can also be segmented in different nanostructured systems. The first two are liposomes and the micellar suspension. After these two, literature and industry start to incorporate different types of NE, which can be produced with oils, usually named NEs, and systems prepared with solid lipids, such as natural kinds of butter and waxes. The latter type is usually defined as SLNs.

10.4.1.1 Liposomes

Liposomes are nanosized vesicles formed by a phospholipid bilayer. Due to this structure, this nanoparticle can carry both hydrophilic and hydrophobic compounds.

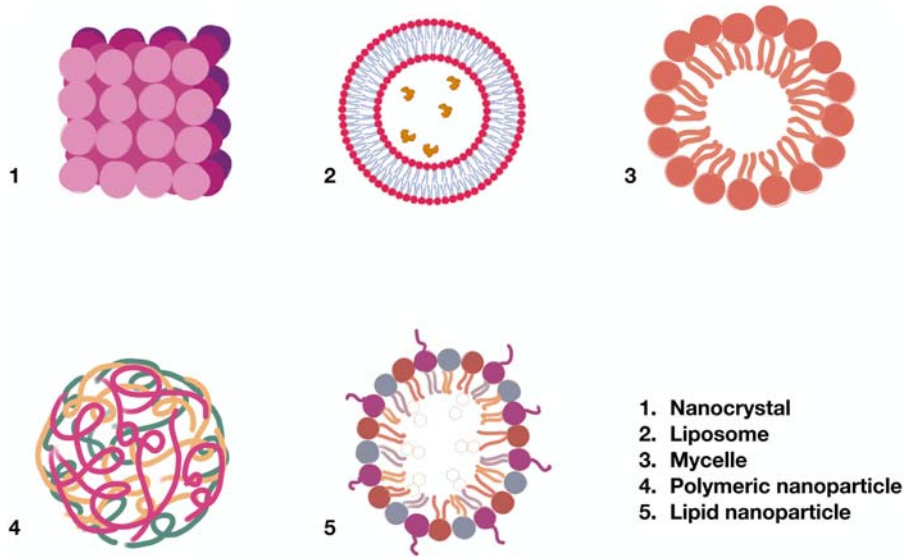

Figure 10.3 Different types of nanoparticles used in cosmetic applications.

The hydrophilic molecules are placed in the central aqueous compartment, and the hydrophobic molecules are carried in the phospholipid bilayer, among the fatty acid chains [11]. These characteristics make liposomes versatile nanocarriers, and they have been extensively used in the cosmetic industry.

Liposome preparation uses the method of phospholipid film hydration, followed by sonication, and size selection in size-specific filters. Briefly, the phospholipids are dissolved in an organic solvent and dried to form a lipid film. Due to their amphiphilic pattern, generated by the presence of fatty acid chains and phosphate groups, these phospholipids spontaneously form liposomal vesicles when hydrated with aqueous solutions. Multilamellar vesicles and micellar vesicles can be formed in this first step in a liposome preparation. Vesicles of different sizes are also formed in this first step.

To harmonize the vesicles populations formed, the sonication process can normally be used. With these procedures, liposome suspensions become more homogeneous in terms of structural organization. The last step consists of passing the liposome suspension through an extrusion membrane with nanosized pores. This last procedure aims to prepare liposome suspension with narrower size distribution, and it also contributes to sterilizing the samples.

For the encapsulation of the active ingredient, if the compound is lipophilic, it can be solubilized in the organic solvent phospholipid solution that will be dried before hydration. If the active compound is hydrophilic, the molecule can be solubilized in the aqueous solution used to hydrate the lipid film. For both situations, future studies are necessary to establish the encapsulation efficacy of the active molecule used.

10.4.1.2 Nanoemulsions and solid lipid nanoparticles

Emulsions are defined as two immiscible materials stabilized in a colloidal suspension. In terms of definitions, polymeric nanoparticles could also be included in this concept; however, the emulsion terminology is traditionally used for lipid suspensions. There are two types of lipid emulsion, oil in water, and water in oil emulsion. In this chapter, we will discuss deeply the oil in water emulsion, due to the wide use of this type in nanocosmetics. For oil in water NEs, there are two major components in a lipid emulsion, the oily dispersed phase, and the aqueous continuous phase. The stabilization of these two immiscible phases is supported by the presence of amphiphilic surfactants that are placed between the dispersed and the continuous phases.

The NE definition is used when we observed the continuous phase with lipid nanodroplets organized in the nanoscale. Both NEs and SLNs could be included in this definition. However, traditionally, the literature uses the NE definition for emulsions prepared with liquid or oily lipids [12]. The SLN terminology is used when the lipid nanodroplets are composed of solid or semisolid lipids, such as natural butter or waxes [13]. In terms of structure, both NEs and SLNs are composed of a lipid core dispersed in a continuous aqueous phase. Due to this structure, these systems are used to encapsulate different types of lipophilic ingredients. The differential behavior of the two systems will be related to the capacity to release the carried ingredients, which will be discussed later.

These two nanosystems are prepared with emulsification methods, and the main difference can be in the amount of energy applied in each protocol. For the NE preparation, there are also methods that can be performed with low-energy procedures. On the other hand, for SLN preparation, due to the solid pattern of the initial ingredients, the methods usually use higher temperatures (70°C−80°C). In both situations the principle of the method is to mix the oil phase (lipids and surfactants) and add the aqueous phase. The formation of nanodroplets is usually achieved with stirring procedures that can also include cooling steps to increase the contact between the surfactants and the lipid molecules [14].

As in other similar systems, the decision to use one or other usually depends on different aspects. First, the lipid ingredient source is considered, if it is solid or liquid, but there is also the capacity to encapsulate active ingredients. For this latter aspect, the nano space created by solid lipids is a slightly different from the liquid one. The presence of a semirigid crystal liquid structure forms more stable and rigid nanodroplets [15]. This pattern affects the structure's stability and its capacity for active ingredient-controlled release, which will be discussed in the next topics of this chapter.

10.4.2 Polymeric nanoparticles

Polymeric nanoparticles are a subtype of colloidal suspension also used for dermocosmetic applications [16]. There are two main types, and the difference is in the core composition, which can be an aqueous or oily compartment surrounded by

a shell layer formed by polymeric constituents. One feature of this kind of nanocarrier is the ability to encapsulate both hydrophilic and hydrophobic active ingredients, when the core composition is aqueous or oily, respectively. In terms of use, they have similar indications, in comparison to lipid nanoparticles; however, the polymer's surface is useful for chemical modifications. This procedure can produce new, innovative surface alterations that can be used to deliver or target some specific tissues.

Furthermore, due to the solid characteristics of the capsules, this system can be used to chemically protect the carried components and to produce different patterns of controlled release [17,18]. The most common polymers used for nanoparticle preparation are poly(lactic acid) and poly(lactic-co-glycolic); however, there are some other examples of polymers, such as methylcellulose, or new ingredients from biodiversity that have been proposed for polymeric nanoparticle preparation.

In terms of nanoparticle preparation, the most common method used in the literature is the nanoprecipitation technique. In these protocols the aqueous-insoluble components (polymer and active ingredient) are dissolved in a polar organic solvent. To form the nanoparticle an aqueous solvent (water or saline buffer) is injected into the system. This last procedure promotes the precipitation of the insoluble polymer, thus forming nanosized dispersed polymeric droplets. With this step the insoluble active ingredient is also associated, eventually encapsulated in the nanoparticles just formed [16].

10.5 Nanocarriers used to improve the cosmetic ingredient

The application of organic nanoparticles described previously can be done at different stages in the cosmetic ingredient journey (Fig. 10.1). There are some applications used to reduce industrial production time, to produce more stable formulations, to chemically protect the active ingredient carried, to increase the effectiveness on the skin or on the hair fiber, and potentially to reduce the toxicity of some ingredients carried. For each of these applications the cosmetic ingredient can benefit from the application of nanotechnologies. And these benefits can impact the cosmetic product from its conception, through its production, to its application by end users.

10.5.1 Dispersion of insoluble actives—reducing industrial production time

One important nanotech application for the cosmetic industry is the dispersion of aqueous-insoluble ingredients. For industry, the use of this kind of insoluble materials is usually time-consuming and can be critical for their use. For example, salicylic acid, a common keratolytic agent, has a low aqueous solubility (0.2 g per 100 mL at 20°C) and is soluble in ethanol; however, the oil solubility can vary depending upon the oil source [19,20]. As an example, 1 g of salicylic acid has 2%

solubility in olive oil and 22% in castor oil [21]. This variation in solubility may pose some difficult challenges during the industrial preparation that includes this type of aqueous-soluble active ingredient.

Nanotechnology can provide some interesting solutions that improve the dispersion of these types of compounds, thus reducing the time for industrial batch production. As an example, there is an interesting method called self-nano emulsification, which has been widely used for this purpose [22]. This strategy was first used for an oral administration of insoluble molecules [23,24] and recently was also applied for cosmetic industrial purposes.

The process involves the development of an oily mixture composed of oils, surfactants, and cosurfactants, and the active ingredient that can spontaneously form stable NEs when mixed with an aqueous solution. The principle is similar to NE preparation; however, in this case, it requires very low energy and uses the hydrophobic chemical forces of the oily mixture to spontaneously form the lipid nanocarriers containing the active insoluble compound [24]. Coming back to salicylic acid, it is possible to prepare this kind of nanotech inputs with higher ingredient concentrations, typically 20%−30% (unpublished data, provided by Nanoceuticals; http://www.nanoceuticals.net).

Thus in conclusion, this incremental innovation can be applied in order to reduce the production time of insoluble active ingredients. It is interesting that this technique can also be used for new ingredients, such as those obtained from biodiversity, or eventually to bring back old ones that are not being used any more due to insolubility issues [25]. Moreover, this application can also be applied to increase formulation stability, due to the encapsulation of insoluble molecules.

10.5.2 Chemical instability

Chemical instability is an important issue in cosmetology. The classical problem of ascorbic acid oxidation is a well-known example in this context. The reason for using nanocarriers to reduce chemical instability is to create nanoscopic spaces that could isolate the carried active molecule from the external environment. In this way the nanostructured components produce a kind of nanosized package or transitory shield, which can isolate the materials carried, thus protecting them from external potential aggressors. As we will explain later, molecular movements from inside to outside the nanostructure carrier are possible, but, with this chemical protection strategy, it would be possible to inhibit the movements of some species to chemically protect the compounds carried. Thus controlling the access of oxidative components to the inner parts of the nanostructures is a suitable strategy for preventing the chemical oxidation of the active ingredient [26−28].

For this application the physical−chemical nature of the active ingredient will define the type of nanoparticle used. For instance, as an aqueous-soluble molecule, ascorbic acid has been widely used in association with liposomes, due to the aqueous core environment. In this situation the ascorbic acid molecule is encapsulated in the liposome's aqueous core. The interesting point is that for the liposome system, the phospholipid bilayer is a useful barrier for polar oxygen species that are

the main chemical aggressors for carried active molecules, such as the ascorbic acid structure in this example (Fig. 10.4).

The importance of chemical protection provided by liposome vesicles was demonstrated during the development of the COVID-19 mRNA vaccines [29]. These new-generation vaccines are based on the internalization of the mRNA molecule and the transcription of an active antigen, which should be expressed in the external cellular membrane. The main problem of these new technologies was that RNA is extremely unstable. It has a short lifetime and is easily degraded by enzymes or cellular chemical conditions. To address this drawback the researchers encapsulated the mRNA sequences in nanosized liposomes to protect the oligonucleotides, thus allowing immunization [30]. The liposomes used have the same technology that the cosmetic industry uses for chemical protection in cosmetic products.

This chemical protection ability was presented as an example for ascorbic acid; however, it has also been used for several other cosmetic active ingredients, including the stabilization of biomolecules [31]. As an important trend, the use of small peptide sequences and new molecules from biodiversity in the use of nanoparticles as chemical stabilizers will be of great importance for industry and research in cosmetology [32]. In a prospective analysis the biggest beneficiaries of this process will be the molecules extracted from biodiversity, because as they are isolated from their natural environments, chemical instabilities may be also detected. And, as

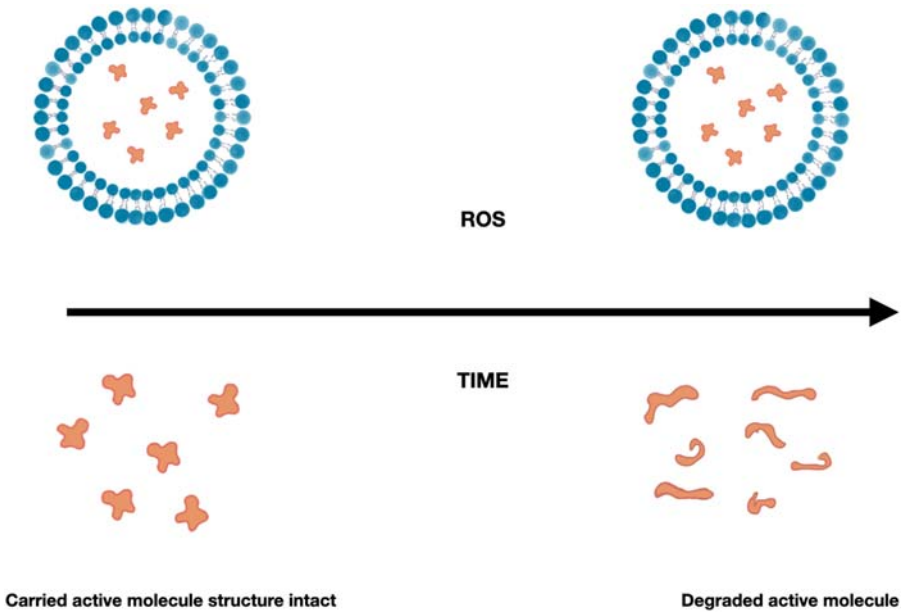

Figure 10.4 Schematic representation of the chemical protection provided by the nanocarriers. The main idea is to create a kind of nanosized package or transitory shield, which can isolate the materials carried, thus protecting them from external potential aggressors.

biodiversity research grows significant over time, it will be an important issue accessed by nanotechnology.

10.5.3 Controlled release

One of the most interesting features of nanoparticles for cosmetics is the possibility to control and sustain the release of encapsulated active ingredients (Fig. 10.5A). This property has been widely used for fragrance [33] and is usually known as the "long-lasting" property. In other words, it is possible to keep releasing fragrance for long periods, throughout the day, or occasionally days [34].

The concept is that the nano spaces created inside nanoparticles can facilitate or hinder the release of active molecules. This characteristic depends upon the materials that compose the nanocarriers and their physical stability. The interesting point is that it is possible to prepare nanoparticles with different behaviors, in terms of control release [35]. The first strategies described in the literature used passive methods for control release, but today some scientific initiatives propose the use of external signals to trigger the release of these active molecules from nanoparticles [36,37].

As an example, Fig. 10.5 presents the pattern of controlled release of a hydrophobic dye (rhodamine) from two different nanocarriers, an NE (Fig. 10.5B) and an SLN (Fig. 10.5C). The dye was used as a model to understand the release pattern of these two nanocarriers. These results confirm that it is possible to control active release by using different nanotechnologies approaches. Furthermore, as discussed previously, the main difference between these two nanoparticles is the physical state of the lipid phase of the core of the particles. The NE is composed mainly of

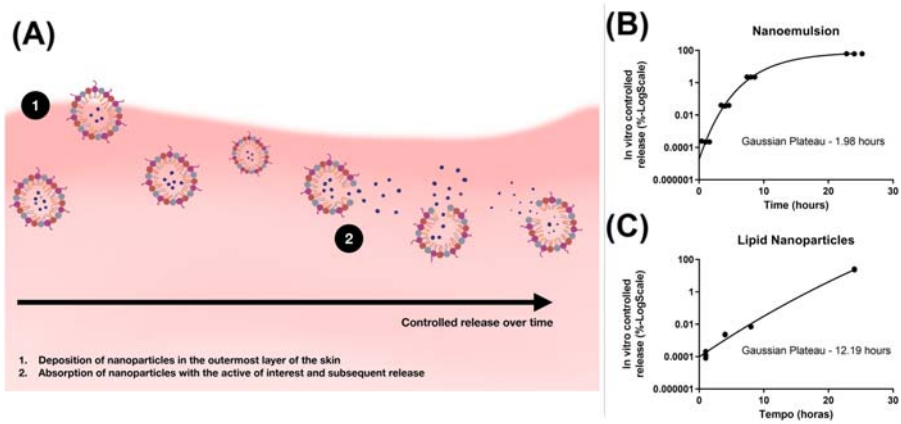

Figure 10.5 Controlled release of carried active molecules. (A) Schematic representation of the controlled release of active ingredients over the skin. (B) and (C) The in vitro controlled release of a fluorescent dye in two different lipid nanocarriers, nanoemulsions (B), and solid lipid nanoparticles (C).

liquid lipids, and the SLN is composed of solid lipid sources, such as butter and waxes [38].

In the graph the dye release profile is shown over time. In the Gaussian curve distribution the release plateau is reached in 1.8 h for the NE and in 12.19 h for the SLN. This experiment shows that different nanosystems can perform differently in terms of active ingredient release over time (unpublished data provided by Nanoceuticals; http://www.nanoceuticals.net). For topical dermal applications, SLN could be used for longer releases, while NE can be indicated as a carrier to produce faster releases. Understanding this kind of nanotechnology allows researchers and innovators to design better products. They can use these differential capabilities to produce products that can, eventually, keep the active ingredient in contact with the skin/hair for longer or shorter periods, depending on the purpose of the product.

In terms of technical explanations the more crystallized the lipid phase, the more stable will be the core of the nanoparticles [39]. In the graph the SLN has a more crystalline lipid core. In this case the lipid core may slow down the diffusion movement of the active ingredient carried from the lipid nanoparticle core to the external continuous compartment. As mentioned before, the active movement is governed by a diffusion process; thus the concentrations inside and outside the particles are important, as well as the presence of skin compartments that can push the diffusion forces in one direction. As an example, lipophilic carried molecules are strongly attracted by the keratinocyte membrane compartments, due to the lipophilic environment present in these cellular structures.

10.5.4 Clinical benefits in nanocosmetics—effectiveness

During the use of an active ingredient, nanotechnology can improve different characteristics that have been discussed in the previous sections. Among them, the increase in the effectiveness of active ingredients is undoubtedly one of the attributes that draw the most attention to nanotechnology applied to cosmetics. These benefits are partially explained by better chemical stability, controlled release of the active ingredient on the skin, and more stable and homogeneous products. Furthermore, some benefits related to the effectiveness of the cosmetic products will be achieved during the contact between the cosmetic nanocarrier and the biological structure, which could be skin or hair fiber.

The first explanation for that is the exponential increase in the material surface area observed when nanostructured cosmetics and conventional cosmetics are compared (Fig. 10.6A). Cosmetics are made of lipid emulsions, and the nanodroplets formed in nanocosmetics have a larger surface area in comparison to conventional emulsions. This feature promotes two main properties. The first one is related to the contact between the active carried and the skin/hair surface, which is much more intense for the nanocarriers (Fig. 10.6B). In this situation, the nanoparticles can put the active molecules in close contact with the biological structures, and the control release property can keep them in contact for longer periods.

The second immediate effect is that the nanoparticles can form a thin film over the skin/hair surface, creating an occlusion zone (Fig. 10.6B), that protects the

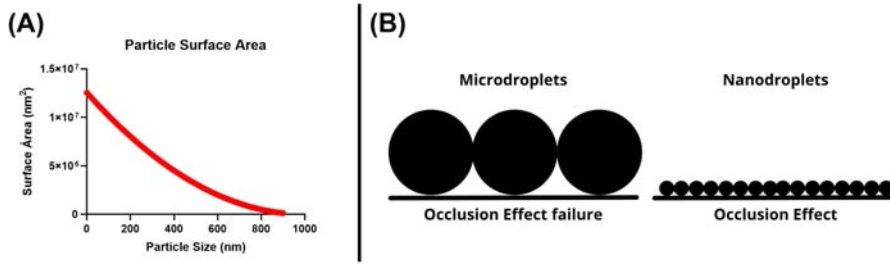

Figure 10.6 (A) We observe the exponential increase in nanoparticles surface area observed when nanostructured are produced with the same amount of material. (B) We observe the occlusion effect produced due to the increased surface area in the nanoparticle's products.

surface against dehydration. This is one of the most important effects of nanotechnology in cosmetology. Since the skin is our largest organ, and the main organ responsible for controlling fluid loss, the presence of this thin film formed by the nanoparticles can prevent water loss, acting as a more effective skin/hair moisturizer (Fig. 10.6B).

Another important and deeply discussed feature of nanotechnology for cosmetology is skin permeation. In the literature, there is no definitive consensus regarding this property. In this chapter, we will discuss the process and present the arguments that can explain, or not, this nanoparticle behavior. First, we must go back to the biological structure of the skin that is composed of connective tissue, mainly formed by fibroblasts and abundant vascular extracellular matrix, named the dermis; and an external layer, mainly composed of keratinocytes with almost no extracellular matrix, named the epidermis.

The epidermis is the first point of contact between the skin and the applied nanoparticles. This layer is composed of several cell layers, with an average thickness of 10−20 μm. The more external cell layers are composed of dead cells that are continuously produced by the basal epidermis cells, placed in the inner part of the epidermis. In terms of chronology the basal cells duplicate by mitosis and the new cells are pushed out through the external epidermis layers. As an avascular tissue, the epidermal cells do not have enough access to nutrients and die during this journey. Thus, as commented earlier, the external cells are dead cells, composed of remains of cytoplasm surrounded by hydrophobic phospholipid membranes [40].

In this biological structure, most of the epidermis compartments are hydrophobic environments, due to the membrane phospholipid bilayers, with a thin extracellular hydrophilic space among the keratinocytes. Thus the epidermis is more suitable to be permeable to hydrophobic components, and the hydrophilic structures will be impaired by these apolar obstacles. For nanoparticle permeation, we can use the same understanding. If the nanoparticle is composed mainly of hydrophobic components, such as lipids, they tend to fuse and be absorbed by the epidermis, and skin permeation can be faster. One important question raised in the literature is if the active compound carried is absorbed alone or encapsulated inside the nanocarriers.

This point is difficult to answer, because it is not easy to image or quantify the nanocarrier and the carried compound in the same space at the same time. This is not correct to say that the nanoparticles can improve the permeation of the active molecules carried, but at least they can be used to keep them for longer periods in contact with the target skin surface, and then the permeation can be facilitated. For the hydrophilic compounds the skin permeation may not occur through the keratinocyte layer, but they can accumulate close to the hair follicles, which can retain nanocarriers for longer periods.

Furthermore, there are also some innovative strategies described in the literature to improve the effectiveness of nanotechnologies for cosmetics. For instance, there are external trigger systems and nanoparticle surface modifications that can improve the product performance. The external signal systems can use temperature, pH, or even light to trigger the release of active components carried by the nanoparticles [41]. In these systems, physical−chemical local alterations can start the process that culminates with the release of the active molecules.

For the nanoparticles' surface modification, the addition of cationic charges can increase the contact among the particles and the skin/hair surface, thus improving the effectiveness of the carried active ingredient [42]. Moreover, some innovations, such as the surface decoration with small sequences of peptides, which can target the particles to specific cells, have also been proposed and produced by different companies. For this strategy the peptide sequences can relate to surface cell receptors that can keep the nanoparticles in close contact with the target skin/hair surface [43].

10.6 Conclusion

As presented in this chapter, nanotechnology can be applied to the development of cosmetic products. In terms of technological evolution the different nonsolutions can be used for cosmetic development from product conception, through industrial production, and reaching the consumers, providing several benefits for the end users. We believe that in the next few years, new innovative approaches, related to nanotechnologies, will bring more benefits and improvements to the cosmetology field.

References

[1] C. Toumey, Does scale matter at the nanoscale? Nat. Nanotechnol. 9 (1) (2014) 6−7.
[2] P. Mulvaney, Nanoscience vs Nanotechnology: Defining the Field. 9 (3) (2015) 2215−2217.
[3] J.P.F. Longo, et al., Issues affecting nanomedicines on the way from the bench to the market, J. Mater. Chem., B 8 (47) (2020) 10681−10685.
[4] K. Miyazaki, N. Islam, Nanotechnology systems of innovation—an analysis of industry and academia research activities, Technovation 27 (11) (2007) 661−675.

[5] T. Karamanidou, et al., A review of the EU's regulatory framework for the production of nano-enhanced cosmetics, Metals 11 (3) (2021) 455−470.
[6] Z.A.A. Aziz, et al., Role of nanotechnology for design and development of cosmeceutical: application in makeup and skin care, Front. Chem. 7 (2019) 739−744.
[7] C. Ferraris, et al., Nanosystems in cosmetic products: a brief overview of functional, market, regulatory and safety concerns, Pharmaceutics 13 (9) (2021) 1408−1438.
[8] S.L. Schneider, H.W. Lim, A review of inorganic UV filters zinc oxide and titanium dioxide, Photodermatol. Photoimmunol. Photomed. 35 (6) (2019) 442−446.
[9] T.G. Smijs, S. Pavel, Titanium dioxide and zinc oxide nanoparticles in sunscreens: focus on their safety and effectiveness, Nanotechnol. Sci. Appl. 4 (2011) 95−112.
[10] A.V. Zvyagin, et al., Imaging of zinc oxide nanoparticle penetration in human skin in vitro and in vivo, J. Biomed. Opt. 13 (6) (2008) 64031.
[11] L.A. Muehlmann, et al., Liposomal photosensitizers: potential platforms for anticancer photodynamic therapy, Braz. J. Med. Biol. Res. 44 (8) (2011) 729−737.
[12] Y. Singh, et al., Nanoemulsion: concepts, development and applications in drug delivery, J. Control. Release 252 (2017) 28−49.
[13] A. Dingler, et al., Solid lipid nanoparticles (SLNTM/LipopearlsTM) a pharmaceutical and cosmetic carrier for the application of vitamin E in dermal products, J. Microencapsul. 16 (6) (1999) 751−767.
[14] R.H. Müller, M. Radtke, S.A. Wissing, Solid lipid nanoparticles (SLN) and nanostructured lipid carriers (NLC) in cosmetic and dermatological preparations, Adv. Drug Delivery Rev. 54 (2002) S131−S155.
[15] S. Gao, D.J. McClements, Formation and stability of solid lipid nanoparticles fabricated using phase inversion temperature method, Colloids Surf., A: Physicochem. Eng. Aspects 499 (2016) 79−87.
[16] Y. Liu, et al., Formulation of nanoparticles using mixing-induced nanoprecipitation for drug delivery, Ind. Eng. Chem. Res. 59 (9) (2019) 4134−4149.
[17] X. Wu, R.H. Guy, Applications of nanoparticles in topical drug delivery and in cosmetics, J. Drug Delivery Sci. Technol. 19 (6) (2009) 371−384.
[18] R. Ganassin, et al., Nanocapsules for the co-delivery of selol and doxorubicin to breast adenocarcinoma 4T1 cells in vitro, Artif. Cells Nanomed, Biotechnol. 46 (8) (2018) 2002−2012.
[19] T. Arif, Salicylic acid as a peeling agent: a comprehensive review, Clin. Cosmet. Invest. Dermatol. 8 (2015) 455−461.
[20] C. Huber, E. Christophers, "Keratolytic" effect of salicylic acid, Arch. Dermatol. Res. 257 (3) (1977) 293−297.
[21] E.A. STRAKOSCH, Studies on ointments: II. Ointments containing salicylic acid, Arch. Dermatol. Syphilol. 47 (1) (1943) 16−26.
[22] F.U. Rehman, et al., From nanoemulsions to self-nanoemulsions, with recent advances in self-nanoemulsifying drug delivery systems (SNEDDS), Expert Opin. Drug Delivery 14 (11) (2016) 1325−1340.
[23] S.V.R. Rao, K. Yajurvedi, J. Shao, Self-nanoemulsifying drug delivery system (SNEDDS) for oral delivery of protein drugs: III. In vivo oral absorption study, Int. J. Pharm. 362 (1) (2008) 16−19.
[24] L.I. de Lima, et al., Self-nanoemulsifying drug-delivery systems improve oral absorption and antischistosomal activity of epiisopiloturine, Nanomedicine 13 (7) (2018) 689−702.
[25] D.J. McClements, Advances in nanoparticle and microparticle delivery systems for increasing the dispersibility, stability, and bioactivity of phytochemicals, Biotechnol. Adv. 38 (2020) 107287−107299.

[26] M. Gallarate, et al., On the stability of ascorbic acid in emulsified systems for topical and cosmetic use, Int. J. Pharm. 188 (2) (1999) 233−241.
[27] S. Gopi, P. Balakrishnan, Evaluation and clinical comparison studies on liposomal and non-liposomal ascorbic acid (vitamin C) and their enhanced bioavailability, J. Liposome Res. 31 (4) (2021) 356−364.
[28] M.I. Ordoñez Lozada, et al., Physicochemical characterization and nano-emulsification of three species of pumpkin seed oils with focus on their physical stability, Food Chem. 343 (2021) 128512−128524.
[29] J.P. Figueiró Longo, L.A. Muehlmann, How has nanomedical innovation contributed to the COVID-19 vaccine development? Nanomedicine (Lond) 16 (14) (2021) 1179−1181.
[30] E.E. Walsh, et al., Safety and immunogenicity of two RNA-based Covid-19 vaccine candidates, N. Engl. J. Med. 383 (25) (2020) 2439−2450.
[31] D.S. Santos, et al., Oral delivery of fish oil in oil-in-water nanoemulsion: development, colloidal stability and modulatory effect on in vivo inflammatory induction in mice, Biomed. Pharmacother. 133 (2021) 110980−110995.
[32] G.C. Carvalho, et al., Lycopene: from tomato to its nutraceutical use and its association with nanotechnology, Trends Food Sci. Technol. 118 (A) (2021) 447−458.
[33] N. Vijaya, et al., Nanomaterials in fragrance products, Nanocosmetics, Elsevier, 2020, pp. 247−265.
[34] U.C. Palmiero, et al., Surfactant-free and rinsing-resistant biodegradable nanoparticles with high adsorption on natural fibers for the long-lasting release of fragrances, Colloids Surf., B: Biointerfaces 190 (2020) 110926−110934.
[35] J. Pardeike, A. Hommoss, R.H. Müller, Lipid nanoparticles (SLN, NLC) in cosmetic and pharmaceutical dermal products, Int. J. Pharm. 366 (1−2) (2009) 170−184.
[36] N. Tiwari, et al., Nanocarriers for skin applications: where do we stand? Angew. Chem. Int. Ed. 60 (2021) 2−28.
[37] A.L.D. Camara, et al., Acid-sensitive lipidated doxorubicin prodrug entrapped in nanoemulsion impairs lung tumor metastasis in a breast cancer model, Nanomedicine 12 (15) (2017) 1751−1765.
[38] S. Jain, et al., Recent advances in lipid-based vesicles and particulate carriers for topical and transdermal application, J. Pharm. Sci. 106 (2) (2017) 423−445.
[39] M.C.O. da Rocha, et al., Docetaxel-loaded solid lipid nanoparticles prevent tumor growth and lung metastasis of 4T1 murine mammary carcinoma cells, J. Nanobiotechnol. 18 (1) (2020) 1−20.
[40] S. Lippens, et al., Cell death in the skin, Apoptosis 14 (4) (2009) 549−569.
[41] V. Marturano, et al., Light-responsive polymer micro-and nano-capsules, Polymers 9 (1) (2017) 8−27.
[42] V.K. Rai, et al., Nanoemulsion as pharmaceutical carrier for dermal and transdermal drug delivery: formulation development, stability issues, basic considerations and applications, J. Control. Release 270 (2018) 203−225.
[43] M.S. Mirtaleb, et al., Advances in biological nano-phospholipid vesicles for transdermal delivery: a review on applications, J. Drug Delivery Sci. Technol. 61 (2021) 102331−102342.

Index

Note: Page numbers followed by "*f*" and "*t*" refer to figures and tables, respectively.

Quantum Materials, Devices, and Applications

Edited by Mohamed Henini and Marcelo Oliveira Rodrigues

One-stop reference on the most relevant current and emerging quantum materials structures and device designs, organized by application in the areas of electronics, photonics, sensing, and more.

Quantum Materials, Devices, and Applications covers the advances made in quantum technologies both in research and mass production for applications in electronics, photonics, sensing, biomedical, environmental, and agricultural applications. It includes new materials, new device structures which are commercially available, and many more which are at the advanced research stage.

The study of what are now called low dimensional structures (LDS) began in the late 1970s when sufficiently thin epitaxial layers were first produced following developments in the technology of epitaxial growth of semiconductors, mainly pioneered in industrial laboratories for device purposes. The LDS are materials structures whose dimensions are comparable with interatomic distances in solids. At the inception of their investigation, it was already clear that such structures were of great scientific interest and excitement and their novel properties caused by quantum effects offered potential for applications in new devices. Moreover, these complex LDS offer device engineers new design opportunities for tailor-made new generation devices.

The book reviews the most relevant current and emerging materials and device structures, organized by key applications. It covers existing devices and technologies and future possibilities within a common framework of high-performance quantum devices, which have already an impact on our every-day life and those that will form the basis for longer-term technology development.

Quantum Materials, Devices, and Applications is suitable for researchers and practitioners in academia and industry and the materials science and engineering, electrical engineering, and physics disciplines.

Key features

- The success of quantum physics is well-known because of its wide range of applications, and the purpose of this book is to convey current ideas and important achievements in nanomaterials, quantum structures and devices which are responsible for the technological advances that make modern life possible, including those used in electronics, photonics, sensing, bio-medical and agricultural applications, rather than achieve a complete coverage of quantum technologies.
- This book will include the advances made in Quantum Materials and Devices for applications in Sensing, Agrochemicals, Environment, Bio-Medical, Health Care, Cancer Diagnosis and Therapy, and Cosmetics

About the Editors

Mohamed Henini: School of Physics and Astronomy, University of Nottingham, Nottingham NG7 2RD, UK.

Professor Mohamed Henini has authored and co-authored over 970 papers in international journals and conference proceedings. He has a H-index of 53 (ISI Web of Science). He edited/co-edited six books in the field of semiconductors and nanoscience which were published by Elsevier and serves on the Editorial Board of several scientific journals. He is one of the Editors of Journal of Alloys and Compounds (Elsevier). He is member of several National and International Professional Organisations including UNESCO-Africa Chair in Nanosciences & Nanotechnology, Nanosciences African-Network Initiative (NANOAFNET), and African Network for Solar Energy (ANSOLE).

He has a strong track record in organising conferences and workshops, and he is the founder of two international conferences namely, Low Dimensional Structures and Devices (LDSD) and Epitaxial Semiconductors on Patterned Substrates and Novel Index Surfaces (ESPS-NIS).

Marcelo Oliveira Rodrigues: Institute of Chemistry, University of Brasilia, Asa Norte, Brasilia 70910-900, Brazil.

Dr Marcelo Rodrigues is a young researcher who has authored and co-authored over 50 papers in international journals and 5 patents. He has an H-index of 24 (Scopus). His expertise lies in the new photoluminescent materials such as nanomaterials, metal-organic framework, ceramic, composites and their application as technological materials. In recent years, Dr Marcelo has devoted efforts to transforming basic science into innovations. He co-founded two start-ups (Krilltech NanoAgtech and Lazutech Nano Solutions) which develop applications of nanomaterials in agriculture aiming to improve crop productivity and pest control.

ISBN 978-0-12-820566-2

9 780128 205662

ELSEVIER elsevier.com/books-and-journals